Advances in
HEAT
TRANSFER

Serial Editors

James P. Hartnett
Energy Resources Center
University of Illinois at Chicago
Chicago, Illinois

Thomas F. Irvine, Jr.
Department of Mechanical Engineering
State University of New York at Stony Brook
Stony Brook, New York

Serial Associate Editor

Young I. Cho
Department of Mechanical
Engineering
Drexel University
Philadelphia, Pennsylvania

George A. Greene
Department of Advanced Technology
Brookhaven National Laboratory
Upton, New York

Volume 30

CONTRIBUTORS

Numbers in parentheses indicate the pages on which the authors' contributions begin.

A. ANSELMO (313), USAF Rome Laboratory, Hanscom Air Force Base, Massachusetts 01731.

VEDAT S. ARPACI (1), Department of Mechanical Engineering and Applied Mechanics, University of Michigan, Ann Arbor, Michigan 48109.

ARTHUR E. BERGLES (197), Department of Mechanical Engineering, Rensselaer Polytechnic Institute, Troy, New York 12180.

P. CHENG (93), Department of Mechanical Engineering, The Hong Kong University of Science and Technology, Clear Water Bay, Kowloon, Hong Kong.

K. D. KIHM (255), Department of Mechanical Engineering, Texas A & M University, College Station, Texas 77843.

V. PRASAD (313), Department of Mechanical Engineering, State University of New York, Stony Brook, New York 11794.

EUAN F. C. SOMERSCALES (197), Department of Mechanical Engineering, Rensselaer Polytechnic Institute, Troy, New York 12180.

C. Y. WANG (93), Department of Mechanical Engineering, Pennsylvania State University, University Park, Pennsylvania 16802.

H. ZHANG (313), Department of Mechanical Engineering, State University of New York, Stony Brook, New York 11794.

PREFACE

For over a third of a century, *Advances in Heat Transfer* has filled the information gap between the regularly published journals and university-level textbooks. The series presents review articles on special topics of current interest. Each contribution starts from widely understood principles and brings the reader up to the forefront on the topic being addressed. The favorable response by the international scientific and engineering community to the 30 volumes published to date is an indication of the success of our authors in fulfilling this purpose.

In recent years, the editors have undertaken to publish topical volumes dedicated to specific fields of endeavor. Several examples of such topical volumes are Bioengineering Heat Transfer (volume 22), Transport Phenomena in Materials Processing (volume 28), and Heat Transfer in Nuclear Reactor Safety (volume 29). The editors intend to continue the practice of publishing topical volumes, as well as the traditional general volumes, as a result of the enthusiastic response of the readers.

The editorial board expresses their appreciation to the contributing authors of Volume 30, who have maintained the high standards associated with *Advances in Heat Transfer*. Last, but not least, the editors acknowledge the efforts of the professional staff at Academic Press, who have been responsible for the attractive presentation of the published volumes over the years.

Microscales of Turbulent Heat and Mass Transfer

VEDAT S. ARPACI

Department of Mechanical Engineering and Applied Mechanics, University of Michigan
Ann Arbor, Michigan

I. Introduction

Although increased attention has been paid to turbulent flows for more than a century, to date, a general approach to their solutions has not been found and is not expected to be in the foreseeable future. One major stumbling block to progress is our failure to solve nonlinear partial differential equations, which are assumed to govern turbulent flows. Recently, because of rapidly increasing computational capabilities, increasing attention is being paid to solution of these equations by direct numerical or large eddy simulations. Despite extensive computational efforts, however, accurate quantitative predictions are still difficult to make without heavily relying on some ad hoc assumptions. In short, the analytical and computational tools available for turbulence, so far, are unable to provide the whole story. We also need intuitive use of dimensional arguments to complete the story between mathematics and actual flows. An inspection of experimental literature clearly shows that some aspects of turbulence depend only on a few transport properties (such as diffusivities and dissipation rates). In such situations dimensional methods readily lead to an answer, except for a numerical coefficient. Outstanding examples are equilibrium range of energy and entropy spectra, and heat and mass transfer correlations. Here, an illustrative example would clarify this fact further. First, note that *although analytical tools for linear problems are quite different from those for nonlinear problems, the same dimensional tools apply equally to both problems.* Accordingly, we use an old linear problem

(semi-infinite, stagnant, viscous fluid suddenly accelerated from boundary)
for our demonstration (Fig. 1(a)). Conversion of the governing equation

$$\frac{\partial u}{\partial t} = \nu \frac{\partial^2 u}{\partial y^2}$$

(by using Fourier transforms in space, Laplace transforms in time, or a
similarity variable) to an ordinary differential equation eventually leads to
the exact solution

$$\frac{u}{U} = \text{erfc}\left(\frac{y}{2\sqrt{\nu t}}\right),$$

which, for the friction coefficient, yields

$$f = \frac{2}{\sqrt{\pi}}\left(\frac{\nu}{tU^2}\right)^{1/2}. \tag{1}$$

Now suppose we do not have the analytical tools (which is the case for
turbulent flows) to solve the problem. For an approximate solution, con-
sider the governing equation integrated over boundary layer δ (Fig. 1(b))

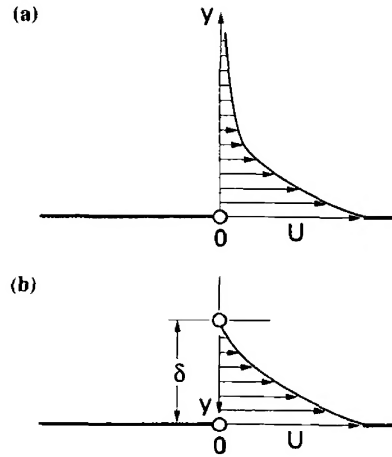$$\frac{d}{dt}\int_0^\delta u\,dy = \nu\left(\frac{\partial u}{\partial y}\right)_w$$

FIG. 1. (a) A semi-infinite stagnant viscous fluid suddenly accelerated from the boundary.
(b) U, velocity; δ, boundary layer.

coupled with

$$\frac{u}{U} = \left(\frac{y}{\delta}\right)^2,$$

which for the boundary thickness, gives

$$\delta = (12\nu t)^{1/2} \tag{2}$$

and for the friction coefficient,

$$f = \frac{2}{\sqrt{3}}\left(\frac{\nu}{tU^2}\right)^{1/2}. \tag{3}$$

Suppose further that we do not have the tools to construct an approximate velocity profile (which is the case for turbulent flows). On dimensional grounds, however, from the governing equation we have

$$\frac{U}{t} \sim \nu\frac{U}{\delta^2},$$

or the boundary layer thickness

$$\delta \sim (\nu t)^{1/2} \tag{4}$$

and the friction coefficient

$$f = \frac{2}{C}\left(\frac{\nu}{tU^2}\right)^{1/2}. \tag{5}$$

Thus we are able to obtain the friction coefficient by dimensional arguments alone, except for a numerical coefficient C.

Clearly the friction coefficient obtained by three different methods has a *universal* part

$$\left(\frac{\nu}{tU^2}\right)^{1/2}$$

that is independent of the method used, and a *structural* (numerical) part C that depends on the method used. Differential formulation leading to the exact solution yields the exact value of $C = \sqrt{\pi}$. An integral formulation coupled with an assumed velocity profile leads to $C = \sqrt{3}$, which is surprisingly accurate in view of the crudeness of the assumed profile. Along with other methods, the *dimensional approach solves the universal part but does not address the numerical value of the constant.*

Our objectives are to review the recent literature [2–9] on dimensional arguments leading to *microscales of complex* (buoyant, two-phase, thermocapillary, reacting, unsteady, etc.) *turbulent flows and to interpret the empirical heat and mass transfer correlations in terms of these scales.*

A. Origin of Microscales

Successively eliminating time and length between the fundamental units of two kinematic concepts, the dissipation rate of the mean kinetic energy per unit mass of turbulent fluctuations

$$[\varepsilon] \equiv L^2/T^3 \tag{6}$$

and the kinematic viscosity

$$[\nu] \equiv L^2/T, \tag{7}$$

Kolmogorov [55] originated a length scale and a time scale:

$$\eta = \left(\frac{\nu^3}{\varepsilon}\right)^{1/4}, \qquad \tau = \left(\frac{\nu}{\varepsilon}\right)^{1/2}, \tag{8}$$

respectively, and from their ratio, a velocity scale:

$$\upsilon = (\nu\varepsilon)^{1/4}. \tag{9}$$

These three scales now are called the microscales of isotropic turbulent flow. The intuitive idea leading to these scales was later extended by Oboukhov [72] and Corrsin [28] to a thermal scale for fluids with vanishing Prandtl number:

$$\eta_\theta^C = \left(\frac{\alpha^3}{\varepsilon}\right)^{1/4}, \qquad \mathrm{Pr} \to 0, \tag{10}$$

which results from the elimination of time between ε and the thermal diffusivity

$$[\alpha] \equiv L^2/T. \tag{11}$$

Kolmogorov's intuitive idea, however, no longer holds for the last of the length scales:

$$\eta_\theta^B = \left(\frac{\nu\alpha^2}{\varepsilon}\right)^{1/4}, \qquad \mathrm{Pr} \to \infty \tag{12}$$

proposed by Batchelor [17] for fluids with large Prandtl numbers, which requires a combination of three, rather than two, thermomechanical transport properties. Clearly a general methodology is needed not only for recovery of the foregoing scales but also for discovery of the microscales of more complex (buoyancy driven, two-phase, thermocapillary, reacting, pulsating, etc.) flows.

The objectives of this review are threefold: first, a general approach by which the microscales of complex flows are constructed; second, interpretation of heat and mass transfer (the latter including reacting flows) in

terms of these scales; third, correlations with the experimental literature. After this introductory part, the remainder of this chapter is divided into two parts. Part II, entitled Heat Transfer, contains three sections on Convection, Two-Phase Film, and Microgravity. Part III, entitled Mass Transfer, contains two sections on Diffusion Flame and Pulsed Combustion.

B. A Novel Approach

In the next two sections we take a general approach to the classic microscales, which is later used in the development of microscales for complex flows.

1. Kinetic Scales

Following the usual practice, let the instantaneous velocity be decomposed into a temporal mean and fluctuations,

$$U_i + u_i, \tag{13}$$

and let U_i be statistically steady.

The balance of the mean kinetic energy of velocity fluctuations is [86]

$$U_j \frac{\partial K}{\partial x_j} = -\frac{\partial \mathcal{D}_j}{\partial x_j} + \mathcal{P} - \varepsilon, \tag{14}$$

where

$$K = \tfrac{1}{2}\overline{u_i u_i} \tag{15}$$

is the mean kinetic energy;

$$\mathcal{D}_j = \frac{1}{\rho}\,\overline{pu_j} + \frac{1}{2}\,\overline{u_i u_i u_j} - 2\nu\overline{u_i s_{ij}} \tag{16}$$

is the mean transport (flux);

$$\mathcal{P} = -\overline{u_i u_j}\,S_{ij} \tag{17}$$

is the inertial production; and

$$\varepsilon = 2\nu\overline{s_{ij} s_{ij}} \tag{18}$$

is the dissipation of turbulent energy. Here s_{ij} denotes the rate of fluctuating strain and S_{ij} that of mean strain.

For a homogeneous pure shear flow (in which all averaged quantities except U_i are independent of position and S_{ij} is a constant), Eq. (14)

reduces to

$$\mathscr{P} = \varepsilon. \tag{19}$$

On dimensional grounds, Eq. (19) gives

$$\mathscr{P} \sim \frac{u^3}{l} \sim \nu \frac{u^2}{\lambda^2} \sim \varepsilon, \tag{20}$$

where l is an integral (or geometry) scale and λ is a dissipation (and diffusion) scale. The velocity from Eq. (20) in terms of the integral scale is

$$u \sim (\varepsilon l)^{1/3}. \tag{21}$$

In terms of the dissipation scale it is

$$u \sim \lambda \left(\frac{\varepsilon}{\nu} \right)^{1/2}. \tag{22}$$

Elimination of the velocity between Eqs. (21) and (22) yields the dissipation scale in terms of the integral scale:

$$\lambda \sim l^{1/3} \left(\frac{\nu^3}{\varepsilon} \right)^{1/6}. \tag{23}$$

This scale was originally proposed by Taylor [84], and hereafter is called the Taylor (micro)scale. Now consider a thin layer of turbulent flow (a sublayer next to a wall, or a vortex tube or sheet) in which the Taylor scale and the integral scale are replaced with an asymptotic limit. Let this limit be η:

$$\left(\frac{\lambda}{l} \right) \to \eta. \tag{24}$$

Then Eq. (23) leads to the length scale:

$$\eta \sim \left(\frac{\nu^3}{\varepsilon} \right)^{1/4}. \tag{25}$$

In terms of this scale, Eq. (21) or (22) gives the velocity scale:

$$\upsilon \sim (\nu \varepsilon)^{1/4}, \tag{26}$$

and the ratio of Eqs. (25) and (26) yields the time scale:

$$\tau \sim \frac{\eta}{\upsilon} \sim \left(\frac{\nu}{\varepsilon} \right)^{1/2}. \tag{27}$$

These smallest (or isotropic flow) scales of turbulence are called the Kolmogorov microscales. From Eqs. (22) and (27),

$$\frac{\eta}{v} \sim \frac{\lambda}{u}, \tag{28}$$

and from the ratio of Eqs. (23) and (25),

$$\left(\frac{\eta}{\lambda}\right)^2 \sim \frac{\lambda}{l}. \tag{29}$$

This is an important relation suggesting a model for the small-scale structure of turbulence discussed next.

One of the outstanding features of this structure is that viscous dissipation is not uniformly distributed in space. The intermittency or spottiness of dissipation must be taken into account. Tennekes [85] has developed a simple model (Fig. 2) consisting of dissipative vortex tubes of diameter η, which are stretched by eddies of size λ (see Corrsin [29] and Frisch [39] for other models). Accordingly, the local dissipation rate in vortex tubes is $\nu(u^2/\eta^2)$. The vortex tubes occupy the volume fraction $\eta^2\lambda/\lambda^3 = (\eta/\lambda)^2$, provided the length of the vortex tubes in a volume λ^3 is proportional to λ. The volume-averaged dissipation rate for this model then becomes

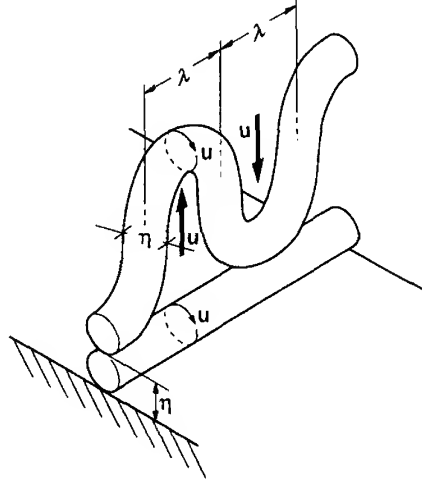$$\varepsilon \sim \nu\frac{u^2}{\eta^2}\left(\frac{\eta}{\lambda}\right)^2 = \nu\frac{u^2}{\lambda^2}. \tag{30}$$

Fig. 2. A simple model consisting of dissipative vortex tubes of diameter η that are stretched by eddies of size λ. Reprinted with permission of Tennekes [85].

In addition, the local and volume-averaged production rates in eddies of size λ are u^3/λ and

$$\mathscr{P} \sim \frac{u^3}{\lambda}\left(\frac{\lambda}{l}\right) = \frac{u^3}{l}, \tag{31}$$

respectively. An alternative form of Eq. (29) leads to

$$\frac{\eta}{l} \sim \left(\frac{\lambda}{l}\right)^{3/2}, \tag{32}$$

which shows the explicit $\eta - \lambda$ relation relative to l.

Now we may introduce a variety of Reynolds numbers based on the foregoing scales. By definition, the Reynolds number based on the Kolmogorov scale is

$$\mathrm{Re}_K \sim \frac{v\eta}{\nu} \sim 1, \tag{33}$$

which implies the slow and viscous nature of the small-scale motion. From Eq. (20),

$$\frac{\lambda}{l} \sim \frac{1}{\mathrm{Re}_\lambda} \sim \frac{1}{\mathrm{Re}_l^{1/2}}, \tag{34}$$

and in view of Eq. (29),

$$\frac{\eta}{\lambda} \sim \frac{1}{\mathrm{Re}_\lambda^{1/2}} \sim \frac{1}{\mathrm{Re}_l^{1/4}}. \tag{35}$$

From the product of Eqs. (34) and (35), we obtain

$$\frac{\eta}{l} \sim \frac{1}{\mathrm{Re}_\lambda^{3/2}} \sim \frac{1}{\mathrm{Re}_l^{3/4}}, \tag{36}$$

where

$$\mathrm{Re}_\lambda = \frac{u\lambda}{\nu}, \qquad \mathrm{Re}_l = \frac{ul}{\nu}. \tag{37}$$

In addition,

$$\mathrm{Re}_\eta = \frac{u\eta}{\nu} \sim \left(\frac{v\eta}{\nu}\right)\frac{u}{v}, \tag{38}$$

which may be rearranged in terms of Eqs. (28) and (33) as

$$\mathrm{Re}_\eta \sim \frac{\lambda}{\eta}. \tag{39}$$

Then in view of Eq. (35),

$$\text{Re}_\eta \sim \text{Re}_l^{1/2} \sim \text{Re}_l^{1/4}, \tag{40}$$

which shows the relation among the Reynolds numbers based on scales of differing lengths.

2. Thermal Scales

The development of thermal microscales is carried out in two parts, dealing with the scales appropriate for forced and natural convection, respectively.

a. Forced Flow Let the instantaneous temperature of turbulent forced convection be decomposed into a temporal mean and fluctuations,

$$\Theta + \theta, \tag{41}$$

and let Θ be statistically steady.

Neglecting buoyant production, the balance of the root mean square (rms) of thermal fluctuations

$$K_\theta = \tfrac{1}{2}\overline{\theta^2} \tag{42}$$

is [13, 86]

$$U_j \frac{\partial K_\theta}{\partial x_j} = -\frac{\partial}{\partial x_j}(\mathcal{D}_\theta)_j + \mathcal{P}_\theta - \varepsilon_\theta, \tag{43}$$

where

$$(\mathcal{D}_\theta)_j = \frac{1}{2}\,\overline{\theta^2 u_j} - \alpha\,\frac{\partial}{\partial x_j}\left(\frac{1}{2}\,\overline{\theta^2}\right) \tag{44}$$

is the mean thermal transport (or turbulent thermal flux);

$$\mathcal{P}_\theta = -\overline{u_j\theta}\,\frac{\partial \Theta}{\partial x_j} \tag{45}$$

is the thermal production; and

$$\varepsilon_\theta = \alpha\,\overline{\left(\frac{\partial \theta}{\partial x_j}\right)\left(\frac{\partial \theta}{\partial x_j}\right)} \tag{46}$$

is the thermal dissipation, with α denoting the thermal diffusivity.

For a homogeneous flow (in which all averaged quantities except U_j and Θ are independent of position and S_{ij} and $\partial\Theta/\partial x_j$ are constants), Eq. (43) becomes

$$\mathcal{P}_\theta = \varepsilon_\theta. \tag{47}$$

On dimensional grounds, Eq. (47) gives

$$\mathscr{P}_\theta \sim u_\theta \frac{\theta^2}{l_\theta} \sim \alpha \frac{\theta^2}{\lambda_\theta^2} \sim \varepsilon_\theta , \tag{48}$$

where λ_θ denotes a thermal counterpart of the Taylor scale. To proceed further, we need a velocity scale that depends on the Prandtl number. This dependence for fluids with $Pr \geq 1$ (air, water, viscous oils) is different from that for fluids with $Pr \ll 1$ (liquid metals).

First, we consider the **case of $Pr \geq 1$**.

From Eq. (48), we have

$$u_\theta \sim \alpha \frac{l}{\lambda_\theta^2} , \tag{49}$$

and from the similarity between velocity and temperature profiles, we have

$$\frac{u}{\lambda} = \frac{u_\theta}{\lambda_\theta} . \tag{50}$$

From Eq. (50), in terms of Eq. (49), we have

$$\frac{u_\theta}{\lambda_\theta} = \frac{u}{\lambda} = \alpha \frac{l}{\lambda_\theta^3} . \tag{51}$$

Elimination of u/λ between Eqs. (22) and (51) yields, after some rearrangement,

$$\lambda_\theta \sim l^{1/3} \left(\frac{\nu \alpha^2}{\varepsilon} \right)^{1/6} , \tag{52}$$

and the ratio between Eqs. (23) and (52) gives

$$\frac{\lambda}{\lambda_\theta} = Pr^{1/3}. \tag{53}$$

Note that assumed similarity makes Eq. (53) an equality. The isotropic limit of Eq. (52) for

$$\left(\frac{\lambda_\theta}{l} \right) \rightarrow \eta_\theta^B \tag{54}$$

leads to the *Batchelor scale*:

$$\eta_\theta^B \sim \left(\frac{\nu \alpha^2}{\varepsilon} \right)^{1/4} . \tag{55}$$

The ratio between Eqs. (25) and (55) gives

$$\frac{\eta}{\eta_\theta^B} = \mathrm{Pr}^{1/2}. \tag{56}$$

As a *second model* for the case of $\mathrm{Pr} \geq 1$, consider another limit of the homogeneous flow for

$$\lambda_\theta \to \eta_\theta, \qquad l \to \eta. \tag{57}$$

Equation (52) for this limit,

$$\eta_\theta \sim \eta^{1/3} \left(\frac{\nu\alpha^2}{\varepsilon} \right)^{1/6}, \tag{58}$$

rearranged in terms of η_θ^B, yields

$$\eta_\theta \sim \left[\eta \left(\eta_\theta^B \right)^2 \right]^{1/3}, \tag{59}$$

which is a *mesomicroscale* based on the weighted geometric average of η and η_θ^B. For any $\mathrm{Pr} \geq 1$,

$$\eta_\theta^B \leq \eta_\theta \leq \eta, \tag{60}$$

with equality holding for the case of $\mathrm{Pr} = 1$. The ratio between η and η_θ,

$$\boxed{\frac{\eta}{\eta_\theta} \sim \left(\frac{\eta}{\eta_\theta^B} \right)^{2/3} = \mathrm{Pr}^{1/3}}, \tag{61}$$

plays a vital role in the rest of this chapter, in which we interpret the well-known heat and mass transfer correlations by turbulent microscales.

Now the ratio between Eqs. (52) and (58),

$$\frac{\eta_\theta}{\lambda_\theta} \sim \left(\frac{\eta}{l} \right)^{1/3}, \tag{62}$$

in view of Eq. (32), gives

$$\left(\frac{\eta_\theta}{\lambda_\theta} \right)^2 \sim \frac{\lambda}{l}, \tag{63}$$

or in view of Eq. (53), gives

$$\left(\frac{\eta_\theta}{\lambda_\theta} \right)^2 \sim \left(\frac{\lambda_\theta}{l} \right) \mathrm{Pr}^{1/3}, \qquad \mathrm{Pr} \geq 1, \tag{64}$$

which helps us to construct a model for *thermal intermittency*. Following Tennekes' model for kinetic intermittency, we conjecture conductive tubes
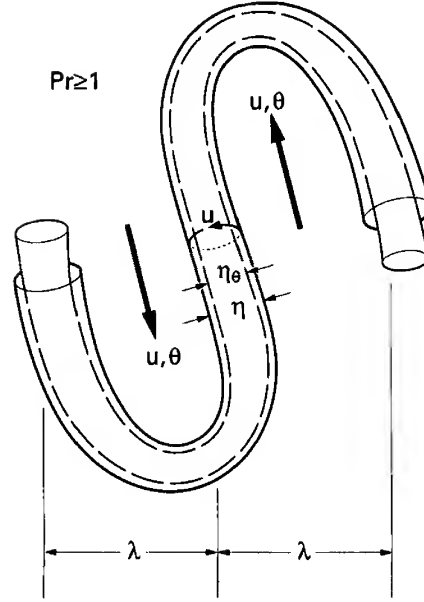
FIG. 3. Thermal intermittency (Pr ≥ 1). Tubes of diameter η_θ with vortex tubes of diameter η stretched by thermal eddies of size λ_θ within kinetic eddies of size λ. Pr, Prandtl; u, rms of velocity fluctuations.

of diameter η_θ within vortex tubes of diameter η stretched by thermal eddies of size λ_θ within kinetic eddies of size λ (Fig. 3).

Next, we consider the **case of Pr ≪ 1**.

Using Eq. (21) for the velocity of enthalpy flow, and eliminating u between Eqs. (21) and (49), we obtain

$$\lambda_\theta \sim l^{1/3}\left(\frac{\alpha^3}{\varepsilon}\right)^{1/6}, \tag{65}$$

and from its isotropic limit, we obtain

$$\left(\frac{\lambda_\theta}{l}\right) \to \eta_\theta^C, \tag{66}$$

which leads to the *Oboukhov-Corrsin* scale:

$$\eta_\theta^C \sim \left(\frac{\alpha^3}{\varepsilon}\right)^{1/4}. \tag{67}$$

Now, in a manner similar to the ratios among η, λ, and l, it readily can be shown that

$$\frac{\lambda_\theta}{l} \sim \frac{1}{\mathrm{Pe}_\lambda} \sim \frac{1}{\mathrm{Pe}_l^{1/2}}, \tag{68}$$

$$\frac{\eta_\theta^C}{l} \sim \frac{1}{\mathrm{Pe}_\eta^3} \sim \frac{1}{\mathrm{Pe}_l^{3/4}}, \tag{69}$$

$$\frac{\eta_\theta^C}{\lambda_\theta} \sim \frac{1}{\mathrm{Pe}_\eta} \sim \frac{1}{\mathrm{Pe}_\lambda^{1/2}} \sim \frac{1}{\mathrm{Pe}_l^{1/4}}, \tag{70}$$

or

$$\boxed{\mathrm{Pe}_\eta \sim \mathrm{Pe}_\lambda^{1/2} \sim \mathrm{Pe}_l^{1/4}}, \tag{71}$$

where $\mathrm{Pe} = \mathrm{Pr}\,\mathrm{Re}$ is the Peclet number and explicitly

$$\mathrm{Pe}_\eta = \frac{u\eta}{\alpha}, \qquad \mathrm{Pe}_\lambda = \frac{u\lambda}{\alpha}, \qquad \mathrm{Pe}_l = \frac{ul}{\alpha}.$$

In addition, the ratio between η and η_θ^C gives

$$\frac{\eta}{\eta_\theta^C} \sim \mathrm{Pr}^{3/4}, \tag{72}$$

and elimination of α^3/ε between Eqs. (65) and (67) yields

$$\left(\frac{\eta_\theta^C}{\lambda_\theta} \right)^2 \sim \frac{\lambda_\theta}{l}, \qquad \mathrm{Pr} \ll 1, \tag{73}$$

which may be used for another thermal intermittency model.

So far, we have systematically obtained the Kolmogorov, Batchelor, and Oboukhov-Corrsin scales. We also have discovered a mesomicroscale for flows with $\mathrm{Pr} \geq 1$. In the next section, following the same methodology, we introduce the scales for buoyancy-driven flows.

b. Buoyancy-Driven Flow As is well known, the independent dimensionless numbers characterizing natural convection are the Rayleigh and Prandtl numbers, respectively. A recent discovered dimensionless number by Arpacı [2, 3, 5–9] explicitly describes natural convection in any fluid by a combination of Ra and Pr. Following a review of this dimensionless number (say, Π_N), the thermal microscales of natural convection are developed in terms of Π_N.

Let the buoyancy-driven momentum balance be

$$F_B \sim F_I + F_V,$$ (74)

where F_B, F_I, and F_V denote, respectively, the buoyant, inertial, and viscous forces. In addition, let the thermal energy balance be

$$Q_H \sim Q_K,$$ (75)

where Q_H and Q_K denote the enthalpy flow and conduction, respectively. Then from Eq. (74),

$$\frac{F_B}{F_I + F_V} \sim \frac{F_B/F_V}{F_I/F_V + 1},$$ (76)

and from Eq. (75),

$$Q_H/Q_K,$$ (77)

with the numeral 1 in Eq. (76) implying order of magnitude. Although the force ratios of Eq. (76) and the energy ratio of Eq. (77) are dimensionless, they are given in terms of velocity, which is a dependent variable in buoyancy driven flows. For example,

$$\frac{F_B}{F_V} \sim \frac{g(\Delta\rho)l^2}{\mu V}, \quad \frac{F_I}{F_V} \sim \frac{\rho Vl}{\mu}, \quad \frac{Q_H}{Q_K} \sim \frac{\rho cVl}{k},$$ (78)

with l being a characteristic length and the other notation being conventional. Now combine Eqs. (76) and (77) for a result independent of velocity:

$$\frac{(F_B/F_V)(Q_H/Q_K)}{(F_I/F_V)(Q_K/Q_H) + 1} \sim \frac{\text{Ra}}{\text{Pr}^{-1} + 1},$$ (79)

or

$$\Pi_N \sim \frac{\text{Ra}}{1 + \text{Pr}^{-1}} = \frac{\text{Ra Pr}}{1 + \text{Pr}},$$ (80)

which is the appropriate dimensionless number for natural convection in any fluid. Two limits of Eq. (80) are

$$\lim_{\text{Pr} \to 0} \Pi_N \to \text{Pr Ra},$$ (81)

$$\lim_{\text{Pr} \to \infty} \Pi_N \to \text{Ra},$$ (82)

as expected. Although the existence of Π_N has never been shown directly, the integral solution for the laminar natural convection near a vertical plate given in 1938 by Squire [82] leads to an expression in terms of Π_N. Since then, the explicit role of Π_N in studies on natural convection usually has been ignored.

We proceed directly to the homogeneous flow (in which all averaged quantities except U_i and Θ are independent of position and S_{ij} and $\partial\Theta/\partial x_i$ are constants) and the mean kinetic energy of turbulent fluctuations,

$$\mathcal{B} = \mathcal{P} + \varepsilon, \tag{83}$$

where

$$\mathcal{B} = -g_i \overline{u_i \theta}/\Theta_0, \tag{84}$$

is the rate of buoyant energy production, with g_i being the vector acceleration of gravity and Θ_0 a characteristic temperature for isobaric ambient. The rate of thermal energy retains its earlier form:

$$\mathcal{P}_\theta = \varepsilon_\theta. \tag{47}$$

On dimensional grounds, Eq. (83) leads to

$$\mathcal{B} \sim \frac{u^3}{l} + \nu \frac{u^2}{\lambda^2}, \tag{85}$$

and in view of $u_\theta \sim u$ for buoyancy-driven flows, Eq. (48) becomes

$$u \frac{\theta^2}{l} \sim \alpha \frac{\theta^2}{\lambda_\theta^2}. \tag{86}$$

Furthermore, following Squire, let $\lambda \sim \lambda_\theta$. Then elimination of velocity between Eqs. (85) and (86) leads to a thermal Taylor scale:

$$\lambda_\theta \sim l^{1/3}\left(1 + \frac{1}{Pr}\right)^{1/6}\left(\frac{\nu\alpha^2}{\mathcal{B}}\right)^{1/6}, \qquad Pr \geq 1, \tag{87}$$

or

$$\lambda_\theta \sim l^{1/3}(1 + Pr)^{1/6}\left(\frac{\alpha^3}{\mathcal{B}}\right)^{1/6}, \qquad Pr \leq 1, \tag{88}$$

where Eq. (87) explicitly includes the limit for $Pr \to \infty$ and is useful for fluids with $Pr \geq 1$, and Eq. (88) explicitly includes the limit for $Pr \to 0$ and is useful for fluids with $Pr \ll 1$.

For the isotropic limit of the homogeneous flow, letting

$$\left(\frac{\lambda_\theta}{l}\right) \to \eta_\theta, \tag{89}$$

Eqs. (87) and (88) are reduced to a thermal Kolmogorov scale introduced by Arpaci [2, 3, 5–9]:

$$\eta_\theta \sim \left(1 + \frac{1}{Pr}\right)^{1/4}\left(\frac{\nu\alpha^2}{\mathcal{B}}\right)^{1/4}, \qquad Pr \geq 1, \tag{90}$$

or

$$\eta_\theta \sim (1 + \mathrm{Pr})^{1/4} \left(\frac{\alpha^3}{\mathscr{B}} \right)^{1/4}, \qquad \mathrm{Pr} \leq 1. \tag{91}$$

Now it is a simple matter to show from Eq. (90) that

$$\lim_{\mathrm{Pr} \to \infty} \eta_\theta \to \left(\frac{\nu\alpha^2}{\mathscr{B}} \right)^{1/4}, \tag{92}$$

which in view of

$$\lim_{\mathrm{Pr} \to \infty} \mathscr{P} \to 0 \tag{93}$$

and

$$\mathscr{B} \to \varepsilon, \tag{94}$$

leads to the Batchelor scale:

$$\lim_{\mathrm{Pr} \to \infty} \eta_\theta \to \eta_\theta{}^B \sim \left(\frac{\nu\alpha^2}{\varepsilon} \right)^{1/4}. \tag{95}$$

In addition, from Eq. (91),

$$\lim_{\mathrm{Pr} \to 0} \eta_\theta \to \left(\frac{\alpha^3}{\mathscr{B}} \right)^{1/4}, \tag{96}$$

which in view of

$$\lim_{\mathrm{Pr} \to 0} \varepsilon \to 0, \tag{97}$$

$$\mathscr{B} \to \mathscr{P}, \tag{98}$$

and in a viscous layer order of magnitude thinner than η_θ,

$$\mathscr{P} \to \varepsilon, \tag{99}$$

leads to the Oboukhov-Corrsin scale:

$$\lim_{\mathrm{Pr} \to \infty} \eta_\theta \to \eta_\theta{}^C \sim \left(\frac{\alpha^3}{\varepsilon} \right)^{1/4}. \tag{100}$$

Finally, for $\mathrm{Pr} \sim 1$, because of the equipartition (on dimensional grounds) of buoyant production into inertial production and viscous dissipation, Eq. (83) becomes

$$\mathscr{B} \sim 2\varepsilon, \tag{101}$$

and both Eqs. (90) and (91) lead to the Kolmogorov scale:

$$\lim_{\mathrm{Pr}\to 1} \eta_\theta \to \eta \sim \left(\frac{\nu^3}{\varepsilon}\right)^{1/4}. \tag{102}$$

The relation between the thermal scales and the integral scale may now be obtained by eliminating the factor $(1 + \mathrm{Pr}^{-1})(\nu\alpha^2/\mathscr{B})$ between Eqs. (87) and (90) or Eqs. (88) and (91). Thus

$$\left(\frac{\eta_\theta}{\lambda_\theta}\right)^2 = \frac{\lambda_\theta}{l}, \tag{103}$$

which leads to a model for *thermal intermittency*.

Note that in the foregoing Kolmogorov scales given by Eqs. (90) and (91), $\mathscr{B}$ depends on velocity, and these scales cannot be the ultimate forms of the Kolmogorov scales for buoyancy-driven flows. To eliminate velocity dependence, reconsider

$$\eta_\theta \sim \left(1 + \frac{1}{\mathrm{Pr}}\right)^{1/4}\left(\frac{\nu\alpha^2}{\mathscr{B}}\right)^{1/4}, \tag{90}$$

and assume, on dimensional grounds, that

$$\mathscr{B} \sim gu\theta/\Theta_0. \tag{104}$$

Noting that

$$\Theta_o^{-1} \sim \beta, \tag{105}$$

where β is the coefficient of thermal expansion, rearrange Eq. (104) as

$$\mathscr{B} \sim gu\beta\theta, \tag{106}$$

or with local velocity obtained from the limit of Eq. (49),

$$u \sim \alpha/\eta_\theta \tag{107}$$

as

$$\mathscr{B} \sim g\alpha\beta\theta/\eta_\theta. \tag{108}$$

Insertion of Eq. (108) into Eq. (90) yields, after some rearrangement,

$$\eta_\theta \sim \left(1 + \frac{1}{\mathrm{Pr}}\right)^{1/3}\left(\frac{\nu\alpha}{g\beta\theta}\right)^{1/3}. \tag{109}$$

Finally, assuming

$$\theta \sim \Delta T, \tag{110}$$

$$\eta_\theta \sim \left(1 + \frac{1}{\mathrm{Pr}}\right)^{1/3}\left(\frac{\nu\alpha}{g\beta\Delta T}\right)^{1/3}, \tag{111}$$

or in terms of an integral scale l,

$$\frac{\eta_\theta}{l} \sim \left(1 + \frac{1}{Pr}\right)^{1/3} Ra^{-1/3} \sim \Pi_N^{-1/3}, \tag{112}$$

where

$$Ra = \frac{g\beta\Delta Tl^3}{\nu\alpha}$$

is the Rayleigh number.

Similarly, the thermal Taylor scale can be expressed in terms of Π_N. Recall and rearranging Eq. (103), we have

$$\frac{\lambda_\theta}{l} \sim \left(\frac{\eta_\theta}{l}\right)^{2/3}, \tag{113}$$

which in terms of Eq. (112), gives

$$\frac{\lambda_\theta}{l} \sim \Pi_N^{-2/9}. \tag{114}$$

Thus we are able to express the Kolmogorov and Taylor thermal scales in terms of Π_N.

In some cases, buoyant flow is driven by internal energy generation rather than by a temperature difference. Assume that energy generated within volume Al, with A being horizontal area and l vertical height, is lost from A by conduction across a thickness layer η_θ. From the balance between generated and lost energies

$$u''' Al \sim kA\frac{\theta}{\eta_\theta}, \tag{115}$$

we have

$$\theta \sim \left(\frac{\eta_\theta l}{\alpha}\right)\Phi, \tag{116}$$

where $\Phi = u'''/\rho c_p$. Now buoyant production given by Eq. (108) becomes, in terms of Eq. (116),

$$\mathscr{B} \sim g\beta l\Phi, \tag{117}$$

and the thermal Kolmogorov scale given by Eq. (90) becomes, in terms of Eq. (117),

$$\eta_\theta \sim \left(1 + \frac{1}{Pr}\right)^{1/4}\left(\frac{\nu\alpha^2}{g\beta l\Phi}\right)^{1/4}. \tag{118}$$

Relative to vertical height l,

$$\frac{\eta_\theta}{l} \sim \left(1 + \frac{1}{Pr}\right)^{1/4} Ra_I^{-1/4}, \tag{119}$$

or

$$\frac{\eta_\theta}{l} \sim \Pi_I^{-1/4}, \tag{120}$$

where

$$\Pi_I \sim \frac{Ra_I}{1 + Pr^{-1}} = \frac{Ra_I Pr}{1 + Pr}, \tag{121}$$

$$Ra_I = \frac{g \beta \Phi l^5}{\nu \alpha^2}. \tag{122}$$

Also, in terms of Eq. (120), Eq. (113) gives

$$\frac{\lambda_\theta}{l} \sim \Pi_I^{-1/6}. \tag{123}$$

Note that we use subscript I to distinguish dimensionless numbers based on u''' from those based on ΔT.

II. Heat Transfer

A. Convection

Here we demonstrate microscale foundations of well-known heat transfer correlations. We also introduce models based on microscales and correlate additional experimental data. We begin with forced convection and end with natural convection.

1. *Forced Convection*

First, from fluid mechanics we recall that any velocity gradient makes a layer of inviscid flow unstable (Kelvin-Helmholtz instability). Under the influence of viscosity, the layer becomes stable within the dissipation layer (of thickness η) over a boundary. Then we extend the Tennekes model by assuming vortex tubes on boundaries to be stable and the ones above unstable.

Now we express the usual definitions of the coefficient of heat transfer and that of skin friction in terms of dissipation scales for friction (u, η) and

for heat transfer (θ, η_θ):

$$q_w \sim h\theta \sim k(\theta/\eta_\theta),\qquad(124)$$

$$\frac{1}{2}f \sim \frac{\tau_w}{\rho u^2} \sim \frac{\mu(u/\eta)}{\rho u^2} \sim \frac{\nu}{u\eta}.\qquad(125)$$

Then we rearrange Eqs. (124) and (125) as

$$h/k \sim \eta_\theta^{-1},\qquad(126)$$

$$u/\nu \sim \left(\tfrac{1}{2}f\right)^{-1}\eta^{-1},\qquad(127)$$

and establish their ratio

$$\frac{h/k}{u/\nu} \sim \frac{1}{2}f\left(\frac{\eta}{\eta_\theta}\right).\qquad(128)$$

Finally, nondimensionalizing the left-hand side of Eq. (128) by an integral scale, we obtain

$$\left(\frac{\mathrm{Nu}}{\mathrm{Re}}\right)_l \sim \frac{1}{2}f\left(\frac{\eta}{\eta_\theta}\right),\qquad(129)$$

where

$$\mathrm{Nu}_l = hl/k \quad \text{and} \quad \mathrm{Re}_l = ul/\nu$$

are the Nusselt and Reynolds numbers.

Next, we consider fluids with $\mathrm{Pr} \geq 1$ and $\mathrm{Pr} \ll 1$, respectively.

a. $\mathrm{Pr} \geq 1$ (Gases, Liquids, Viscous Oils) In this case, the analogy between momentum and heat makes the ratio between Eqs. (126) and (127) given by Eqs. (128) and (129) an equality. Then from Eq. (129), in terms of Eq. (61), we have

$$\left(\frac{\mathrm{Nu}}{\mathrm{Re}}\right)_l = \left(\frac{1}{2}f\right)\mathrm{Pr}^{1/3}.\qquad(130)$$

An alternative form of Eq. (130) expressed in terms of the Stanton number,

$$\mathrm{St} = \frac{\mathrm{Nu}}{\mathrm{Re}\,\mathrm{Pr}}\qquad(131)$$

is

$$\mathrm{St}\,\mathrm{Pr}^{2/3} = \tfrac{1}{2}f,\qquad \mathrm{Pr} \geq 1.\qquad(132)$$

Equation (132) is the well-known *Colburn correlation* relating heat transfer to skin friction. The foregoing development established this relation in terms of the microscales of turbulence, rather than the usual approach

which is the correlation of turbulent experimental data. Note that Eqs. (130) and (132), also may be obtained from (the similarity solution of the differential formulation or with approximate profiles satisfying the integral formulation of) laminar boundary layers. Consequently, they are *universal relations* valid for turbulent as well as laminar forced convection in fluids, with $\Pr \geq 1$. Only the explicitly stated friction coefficient distinguishes Eqs. (130) and (132) for turbulent flows from those for laminar flows.

The friction coefficient for turbulent flows is usually available from the correlation of experimental data. However, in tune with the philosophy of this monograph, a model based on the local dissipation scales is constructed here. Recall and rearrange Eq. (125) as

$$\tfrac{1}{2}f \sim \mathrm{Re}_\eta^{-1}, \tag{133}$$

where

$$\mathrm{Re}_\eta = u\eta/\nu. \tag{134}$$

Then in view of Eq. (40),

$$\tfrac{1}{2}f \sim \mathrm{Re}_l^{-1/4}. \tag{135}$$

Now the combination of Eqs. (130) and (135) yields

$$\mathrm{Nu}_l \sim \mathrm{Re}_l^{3/4}\,\Pr^{1/3}, \qquad \Pr \geq 1. \tag{136}$$

The experimental data confirms the validity of this relation for turbulent heat transfer over a flat plate and in a pipe, provided the Reynolds number remains moderate in the latter case.

A second model takes into account a core effect above the viscous sublayer. Now assume that

$$U \sim u + u_c, \tag{137}$$

where the subscript c denotes the core effect. For the sublayer, noting $u \sim \nu/\eta$, let

$$\tau \sim \mu\,\frac{u}{\eta} \sim \rho u^2, \tag{138}$$

which states the same order of magnitude contribution from both viscous and Reynolds stresses. For the core, neglecting the viscous effect, let

$$\tau_c \sim \rho u_c^2. \tag{139}$$

Then assuming

$$\tau \sim \tau_c \tag{140}$$

and using Eqs. (138) and (139), rearrange Eq. (137) as

$$\tau \sim \frac{\mu(U/\eta)}{(1 + (\nu/\eta u_c))}.\tag{141}$$

Next, consider Eq. (20) for u_c, noting that

$$\frac{u_c l}{\nu} \sim \left(\frac{l}{\lambda}\right)^2,\tag{142}$$

and rearrange $\nu/\eta u_c$ of Eq. (141) as

$$\frac{\nu}{\eta u_c} \sim \frac{\nu}{u_c l}\left(\frac{l}{\eta}\right) \sim \left(\frac{\lambda}{l}\right)^2 \frac{l}{\eta}.\tag{143}$$

Thus

$$\tau \sim \frac{\mu(U/\eta)}{1 + (\lambda/l)^2 l/\eta},\tag{144}$$

or, in terms of Eqs. (34) and (36),

$$\tau \sim \frac{\mu(U/\eta)}{1 + (1/\mathrm{Re}_l^{1/4})}.\tag{145}$$

Next, we repeat the steps between Eqs. (137) and (145) for thermal energy. First, replace Eq. (110) by

$$\Delta T \sim \theta + \theta_c,\tag{146}$$

where the subscript c denotes the core effect. For the thermal sublayer, noting $u_\theta \sim \alpha/\eta_\theta$, let

$$q \sim k\frac{\theta}{\eta_\theta} \sim \rho c_p u_\theta \theta,\tag{147}$$

which states the same order of magnitude for conduction and Reynolds flux. For the thermal core,

$$q_c \sim \rho c_p (u_\theta)_c \theta_c.\tag{148}$$

Then assuming

$$q \sim q_c\tag{149}$$

and using Eqs. (147) and (148), rearrange Eq. (146) as

$$q \sim \frac{k(\Delta T/\eta_\theta)}{1 + (\alpha/(u_\theta)_c \eta_\theta)}.\tag{150}$$

For the denominator, consider

$$\frac{(u_\theta)_c \eta_\theta}{\alpha} = \frac{u_c l}{\nu} \frac{\eta}{l} \frac{\eta_\theta}{\eta} \frac{(u_\theta)_c}{u_c} \frac{\nu}{\alpha},$$

or in terms of Eqs. (142), (34), (36), (61), (50) for core effect, and (53),

$$\frac{(u_\theta)_c \eta_\theta}{\alpha} \sim \text{Re}_l^{1/4} \text{Pr}^{1/3}. \tag{151}$$

Thus, in terms of Eq. (151), Eq. (150) becomes

$$q \sim \frac{k(\Delta T / \eta_\theta)}{1 + \left(1/\text{Re}_l^{1/4} \text{Pr}^{1/3}\right)}. \tag{152}$$

Now we return to the definitions of the coefficient of heat transfer and skin friction in terms of Eqs. (145) and (152), and we replace Eqs. (126) and (127) with

$$\frac{h}{k} \sim \frac{\eta_\theta^{-1}}{1 + \left(1/\text{Re}_l^{1/4} \text{Pr}^{1/3}\right)}, \tag{153}$$

$$\frac{U}{\nu} \sim \frac{\eta^{-1}}{1 + \left(1/\text{Re}_l^{1/4}\right)}. \tag{154}$$

Then from the ratio of Eqs. (153) and (154), and noting that $(h/k)/(U/\nu) = \text{Nu}/\text{Re}_l$ and recalling the analogy between momentum and heat, we have

$$\frac{\text{Nu}}{\text{Re}_l} = \frac{1}{2} f\left(\frac{\eta}{\eta_\theta}\right) \Phi(\text{Re}_l, \text{Pr}), \qquad \text{Pr} \geq 1, \tag{155}$$

or in terms of Eqs. (61) and (131),

$$\text{St} \, \text{Pr}^{2/3} = \left(\frac{1}{2} f\right) \Phi(\text{Re}_l, \text{Pr}), \qquad \text{Pr} \geq 1, \tag{156}$$

where

$$\Phi = \frac{1 + \left(C/\text{Re}_l^{1/4}\right)}{1 + \left(C/\text{Re}_l^{1/4} \text{Pr}^{1/3}\right)} \tag{157}$$

is the core effect, with C being a constant depending on the structure. Note that the core effect diminishes for $\text{Re}_l \to \infty$, as expected.

With an approximate value of $C \approx 5$, obtained somewhat loosely by fitting Eq. (156) for $\text{Re}_l = 3 \times 10^4$ and $\text{Pr} = 100$ to the empirical correla-

tion of Ribaud [76], we have

$$\frac{\text{St}}{\frac{1}{2}f} = \frac{1}{1 + 0.75(\text{Pr}^{2/3} - 1)} .$$

In Fig. 4, we compare the present model with some earlier models based on eddy diffusivity and the law of the wall. Figure 4 also includes a three-layer model of Karman.

We proceed to a model for liquid metals.

b. Pr $\ll$ 1 (Liquid Metals) In this case, in terms of Eqs. (135) and (72), Eq. (129) yields

$$\text{Nu}_l \sim \text{Pe}_l^{3/4}, \qquad \text{Pr} \to 0. \tag{158}$$

An alternative is the use of the Nusselt number:

$$\text{Nu} \sim \frac{l}{\eta_\theta^C}, \tag{159}$$

which, in view of Eq. (69), leads directly to Eq. (158). A two-layer model including the Prandtl effect for liquid metals is left to the reader.

Because of wide data scatter in experimental literature, there are a number of correlations with liquid metal heat transfer. Equation (158) is consistent with some of these correlations. However, new data are needed for further comparison. These data should distinguish the surface wetting and nonwetting liquid metals, should explicitly include the effect of the Prandtl number, and should be correlated with an improved model depending on Pr.
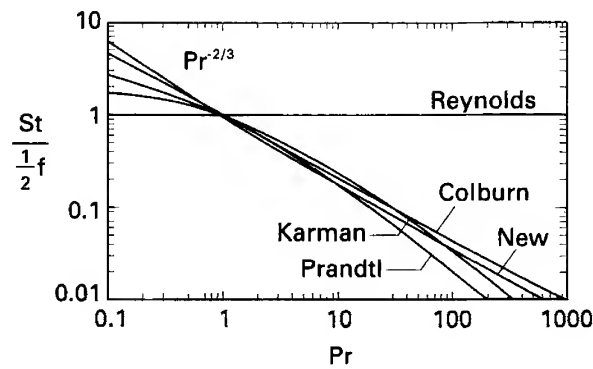

FIG. 4. Comparison of various models for heat transfer. Pr, Prandtl; St, Stanton; f, friction factor.

2. Natural Convection

Here we consider two cases: the vertical plate and the classic Rayleigh-Bénard problem.

a. Vertical Plate   A mathematical model by Churchill and Chu [25] correlates the extensive laminar and turbulent data with one correlation:

$$\text{Nu}^{1/2} = 0.825 + \frac{0.387 \, \text{Ra}^{1/6}}{\left[1 + (0.492/\text{Pr})^{9/16}\right]^{8/27}} . \tag{160}$$

Because each regime is fundamentally different from the other, Eq. (160) may be considered an approximate representation of both regimes, rather than being accurate for each one.

A model based on microscales, obtained from the inverse of Eq. (112), is

$$\text{Nu} \sim \frac{l}{\eta_\theta} \sim \Pi_N^{1/3}, \tag{161}$$

or explicitly

$$\text{Nu} = C_1 \Pi_N^{1/3}, \qquad \Pi_N = \frac{\text{Ra}}{1 + C_0 \, \text{Pr}^{-1}} . \tag{162}$$

Using a least squares fit to the Churchill and Chu correlation, Arpacı and Kao [11] have obtained $C_0 = 0.164$ and $C_1 = 0.150$ for the turbulent regime of Eq. (160) or explicitly, for $10^9 \leq \Pi_N \leq 10^{12}$,

$$\text{Nu} = 0.15 \Pi_N^{1/3}, \qquad \Pi_N = \frac{\text{Ra}}{1 + 0.164 \, \text{Pr}^{-1}} . \tag{163}$$

Between the two constants, C_0 is extremely sensitive to data. The numerical value of C_1 is expected to be quite accurate but that of C_0 needs further examination.

Next, we consider the classic Rayleigh-Bénard problem of buoyancy-driven flow between two horizontal plates.

b. Rayleigh-Bénard Problem   Assume that the temperature difference between the plates is large and that fully developed turbulent conditions prevail. This is an ideal problem for testing models based on microscales because of the wealth of experimental, analytical, and computational literature.

In a manner similar to the two-layer turbulence model of Prandtl and Taylor for forced convection, let the buoyancy-driven turbulent flow be described by a sublayer next to each plate and a core between these layers.

Assume that each sublayer is characterized by local dissipation scales and the core by volume-averaged dissipation scales.

In terms of local dissipation and $u \sim \alpha/\eta_\theta$ or $k/\eta_\theta \sim \rho c_p u$, the mean heat flux in the sublayer is

$$q \sim k \frac{\theta}{\eta_\theta} \sim \rho c_p u \theta, \tag{164}$$

which shows the same order of magnitude for conduction and convection. After neglecting the small effect of conduction, the heat flux in the core is

$$q_c \sim \rho c_p u_c \theta_c, \tag{165}$$

where the subscript c indicates the core. At the interface between the sublayer and core,

$$q \sim q_c. \tag{166}$$

In view of the temperature reversal in the core (Fig. 5), demonstrated experimentally by Thomas and Townsend [87], Gill [43], and Chu and

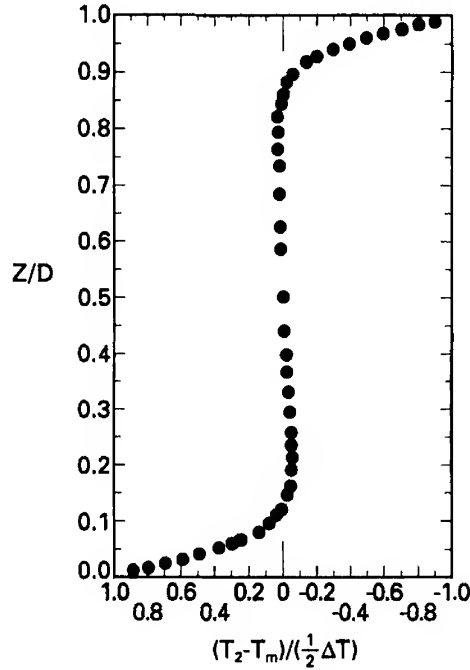Fig. 5. A typical mean temperature profile in a water layer with a gradient reversal. Ra = 3.97 × 10⁶, D = 3.8 cm, ΔT = 0.441°C [24]. Z/D, dimensionless vertical distance.

Goldstein [24], and numerically by Herring [49] and Elder [33], we let

$$\theta \sim \Delta T + \theta_c , \tag{167}$$

where ΔT is the imposed temperature difference across the plates. Inserting θ of Eq. (164) and θ_c of Eq. (165) into Eq. (167) and noting Eq. (166), we have

$$q(1 - \alpha/u_c\eta_\theta) \sim k \Delta T/\eta_\theta , \tag{168}$$

which in terms of the Nusselt number,

$$Nu = \frac{q}{k(\Delta T/l)} , \tag{169}$$

leads to

$$Nu \sim \frac{l/\eta_\theta}{1 - (l/\eta_\theta)(u_c l/\alpha)^{-1}} , \tag{170}$$

where the numerator shows the contribution to heat transfer of the sublayer and $(l/\eta_\theta)(u_c l/\alpha)^{-1}$ that of the core. In addition, for Eq. (170) in length scales alone, consider the velocity obtained from Eq. (49) by replacing u_θ with u,

$$u_c \sim \alpha \frac{l}{\lambda_\theta^2} , \tag{171}$$

or its equivalent

$$\frac{u_c l}{\alpha} \sim \left(\frac{l}{\lambda_\theta} \right)^2 . \tag{172}$$

With this relation, Eq. (170) becomes

$$Nu \sim \frac{l/\eta_\theta}{1 - (l/\eta_\theta)(l/\lambda_\theta)^{-2}} , \tag{173}$$

and in view of Eqs. (112) and (114), it yields

$$Nu \sim \frac{\Pi_N^{1/3}}{1 - \Pi_N^{-2/9}} , \tag{174}$$

which may now be converted to an equality by three constants C_0, C_1, and C_2:

$$Nu = \frac{C_1 \Pi_N^{1/3}}{1 - C_2 \Pi_N^{-2/9}} , \tag{175}$$

where

$$\Pi_N = \left(\frac{\text{Pr}}{C_0 + \text{Pr}}\right)\text{Ra}. \tag{176}$$

Equation (175) provides a heat transfer correlation for natural convection between two parallel plates. This correlation applies for fluids of any Prandtl number and Rayleigh number under turbulent conditions. Although the numerical values of the constants need to be determined from experimental data, they are expected to be universal.

Arpacı and Dec [10] computed these values by least squares fit of Eq. (175) to experimental data from the literature. The available experimental data and the selection of the best liquid metal, air, and water data for computation of the constants are discussed in the following literature review. Silveston [78] covers a range of high Prandtl number liquids, Globe and Dropkin [44] cover liquid metals, water, and viscous oils. However, these data—except for those of liquid metals ($\text{Pr} \approx 0.02$)—have been superseded by later work. Because the value of C_0 requires low Prandtl data, the liquid metal data of Globe and Dropkin are used. Gases ($\text{Pr} \approx 0.7$) are covered by Threlfall [88], Fitzjarrald [36], and Goldstein and Chu [45]. All these authors show plotted data rather than tabulated values. The data of Goldstein and Chu have the least scatter and some tabulated values and therefore they are the data used for air. Water ($\text{Pr} \approx 6$) is covered by Chu and Goldstein [24], Garon and Goldstein [42], and Goldstein and Tokuda [46]. The data of Garon and Goldstein are tabulated and cover the widest range of Rayleigh numbers, and therefore they are the data used for water. Viscous oil data ($\text{Pr} > 6$) are omitted from these computations for two reasons: There is a lack of high-quality recent data, and the constants are not sensitive to Prandtl effects for $\text{Pr} \gg 1$. The only recent data for viscous oils are that of Somerscales and Gazda [79], which are not very extensive and differ considerably from those of Goldstein and others.

Before computing the constants, the following modifications were made to the selected data. The data of Globe and Dropkin for $\text{Ra} < 10^6$ were omitted because they are likely not to be fully turbulent. In addition, the data of Goldstein and Chu, which have an aspect ratio (width-to-height) of one, are omitted because they cannot be considered free of edge effects. From a least squares fit of the selected data, the numerical constants are found by Arpacı and Dec [10] to be $C_0 = 0.04140$, $C_1 = 0.04707$, and $C_2 = 1.734$. These values are accurate for the data used; however, improved future data may lead to refinement. This is especially true for C_0, because its value relies heavily on low Prandtl number (liquid metal) data, which is quite old and does not extend beyond $\text{Ra} = 3.4 \times 10^7$.
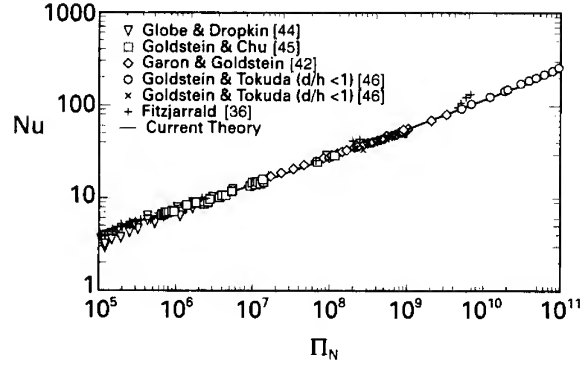
FIG. 6. Comparison of a proposed model with experimental literature for $0.02 \leq Pr \leq 6$ and $10^6 \leq Ra \leq 10^{11}$. Nu, Nusselt, Π_N, dimensionless number.

Figure 6 shows the correlation of the experimental data with the proposed model. In addition to the data used to compute constants, the data of Fitzjarrald, and Goldstein and Tokuda—as well as the omitted points of Globe and Dropkin—and Goldstein and Chu are plotted. The omitted low Ra (and low Π_N) data of Globe and Dropkin and the low aspect ratio data of Goldstein and Tokuda (high Π_N) deviate from the curve. It can be seen that, when converted into terms of Π_N, data from fluids of all Prandtl numbers collapse onto a single curve. It should be noted that the plot of the proposed model in Fig. 6 is not a straight line due to the core effect. This fact has been noted by several previous researchers, who interpreted it in terms of a series of discrete transitions. A review and discussion of these proposed transitions may be found in Chu and Goldstein [24]. It is important to note that the discussion is limited to proposed transitions in the fully turbulent range, $Ra > 10^6$. These transitions should not be confused with those for $Ra < 10^6$, which Krishnamurti [56–58] has shown—through flow visualization techniques—to be due to changing flow patterns. The experiments of Krishnamurti are impressively complemented by the analytical and computational studies of Busse et al. summarized in Ref. [21]. Four transitions in a fully turbulent regime $(Ra > 10^6)$ are explicitly reported by Garon and Goldstein [42], although they note that "their [transitions] validity is open to question." The plot for these transitions by these authors is reproduced in Fig. 7. The model developed in this paper offers an alternative interpretation of these data. In the model, curvature resulting from the core effect produces a smooth curve through these apparent transitions. This may be
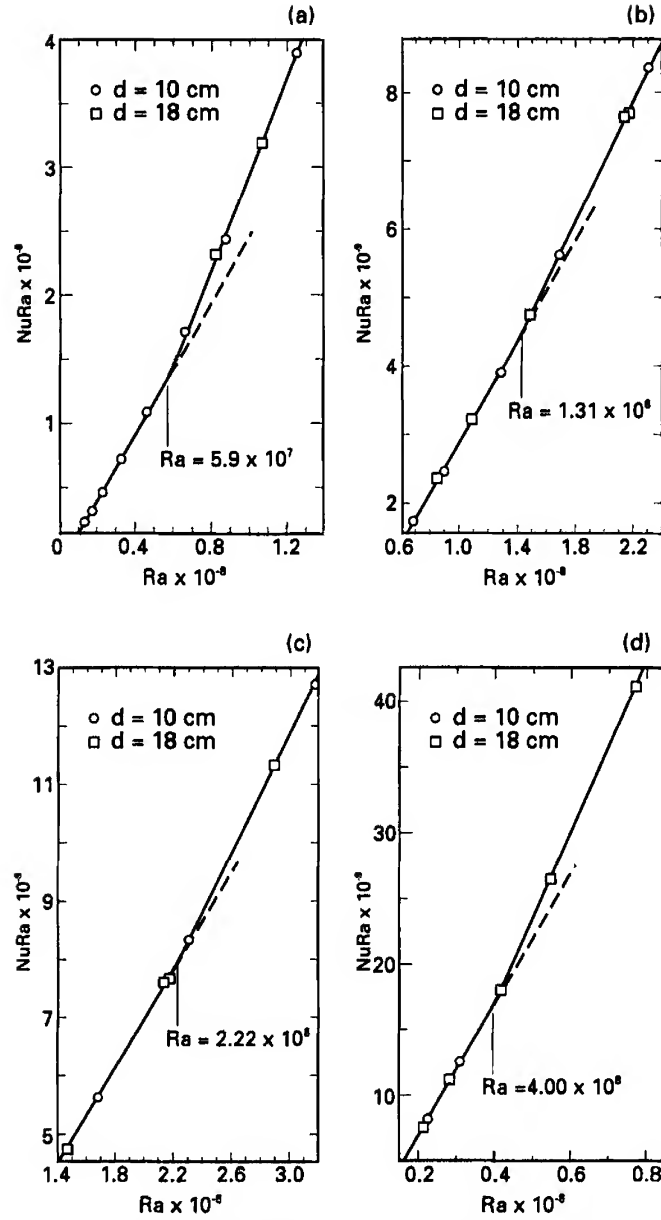
FIG. 7. (a–d) Four transitions. Nu, Nusselt; Ra, Rayleigh. Reprinted with permission of Garon and Goldstein [42].
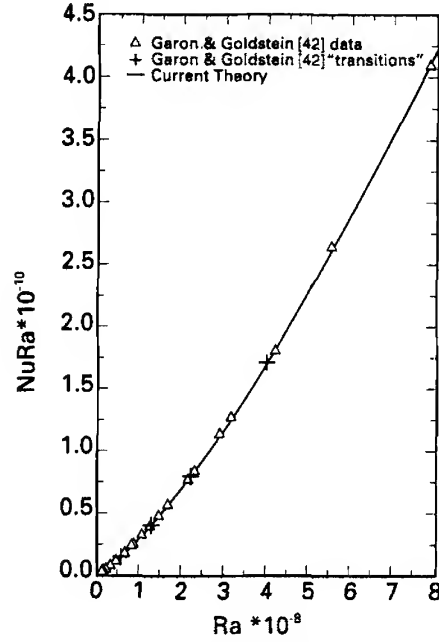
Fig. 8. Comparison of a proposed model with experimental data about four transitions plotted from Garon and Goldstein [42]. Ra, Rayleigh; Nu, Nusselt.

seen in Fig. 8, which presents the proposed model and the data and transitions of Garon and Goldstein, plotted in the same linear fashion as in Fig. 7. The linear plotting dramatizes the core effect noted in Fig. 8. The continuous curve produced by the present model may be seen to fit the data very well.

An earlier model by Long [64] also refutes these proposed transitions in the fully turbulent regime. The Long model leads to

$$Nu = \frac{Ra^{1/3} Pr^{2/3}}{\left[A_0 \delta + 2C\Delta - \gamma(Nu\,Ra)^{-s/4} \right]^{4/3}}, \qquad (177)$$

which explicitly includes the core effect. Here A_0, δ, C, δ, and γ are functions of Pr and s is a constant exponent. Equation (177) ultimately reduces to

$$Nu = \frac{C_1 Ra^{1/3}}{\left[1 - C_2(Nu\,Ra)^{-s/4} \right]^{4/3}}, \qquad (178)$$

where the constants are functions of the Prandtl number, and therefore different numerical values must be calculated for each fluid. In contrast, the present model is valid for any Prandtl number, as well as for any Rayleigh number in the turbulent range. It is general in that the parameters involved with the theory are numerical constants independent of the Prandtl number.

For buoyant flow driven by energy generation rather than a temperature difference, inserting Eqs. (120) and (123) into Eq. (173), we obtain

$$\text{Nu} \sim \frac{\Pi_I^{1/4}}{1 - \Pi_I^{-1/12}}. \tag{179}$$

The two limits of this result are identical to the models already proposed by Cheung [23]:

$$\lim_{\text{Pr} \to 0} \text{Nu} \sim \frac{(\text{Pr Ra}_I)^{1/4}}{1 - (\text{Pr Ra}_I)^{-1/12}}, \tag{180}$$

$$\lim_{\text{Pr} \to \infty} \text{Nu} \sim \frac{\text{Ra}_I^{1/4}}{1 - \text{Ra}_I^{-1/12}}. \tag{181}$$

Thus the present study generalizes, via microscales introduced for buoyancy-driven flows, two Cheung correlations into Eq. (179), which is valid for fluids of any Prandtl number. Now Eq. (179) may be written as an equality in terms of three constants:

$$\text{Nu} = \frac{C_1 \Pi_I^{1/4}}{1 - C_2 \Pi_I^{-1/12}}, \qquad \Pi_I = \left(\frac{\text{Pr}}{C_0 + \text{Pr}}\right) \text{Ra}_I. \tag{182}$$

Equation (182) provides a heat transfer correlation for turbulent natural convection driven by energy generation between two parallel plates.

The experimental literature on the buoyant turbulent flow driven by volumetric internal energy generation is confined to the studies of Tritton and Zarraga [89], Fiedler and Wille [35], Kulacki and Nagle [60], and Kulacki and Emara [59]. These studies employ electrolytically heated water for which Pr remains within the narrow range of 6 to 7. If we assume that $C_0 \ll 1$, indicating a small inertial effect [5], the numerical value of

$$\left(\frac{\text{Pr}}{C_0 + \text{Pr}}\right)^{1/4}$$

can be very closely approximated by unity. Then

$$\Pi_I \to \text{Ra}_I, \qquad \text{Pr} > 1,$$

and Nu given by Eq. (182) is reduced to

$$Nu = \frac{C_1 \, Ra_I^{1/4}}{1 - C_2 \, Ra_I^{-1/12}}.$$ (183)

Cheung employs the data of Kulacki and Emara and proposes that

$$Nu = \frac{0.206 \, Ra_I^{1/4}}{1 - 0.847 \, Ra_I^{-1/12}}.$$ (184)

Figure 9 taken from Cheung [23] shows the correlation of data by Eq. (184). A correlation for any Prandtl number incorporating the numerical values of C_0, C_1, and C_2 into Eq. (182) needs data for another Prandtl range (preferably for liquid metals), which are not presently available.

B. Two-Phase Film

The literature on heat transfer in two-phase films involving condensation and boiling is usually described by

$$Nu = f(Ra/Ja),$$ (185)
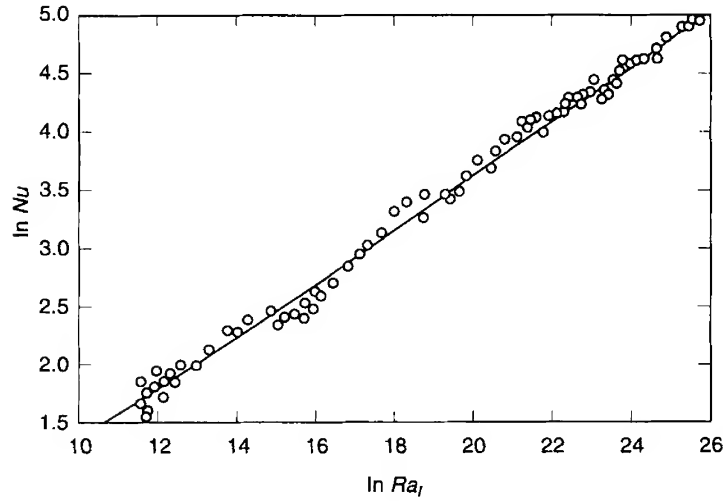

FIG. 9. In Nu versus ln Ra_I. Solid line indicates the Cheung model given by Eq. (181); open circles indicate the data of Kulacki and Emara [59]. Reprinted with permission by Cheung [23]. Nu, Nusselt; Ra_1, Rayleigh for energy generation.

which shows the dependence of the Nusselt number on the ratio between Rayleigh and Jacob numbers [71]. The relation given by Eq. (185) ignores the effect of inertial force, which is characterized by a Jacob to Prandtl number ratio. The heat transfer including this effect leads to

$$Nu = f(Ra/Ja, Ja/Pr). \tag{186}$$

This relation is implicit in the similarity solution of Sparrow and Gregg [81] for the laminar film condensation of saturated vapor next to a vertical isothermal wall [54].

The foregoing dimensionless numbers result from coupling appropriate (inertial, viscous, and buoyant) forces of the momentum balance with (enthalpy flow and conduction of) the thermal energy balance. Here we introduce a dimensionless number (say Π_2 for two-phase) that includes a combination of Ra/Ja and Ja/Pr. The objective of this section is to show that

$$Nu = f(\Pi_2), \tag{187}$$

which so far appears to have been overlooked, except for a recent attempt by Arpacı and Kao [12].

1. A Dimensionless Number (Π_2)

Let the balance among body and surface forces acting on a control volume shown in Fig. 10 be

$$F_I + F_V \sim F_B, \tag{188}$$

where F_I is the inertial force, F_V the viscous force, and F_B the buoyant force. In addition, let the balance of thermal energy for the control volume be

$$Q_H + Q_2 \sim Q_K, \tag{189}$$

where Q_H is the net enthalpy flow, Q_2 the enthalpy flow across a two-phase interface, and Q_K the conduction. In situations involving phase change the Jacob number denoting the ratio of sensible heat to latent heat

$$\frac{Q_H}{Q_2} \sim \frac{c_p \Delta T}{h_{fg}} = Ja \ll 1 \tag{190}$$

is customarily used where c_p is the specific heat at constant pressure, ΔT a longitudinal temperature difference, and h_{fg} the latent heat. In view of Eq. (190), however, $Q_H \ll Q_2$ and Eq. (189) is reduced to
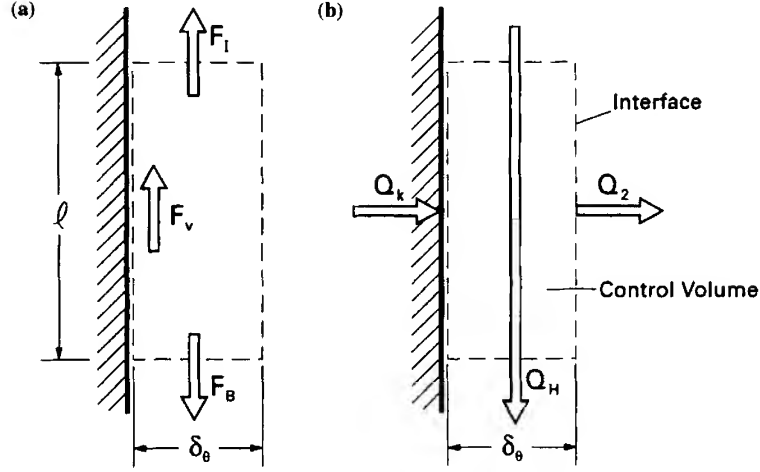
$$Q_2 \sim Q_K. \tag{191}$$

FIG. 10. Control volume for momentum and energy balances. (a) Momentum balance. (b) Thermal energy balance. F_I, inertial force; F_V, viscous force; F_B, buoyant force; Q_H, net enthalpy flow; Q_2, enthalpy flow across a two-plane interface; Q_k, the conduction.

A dimensionless number resulting from Eq. (188) is

$$\frac{F_B}{F_I + F_V} \tag{192}$$

or

$$\frac{F_B/F_V}{F_I/F_V + 1}. \tag{193}$$

In addition, a dimensionless number associated with Eq. (191) is

$$Q_2/Q_K. \tag{194}$$

On dimensional grounds,

$$\frac{F_B}{F_V} \sim \frac{g(\Delta\rho)l^2}{\mu V}, \quad \frac{F_I}{F_V} \sim \frac{\rho Vl}{\mu}, \quad \frac{Q_2}{Q_K} \sim \frac{\rho Vl h_{fg}}{k\,\Delta T},$$

where l is of characteristic length and the rest of the notation is conventional. The foregoing nondimensionalizations in terms of a characteristic velocity V are not appropriate for buoyancy-driven two-phase flows because V is a dependent variable and should not appear in dimensionless

numbers. Accordingly, we need to combine Eq. (194) with Eq. (193) for a result independent of V. The only combination that eliminates velocity is

$$\Pi_2 \sim \frac{(F_B/F_V)(Q_2/Q_K)}{(F_I/F_V)(Q_K/Q_2) + 1} \sim \frac{\text{Ra}_2}{\text{Pr}_2^{-1} + 1},\qquad (195)$$

and its limit

$$\lim_{\text{Pr}_2 \to \infty} \Pi_2 \sim \text{Ra}_2,\qquad (196)$$

where

$$\text{Pr}_2 \sim \left(\frac{F_V}{F_I}\right)\left(\frac{Q_2}{Q_K}\right) \sim \frac{\mu h_{fg}}{k\,\Delta T},\qquad (197)$$

$$\text{Ra}_2 \sim \left(\frac{F_B}{F_V}\right)\left(\frac{Q_2}{Q_K}\right) \sim \frac{g(\Delta\rho)\rho h_{fg} l^3}{\mu k(\Delta T)},\qquad (198)$$

which clearly demonstrate that Π_2 does not include the Jacob number. This fact should not be surprising in view of Eq. (190). Actually, either Pr_2 or Ra_2 would have been a more appropriate definition for the Jacob number.

The heat transfer across a two-phase film is then represented by

$$\text{Nu} = f(\Pi_2),\qquad (199)$$

or its limit

$$\lim_{\text{Pr}_2 \to \infty} \text{Nu} = f(\text{Ra}_2).\qquad (200)$$

Note that a *two-phase specific heat*

$$(c_p)_2 = h_{fg}/\Delta T \qquad (201)$$

may be defined as the natural limit of $(\partial h/\partial T)_p$, where ΔT is the temperature jump across interface. In terms of this definition,

$$\alpha_2 = \frac{k}{\rho(c_p)_2},\quad \text{Pr}_2 = \frac{\nu}{\alpha_2},\quad \text{Ra}_2 = \frac{g}{\nu\alpha_2}\left(\frac{\Delta\rho}{\rho}\right)l^3,\qquad (202)$$

and Pr_2 and Ra_2 assume their conventional forms.

Here, for customary reasons only, Eqs. (197) and (198) are rearranged by Q_H:

$$\text{Pr}_2 \sim \left(\frac{F_V}{F_I}\right)\left(\frac{Q_H}{Q_K}\right)\left(\frac{Q_2}{Q_H}\right),\qquad (203)$$

$$\text{Ra}_2 \sim \left(\frac{F_B}{F_V}\right)\left(\frac{Q_H}{Q_K}\right)\left(\frac{Q_2}{Q_H}\right),\qquad (204)$$

which, in terms of the usual Prandtl and Rayleigh numbers

$$\text{Pr} \sim \left(\frac{F_V}{F_I}\right)\left(\frac{Q_H}{Q_K}\right) \sim \frac{\nu}{\alpha},\tag{205}$$

$$\text{Ra} \sim \left(\frac{F_B}{F_V}\right)\left(\frac{Q_H}{Q_K}\right) \sim \frac{g}{\nu\alpha}\left(\frac{\Delta\rho}{\rho}\right)l^3,\tag{206}$$

become

$$\text{Pr}_2 = \text{Pr}/\text{Ja}, \qquad \text{Ra}_2 = \text{Ra}/\text{Ja}.\tag{207}$$

Then, Eq. (195) gives

$$\Pi_2 \sim \frac{\text{Ra}/\text{Ja}}{\text{Ja}/\text{Pr} + 1},\tag{208}$$

$$\lim_{\text{Pr}\to\infty} \Pi_2 = \text{Ra}/\text{Ja}.\tag{209}$$

The next two sections develop two explicit forms of Eq. (199) corresponding to laminar and turbulent films of two-phase flows, respectively.

2. Laminar Two-Phase Flow

In terms of a flow scale l (or x) and a diffusion scale δ, an explicit dimensionless form of Eq. (188) is

$$u\frac{u}{l} + \nu\frac{u}{\delta^2} \sim g\left(\frac{\Delta\rho}{\rho}\right),\tag{210}$$

and an explicit dimensionless form of Eq. (191) is

$$\rho\left(\frac{u\delta_\theta}{l}\right)h_{fg} \sim k\frac{\Delta T}{\delta_\theta},\tag{211}$$

where $u\delta_\theta/l$ is the interface velocity of transversal mass flow expressed in terms of the longitudinal mass flow.

Noting that the thicknesses of the momentum and thermal boundary layers are about the same,

$$\delta \sim \delta_\theta,\tag{212}$$

and rearranging Eq. (210) in terms of Eq. (212) yields

$$\frac{u}{\delta_\theta^2}\left(1 + \frac{u\delta_\theta^2}{\nu l}\right) \sim \frac{g}{\nu}\left(\frac{\Delta\rho}{\rho}\right).\tag{213}$$

Separately, Eq. (211) gives

$$\frac{u \delta_\theta^2}{l} \sim \frac{k \Delta T}{\rho h_{fg}},$$ (214)

which may be rearranged in terms of Eqs. (201) and (202) as

$$\frac{u \delta_\theta^2}{l} \sim \frac{k}{\rho(c_p)_2} = \alpha_2,$$ (215)

or

$$u \sim \frac{\alpha_2 l}{\delta_\theta^2}.$$ (216)

Insertion of Eq. (216) into Eq. (213) leads to

$$\frac{l}{\delta_\theta^4} \sim \frac{(g/\nu\alpha_2)(\Delta\rho/\rho)}{1 + Pr_2^{-1}},$$ (217)

or in terms of Eq. (195), to

$$\frac{l}{\delta_\theta} \sim \Pi_2^{1/4} \sim Nu.$$ (218)

As Pr_2 (or Pr) $\to \infty$, the inertial effect becomes negligible and Eq. (218) is reduced to

$$Nu \sim Ra_2^{1/4}.$$ (219)

An integral approach by Arpacı and Larsen [13] to laminar film condensation of saturated vapor next to an isothermal vertical wall for local heat transfer (Fig. 11), gives

$$Nu_x = \left[\frac{Ra_x/Ja}{4(1 + \frac{2}{3} Ja/Pr)} \right]^{1/4} = \left(\frac{Ra_x}{4Ja} \right)^{1/4} f_3\left(\frac{Ja}{Pr} \right),$$ (220)

where $f_3(Ja/Pr)$ denotes the inertial effect. Equation (220) can be reduced in terms of

$$(\Pi_2)_x = \frac{Ra_x/Ja}{1 + \frac{2}{3} Ja/Pr}$$ (221)

to

$$Nu_x = \left(\tfrac{1}{4}\Pi_2 \right)_x^{1/4}.$$ (222)

This result agrees well with the similarity solution of Koh *et al.* [54], and also shows the deviation from the Nusselt relation due to inertial effects.
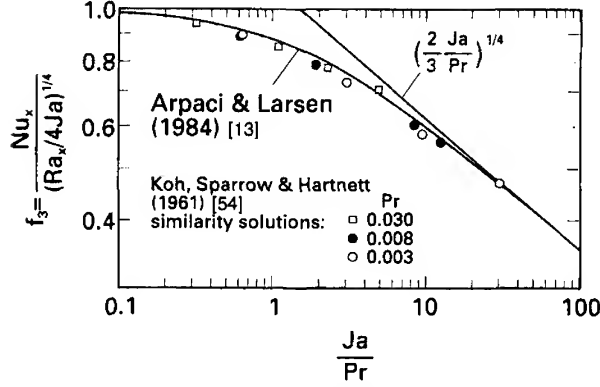
FIG. 11. Departure from Nusselt ($f_3 = 1$) for liquid metals. Nu, Nusselt; Ra, Rayleigh; Ja, Jacob; Pr, Prandtl.

Following Bromley [19], the existing correlations for film boiling on an immersed plate, cylinder, or sphere, assume the form of those on film condensation. The difference between the two cases is that, in condensation, liquid film flows downward and is slightly influenced by the adjacent vapor, whereas in boiling, vapor film flows upward and is strongly influenced by the adjacent liquid. However, this difference only makes the vapor film thicker, which lead to constants smaller than those involved with condensation. The literature gives

$$\bar{h} = C \left[\frac{(\rho_l - \rho_v) g h'_{fg} k_v^3}{\nu_v (T_w - T_{sat}) L} \right]^{1/4}, \tag{223}$$

where L is the height of a vertical plate, L equals D for sphere and cylinder, and $h'_{fg} = h_{fg} + 0.35 c_{pv}(T_w - T_{sat})$. The numerical value of C is 0.71 for the vertical plate, 0.62 for the horizontal cylinder, and 0.67 for the sphere, respectively [38]. Clearly Eq. (223) neglects the inertial effect and in view of Eq. (219) can be represented by

$$Nu = C \, Ra_2^{1/4}. \tag{224}$$

3. Turbulent Two-Phase Flow

Let the instantaneous velocity and temperature of a buoyancy-driven flow be decomposed into temporal means and fluctuations:

$$U_i + u_i, \qquad \Theta + \theta.$$

In addition, let U_i and Θ be statistically steady. Then the balance of the mean kinetic energy of homogenous velocity fluctuations gives

$$\mathscr{B} = \mathscr{P} + \varepsilon, \tag{225}$$

where

$$\mathscr{B} = -g_i \overline{u_i \theta} / \Theta_0 \tag{226}$$

is the buoyant production, with g_i being the vector acceleration of gravity and Θ_0 a characteristic temperature for isobaric ambient; and where

$$\mathscr{P} = -\overline{u_i u_j} S_{ij} \tag{227}$$

is the inertial production, with S_{ij} being the rate of the mean strain; and where

$$\varepsilon = 2\nu \overline{s_{ij} s_{ij}} \tag{228}$$

is the dissipation of turbulent energy, with s_{ij} being the rate of fluctuating strain.

In addition, the balance of the rms of homogeneous thermal fluctuations involving phase change yields

$$(\mathscr{P}_\theta)_2 = (\varepsilon_\theta)_2, \tag{229}$$

where

$$(\mathscr{P}_\theta)_2 = -\overline{u_i \theta} \, \frac{\partial \Theta}{\partial x_i} \tag{230}$$

is the mean thermal production and

$$(\varepsilon_\theta)_2 = \alpha_2 \overline{\left(\frac{\partial \theta}{\partial x_i}\right)\left(\frac{\partial \theta}{\partial x_i}\right)} \tag{231}$$

is the thermal dissipation, with $\alpha_2 = k/\rho(c_p)_2$ and $(c_p)_2 = h_{fg}/\Delta T$ already defined by Eqs. (202) and (201).

On dimensional grounds, the turbulent kinetic energy associated with Eq. (188) is

$$\mathscr{B} \sim \frac{u^3}{l} + \nu \frac{u^2}{\lambda^2}, \tag{232}$$

where u is the rms value of velocity fluctuations, l is an integral scale, and λ is the Taylor scale.

In addition, the turbulent thermal energy of the interface as associated with Eq. (191) is

$$(\mathscr{P}_\theta)_2 \sim u \frac{\theta^2}{l} \sim \alpha_2 \frac{\theta^2}{\lambda_\theta^2} \sim (\varepsilon_\theta)_2, \tag{233}$$

with λ_θ being a thermal Taylor scale characterizing the film thickness.

In a manner similar to Eq. (212), assuming that

$$\lambda \sim \lambda_\theta, \tag{234}$$

rearranging Eq. (232) in terms of Eq. (233), and solving the result for λ_θ, yields

$$\lambda_\theta \sim l^{1/3} \left(1 + \frac{1}{\mathrm{Pr}_2} \right)^{1/6} \left(\frac{\nu \alpha_2^2}{\mathscr{B}} \right)^{1/6} \tag{235}$$

and its limit

$$\lim_{\mathrm{Pr}_2 \to \infty} \lambda_\theta \sim l^{1/3} \left(\frac{\nu \alpha_2^2}{\mathscr{B}} \right)^{1/6}. \tag{236}$$

Although λ_θ and l are two different scales, let both approach the scale η_θ of the isotropic flow as the limit of the homogeneous flow

$$\left(\frac{\lambda_\theta}{l} \right) \to \eta_\theta. \tag{237}$$

Then, Eq. (235) is reduced to a thermal Kolmogorov scale for two-phase turbulent flows:

$$\eta_\theta \sim \left(1 + \frac{1}{\mathrm{Pr}_2} \right)^{1/4} \left(\frac{\nu \alpha_2^2}{\mathscr{B}} \right)^{1/4} \tag{238}$$

and its limit

$$\lim_{\mathrm{Pr}_2 \to \infty} \eta_\theta \sim \left(\frac{\nu \alpha_2^2}{\mathscr{B}} \right)^{1/4}, \tag{239}$$

which is a Batchelor scale. For $\alpha_2 = \alpha$ and $\mathrm{Pr}_2 = \mathrm{Pr}$, Eq. (238) is reduced to Eq. (90) introduced in Part II.

As demonstrated in the development leading to Π_2, a dimensionless number appropriate for buoyancy-driven flows should be independent of velocity. Because $\mathscr{B}$ depends on velocity, Eq. (238) cannot be the ultimate form of the microscale for buoyancy-driven flows. To eliminate velocity, consider $\mathscr{B}$ in terms of the buoyant force $\mathscr{F}$. On dimensional grounds,

$$\mathscr{B} \sim u\mathscr{F}, \tag{240}$$

which may be rearranged in terms of the isotropic velocity obtained from Eq. (233),

$$u \sim \alpha_2 / \eta_\theta, \tag{241}$$

as

$$\mathscr{B} \sim \alpha_2 \mathscr{F} / \eta_\theta. \tag{242}$$

In terms of $\mathcal{F}$, Eq. (238) becomes

$$\eta_\theta \sim \left(1 + \frac{1}{Pr_2}\right)^{1/3}\left(\frac{\nu\alpha_2}{\mathcal{F}}\right)^{1/3}, \tag{243}$$

which, by introducing a two-phase Rayleigh number

$$Ra_2 = \mathcal{F}l^3/\nu\alpha_2, \tag{244}$$

yields

$$\frac{\eta_\theta}{l} \sim \left(1 + \frac{1}{Pr_2}\right)^{1/3} Ra_2^{-1/3} \tag{245}$$

relative to the integral scale, or in terms of Π_2,

$$(l/\eta_\theta) \sim \Pi_2^{1/3} \sim Nu, \tag{246}$$

and

$$\lim_{Pr_2 \to \infty} Nu \sim (Ra_2)^{1/3}. \tag{247}$$

The heat transfer relation suggested by Eq. (246) finds strong support in experimental literature on buoyancy-driven flows.

For film boiling of cryogenic liquids at atmospheric pressure, correlating experimental data for liquid nitrogen, Frederkin and Clark [37] recommend the correlation

$$\bar{h} = 0.15\left[\frac{(\rho_l - \rho_v)gh'_{fg}k_v^2}{\nu_v(T_w - T_{sat})}\right]^{1/3}, \qquad \frac{(\rho_l - \rho_v)gh'_{fg}L^3}{k_v\nu_v(T_w - T_{sat})} > 5 \times 10^7, \tag{248}$$

where $h'_{fg} = h_{fg} + 0.5c_{pv}(T_w - T_{sat})$. This correlation can be expressed readily in terms of Eq. (243), leading to

$$Nu = 0.15 Ra_2^{1/3}, \qquad Ra_2 > 5 \times 10^7. \tag{249}$$

In addition, a recent study by Arpacı and Kao [12] on film boiling of liquid metals, correlates the atmospheric (10^2 kPa) mercury data of Lyon [65] and the low-pressure (39 kPa and 97 kPa) potassium data of Padilla [73] by

$$Nu = 0.22\Pi_2^{1/3}, \qquad \Pi_2 = \frac{Ra_2\,Pr_2}{1 + 0.036\,Pr_2}. \tag{250}$$

The bubble departure diameter is the characteristic length used for Nu and Ra_2. However, Eq. (250), like other buoyancy-driven correlations based on the one-third power law, is independent of any characteristic length. Figure 12 shows the correlation of the experimental data with Eq. (250). New data are needed for a more reliable correlation, which would
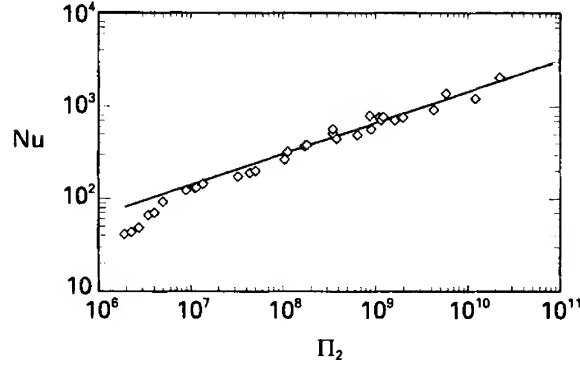
FIG. 12. Correlation of experimental data with Eq. (250). Nu, Nusselt; Π_2, two-phase dimensionless number.

include the effect of geometric orientation as well as that of surface wetting.

C. MICROGRAVITY

Thermocapillary (surface tension)-driven flows continue to attract increased experimental, analytical, and computational attention because of their importance to space exploration. Experimental observations by Block [18]—supported by Pearson's [75] analytical study about four decades after Rayleigh—demonstrated that thermocapillary-driven flow rather than buoyancy-driven flow is responsible for instability in some of the Bénard experiments. For example, drying paints are now known to display steady cellular circulatory flow of Bénard type whether the free surface is at the top or bottom of the paint layer. In some of these cases, the critical Rayleigh number fails to predict the flow initiation. Pearson has shown in terms of classic theory that the thermocapillary forces are sufficient to cause this instability characterized by the Marangoni number

$$\text{Ma} = \frac{\Delta\sigma l}{\mu\alpha}, \tag{251}$$

where $\Delta\sigma$ is the net surface tension, l thickness of the horizontal liquid layer, μ dynamic viscosity, and α thermal diffusivity. Note that by definition

$$\text{Ma} = \left(\frac{F_S}{F_V}\right)\left(\frac{Q_H}{Q_K}\right), \tag{252}$$

where F_S and F_V are the thermocapillary tension and viscous forces, respectively, and Q_H and Q_K are the enthalpy flow and conduction, respectively. In addition, by definition the Prandtl number is

$$\mathrm{Pr} = \left(\frac{Q_H}{Q_K}\right)\left(\frac{F_V}{F_I}\right), \tag{253}$$

where F_I is the inertial force. An infinitesimal theory, resting on linearized governing equations, ignores the nonlinear inertial effects and is independent of the Prandtl number. It is then governed by the Marangoni number alone. A nonlinear theory for thermocapillary-driven flows past the Marangoni instability depends on the Prandtl number as well as the Marangoni number. A fundamental dimensionless number including the effect of both Ma and Pr so far appears to have been overlooked in the archival literature. Our first objective is to introduce this dimensionless number and to discuss thermocapillary-driven flow in terms of this number.

1. Dimensional Considerations

On dimensional grounds, we first consider a flow driven by thermocapillary forces F_S:

$$F_S \sim F_I + F_V, \tag{254}$$

where F_I and F_V are the inertial and viscous forces, respectively. The thermal energy balance for this flow is

$$Q_H \sim Q_K, \tag{255}$$

where Q_H and Q_K are the enthalpy flow and heat conduction, respectively. Now rearrange Eq. (254) as

$$\frac{F_S}{F_I + F_V} \sim \frac{F_S/F_V}{1 + F_I/F_V} \tag{256}$$

and Eq. (255) as

$$Q_H/Q_K. \tag{257}$$

Note that the numeral 1 in the denominator of Eq. (256) implies order of magnitude. Explicitly,

$$F_S \sim \Delta\sigma l, \quad F_I \sim \rho V^2 l^2, \quad F_V \sim \mu V l,$$

$$Q_H \sim \rho c_p V T l^2, \quad Q_K \sim kTl,$$

and

$$\frac{F_S}{F_V} \sim \frac{\Delta\sigma}{\mu V}, \qquad \frac{F_I}{F_V} \sim \frac{\rho Vl}{\mu}, \tag{258}$$

$$\frac{Q_H}{Q_K} \sim \frac{\rho c_p Vl}{k}, \tag{259}$$

where ρ is the density, c_p specific heat at constant pressure, V velocity, T temperature, l a characteristic length, and Δ the difference in surface tension.

In terms of Eq. (258), Eq. (256) yields

$$\frac{\Delta\sigma/\mu V}{1 + \rho Vl/\mu}. \tag{260}$$

In terms of Eq. (259), Eq. (257) gives

$$\rho c_p Vl/k. \tag{261}$$

For thermocapillary driven flow, V is a dependent variable. Consequently, neither Eq. (260) nor Eq. (261) is an ultimate dimensionless number characterizing these flows. The elimination of V between Eq. (260) and Eq. (261) leads to this number,

$$\frac{(F_S/F_V)Q_H/Q_K}{(1 + F_I/F_V)Q_K/Q_H},$$

or explicitly

$$\Pi_S \sim \frac{\Delta\sigma l/\mu\alpha}{1 + \alpha/\nu}, \tag{262}$$

or

$$\Pi_S \sim \frac{\mathrm{Ma}}{1 + \mathrm{Pr}^{-1}} = \frac{\mathrm{Ma\,Pr}}{1 + \mathrm{Pr}}. \tag{263}$$

The two limits of Eq. (263) corresponding to large and small Prandtl numbers, respectively, are

$$\lim_{\mathrm{Pr}\to\infty} \Pi_S \to \mathrm{Ma}, \tag{264}$$

$$\lim_{\mathrm{Pr}\to 0} \Pi_S \to \mathrm{Ma\,Pr}. \tag{265}$$

The next section is devoted to the laminar boundary layer in terms of Π_S.

2. Laminar Flow

On dimensional grounds, let the momentum balance given by Eq. (254) be

$$\frac{\Delta\sigma}{\rho l^2} \sim u\frac{u}{l} + \nu\frac{u}{\delta},\tag{266}$$

where δ is the thickness of the momentum boundary layer and l is an integral scale characterizing geometry. In addition, let the thermal energy balance be

$$u\frac{\theta}{l} \sim \alpha\frac{\theta}{\delta_\theta^2},\tag{267}$$

where δ_θ is the thickness of the thermal boundary layer. Solve Eq. (267) for velocity:

$$u \sim \alpha\frac{l}{\delta_\theta^2}.\tag{268}$$

To proceed further, following Squire [82], let

$$\delta \sim \delta_\theta\tag{269}$$

in Eq. (266), and eliminate velocity with Eq. (268). Thus

$$\frac{\Delta\sigma}{\rho l^2} \sim \frac{l}{\delta_\theta^4}\left(1 + \frac{\nu}{\alpha}\right),\tag{270}$$

or in terms of Π_S,

$$\frac{l}{\delta_\theta} \sim \Pi_S^{1/4}.\tag{271}$$

The next section is devoted to turbulent thermal microscales in terms of Π_S.

3. Turbulent Flow

For the homogeneous flow (in which all averaged quantities except U_i and Θ are independent of position and S_{ij} and $\partial\Theta/\partial x_i$ are constants) the mean kinetic energy of turbulent fluctuations [2, 3, 5–9] is reduced to

$$\mathscr{P}_S = \mathscr{P} + \varepsilon.\tag{272}$$

Here $\mathscr{P}$ is the inertial production rate of turbulent energy by Reynolds stresses and ε is the rate of viscous dissipation of turbulent fluctuations, where

$$\mathscr{P}_S = \sigma_T\overline{u_i\theta}/\rho l^2\tag{273}$$

is the rate of thermocapillary energy production, with σ_T being the surface tension expansion coefficient. In addition, the rate of thermal energy is

$$\mathscr{P}_\theta = \varepsilon_\theta, \tag{274}$$

where $\mathscr{P}_\theta$ and ε_θ are the thermal production and dissipation, respectively.

On dimensional grounds, Eqs. (272) and (274) lead to

$$\mathscr{P}_S \sim \frac{u^3}{l} + \nu \frac{u^2}{\lambda^2}, \tag{275}$$

and using $u \sim u_\theta$ for surface-driven flows,

$$u \frac{\theta^2}{l} \sim \alpha \frac{\theta^2}{\lambda_\theta^2}. \tag{276}$$

It seems reasonable to assume that Eq. (269) is a general property of body or surface-force driven flows and is also valid under turbulent conditions. Accordingly, let $\lambda \sim \lambda_\theta$. Then elimination of velocity between Eqs. (275) and (276) leads to a thermal Taylor scale

$$\lambda_\theta \sim l^{1/3}\left(1 + \frac{1}{\mathrm{Pr}}\right)^{1/6}\left(\frac{\nu\alpha^2}{\mathscr{P}_S}\right)^{1/6}, \qquad \mathrm{Pr} \geq 1, \tag{277}$$

or

$$\lambda_\theta \sim l^{1/3}(1 + \mathrm{Pr})^{1/6}\left(\frac{\alpha^3}{\mathscr{P}_S}\right)^{1/6}, \qquad \mathrm{Pr} \leq 1, \tag{278}$$

where Eq. (277) explicitly includes the limit for $\mathrm{Pr} \to \infty$ and is useful for fluids with $\mathrm{Pr} \geq 1$, and Eq. (278) explicitly includes the limit for $\mathrm{Pr} \to 0$ and is useful for fluids with $\mathrm{Pr} \leq 1$.

For the isotropic limit of the homogeneous flow, letting

$$\left(\frac{\lambda_\theta}{l}\right) \to \eta_\theta, \tag{279}$$

Eqs. (277) and (278) are reduced to a thermal Kolmogorov scale

$$\eta_\theta \sim \left(1 + \frac{1}{\mathrm{Pr}}\right)^{1/4}\left(\frac{\nu\alpha^2}{\mathscr{P}_S}\right)^{1/4}, \qquad \mathrm{Pr} \geq 1, \tag{280}$$

or

$$\eta_\theta \sim (1 + \mathrm{Pr})^{1/4}\left(\frac{\alpha^3}{\mathscr{P}_S}\right)^{1/4}, \qquad \mathrm{Pr} \leq 1. \tag{281}$$

Now, it is a simple matter to show from Eq. (280) that

$$\lim_{\mathrm{Pr}\to\infty} \eta_\theta \to \left(\frac{\nu\alpha^2}{\mathscr{P}_S}\right)^{1/4}, \tag{282}$$

which in view of

$$\lim_{\mathrm{Pr}\to\infty} \mathscr{P} \to 0 \tag{283}$$

and

$$\mathscr{P}_S \to \varepsilon, \tag{284}$$

leads to the Batchelor scale:

$$\lim_{\mathrm{Pr}\to\infty} \eta_\theta \to \eta_\theta^B \sim \left(\frac{\nu\alpha^2}{\varepsilon}\right)^{1/4}. \tag{285}$$

In addition, from Eq. (281),

$$\lim_{\mathrm{Pr}\to 0} \eta_\theta \to \left(\frac{\alpha^3}{\mathscr{P}_S}\right)^{1/4}, \tag{286}$$

which in view of

$$\lim_{\mathrm{Pr}\to 0} \varepsilon \to 0, \tag{287}$$

$$\mathscr{P}_S \to \mathscr{P}, \tag{288}$$

and in a viscous layer order of magnitude thinner than η_θ,

$$\mathscr{P} \to \varepsilon, \tag{289}$$

leads to the Oboukhov-Corrsin scale:

$$\lim_{\mathrm{Pr}\to\infty} \eta_\theta \to \eta_\theta^C \sim \left(\frac{\alpha^3}{\varepsilon}\right)^{1/4}. \tag{290}$$

Finally, for $\mathrm{Pr} \sim 1$, because of the equipartition (on dimensional grounds) of thermocapillary production into inertial production and viscous dissipation, Eq. (272) becomes

$$\mathscr{P}_S \sim 2\varepsilon, \tag{291}$$

and both Eqs. (280) and (281) lead to the Kolmogorov scale:

$$\lim_{\mathrm{Pr}\to 1} \eta_\theta \to \eta \sim \left(\frac{\nu^3}{\varepsilon}\right)^{1/4}. \tag{292}$$

The relation between the thermal scales and the integral scale may now be obtained by eliminating the factor $(1 + \mathrm{Pr}^{-1})(\nu\alpha^2/\mathscr{P}_S)$ between Eqs.

(277) and (280) or Eqs. (278) and (281). Thus

$$\left(\frac{\eta_\theta}{\lambda_\theta}\right)^2 = \frac{\lambda_\theta}{l}, \tag{293}$$

which is analogous to a model proposed by Tennekes [85] for dynamic intermittency.

Note that in the Kolmogorov scales given by Eqs. (280) and (281), $\mathscr{P}_S$ depends on velocity, and these scales cannot be ultimate forms of the Kolmogorov scales for surface tension-driven flows. To eliminate velocity dependence, reconsider Eq. (280):

$$\eta_\theta \sim \left(1 + \frac{1}{\mathrm{Pr}}\right)^{1/4}\left(\frac{\nu\alpha^2}{\mathscr{P}_S}\right)^{1/4}$$

In addition, assume that on dimensional grounds

$$\mathscr{P}_S \sim \sigma_T u\theta/\rho l^2, \tag{294}$$

or with local velocity obtained from the limit of Eq. (276),

$$u \sim \alpha/\eta_\theta, \tag{295}$$

as

$$\mathscr{P}_S \sim \sigma_T \alpha\theta/\rho l\eta_\theta. \tag{296}$$

Insertion of Eq. (296) into Eq. (280), after some rearrangement, yields,

$$\eta_\theta \sim \left(1 + \frac{1}{\mathrm{Pr}}\right)^{1/3}\left(\frac{\mu\alpha l^2}{\sigma_T \theta}\right)^{1/3}. \tag{297}$$

Finally, assuming the rms of the temperature fluctuations to be proportional to the imposed temperature difference, we have

$$\theta \sim \Delta T, \qquad \sigma_T \theta \sim \sigma_T \Delta T \sim \Delta\sigma, \tag{298}$$

$$\eta_\theta \sim \left(1 + \frac{1}{\mathrm{Pr}}\right)^{1/3}\left(\frac{\mu\alpha l^2}{\Delta\sigma}\right)^{1/3}, \tag{299}$$

or in terms of an integral scale l,

$$\frac{\eta_\theta}{l} \sim \left(1 + \frac{1}{\mathrm{Pr}}\right)^{1/3}\mathrm{Ma}^{-1/3} \sim \Pi_S^{-1/3}, \tag{300}$$

where

$$\mathrm{Ma} = \frac{\Delta\sigma\,l}{\mu\alpha}$$

is the Marangoni number.

4. Heat Transfer

a. Flow Past Marginal Stability Dimensional arguments of the preceding sections demonstrate that in the case of steady (or steady on the mean) convection, a balance is maintained between production and dissipation of energy. It was Landau [61] who originally suggested from general considerations that the amplitude of disturbances past marginal stability must increase as

$$A \sim (\mathrm{Re} - \mathrm{Re}_c)^{1/2}, \tag{301}$$

where Re is the Reynolds number characterizing flow beyond the onset of instability at Re_c. Chandrasekhar [22] extended the idea to buoyancy-driven flows and explicitly showed from variational considerations that

$$A \sim (\mathrm{Ra} - \mathrm{Ra}_c)^{1/2}, \tag{302}$$

where Ra is the Rayleigh number (also, for some earlier work, refer to Malkus [66], Malkus and Veronis [67], Gorkov [47], Stuart [83], Veronis [90], and Nakagawa [70]). It is clear from Landau's general considerations, as well as from Chandrasekhar's explicit variational demonstration, that the amplitude of thermocapillary flow past marginal stability is

$$\frac{A}{k\,\Delta T/l} \sim (\mathrm{Ma} - \mathrm{Ma}_c)^{1/2}, \tag{303}$$

where k is the thermal conductivity, l a characteristic length for geometry, and ΔT the imposed temperature difference. Then relative to conduction prevailing up to marginal stability,

$$\left(h - \frac{k}{l}\right)\Delta T \sim A, \tag{304}$$

which in view of Eq. (303), yields

$$\mathrm{Nu} - 1 \sim (\mathrm{Ma} - \mathrm{Ma}_c)^{1/2}. \tag{305}$$

b. Laminar Flow The usual definition of the coefficient of heat transfer, in terms of the thermal boundary layer thickness, gives

$$q_w \sim h\theta \sim k\left(\frac{l}{\delta_\theta}\right), \tag{306}$$

which can be rearranged as

$$\mathrm{Nu} = \frac{hl}{k} \sim \frac{l}{\delta_\theta}. \tag{307}$$

Then in terms of Eq. (271),

$$Nu \sim \frac{l}{\delta_\theta} \sim \Pi_S^{1/4} \tag{308}$$

whose limits for large and small Prandtl numbers are

$$\lim_{Pr \to \infty} Nu \to Ma^{1/4}, \tag{309}$$

$$\lim_{Pr \to 0} Nu \sim (Ma\,Pr)^{1/4}. \tag{310}$$

c. Turbulent Flow The usual definition of the coefficient of heat transfer, in terms of the Kolmogorov scale, gives

$$q_w \sim h_\theta \sim k\left(\frac{l}{\eta_\theta}\right), \tag{311}$$

which can be rearranged as

$$Nu = \frac{hl}{k} \sim \frac{l}{\eta_\theta}. \tag{312}$$

Then in terms of Eq. (300),

$$Nu \sim \frac{l}{\delta_\theta} \sim \Pi_S^{1/3}, \tag{313}$$

whose limits for large and small Prandtl numbers are

$$\lim_{Pr \to \infty} Nu \sim Ma^{1/3}, \tag{314}$$

$$\lim_{Pr \to 0} Nu \sim (Ma\,Pr)^{1/3}. \tag{315}$$

For thermocapillary driven flows, we explain the foundations of the flow regimes described by $Ma^{1/2}$ and $Ma^{1/3}$ in the recent dimensional, computational, and experimental study of Kamotani et al. [50], who follow different arguments from those presented here. We also introduce another regime described by $Ma^{1/4}$ for laminar flow. Figure 13, which is borrowed from Kamotani et al. [50], illustrates the three-flow regimes.

III. Mass Transfer

The microscale foundations of mass transfer correlations is illustrated in this part in terms of fuel consumption in turbulent diffusion flames. However, first we consider a dimensional interpretation of classic laminar flame theories, which proves convenient later.
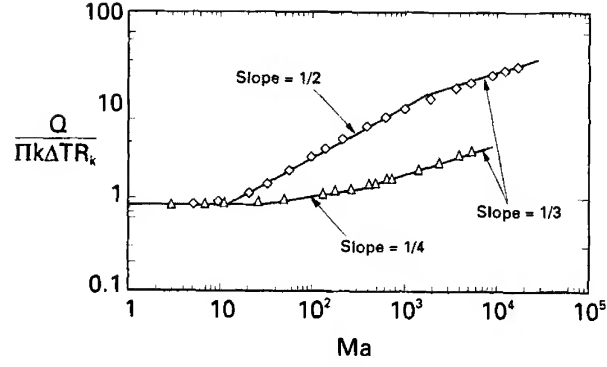
FIG. 13. Three flow regimes. Reprinted with permission by Kamotani *et al* [50]. Ma, Marangoni.

A. DIFFUSION FLAME

1. *Forced Flame*

a. Laminar Flame Reconsider the pioneering work of Spalding [80], which deals with forced flame boundary layers on a flat plate (Fig. 14). The balance of momentum integrated over the momentum boundary layer thickness δ is

$$\rho U^2 \frac{d}{dx} \int_0^\delta \left(1 - \frac{u}{U}\right)\left(\frac{u}{U}\right) dy - \rho U v_w = \mu \left(\frac{\partial u}{\partial y}\right)_w \tag{316}$$

where ρ is the density, μ dynamic viscosity, u longitudinal velocity, U free stream value, and v_w velocity normal to the fuel surface. Also assume that $Le = \alpha/D = 1$, where Le is the Lewis number and α and D are the thermal and mass diffusivities, respectively. The balance of the generalized
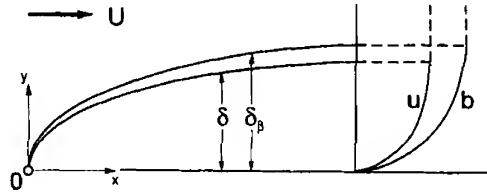

FIG. 14. Forced flame boundary layers on a flat plate. U, free stream value; b, balance of generalized diffusion property; u, longitudinal velocity.

diffusion property b, assumed to be the Schvab-Zeldovich (heat plus oxidizer) property and integrated over its boundary layer thickness δ_β, is

$$\rho UB \frac{d}{dx} \int_0^{\delta_\beta} \frac{u}{U} \left(\frac{b_\infty - b}{B} \right) dy - \rho B v_w = \rho D \left(\frac{\partial b}{\partial y} \right)_w . \qquad (317)$$

Here b and the transfer number B are defined as

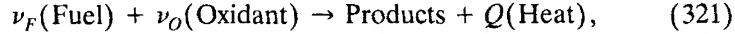$$b = (Y_O Q / \nu_O M_O + h) / h_{fg} \qquad (318)$$

and

$$B = b_\infty - b_w , \qquad (319)$$

respectively, or in terms of Eq. (318), explicitly as

$$B = (Y_{O\infty} Q / \nu_O M_O - h_w) / h_{fg} . \qquad (320)$$

Here Y_O is the mass fraction of the oxidizer, $Y_{O\infty}$ its ambient value, and Q the heat released according to a single global chemical reaction:

$$\nu_F(\text{Fuel}) + \nu_O(\text{Oxidant}) \rightarrow \text{Products} + Q(\text{Heat}), \qquad (321)$$

where

$$\frac{Q}{\nu_O M_O} = \left(\frac{Q}{\nu_F M_F} \right) \left(\frac{\nu_F M_F}{\nu_O M_O} \right) \qquad (322)$$

is the heat released per unit mass of oxidizer. Here $Q / \nu_F M_F$ is the lower heating value (heat released per kg of fuel); $\nu_F M_F / \nu_O M_O$ is the stoichiometric fuel-to-oxidant ratio (kg fuel per kg oxidant); ν_F, ν_O and M_F, M_O are the fuel and oxidant stoichiometric coefficients and molecular weights, respectively; h is the specific enthalpy of gas relative to ambient temperature; h_w equals $c_p(T_w - T_\infty)$; c_p is the specific heat of gas; T_w and T_∞ are the fuel surface and ambient temperatures, respectively; and h_{fg} is the heat of evaporation. The local mass transfer (burning rate per unit area) is

$$M'' = \rho v_w = \rho D \left(\frac{\partial b}{\partial y} \right)_w , \qquad (323)$$

and the mass transfer averaged over a length l is

$$M' = \int_0^l M'' \, dx . \qquad (324)$$

Now consider a dimensional interpretation of the foregoing formulation.

Following Arpacı and Li [14], the balance of momentum given by Eq. (316) may be written as

$$U \frac{U}{l} \sim v_w \frac{U}{\delta} + \nu \frac{U}{\delta^2} , \qquad (325)$$

and the balance of b-property given by Eq. (317) as

$$U_\beta \frac{B}{l} \sim v_w \frac{B}{\delta_\beta} + D \frac{B}{\delta_\beta^2}. \tag{326}$$

In terms of the mass balance on the fuel surface

$$\rho v_w \sim \rho D \frac{B}{\delta_\beta}, \tag{327}$$

Eqs. (325) and (326) may be rearranged as

$$U \frac{U}{l} \sim v \left(1 + \frac{\delta}{\delta_\beta} \frac{B}{\sigma}\right) \frac{U}{\delta^2}, \tag{328}$$

$$U_\beta \frac{B}{l} \sim D(1 + B) \frac{B}{\delta_\beta^2}. \tag{329}$$

For notational convenience, let

$$v_\beta = v(1 + B'), \qquad D_\beta = D(1 + B), \tag{330}$$

where

$$B' = \chi \frac{B}{\sigma}, \qquad \chi = \frac{\delta}{\delta_\beta}, \tag{331}$$

with $\sigma = v/D$ being the Schmidt number. Then Eqs. (328) and (329) are reduced to

$$U \frac{U}{l} \sim v_\beta \frac{U}{\delta^2}, \tag{332}$$

$$U_\beta \frac{B}{l} \sim D_\beta \frac{B}{\delta_\beta^2}. \tag{333}$$

In view of the assumed similarity between Eqs. (332) and (333),

$$U_\beta = U \frac{\delta_\beta}{\delta}, \tag{334}$$

$$\chi = \sigma_\beta^{1/3}, \tag{335}$$

with σ_β being the flame Schmidt number

$$\sigma_\beta = \frac{v_\beta}{D_\beta} = \left(\frac{v_\beta}{v}\right)\left(\frac{D}{D_\beta}\right)\left(\frac{v}{D}\right) = \left(\frac{1 + B'}{1 + B}\right)\sigma. \tag{336}$$

Equations (334) and (335) are strictly valid when $\chi \geq 1$, which is not the case here. However, χ remains near unity and the error introduced by this assumption remains small.

From Eq. (332),

$$\frac{l}{\delta} \sim \mathrm{Re}_\beta^{1/2}, \tag{337}$$

where

$$\mathrm{Re}_\beta = \frac{Ul}{\nu_\beta} = \left(\frac{\nu}{\nu_\beta}\right)\frac{Ul}{\nu} = \frac{\mathrm{Re}}{(1 + B')}, \tag{338}$$

with $\mathrm{Re} = Ul/\nu$ being the Reynolds number. Now the burning rate over a length l,

$$\frac{M'}{\rho D} \sim B \frac{l}{\delta_\beta} = \chi B\left(\frac{l}{\delta}\right), \tag{339}$$

becomes, in terms of Eqs. (335) and (338),

$$\frac{M'}{\rho D} \sim B \, \mathrm{Re}_\beta^{1/2} \, \sigma_\beta^{1/3}, \tag{340}$$

which explicitly is

$$\frac{M'}{\rho D} \sim \frac{B \, \mathrm{Re}^{1/2}}{(1 + B')^{1/2}} \left(\frac{1 + B'}{1 + B}\right)^{1/3} \sigma^{1/3}, \tag{341}$$

or

$$\frac{M'}{\rho D \, \mathrm{Re}^{1/2} \, \sigma^{1/3}} \sim \frac{B}{(1 + B')^{1/6}(1 + B)^{1/3}}. \tag{342}$$

For $\chi \sim 1$ and $\sigma \sim 1$, $B \sim B'$, and Eq. (342) is reduced, with a parameter C, to

$$\frac{M'}{\mu \, \mathrm{Re}^{1/2}} = \frac{CB}{(1 + B)^{1/2}}, \tag{343}$$

which in the sense of explicit B-dependence, is identical to

$$\frac{M'}{\mu \, \mathrm{Re}^{1/2}} = B\left[\frac{a_1(\delta_m/\delta)}{2(1 + B)}\right]^{1/2}. \tag{344}$$

Equation (344) is the result obtained by Spalding [80], where a_1 is the coefficient of the linear term in the assumed cubic velocity profile, δ_m momentum thickness, and δ boundary layer thickness. From Eqs. (343) and (344),

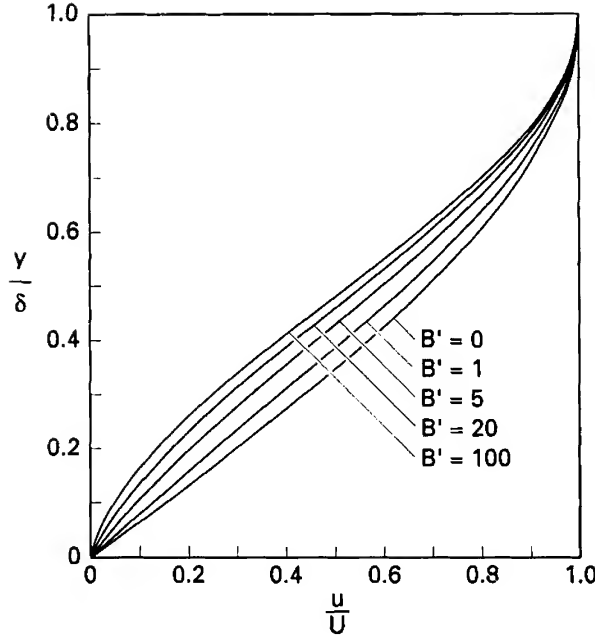$$C = \left[\frac{a_1}{2}\left(\frac{\delta_m}{\delta}\right)\right]^{1/2}. \tag{345}$$

FIG. 15. Momentum and Schvab-Zeldovich boundary layers.

An inspection of Spalding's result reveals that δ_m/δ remains almost constant but that a_1 decays monotonically and is mainly responsible for the B-dependence of C. In addition, the velocity assumes a curvature reversal (inflection) depending on B (Fig. 15). The foregoing dimensional considerations then need to be complemented by including this dependence in Eq. (343). Spalding includes the boundary condition

$$\rho v \, \frac{db}{dy} = \rho D \, \frac{d^2 b}{dy^2}, \qquad y = 0, \tag{346}$$

whose effect is missing from these considerations. Now, assume that Eq. (346) applies for $0 \le y \le \delta$, and recover from twice integration the burning rate obtained from the stagnant film theory

$$\frac{M'}{\rho D} = \chi \ln(1 + B) \frac{l}{\delta}. \tag{347}$$

This suggests a somewhat logarithmic rather than linear behavior for the numerator of Eq. (343). By expansion and inversion it can be shown that

$$\ln(1 + B) = \frac{B}{1 + \dfrac{B}{2} - \dfrac{B^2}{12} + \cdots}, \qquad (348)$$

which can be simulated by

$$\frac{B}{(1 + C_0 B)^n}. \qquad (349)$$

For $n < 1$, the denominator of Eq. (349) is an alternating series such as that in the denominator of Eq. (348). In terms of

$$C = \frac{C_1}{(1 + C_0 B)^n}, \qquad (350)$$

the burning rate now becomes

$$\frac{M'}{\mu \, \mathrm{Re}^{1/2}} = \frac{C_1 B}{(1 + C_0 B)^n (1 + B)^{1/2}}. \qquad (351)$$

For $B = 0$, the heat transfer literature based on cubic profiles gives

$$C_1 = 0.646.$$

For $B \to \infty$, Spalding's result approaches $B^{1/4}$, which requires that

$$n = \tfrac{1}{4}.$$

Thus

$$\frac{M'}{\mu \, \mathrm{Re}^{1/2}} = \frac{0.646 B}{(1 + C_0 B)^{1/4} (1 + B)^{1/2}}. \qquad (352)$$

An inspection of the literature [52] reveals an approximate upper bound of $B \sim 10$ for liquid fuels. A least squares fit of Eq. (352) to Spalding's result for $B \leq 20$ yields

$$C_0 = 0.525$$

and

$$\frac{M'}{\mu \, \mathrm{Re}^{1/2}} = \frac{0.646 B}{(1 + 0.525 B)^{1/4} (1 + B)^{1/2}}. \qquad (353)$$

Figure 16 shows the comparison of Eq. (353) with Spalding's result against $B \leq 20$.
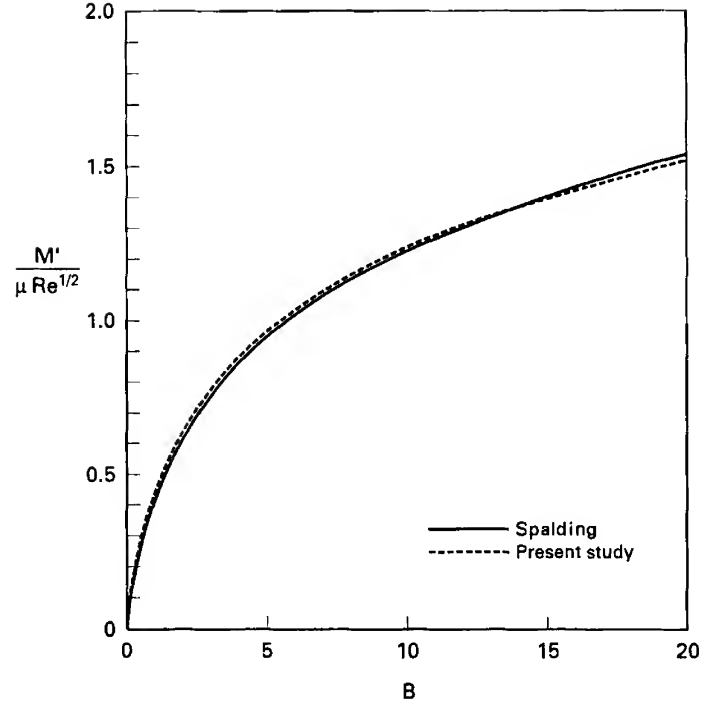
FIG. 16. Comparison of Eq. (353) with Spalding against $B \leq 20$. Re, Reynolds.

So that our reasoning is clear in the next section, we also consider the exact solution obtained by Emmons [34]. For $B = 0$, the literature based on the similarity solution gives

$$C_1 = 0.664.$$

For $B \to \infty$, Emmons' solution approaches a constant that requires

$$n = \tfrac{1}{2}.$$

Thus

$$\frac{M'}{\mu \, \mathrm{Re}^{1/2}} = \frac{0.664B}{(1 + C_0 B)^{1/2}(1 + B)^{1/2}}. \tag{354}$$

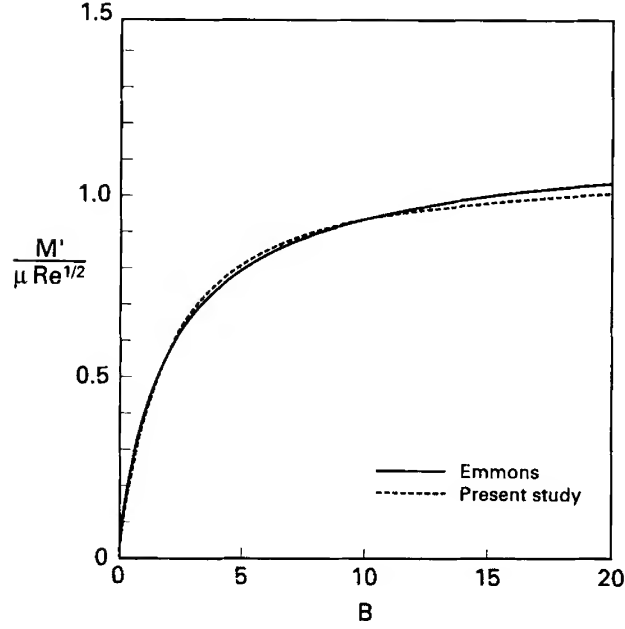A least squares fit of Eq. (354) to Emmons' solution for $B \leq 20$ yields

$$C_0 = 0.354$$

FIG. 17. Comparison of Eq. (355) with Emmons against $B \leq 20$. Re, Reynolds.

and

$$\frac{M'}{\mu\,\mathrm{Re}^{1/2}} = \frac{0.664B}{(1 + 0.354B)^{1/2}(1 + B)^{1/2}}.$$ (355)

Figure 17 shows the comparison of Eq. (355) with Emmons' solution against $B \leq 20$.

Although the main interest lies in fuel consumption, for convenience in the next section on turbulent diffusion flames, we also consider heat transfer and skin friction. As is well known, for $B \sim B'$ and $\chi \sim 1$, the similarity leads to

$$\lim_{B \to 0} \left(\frac{M'}{\mu B} \right) = N = C_f,$$ (356)

or

$$\frac{N}{N_{B=0}} = \frac{C_f}{(C_f)_{B=0}} = \frac{1}{(1 + C_0 B)^n (1 + B)^{1/2}},$$ (357)

where N is the Nusselt number and C_f the drag coefficient, and where the subscript $B = 0$ corresponding to the case without boundary mass transfer.
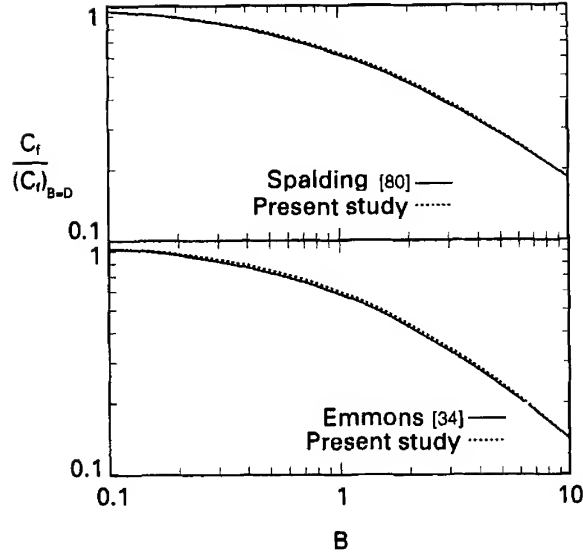
FIG. 18. Comparison of Spalding and Emmons with present study.

The values for n and C_0 are those assumed for the fuel consumption. Figure 18 shows that $N/N_{B=0} = C_f/(C_f)_{B=0}$ versus $B \leq 20$.

The foregoing dimensional arguments are now extended to turbulent flames.

b. Turbulent Flame Following the usual practice, decompose the instantaneous velocity $\tilde{u}_i$, and the Schvab-Zeldovich property of a turbulent diffusion flame $\tilde{b}$ into a temporal mean (denoted by capital letters) and fluctuations,

$$\tilde{u}_i = U_i + u_i \quad \text{and} \quad \tilde{b} = B + b.$$

For a homogeneous pure shear flow (in which all averages except U_i and B are independent of position and in which the $\partial B / \partial x_i$ and S_{ij} are constant), the mean kinetic energy of velocity fluctuations and the mean of the Schvab-Zeldovich property yield

$$\mathscr{P} = \varepsilon, \tag{358}$$

and

$$\mathscr{P}_\beta = \varepsilon_\beta, \tag{359}$$

where

$$\mathscr{P} = -\overline{u_i u_j} S_{ij} \tag{360}$$

is the inertial production; where

$$\varepsilon = 2\nu_\beta \overline{s_{ij} s_{ij}}$$

(361)

is the dissipation of turbulent energy; and where

$$\mathscr{P}_\beta = -\overline{u_i b} \, \frac{\partial B}{\partial x_i}$$

(362)

and

$$\varepsilon_B = D_\beta \overline{\left(\frac{\partial b}{\partial x_i}\right)\left(\frac{\partial b}{\partial x_i}\right)}$$

(363)

are the production and dissipation of the Schvab-Zeldovich property, respectively. Note that the incorporation of the boundary mass transfer into Eqs. (358) and (359) is taken into account in terms of ν_β and D_β.

Following Arpacı and Li [14], on dimensional grounds Eqs. (358) and (359) lead to

$$\mathscr{P} \sim \frac{u^3}{l} \sim \nu_\beta \frac{u^2}{\lambda^2} \sim \varepsilon,$$

(364)

$$u_\beta \frac{b^3}{l} \sim D_\beta \frac{b^2}{\lambda_\beta^2},$$

(365)

where λ and λ_β are the Taylor microscales associated with momentum and the Schvab-Zeldovich property.

From Eq. (364),

$$\frac{\lambda}{l} \sim \mathrm{Re}_\beta^{-1/2}.$$

(366)

In addition, from Eq. (364), an inertial estimate for u is

$$u \sim (\varepsilon l)^{1/3},$$

(367)

and a viscous estimate is

$$u \sim \lambda(\varepsilon/\nu_\beta)^{1/2}.$$

(368)

Elimination of velocity between Eqs. (367) and (368) yields a Taylor scale:

$$\lambda \sim l^{1/3}\left(\frac{\nu_\beta^3}{\varepsilon}\right)^{1/6}.$$

(369)

For the isotropic flow, replacing λ and l with one scale,

$$\left(\frac{\lambda}{l}\right) \to \eta,$$

(370)

leads to a Kolmogorov scale:

$$\eta \sim \left(\frac{\nu_\beta^3}{\varepsilon} \right)^{1/4}. \tag{371}$$

Elimination of ν_β^3/ε between Eqs. (369) and (371) yields

$$\frac{\eta}{l} \sim \left(\frac{\lambda}{l} \right)^{3/2}, \tag{372}$$

or in terms of Eq. (366),

$$\frac{\eta}{l} \sim \mathrm{Re}_\beta^{-3/4}. \tag{373}$$

Now, assume that the momentum in terms of λ and the b-property in terms of λ_β are similar (recall the similarity between the momentum and thermal energy of forced convection). Then in terms of

$$u_\beta = u\left(\frac{\lambda_\beta}{\lambda} \right), \tag{374}$$

Eq. (365) becomes

$$\frac{u}{l}\left(\frac{\lambda_\beta}{\lambda} \right) \sim \frac{D_\beta}{\lambda_\beta^2}, \tag{375}$$

which in terms of Eq. (368), leads to

$$\frac{\lambda_\beta}{l}\left(\frac{\varepsilon}{\nu_\beta} \right)^{1/2} \sim \frac{D_\beta}{\lambda_\beta^2}, \tag{376}$$

or after some rearrangement, to a Taylor scale:

$$\lambda_\beta \sim l^{1/3}\left(\frac{\nu_\beta D_\beta^2}{\varepsilon} \right)^{1/6}. \tag{377}$$

The ratio of Eqs. (369) and (377) gives

$$\frac{\lambda}{\lambda_\beta} = \left(\frac{\nu_\beta}{D_\beta} \right)^{1/3} = \sigma_\beta^{1/3}. \tag{378}$$

In the isotropic limit,

$$\left(\frac{\lambda_\beta}{l} \right) \rightarrow \eta_B, \tag{379}$$

and Eq. (377) is reduced to a Batchelor scale:

$$\eta_B \sim \left(\frac{\nu_\beta D_\beta^2}{\varepsilon} \right)^{1/4}.$$

(380)

However, Eq. (370) already sets forth

$$l \to \eta.$$

(381)

In addition, now let

$$l_\beta \to \eta_\beta.$$

(382)

Then, in terms of Eqs. (381) and (382), Eq. (377) is reduced to an original microscale:

$$\eta_\beta \sim \eta^{1/3} \left(\frac{\nu_\beta D_\beta^2}{\varepsilon} \right)^{1/6}.$$

(383)

In terms of Eq. (380) this can be rearranged as

$$\eta_\beta \sim \left(\eta \eta_B^2 \right)^{1/3},$$

(384)

a *mesomicroscale* based on a weighted average of the Kolmogorov and Batchelor scales, or in terms of Eq. (371), as

$$\eta_\beta \sim \left(\frac{\nu_\beta^{5/3} D_\beta^{4/3}}{\varepsilon} \right)^{1/4}.$$

(385)

Note that η_B is the isotropic scale of the isotropic b-balance, while η_β is the isotropic scale of the lower limit of the homogeneous b-balance. In a manner identical to that of Eqs. (369) and (377), the ratio of Eqs (371) and (385) yields (recall Eq. 378)

$$\frac{\eta}{\eta_\beta} = \sigma_\beta^{1/3}.$$

(386)

Experimental literature supports the relevance of η_β rather than η_B for mass transfer.

Now let the turbulent forced diffusion flame over a horizontal fuel be controlled by a sublayer of thickness η_β. Then the averaged burning rate over a length l of the fuel becomes.

$$\frac{M'}{\rho D} = B \frac{l}{\eta_\beta} = CB \left(\frac{l}{\eta} \right) \left(\frac{\eta}{\eta_\beta} \right),$$

(387)

or in terms of Eqs. (349), (373) and (386),

$$\frac{M'}{\rho D} = \frac{C_1 B \, \mathrm{Re}_\beta^{3/4} \sigma_\beta^{1/3}}{(1 + C_0 B)^n},$$

(388)

or in terms of Eqs. (336) and (338),

$$\frac{M'}{\rho D} = \frac{C_1 B}{(1 + C_0 B)^n} \left(\frac{\text{Re}}{1 + B'} \right)^{3/4} \left(\frac{1 + B'}{1 + B} \right)^{1/3} \sigma^{1/3}. \tag{389}$$

This leads to

$$\frac{M'}{\rho D} = \frac{C_1 B \, \text{Re}^{3/4} \sigma^{1/3}}{(1 + C_0 B)^n (1 + B')^{5/12} (1 + B)^{1/3}}. \tag{390}$$

For $\chi \sim 1$ and $\sigma \sim 1$, $B' \sim B$, and Eq. (390) reduces to

$$\frac{M'}{\mu \, \text{Re}^{3/4}} = \frac{C_1 B}{(1 + C_0 B)^n (1 + B)^{3/4}}. \tag{391}$$

For $B = 0$, the experimental literature gives

$$C_1 = 0.0396, \qquad \text{Re} \leq 10^5.$$

For $B \to \infty$, noting the unavailability of a Spalding-flavored turbulent study, assume that the fuel consumption approaches a constant (different from that of Emmons). This requires that

$$n = \tfrac{1}{4}.$$

Then

$$\frac{M'}{\mu \, \text{Re}^{3/4}} = \frac{0.0396 B}{(1 + C_0 B)^{1/4} (1 + B)^{3/4}}, \tag{392}$$

and the skin friction

$$C_f \, \text{Re}^{1/4} = \frac{0.0791}{(1 + C_0 B)^{1/4} (1 + B)^{3/4}}. \tag{393}$$

The aforementioned Arpaci studies on natural convection usually lead to $C_0 \ll 1$. The experimental literature on the present problem is quite scarce for a reliable estimate of C_0. Here the past experiments on skin friction considered by Marxman and Gilbert [69] and Marxman [68] are used for an estimate. A least squares fit also leads to a very small C_0, which is well within the uncertainty of the data. Accordingly,

$$C_0 \cong 0 \tag{394}$$

is assumed. Then to first order,

$$\frac{C_f}{(C_f)_{B=0}} = \frac{1}{(1 + B)^{3/4}}. \tag{395}$$

Figure 19 shows the correlation of the data with Eq. (395). Extensive new data are needed before a reasonable estimate can be made for C_0.
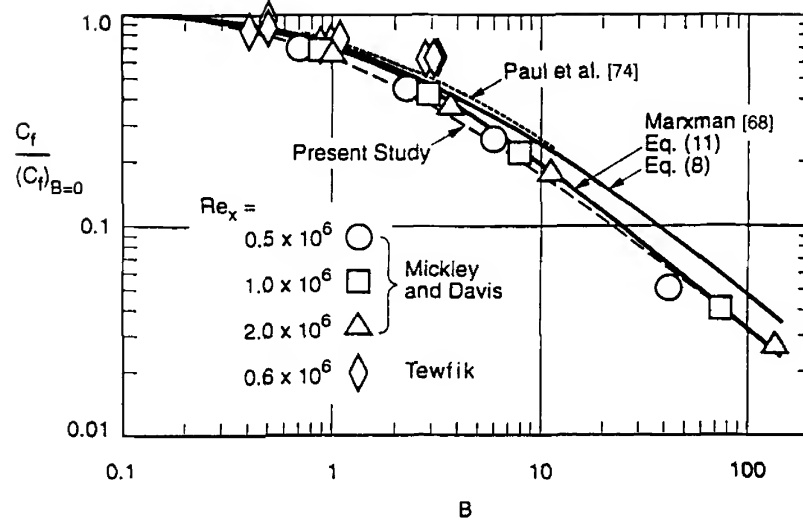
Fig. 19. Correlation data with Eq. (395). Re, Reynolds; B, transfer number.

2. Natural Flame (Pool Fire)

Again, we consider a dimensional review of laminar flames that proves convenient later.

a. Laminar Flame From the work of Spalding [80] on natural flames, the balance of momentum integrated over the boundary layer thickness δ is

$$\frac{d}{dx} \int_0^\delta \rho u^2 \, dy + \left(\mu \frac{\partial u}{\partial y} \right)_w = g \int_0^\delta (\rho_\infty - \rho) \, dy, \qquad (396)$$

where ρ is the density, u longitudinal velocity, μ dynamic viscosity, and the subscripts w and ∞ are the wall (fuel surface) and ambient conditions, respectively. In addition, the balance of the Schvab-Zeldovich (heat plus oxidizer) property integrated over the boundary layer thickness δ_β is

$$\frac{d}{dx} \int_0^{\delta_\beta} \rho u (b_\infty - b) \, dy - B(\rho v)_w = \left(\rho D \frac{\partial b}{\partial y} \right)_w, \qquad (317)$$

where b and B are already defined in Eqs. (318) to (320).

Following Arpaci and Selamet [15], on dimensional grounds Eq. (396) yields

$$U \frac{U}{l} \delta + \nu \frac{U}{\delta} \sim g \left(\frac{\Delta \rho}{\rho} \right) \delta, \qquad (397)$$

where U is a characteristic longitudinal velocity and l is a length scale characterizing the direction of flow. Similarly, Eq. (317) yields

$$U\frac{B}{l} \sim v_w\frac{B}{\delta_\beta} + D\frac{B}{\delta_\beta^2}.$$ (326)

In terms of the surface mass balance

$$\rho v_w \sim \rho D\frac{B}{\delta_\beta},$$ (327)

Eq. (326) may be rearranged as

$$U\frac{B}{l} \sim D(1 + B)\frac{B}{\delta_\beta^2},$$ (398)

and in terms of the Squire postulate

$$\delta \sim \delta_\beta,$$ (399)

Eq. (397) becomes

$$U\frac{U}{l} + \nu\frac{U}{\delta_\beta^2} \sim g\left(\frac{\Delta\rho}{\rho}\right).$$ (400)

For notational convenience, let

$$D_\beta = D(1 + B).$$ (401)

Then, Eq. (398) is reduced to

$$U\frac{B}{l} \sim D_\beta\frac{B}{\delta_\beta^2}.$$ (402)

Clearly Eqs. (400) and (402) can be obtained directly from the corresponding differential formulations, provided D_β is assumed for diffusivity in the latter.

A dimensionless number that describes buoyancy-driven diffusion flames may now be obtained by coupling Eqs. (400) and (402). Because velocity is a dependent variable for any buoyancy-driven flow, its elimination between these equations yields

$$\frac{l}{\delta_\beta^4}\left(1 + \frac{D_\beta}{\nu}\right) \sim \frac{g}{\nu D_\beta}\left(\frac{\Delta\rho}{\rho}\right),$$ (403)

which in terms of a flame Schmidt number

$$\sigma_\beta \sim \frac{\nu}{D_\beta}$$ (404)

and a flame Rayleigh number

$$\mathrm{Ra}_\beta = \frac{g}{\nu D_\beta}\left(\frac{\Delta\rho}{\rho}\right)l^3, \tag{405}$$

may be rearranged as

$$\frac{l}{\delta_\beta} \sim \Pi_\beta^{1/4}, \tag{406}$$

where

$$\Pi_\beta \sim \left(\frac{\sigma_\beta}{1 + \sigma_\beta}\right)\mathrm{Ra}_\beta \tag{407}$$

is the dimensionless number appropriate for buoyancy-driven diffusion flames. Actually, the numerical 1 in Eq. (407) is an unknown constant because of the dimensional nature of the foregoing arguments. In addition, in view of

$$\frac{\Delta\rho}{\rho} \sim \frac{\rho_\infty - \rho_f}{\rho_f} = \frac{T_f - T_\infty}{T_\infty}, \tag{408}$$

the Rayleigh number may be written more appropriately as

$$\mathrm{Ra}_\beta = \frac{g(T_f - T_\infty)l^3}{\nu D_\beta T_\infty}. \tag{409}$$

Now in terms of a (fuel) mass transfer coefficient h_β,

$$\mathrm{Sh}_\beta = \frac{h_\beta l}{D} \sim \frac{l}{\delta_\beta}, \tag{410}$$

where Sh_β is a flame Sherwood number. Then the fuel consumption in a laminar diffusion flame of size l,

$$\frac{M'}{\rho D} = \frac{m''_w l}{\rho D} = \mathrm{Sh}_\beta B \sim B \frac{l}{\delta_\beta} \tag{411}$$

(m''_w being the fuel consumption per unit area), may be written in terms of Eq. (406) as

$$\frac{M'}{\rho D} \sim B\Pi_\beta^{1/4}, \tag{412}$$

or explicitly as

$$\frac{M'}{\rho D} \sim B\left(\frac{\sigma_\beta}{1 + \sigma_\beta}\right)^{1/4}\mathrm{Ra}_\beta^{1/4}, \tag{413}$$

or in terms of the usual Rayleigh number for mass transfer,

$$\mathrm{Ra} = \frac{g}{\nu\alpha}\left(\frac{\Delta\rho}{\rho}\right)l^3 \tag{414}$$

as

$$\frac{M'}{\rho D\,\mathrm{Ra}^{1/4}} \sim B\left(\frac{\sigma_\beta}{1+\sigma_\beta}\right)^{1/4}\left(\frac{D}{D_\beta}\right)^{1/4}. \tag{415}$$

Now, we introduce the definition of the usual Schmidt number

$$\sigma = \frac{\nu}{D} \tag{416}$$

and combine Eqs. (401), (404), and (416) for

$$\frac{\sigma_\beta}{\sigma} \sim \frac{D}{D_\beta} = \frac{1}{1+B}. \tag{417}$$

Then, noting the proportionality and equality relations of Eq. (417), an equality replacing Eq. (415) may be written as

$$\frac{M'}{\rho D\,\mathrm{Ra}^{1/4}} \approx \frac{C_1 B}{(C_0 + B)^{1/4}(1 + B)^{1/4}}, \tag{418}$$

where C_0 and C_1 remain to be determined from a computer or laboratory experiment, or from an analytical solution. Before proceeding to these coefficients, however, a number of important facts can be deduced from Eq. (418).

For small values of B,

$$\lim_{B\to 0}\left(\frac{M'}{\rho D\,\mathrm{Ra}^{1/4}}\right) \to B. \tag{419}$$

For $B > 1$, inertial effects are negligible. Either eliminating the inertial term of the momentum balance (Eq. (400)), or noting Eq. (417) and the definition of

$$\sigma_\beta = \left(\frac{\text{Viscous force}}{\text{Inertial force}}\right)\left(\frac{\text{Flow of } B}{\text{Diffusion of } B}\right), \tag{420}$$

and letting $\sigma_\beta \to \infty$ in

$$\frac{\sigma_\beta}{1+\sigma_\beta} = \frac{1}{1+\sigma_\beta^{-1}} \to 1, \tag{421}$$

Eq. (418) is reduced to

$$\frac{M'}{\rho D\,\mathrm{Ra}^{1/4}} \to B^{3/4}, \qquad B > 1. \tag{422}$$

This is a well known but, so far, assumed to be an experimentally supported empirical result. For $B \gg 1$,

$$\lim_{B \to \infty} \left(\frac{M'}{\rho D \, \mathrm{Ra}^{1/4}} \right) \to B^{1/2}. \tag{423}$$

Hereafter, Eq. (418) is called LM (laminar model).

Now for numerical values of C_0 and C_1, reconsider Spalding's result, which, after a minor algebraic correction,[1] yields for the fuel consumption averaged over a length l

$$\frac{M'}{\rho D \, \mathrm{Ra}^{1/4}} = \frac{0.34115B}{\left[\frac{1}{a^2} \left(\frac{1+B}{5.5-a} \right)^2 + 0.6\sigma \frac{1}{a^3} \left(\frac{1+B}{5.5-a} \right) \right]^{1/4}}, \tag{424}$$

or with some rearrangement,

$$\frac{M'}{\rho D \, \mathrm{Ra}^{1/4}} = \frac{0.34115[a(5.5-a)]^{1/2}B}{\left[\left(1 + \frac{0.6(5.5-a)\sigma}{a} \right) + B \right]^{1/4} (1+B)^{1/4}}, \tag{425}$$

where

$$a = \frac{2}{B} \left[\left(1 + \frac{3}{2} B \right)^{1/2} - 1 \right]. \tag{426}$$

A comparison of Eqs. (418) and (425) readily suggests that C_0 and C_1 are not actually constants but depend on B, as expected in view of the B-dependence of the b-profiles (Fig. 20). Thus

$$\frac{M'}{\rho D \, \mathrm{Ra}^{1/4}} = \frac{C_1(B)B}{[C_0(B) + B]^{1/4}(1+B)^{1/4}}, \tag{427}$$

where

$$C_0(B) = 1 + \frac{0.6(5.5-a)\sigma}{a}, \tag{428}$$

$$C_1(B) = 0.34115[a(5.5-a)]^{1/2}. \tag{429}$$

Figure 21 shows the dependence of C_0 and C_1 on B. Note that when Spalding is repeated with a linear b-profile, Eqs. (424) and (425) are

---

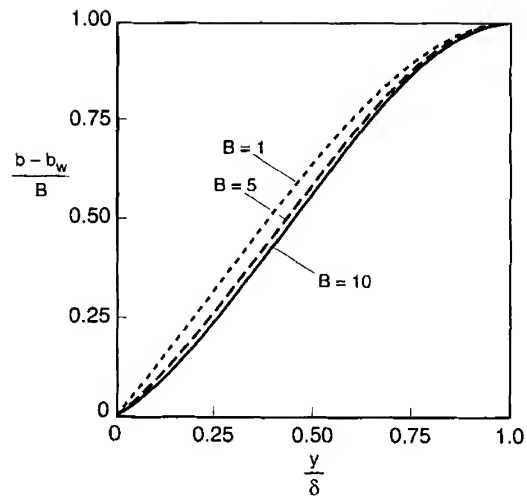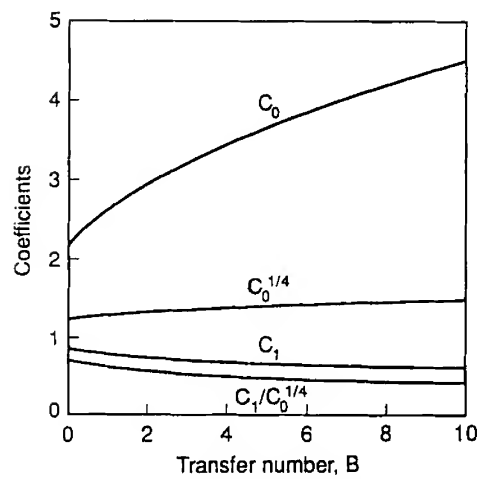[1] Each factor $(3.25 + a)$ in Spalding's result needs to be replaced by $(5.5 - a)$.

FIG. 20. Schvab-Zeldovich profiles.

FIG. 21. Dependence of C_0 and C_1 on the transfer number B is shown.

reduced to

$$\frac{M'}{\rho D \, \text{Ra}^{1/4}} = \frac{0.34115}{\left[\left(\dfrac{1+B}{5.25}\right)^2 + 0.6\sigma\left(\dfrac{1+B}{5.25}\right)\right]^{1/4}}, \tag{430}$$

$$\frac{M'}{\rho D \, \text{Ra}^{1/4}} = \frac{0.34115(5.25)^{1/2}B}{\left[1 + (0.6)(5.25)\sigma + B\right]^{1/4}(1+B)^{1/4}}. \tag{431}$$

and the B-dependence[2] of Eq. (431) turns out to be identical to that of Eq. (418).

For an evaluation of the constants involved with LM, first consider the practical range of B. Assuming an approximate upper bound of 10 for both B and B', the fuel consumption versus B obtained by Spalding, as well as from the computational study of Kim, de Ris, and Kroesser [53] (KRK), are plotted in Fig. 22. Because Spalding employs the Squire postulate but KRK does not, the close agreement also indicates the validity of this postulate for buoyancy-driven diffusion flames. An overprediction of the burning rate by Spalding should be expected in view of the fact that Spalding assumes a constant $\Delta\rho/\rho$ based on maximum buoyancy. Thus it

[2] It is interesting to note that for small values of B, $a \rightarrow 3/2$, and Eq. (425) is reduced to

$$\frac{M'}{\rho D \, \text{Ra}^{1/4}} = \frac{0.34115(6)^{1/2}B}{\left[1 + (0.6)(2.6667)\sigma + B\right]^{1/4}(1+B)^{1/4}}$$

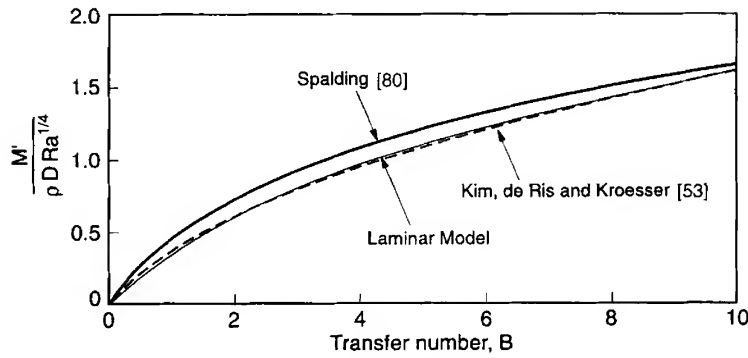whose B-dependence also is identical to that of Eq. (418).

FIG. 22. Fuel consumption versus the transfer number B, obtained from Spalding and from the computational study of Kim, de Ris, and Kroesser (KRK) [53]. Ra, Rayleigh.

is reasonable to assume that KRK is numerically somewhat more accurate than Spalding's result because of its computational rather than approximate integral solution. Here, a least square fit of Eq. (418) to KRK over the range $0 \leq B \leq 10$ should be expected. Instead, a simpler curve-fitting procedure in parallel to that employed for turbulent flame is followed here.

In the limit of $B \to 0$, the fuel consumption approaches the heat transfer correlation; that is

$$\lim_{B \to 0} \left(\frac{M'}{\rho DB} \right) \to \mathrm{Nu}. \tag{432}$$

The computational solution, available for the classic problem of natural convection next to a vertical flat plate, for $\mathrm{Pr} = 0.73$, gives

$$\mathrm{Nu} = 0.52\,\mathrm{Ra}^{1/4}, \tag{433}$$

where the coefficient of 0.52 is based on the experimental results of Schmidt and Beckmann [77]. Thus in view of Eq. (418),

$$\lim_{B \to 0} \left(\frac{M'}{\rho DB} \right) \to \frac{C_1}{C_0^{1/4}}\,\mathrm{Ra}^{1/4}. \tag{434}$$

Equations (432) and (433) yield

$$\frac{C_1}{C_0^{1/4}} = 0.52. \tag{435}$$

Then $1/C_0 = 0.90$ is found by matching Eq. (418) with KRK at $B = 2$. With these values, Eq. (418) becomes

$$\frac{M'}{\rho D\,\mathrm{Ra}^{1/4}} = \frac{0.52B}{(1 + 0.90B)^{1/4}(1 + B)^{1/4}}, \quad B \leq 10. \tag{436}$$

Figure 22 shows the close agreement between Eq. (436) and KRK despite one point-matching. Also interesting is the fact that the correlation is obtained with some mean values of C_0 and C_1 without taking into account their dependence on B. However, because the dependence of C_1 on B is weak and that of C_0 is weakened by its fractional power involved with Eq. (436), the result is not surprising. This is indeed an important fact because, under turbulent conditions, the dependence of these coefficients on B is difficult to estimate.

Next, the foregoing dimensional arguments on laminar flames are extended to turbulent flames and pool fires by following the recent work of Arpaci and Selamet [15].

b. Turbulent Flame Let the instantaneous velocity and the Schvab-Zeldovich (heat plus oxidizer) property of a buoyancy-driven turbulent diffusion flame be decomposed into a temporal mean (denoted by capital letters) and fluctuations,

$$\tilde{u}_i = U_i + u_i \quad \text{and} \quad \tilde{b} = B + b.$$

For a homogeneous pure shear flow (in which all averaged except U_i and B are independent of position and in which $\partial B/\partial x_i$ and S_{ij} are constant), the mean kinetic energy of velocity fluctuations and the rms of the Schvab-Zeldovich property yield

$$\mathscr{B} = \mathscr{P} + \varepsilon \tag{437}$$

and

$$\mathscr{P}_\beta = \varepsilon_\beta, \tag{359}$$

where

$$\mathscr{B} = -g_i \overline{u_i \theta}/\Theta_o \tag{438}$$

is the buoyant production (imposed); where

$$\mathscr{P} = -\overline{u_i u_j} S_{ij} \tag{360}$$

is the inertial production (induced); where

$$\varepsilon = 2\nu_\beta \overline{s_{ij} s_{ij}} \tag{361}$$

is the dissipation of turbulent energy; and where

$$\mathscr{P}_\beta = -\overline{u_i b} \frac{\partial B}{\partial x_i} \tag{362}$$

and

$$\varepsilon_\beta = D_\beta \overline{\left(\frac{\partial b}{\partial x_i}\right)\left(\frac{\partial b}{\partial x_i}\right)} \tag{363}$$

are the production and dissipation of the Schvab-Zeldovich property, respectively. Note that incorporation of the boundary mass transfer into the b-balance is taken into account by considering the b-dissipation in terms of D_β. For buoyancy-driven flows, kinetic dissipation retains its usual form.

On dimensional grounds, Eqs. (437) and (359) lead to

$$\mathscr{B} \sim \frac{u^3}{l} + \nu \frac{u^2}{\lambda^2}, \tag{439}$$

$$u_\beta \frac{b^3}{l} \sim D_\beta \frac{b^2}{\lambda_\beta^2}. \tag{365}$$

Here λ and λ_β are the Taylor microscales associated with momentum and the Schvab-Zeldovich property. Note that dimensional arguments lead to the same scales for homogeneous as well as nonhomogeneous flows.

Now, for a buoyancy-driven turbulent diffusion flame, following the Squire postulate, assume that

$$u \sim u_\beta, \qquad \lambda \sim \lambda_\beta. \tag{440}$$

Then elimination of the velocity between Eqs. (439) and (365) gives

$$\lambda_\beta \sim l^{1/3}(1 + \sigma_\beta)^{1/6}\left(\frac{D_\beta^3}{\mathscr{B}}\right)^{1/6}. \tag{441}$$

Under conditions of isotropic flow,

$$\left(\frac{\lambda_\beta}{l}\right) \rightarrow \eta_\beta, \tag{442}$$

and Eq. (441) leads to a Kolmogorov microscale:

$$\eta_\beta \sim (1 + \sigma_\beta)^{1/4}\left(\frac{D_\beta^3}{\mathscr{B}}\right)^{1/4}, \tag{443}$$

where, on dimensional grounds,

$$\mathscr{B} \sim gu\,\theta/\Theta_o, \tag{444}$$

with θ_o being the temperature of isobaric ambient. The foregoing microscale is identical in form to that recently discovered by Arpaci [2, 3] for buoyancy-driven turbulent flows. Furthermore, for $\sigma_\beta \rightarrow 0$, Eq. (443) is reduced in form to the microscale introduced by Oboukhov [72] and Corrsin [28]:

$$\eta_\beta \sim \left(\frac{D_\beta^3}{\mathscr{B}}\right)^{1/4}. \tag{445}$$

In addition, for $\sigma_\beta \rightarrow \infty$, Eq. (443) is reduced in form to the scale proposed by Batchelor [17]:

$$\eta_\beta \sim \left(\frac{\sigma_\beta D_\beta^3}{\mathscr{B}}\right)^{1/4} = \left(\frac{\nu D_\beta^2}{\mathscr{B}}\right)^{1/4}. \tag{446}$$

Now let

$$\theta \sim \Delta T, \tag{447}$$

where ΔT is the imposed temperature difference, and note for gaseous media that

$$\Theta_o^{-1} = \beta. \tag{448}$$

Then, Eq. (444) becomes

$$\mathscr{B} \sim g\,\beta u\,\Delta T, \qquad (449)$$

or in view of Eq. (365),

$$\mathscr{B} \sim g\,\beta D_\beta l\,\Delta T/\lambda_\beta^2. \qquad (450)$$

Insertion of Eq. (450) into Eq. (441), in terms of the buoyant force rather than buoyant energy, leads to the Taylor microscale:

$$\lambda_\beta \sim l^{1/4}\bigl(1 + \sigma_\beta\bigr)^{1/4}\left(\frac{D_\beta^2}{g\beta\,\Delta T}\right)^{1/4}, \qquad (451)$$

or under the isotropy stated by Eq. (442), to the Kolmogorov microscale:

$$\eta_\beta \sim \bigl(1 + \sigma_\beta\bigr)^{1/3}\left(\frac{D_\beta^2}{g\beta\,\Delta T}\right)^{1/3}. \qquad (452)$$

Now the Taylor and Kolmogorov scales for any σ_β may be rearranged in terms of Π_β as

$$\frac{\lambda_\beta}{l} \sim \Pi_\beta^{-1/4}, \qquad (453)$$

$$\frac{\eta_\beta}{l} \sim \Pi_\beta^{-1/3}. \qquad (454)$$

Let the turbulent diffusion flame near a vertical fuel or the pool fire over a horizontal fuel be controlled by a turbulent sublayer. Assume that the thickness of this layer is characterized by η_β. Then in terms of Eq. (339), the averaged fuel consumption may be written as

$$\frac{M'}{\rho D} = B\,\frac{l}{\eta_\beta} \sim B\Pi_\beta^{1/3}, \qquad (455)$$

or explicitly as

$$\frac{M'}{\rho D} \sim B\left(\frac{\sigma_\beta}{1 + \sigma_\beta}\right)^{1/3}\mathrm{Ra}_\beta^{1/3}, \qquad (456)$$

or in terms of the usual Rayleigh number as

$$\frac{M'}{\rho D\,\mathrm{Ra}^{1/3}} \sim B\left(\frac{\sigma_\beta}{1 + \sigma_\beta}\right)^{1/3}\left(\frac{D}{D_\beta}\right)^{1/3}. \qquad (457)$$

Now rearranging Eq. (457) in terms of Eq. (401), we have

$$\frac{M'}{\rho D \, \mathrm{Ra}^{1/3}} = \frac{C_1 B}{(C_0 + B)^{1/3}(1 + B)^{1/3}}, \tag{458}$$

where C_0 and C_1 (different from those of Eq. (418)) are to be determined from the experimental literature. The one-third power law of the Rayleigh number in pool fires is supported experimentally [51, 63]. Hereafter Eq. (458) is called TM (turbulent model).

Now in a manner similar to the three regimes of laminar flames, the regimes of turbulent flames may be identified. For small values of B,

$$\lim_{B \to 0} \left(\frac{M'}{\rho D \, \mathrm{Ra}^{1/3}} \right) \to B. \tag{459}$$

For $B > 1$, inertial effects are negligible and Eq. (458) is reduced to

$$\frac{M'}{\rho D \, \mathrm{Ra}^{1/3}} \to B^{2/3}. \tag{460}$$

For $B \gg 1$,

$$\lim_{B \to \infty} \left(\frac{M'}{\rho D \, \mathrm{Ra}^{1/3}} \right) \to B^{1/3}. \tag{461}$$

The experimental data on small fires [20, 26, 27, 32] appear to correlate well with TM, as shown in Fig. 23. The original figure is taken from de Ris
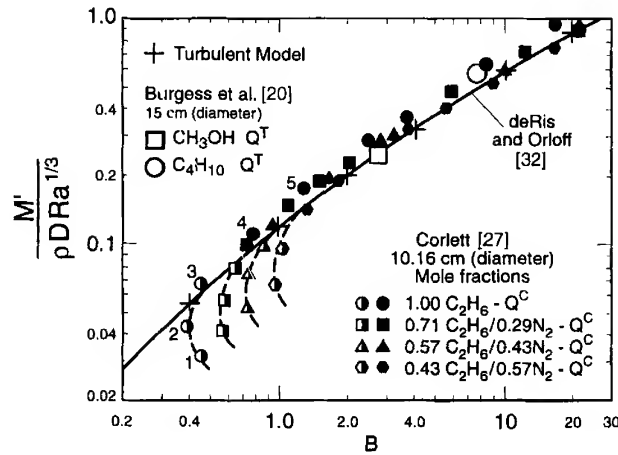
FIG. 23. Ra, Rayleigh; B, transfer number.

and Orloff who rearranged Fig. 11 of Corlett [27] for ethane–nitrogen flames burning above a 10.16-cm diameter burner and compared with their model. The open symbols in the original figure for pure ethane are deleted here because they include a radiative heat transfer component toward the burner surface. Remaining data from Corlett represents the dominant convective component of the surface heat transfer. Half-filled symbols indicate increasing heat transfer with increasing velocity of gases leaving the burner surface. Also included in Fig. 23 are two data points from Burgess *et al.* for liquid methanol and liquid butane, shown by open symbols. The low B-range is the vicinity of extinction of the flames.

Arpacı and Dec [10] recently have demonstrated, with a correlation on natural convection, the sensitivity of C_0 to experimental data. A preliminary attempt to evaluate C_0 and C_1 by a least square fit of Eq. (458) to the data of Corlett demonstrates a similar sensitivity. Here, following the approach taken in the preceding section on laminar flames, the value of $C_1/C_0^{1/3} = 0.16$ is taken from recent data of Fujii and Imura [40]. Then, at $B = 5$, $1/C_0 = 0.05$ is evaluated by fitting Eq. (458) to Corlett's data. With these values, Eq. (458) becomes

$$\frac{M'}{\rho D\, \mathrm{Ra}^{1/3}} = \frac{0.16B}{(1 + 0.05B)^{1/3}(1 + B)^{1/3}}, \tag{462}$$

which agrees very well with the correlation already given by de Ris and Orloff [32]

$$\frac{M'}{\rho D\, \mathrm{Ra}^{1/3}} = 0.16B\left[\frac{\ln(1 + B)}{B}\right]^{2/3}, \tag{463}$$

which was obtained from the stagnant film theory coupled with the empirically assumed two-thirds power law. The maximum difference between the two correlations remains less than 1.8% for the entire B-range. Despite the fact that the correlations are developed by following quite different arguments, this agreement is remarkable. Both models predict only the region beyond bifurcation for $B \le 1$.

So far, the proposed models for laminar and turbulent flames and fires exclude any effect of radiation. Because of the different intrinsic nature of radiation and conduction (or any diffusion), the Schvab-Zeldovich transformation used in the present study no longer applies to radiation-affected flames. On intuitive grounds, the emission effect of radiation (hotness of flame) already has been incorporated into the heat of combustion and the latent heat of evaporation by fractional lowering of these properties [51].
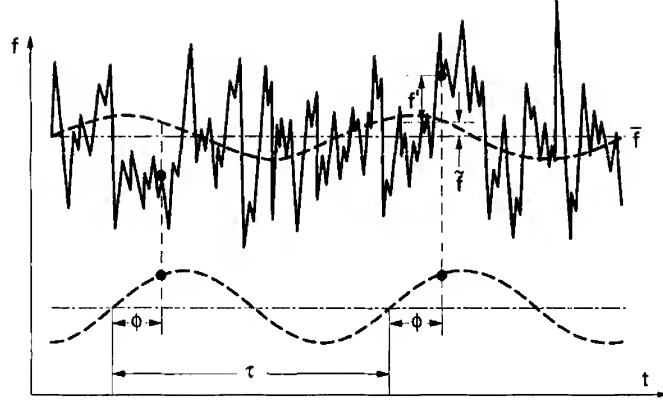
FIG. 24. Decomposition of unsteady turbulence. $\tilde{f}$, mean; f, contribution of the organized wave; f', turbulent fluctuations. Reprinted with permission by Hussain and Reynolds [49a].

B. PULSED COMBUSTION

1. Dynamics of Unsteady Turbulence

Heat transfer correlation for oscillating turbulent flows is difficult to determine solely on empirical grounds. Here, the difficulty is resolved by followed Arpaci et al. [16]. First, microscales of oscillating turbulent flows are developed. Here, results are applied to heat transfer in pulse combustor tailpipes.

Let an instantaneous fluctuating quantity $f(\mathbf{x}, t)$ with an organized wave motion be decomposed as

$$f(\mathbf{x}, t) = \bar{f}(\mathbf{x}) + \tilde{f}(\mathbf{x}, t) + f'(\mathbf{x}, t), \tag{464}$$

where $\bar{f}$ is the mean (temporal average), $\tilde{f}$ the (statistical) contribution of the organized wave, and f' the turbulent fluctuations (Fig. 24). The temporal average is

$$\bar{f}(\mathbf{x}) = \lim_{T \to \infty} \frac{1}{T} \int_0^T f(\mathbf{x}, t) \, dt, \tag{465}$$

and the phase average is

$$\langle f(\mathbf{x}, t) \rangle = \lim_{N \to \infty} \frac{1}{N} \sum_{n=0}^{N} f(\mathbf{x}, t + n\tau), \tag{466}$$

where τ is the period of the imposed wave. Then

$$\tilde{f} = \langle f \rangle - \bar{f}. \tag{467}$$

Dynamical equations are available in the literature. The phase-averaged kinetic energy of velocity fluctuations

$$K = \tfrac{1}{2}\langle u_i' u_i' \rangle \tag{468}$$

satisfies

$$\frac{DK}{Dt} = -\frac{\partial D_j}{\partial x_j} + \mathscr{P} - \varepsilon, \tag{469}$$

where

$$D_j = \left\langle u_j'\left(\frac{p'}{\rho} + \frac{1}{2}\, u_i' u_i'\right)\right\rangle + \left\langle \tilde{u}_j\, \frac{1}{2}\, u_i' u_i'\right\rangle - 2\nu\langle u_i' s_{ij}'\rangle \tag{470}$$

denotes the diffusion;

$$\mathscr{P} = -\langle u_i' u_j'\rangle\left(\bar{S}_{ij} + \tilde{S}_{ij}\right) \tag{471}$$

denotes the inertial production; and

$$\varepsilon = 2\nu\langle s_{ij}' s_{ij}'\rangle \tag{472}$$

denotes the dissipation of turbulent energy.

Thermal equations can be obtained in a similar manner. The phase-averaged rms of thermal fluctuations

$$K_\theta = \tfrac{1}{2}\langle \theta' \theta'\rangle \tag{473}$$

satisfies

$$\frac{DK_\theta}{Dt} = -\frac{\partial D_{\theta,j}}{\partial x_j} + \mathscr{P}_\theta - \varepsilon_\theta, \tag{474}$$

where

$$D_{\theta,j} = \left\langle u_j'\, \frac{1}{2}\, \theta' \theta'\right\rangle + \left\langle \tilde{u}_j\, \frac{1}{2}\, \theta' \theta'\right\rangle - \alpha\, \frac{\partial}{\partial x_j}\left\langle \frac{1}{2}\, \theta' \theta'\right\rangle \tag{475}$$

denotes the thermal flux;

$$\mathscr{P}_\theta = -\langle u_j' \theta'\rangle\left(\frac{\partial \bar{\theta}}{\partial x_j} + \frac{\partial \tilde{\theta}}{\partial x_j}\right) \tag{476}$$

denotes the thermal production; and

$$\varepsilon_\theta = \alpha\left\langle \frac{\partial \theta'}{\partial x_j}\, \frac{\partial \theta'}{\partial x_j}\right\rangle \tag{477}$$

denotes the thermal dissipation. For a homogeneous flow, Eqs. (469) and (474) are reduced to

$$\frac{\partial K}{\partial t} = \mathscr{P} - \varepsilon, \tag{478}$$

$$\frac{\partial K_\theta}{\partial t} = \mathscr{P}_\theta - \varepsilon_\theta. \tag{479}$$

In the next section, kinetic and thermal microscales for a pulsating turbulent flow are developed.

2. Microscales

On dimensional grounds, Eqs. (478) and (479) lead to

$$\omega u^2 + u^2 \left(\frac{U + U_0}{l} \right) \sim \nu \frac{u^2}{\lambda^2}, \tag{480}$$

$$\omega \theta^2 + u_\theta \theta \left(\frac{\Theta + \Theta_0}{l} \right) \sim \alpha \frac{\theta^2}{\lambda_\theta^2}, \tag{481}$$

where u, u_θ, and θ denote the rms of velocity and temperature fluctuations, respectively; U_0 and Θ_0 are the amplitude of velocity and temperature oscillations, respectively; ω is the imposed frequency; l is the integral scale; and λ and λ_θ are the kinetic and thermal Taylor scales, respectively. Let

$$u \sim U + U_0, \qquad \theta \sim \Theta + \Theta_0. \tag{482}$$

Then Eqs. (480) and (481) become

$$\omega u^2 + \frac{u^3}{l} \sim \nu \frac{u^2}{\lambda^2}, \tag{483}$$

$$\omega \theta^2 + u_\theta \frac{\theta^2}{l} \sim \alpha \frac{\theta^2}{\lambda_\theta^2}, \tag{484}$$

or relative to spatial production

$$\frac{u^3}{l} \left(1 + \frac{\omega l}{u} \right) \sim \nu \frac{u^2}{\lambda^2}, \tag{485}$$

$$u_\theta \frac{\theta^2}{l} \left(1 + \frac{\omega l}{u_\theta} \right) \sim \alpha \frac{\theta^2}{\lambda_\theta^2}. \tag{486}$$

The ratio between Eqs. (485) and (486) gives

$$\frac{u}{u_\theta}\left(\frac{1 + (\omega l/u)}{1 + (\omega\lambda/u_\theta)}\right) \sim \frac{\nu}{\alpha}\left(\frac{\lambda_\theta}{\lambda}\right)^2. \tag{487}$$

For small departures from the analogy existing between momentum and heat,

$$\frac{u}{u_\theta} \sim \frac{\lambda_\theta}{\lambda}, \tag{488}$$

and Eq. (487) becomes

$$\frac{\lambda}{\lambda_\theta} = \mathrm{Pr}^{1/3}\left(\frac{1 + (\omega l/u_\theta)}{1 + (\omega l/u)}\right)^{1/3}. \tag{489}$$

In addition, following arguments similar to those leading to the mesomicroscale introduced in Part I,

$$\frac{\eta}{\eta_\theta} = \mathrm{Pr}^{1/3}\left(\frac{1 + (\omega\lambda/u_\theta)}{1 + (\omega\lambda/u)}\right)^{1/3}, \tag{490}$$

or in terms of Eq. (488),

$$\frac{\eta}{\eta_\theta} = \mathrm{Pr}^{1/3}\left[1 + \frac{\omega\lambda}{u}(\mathrm{Pr}^{1/3} - 1)\right]^{1/3}. \tag{491}$$

Furthermore, for local scales, Eqs. (485) and (486) become

$$\frac{u^3}{\lambda}\left(1 + \frac{\omega\lambda}{u}\right) \sim \nu\frac{u^2}{\eta^2}, \tag{492}$$

$$u_\theta\frac{\theta^2}{\lambda}\left(1 + \frac{\omega\lambda}{u_\theta}\right) \sim \alpha\frac{\theta^2}{\eta_\theta^2}, \tag{493}$$

and the ratio between Eqs. (485) and (492) and that between Eqs. (486) and (493) give

$$\left(\frac{\eta}{\lambda}\right)^2 \sim \frac{\lambda}{l}\left(\frac{1 + (\omega l/u)}{1 + (\omega\lambda/u)}\right), \tag{494}$$

$$\left(\frac{\eta_\theta}{\lambda_\theta}\right)^2 \sim \frac{\lambda}{l}\left(\frac{1 + (\omega l/u_\theta)}{1 + (\omega\lambda/u_\theta)}\right), \tag{495}$$

which are the extensions of Tennekes model to thermal intermittency.

The foregoing kinetic and thermal scales are employed in the next section dealing with models for skin friction and heat transfer in oscillating turbulent flows.

3. Skin Friction and Heat Transfer

Let the momentum sublayer of a turbulent flow be characterized by η, and let the entire dissipation be confined to this layer. Then, the usual definition of skin friction can be written in terms of local scales as

$$f = \frac{\tau_w}{\frac{1}{2}\rho u^2} \sim \frac{\mu(u/\eta)}{\frac{1}{2}\rho u^2},$$ (496)

or as

$$\left(\tfrac{1}{2}f\right)\mathrm{Re} \sim \frac{l}{\eta},$$ (497)

where

$$\mathrm{Re} = \frac{ul}{\nu},$$ (498)

is the Reynolds number based on u and l. Now rearrange Eq. (485) and the limit of Eq. (494) for $\omega \to \infty$ as

$$\frac{l}{\lambda} \sim \mathrm{Re}^{1/2}\left(1 + \frac{\omega l}{u}\right)^{1/2}$$ (499)

and

$$\frac{\eta}{l} \sim \left(\frac{\lambda}{l}\right)^{3/2}.$$ (500)

Then in terms of Eqs. (500) and (499), Eq. (497) becomes

$$\frac{1}{2}f \sim \mathrm{Re}^{-1/4}\left(1 + \frac{\omega l}{u}\right)^{3/4}.$$ (501)

The limit of Eq. (501) for $\omega \to 0$,

$$\tfrac{1}{2}f \sim \mathrm{Re}^{-1/4},$$ (502)

is known to correlate turbulent data on flat plates.

Now let the heat transfer be expressed in terms of the local thermal scale η_θ:

$$\mathrm{Nu} \sim \frac{l}{\eta_\theta},$$ (503)

where Nu is the usual Nusselt number. The ratio of Eqs. (497) and (503) gives

$$\frac{\mathrm{Nu}}{\mathrm{Re}} \sim \frac{1}{2}f\left(\frac{\eta}{\eta_\theta}\right),$$ (504)

which in terms of Eq. (491) can be rearranged for the Stanton number:

$$\mathrm{St}\,\mathrm{Pr}^{2/3} = \frac{1}{2}f\left[1 + \frac{\omega\lambda}{u}(\mathrm{Pr}^{1/3} - 1)\right]^{1/3}, \qquad (505)$$

or in terms of Eqs. (491) and (501) as

$$\mathrm{Nu} \sim \mathrm{Re}^{3/4}\left(1 + \frac{\omega l}{u}\right)^{3/4}\left[1 + \frac{\omega\lambda}{u}(\mathrm{Pr}^{1/3} - 1)\right]^{1/3}. \qquad (506)$$

Finally, recalling Eq. (482) and assuming that $U \gg U_0$, Eq. (506) is rearranged as

$$\mathrm{Nu} \sim \overline{\mathrm{Re}}^{3/4}\left(1 + \frac{U_0}{U}\right)^{3/4}\left(1 + \frac{\omega l}{U}\right)^{3/4}\left[1 + \frac{\omega l}{U}\overline{\mathrm{Re}}^{1/2}(\mathrm{Pr}^{1/3} - 1)\right]^{1/3}, \qquad (507)$$

or for $\mathrm{Pr} = 1$ as

$$\mathrm{Nu} \sim \overline{\mathrm{Re}}^{3/4}\left(1 + \frac{U_0}{U}\right)^{3/4}\left(1 + \frac{\omega l}{U}\right)^{3/4}, \qquad (508)$$

where $\overline{\mathrm{Re}} = Ul/\nu$.

Using this model in the next section, we correlate the heat transfer data on pulse combustor tailpipes.

4. Pulse Combustion

Enhanced rates of heat transfer in pulse combustor tailpipes result from large flow oscillations (caused by the acoustic resonance of the combustor) superimposed on turbulent velocity fluctuations. The literature on the effect of flow oscillations on heat transfer rates in turbulent flows is rather controversial. Heat transfer rates in pulse combustor tailpipes have been found to vary from 70% less [1], to 240% greater [48] than those of steady flow at the same mean Reynolds number. Other oscillating flows have shown decreases in the heat transfer coefficient of up to 20% [62] and increases of up to a factor of 5 [41] over steady flow conditions. Part of these inconsistencies may be explained by the greatly different flow conditions investigated. In addition, these studies lacked systematic variation of the important flow parameters, and many were conducted at frequencies much lower than the 45 to 200 Hz range typical of pulse combustors. The effect of flow oscillations on pulse combustor tailpipe heat transfer has recently been clarified by the experimental study of Dec and Keller [30]. These authors systematically varied the important flow parameters—e.g., frequency, velocity oscillation amplitude, and mean flow rate—and assessed the effects of these parameters on heat transfer.

The heat transfer model introduced in the preceding section is used here for a correlation of the experimental data of Dec and Keller. Previous modeling of oscillating flow heat transfer has been based on quasi-steady assumptions, which are valid only in flows with oscillation frequencies lower than those typical of pulse combustors, and results in a heat transfer correlation that is independent of frequency. The heat transfer data of Dec and Keller, which were obtained over a range of typical pulse combustor frequencies (54 to 101 Hz), clearly show a frequency dependence that cannot be explained by a quasi-steady model.

Now, with some constants, replacing Eq. (508) with an equality and following Arpaci et $al.$ [16], we have

$$\text{Nu} = C_0 \overline{\text{Re}}^{3/4}\left(1 + C_1 \frac{U_0}{U} + C_3 \frac{\omega l}{U} + C_4 \frac{U_0 \omega l}{U^2}\right). \tag{509}$$

Experimental results show that

$$C_3 \ll C_1, C_4. \tag{510}$$

After dropping $C_3(\omega l/U)$ and introducing $C_2 = C_4/C_1$, Eq. (509) becomes

$$\text{Nu} = C_0 \overline{\text{Re}}^{3/4}\left[1 + C_1 \frac{U_0}{U}\left(1 + C_2 \frac{\omega l}{U}\right)\right]^{3/4}. \tag{511}$$

Furthermore, let the integral scale l be the hydraulic diameter D of the tailpipe,[3] and following Dec and Keller, assume that $\omega l = (\omega - \omega_0)D$, where ω_0 is the pulsating frequency below which a quasi-steady model independent of frequency yields correct results. Numerical constants determined by a least squares fit of experimental data are $C_0 = 0.0291$, $C_1 = 0.1762$, $C_2 = 8.483$, and $f_0 = \omega_0/2\pi = 45.44$, with a variance of 3.23. With these values, Eq. (511) becomes

$$\text{Nu} = 0.0291 \overline{\text{Re}}^{3/4}\left\{1 + 0.176 \frac{U_0}{U}\left[1 + 8.48 \frac{(f - 45)D}{U}\right]\right\}^{3/4}. \tag{512}$$

Figure 25 shows the results of Eq. (512). In view of the complexity of the problem, the agreement between the data and the correlation is remarkably good. For $f \leq f_0$, Eq. (512) reduces to a quasi-steady model:

$$\text{Nu} = 0.029 \overline{\text{Re}}^{3/4}\left(1 + 0.21 \frac{U_0}{U}\right)^{3/4}. \tag{513}$$

[3] The natural frequency of a resonator depends on the length of the orifice or tailpipe. Using a sectional tailpipe, Dec and Keller are able to operate a pulse combustor over a frequency range. In a correlation given by Eq. (512), frequency is a measured input and the length scale involved with $\omega l/U$ is immaterial.
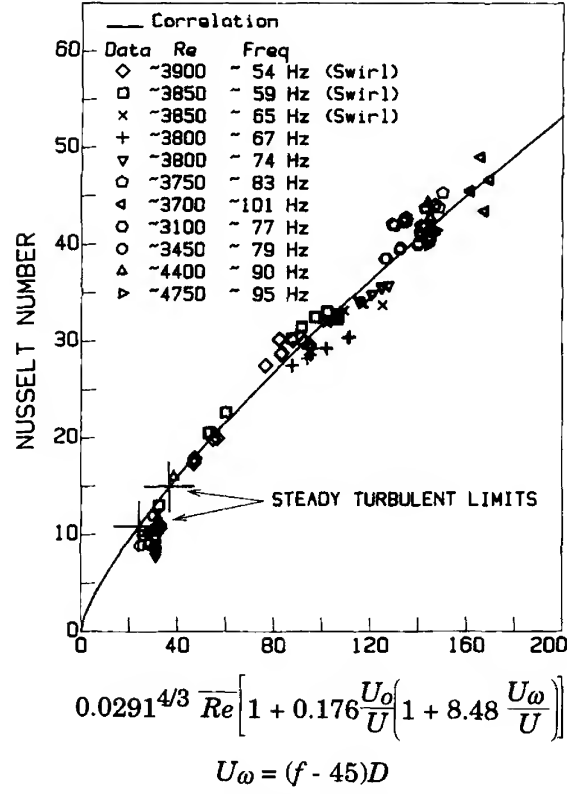
$$0.0291^{4/3} \, \overline{Re}\left[1 + 0.176\frac{U_o}{U}\left(1 + 8.48 \, \frac{U\omega}{U}\right)\right]$$

$$U\omega = (f - 45)D$$

Fig. 25. Correlation of the experimental data with Eq. (512).

For steady flow, $U_0 = 0$, and Eq. (513) reduces to a steady model:

$$Nu = 0.029\overline{Re}^{3/4}. \qquad (514)$$

This model is quite close to the Colburn correlation for heat transfer in steady turbulent flows with $Pr = 1$:

$$Nu = 0.023\overline{Re}^{0.8}. \qquad (515)$$

Thus the correlation given by Eq. (512) not only collapses and correlates all the experimental data, but also reduces to the correct limits for $f \to f_0$ and $U_0 \to 0$. However, before any claim on the universal nature of this correlation, or the values of the constants presented here, a more extensive database than the one presently available is needed.

Nomenclature

$a_1(B)$ function of B

b Schvab-Zeldovich property in laminar flow; fluctuating component in turbulent flow

$\bar{b}$ Schvab-Zeldovich property in turbulent flow

B transfer number in laminar flow; mean transfer number in turbulent flow

B' function of B

c_F specific heat of fuel

c_p specific heat at constant pressure

c_{p2} two-phase specific heat, $h_{fg}/\Delta T$

$C(B)$ function of B

C_f friction coefficient

C_0, C_1, C_2, C_3, C_4 constants

D mass diffusivity; diameter

D_β modified mass diffusivity

f friction coefficient

F_B buoyant force

F_I inertial force

F_S capillary force

F_V viscous force

g gravitational acceleration

g_i gravitational acceleration vector

Gr Grashof number

h specific enthalpy; heat transfer coefficient

h_β mass transfer coefficient

h_{fg} heat of evaporation

Ja Jacob number

k thermal conductivity

K mean kinetic energy

K_θ root mean square of temperature fluctuations

l integral scale

L length

Le Lewis number

M' burning rate per unit length

M'' burning rate per unit area

M molecular weight

Ma Marangoni number

Nu Nusselt number, hl/k or $\Phi l^2/\alpha \Delta T$

p pressure

Pe_N Peclet number for buoyancy driven flows

Pr Prandtl number

Pr_2 two-phase Prandtl number, ν/α_2

q heat flux

q_c core heat flux

Q heat release

Q_2 enthalpy flow across two-phase interface

Q_H enthalpy flow

Q_K conduction heat flux

Ra Rayleigh number

Ra_β flame Rayleigh number

Ra_c critical Rayleigh number

Ra_2 two-phase Rayleigh number

Re Reynolds number

Re_β flame Reynolds number

Re_K Reynolds number of Kolmogorov scales

Re_l Reynolds number, ul/ν

Re_λ Reynolds number, $u\lambda/\nu$

Re_η Reynolds number, $u\eta/\nu$

s_{ij} fluctuating rate of strain

S_{ij} mean rate of strain

Sh_β flame Sherwood number

St Stanton number

T temperature

u longitudinal velocity; velocity fluctuation (root mean square)

u_c core velocity

u_i, u_j velocity fluctuation

u''' rate of energy generation-to-volume

$\bar{u}_i$ instantaneous velocity; pulsation velocity

U characteristic laminar velocity; mean velocity

U_0 amplitude of oscillating velocity

U_i mean turbulent velocity

v transverse velocity; Kolmogorov velocity

v_w transverse velocity at wall

V a characteristic velocity

x, y coordinate velocity

Y mass friction

GREEK SYMBOLS

α thermal diffusivity

α_2 two-phase thermal diffusivity, $k/\rho c_{p2}$

β	coefficient of thermal expansion	σ	Schmidt number; surface tension
δ	momentum boundary layer thickness	σ_β	flame Schmidt number
δ_β	Schvab-Zeldovich property boundary layer thickness	τ	shear stress; Kolmogorov time scale
δ_m	momentum thickness	χ	ratio of boundary layer thicknesses
δ_θ	thermal boundary layer thickness	ω	frequency
Δ	difference		
ε	viscous dissipation		

SCRIPT SYMBOLS

ε_θ	thermal dissipation	$\mathscr{B}$	buoyant production
η	Kolmogorov scale	$\mathscr{D}_i$	mean transport
η_θ	thermal mesomicroscale	$(\mathscr{D}_\theta)_i$	thermal transport
η_θ^B	Batchelor scale	$\mathscr{F}$	buoyant force
η_θ^C	Oboukhov-Corrsin scale	$\mathscr{P}$	inertial production
θ	temperature fluctuation	$\mathscr{P}_\beta$	buoyant production of b property
θ_c	core temperature	$\mathscr{P}_\theta$	thermal production
Θ	mean temperature	$\mathscr{P}_S$	thermocapillary production
Θ_0	temperature of isobaric ambient; amplitude of oscillating temperature		

SUPERSCRIPTS

λ	Taylor scale	$\sim$	instantaneous value; pulsation value
λ_β	Taylor scale for Schvab-Zeldovich property	$-$	mean value
λ_θ	thermal Taylor scale	$\prime$	turbulent value
μ	dynamic viscosity		
ν	kinematic viscosity		**SUBSCRIPTS**
ν_β	modified kinematic viscosity		
ν_O	stoichiometric coefficient of oxidizer	B	b-property related
ν_F	stoichiometric coefficient of fuel	f	flame
Π_β	dimensionless number for buoyancy-driven diffusion flame	F	fuel
		g	gas
$\Pi_{N,l}$	dimensionless number for buoyancy-driven flows	l	liquid
		m	mean
Π_2	dimensionless number for two-phase flow	O	oxidant
		s, sat	saturation
Π_S	dimensionless number for thermocapillary flow	v	vapor
		w	wall
ρ	density	x	local value
		∞	ambient

References

1. Alhaddad, A. A., and Coulman, G. A. (1982). Experimental and theoretical study of heat transfer in pulse-combustion heaters. *Proc. Symp. Pulse Combust. Appl.*, Atlanta, GA, Vol. I; GRI-82/0009.2.

2. Arpacı, V. S. (1986). Microscales of turbulence and heat transfer correlations. *Int. J. Heat Mass Transfer* **29**, 1071–1078.

3. Arpaci, V. S. (1986). Two thermal microscales for natural convection and heat transfer correlations. In *Significant Questions in Buoyancy Affected Enclosure or Cavity Flows*, ASME HTD-60, pp. 117–121. ASME, New York.

4. Arpaci, V. S. (1987). A thermal microscale via lost heat into entropy. In *Second Law Analysis of Heat Transfer in Energy Systems*, ASME HTD-80, pp. 21–25. ASME, New York.

5. Arpaci, V. S. (1990). Microscales of turbulence and heat transfer correlations. *Ann. Rev. Heat Transfer* **3**, 195–231.

6. Arpaci, V. S. (1994). Microscales of turbulence, mass transfer correlations. *Int. Symp. Turbulence, Heat Mass Transfer*, Lisbon, Portugal. Keynote Lecture.

7. Arpaci, V. S. (1994). Microscales of turbulence, heat transfer correlations. *Int. Heat Transfer Conf. 10th*, Brighton, UK. Keynote Lecture.

8. Arpaci, V. S. (1995). Buoyant turbulent flow driven by internal energy generation. *Int. J. Heat Mass Transfer* **38**, 2761–2770.

9. Arpaci, V. S. (1995). Microscales of turbulent combustion. *Prog. Energy Combust. Sci.* **21**, 153–171.

10. Arpaci, V. S., and Dec, J. E. (1987). A theory for buoyancy driven turbulent flows. *24th Nat. Heat Transfer Conf.*, Pittsburgh, Pap. No. 87-HT-55.

11. Arpaci, V. S., and Kao, S.-H. (1997). Foundations of buoyancy driven heat transfer correlations. In preparation.

12. Arpaci, V. S., and Kao, S.-H. (1996). Microscales of turbulent two-phase film 1996. *Nat. Heat Tranfer Conf.*, HTC-Vol. 9, Houston, TX.

13. Arpaci, V. S., and Larsen, P. S. (1984). *Convection Heat Transfer*. Prentice Hall, Englewood Cliffs, NJ.

14. Arpaci, V. S., and Li, C. Y. (1995). Turbulent forced diffusion flames. *Combust. Flame* **102**, 170–178.

15. Arpaci, V. S., and Selamet, A. (1991). Buoyancy driven turbulent diffusion flames. *Combust. Flame* **86**, 203–215.

16. Arpaci, V. S., Dec, J. E., and Keller, J. O. (1993). Heat transfer in pulse combustor tailpipes. *Combust. Sci. Technol.* **94**, 131.

17. Batchelor, G. K. (1959). Small-scale variation of convected quantities like temperature in a turbulent fluid. *J. Fluid Mech.* **5**, 113–133.

18. Block, M. J. (1956). Surface tension as the cause of Bénard cells and surface deformation in a liquid film. *Nature (London)* **178**, 650.

19. Bromley, L. A. (1950). Heat transfer in stable film boiling. *Chem. Eng. Prog.* **46**, 221.

20. Burgess, D. S., Strasser, A., and Grumer, J. (1961). *Fire Res. Abstr. Rev.* **3**, 177–192.

21. Busse, F. H. (1981). Transition to turbulence in Rayleigh-Bénard convection. In *Hydrodynamic Instabilities and the Transition to Turbulence* (H. L. Swinney and J. P. Gollub, eds.), Vol. 45, p. 97. Springer-Verlag, Berlin.

22. Chandrasekhar, S. (1961). *Hydrodynamic and Hydromagnetic Stability*. Oxford University Press, Oxford.

23. Cheung, F. B. (1980). Heat source-driven thermal convection at arbitrary Prandtl number. *J. Fluid Mech.* **97**, 743.

24. Chu, T. Y., and Goldstein, R. J. (1973). Turbulent convection in a horizontal layer of water. *J. Fluid Mech.* **60**, 141.

25. Churchill, S. W., and Chu, H. H. S. (1975). Correlating equations for laminar and turbulent free convection from a vertical plate. *Int. J. Heat Mass Transfer* **18**, 1323–1329.

26. Corlett, R. C. (1968). Gas fires with pool-like boundary conditions. *Combust. Flame* **12**, 19.

27. Corlett, R. C. (1970). Gas fires with pool-like boundary conditions: Further results and interpretation. *Combust. Flame* **14**, 351–360.

28. Corrsin, S. (1951). On the spectrum of isotropic temperature fluctuations in isotropic turbulence. *J. Appl. Phys.* **22**, 469.

29. Corrsin, S. (1962). Turbulent dissipation fluctuations. *Phys. Fluids* **5**, 1301.

30. Dec. J. E., and Keller, J. O. (1989). Pulse combustor tail-pipe heat-transfer dependence on frequency, amplitude, and mean flow rate. *Combust. Flame* **77**, 359–374.

31. Dec. J. E., Keller, J. O., and Arpaci, V. S. (1992). Heat transfer enhancement in the oscillating turbulent flow of a pulse combustor tailpipe. *Int. J. Heat Mass Transfer* **35**, 2311.

32. de Ris, J., and Orloff, L. (1972). A dimensionless correlation of pool burning data. *Combust. Flame* **18**, 381.

33. Elder, J. W. (1969). The temporal development of a model of high Rayleigh number convection. *J. Fluid Mech.* **35**, 417.

34. Emmons, H. W. (1956). The film combustion of liquid fuel. *Z. Angew. Math. Mech.* **36**, 60.

35. Fiedler, H., and Wille, R. (1971). Warmetransport bie frier Konvektion in einer horizontalen Flussigkeitsschicht mit Volumenheizung, Teil 1: Integraler Warmetransport. *Forschungsber.—Dtsch. Forsch. Versuchsanst. Luft Raumfahrt,* Inst. Trubulenzfenschung, Berlin.

36. Fitzjarrald, D. E. (1976). An experimental study of turbulent convection in air. *J. Fluid Mech.* **73**, 693.

37. Frederkin, T. H. K., and Clark, J. A. (1962). Natural convection film boiling on a sphere. *Adv. Cryogen. Eng.* **8**, 501.

38. Frederkin, T. H. K., and Daniels, D. J. (1966). The relation between bubble diameter and frequency of removal from a sphere during film boiling. *J. Heat Transfer* **88**, 87.

39. Frisch, U. (1965). *Turbulence. The Legacy of A. N. Kolmogorov.* Cambridge University Press, Cambridge, U.K.

40. Fujii, T., and Imura, H. (1972). Natural convection heat transfer from a plate with arbitrary inclination. *Int. J. Heat Mass Transfer.* **15**, 755.

41. Galitseyskiy, B. M., and Ryzhov, Y. A. (1977). Heat transfer in turbulent gas flows in the case of high-frequency pressure fluctuations. *Heat Transfer—Sov. Res.* **8**(4), 178–183.

42. Garon, A. M., and Goldstein, R. J. (1973). Velocity and heat transfer measurements in thermal convection. *Phys. Fluids* **16**, 1818.

43. Gill, J. (1967). Interferometric measurement of temperature gradient reversal in a layer of convecting air. *J. Fluid Mech.* **30**, 371.

44. Globe S., and Dropkin, D. (1959). Natural convection heat transfer in liquids confined by two horizontal plates and heated from below. *J. Heat Transfer* **81**, 24.

45. Goldstein, R. J., and Chu, T. Y. (1969). Thermal convection in a horizontal layer of air. *Prog. Heat Mass Transfer* **2**, 55–75.

46. Goldstein, R. J., and Tokuda, S. (1980). Heat transfer by thermal convection at high Rayleigh numbers. *Int. J. Heat Mass Transfer* **23**, 738.

47. Gorkow, L. P. (1958). Stationary convection in a plane liquid layer near the critical heat transfer point. *Soviet Phys.—JETP (Engl. Transl.)* **6**, 311–315.

48. Hanby, V. I. (1969). Convective heat transfer in a gas-fired pulsating combustor. *J. Eng. Power* **91**, 48–52.

49. Herring, J. R. (1963). Investigation of problems in thermal convection. *J. Atmos. Sci.* **20**, 325.

50. Kamotani, Y., Chang, A., and Ostrach, S. (1996). Effects of heating mode of steady axisymmetric thermocapillary flows in microgravity. *J. Heat Transfer* **118**, 191–197.

51. Kanury, A. M. (1975). Modeling of pool fires with a variety of polymers. *Symp. (Int.) Combust. [Proc.]* **15**, 193.

52. Kanury, A. M. (1977). *Introduction to Combustion Phenomena*. Gordon & Breach, New York.

53. Kim, J. S., de Ris, J., and Kroesser, F. W. (1971). Laminar free convective burning of fuel surfaces. *Symp. (Int.) Combust. [Proc.]* **13**, 949.

54. Koh, J. C. Y., Sparrow, E. M., and Hartnett, J. P. (1961). Two phase boundary layer in laminar film condensation. *Int. J. Heat Mass Transfer* **2**, 69.

55. Kolmogorov, A. N. (1941). Local structure of turbulence in incompressible viscous fluid for very large Reynolds numbers. *C. R. Acad. Sci. URSS* **30**, 301.

56. Krishnamurti, R. (1970). On the transition to turbulent convection. Part 1. The transition from two- to three-dimensional flow. *J. Fluid Mech.* **42**, 295-307.

57. Krishnamurti, R. (1970). On the transition to turbulent convection. Part 2. The transition to time-dependent flow. *J. Fluid Mech.* **42**, 309-320.

58. Krishnamurti, R. (1973). Some further studies on the transition to turbulent convection. *J. Fluid Mech.* **60**, 285-303.

59. Kulacki, F. A., and Emara, A. A. (1977). Steady and transient thermal convection in a fluid layer with uniform volumetric energy sources. *J. Fluid Mech.* **83**, 375.

60. Kulacki, F. A., and Nagle, M. E. (1975). Natural convection in a horizontal fluid layer with volumetric energy sources. *J. Heat Transfer* **91**, 204.

61. Landau, L. D. (1944). On the problem of turbulence. *C. R. (Dokl.) Acad. Sci. URSS* **44**, 311-314.

62. Liao, N. S., Wang, C. C., and Hong, J. T. (1985). An investigation of heat transfer in pulsating turbulent pipe flow. *23rd Nat. Heat Transfer Conf.*, Denver, CO. ASME HTD, Vol. 42.

63. Lockwood, R. W., and Corlett, R. C. (1987). Radiative and convective feedback heat flux in small turbulent pool fires with variable pressure and ambient oxygen. In *Heat Mass Transfer Fires*, ASME HTD-73, 421. ASME, New York.

64. Long, R. R. (1976). Relation between Nusselt number and Rayleigh number in turbulent thermal convection. *J. Fluid Mech.* **73**, 445.

65. Lyon, R. N. (1952). *Liquid Metals Handbook*, 3rd ed. Atomic Energy Commission and Department of the Navy, Washington, DC.

66. Malkus, W. (1954). The heat transport and spectrum of thermal turbulence. *Proc. R. Soc. London, Ser. A* **225**, 196-212.

67. Malkus, W., and Veronis, G. (1958). Finite amplitude cellular convection. *J. Fluid Mech.* **4**, 225.

68. Marxman, G. A. (1967). Boundary-layer combustion in propulsion. *Symp. (Int.) Combust. [Proc.]* **11**, 269.

69. Marxman, G. A., and Gilbert, M. (1963). Turbulent boundary layer combustion in the hybrid rocket. *Symp. (Int.) Combust. [Proc.]* **9**, 371.

70. Nakagawa, Y. (1960). Heat transport by convection. *Phys. Fluids* **3**, 82-86.

71. Nusselt, W. (1916). Die Oberflachenkondensation des Wasser Dampfes. *VDI-Z* **60**, 541.

72. Oboukhov, A. M. (1949), Structure of the temperature field in turbulent flows. *Izv. Akad. Nauk SSSR, Ser. Geogr. Geofiz.* **13**, 58.

73. Padilla, A., Jr. (1966). Film boiling of potassium on a horizontal plate. Ph.D. Thesis, University of Michigan, Ann Arbor.

74. Paul, P. J., Mukunda, H. S., and Jain, V. K. (1982). Regretion rates in boundary layer combustion. *Symp. (Int.) Combust. [Proc.]* **19**, 717-729.

75. Pearson, J. R. A. (1958). On convection cells induced by surface tension. *J. Fluid Mech.* **4**, 489-500.

76. Ribaud, G. (1941). Nouvelle expression du coefficient de convection de la chaleur en régime découlement turbulent. *J. Phys. Radium* **2**, 12.

77. Schmidt, E., and Beckmann, W. (1930). *Tech. Mech. Thermodyn.* **1**, 341.

78. Silveston, P. L. (1958). Warmedurchgang in waagerechten flussigkeitschichten. *Forsch. Geb. Ingenieurwes.* **29**, 59.

79. Somerscales, E. F. C., and Gazda, I. W. (1969). Thermal convection in high Prandtl number liquids at high Rayleigh number. *Int. J. Heat Mass Transfer* **12**, 1491.

80. Spalding, D. B. (1954). Mass transfer in laminar flow. *Proc. R. Soc. London, Ser. A* **221**, 78.

81. Sparrow, E. M., and Gregg, J. L. (1959). A boundary layer treatment of laminar film condensation. *J. Heat Transfer* **81**, 13.

82. Squire, H. B. (1938). Free convection from a heated vertical plates. *Mod. Dev. Fluid Mech.* **2**, 638.

83. Stuart, J. T. (1958). On the nonlinear mechanics of hydrodynamic stability. *J. Fluid Mech.* **4**, 1–21.

84. Taylor, G. I. (1935). Statistical theory of turbulence. *Proc. R. Soc. London, Ser. A* **151**, 421.

85. Tennekes, H. (1968). Simple model for the small scale structure of turbulence. *Phys. Fluids* **11**, 669.

86. Tennekes, H., and Lumley, O. L. (1972). *A First Course in Turbulence*. MIT Press, Cambridge, MA.

87. Thomas, D. B., and Townsend, A. A. (1957). Turbulent convection over a heated horizontal surface. *J. Fluid. Mech.* **2**, 473.

88. Threlfall, D. C. (1975). Free convection in low-temperature gaseous helium. *J. Fluid Mech.* **67**, 17.

89. Tritton, D. J., and Zarraga, M. N. (1967). Convection in horizontal layers with internal heat generation. *J. Fluid. Mech.* **30**, 21.

90. Veronis, G. (1959). Cellular convection with finite amplitude in a rotating fluid. *J. Fluid Mech.* **5**, 401–435.

Multiphase Flow and Heat Transfer
in Porous Media

C. Y. WANG

Department of Mechanical Engineering, Pennsylvania State University,
University Park, Pennsylvania

P. CHENG

Department of Mechanical Engineering, The Hong Kong University of Science
and Technology, Clear Water Bay, Kowloon, Hong Kong

I. Introduction

Problems involving multiphase flow, heat transfer, and multicomponent mass transport in porous media arise in a number of scientific and engineering disciplines. Important technological applications include thermally enhanced oil recovery [1], subsurface contamination and remediation [2], capillary-assisted thermal technologies [3], drying process [4], thermal insulation materials [4a], multiphase trickle bed reactors [5], nuclear reactor safety analysis [6], high-level radioactive waste repositories [7], and geothermal energy exploitation [8].

A number of complex, interacting transport phenomena may take place in a nonisothermal, multiphase system. In general, multiphase flows in porous media are driven by gravitational, capillary, and viscous forces. Gravity causes phase migration in the direction of the gravitational field. A common example is gravity override of steam as commonly encountered in steam injection for enhanced oil recovery and subsurface remediation, where the injected steam tends to rise to the top of a formation thus leading to a premature breakthrough of steam into production wells. The detrimental outcome of steam override is a large reduction in the recovery of oil or contaminant and a significant waste of latent-heat thermal energy.

93

Another example of the influence of gravity is thermosolutal convection in each fluid phase as a result of density variations due to combined temperature and concentration gradients. Thermosolutal convection directly controls distillation of light components in oil recovery processes, evaporation rates in drying processes, and the gas phase transport of contaminants in the subsurface environment and in remediation processes (e.g., during soil vapor extraction).

Capillary forces play fundamental roles in controlling the phase distribution and hence multiphase flow and transport in heterogeneous porous media. In the context of groundwater contamination, the capillary forces due to interfacial tension are largely responsible for the extent of lateral spreading of a contaminant as it encounters a low-permeability layer. Viscous forces influence relative phase motion: Fluids with lower viscosity tend to migrate more rapidly due to their reduced resistance to flow. When a denser, less viscous fluid displaces another fluid of lower density and higher viscosity, the process is inherently unstable, leading to fingering of phase interfaces [9].

Due to the complicated transport phenomena involved, the multiphase flow and transport in porous media remains poorly understood and analytically intractable. This chapter summarizes the most recent theoretical and experimental work in this field in order to identify current capabilities and thus provide a basis for further developments. Nonisothermal flows with heat transfer are the focus, whereas isothermal multiphase flows in porous media have been extensively discussed in several excellent reviews by Morel-Seytoux [10], Wooding and Morel-Seytoux [9], Adler and Brenner [11], and De Santos et al. [12]. Previous major articles and chapters addressing various aspects of multiphase heat transfer in porous media include those by Whitaker [4], Tien and Vafai [13], Vakai and Sözen [13a], Kaviany [14], Dhir [6], and Catton and Chung [15]. The purpose of this chapter is to compile and summarize the many ongoing studies of the fundamental phenomena and new analytical and experimental techniques for *simultaneous* multiphase flows. These are a class of the most difficult problems to deal with, and include, as limiting cases, the situation where one or more phases are immobile. Both pure and multicomponent systems are addressed. Ample references to the original literature are included in this chapter, but no attempt has been made to be complete.

The review is divided into sections devoted to fundamental systems rather than specific applications. Part II outlines several theoretical models currently prevailing in the literature for multiphase flow and heat transfer in porous media. In particular, a multiphase mixture model that we recently developed [16] is elaborated on and compared with the traditional multiphase flow model [17] and unsaturated flow theory [10].

Part III reviews both theoretical and experimental work for single-component two-phase systems with major applications to thermal engineering, while Part IV is devoted to general multiphase, multicomponent systems in connection with a wide variety of engineering applications, such as drying of porous materials, groundwater contamination, and remediation. The last part summarizes the conclusions and indicates areas for future research.

II. Theoretical Considerations

This section surveys and assesses the mathematical models available in the literature to describe multiphase transport phenomena in porous media. The summary includes only the most generic models that can be applied to various situations. The earliest modeling efforts involving multiphase flow in porous media began in the petroleum industry [18]. These models then provided the basis for many of the current multiphase flow and transport models in hydrology [17], chemical engineering [19], and thermal-fluid engineering [14]. The starting points for development of any multiphase model are the principles of mass, momentum, species, and energy conservation. Because multiphase flow in porous media is generally a special subset of multiphase systems, many of the recent advances in multiphase theories have influenced the porous media research. For example, the technique of volume averaging was widely utilized to rigorously derive macroscopic transport equations [20, 21]. Microscopic modeling efforts were made to accurately incorporate microscopic interfacial phenomena [14, 22]. Multiscale modeling approaches were attempted in order to transmit information over various length scales, ranging from microscale, mesoscale, macroscale, and finally to the field scale [23-26].

A. Basic Concepts

To establish a fundamental theoretical framework, basic concepts associated with multiphase transport in porous media are first discussed.

1. Phase Saturation

Saturation of a fluid is defined as the volume fraction of the total pore space occupied by that fluid. Saturations vary from zero to unity and the saturations of all phases add up to unity. The saturation geometrically quantifies the phase distribution in a porous medium and thus influences the resistance to the flow of each phase. It is an important parameter on

which many other properties (e.g., capillary pressure and relative permeability) depend.

Direct measurement of phase saturations within a porous medium would normally disturb the sample. Indirect determination of phase saturations is usually made by measuring the change in the sample mass, by measuring the change in attenuation of gamma ray energy [27], and through three-dimensional (3D) imaging technology such as X-ray tomography [28] or magnetic resonance imaging [29]. Because of resolution limitations inherent to these techniques, their utility is restricted to providing saturation information over relatively large areas. Most recently, a photoluminescent volumetric imaging (PVI) technique was developed by Montemagno and Gray [30] to overcome this drawback. With a measurement resolution better than 1 μm, the PVI technique provides a powerful tool to quantify the microscopic distribution of the fluid phases as well as their interfaces within a porous medium. Another recent experimental technique to measure phase saturations is called transmitted light imaging [31]. The technique relies on a uniform, controlled, diffuse light source passing through a translucent sample, and uses a digital imaging system to capture the saturation field. The technique allows for whole-field saturation measurements with high spatial and temporal resolutions. Despite the fact that its utility has been limited to thin slab samples (~ 1 cm) under isothermal flow conditions, this technique appears to hold great promise for adaptation to heat transfer studies under both steady and transient conditions.

2. Interfacial Tension

Interfacial tension is referred to as the free surface energy at the interface formed between two immiscible or nearly immiscible fluids. It results from the difference between the mutual attraction of like molecules within each fluid and the attraction of dissimilar molecules across the fluid interface. Interfacial tension is directly responsible for capillary effects. For nonisothermal multicomponent systems, interfacial tension depends strongly on temperature and species concentration.

3. Capillary Pressure

If two immiscible fluids are in contact, a curved surface tends to develop at the phase interface. By measuring the pore pressure near the interface in each phase, we find that the pressures are not the same. The difference is the capillary pressure, which is defined as

$$p_{cjk} = p_j - p_k. \tag{1}$$

Capillary pressure is directly proportional to the interfacial tension and inversely proportional to the radius of curvature. The radius curvature, in turn, is dependent on the pore size and the amount of each fluid present, that is, phase saturations. Hence, the capillary pressure can be expressed as a function of the interfacial tensions and phase saturations for multiphase systems. This function is generally multivalued, and exhibits hysteretic behaviors. Figure 1 shows typical capillary pressure curves in a liquid–gas two-phase system, where the liquid is the wetting phase and the gas is the nonwetting fluid. Changes in capillary pressure with saturation depend on whether the medium is undergoing wetting (imbibition) or draining of the wetting fluid. In the drainage process, the capillary pressure increases as the liquid saturation decreases. Eventually, no more liquid phase will be displaced by the gas phase, even with further increases in capillary pressure. This saturation value is known as the residual or irreducible liquid saturation s_{lr}. Conversely, when the imbibition curve reaches zero capillary pressure, some of the gas phase remains in the
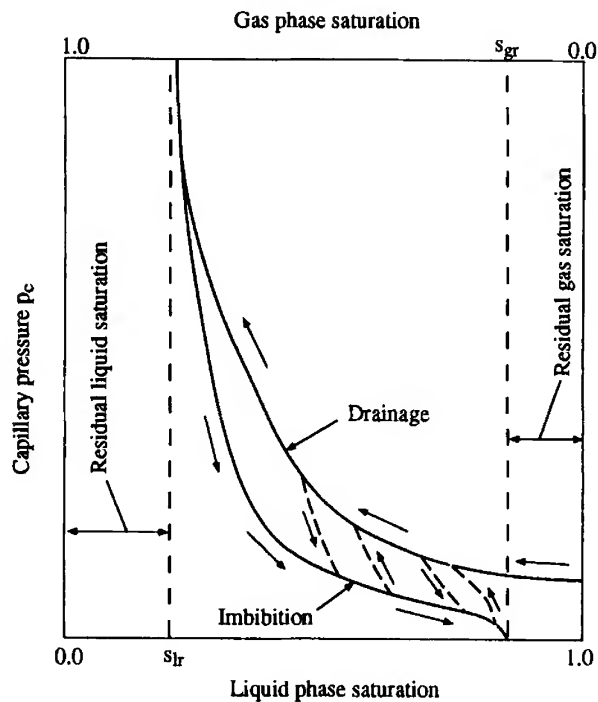
FIG. 1. Capillary pressure curves for liquid–gas two-phase systems. s_{gr}, the residual or irreducible gas saturation; s_{lr}, the residual or irreducible liquid saturation.

porous medium. This saturation is known as the residual or irreducible gas saturation s_{gr}.

An example of the capillary pressure function for an air–water system is given by Udell [32]. Lenhard and Parker [33] evaluated a scaling procedure to derive capillary pressure relations of air–water, air–NAPL and NAPL–water porous media systems (where NAPL stands for nonaqueous phase liquids). Using this procedure, three-phase capillary pressures can also be predicted from two-phase relationships [34].

4. Relative Permeability

During simultaneous multiphase flow, the available pore space is shared by multiple fluids. The cross-sectional area of the pore space available for each fluid phase is thus less than the total pore space. This leads to the concept of relative permeability. The relative permeability k_r, is defined as the ratio of the intrinsic permeability for a phase at a given saturation to the total intrinsic permeability of the porous medium. Figure 2(a) schematically shows two-phase relative permeability curves for both wetting and nonwetting fluids, where the irreducible phase saturation denotes the threshold value at which the phase no longer flows. Figure 2(b) is a ternary relative permeability diagram for the NAPL in an air–water–NAPL system [35]. In general, relative permeabilities are assumed to be known functions of the phase saturations, which are determined empirically.

B. MULTIPHASE FLOW MODEL (MFM)

Traditionally, macroscopic problems of multiphase flow and transport in porous media are modeled by a multiphase approach [17, 36], in which various phases are regarded as distinct fluids with individual thermodynamic and transport properties and with different flow velocities. The transport phenomena are mathematically described separately by the basic principles of conservation for each phase and by appropriate interfacial conditions between various phases. The generalized Darcy law is employed to represent momentum conservation in each phase, with the relative permeabilities of each phase introduced to account for a decrease in the effective flow cross section due to the presence of other phases. An important assumption usually made in this model is interfacial thermal and chemical equilibrium between the fluid phases. A brief summary of the multiphase flow formulation for multiphase, multicomponent transport in a porous medium is given below. Note that the following set of macroscopic equations can be derived either heuristically or by the method of volume averaging [20, 21].
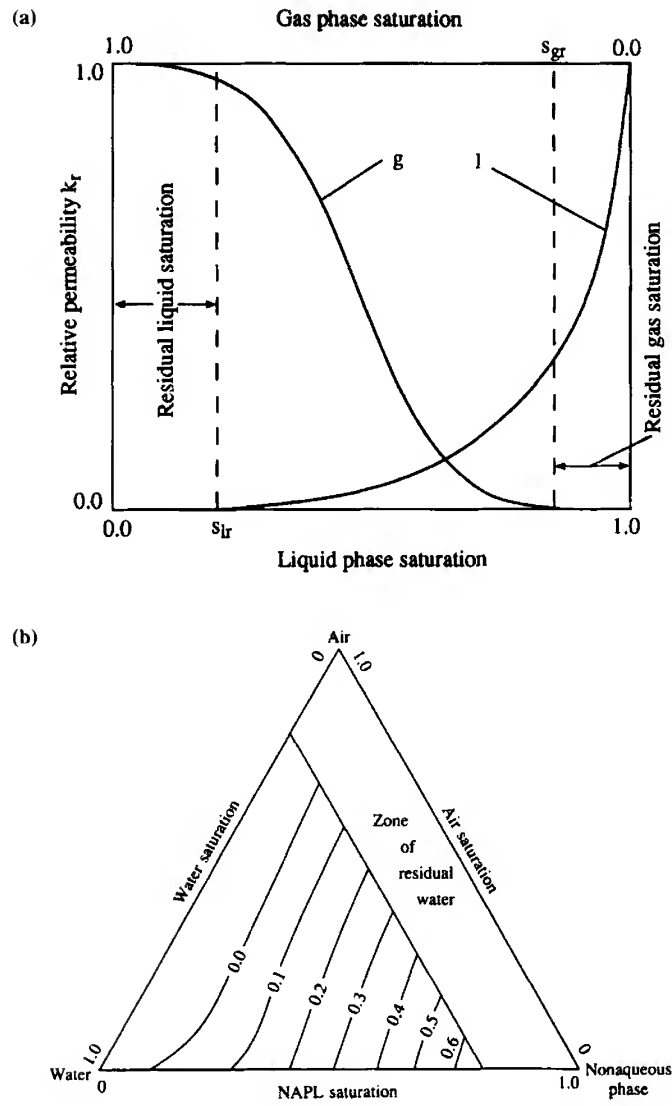
FIG. 2. Two-phase and three-phase relative permeability curves. (a) NAPL, nonaqueous phase liquids. (b) Reprinted with permission by Faust [35]. s_{gr}, the residual or irreducible gas saturation; s_{lr}, the residual or irreducible liquid saturation.

1. *Mass conservation in phase k:*

$$\varepsilon \frac{\partial(\rho_k s_k)}{\partial t} + \nabla \cdot (\rho_k \mathbf{u}_k) = \overline{m}_k, \tag{2}$$

where ε is the porosity of the porous medium, s_k is the phase saturation denoting the volumetric fraction of the void space occupied by phase k, and $\mathbf{u}_k$ is the superficial (or Darcian) velocity vector based on the total cross-sectional area of multiple fluids and porous medium. The term $\overline{m}_k$ represents an interfacial mass transfer rate from all other phases to phase k. In the absence of any external mass source or sink, it follows that

$$\sum_k \overline{m}_k = 0. \tag{3}$$

Equations (2) and (3) assume that the porous medium is not deformable.

2. *Momentum conservation in phase k:*

$$\mathbf{u}_k = -K \frac{k_{rk}}{\mu_k} (\nabla p_k - \rho_k \mathbf{g}), \tag{4}$$

where the presence of the gravitational force has been taken into account. The difference between the pressures for two adjacent phases k and j is described by the capillary pressure defined in Eq. (1). This generalized Darcy's equation is valid if inertia as well as (macroscopic) viscous effects can be neglected.

3. *Mass conservation of species α in phase k:*

$$\frac{\partial}{\partial t}(\varepsilon \rho_k s_k C_k^\alpha) + \nabla \cdot (\rho_k \mathbf{u}_k C_k^\alpha) = -\nabla \cdot \mathbf{j}_k^\alpha + \overline{J}_k^\alpha, \tag{5}$$

where C_k^α is the mass concentration of species α in phase k, and $\mathbf{j}_k^\alpha$ is a diffusive flux of species α in phase k due to molecular diffusion, hydrodynamic dispersion, or both. The latter is usually expressed in Fickian form:

$$\mathbf{j}_k^\alpha = -\varepsilon \rho s_k D_k^\alpha \nabla C_k^\alpha, \tag{6}$$

where D_k^α is a macroscopic second-order tensor and depends on the molecular diffusion coefficient and fluid velocity. Presently, much effort is being expended to model the hydrodynamic dispersion phenomenon (see, e.g., Brenner and Edwards [22]).

The last term in Eq. (5), $\overline{J}_k^\alpha$, denotes the interphase species transfer rate caused by chemical reaction, phase change, or both at the interfaces between phase k and all other phases. Recognizing that the production of species α in phase k must be accompanied by

destructions of species α in other phases, it follows that

$$\sum_k J_k^\alpha = 0, \qquad (7)$$

provided there is no extrinsic species generation due to chemical or biological reactions.

4. *Energy conservation in phase k:*

$$\frac{\partial}{\partial t}(\varepsilon \rho_k s_k h_k) + \nabla \cdot (\rho_k \mathbf{u}_k h_k) = \nabla \cdot (s_k k_k \nabla T) + \bar{q}_k, \qquad (8)$$

where local thermal equilibrium among phases has been assumed $(T_k = T)$, and k_k and $\bar{q}_k$ represent the effective thermal conductivity of phase k and the interphase heat transfer rate associated with phase k, respectively. Hence,

$$\sum_k \bar{q}_k = \dot{q}, \qquad (9)$$

where $\dot{q}$ stands for an external volumetric heat source or sink. The phase enthalpy h_k is related to the common temperature T via

$$h_k = \int_0^T c_k \, dT + h_k^0, \qquad (10)$$

where c_k and h_k^0 represent the effective specific heat and the reference enthalpy of phase k, respectively.

The previous basic conservation laws provide a full system of governing equations for the unknown vector velocities $\mathbf{u}_k$, scalar pressures p_k, scalar liquid saturations s_k, mass concentrations C_k^α, and the common temperature T. Due to this large number of primary variables and their highly nonlinear equations, exact solutions to multiphase flow and transport problems are limited to a very small class of problems in one dimension and with many simplifying assumptions [37]. Solving practical problems, which usually involve multidimensional effects, gravity, capillarity, and phase change, requires sophisticated numerical procedures and represents a challenging task [38].

Another fundamental difficulty of MFM in simulating multiphase flow and transport in porous media lies in the presence of moving and irregular phase interfaces separating the single-phase and multiphase subregions that co-exist in a physical system. The locations of these interfaces are not known *a priori* but must be determined by the coupled flows in adjacent regions. A numerical procedure for such a multiregion problem based on MFM needs to explicitly track the moving interfaces, thus calling for complex coordinate mapping or numerical remeshing [39]. Alternatively, in

the water resources literature [40] the procedure of switching the primary variables and governing equations in various regions is usually adopted, which may severely affect numerical stability and convergence speed.

C. Unsaturated Flow Theory (UFT)

In order to alleviate the analytical difficulties associated with the multiphase flow model, an approximate model called the unsaturated flow theory was developed and popularly used by hydrologists [10, 41]. Applications of UFT to condensation heat transfer problems in porous media were also demonstrated [42, 43]. In the following, we briefly derive the well-known Richards equation in UFT to gain insight into the important assumptions made in the theory and thus identify its limitations in certain situations.

Substitution of Eq. (4) into Eq. (2) for a liquid phase (e.g., water in hydrology) yields

$$\varepsilon \frac{\partial(\rho_l s_l)}{\partial t} + \nabla \cdot \left(-K \frac{k_{rl}}{\nu_l} \nabla p_l + K \frac{k_{rl}}{\nu_l} \rho_l \mathbf{g} \right) = \bar{m}_l. \tag{11}$$

This provides a single equation for two unknowns, s_l and p_l. To close the mathematical system, it is traditionally assumed that the gas phase (e.g., air in hydrology) essentially remains at a constant pressure, equal to atmospheric pressure, so that ∇p_l is simple given by

$$\nabla p_l = \nabla p_g - \nabla p_c = \nabla(\rho_g \mathbf{g}) - \frac{dp_c}{ds_l} \nabla s_l. \tag{12}$$

With this identity, Eq. (11) can be rearranged as

$$\varepsilon \frac{\partial(\rho_l s_l)}{\partial t} + \nabla \cdot \left(K \frac{k_{rl}}{\nu_l} \frac{dp_c}{ds_l} \nabla s_l \right) + \nabla \cdot \left[K \frac{k_{rl}}{\nu_l}(\rho_l - \rho_g)\mathbf{g} \right] = \bar{m}_l. \tag{13}$$

Furthermore, a diffusivity is defined as

$$D(s_l) = -K \frac{k_{rl}}{\nu_l} \frac{dp_c}{ds_l}. \tag{14}$$

By its definition, $D(s_l)$ is always positive. Equation (13) then takes the final form of

$$\varepsilon \frac{\partial(\rho_l s_l)}{\partial t} - \nabla \cdot (D\nabla s_l) + \nabla \cdot \left[K \frac{k_{rl}}{\nu_l}(\rho_l - p_g)\mathbf{g} \right] = \bar{m}_l. \tag{15}$$

This equation, with the interphase mass transfer $\bar{m}_l$ and the gas phase density neglected, is usually known as the *Richards equation* and can be solved similarly to a diffusion equation.

D. MULTIPHASE MIXTURE MODEL (MMM)

Most recently, an alternative approach was developed to the modeling of multiphase flow and multicomponent transport in porous media [16]. In this so-called multiphase mixture model, the multiphase system is viewed as being a chemical mixture. Multiphase flow is then described in terms of a mass-averaged mixture velocity and a diffusive flux, representing the difference between the mixture velocity and an individual phase velocity. Without making any assumptions, a new set of transport equations for the multiphase mixture was derived from the classic multiphase flow model. Moreover, explicit relations describing the relative motions between the multiphase mixture and an individual phase are found that can be used to determine the intrinsic characteristics of the phase dynamics (e.g., the phase velocity fields). An overview of the multiphase mixture model is presented subsequently.

1. Basic Definitions

As in a classic multicomponent mixture, all physical properties of the multiphase mixture are consequences of the properties of its constituents; however, their functional forms are not assumed *a priori*, but are derived strictly from the multiphase flow model. The mixture density, velocity, species concentration, enthalpy, and pressure are defined, respectively, as

$$\rho = \sum_k \rho_k s_k, \tag{16}$$

$$\rho\mathbf{u} = \sum_k \rho_k \mathbf{u}_k, \tag{17}$$

$$\rho C^\alpha = \sum_k \rho_k s_k C_k^\alpha, \tag{18}$$

$$\rho h = \sum_k \rho_k s_k h_k, \tag{19}$$

$$p = p_k + \sum_i \int_0^{s_i} Ca_{ik} \, ds_i + \sum_\alpha \int_0^{C^\alpha} Cs_{\alpha k} \, dC^\alpha + \int_0^T Ct_k \, dT, \tag{20}$$

where a quantity without a subscript is reserved for the multiphase mixture, and the subscript k denotes phase k. The symbols are defined in the section on Nomenclature. The superficial velocity of phase k, $\mathbf{u}_k$, is related to its intrinsic velocity by the phase volume fraction, and thus Eq. (17) implies that the mixture velocity is a mass-weighted average of the intrinsic phase velocities.

The definition of the mixture pressure in Eq. (20) is somewhat nonconventional; however, inspection in several limiting cases reveals that the definition is indeed consistent with a mixture theory [16]. As we shall see, the definition given in Eq. (20) greatly simplifies the momentum conservation equation for a bulk mixture. The terms Ca_{ik}, $Cs_{\alpha k}$, and Ct_k in Eq. (20) are called the capillary, solutal-capillary, and thermocapillary factors, respectively, and can be expressed as functions of capillary pressure gradients with respect to saturation, species concentration, and temperature.

In addition, the mixture kinematic viscosity and the mobility of each phase in the multiphase mixture are introduced, respectively, as follows:

$$\nu = \left(\sum_k \frac{k_{rk}}{\nu_k} \right)^{-1}, \tag{21}$$

$$\lambda_k = \frac{k_{rk}}{\nu_k} \nu, \qquad \sum_k \lambda_k = 1. \tag{22}$$

2. Model Equations

The multiphase mixture model consists of the governing equations written only in terms of the mixture variables defined previously, which can be summarized as follows [16].

1. *Mass conservation of the multiphase mixture:*

$$\varepsilon \frac{\partial \rho}{\partial t} + \nabla \cdot (\rho \mathbf{u}) = 0. \tag{23}$$

It is clear that this continuity equation is just a duplicate of the corresponding equation for a single-phase mixture flow. Since the mixture density ρ is strongly variable, the multiphase mixture flow should be categorized as highly compressible.

2. *Momentum conservation of the multiphase mixture:*

$$\rho \mathbf{u} = -\frac{K}{\nu} (\nabla p - \gamma_\rho \rho \mathbf{g}), \tag{24}$$

where γ_ρ is called the density correlation factor and is defined as

$$\gamma_\rho = \frac{\sum_k \rho_k \lambda_k}{\sum_k \rho_k s_k}. \tag{25}$$

It should be noted that this correction factor is a sole function of phase saturations, and thus can be regarded as a property of the

multiphase mixture. The physical reason that a correction factor appears in the body force for a multiphase mixture is the relative motion between phases, so that the effective mixture density for the gravitational force contains certain dynamic properties of phases (i.e., λ_k and hence ν_k). Only when $\gamma_\rho = 1$, can the body force for the multiphase mixture be represented by the mixture density defined in Eq. (16). This is the case of single-phase multicomponent mixtures.

3. *Diffusive flux.*

As in a traditional mixture theory, we can define a diffusive mass flux of phase k relative to the whole multiphase mixture, such that

$$\mathbf{j}_k = \rho_k \mathbf{u}_k - \lambda_k \rho \mathbf{u}, \qquad \sum_k \mathbf{j}_k = 0, \tag{26}$$

or alternatively,

$$\rho_k \mathbf{u}_k = \mathbf{j}_k + \lambda_k \rho \mathbf{u}. \tag{27}$$

Wang and Cheng [16] found that the diffusive flux can be expressed as

$$\mathbf{j}_k = \sum_i \left[-\rho_k D_{cik} \nabla s_i + \frac{\lambda_k \lambda_i K(\rho_k - \rho_i)}{\nu} \mathbf{g} \right] + \sum_\alpha \left[-\rho_k D_{sak} \nabla C^\alpha \right] + (-\rho_k D_{tk}) \nabla T, \tag{28}$$

where the capillary diffusion coefficient D_{cik}, the solutal-capillary diffusion coefficient D_{sak}, and the thermocapillary diffusion coefficient D_{tk}, are given by

$$D_{cik} = \frac{K}{\rho_k \nu} \lambda_k \sum_j \lambda_j \left[-\frac{\partial p_{cjk}}{\partial s_i} \right], \tag{29}$$

$$D_{sak} = \frac{K}{\rho_k \nu} \lambda_k \sum_j \lambda_j \left[-\frac{\partial p_{cjk}}{\partial \sigma_{jk}} \frac{\partial \sigma_{jk}}{\partial C^\alpha} \right], \tag{30}$$

$$D_{tk} = \frac{K}{\rho_k \nu} \lambda_k \sum_j \lambda_j \left[-\frac{\partial p_{cjk}}{\partial \sigma_{jk}} \frac{\partial \sigma_{jk}}{\partial T} \right]. \tag{31}$$

Physically, Eq. (28) implies that the diffusive flux of phase k within the multiphase mixture results from the capillary forces due to saturation gradients, as well as concentration and temperature gradients through their effects on the interfacial tensions. In addition, the second term on the right-hand side of Eq. (28) reflects the gravitational separation due to the difference between phase densities. Note also that the diffusion coefficients defined by Eqs.

(29) to (31) depend only on phase saturations and, hence, are properties of the multiphase mixture.

4. *Conservation of species α in the multiphase mixture:*

$$\varepsilon \frac{\partial}{\partial t}(\rho C^\alpha) + \nabla \cdot (\gamma_\alpha \rho \mathbf{u} C^\alpha)$$

$$= \nabla \cdot [\varepsilon \rho D \nabla C^\alpha] + \nabla \cdot \left\{ \varepsilon \sum_k [\rho_k s_k D_k^\alpha (\nabla C_k^\alpha - \nabla C^\alpha)] \right\}$$

$$- \nabla \cdot \left(\sum_k C_k^\alpha \mathbf{j}_k \right), \tag{32}$$

where the correction factor for species advection γ_α, is defined as

$$\gamma_\alpha = \frac{\rho \sum\limits_k \lambda_k C_k^\alpha}{\sum\limits_k \rho_k s_k C_k^\alpha}, \tag{33}$$

and the effective diffusion coefficient for the multiphase mixture is defined as

$$\rho D = \sum_k \rho_k s_k D_k^\alpha. \tag{34}$$

The second term on the left-hand side of Eq. (32) indicates that species α is advected, on the mixture level, by a modified velocity field $\gamma_\alpha \mathbf{u}$ rather than by the original mixture velocity field. This peculiar feature resembles that related to the gravitational term in the momentum equation, Eq. (24). The first two terms on the right-hand side of Eq. (32) combine to represent the net Fickian diffusion fluxes within various phases, whereas the last term on the right-hand side represents the diffusive flux across phases. Also, note that the second term on the right-hand side of Eq. (32) vanishes in single-phase regions or when the phase compositions C_k^α are identical in all phases.

It is worth mentioning that the mixture concentration C^α in a multiphase region essentially corresponds to the phase saturation s_k through Eq. (18) because the phase compositions C_k^α are given by the corresponding phase diagram under the assumption of local chemical equilibrium. Therefore, solving C^α from Eq. (32) determines all the phase saturations that, in turn, are used to calculate the mixture properties.

5. *Energy conservation for the multiphase mixture:*

$$\frac{\partial}{\partial t}[(1 - \varepsilon)\rho_s h_s + \varepsilon\rho h] + \nabla \cdot (\gamma_h \rho \mathbf{u} h)$$

$$= \nabla \cdot (k_{\text{eff}} \nabla T) + \nabla \cdot \left[\sum_k (h_k \mathbf{j}_k)\right] + \dot{q}, \quad (35)$$

where local thermal equilibrium among contiguous phases is invoked, and the correction factor for energy advection γ_h, is defined as

$$\gamma_h = \frac{\rho \sum_k \gamma_k h_k}{\sum_k \rho_k s_k h_k}. \quad (36)$$

The second term on the right-hand side of Eq. (35) describes the energy flux due to relative phase motions, including both sensible and latent heat transport.

3. Model Summary

Equations (23), (24), (32), and (35) represent a full system of governing equations for four mixture variables, that is, mixture velocity $\mathbf{u}$, mixture pressure p, mixture concentration C^α, and the mixture temperature T. As can be seen, striking similarities exist between the MMM equations and those in the single-phase transport theory; the two sets differ only in that property coefficients are variable and additional source terms appear (in the mixture species and energy equations) in MMM. The similarities are physically conceivable because on the mixture level, a multiphase system is not much different from a single-phase fluid. The variable properties contained in the model equations precisely reflect the physics that multiphase flow problems are inherently nonlinear. The source terms arise from the interfacial mass and heat transfer processes occurring internally within the multiphase mixture. For single-phase flows, these source terms vanish and the variable properties reduce identically to those corresponding to the single-phase transport theory.

Recognizing the similar structure of MMM to the single-phase transport theory, it is clear that the new model equations for multiphase flows are amenable to well-established single-phase computational fluid dynamics (CFD) algorithms. The solution sequence may be as follows:

1. From the transport equations for the multiphase mixture, the mixture pressure, velocity, concentration, and temperature fields are determined.

2. From the mixture pressure, concentration and temperature at a nodal point, the thermodynamic state of this cell is identified (see Wang and Cheng [16] for details).
3. Phase concentrations are then calculated from equilibrium phase diagrams, and the phase saturations are determined from the mixture concentration solved from the species transport equation.
4. Effective thermophysical properties of the multiphase mixture are then evaluated with the knowledge of phase saturations, and finally these properties are substituted back into the transport equations for updating.

The entire procedure is repeated iteratively until convergence is achieved. Successful calculations for several practical problems have been made [44–48].

In closing, it should be mentioned that the mixture pressure, Eq. (20), introduced to facilitate the development of MMM is similar to the "global pressure" previously proposed by Chavent [49] and Yortsos [50] in an attempt to obtain a simplified mathematical system describing immiscible displacement in porous media. The slight difference lies only in the fact that the present definition is generally applicable to multiphase flows with and without phase change, whereas the previous concept is limited to immiscible flow without phase change and interphase mass transfer. Nonetheless, the fundamental novelty of the present formulation is Eqs. (26) to (28), which allow the calculation of individual phase velocities, thus maintaining the mathematical equivalence between MFM and MMM. The key equation, Eq. (28), was first derived by Wang and Beckermann [51] for two-phase systems and was extended by Wang and Cheng [16] for general multiphase systems.

E. COMPARISONS OF VARIOUS MODELS

Compared with the traditional MFM, MMM offers the following advantages:

1. It strongly resembles the single-phase transport theory, thus facilitating both theoretical and numerical analyses.
2. It requires much fewer nonlinear and coupled differential equations to be solved. For example, for a three-phase isothermal flow, the MFM requires a total of 12 primary variables: 2 phase saturations, 9 velocity components for 3 phases in 3 dimensions and any one phase pressure. In contrast, MMM contains only 6 primary variables: 2 mixture concentrations (or equivalently 2 phase saturations), 3 mixture velocity components, and the mixture pressure. This unique feature

renders MMM particularly suitable for numerical simulations with even moderate computer resources.

3. It is a mixture formulation, thus eliminating the need to handle phase appearance or disappearance and to track interfaces separating single-phase from multiphase regions. The mixture variables are always present.

4. Most importantly, MMM provides the same predictive capabilities as does the conventional MFM. With the aid of Eqs. (27) and (28), the flow characteristics of individual phases can be obtained readily after the flow problem of the bulk mixture has been solved. Thus the detailed flow aspects of each phase are not smeared out in MMM. Similarly, the phase pressures p_k can be obtained from Eq. (20) after the mixture pressure, temperature, concentration, and phase saturation fields are determined. Moreover, these types of calculations, if needed, can be done in a postprocessing manner. This is why the model is called the *multiphase mixture model*, rather than simply a mixture model, implying that, in the latter, the intrinsic multiphase characteristics usually are lost.

In essence, MMM is a mathematically equivalent but reformulated version of MFM (i.e., without making any additional approximations). The model reduction was achieved by replacing some differential equations contained in MFM by the corresponding algebraic equations in MMM.

To compare MMM with UFT, it is instructive to substitute Eq. (27) for the liquid mass flux $\rho_l \mathbf{u}_l$ into the mass conservation equation for the liquid phase, Eq. (2). This results in

$$\varepsilon \frac{\partial(\rho_l s_l)}{\partial t} + \nabla \cdot (\rho \mathbf{u} \lambda_l) = -\nabla \cdot \mathbf{j}_l + \overline{m}_l, \qquad (37)$$

where the diffusive mass flux $\mathbf{j}_l$ can be simplified, in the case of isothermal two-phase flow, to

$$\mathbf{j}_l = -\rho_l D_c \nabla s_l + \frac{\lambda_l \lambda_g K(\rho_l - \rho_g)}{\nu} \mathbf{g}. \qquad (38)$$

Substitution of Eq. (38) into Eq. (37) yields

$$\varepsilon \frac{\partial(\rho_l s_l)}{\partial t} + \nabla \cdot (\rho \mathbf{u} \lambda_l)$$

$$= \nabla \cdot (\rho_l D_c \nabla s_l) - \nabla \cdot \left(\frac{\lambda_l \lambda_g K(\rho_l - \rho_g)}{\nu} \mathbf{g} \right) + \overline{m}_l. \qquad (39)$$

This equation can be referred to as the generalized Richards equation because it identically reduces to the Richards equation in the limit of the

constant gas phase pressure or, equivalently, zero gas viscosity. In this case, it can be easily shown from Eqs. (21), (22), and (29) that

$$\lambda_l \to 0, \quad \lambda_g \to 1, \quad \frac{\lambda_l}{\nu} \to \frac{k_{rl}}{\nu_l}, \quad \rho_l D_c \to D(s_l). \tag{40}$$

Substitution of these asymptotes into Eq. (39) recovers the Richards equation of UFT. Thus it is clear that the Richards approximation elegantly eliminates the advective term in Eq. (39), thereby resulting in a single equation having a diffusion nature for the liquid saturation. Whereas this yields great simplifications, the applicability of UFT to general multiphase flow problems is severely limited because the gas phase motion cannot be determined.

The Richards equation can also be derived from Eq. (39) using the limit $\nu_1 \to \infty$. Collectively, it can be concluded that UFT holds true in the limit of the viscosity ratio ν_l/ν_g approaching infinity. A numerical experiment for a boundary layer–type two-phase flow indicated that this condition corresponds to such a high threshold value that practically no fluid pair could possibly match it (see Part III, Section D.4 for further discussion).

In the absence of the Richards approximation, Eq. (39) contains both diffusion and advective terms, where the mixture velocity field must be determined from the continuity and momentum equations given by Eqs. (23) and (24). In view of the fact that UFT introduces approximations that are difficult to justify and ascertain in general situations, the exact nature of Eq. (39) may open new prospects for a more accurate understanding of multiphase flow through porous media.

F. NONEQUILIBRIUM EFFECTS

In all the foregoing mathematical models, interfacial thermal and chemical equilibrium is assumed implicitly. In most circumstances, the assumption is adequate; however, in other practical applications, interfacial heat and mass transfer may become rate-limited.

Interfacial thermal equilibrium has been under investigation for many years. Whitaker [52] attempted to define the domain of validity of local thermal equilibrium by an order of magnitude estimate. Using the method of volume averaging, Kaviany [14] extensively examined local thermal nonequilibrium effects and developed a two-equation model for the averaged temperatures in each phase. The form of the two-equation model in the case of pure diffusion was further explored by Quintard and Whitaker [53].

Interfacial chemical nonequilibrium recently received intensive attention in the field of groundwater contamination and remediation. Results of a series of laboratory-scale experiments [54] demonstrated several potential limitations of the local chemical equilibrium assumption. In particular, the dissolution of contaminants into the aqueous phase was found to be rate-limited by interfacial mass transfer under low NAPL saturation or high aqueous phase flow conditions typically encountered during pump-and-treat remediation [55–57]. In relation to the popular soil vapor extraction technique for subsurface remediation, the interfacial mass transfer between NAPL and air has been determined experimentally [58]. Most recently, Quintard and Whitaker [59] derived a macroscopic multiphase flow model that rigorously accounts for interfacial mass transfer between phases.

Whereas the multiphase flow model can easily be extended to include interfacial nonequilibrium effects, it is of interest to explore the potential of MMM in describing nonequilibrium processes. It should be noted that MMM is not inherently an equilibrium model; in fact, the model has accounted for dynamic nonequilibrium because it allows for different phase velocities, as discussed in the preceding section. Similarly, the assumptions of interfacial thermal and chemical equilibrium can be relaxed. Under such circumstances, the model differential equations summarized previously remain valid, whereas only the supplementary relationships for determining phase saturations, phase temperatures, and compositions need to be modified. In the absence of thermal and chemical equilibrium, the bulk phase temperature and concentration depart from their interfacial values (as determined from equilibrium phase diagrams), with the magnitudes of departures measured by the local heat and mass transfer coefficients.

G. Non-Darcian Effects

Non-Darcian effects, such as inertial, boundary, and dispersion effects, have been widely investigated for single-phase flows [14, 60]. Forchheimer and Brinkman's extensions of Darcy's law have been well established, and species and thermal dispersion coefficients have been determined by, for example, Koch and Brady [61] and Hsu and Cheng [62]. This situation clearly is different for multiphase flows. While the non-Darcian effects may be equally important in certain multiphase problems (i.e., the boundary effect in two-phase condensing flow and the inertia effect in trickle beds), it remains largely unknown how to incorporate these effects into a multiphase flow model. This point of view is particularly evident in the recent monograph by Kaviany [14]. Much more fundamental research on

multiphase flows in porous media is needed before these non-Darcian effects can be rigorously incorporated. Preliminary attempts at modeling the inertia effect in the literature are reviewed subsequently to show how little is known in this area.

Based on visual observations of co-current and countercurrent flow of air and water in beds composed of large-diameter particles ($d_p \geq 3$ mm), Tung and Dhir [63] derived a hydrodynamic model that includes the generalized Darcy term, quadratic inertia term, and an interfacial drag. The expressions for relative permeability and interfacial drag were also developed. The model prediction for one-dimensional (1D) co-current and countercurrent two-phase flows was found to be in good agreement with the experimental measurements.

Using the volume averaging theory, Grosser et al. [64] and Dankworth et al. [65] derived a set of macroscopic equations for gas–liquid flow in trickled beds, which is in a form similar to that of two-phase flow without porous media. The momentum equation for each phase contains an interfacial drag accounting for the total forces exerted on that phase by the other fluid phases as well as by the stationary solid matrix. A constitutive relationship for the interfacial drag was developed, which resembles the single-phase Ergun correlation.

A semiheuristic approach to incorporate the effect of inertia was proposed by Kaviany [14]. The two-phase momentum equations were obtained simply by multiplying the relative permeability to the Darcy term and another "microscopic inertia coefficient" to the inertia term of the single-phase Forchheimer equation. Both coefficients are assumed to depend only on the saturation and must be determined empirically. Although the previous models possess appropriate asymptotic behaviors in the limits of zero and unity liquid saturation, they apparently lack in taking into account fundamental pore-level fluid mechanics. The models with and without interfacial drag are inconsistent. The modeling burden is simply shifted to the calibration of the empirical coefficients introduced. It is expected that the general framework established in MMM may provide a novel approach (from the perspective of the multiphase mixture) to the fundamental modeling of non-Darcian effects in multiphase flows.

III. Two-Phase, Single-Component Systems

Two-phase flow and heat transfer in porous media saturated with pure fluids has historically received intensive attention due to its enormous technological importance and academic interest. Three distinct regions

may appear in a two-phase, single-component system with heat transfer:

1. A single-phase vapor region where the voids are filled with superheated vapor
2. A nearly isothermal two-phase zone in which vapor and liquid co-exist at equilibrium
3. A single-phase liquid region with the pore spaces occupied by the subcooled liquid.

Such a thermodynamic state is conveniently sketched in Fig. 3 with a 1D geometry. Evaporation occurs at the lower boundary of the two-phase zone with bottom heating or volumetrically with internal heating, while vapor condensation takes place at the upper boundary of the two-phase zone in the case of top cooling. The countercurrent liquid–vapor percolation provides a net upward heat flow.
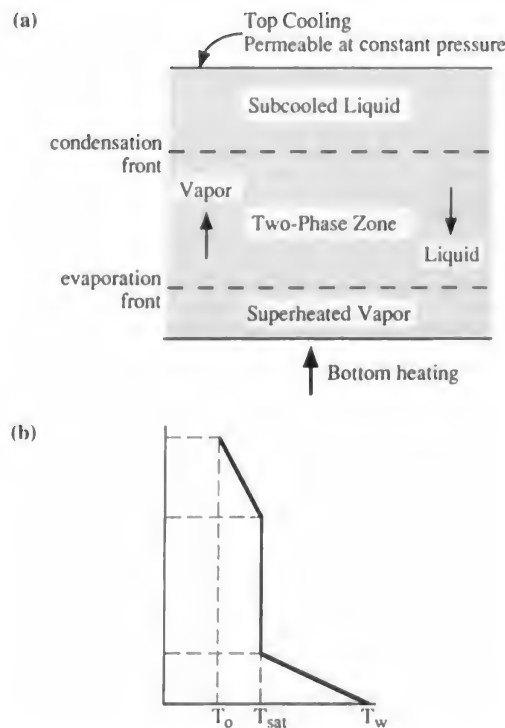
FIG. 3. Schematic illustration of (a) boiling in a one-dimensional porous medium, and (b) the temperature profile.

Using Kelvin and Clapeyron equations, Udell [32] determined the saturated temperature in the two-phase zone as follows:

$$T = \frac{T_0 \left[1 + \dfrac{p_c}{h_{fg}\, \rho_l} \right]}{1 - \dfrac{RT_0}{h_{fg}} \ln \dfrac{p_v}{p_0}},$$ (41)

where T_0 and p_0 are the reference temperature and its saturation pressure at which the capillary pressure is zero and hence the vapor pressure p_v becomes equal to the reference p_0. The subscripts l and v in Eq. (41) and throughout this section denote liquid and vapor phases, respectively. The temperature in the two-phase zone is practically constant under most conditions except for geothermal situations, where the relevant length scale is on the order of kilometers and hence the pressure variation is substantial. Satik $et\ al.$ [66] found that the importance of heat conduction due to the temperature difference in the two-phase zone is quantified by a single dimensionless group

$$\frac{Kh_{fg}^2 M_w p_0\, \rho_v}{\mu_v k_{\mathrm{eff}} RT_0^2},$$

where M_w is the molecular weight of the fluid component and R is the universal gas constant. Typically, this dimensionless parameter is large and heat conduction is negligible.

A. One-Dimensional Situations

One-dimensional two-phase flow in porous media is of theoretical interest for understanding the transport processes occurring in a variety of engineering systems such as heat pipes, geothermal reservoirs, and nuclear debris beds. This is also the only class of two-phase flow problems that admit exact solutions. Extensive research has been carried out in both steady-state and transient cases.

In a 1D situation, the continuity and liquid mass conservation equations given by Eqs. (23) and (39) are simplified, respectively, to

$$\varepsilon\, \frac{\partial \rho}{\partial t} + \frac{\partial(\rho u)}{\partial x} = 0,$$ (42)

$$\varepsilon\, \frac{\partial(\rho_l s_l)}{\partial t} + \frac{\partial(\rho u \lambda_l)}{\partial x} = \frac{\partial}{\partial x}\left(\rho_l D_c\, \frac{\partial s_l}{\partial x} \right)$$
$$- \frac{\partial}{\partial x}\left(\frac{\lambda_l \lambda_v K(\rho_l - \rho_v) g_x}{\nu} \right) + \overline{m}_l,$$ (43)
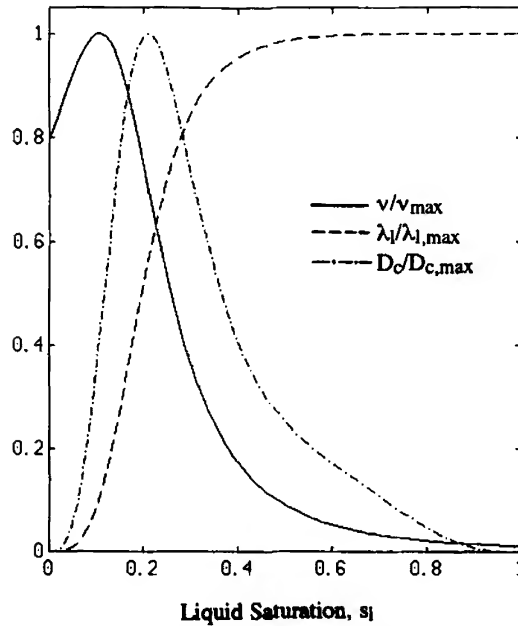
FIG. 4. Variations of two-phase mixture properties with respect to the liquid saturation.

where g_x denotes the x-component of the gravity vector. It is evident that the mixture velocity u and liquid saturation s_l represent the only primary variables for 1D problems, while other variables such as phase velocities and pressures can be algebraically determined, from the various relations given in Part II, Section D, after Eqs. (42) and (43) are solved. Hence, Eqs. (42) and (43) form a theoretical basis for 1D two-phase flow in porous media with and without phase change. Furthermore, the familiar form of this equation set can shed considerable light on finding possible analytical solutions, as will be discussed later. Note that the two-phase property coefficients in Eqs. (42) and (43) are strongly dependent on the liquid saturation s_l. Figure 4 displays typical variations of these coefficients, which include the mixture viscosity ν, relative mobility λ_l (and $\lambda_r = 1 - \lambda_l$), and capillary diffusion coefficient D_c.

1. Steady Two-Phase Flows

Various analytical solutions exist for steady, 1D two-phase flow problems, as summarized by Lipinski [67] with application to the nuclear reactor safety analysis. These flows are induced by bottom heating, volumetric heating, or both. Under the steady-state conditions, the continuity

equation, Eq. (42), requires that

$$\rho u = \dot{m}_w, \tag{44}$$

where $\dot{m}_w$ denotes a constant mass flux across the two-phase zone. If the two-phase zone is bounded by an impermeable wall, that is, $\dot{m}_w = 0$, Eq. (44) leads to a uniformly zero mixture velocity within the two-phase zone. Assuming an isothermal two-phase zone, the interphase mass transfer rate $\overline{m}_l$ is equal to $-\dot{q}/h_{fg}$. Integration of Eq. (43) subject to appropriate boundary conditions yields

$$\rho_l D_c(s) \frac{\partial s_l}{\partial x} - \frac{\lambda_l \lambda_v K(\rho_l - \rho_v) g_x}{\nu}$$

$$= \frac{1}{h_{fg}} \left(q_w + \int \dot{q} \, dx \right) + \dot{m}_w(\lambda_l - \lambda_{l,w}). \tag{45}$$

This equation is a key theoretical tool for studying steady 1D two-phase flows in porous media with phase change. Physically Eq. (45) implies that the two-phase flow may be driven by capillary forces, gravitational forces, or both. The last term on the right-hand side would vanish if either boundary of the two-phase zone were impermeable. As will be shown subsequently, exploration of various limiting cases of Eq. (45) allows for an overview of previous theoretical studies on steady 1D two-phase flow and heat transfer in porous media.

In the absence of capillary forces (i.e., in the gravity-driven case), Eq. (45) reduces to an algebraic equation, implying that a two-phase zone of constant liquid saturation results. Moreover, there are two solutions for a given heat flow rate, one corresponding to low liquid saturation (vapor dominated, VD) and the other corresponding to high liquid saturation (liquid dominated, LD). The multiple solutions arise from the fact that the product of the two relative mobilities varies nonmonotonically with the liquid saturation, as clearly shown in Fig. 4. Figure 5 illustrates the multiple possible solutions to a two-phase problem with bottom heating for a special choice of relative permeabilities given by Bau and Torrance [68]: $k_{rl} = s_l$ and $k_{rv} = (1 - s_l)$. The selection of a particular solution in reality depends on the past history of the system. For instance, in the case of boiling (bottom heating), it is the LD branch that is followed, while in condensation of a superheated vapor (top cooling), it is the VD branch that is selected [66]. Using a singular perturbation method, McGuinness [69] rigorously analyzed Eq. (45), and proposed a concept called *capillary boundary layer* to explain the selection process of either LD or VD solution.
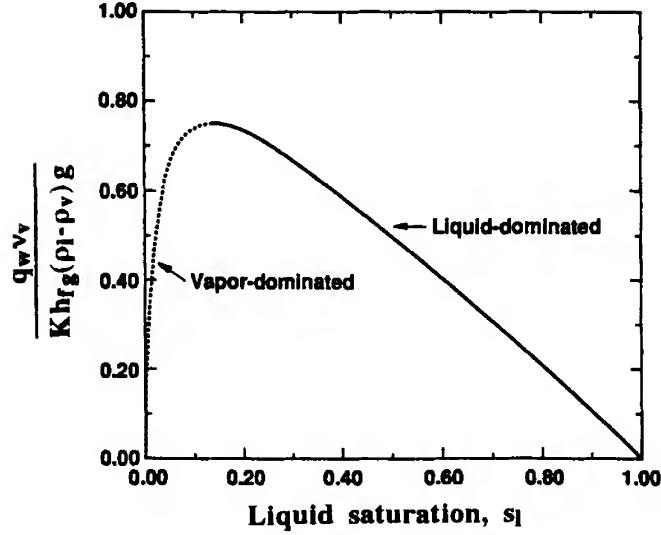
FIG. 5. Multiple solutions for the two-phase zone with negligible capillarity [68].

Figure 5 also showed that there exists a maximum heat flux at a particular value of the liquid saturation. The limit represents the peak heat flux that can be transported through a two-phase zone by the counter-current percolation mechanism. When the applied heat flux exceeds this maximum, the two-phase zone must disappear and be replaced by a superheated vapor layer. Thus the limit is also called the dryout heat flux, which can be predicted from Eq. (45) with the capillary term neglected; that is,

$$\frac{q_{\text{dry}} \nu_{v}}{Kh_{fg}(\rho_{l} - \rho_{v})(-g_{x})} = \max_{s_{l}}\left\{\frac{\lambda_{l}\lambda_{v}\nu_{v}}{\nu}\right\} = \max_{s_{l}}\left\{\frac{k_{rl}k_{rv}}{k_{rl} + (\nu_{l}/\nu_{v})k_{rv}}\right\}.$$

(46)

Apparently the dryout limit is dependent on the particular form of relative permeabilities. Including the capillary effect, Udell [32] solved Eq. (45) numerically to obtain the dryout heat flux for the cases of bottom and top heating, and compared them with his experiments for a steam–water system.

The effects of medium heterogeneity on two-phase flow and resultant dryout with bottom heating were explored by Chuah and Carey [70], Wang et al. [71], and Stubos et al. [72], among others. Chuah and Carey studied two-phase flow in a continuously variable porosity layer, but did not

consider the associated dryout limit. Wang *et al.* [71] numerically investigated two-phase flow and dryout in a composite porous layer heated from below. The porous bed consisted of two homogeneous sublayers of different particle diameter. A saturation jump was found to exist at the interface between the two sublayers due to the capillary force resulting from medium heterogeneity. The jump may have a positive or negative effect on the dryout heat flux, depending on whether a high-permeability sublayer overlies one of low permeability, or vice versa. In the enhanced case, the optimal thickness of the high-permeability sublayer was determined to be around 60% of the total bed height for the maximum dryout heat flux. Stubos *et al.* [72] further explored the effects of medium heterogeneity on vapor–liquid counterflow in porous heat pipes, and showed that the capillary heterogeneity is analogous to an external body force, aiding or opposing the gravity roles in the operation of heat pipes.

Dryout limits in volumetrically heated beds were compiled by Lipinski [67] for various particle diameters using water and Freon as the working fluids, as shown in Fig. 6. In Fig. 6 the available experimental data are also compared with the theoretical predictions based on a generalized version of Eq. (45) with the inertia effect included. Reasonable agreement is found, indicating that a hydrodynamic model is adequate to describe the dryout phenomenon of boiling in a wide variety of porous beds. Dhir [6] summarized experimental data on the effects of system variables on the dryout heat flux, such as vapor channeling, liquid subcooling, and forced flow through porous beds. The effect of liquid throughflow is readily seen from Eq. (45) where $\lambda_{l,w}$ is equal to unity due to liquid feeding from the bottom. It then can be deduced that the dryout heat flux increases with the liquid throughflow rate $\dot{m}_w$. Furthermore, Eq. (45) reveals that the lower bound of the dryout heat flux with the feeding of liquid from below should be given by $\dot{m}_w h_{fg}$, which is exactly the amount of energy needed to convert all of the incoming liquid into vapor. The dryout heat flux data obtained by Tsai and Catton [73] for the case of forced flow, as displayed in Fig. 7, indeed shows such an asymptotic behavior. The difference between the measured data and their lower bound represents the contribution of the countercurrent two-phase flow driven by gravity. As the throughflow rate increases, the gravity-induced contribution diminishes and a co-current flow pattern begins to prevail in most of the porous bed.

In geothermal systems the capillary term is often negligible because of the system's large length scales, and typically there is neither a surface nor volumetric heat source to sustain the two-phase zone in the shallow subsurface. Instead, the decrease in pressure, which occurs on approaching the ground surface, acts as a volumetric heat source to generate the vapor. For a given pressure variation with depth, an equivalent heat generation
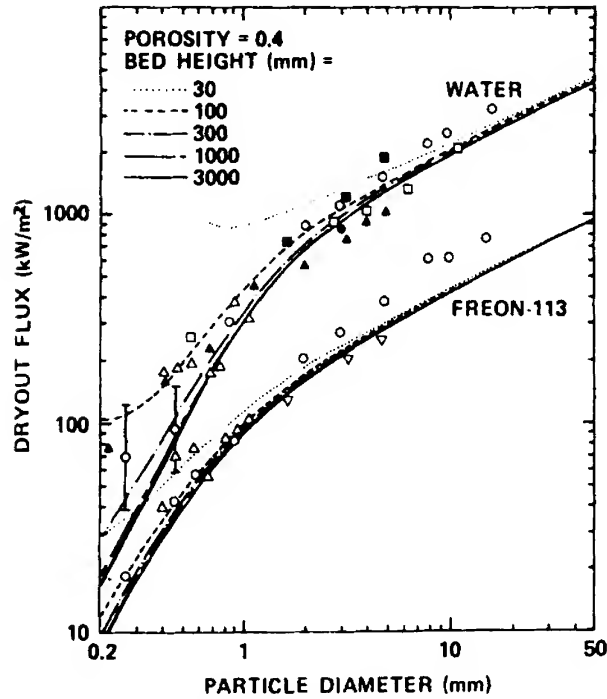
FIG. 6. Experimental (symbols) and theoretical (lines) dryout heat fluxes in a variety of packed beds saturated with water and Freon-113 [67].

rate can be calculated from the energy equation, requiring the temperature to follow on the Clapeyron curve for saturated temperature and pressure. Sheu *et al.* [74] investigated a system with steady flow through the two-phase zone (i.e., $\dot{m}_w \neq 0$) in order to model geothermal reservoirs above cooling igneous intrusions. Pressure release boiling results in a two-phase zone of variable saturation as the heat generation rate varies with location. Within this zone, steam percolates upward relative to water and condenses at the upper boundary due to conductive heat loss to the cold ground surface. Numerical results were compared with temperature and pressure logs from drill holes in the thermal systems of Steamboat Springs, Nevada, and Yellowstone National Park, Wyoming. Schubert and Straus [75] analytically explored the case without vertical throughflow (i.e., $\dot{m}_w = 0$).
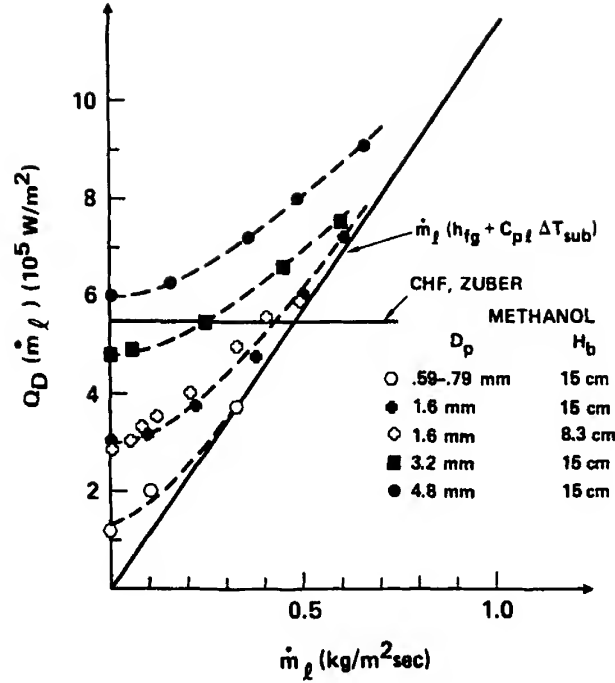
Fig. 7. Dryout heat flux data for a methanol-saturated bed with liquid feeding from below. The solid line denotes an asymptotic limit. CHF, the critical heat flux of pool boiling [73].

2. Transient Two-Phase Flows

Exact similarity solutions can be obtained for transient two-phase flows in porous media under certain types of initial and boundary conditions [37, 77]. To show this, we neglect the interphase mass transfer rate and the gravity effect in Eq. (43). The governing equations then become

$$\varepsilon \frac{\partial \rho}{\partial t} + \frac{\partial(\rho u)}{\partial x} = 0,$$

$$\varepsilon \frac{\partial(\rho_l s_l)}{\partial t} + \frac{(\rho u \lambda_l)}{\partial x} = \frac{\partial}{\partial x}\left(\rho_l D_c \frac{\partial s_l}{\partial x}\right). \tag{47}$$

If the boundary condition for the velocity u varies inversely proportional to the square root of time, a similarity variable, $\eta = x/\sqrt{t}$, reduces Eq. (47) to a set of ordinary differential equations. This change of variables, known as the Boltzmann transformation in heat conduction, is the tool employed by Morrison [76], Doughty and Pruess [77], and McWhorster and

Sunada [37] to arrive at an exact solution for various two-phase flows with and without phase change.

Morrison [76] numerically analyzed a transient condensing two-phase flow by applying the foregoing similarity transformation, and showed that a discontinuity in saturation occurs at the condensation front. This shocklike behavior is attributed to the neglect of capillary effects from Eq. (47). Similarity solutions were also obtained by Nilson and Romero [78] for the propagation of a condensation front into an initially dry porous matrix that received an inflow of saturated vapor. Once again, the capillarity was ignored, thus leading to the hyperbolic equations, as can be seen from Eq. (47). Later, their analysis was extended to various types of initial and boundary conditions [79]. In addition, an experimental study [80] was performed to validate the theoretical prediction of temperature and pressure profiles. Recently, Tsurata et al. [81] experimentally and analytically investigated condensing flow through an initially subcooled porous medium. It is worth mentioning that all these studies on phase change flows failed to recognize that the same similarity transformation exists even with the inclusion of capillarity. Therefore, it is of interest for future research to explore the effects of capillarity in altering the shocklike behavior of transient two-phase flows in porous media.

Doughty and Pruess [77] studied the thermal and geological behavior resulting from the emplacement of a heat source, such as a high-level nuclear waste package, into a geological medium. The above-mentioned similarity transformation was applied to obtain a coupled set of ordinary differential equation that were solved numerically in the cylindrical coordinates.

McWhorster and Sunada [37] considered two-phase flow in porous media without phase change for hydrological applications. Using the foregoing similarity transformation, they developed the first "exact" solution in the presence of capillarity. A limit of their solution in the absence of capillarity is the well-known Buckley-Leverett case. McWhorster and Sunada's solutions is now widely used as a benchmark for validation and testing of complex 2D and 3D numerical codes for multiphase flow and transport in porous media [82].

Transient two-phase flow inside a heat pipe wick was investigated experimentally and analytically by Ambrose et al. [83], who reported the transient liquid saturation profiles along a heat pipe as a function of heat input to the evaporator section. Measurements of the liquid saturation distribution was made by X-ray radiography. The theoretical equation derived to predict the liquid distribution inside the porous wick strongly resembled the UFT version of Eq. (43). The predicted and measured liquid saturation distributions were compared favorably.

B. INTERNAL BOILING AND NATURAL CONVECTION

The two-phase Bérnard-like problem in a horizontal porous layer with bottom or internal heating has been the subject of recent research. Both experimental [68, 84] and theoretical [39, 44, 45, 86, 87] investigations were performed. An important finding from the latest numerical study by Wang *et al.* [45] is that various transient effects may well exist in this inherently nonlinear two-phase system. Separate discussion for each heating mode follows.

1. *Bottom Heating*

Single-phase natural convection inside a horizontal liquid-saturated porous layer heated from below has been a classic topic and has received extensive research attention for many years [60]. When the bottom heat flux exceeds a critical value, boiling or evaporation starts adjacent to the heated surface, and the thermodynamic state of the system then consists of a two-phase zone underneath a subcooled liquid region, as schematically shown in Fig. 8. Convection in the upper liquid region affects the boiling behavior in the underlying two-phase zone, and the two-phase flow, in turn, influences natural convection in the overlying liquid region. It is this interactive nature that rendered this fundamentally interesting problem unsolved until the 1990s.
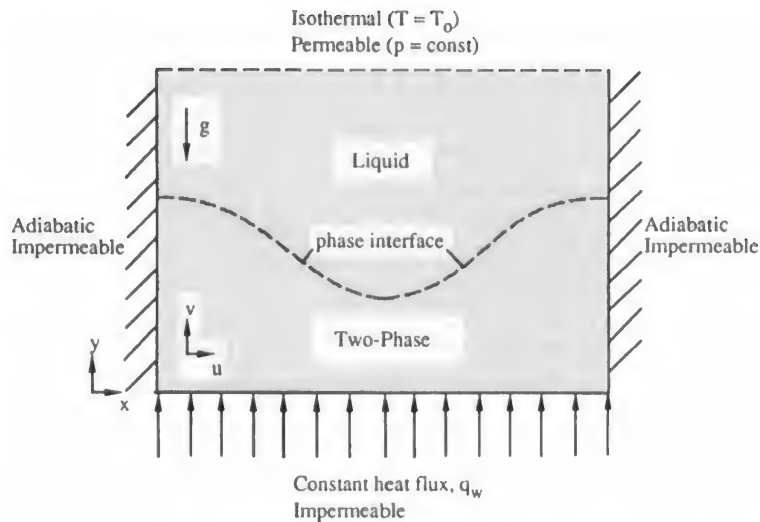
FIG. 8. Schematic illustration of boiling and two-phase flow in a horizontal porous cavity heated from below.

a. Linear Stability Analysis   When the liquid region overlies the two-phase zone, there are two instability mechanisms: buoyancy and gravitational instabilities. The gravitational instability of vapor–liquid counterflow, referred to as the heavier full-liquid region overlying the lighter two-phase zone, differs from the classic Rayleigh-Taylor instability of superposed fluids in that the phase interface is permeable and thus allows both mass and heat transfer across it. Schubert and Straus [88] performed a linear stability analysis and found that such systems are stable, provided the permeability is sufficiently small. The stability is maintained because when liquid penetrates the phase interface, that interface is distorted along the Clapeyron curve, thereby creating a pressure gradient that acts to restore the system to equilibrium.

The onset of 2D polyhedral-shaped convection in the configuration of Fig. 8 was studied by Ramesh and Torrance [86] using a linear stability analysis. Their analysis revealed that the governing parameters include the Rayleigh numbers Ra and $Ra_{2\phi}$ for the liquid and two-phase regions as well as the dimensionless bottom heat flux Q_w. These parameters are defined, respectively, as

$$Ra = \frac{\beta_l(T_{sat} - T_0)KL_h g}{\nu_l \alpha_l}, \qquad Ra_{2\phi} = \frac{(1 - \rho_v/\rho_l)KL_h g}{\nu_l \alpha_l},$$

$$Q_w = \frac{q_w L_h}{k_{eff}(T_{sat} - T_0)}. \tag{48}$$

The two Rayleigh numbers are related through a density ratio; that is,

$$\frac{Ra}{Ra_{2\phi}} = \frac{\beta_l(T_{sat} - T_0)}{1 - \rho_v/\rho_l} = \frac{\rho_l \beta_l(T_{sat} - T_0)}{\rho_l - \rho_v}, \tag{49}$$

where the numerator is simply the maximum density variation in the liquid region and the denominator is the density difference between the phases in the two-phase zone. If the boundary temperature T_0 is fixed, the two Rayleigh numbers are not independent.

For liquid-dominated systems, Ramesh and Torrance [86] obtained a comprehensive map of conductive and convective solutions in the Ra–Q_w parameter space, as shown in Fig. 9. Four distinct regions can be identified from this stability map:

1. Conductive liquid layer
2. Convective liquid layer
3. Conductive liquid layer above a two-phase zone
4. Convective liquid layer above a two-phase zone.

The onset of boiling is indicated by curve ABE in Fig. 9. For Q_w values above this curve, boiling occurs with a liquid layer overlying a two-phase
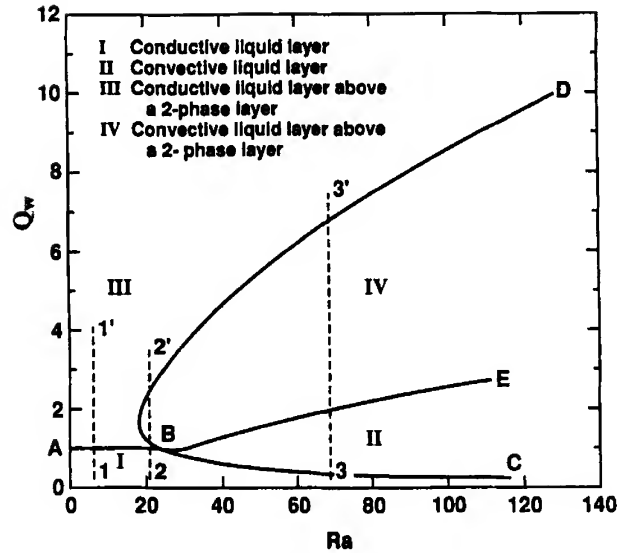
FIG. 9. Map of conductive and convective solutions for liquid-dominated two-phase systems [86]. Q_w, dimensionless heat flux; Ra, Rayleigh number.

zone. For Q_w values below ABE, boiling does not occur. The onset of convection in the liquid is denoted by curve CBD. Convection occurs only to the right of the curve. Curve CBD thus defines the critical Rayleigh number Ra_{cr} as a function of Q_w for a wave number fixed at π.

The map in Fig. 9 is extremely useful for interpreting various boiling experiments. Consider a series of experiments conducted by varying the bottom heat flux and with constant fluid and matrix properties. At low Ra (as indicated by line 1–1′) the liquid region is conductive before and after the onset of boiling. This is consistent with the experiments of Bau and Torrance [68] for low permeability beds ($K = 11 \times 10^{-12}$ m²). At higher Ra (as indicated by line 2–2′), the liquid region is conductive before the onset of boiling, but becomes convective almost immediately when boiling starts, which is in agreement with the observations of Sondergeld and Turcotte [84] ($K = 70 \times 10^{-12}$ m²). For large Ra (as denoted by line 3–3′) the liquid region becomes convective before the onset of boiling and stays convective after the onset of boiling, which coincides with the experiments of Bau and Torrance [85] on high permeability beds ($K = 1600 \times 10^{-12}$ m²). The latter study also showed that at high heat fluxes the liquid region reverts back to a conductive state, which is again predicted by Fig. 9.
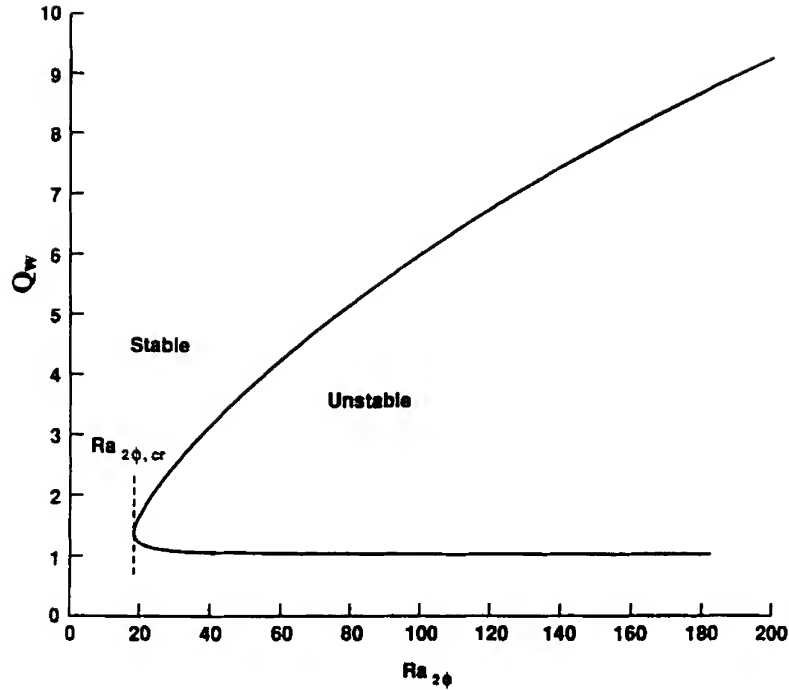
FIG. 10. Stability curves for vapor-dominated two-phase systems with Ra = 0 [86]. Q_w, dimensionless heat flux; Ra, Rayleigh number.

For vapor-dominated systems, the density difference between the liquid and two-phase regions becomes significant, and thus gravitational instability is expected to dominate over buoyancy instability. Neglecting the buoyancy effects (i.e., Ra = 0), Ramesh and Torrance [86] obtained the stability diagram shown in Fig. 10 for vapor-dominated systems. The diagram was obtained for water as the working fluid and for a top surface temperature of 30°C. For the wave number of π, the minimum value of $Ra_{2\phi}$ for the onset convection was found to be 18.95, occurring at $Q_w = 1.4$.

b. Experimental Observations   Observations of boiling in porous materials have been made in several studies. Sondergeld and Turcotte [84] carried out an experimental investigation in a horizontal porous cavity heated from below and cooled from the top. The experimental setup was designed to model a geological thermal reservoir on a laboratory scale. The two-dimensional (2D) porous layer was composed of spherical glass

media ($K = 7.04 \times 10^{-11}$ m^2, $d_p = 0.53$ mm, and $\varepsilon = 0.347$). The rate of heat input was varied over a range of $1.8 < Q_w < 26.0$, where Q_w is the dimensionless bottom heat flux defined in Eq. (48). The case of $Q_w = 1$ corresponds to pure heat conduction occurring inside the bed at the onset of boiling. Sondergeld and Turcotte [84] observed that as Q_w was increased to greater than unity, a single-phase polyhedral-shaped convection flow pattern with central downwelling and peripheral upwelling began to appear. Further increases in Q_w resulted in the appearance of a two-phase zone, and the buoyancy-driven convection cell remained similar to the single-phase case except for penetration into the two-phase zone. The two-phase layer was stable up to the point where $Q_w = 18$, after which a superheated vapor zone eventually appeared.

A similar system, but of cylindrical geometry, was studied by Bau and Torrance [68]. This bed consisted of closely packed glass beads with heating from the base and cooling from the top ($K = 8.5 \times 10^{-12}$ m^2, $d_p = 0.11$ mm, and $\varepsilon = 0.37$). One-dimensional boiling was observed, with the two-phase zone uniformly expanding as the bottom heat flux increases. When the height of the two-phase zone reached about 70% to 80% of the total bed height, the temperature field in the overlying liquid region became time-periodic.

In another study by Bau and Torrance [85], a bed of Ottawa sand was used ($K = 1.4 \times 10^{-9}$ m^2, $d_p = 1.06$ mm, and $\varepsilon = 0.42$). Steady single-phase convection was reported in the system up to a dimensionless heat flux of around $Q_w = 4$. For higher Q_w, boiling occurred and the system consisted of both liquid and two-phase regions. At much higher Q_w values, the cellular convection flow disappeared, and a horizontal liquid layer was then observed to overlie the two-phase zone.

An extensive series of boiling experiments in a rectangular porous bed, again heated from below and with an isothermal top condition, was undertaken by Tewari [89] for five different media permeabilities (5.0×10^{-11} m^2 $< K < 2600 \times 10^{-11}$ m^2, 0.11 mm $< d_p < 1.54$ mm, and $\varepsilon = 0.41$). He found that by increasing the dimensionless heat flux Q_w, the flow structure generally evolved in the following sequence:

1. Quiescent conduction
2. Single-phase convective flow across the entire bed
3. Two-phase convective flow either across both liquid and two-phase regions or isolated within the individual regions
4. Stratification of the two regions with heat transfer by conduction in the liquid region and by countercurrent liquid–vapor percolation in the two-phase zone.

In addition, Tewari [89] observed bubble formation and migration in the most permeable bed, suggesting that channeling usually occurs in coarse

porous media, accompanying the non-Darcian effects discussed in Part II, Section G.

c. Numerical Analysis Using the Multiphase Flow Model (MFM) Finite-amplitude solutions of two-phase boiling convection were attempted by Ramesh and Torrance [39] using the multiphase flow model (MFM). A numerical algorithm was developed to solve the equations in the liquid and two-phase regions separately as well as to track the phase interface using the Landau coordinate transformation. Convergence and accuracy considerations of the algorithm were discussed and solutions presented for only one case based on coarse grids. Qualitative agreement between the numerical prediction and previous experimental work involving cavity boiling was noted. A major drawback of this algorithm (which is inherent in MFM) was its intensive computer time, that is, obtaining an accurate solution on a sufficiently fine grid would require substantial computational efforts. In a subsequent study [87] the algorithm was employed to perform a parametric study for various values of the liquid Rayleigh number Ra and the dimensionless bottom heat flux Q_w. Three solution regimes were found:

1. Conduction-dominated at low Ra
2. Convection-dominated at intermediate Ra
3. Oscillatory convection at high Ra.

Oscillatory convection appeared to be triggered by asymmetric disturbances in the system.

d. Numerical Analysis Using the Multiphase Mixture Model (MMM) Based on the two-phase version [51] of MMM, direct simulations of the nonlinear, 2D problem were carried out by Wang *et al.* [44]. This steady-state study successfully captured four flow patterns observed in previous experiments:

1. Conductive liquid layer before and after the onset of boiling in low-permeability media [68]
2. Conductive liquid layer before the onset of boiling but convective liquid layer after the onset of boiling for intermediate permeabilities [84]
3. Convective liquid layer before and after the onset of boiling for high permeabilities [85]
4. Convective liquid layer at low heat fluxes, but conductive liquid layer at high heat fluxes in the presence of boiling [85].

Selected results are presented below to further illustrate the intricate interplay between natural convection in the upper liquid region and boiling flow in the two-phase zone.

As observed by Sondergeld and Turcotte [84], thermal convection does not occur in porous media of intermediate permeabilities in the absence of boiling, but starts with the onset of boiling. Furthermore, a visualization study by the same authors [90] revealed distinct cellular convection patterns that involved both the overlying liquid layer and the underlying two-phase zone. These experimental runs were numerically simulated by Wang et al. [44]. The numerical results for a representative case are displayed in Fig. 11, which includes the isotherms, iso-liquid saturation lines, streamlines, and phase velocity distributions. This case corresponds to a dimensionless bottom heat flux, Q_w, of 4.0 and a Rayleigh number, Ra, of 60, which translate to a permeability of 7.0×10^{-11} m^2 as in the experiments by Sondergeld and Turcotte [84]. The isotherms denote lines of constant $\theta = (T - T_0)/(T_{sat} - T_0)$, with the top boundary and the
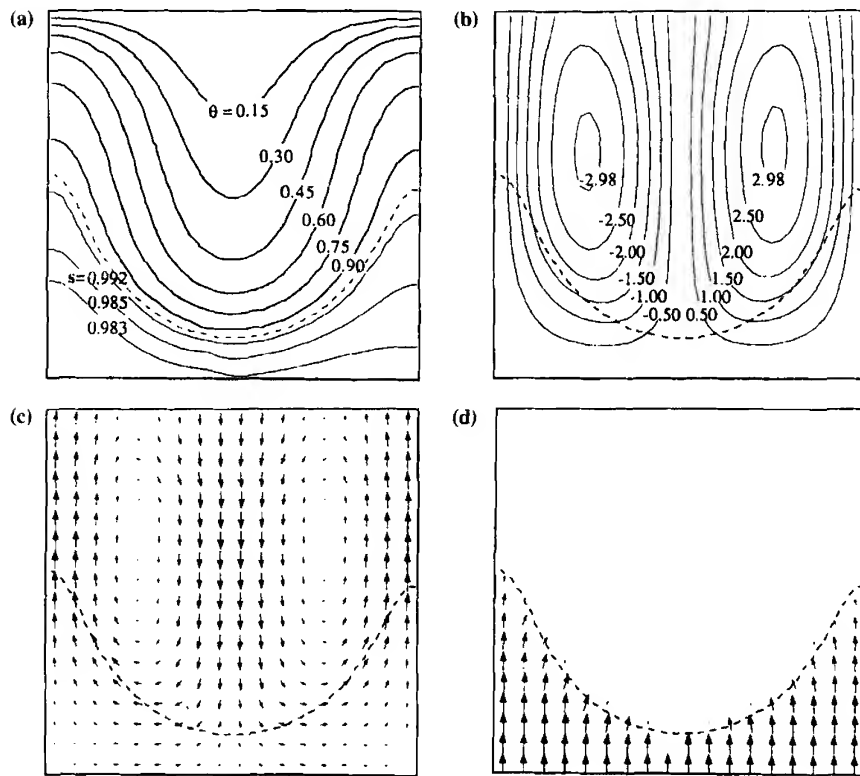
FIG. 11. Numerical results for Ra = 60 and Q_w = 4: (a) composite plots of isotherms and iso-liquid saturation lines; (b) streamlines for the two-phase mixture; (c) liquid velocity; and (d) vapor velocity. The dashed line denotes the phase interface between the subcooled liquid and two-phase regions. Q_w, dimensionless heat flux; Ra, Rayleigh number.

phase interface represented by $\theta = 0$ and 1, respectively. The iso-liquid saturation lines, however, denote absolute values. The steamlines are based on the dimensionless mixture velocity (which is the liquid velocity in the liquid region), and the liquid and vapor velocity vector plots correspond to $\mathbf{u}_l$ and $\bar{\rho}\mathbf{u}_v$, respectively (where $\bar{\rho}$ is the density ratio of vapor to liquid). It can be seen from Fig. 11(a) that thermal convection is so strong that the phase interface (represented by a dashed line) is highly distorted. There are two convective cells present in the liquid region with the steamlines penetrating into the two-phase zone (Fig. 11(b)). Whereas the liquid phase has considerable lateral motion (Fig. 11(c)), the vapor flows primarily vertically upward (Fig. 11(d)). These simulation results are in excellent agreement with the experimental observations by Sondergeld and Turcotte [84, 90]. The fact that the formation of a two-phase zone can drive thermal convection can be understood by recalling that the two-phase Rayleigh number $\mathrm{Ra}_{2\phi}$ is substantially higher than the critical single-phase Rayleigh number Ra. While such a steady-state investigation supported the available experiments, the fundamental process of boiling inducing natural convection can only be revealed through a fully transient analysis, as discussed below.

Another simulation was conducted by Wang *et al.* [44] for a relatively high permeability ($K = 10^{-10}$ m^2) for comparison with the experiments by Bau and Torrance [85]. In this case, the Rayleigh number (Ra = 85) was larger than the critical value for the onset of single-phase natural convection, so that steady cellular convection prevails before the onset of boiling. This is shown by the temperature and streamline contours depicted in Figs. 12(a) and 12(b) for $Q_w = 2.0$. The dashed line at the very left and right corners adjacent to the bottom heated surface suggests that this case is
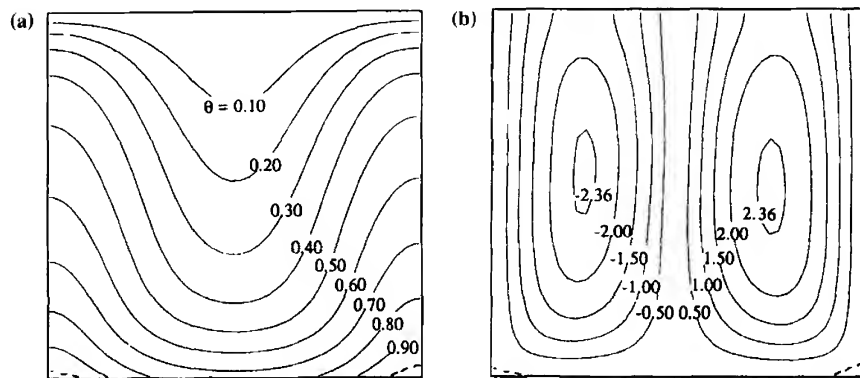
FIG. 12. Numerical results for Ra = 85 and Q_w = 2: (a) isotherms and (b) streamlines [44]. Q_w, dimensionless heat flux; Ra, Rayleigh number.
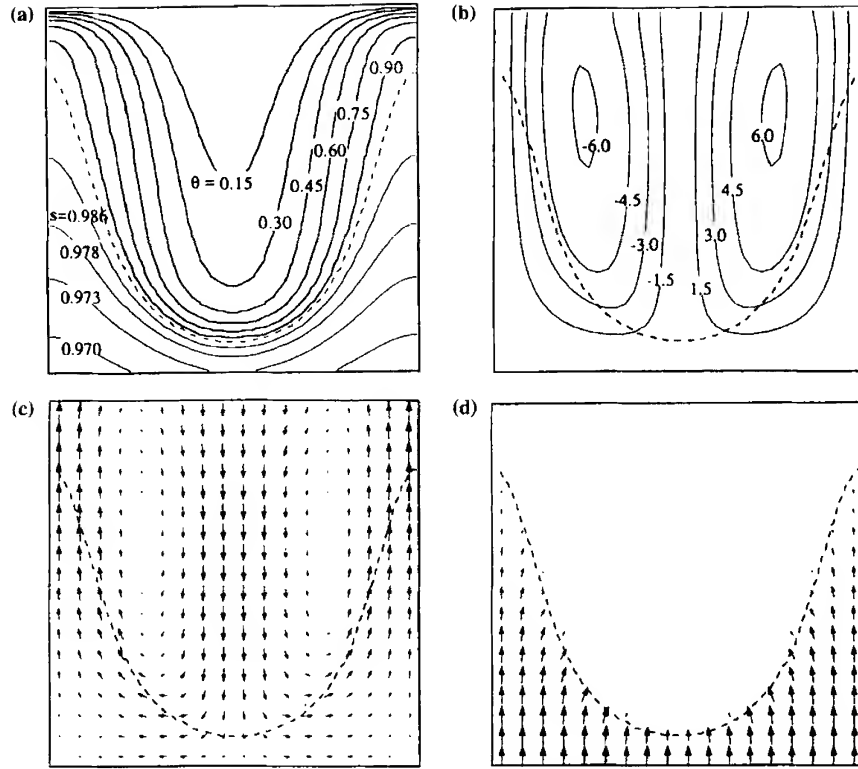
FIG. 13. Numerical results for Ra = 85 and Q_w = 10 [44]. See Fig. 11 for (a) to (d). Q_w, dimensionless heat flux; Ra, Rayleigh number.

marginal to the onset of boiling. After Q_w was raised to 5.0, a two-phase region started to develop at the bottom and thermal convection persisted. When Q_w was further increased, the two-phase zone occupied almost half of the porous bed, and the interaction between boiling and natural convection became more pronounced (see Fig. 13). However, when Q_w was finally raised to 15.0, convection in the liquid region disappeared and the phase interface became horizontally flat [44]. The high heat flux, instead, was acquired by conduction through a thin liquid layer. Clearly these results for high permeability porous media showed that the liquid layer is convective before the onset of boiling and stays convective after boiling, which is consistent with the experiments of Bau and Torrance [85]. Furthermore, it was confirmed that at large bottom heat fluxes (e.g., q_w = 7 kW/m^2 in the experiments), the overlying liquid region reverts back to a conductive heat transfer mode, as observed by Bau and Torrance [85].

Quantitative comparison was also attempted in Wang *et al.* [44]. Figure 14 displays the predicted and measured [84] vapor volume fractions in the test cell as a function of the bottom heat flux Q_w. The solid line represents the 2D simulation results, and the dashed line corresponds to a 1D semi-analytical solution that is applicable only to cases where the overlying liquid layer is conduction-controlled and the two-phase zone is dominated by two-phase countercurrent percolation [44]. The squares represent the data points measured by Sondergeld and Turcotte [84]. It can be seen that at low and intermediate bottom heat fluxes, the 2D numerical model predicts the experimental data reasonably well, whereas the 1D analytical model leads to considerable overpredictions. Beyond a certain value of the bottom heat flux, the 2D results merge into the 1D solution curve. This is because, at high heat fluxes, the liquid region shrinks and reverts to the conduction regime, and the flow inside the two-phase zone becomes a 1D flow, as discussed earlier. It is noteworthy that the experimental data of vapor fraction deviates from the prediction at high heat fluxes, likely due to fluidization of the solid matrix under violent boiling that created additional void spaces through which the vapor could escape [84]. However, the experiments performed by Bau and Torrance [85] do confirm the
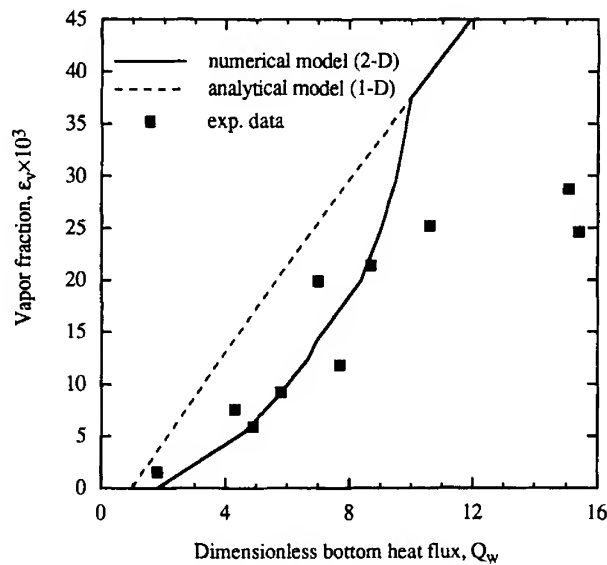
FIG. 14. Comparison of the measured and predicted vapor volume fractions in a two-phase porous layer heated from below [44]. Q_w, dimensionless heat flux; 2D, two-dimensional; 1D, one-dimensional.

transition of the flow from a 2D to a 1D mode at high fluxes. More experiments are needed to thoroughly resolve this issue.

It is also of interest to compare the numerical results of Wang *et al.* [44] with the linear stability results of Ramesh and Torrance [86], since MMM is mathematically exactly equivalent to MFM. We now return to Fig. 12, which shows that the onset of boiling takes place at a dimensionless bottom heat, Q_w, of approximately 2.0 in a porous layer with Ra $\approx$ 85. This finding validates the boiling onset curve labeled BE in the stability map shown in Fig. 9. In addition, the transition from a convective to a conductive overlying liquid layer was numerically predicted to occur at a heat flux between 10 and 15. However, the convection onset curve labeled BD in Fig. 9 indicates $Q_w \approx 7.5$ for the transition. This quantitative discrepancy was found to be related to a hysteresis effect present in the system under consideration. By performing a transient analysis, Wang *et al.* [45] showed that the transition from a convective to a conductive overlying liquid layer can occur over a wide range of bottom heat fluxes; that is, $8.9 \le Q_w \le 17.5$, depending on whether the applied heat flux is decreasing or increasing. The slight difference between the linear stability result and the numerically predicted minimum heat flux (i.e., $Q_w = 8.9$) for the transition is possibly due to the fact that the numerical analysis included the capillary effect, which was neglected in the linear stability analysis.

In order to understand the dynamic evolution of a two-phase boiling system and, hence, the underlying physical mechanisms leading to different flow patterns under various conditions, a transient analysis was performed by Wang *et al.* [45] using a fully implicit method. Based on a 42 × 42 grid, a typical simulation for this transient problem required a CPU (central processing unit) time of about 30 min on a Hewlett Packard (Colorado Springs, CO) 715/75 workstation. Such a CPU time is comparable to those reported in the literature for transient single-phase flows with heat transfer and similar complexity. Selected transient results are shown in Fig. 15 for a system with the following parameters: $L_w = L_h = 0.2$ m, $K = 7 \times 10^{-11}$ m^2, $\varepsilon = 0.35$, $T_0 = 293$ K and $q_w = 1020$ W/m^2 (which corresponds to $Q_w = 3.0$ and Ra = 60). This case is chosen to show the transition of the conductive liquid layer before boiling to the convection mode after boiling.

As can be seen from Fig. 15(a), boiling occurs at $t = 3.2 \times 10^4$ sec, and the two-phase region occupies the lower third of the cavity. The phase interface still remains horizontal. The liquid velocity plot shows that the liquid in the two-phase zone moves downward to replenish the bottom boiling surface. The liquid in the upper liquid region, however, is displaced upward out of the top permeable boundary because of the expansion of
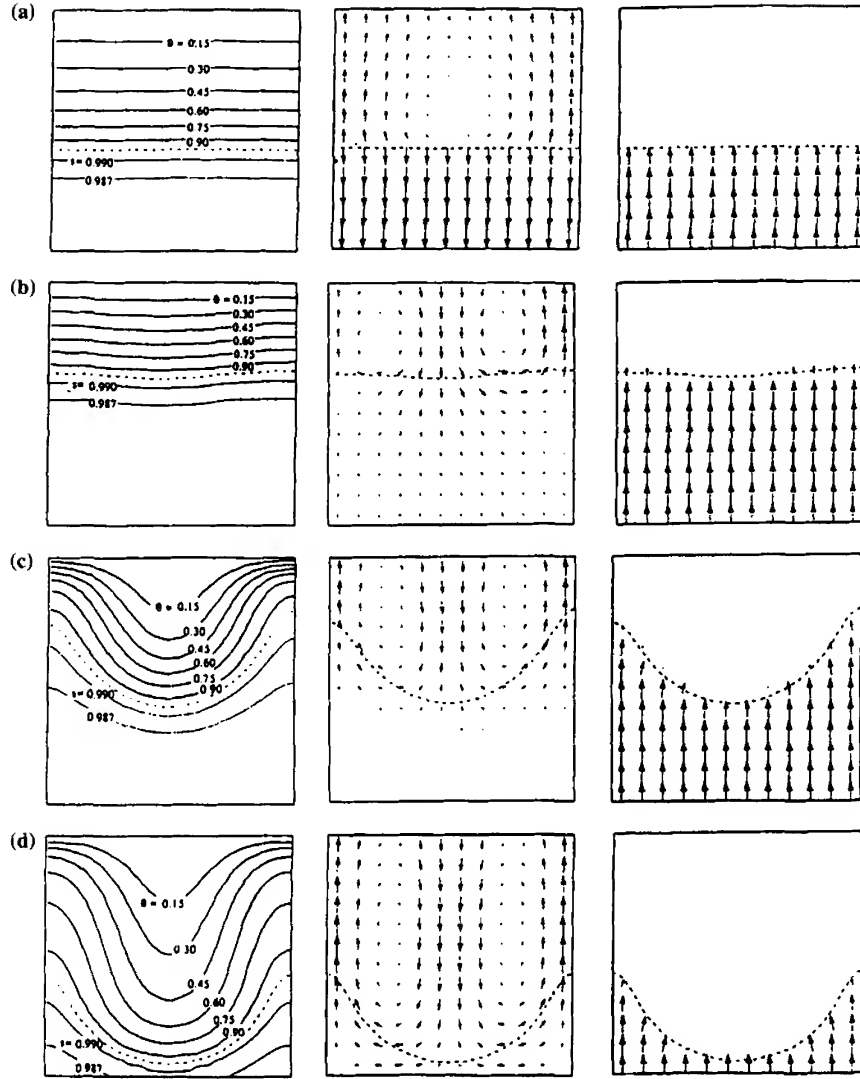
FIG. 15. Numerical results of transient boiling and natural convection in a porous cavity, including isotherms (dimensionless values), iso-liquid saturation lines, liquid and vapor velocities for $Q_w = 3.0$ and $Ra = 60$ [45]. The vapor velocity is normalized by the density ratio ρ_v/ρ_l. (a) $t = 3.5 \times 10^4$ sec, $|u_l|_{max} = 4.57 \times 10^{-7}$ m/sec, $|u_v|_{max} = 4.54 \times 10^{-7}$ m/sec. (b) $t = 5.2 \times 10^4$ sec, $|u_l|_{max} = 2.23 \times 10^{-6}$ m/sec, $|u_v|_{max} = 4.60 \times 10^{-7}$ m/sec. (c) $t = 6.2 \times 10^4$ sec, $|u_l|_{max} = 2.32 \times 10^{-5}$ m/sec. $|u_v|_{max} = 4.61 \times 10^{-7}$ m/sec. (d) $t = 8.0 \times 10^4$ sec, $|u_l|_{max} = 1.78 \times 10^{-5}$ m/sec, $|u_v|_{max} = 4.62 \times 10^{-7}$ m/sec. Q_w, dimensionless heat flux; Ra, Rayleigh number.

the two-phase zone. In Fig. 15(a), the velocity field in the liquid layer has been magnified by a factor of 25 for clarity. Figure 15(a) shows that the vapor generated on the bottom rises up to the phase-change interface, where it condenses. At $t = 5.2 \times 10^4$ sec, the two-phase zone has further expanded, and the system evolves into a state such that small disturbances can be amplified and 2D convection is imminent. This can be seen from the slightly distorted phase change interface shown in Fig. 15(b). The velocity fields of the two phases retain the same features as in Fig. 15(a), except that the liquid velocity in the upper region is no longer magnified.

At $t = 6.2 \times 10^4$ sec, as shown in Fig. 15(c), convection in the liquid region has fully developed. The condensation heat transfer at the phase interface is thus enhanced so that the two-phase region shrinks. The liquid velocity plot reveals two convection cells that are slightly asymmetric and able to penetrate into the lower two-phase zone. At $t = 8 \times 10^4$ sec, as shown in Fig. 15(d), the system acquires a steady state, and the two convection cells become symmetric.

2. Internal Heating

Multidimensional phase-change flow in porous media with volumetric heating also has been studied extensively, particularly with application to nuclear reactor safety assessment [91–93]. Experimental results of boiling in a 2D internally heated porous bed were reported by Hardee and Nilson [91] for water–glass and water–silica sand media. Akin to the case of bottom heating, the two-phase flow structure was observed to consist of a subcooled liquid region overlying a two-phase zone. The liquid region was found to decrease in size with an increase in the heat generation rate. A summary of the experimental data of Hardee and Nilson for $\dot{Q}$ versus Ra is shown in Fig. 16, where the dimensionless volumetric heat generation rate and the Rayleigh number are defined, respectively, as

$$\dot{Q} = \frac{\dot{q}L_h^2}{2k_{\text{eff}}(T_w - T_0)}, \qquad \text{Ra} = \frac{g\beta_l L_h K\left(\dfrac{\dot{q}L_h^2}{2k_{\text{eff}}}\right)}{\nu_l \alpha_l}. \tag{50}$$

In the single-phase regime, $\dot{Q}$ is identical to the Nusselt number; hence $\dot{Q}$ is unity for conduction, and there exists a single curve between $\dot{Q}$ and Ra for single-phase convection. These features are clearly shown in Fig. 16. The single-phase convection curve is in agreement with the following theoretical correlation:

$$\dot{Q} = \left(\frac{1}{32}\,\text{Ra}\right)^{1/2}. \tag{51}$$

Bed Height (cm)	Permeability (Darcy)	Aspect Ratio (L/D)
5	100	0.2
12	100	0.4
36	100	1.2
36	300	6.0
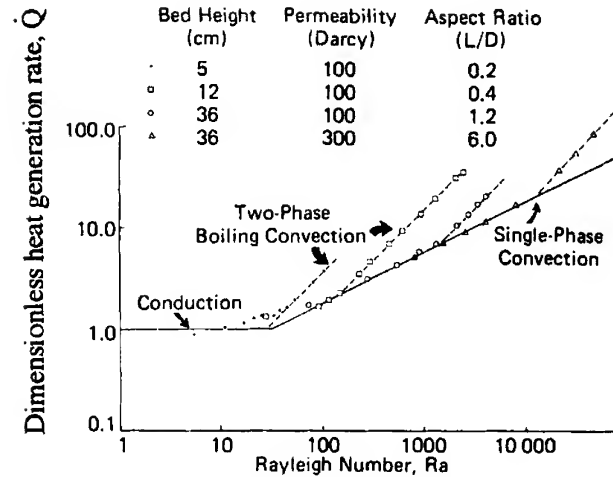
FIG. 16. Summary of conduction, convection, and boiling heat transfer data in porous media with internal heating [91].

Figure 16 or Eq. (51) indicates that the transition from conduction to convection occurs at Ra_{cr} = 32. The family of dotted lines in Fig. 16, which branch from the conduction–convection curve, represents the boiling regimes. In these regimes, the bottom wall temperature T_w remains constant at the saturation temperature, so that Q is linearly dependent on Ra. The Rayleigh numbers at the onset of boiling depend on the characteristics of a porous bed and are not universal.

Various attempts have been made to obtain numerical solutions of multidimensional phase-change flows after the onset of boiling. Tsai and Catton [73] used the finite difference method to simulate two-phase flow and dryout in volumetrically heated particles surrounded by nonheated gas particles. Unfortunately, the numerical scheme was not robust and stable, and the calculations had to be terminated prior to dryout. There was, however, a fair agreement between the numerical prediction and experimental data. Later, Tung and Dhir [92] used a finite-element scheme to analyze the same problem, as examined by Tsai and Catton [73]. The mechanistically derived relative permeabilities, as described in Part II, Section G, were used in their numerical model, and the interfacial drag between liquid and vapor phases was also incorporated.

Post-dryout heat transfer in a porous bed is of practical significance because excessive heat can still be removed effectively as long as the maximum temperature of the bed is kept below a critical value, such as the melting point of the bed. These problems are characterized by the simultaneous presence of all three regions: subcooled liquid, two-phase, and

superheated vapor. Neglecting the full-liquid region, Chung and Catton [93] first tackled such a multiple-region problem by coupling the transport equations in the two-phase zone with the energy equation in the superheated vapor region, taking thermal radiation into account. They reported that their solution scheme suffered from a very narrow choice of grid distribution and iteration parameters for convergence. Their results were found to be in fairly good agreement with corresponding experimental data.

Studies of transient two-phase flow and heat transfer in porous media with internal heating are rather scarce. The work of Stubos and Buchlin [94] is an exception. Within the same context of nuclear reactor debris beds, this study differs from all others in that the generalized Darcy law was used (i.e., the model is only applicable to beds of small particles) and the time response of the bed to applied power transients was modeled. The model was claimed to be multidimensional; however, only 1D results were presented and compared with the data from the Sandia National Laboratories (Albuquerque, New Mexico) and European in-pile tests. In one recent study, Stubos et al. [95] proposed a micro-macroscopic modeling approach in which the structural and transport properties of the porous medium, such as porosity and effective thermal conductivity, were calculated by a microscopic discrete method, such as the 3D off-lattice algorithm, whereas the transport behavior was computed from a macroscopic, continuum model (i.e., MFM). Although at first sight it appeared sophisticated, a closer examination revealed that the approach of Stubos et al. [95] is essentially a two-step decoupled calculation without accounting for dynamic interactions between different length scales. A tight coupling between microscopic interfacial phenomena and macroscopic transport was not established, and thus the effects of phase dynamics on the pore-level would not be captured by such an approach.

C. INTERNAL BOILING AND FORCED CONVECTION

We now consider liquid forced flow through a partially heated porous formation. When the heat input increases, boiling occurs adjacent to the heated surface and the thermodynamic state of the system then consists of a liquid region and a developing two-phase zone. If the heat flux is sufficiently large, a superheated vapor region may also appear. In these problems the resulting two-phase flow patterns are not only determined by the buoyancy forces along the gravitational direction, but also are affected by the pressure difference in the main flow direction. Such complicated two-phase flow and heat transfer processes are reviewed and discussed in this section.

1. *Experimental Studies*

An experimental study on forced convection with boiling inside a vertical porous channel heated symmetrically or asymmetrically was conducted by Cioulachtjian *et al.* [96]. The working fluid was pentane, mainly chosen for its low boiling point. The channel with an aspect ratio of 10 was packed with spherical bronze media ($K = 2.7 \times 10^{-11}$ m^2, $d_p = 0.165$ mm, and $\varepsilon = 0.40$) and was heated from either one or both vertical walls. The Reynolds numbers (based on the particle diameter) for liquid and vapor flow are smaller than 1 and 5, respectively; hence, the experiments were approximately in the Darcy flow regime. Temperature distributions were measured using an array of 130 thermocouples. Although this experimental work was able to generate a 3D temperature distribution, only the 2D results at the midplane were presented. Interesting findings from this study include: (i) a systemic progression of single-phase liquid, to two-phase, and to single-phase vapor structure occurs with time, or with increase in power input, or both, and (ii) all three regions can co-exist within the flow channel at a nonzero liquid flow rate from the bottom. No quantitative information on the two-phase zone could be yielded using thermocouples because it is nearly isothermal.

Most recently, a visualization study of interactive boiling and forced flow in a horizontal, 2D porous formation was performed by Easterday *et al.* [46]. A rectangular test cell was made of acrylic, with inner dimensions of 152.4 mm wide, 58 mm high, and 25.4 mm deep. A heat flux of 10^5 W/m^2 was applied over the central one-third portion of the bottom surface. Numerous thermocouples were mounted inside the test section from the back; the front side was a double-pane insulating window, allowing for direct observations. The other sides of the test section were well insulated, with the front insulation briefly removed at intervals to observe flow conditions, interface location, and two-phase structure, via a camera. The test cell was randomly packed with spherical soda-lime 0.5-mm-diameter glass beads, for which the porosity and absolute permeability were determined to be 0.37 and 1.77×10^{-10} m^2, respectively. Visualization of the two-phase structure on boiling was made by use of black india ink that is fully dissolved into the liquid, but that is nonvolatile. Thus the light intensity level at a certain location directly corresponds to the local liquid saturation. A charge-coupled device (CCD) camera was used to record the location of the phase interface and the light intensity field. The intensity images were then processed to generate liquid saturation plots.

The experimental images of liquid saturation are shown in Figs. 17(a), 18(a), and 19(a) corresponding to the inlet velocities of 0.15, 0.25, and 0.35 mm/s, respectively. In these images the gray scale ranges from black for

(a) experimental image of liquid saturation

(b) numerical image of liquid saturation

(c) predicted vapor velocity field

(d) predicted liquid velocity field
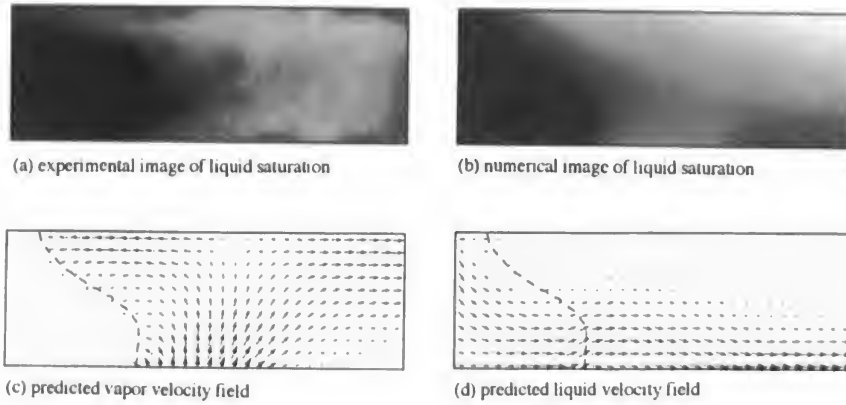
FIG. 17. Experimental and numerical results for u_{in} = 0.15 mm/sec [46].

(a) experimental image of liquid saturation

(b) numerical image of liquid saturation

(c) predicted vapor velocity field

(d) predicted liquid velocity field
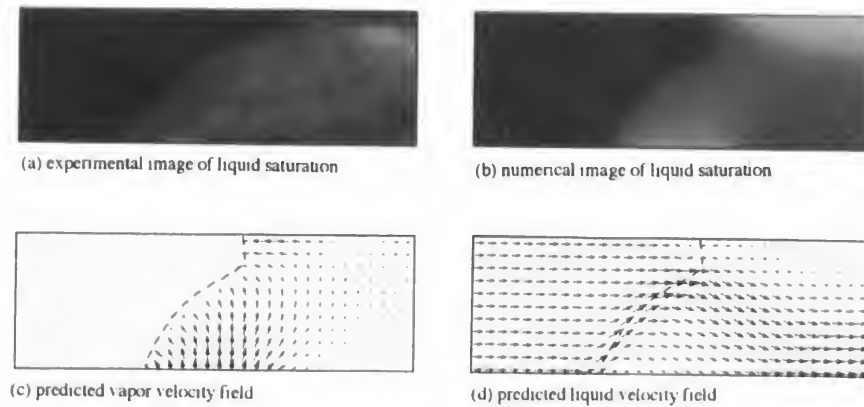
FIG. 18. Experimental and numerical results for u_{in} = 0.25 mm/sec [46].

the pure liquid to white for the pure vapor. It can be seen from Fig. 17(a) that the two-phase zone is extensive and the phase interface protrudes forward at the top, reminiscent of the numerical image shown in Fig. 17(b). In addition, the liquid saturation is apparently lower in the upper right-hand region than it is in the vicinity of the heated element. Physically, this phenomenon arises because the much lighter vapor migrates upward on evaporation and subsequently accumulates at the top of the formation. An engineering implication of this result is that in a vapor-dominated geothermal reservoir, the region with most thermal energy (i.e., richest in vapor) may be located significantly away from the heat source. This peculiar

(a) experimental image of liquid saturation

(b) numerical image of liquid saturation

(c) predicted vapor velocity field

(d) predicted liquid velocity field
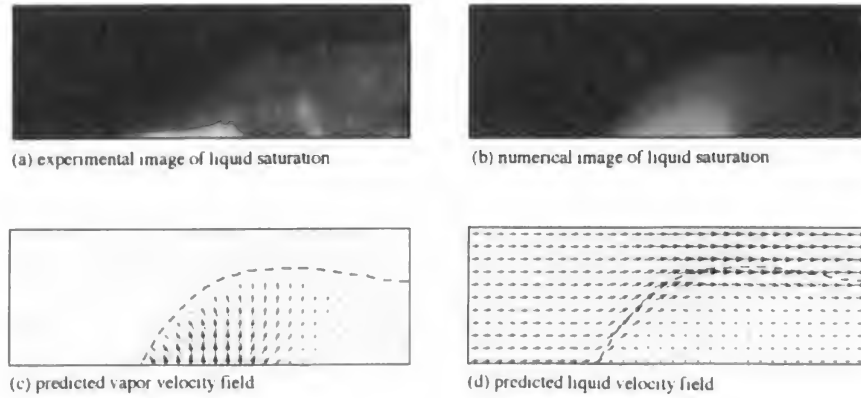
FIG. 19. Experimental and numerical results for u_{in} = 0.35 mm/sec [46].

feature of two-phase systems, which contradicts the common knowledge of single-phase heat transfer, clearly demonstrates the need for two-phase flow studies.

At a higher incoming flow (i.e., u_{in} = 0.25 mm/sec), the experimental image displayed in Fig. 18(a) shows a receding two-phase zone away from the inlet. It also is clearly visible that the upper right-hand region is saturated more with vapor (lighter in color), whereas the lower right-hand corner is full of liquid (darker). Again, this experiment confirms the second type of two-phase structures predicted by the numerical model (Fig. 18(b)). For the highest flow rate, both the experimental (Fig. 19(a)) and numerical (Fig. 19(b)) images show a dome-shaped two-phase zone underlying a pure liquid region. Despite the gravitational instability, the structure of the liquid layer over the two-phase zone appears stable, as shown in Fig. 19(a). The theoretical underpinning for this stable structure remains unknown.

2. Numerical Analysis Using the Multiphase Mixture Model (MMM)

The previous numerical images of the liquid saturation were obtained by Easterday et al. [46] based on the two-phase mixture model of Wang and Beckermann [51]. Employing a 62 × 22 grid, a typical simulation for this problem required CPU time of only 10 min on a Hewlett Packard 715/75 workstation. To help understand the formation of the two-phase patterns displayed in panels (a) and (b) of Figs. 17 to 19, more detailed numerical results of vapor and liquid velocity fields are presented in panels (c) and (d) of Figs. 17 to 19.

For the case of a low inlet velocity (i.e., $u_{in} = 0.15$ mm/sec), strong vapor upward flow is seen (Fig. 17(c)). When the vapor rising from the bottom heater reaches the impermeable top surface, it spreads over along both directions. The vapor flowing toward the phase interface is condensed, while the other vapor stream is carried away by the liquid toward the exit. Figure 17(d) shows that the liquid preferentially flows along the bottom surface of the channel where the liquid saturation is higher, bypassing the upper region where liquid saturation is lower and therefore resistance to liquid flow is higher. This preferential liquid flow provides an effective means to wet the heated surface.

When the inlet velocity of the liquid increases to 0.25 mm/sec (Fig. 18(c)), the vapor flow splits into two before reaching the top surface, one flowing toward the phase interface (i.e., the condensation front), and the other mixing with the liquid to exit from the channel. The liquid velocity shown in Fig. 18(d) indicates that the liquid flow remains nearly horizontal until reaching the phase interface. Inside the two-phase zone, the liquid tends to bypass both regions that are rich in vapor, namely, around the bottom heated surface and along the top of the formation.

Inspection of Fig. 19(c) for the highest liquid incoming velocity (i.e., 0.35 mm/sec) reveals that the vapor generated from the bottom surface rises to the phase interface lying above and is condensed completely there. Thus the upper one-third portion of the channel is fully saturated with liquid. In this region, the pure liquid flows over the two-phase dome despite the gravitational instability (Fig. 19(d)). The underlying two-phase dome acts as a restriction to the liquid flow and forces the liquid to bypass it.

Most recently, a fixed-grid numerical algorithm based on MMM was developed for general problems that may simultaneously involve all three regions: superheated vapor, two-phase, and subcooled liquid [46a]. The algorithm was successfully applied to simulate the above problem under post-dryout conditions.

3. Large-Scale Numerical Simulation

Although the foregoing laboratory-scale experimental and numerical studies have shed considerable light on the fundamental processes of boiling in a forced flow through porous media, there is a need to conduct large-scale numerical simulation for geothermal applications involving length scales on the order of kilometers. Such work has been extensively reported in a separate branch of research focused on geothermal energy exploitation [97–99]. A primary objective of these modeling studies has been to provide answers to reservoir management questions relating to well decline, well spacing, generating capacity (power potential) of the

reservoir, injection effects, and scaling problems. The numerical simulations also aimed at predicting premature breakthrough at the production wells during cold-water injection for reservoir recharge. The preferential passing would drastically reduce the enthalpy and temperature of the produced fluids. Figure 20 schematically illustrates a typical production–injection system for a doublet in a geothermal reservoir [97]. It is of particular interest to predict the movement of cold-water fronts in the modeling of fluid injection processes. Such fronts cannot be adequately resolved on the spatial scale traditionally used in discretizing flow domains (10 to 100 m or more) based on the MFM, and hence large numerical diffusion is inevitable [97]. Conversely, if based on the newly developed MMM, spatial resolution of the large-scale reservoir simulation can be greatly improved due to the much reduced computational time associated with MMM. This may be a promising area for future research.

D. External Condensing Flows

Phase change flows in unbounded porous media are encountered in numerous important technological applications. Examples include boiling flow along an igneous intrusion in geothermal reservoirs and condensing flow adjacent to a cold surface in heat pipes and porous insulation materials. Recently, there has been much research on the external condensing flow as related to enhanced condensation heat transfer in porous
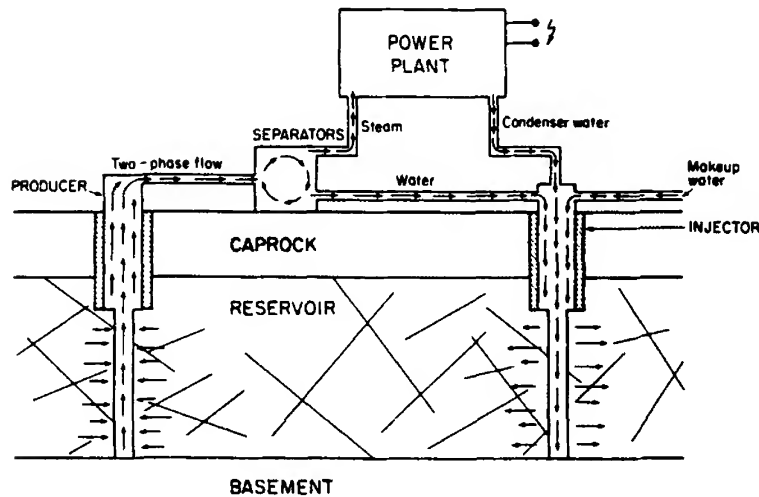
Fig. 20. Schematic illustration of an injection–production geothermal system [97].
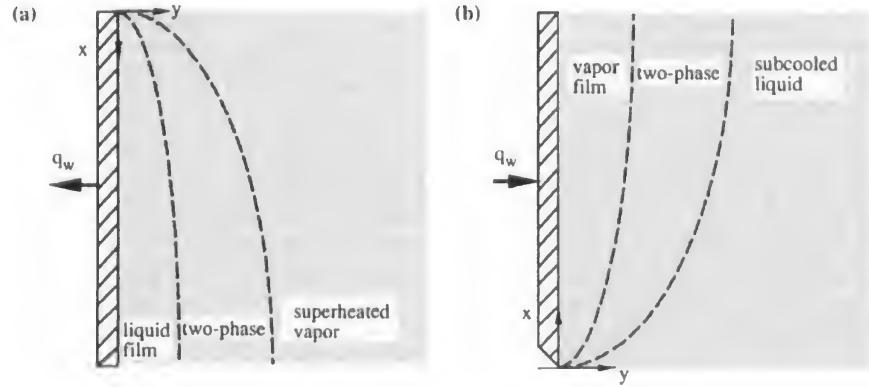
FIG. 21. External (a) condensing flow and (b) boiling flow in porous media. q_w, wall heat flux.

media [43, 100–102]. Figure 21(a) illustrates a typical three-region structure of external condensing flow in porous media, where the two-phase zone arises from the capillary effect. As the heat extraction rate increases, the liquid saturation on the cold wall increases up to unity, after which a pure liquid film begins to form adjacent to the wall. A complete problem of external condensation then involves multiple regions consisting of the pure liquid film, the two-phase zone, and the infinitely large superheated vapor region. The flow dynamics in such systems are driven by relative buoyancy forces between liquid and vapor, external pressure gradients, or both.

1. Single-Phase Analysis

If we neglect the two-phase zone, following the original study of Cheng [100], the condensation problem is then reduced to a single-phase transport counterpart within the liquid condensate film. Such analyses would be conceptually similar to the pioneering work by Nusselt [103] for vapor condensation in the absence of porous materials. Typical assumptions made in these analyses include

1. The interface between vapor and liquid is sharp and smooth
2. Classic boundary layer approximations are valid
3. The porous medium is isotropic.

Further assuming Darcy flow, Cheng [100] obtained the following similarity solution:

$$\mathrm{Nu}_x/\mathrm{Ra}_x^{1/2} = \left(\frac{1}{2\mathrm{Ja}} + \frac{1}{\pi} \right)^{1/2}, \tag{52}$$

where Nusselt, Rayleigh, and Jacob numbers are defined, respectively, as

$$\mathrm{Nu}_x = \frac{hx}{k_{\mathrm{eff}}}, \quad \mathrm{Ra}_x = \frac{K(\rho_l - \rho_v)gx}{\mu_l \alpha_l}, \quad \mathrm{Ja} = \frac{c_l(T_{\mathrm{sat}} - T_w)}{h_{fg}}. \quad (53)$$

2. Two-Phase Boundary Layer Approximations

In view of the fact that the mathematical characteristics of the governing equations in MMM for two-phase flow are similar to those governing single-phase flow, a two-phase boundary layer theory, that parallels the single-phase boundary layer theory of Schlichting [104], is conceivable. By carrying out a formal perturbation analysis, Wang and Beckermann [105] found that the two-phase boundary layer approximations are valid when the two-phase Peclet number is much larger than unity; namely,

$$\mathrm{Pe}_{2\phi} \equiv \frac{u_\infty L}{(\varepsilon K)^{1/2} \sigma/\mu_l} \gg 1, \quad (54)$$

where u_∞ is the uniform velocity at infinity in pressure-driven flows or the scaling velocity $K(\rho_l - \rho_v)g/\mu_l$ in buoyancy-driven flows. Physically, the two-phase boundary layer approximations imply that the mixture velocity component along the surface dominates the one perpendicular to it, and that changes across the two-phase boundary layer are much steeper than those along it.

3. Two-Phase Analysis Using the Unsaturated Flow Theory

Several attempts have been made to include the two-phase zone and, hence, the capillary effect in the analysis of condensation heat transfer inside porous media [42, 43, 101]. In order to render the problem analytically tractable, these theoretical studies based on MFM had to neglect the vapor flow. More specifically, the vapor phase was assumed to remain at a constant pressure and a two-phase flow problem thus was essentially reduced to the consideration of the liquid phase flow only. This approach is equivalent to the unsaturated flow theory discussed in Part II, Section C. The key equation governing the two-phase condensing flow based on UFT is [43]

$$\frac{(\varepsilon K)^{1/2}\sigma}{\nu_l} \frac{\partial}{\partial y}\left\{k_{rl}(s_l)[-J'(s_l)]\frac{\partial s_l}{\partial y}\right\} - \frac{K\Delta\rho}{\nu_l}g\frac{dk_{rl}}{ds_l}\frac{\partial s_l}{\partial x} = 0. \quad (55)$$

The solution to Eq. (55) along with appropriate boundary conditions eventually determines the capillary effect on condensation heat transfer in porous materials.

4. Two-Phase Analysis Using the Multiphase Mixture Model (MMM)

Within the framework of MMM, a set of boundary layer equations has been rigorously derived by Wang and Beckermann [105] without invoking the Richards approximation associated with UFT. In the Cartesian coordinate system shown in Fig. 21, the mixture continuity equation, the mixture Darcy law, and the liquid mass conservation equation can be written explicitly as

$$\frac{\partial(\rho u)}{\partial x} + \frac{\partial(\rho v)}{\partial y} = 0, \tag{56}$$

$$\rho u = -\frac{K}{\nu}\left(\frac{\partial p}{\partial x} - \rho_k g\right), \tag{57}$$

$$\rho \frac{d\lambda}{ds_l}\left(u\frac{\partial s_l}{\partial x} + v\frac{\partial s_l}{\partial y}\right) = \frac{\partial}{\partial y}\left(\rho D_c \frac{\partial s_l}{\partial y}\right) - \frac{K\Delta\rho}{\nu_v} g \frac{df}{ds_l}\frac{\partial s_l}{\partial x}, \tag{58}$$

where the mixture transport properties are all functions of the local liquid saturation s_l. It is worth noting that Eqs. (56) to (58) strongly resemble the boundary layer equations for single-phase binary mixture flow and transport in porous media. In the limit corresponding to UFT (i.e., $\bar{\nu} \to \infty$), it was shown by Wang and Beckermann [106] that

$$\frac{d\lambda}{ds_l} = O(\bar{\nu}^{-1}) \to 0; \quad \rho D_c \to \frac{(\varepsilon K)^{1/2}\sigma}{\nu_l} k_{rl}(s_l)\left[-J'(s_l)\right];$$

$$\frac{1}{\nu_v}\frac{df}{ds_l} \to \frac{1}{\nu_l}\frac{dk_{rl}}{ds_l} \tag{59}$$

so that Eq. (58) identically reduces to Eq. (55) of UFT.

In the case of buoyancy-driven condensing flow, Eqs. (56) to (58) admit a similarity solution in terms of the following similarity variables [106]:

$$\eta = \frac{y}{x}\text{Ra}_{2\phi}^{1/2}, \quad \Psi = \rho D_c \text{Ra}_{2\phi}^{1/2}F(\eta), \quad s_l = s_l(\eta), \tag{60}$$

where the two-phase Rayleigh number $\text{Ra}_{2\phi}$ is defined as

$$\text{Ra}_{2\phi} = \frac{K(\rho_l - \rho_v)gx}{(\varepsilon K)^{1/2}\sigma}, \tag{61}$$

and Ψ is a stream function of the two-phase mixture such that

$$\rho u = \frac{\partial\Psi}{\partial y} \qquad \rho v = -\frac{\partial\Psi}{\partial x}. \tag{62}$$
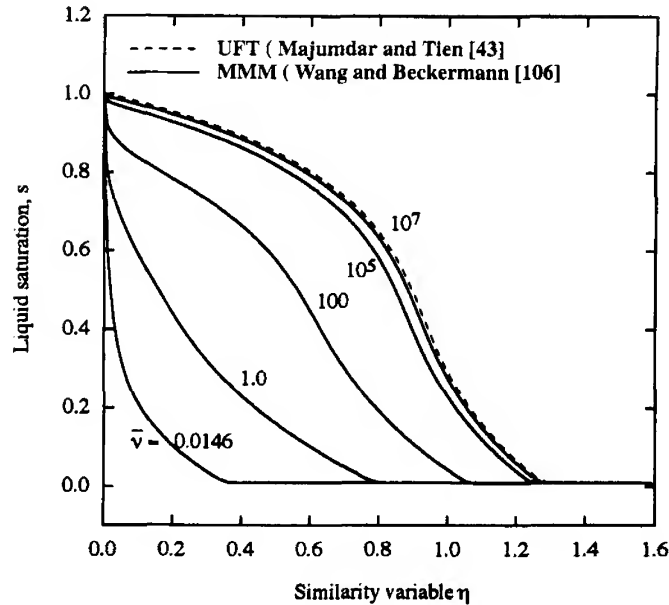
FIG. 22. Saturation profiles of two-phase boundary condensing flow as predicted by the two-phase mixture model [106] and the unsaturated flow theory [43]. UFT, unsaturated flow theory; MMM, multiphase mixture model.

Figure 22 shows the liquid saturation profiles for different values of the viscosity ratio along with the curve obtained using UFT. The latter is independent of the viscosity ratio $\bar{\nu}$ [43]. It can be seen that the curves indeed approach the limiting case represented by UFT. However, the value of $\bar{\nu}$ needed for UFT to hold true is surprisingly large—$\bar{\nu} = 10^7$! Obviously, for all common fluids, this condition cannot be satisfied, implying that UFT is generally questionable when applied to the condensation problem under consideration. In fact, for a water–steam system at atmospheric pressure ($\bar{\nu} = 0.01466$), the saturation profile predicted by MMM greatly deviates from that of UFT.

The capillary effect on condensation heat transfer is reflected by the liquid mass flux across the interface between the two-phase zone and the pure liquid film. It was shown by Wang and Beckermann [106] that UFT overpredicts this flux by a factor of 66, suggesting that the previous theoretical studies based on UFT [43, 101] have probably exaggerated the effect of capillary forces on condensation heat transfer in porous media. The overprediction results from the neglect of the vapor flow, which is actually very strong due to the low vapor density.
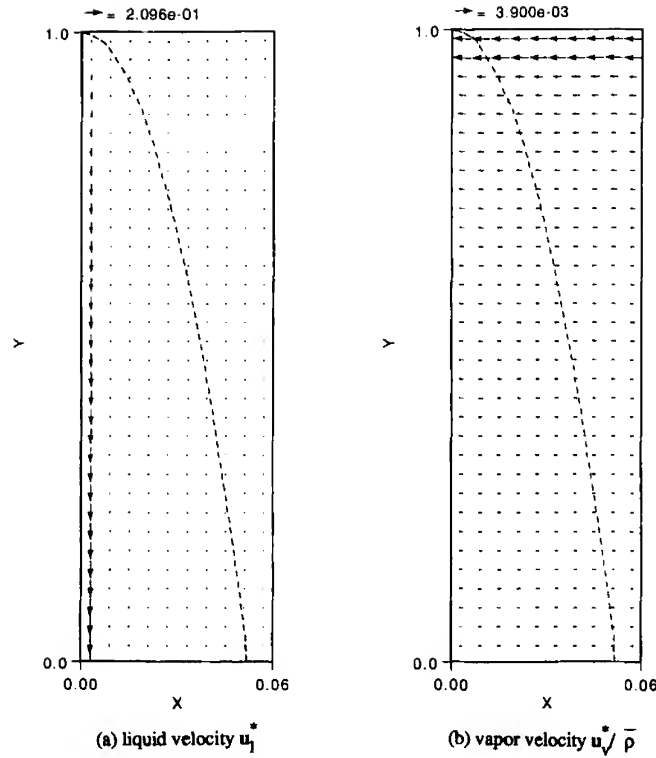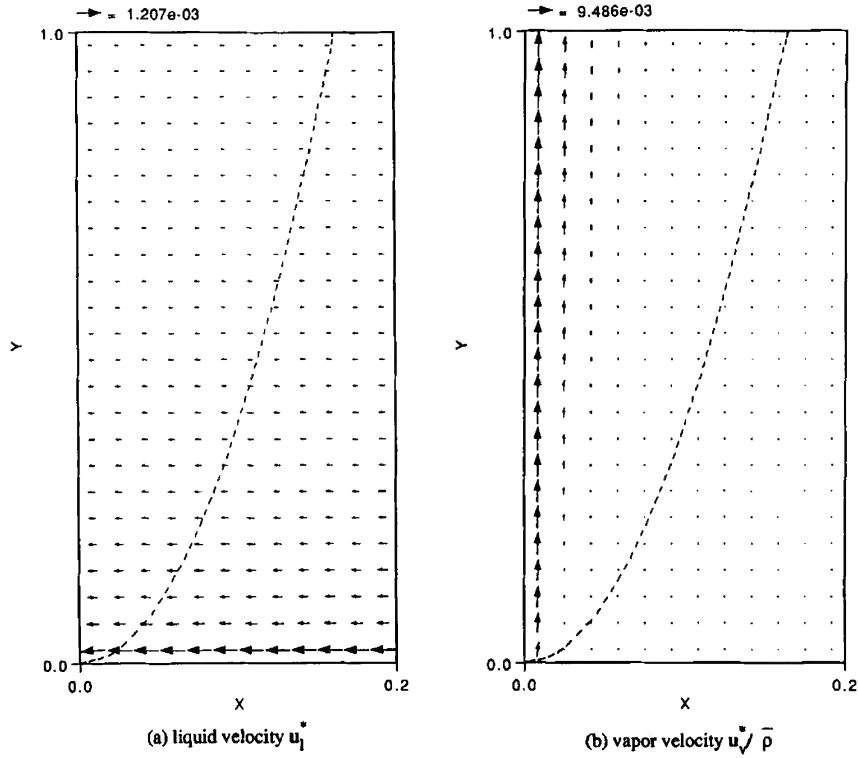
FIG. 23. Two-phase flow pattern in the external condensing case: (a) liquid velocity u_l^*, and (b) vapor velocity $u_v^* \bar{\rho}$ [106]. Dashed line, edge of the boundary layer.

Figure 23 displays representative liquid and vapor flow fields in a two-phase boundary layer of buoyancy-driven flow along a cooled vertical flat plate. The dashed line in these plots denotes the edge of the boundary layer. The liquid flow is essentially confined to a region adjacent to the cooled wall, where the vapor condenses into the liquid. As a result of its large density, the liquid moves primarily downward (see Fig. 23(a)). The downward liquid velocity quickly diminishes with the distance away from the wall, because it is proportional to the cubic of the liquid saturation, which furthermore has an extremely steep profile (see Fig. 22). Figure 23(b) shows that the vapor is only laterally entrained into the two-phase boundary layer. A two-phase cross-flow pattern is characteristic of condensing buoyancy-driven flows.

5. Experimental Studies

Quantitative comparisons of the foregoing two-phase analysis with the available condensation experiments [102, 107] have not been attempted for the reasons explained in Wang and Beckermann [106]. However, qualitative insight into the capillary effect can be gained from Fig. 24, which compares the single-phase theory of Cheng, the UFT model of Majumdar and Tien, and the refined two-phase model of Chung et al. with the experimental data for a porous medium consisting of small glass beads by Chung et al. Under the experimental conditions, the Darcy flow assumption is likely to be valid, and therefore the differences between various model predictions are mainly attributed to the capillary effect and, hence, the inclusion of the two-phase zone. As is clearly seen, the experimental data suggest that the UFT model of Majumdar and Tien significantly overpredicts the capillary effect, confirming the argument made earlier.
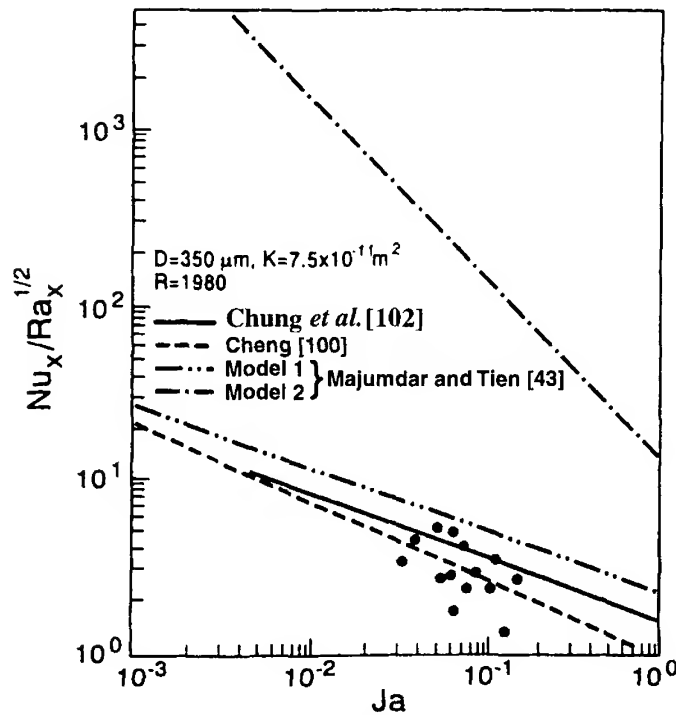
FIG. 24. Comparison of condensation heat transfer data with theories [102]. Nu, Nusselt; Ra, Rayleigh; Ja, Jacob.

The difference between the curves of Cheng and Chung is relatively small, implying that the capillary effect is insignificant in these experimental situations.

6. Additional Issues

The two-phase analysis of Wang and Beckermann [106] for boundary layer condensing flows focused on the development of the two-phase zone before a condensate film appears along the cold wall. Beyond the marginal condition, at which the liquid saturation at the wall becomes equal to unity, the two-phase analysis presented in the previous section needs to be modified to couple the single-phase flow within the liquid film; this can be done readily, as in many previous models. The two-phase analysis still would be valid, except that the phase interface now becomes permeable. As a result, the normal mixture velocity v is no longer zero, as specified in the above analysis, but must be obtained from the coupling between the single-phase and two-phase flows. Such an extension, although straightforward, needs to be performed in the future. In addition, neither analysis nor experiment has been performed on pressure-driven condensing flows in porous media with two-phase effects.

E. EXTERNAL BOILING FLOWS

Pool and external boiling in porous media is a time-honored research area. To date, theoretical work in the literature typically followed the standard film boiling model in the absence of porous media. The analyses were developed in parallel with that for condensing flow, as discussed in the preceding section. Hence, the following discussion on the theoretical aspects of boiling in porous media will be brief. To facilitate discussion, a sketch of the flow structure and nomenclature for external boiling along a vertical wall is illustrated in Fig. 21(b).

1. Single-Phase Analysis of Film Boiling

In one of the first studies on external boiling in porous media, Parmentier [108] assumed that a thin vapor film forms adjacent to the heated surface when boiling occurs, and that the vapor film and the pure liquid region of semi-infinite extent are separated by a sharp interface with no mixed region in between. As a result of this approximation, the mathematical formulation of the boiling problem was simplified to a single-phase version. Within this theoretical framework, Cheng and Verma [109] subsequently studied subcooled boiling on a vertical surface. They

reported that the following relationship exists:

$$\mathrm{Nu}_x \sim \sqrt{\mathrm{Ra}_x},\tag{63}$$

where the proportionality constant is a function of various dimensionless parameters defined as

$$\mathrm{Nu}_x = \frac{hx}{k_{\mathrm{eff}}}, \quad \mathrm{Ra}_x = \frac{K(\rho_l - \rho_v)gx}{\mu_v \alpha_v}, \quad R = \frac{\rho_v}{\rho_l}\left[\frac{\mu_l \alpha_v (\rho_l - \rho_v)c_l}{\mu_v \alpha_l \rho_l \beta_l h_{fg}}\right]^{1/2},$$

$$\mathrm{Ja} = \frac{c_l(T_{\mathrm{sat}} - T_\infty)}{h_{fg}}, \qquad \mathrm{Sh} = \frac{c_c(T_w - T_{\mathrm{sat}})}{h_{fg}}.\tag{64}$$

Figure 25 shows the dependence of the Nusselt number on wall superheat Sh for $R = 0.05$ and various liquid subcooling Ja. As can be expected, the heat transfer coefficient decreases with wall superheat but increases with liquid subcooling. It should be mentioned that this theory neglecting the presence of a two-phase zone has not been directly verified by experiments.

2. Two-Phase Analysis Using the Multiphase Mixture Model

In a unified treatment, Wang and Beckermann [106] also studied buoyancy-driven boiling flow in the two-phase zone adjacent to a heated vertical flat plate, and developed a similarity solution. An important result
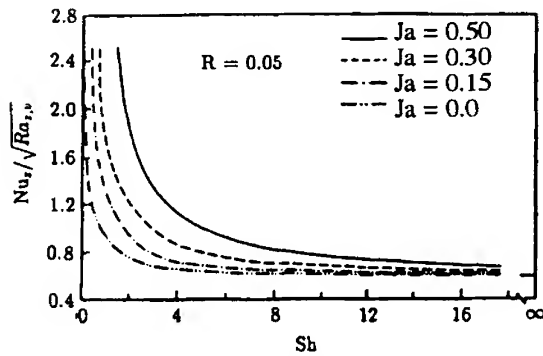
FIG. 25. Single-phase predictions of subcooled film boiling heat transfer in porous materials [109]. Nu, Nusselt; Ra, Rayleigh; Sh, Sherwood; Ja, Jacob.

from that study is the dryout heat flux corresponding to zero liquid saturation at the wall, which is given by

$$q_{dry} = 2.716 \times 10^{-3} \frac{h_{fg}\sigma}{\nu_l} \left(\frac{\varepsilon K}{L^2}\right)^{1/4} \left[\frac{(\rho_l - \rho_v)gK}{\sigma}\right]^{1/2}. \quad (65)$$

For a water–steam system with $\varepsilon = 0.4$, $K = 10^{-10}$ m^2, and $L = 0.1$ m, this equation estimates a dryout heat flux of 2.45×10^4 W/m^2. Note that the dryout heat flux is proportional to the three-fourths power of permeability and is inversely proportional to the square root of the heating length.

Figure 26 depicts the liquid and vapor phase velocity fields, respectively, in a typical two-phase boiling boundary layer at $Ra_{2\phi,L} = 50$ [106]. The dashed lines in these plots represent the edge of the boundary layer. The

FIG. 26. Two-phase flow pattern in the external boiling case: (a) liquid velocity u_l^*, and (b) vapor velocity $u_v^* \bar{\rho}$ [106].

vapor moves primarily vertically upward due to the large density difference between liquid and vapor. The liquid is laterally entrained into the boundary layer. Once again, the two-phase cross-flow pattern is characteristic of buoyancy-driven boiling flows in porous media.

In contrast, the dryout heat flux in a pressure-driven boiling flow was found to be given by [105]

$$q_{dry} = 2.9 \times 10^{-3} \frac{h_{fg}\sigma}{v_l} \left(\frac{\varepsilon K}{L^2}\right)^{1/4} \left(\frac{u_\infty \mu_l}{\sigma}\right)^{1/2}. \tag{66}$$

Equation (66) gives a dryout heat flux of 4.04×10^4 W/m^2 for a water–steam system with $\varepsilon = 0.4$, $K = 10^{-10}$ m^2, and $L = 0.1$ m, and with an upward flow of $u_\infty = 5$ mm/sec. Neither Eq. (65) nor (66) has been verified experimentally. Nonetheless, it provides a simple estimate and a useful boundary of the dryout heat flux in various types of external boiling flow.

3. Experimental Studies

Limited experimental studies of boiling in porous media are available. Schrock et al. [110] performed the first study on boiling from horizontal cylinders placed in liquid-saturated sands with the particle diameters ranging from 0.16 to 1.5 mm. It was noted that with smaller particles the critical heat flux was lower than that without particles and a smooth transition occurred from nucleate boiling to film boiling regimes. The lower critical heat flux is probably caused by the difficulty in removing vapor from the heated surface through interstitial spaces. Fukusako et al. [111] obtained experimental curves of boiling over a horizontal heated plate embedded in a liquid-saturated porous layer. Steel, glass, and worked iron particles of 1 to 16.5 mm in diameter were used. Water, Freon-11, and Freon-113 were the test fluids. Fukusako et al. also found that for small particles (i.e., $d_p = 1$ to 2 mm), the heat flux increased monotonically with temperature during the transition from nucleate to film boiling, as shown in Fig. 27. Moreover, the heat flux in nucleate boiling was higher with small particles than that for large particles or without particles for the same superheat. They hypothesized that the particles constituting the porous medium serve as additional nucleation sites that are activated at low wall superheats, and furthermore, enhance heat transfer through fin effects. Nucleate boiling on a sphere placed in a coarse porous medium ($d_p = 2.9$ to 19 mm) saturated with Freon-113 was investigated by Tung and Dhir [112]. Similar behavior was observed.

Presently, there is a lack of the fundamental understanding of microscopic evaporation and bubble dynamics on the pore level, macroscopic
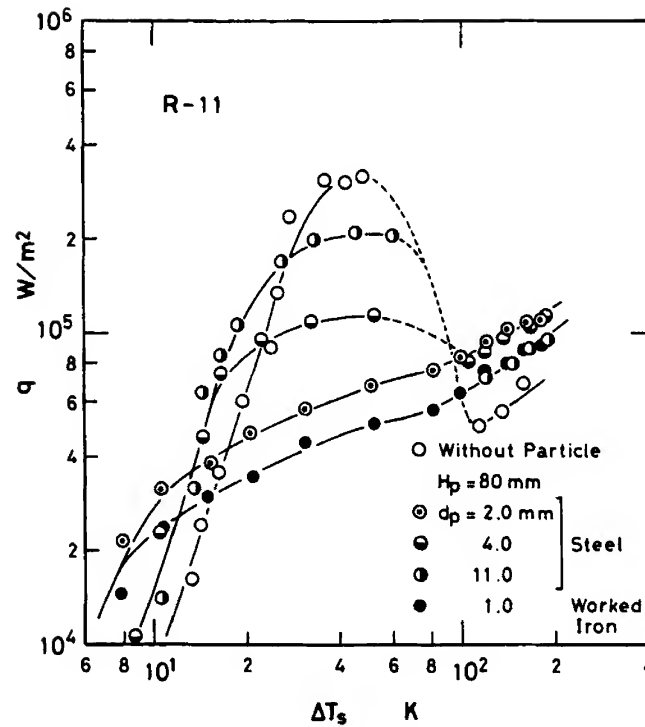
FIG. 27. Boiling curves in particulate beds saturated with Freon-11 for various particle diameters [111].

two-phase transport on the system scale, and their couplings during boiling in porous media. For example, it remains unclear how the capillary forces would influence movement of vapor bubbles away from the heated surface and liquid toward the heated surface. Dhir [6] has presented an insightful discussion on various fundamental issues related to boiling in porous media. This excellent review excluded the abundant literature of boiling in heat pipes and structured surfaces for heat transfer augmentation, because these problems typically feature a thin layer of porous materials, thus invalidating a continuum treatment of multiphase flow and heat transfer in porous media.

F. STEAM INJECTION

Another type of two-phase flow and heat transfer problems occurs during immiscible displacement in porous media, as usually encountered in enhanced oil recovery and remediation of contaminated soils. For exam-

ple, steam injection into a reservoir results in displacement of the initial pore fluids. Thus the rate of mass displaced out of the reservoir is substantially greater than the injection mass flow rate of steam. Figure 28 schematically illustrates the process of steam injection into a porous formation that is partially filled with either petroleum hydrocarbons in an oil recovery scenario or with water-immiscible contaminants in a ground-water contamination context. Steam is injected into the reservoir through vertical wells, allowed to sweep through the oil- or contaminant-rich regions, and then removed together with the mobilized volatile and semivolatile hydrocarbons. The principal mechanisms for oil or contaminant recovery in steam injection include

1. Steam distillation
2. Increased mobilization due to the decreasing viscosities with temperature
3. Displacement and dilution by the steam condensation front
4. Reduction in the amount of absorption into soil at elevated temperatures.

All these mechanisms are largely controlled by complex transport phenomena that occur during steam injection. They include phase change heat transfer, mass transfer of components between the phases, and multiphase simultaneous flows driven by the viscous, gravitational, and capillary forces.
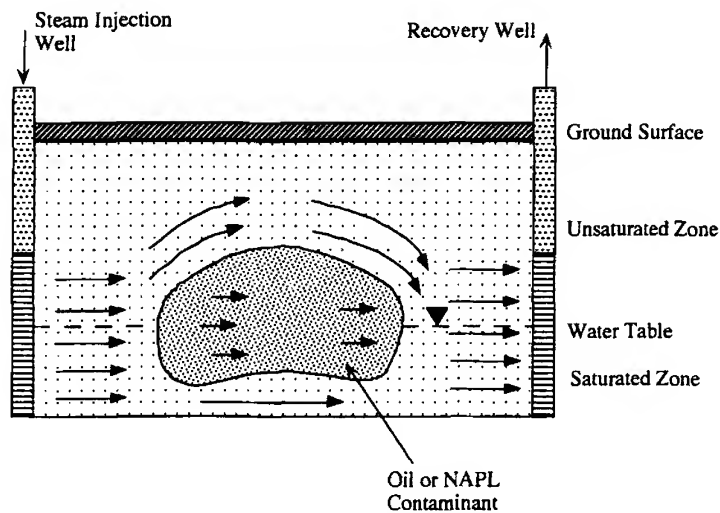
FIG. 28. Schematic illustration of steam injection into porous media. NAPL, nonaqueous phase liquids.

Moreover, these transport phenomena are inherently transient and multi-dimensional. Even in an idealized homogeneous reservoir, the injected steam tends to bypass the oil- or contaminant-present zones because they offer lower permeabilities to steam flow, thus resulting in a multidimensional scenario as shown in Fig. 28. In realistic geologic media, the multidimensional behavior of steam injection is further exacerbated by the reservoir heterogeneity. Certain physical phenomena may also contribute to multidimensional characteristics; for example, gravity override of steam where the light steam tends to rise to the top of the formation, thus leading to a premature breakthrough of steam into production wells. The detrimental outcome of steam override is a large reduction in the recovery rate and a significant waste of applied thermal energy (i.e., latent heat energy). In addition, buoyancy-driven flows in various phases due to both thermal and solutal gradients can result in the strongly multidimensional behavior and alter evaporation rates of oil or NAPL components at the condensation front. The role of natural convection in multiphase transport in porous media so far, has been little explored.

There is a wealth of information on steam injection for enhanced oil recovery in the petroleum industry. Examples are the experimental study of Baker [113], and the numerical work of Coats [114, 115]. However, because of the considerable commercial value of this technology, limited studies have been published in the open literature, and a fundamental understanding of the steam injection process remains proprietary. This is why a recent environmental application, that is, groundwater contamination by NAPLs and subsequent remediation by steam injection, has renewed great interest in this rather old problem [48, 55, 116, 117]. In addition, there are fundamentally different issues and approaches involved in the two types of applications. For example, in groundwater remediation, considerable attention must be given to the critical issue of complete disappearance of the NAPL, while the objective of oil recovery is to remove as much hydrocarbon from a formation as is economically feasible.

This review thus is restricted to the most recent work existing in the open literature and is focused on the fundamentals. While vapor displacement of the same-component liquid will be reviewed shortly, the topic of displacement of multicomponent fluids is deferred to Part IV.

1. Experimental Studies

Several experimental studies of 1D steam injection systems have appeared in the literature [55, 118–120]. In the absence of gravity, a steam condensation front propagates in the direction perpendicular to the injec-

tion velocity. The laboratory-scale experimental data demonstrated that steam injection is a viable method for contaminant recovery [55].

Experimental data of multidimensional steam injection are quite scarce. An injection of dry steam into an initially water-saturated porous medium was undertaken by Basel and Udell [116]. The test section consisted of a 2D rectangular bed. It was observed that the angle of the propagating steam front (with respect to the gravity direction) was a function of the ratio of gravitational to viscous forces. Basel and Udell [116] mapped the location of the steam front using liquid crystals formulated for color change at the boiling temperature of water. A thin layer of crystals was painted onto the innermost pane of the front side of the test section. Propagation of the front with time for different media permeabilities was reported. Later, Basel and Udell [121] experimentally examined the condensation front location in steam injection into a heterogeneous porous medium consisting of three homogeneous horizontal layers of different permeabilities.

2. One-Dimensional Analytical Studies

Basel and Udell [116] also developed a 1D analytical model for a dry steam front infiltrating an initially water-saturated bed. Neglecting capillary forces, the model formulated the hydrodynamic force and energy balance equations, and predicted the propagation velocity and angle (with respect to gravity) of the steam front. It was found that the angle of the steam condensation front is critically dependent on the ratio of gravitational forces to vapor phase viscous forces. A qualitatively good agreement was achieved between their model prediction and experimental data.

3. Multidimensional Numerical Modeling

Accurate analysis of multidimensional two-phase flow and heat transfer in porous media is intrinsically complicated and prohibitive for the reasons discussed in Part II. Chung and Catton [122] studied numerically the steam injection process into a forced water flow through a porous medium. A steam bubble develops around the injector that can either grow or become steady with time, depending on the heat removal rate at the phase interface separating the vapor and subcooled liquid regions. An important assumption made in this analysis was that there exists no two-phase zone between the two single-phase regions. Despite this simplification, the fundamental difficulty of tracking the moving and irregular phase interface is still present. A coordinate transformation was employed to find the location of the phase interface under steady-state conditions. An integral

solution was obtained to predict the vapor bubble size. It was concluded that the thermal dispersion effect is of paramount importance to achieve good agreement between theory and experiment. Applicability of this conclusion to transient steam injection processes, however, seems invalid. In fact, in a most recent study on steam injection into multidimensional porous reservoirs, Wang [48] found that the phase interface location was not affected by thermal dispersion in the subcooled liquid region.

Wang [48] described a fundamental study of steam injection into an initially water-saturated 2D reservoir. Emphasis was placed on elucidating various fundamental phenomena such as steam override, two-phase flow patterns, evaporation heat transfer, and natural convection in both phases caused by thermal gradients. The theoretical basis of this numerical study was MMM. Model assumptions included: (i) the generalized Darcy law for two-phase flow, (ii) isothermal two-phase zone, and (iii) local thermal equilibrium among the vapor, liquid, and solid phases. The numerical model was first validated against the 1D experiments of Hunt et al. [55], and good agreement was found between the measured and calculated steam front locations, as shown in Fig. 29. The 2D simulations were then compared with the three experiments of Basel and Udell [116], corresponding to different injection mass fluxes. Such a comparison is shown in Fig. 30, in which the steam condensation front profiles are plotted at various dimensionless times known also as the pore volumes. The pore volume is defined as the number of pore volumes filled with injected steam; namely,

$$\text{Pore volumes} = \frac{\text{Volume of injected steam}}{\text{Pore volume of formation}} = \left(\frac{\dot{m}_{in}}{\rho_{\ell} \varepsilon L_w}\right) t. \qquad (67)$$
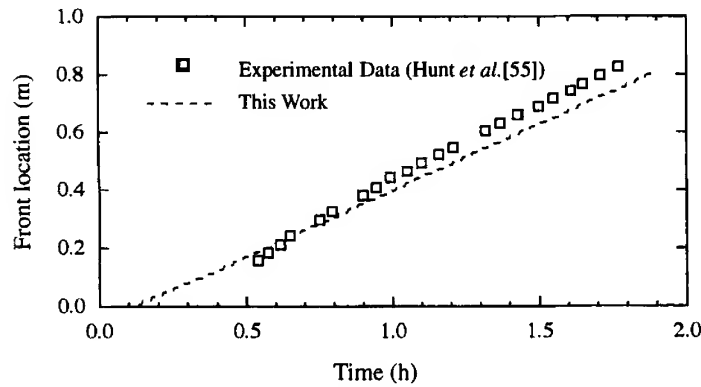
Fig. 29. Comparison of experimental and predicted steam front locations in a one-dimensional silica sand column [48].

**Pore volumes
of injected steam**

(a) experimental
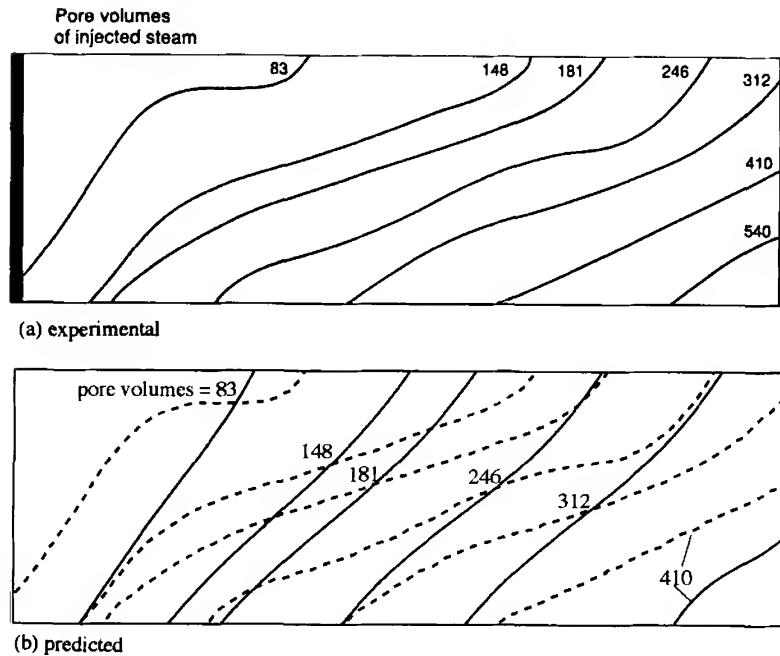
(b) predicted

Fig. 30. Comparison of predicted (solid lines [48]) and measured (dashed lines [116]) two-dimensional steam front profiles for the injection mass flux of $0.0274 \text{ kg/m}^2 \cdot \text{sec}$.

Apparently, the pore volume is equivalent to a dimensionless time. It can be seen from Fig. 30 that the predicted curves are in reasonable agreement with those measured experimentally [116]. In particular, there seems to be good agreement in terms of the mean front location as a function of time. The experimental fronts, however, are more inclined from the vertical than are the predicted counterparts. This can be explained by the fact that during experimental preparation a high permeability zone is created at the top of the sandpack, which allows the injected steam to preferentially invade along the top [116, 123]. The influence of this more permeable layer at the top of the sandpack on the measured steam front profiles is clearly visible, (see the dashed lines in Fig. 30). No attempt was made by Wang [48] to adjust the permeability of the upper region of the sandpack to reconcile the discrepancies displayed in Figs. 30.

To elucidate the fundamental transport phenomena occurring during steam injection, representative results of the temperature distribution ahead of the condensation front, liquid saturation contours within the
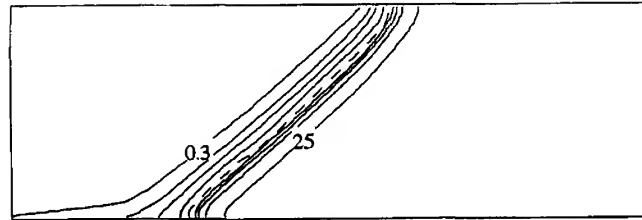
(a) Liquid saturation contours and isotherms
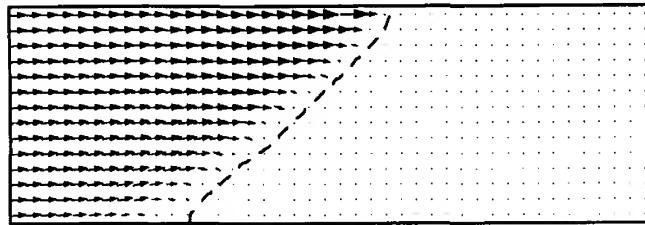
(b) vapor velocity vectors (m/s)

➡ = 8.48e-02
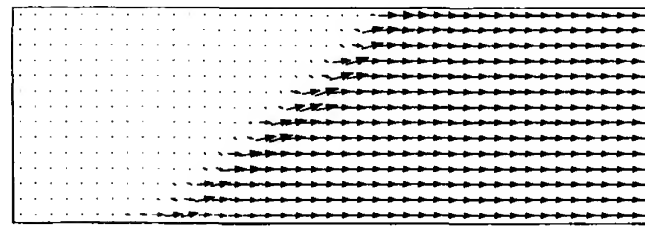
(c) liquid velocity vectors (m/s)

➡ = 1.75e-04

FIG. 31. Numerical results for two-dimensional steam injection at the instant of 0.4 h: (a) liquid saturation contours ($\Delta s = 0.2$) in the two-phase zone (left to the dashed line) and isotherms ($\Delta T = 15°C$) in the pure liquid region (right to the dashed line); (b) vapor velocity field; and (c) liquid velocity field. The steam front is denoted by the dashed line [48].

two-phase zone, and vapor and liquid velocity fields are shown in Fig. 31 for the injection mass fluxes of $0.0274 \text{ kg/m}^2 \cdot \text{sec}$. In Fig. 31, the isotherms are plotted for temperatures between 25 and 70°C, with an equal increment of 15°C, and the liquid saturation contours from 0.3 to 0.9, with an increment of 0.2. It can be seen from Fig. 31(a) that the steam front denoted by the dashed line is rather inclined, indicating that the gravita-

tional forces dominate the viscous forces. Far behind the steam front, the liquid saturation is nearly constant at the residual value, that is, 0.2. Major changes in the temperature and liquid saturation occur over very small distances in the proximity of the steam condensation front. This unique feature of the steam front would invalidate the use of coarse grids, as was done by Falta [123]. The vapor motion in the two-phase zone is primarily horizontal and uniform except in the neighborhood of the condensation front (as shown in Fig. 31(b)) where the vapor velocity drastically decreases due to steam condensation. As a result, the liquid saturation increases rapidly, as can be seen from Fig. 31(a). The liquid motion features somewhat intricate characteristics in the vicinity of the condensation front, as shown in Fig. 31(c). Immediately behind the front and within the two-phase zone, liquid tends to migrate downward because its density is much larger than that of the vapor. The migration, however, occurs at a low speed because of the large resistance against liquid flow in the two-phase zone. Ahead of the front and in the full-liquid region, the liquid ascends owing to thermal buoyancy forces. Away from the steam front, the liquid velocity field becomes horizontal.

Overall assessment of steam displacement for oil recovery or contaminant removal can be made by examining the cumulative mass displaced out of the reservoir; namely,

$$m_{\text{out}} = \frac{1}{A} \int_0^t \int_A (\rho u)_{\text{out}} \, dA \, dt \qquad (68)$$

From an experimental point of view, the displaced mass is also a convenient quantity to measure. Numerical results of cumulative displaced mass for three injection rates (shown as circles in Fig. 32) indicate that displaced mass increases almost linearly with time, implying that steam displacement occurs at a constant mean speed. Steam breakthrough is seen to be characterized by a sharp change in the slope of a displacement curve. At times sufficiently later than the steam breakthrough, the slope of the displacement curve should asymptotically approach the injection mass flux because the system has reached steady state. The slopes of the displacement curves, shown in Fig. 32 before steam breakthrough, range between 3.0 and 3.3 times larger than their respective injection mass fluxes, indicating that steam injection is a viable method of removing oil or contaminants from the subsurface. Also plotted in Fig. 32 are the solid lines obtained from 1D simulations in which the gravitational acceleration is set to zero, with other conditions remaining the same. Apparently, 2D displacement can be well approximated by the 1D behavior, regardless of the severe steam override and natural convection present in some of the cases. This might provide a reason why most 1D models give good predictions of the
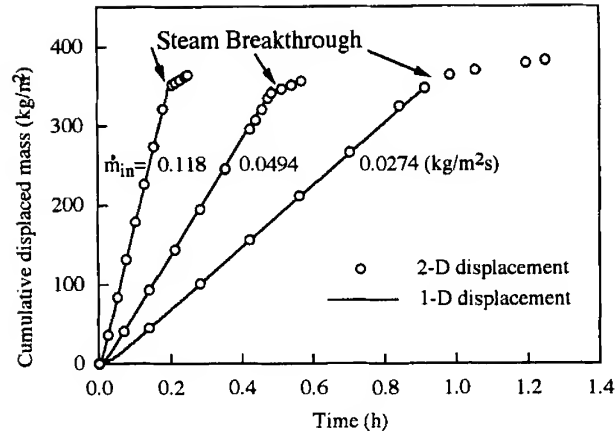
FIG. 32. Cumulative displaced mass for various injection fluxes and comparison to one-dimensional (1D) predictions [48]. 2D, two-dimensional.

performance curves, even though steam override is a complex multidimensional phenomenon.

The thermal dispersion effect on convection in the full-liquid region and, hence, steam displacement can be qualitatively assessed by artificially increasing the effective thermal conductivity. Figure 33 shows that doubling the effective thermal conductivity does not influence the displacement curve, demonstrating that heat conduction into the liquid ahead
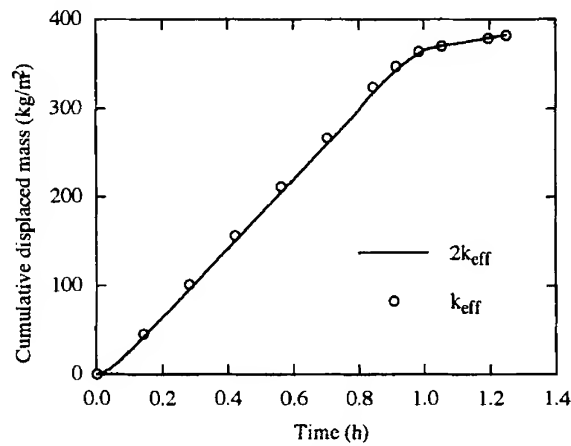
FIG. 33. Effect of thermal dispersion on steam displacement [48].
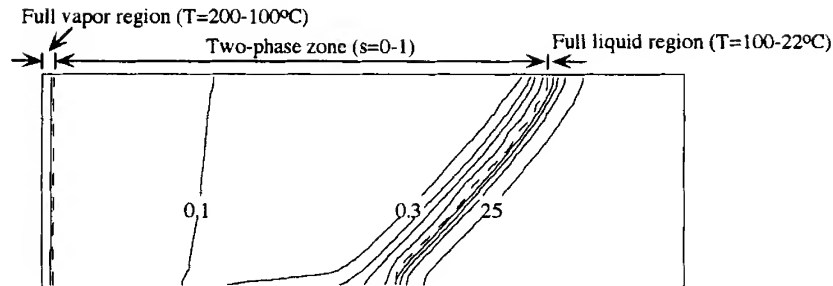
FIG. 34. Numerical results for superheated steam injection with ΔT_{sup} = 100°C, displaying evaporation and condensation front locations, isotherms, and liquid saturation contours (Δs = 0.2). The isotherms in the full vapor region are for T = 200, 150, and 100°C, whereas the isotherms in the full liquid region are in increments of 15°C [48].

of the condensation front plays a negligible role in controlling steam displacement.

Finally, superheated steam injection was studied for a moderate superheat of 100°C. It was found that the superheat helps to displace more liquid out of the porous formation due to the evaporation of residual water as stimulated by the superheated steam. Inspection of the liquid saturation contours shown in Fig. 34 for superheated steam injection indeed reveals that the liquid saturation in a large portion of the two-phase zone becomes lower than the residual value of the water saturation (i.e., 0.2). Figure 34 also illustrates the capability of the present model of handling a three-region problem encompassing superheated vapor, two-phase, and liquid zones, despite the fact that the superheated vapor region is quite narrow due to the small specific heat of the vapor.

G. SUMMARY

This section has presented a review of existing theoretical and experimental work for two-phase, single-component systems in porous media. Considerable progress has been made in the theoretical analysis of these systems in recent years. In particular, with the development of the multiphase mixture model (MMM), numerical solution of multidimensional, two-phase flow, and heat transfer problems in porous media can now be routinely performed on engineering workstations. Several examples reviewed indicate clearly that the computer time using MMM has decreased to a fraction of that required for MFM. The numerical capabilities and advantages of MMM have been fully demonstrated by successful applications to three-region problems including the liquid, two-phase, and super-

heated vapor zones simultaneously [46a, 48]. In addition, the MMM also shed new light on the analytical aspects of two-phase flow and heat transfer in porous media. A number of exact or similarity solutions have been found or expected.

While more applications of MMM to important engineering systems continue, a parallel development of new, accurate, experimental techniques for studying two-phase flow and heat transfer characteristics in porous media cannot be overemphasized. Careful experimentation is required both for gaining a thorough understanding of the two-phase transport phenomena inside porous media and for validating theoretical predictions to be produced. In particular, nonintrusive techniques to measure liquid saturations and phase velocities in the two-phase zone are highly desirable. In addition, the following fundamental issues also require special attention:

- Effects of medium heterogeneity on two-phase flow and heat transfer, and exploitation of heterogeneous materials for dramatic improvement of conventional capillary systems
- A fundamental model describing highly transient, localized, two-phase transport phenomena to be used in the modeling of nucleate and transitional boiling in porous media
- Thermal nonequilibrium models to capture the physics of boiling in porous materials
- Multidimensional solutions of non-Darcian two-phase flows that occur in coarse porous media
- Micro-macroscopic models to rigorously address the couplings between the vapor dynamics on the pore level and two-phase transport phenomena on the system level
- Design of novel thermal devices by taking advantage of two-phase transport principles in porous capillary materials, such as a capillary evaporator

VI. Multiphase, Multicomponent Systems

Multiphase flow and transport in multicomponent systems differ markedly from what was discussed in the preceding section for single-component systems. The fundamental differences arise from the thermodynamics of gas–liquid phase equilibrium of mixtures that allow the gas and liquid phases to be of differing compositions. This is exemplified in Fig. 35 for a typical binary phase diagram. As can be seen, in binary and multicomponent systems the various phases can co-exist in equilibrium
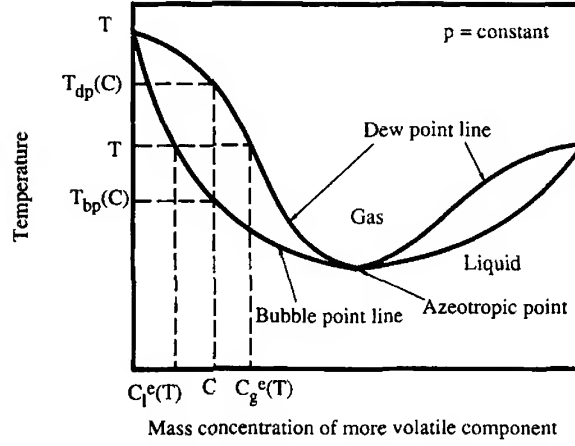
FIG. 35. A typical equilibrium phase diagram for an azeotropic mixture.

over a range of temperatures, thus leading to a nonisothermal multiphase zone. In the case of binary mixtures with a noncondensable gas, Eq. (41) for the equilibrium temperature in a two-phase zone is modified as [124]

$$
T = \frac{T_0 \left[1 + \dfrac{p_c - y p_g}{h_{fg}\, \rho_l} \right]}{1 - \dfrac{RT_0}{h_{fg}} \ln \dfrac{p_g (1 - y)}{p_0}},
\tag{69}
$$

where the vapor partial pressure is expressed by $p_g(1 - y)$, with y being the molar fraction of the noncondensable gas. It is clear from Eq. (69) that the two-phase temperature strongly varies with the content of the noncondensable gas. Note that in this section the liquid and gas phases are denoted by subscripts l and g, respectively, while the subscript v is reserved for the vapor component in the gas phase.

The second consequence of the phase diagram of mixtures shown in Fig. 35 is that during phase change a chemical species may be preferentially incorporated or released at the interphase boundary because of the differing solubilities in various phases. Thus mass transfer, in addition to heat transfer, plays a critical role in controlling phase change of multicomponent fluids. Moreover, the mass transfer process is often dominant because the rate of mass diffusion is normally much lower than that of heat diffusion in the liquid phase. In addition, the presence of species gradients may cause thermosolutal convection in each fluid phase. The

topic of thermosolutal convection in porous media—although it has received wide attention for single-phase systems over recent years—remains to be explored in multiphase systems. It is well known that thermosolutal convection patterns can be extremely intriguing in situations where the rates of heat and mass diffusion are vastly different.

The strong dependence of interfacial tension on species concentration gives rise to yet another new phenomenon called solutal-capillary flow in multicomponent systems. The capillary forces altered by species concentration (and temperature) variations may either accelerate or retard multiphase flow and transport in porous media.

The objective of this section is to review the significant advances in the understanding of multiphase flow and transport processes in porous media germane to mixtures. Section A explores 1D systems for basic insight into the physical phenomena involved and to establish a basis for further discussion of more complicated configurations arising from practical applications. Section B considers a particular subset of general multiphase systems, that is, liquid–gas systems that are of technical relevance in innumerable applications. Section C presents an overview of the recent efforts toward understanding dynamics of three-phase systems consisting of a gas and two immiscible liquid phases, with particular application to groundwater contamination and remediation. Finally, Section D gives a summary of future research needs in the area of multiphase, multicomponent transport in porous media.

A. ONE-DIMENSIONAL SYSTEMS

To delineate the general characteristics of multiphase flow and transport of mixtures in porous media, it is instructive to consider 1D situations in which the governing equations are still represented by Eqs. (42) and (43) but rewritten in terms of the subscripts l and g; that is,

$$\varepsilon \frac{\partial \rho}{\partial t} + \frac{\partial(\rho u)}{\partial x} = 0, \tag{70}$$

$$\varepsilon \frac{\partial(\rho_l s_l)}{\partial t} + \frac{\partial(\rho u \lambda_l)}{\partial x} = \frac{\partial}{\partial x}\left(\rho_l D_c \frac{\partial s_l}{\partial x}\right)$$

$$- \frac{\partial}{\partial x}\left(\frac{\lambda_l \lambda_g K(\rho_l - \rho_g) g_x}{\nu}\right) + \overline{m}_l. \tag{71}$$

Subject to the appropriate initial and boundary conditions, this equation set can be solved for the mixture velocity u and liquid saturation s_l. Other

secondary variables such as phase velocities and pressures are determined algebraically thereafter.

1. Steady Multiphase Flows

As an example of multiphase flows, consider two-phase, two-component flow in a 1D porous medium, as shown in Fig. 3(a). The two components are taken to be air and water, with air being initially present in the porous medium. Thus the liquid phase consists of pure water, whereas the gas phase is binary in water vapor and air. To investigate two-phase flow characteristics in this situation, we can integrate Eqs. (70) and (71) in much the same way as in Part III, Section A.1, except for two notable differences. First, the actual energy used for liquid–vapor phase transformation is now equal to $[q_w - (-k\partial T/\partial x)]$, where the second term accounts for the flux by heat conduction through a nonisothermal two-phase zone. Second, the mixture mass flux across the condensation front $\dot{m}_w$ is no longer zero because the mass transfer of components amounts to a net flow perpendicular to the front. Because the condensation front is impermeable to the noncondensable gas, the mixture mass flux must be given by

$$\dot{m}_w = -\rho_g D \frac{\partial y}{\partial x}, \tag{72}$$

where D is the binary diffusion coefficient of the gas phase. The net mixture flow is to counteract mass diffusion of the noncondensable gas toward the condensation front. Taking these differences into account, Eq. (45) can be modified into the following form for a binary mixture:

$$\rho_l D_c(s) \frac{\partial s_l}{\partial x} - \frac{\lambda_l \lambda_g K(\rho_l - \rho_g)g_x}{\nu} = \frac{1}{h_{fg}}\left(q_w + k\frac{\partial T}{\partial x}\right) - \lambda_l \rho_g D \frac{\partial y}{\partial x}. \tag{73}$$

The last two terms of this equation reflect the effects of heat conduction and mass diffusion on the two-phase characteristics of a binary mixture. The two mechanisms are further interlinked via Eq. (69), which relates the two-phase temperature to the molar fraction of the noncondensable gas. Figure 36 compares the liquid saturation profiles predicted by Eq. (73) for cases with and without a noncondensable gas [124]. The curve for the condensation front temperature equal to 100°C corresponds to the absence of noncondensable gas at atmospheric pressure, whereas the cases denoted by lower temperatures indicate increasingly higher contents of the noncondensable gas. It is seen that the liquid saturation gradients decrease as the
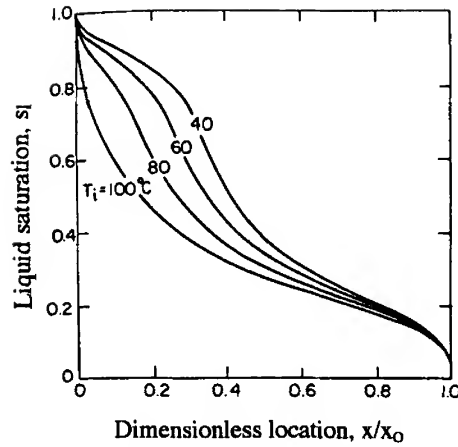
FIG. 36. Effects of a noncondensable gas on a two-phase flow pattern [124].

concentration of the noncondensable gas increases. The smaller saturation gradients, in turn, increase the wicking limit of heat transfer [124].

2. Transient Multiphase, Multicomponent Flows

Under transient conditions and ignoring the interphase mass transfer $\overline{m}_l$, Eqs. (70) and (71) may admit two possible similarity solutions, depending on particular types of boundary conditions. One corresponds to constant mixture velocity at the boundaries of a multiphase zone. In this situation, a similarity transformation $\eta = x - v_c t$ can be derived from Eqs. (70) and (71), where v_c represents the constant characteristic velocity of the moving boundary. Examples of this family of exact solutions include constant rate injection of steam into porous media. Yuan and Udell [125] studied steam distillation of a single component hydrocarbon liquid in a 1D porous media, both theoretically and experimentally. Assuming a constant injection rate of the steam with constant quality, the previously mentioned similarity solution was obtained, and the characteristic velocity of the distillation front was found to be a function of the residual saturation of the hydrocarbon liquid as well as the thermodynamic properties of water and the hydrocarbon liquid. Experimental results confirmed this similarity theory and, furthermore, determined that the interphase mass transfer coefficient (a parameter gauging the departure from local chemical nonequilibrium) increases linearly with the saturation of the liquid hydrocarbon [125].

The other family of similarity solutions that can be foreseen from Eqs. (70) and (71) assumes the negligible gravity effect and the boundary velocity of the mixture to follow the $t^{-1/2}$ profile. Then the similarity transformation $\eta = x/\sqrt{t}$ exists. This type of solution is applicable to situations such as constant pressure injection (the relationship $u \sim x^{-1} \sim t^{-1/2}$ is evident from the Darcy equation) and drying of porous slabs. Within this family, Morrison [76] obtained an analytical solution for a two-phase binary system under the assumption of negligible capillary pressure; however, this assumption is unnecessary in light of MMM, as has been explained earlier in Section II.

B. Liquid–Gas Systems

Liquid–gas multicomponent systems represent an important subset of general multiphase, multicomponent systems, and arise in a wide variety of applications in thermal, chemical, and environmental engineering.

1. Convection in Unsaturated Media

The topic of convection in unsaturated porous media, with and without evaporation or condensation, was systematically discussed by Plumb [126], who also concluded that very little work has been done on convection in the vadose zone of the subsurface. Technological examples where this subject may be important include heat losses from underground thermal structures, ground coupled heat pumps, repositories of high-level radioactive waste, and trickled-bed chemical reactors. Plumb [127] considered convection in a parallel flow from a heated horizontal surface embedded in the vadose zone. Assuming the Richards approximation in UFT (i.e., neglecting the gas phase motion), Plumb [127] obtained a boundary layer solution to the convective heat transfer problem. The interrelation between heat transfer and capillary-driven flow was shown. The analytical solution, however, has not been verified experimentally. In view of the similarities between UFT and MMM discussed in Section II, it appears possible and straightforward to remove the Richards assumption from the Plumb analysis, and to carry out a more accurate analysis of convection in unsaturated porous media using MMM.

Recent application to repositories of high-level radioactive waste has prompted renewed research interest in convection in unsaturated media. A large amount of decay heat is expected to be generated as a result of placing spent nuclear fuel in a potential repository site. Understanding the resulting thermal–hydrological scenarios is essential for repository assess-

ment. Pollock [128] employed a 1D mathematical model of the coupled heat and mass transfer to analyze vertical transport of energy and moisture above and below a horizontal repository. However, the 1D model is inherently incapable of describing the thermally induced gas circulation around a repository. Most recently, Chen and Boehm [129] presented an overview of heat transfer around an underground storage of high-level radioactive waste, and pointed out the need for careful experimentation in order to calibrate various existing models. Several experiments were carried out to measure the temperature distribution throughout an unsaturated packed bed. It was found that water vapor generated in the vicinity of the heater could be advected over a large portion of the bed, thus significantly altering the entire temperature field. Conduction was identified as a principal mechanism for heat transfer around the heater; however, convection and two-phase transport combined to contribute to heat transfer far away from the heater.

Another potential application of convection in liquid–gas systems concerns trickled-bed chemical reactors featuring liquid–gas co-current and countercurrent flows in packed beds [5]. Heat transfer in such two-phase systems is crucially important for reactor design, especially when higher exothermic reactions such as hydrogenation and oxidation take place. There appears to be only a few articles in the literature on the thermal aspects of trickle bed reactors. Weekman and Myers [130] measured radial temperature profiles in a co-current air–water downward flow through a packed column. Three types of packings with beads of 3.8 to 6.5 mm in diameter were examined. The experimental data was then interpreted by a simple heat transfer model for the two-phase mixture with the effective thermal conductivity being an adjustable parameter. Specchia and Baldi [131] interpreted similar experiments but employed a two-parameter heat transfer model (i.e., the effective thermal conductivity and the wall-to-bed heat transfer coefficient are adjustable). These authors proposed correlations of both parameters as functions of the operating conditions. It should be mentioned that all these primitive models have ignored the complicated two-phase flow patterns in trickled beds. Crine [132] took an important step toward establishing the effects of the two-phase distribution on the heat transfer phenomena using a percolation theory. However, much more research, both experimental and theoretical, is left to unravel the coupling between heat transfer and two-phase hydrodynamics in packed beds.

2. Drying of Porous Materials

Within the general area of multiphase, multicomponent heat and mass transfer in porous media, the problem of drying has probably received the most research attention. Classic work includes Krischer [33], Luikov [134],

Whitaker [4], and Eckert and Faghri [135]. Recent literature of drying was reviewed by Plumb [136] and Bories [137]. Additional references were cited in a general review on porous media transport by Tien and Vafai [13].

Without attempting an exhaustive review on drying, suffice it to mention the pioneering work of Luikov [134] and Whitaker [4]. These models constitute the theoretical basis of a large body of previous work. Luikov's model assumed that moisture transfer in a porous material is driven by gradients of moisture content, temperature, and pressure in a diffusion-like fashion. Whitaker [4] developed a comprehensive theory of drying using the technique of volume averaging. In a later study, Whitaker [138] specifically demonstrated that for low-intensity drying conditions the liquid transport is only due to capillary action and the governing transport equation can be written in terms of the liquid saturation:

$$\varepsilon \frac{\partial(\rho_l s_l)}{\partial t} = \frac{\partial}{\partial x}\left(D \frac{\partial s_l}{\partial x}\right) + \frac{\partial}{\partial x}\left(K \frac{k_{rl}}{\nu_l}\rho_l g\right),$$

(74)

where D is given by

$$D = \frac{Kk_{rl}}{\nu_l}\frac{dp_c}{ds_l}.$$

(75)

A comparison with Eq. (15) shows that Eq. (74) is exactly the duplicate of UFT for problems of drying. Thus implicit in Eq. (74) is the assumption that the gas phase pressure remains constant. This assumption has been commonly invoked, both implicitly and explicitly, in the majority of current drying models. Apparently, the assumption is likely to break down for rapid drying processes where the gas phase dynamics become critical. As a significant departure from previous reviews on drying, the following discussion concentrates on systems in which simultaneous liquid and gas flows take place.

Consider a porous medium initially saturated or near-saturated with liquid. When drying occurs by passing heated air or vapor over the surface of the porous material, as illustrated in Fig. 37, three distinct regions may appear inside the porous medium. Near to the drying surface, a super-heated vapor region results due to high drying rates. Adjacent to this region and extending into the porous material will be a two-phase zone in which the two-phase flow and transport is driven by both gravitational and capillary forces. Ahead of this zone the medium will remain saturated with liquid. The temperature profile in each region is also sketched in Fig. 37.

In 1D situations, an exact similarity solution can be developed for the problem. This was first shown by Udell [139] for the case of superheated steam drying of a semi-infinite slab initially saturated with liquid water. Analytical profiles of temperature and liquid saturation were found using
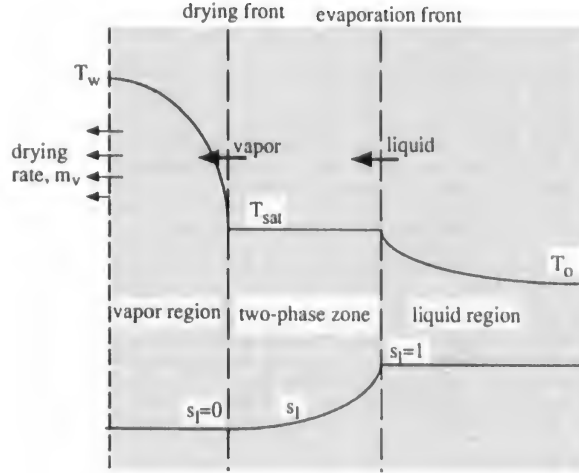
FIG. 37. Schematic illustration of drying of porous material and the different drying regimes.

the similarity transformation $x/\sqrt{t}$, as predicted in Part IV, Section A.2. While accounting fully for the two-phase simultaneous flows, however, Udell did make a quasi-steady assumption, namely that the two-phase dynamics is steady within the moving coordinate attached to the evaporation front. While this assumption was instrumental in Udell [139] arriving at the similarity solution based on MFM, it appears unnecessary within the framework of MMM. To elaborate on this, we can apply the energy equation of MMM, Eq. (35), to the current 1D problem; that is,

$$\frac{\partial}{\partial t}\left[(1 - \varepsilon)\rho_s h_s + \varepsilon\rho h\right] + \frac{\partial}{\partial x}(\gamma_h \rho u h)$$

$$= \frac{\partial}{\partial x}\left(k_g \frac{\partial T}{\partial x}\right) + \frac{\partial}{\partial x}\left(-h_{fg} \rho_l D_c \frac{\partial s_l}{\partial x}\right). \quad (76)$$

This equation, together with Eq. (70), then constitutes a complete mathematical system for two unknowns: the mixture enthalpy h and velocity u. The mixture enthalpy in a single-phase region is nothing more than the temperature T times a specific heat, whereas in the two-phase zone the temperature corresponds to the known saturation state, and thus the enthalpy h is linearly proportional to the liquid saturation s_l. Equations (70) and (76) admit a similarity solution provided that the boundary

conditions are as follows:

$$\text{at } t = 0, \quad h = c_l T_0 = \text{const}, \quad u = 0, \tag{77}$$

$$\text{at } x = 0, \quad h = h_{fg} + c_l T_w = \text{const}, \tag{78}$$

$$\text{at } x \to \infty, \quad h = c_l T_0 = \text{const}, \quad u = 0. \tag{79}$$

With a similarity transformation $\eta = x/\sqrt{t}$, Eqs. (70) and (76) are readily cast into two ordinary differential equations, which can then be solved using routine numerical methods such as the Runge-Kutta scheme. Results of this analytical study will be detailed in a forthcoming publication. Note that no quasi-steady assumption needs to be employed, and thus the exact nature of the solution is retained. Such more exact solutions will be useful in providing physical insight into the drying process as well as a benchmark to validate sophisticated numerical models. For instance, as revealed in Part IV, Section A.2, the similarity solution indicates that the drying rate, that is, the mixture velocity at the drying surface, is inversely proportional to the square root of time.

For drying samples of finite dimension, numerical methods are usually required. An example was given by Rogers and Kaviany [140] who experimentally and numerically studied drying of an initially partially saturated packed bed during both funicular and drying-front periods. In the funicular regime, the liquid phase is continuous, and simultaneous two-phase flow occurs. In the second period, the liquid saturation at the drying surface drops below the irreducible value, and a superheated gas region begins to develop at the surface and to expand into the porous medium. Rogers and Kaviany [140] used MFM to simulate the funicular drying process, but had to terminate the numerical simulation when the drying front regime was reached. This numerical difficulty arises from the inherent nature of MFM; that is, MFM is inconvenient to handle a multiregion problem encompassing single- and two-phase subregions simultaneously or a problem involving phase appearance and disappearance. Figure 38 shows the predicted and measured mass transfer rates as a function of time [140]. As seen, the drying rate decreases initially, and then remains constant, signifying that the surface lies within a two-phase zone. The mass transfer rate drastically decreases when reaching the drying front regime (called the evaporative front in the original article and Fig. 38), where the surface becomes completely dry. The numerical prediction in the funicular regime compared favorably with the experimental data.

While it still may be possible to use MFM and track a moving front separating various regions for 1D drying problems, significantly more difficulties will be experienced in multidimensional problems. The numerical problem of interface tracking and various remedial methods have been
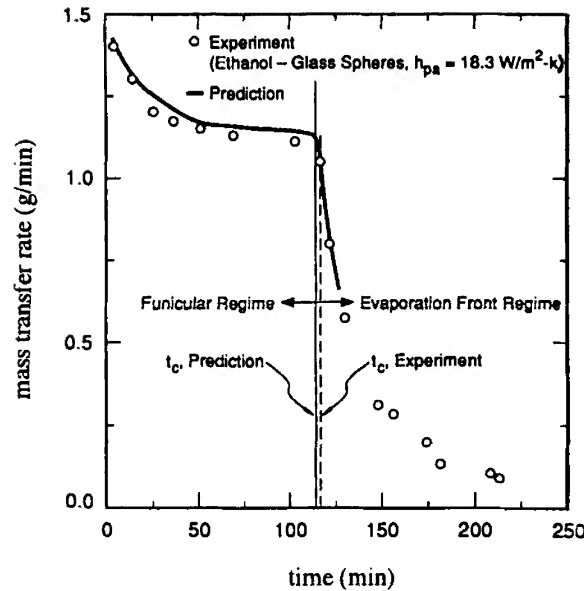
FIG. 38. Variation of the drying rate with respect to time in both the funicular and drying front regimes [140].

discussed in the work of Perre et al. [141, 142] on 2D drying. Unfortunately, all of these methods require certain approximations. On the other hand, if MMM is used, the numerical difficulty would vanish, making it possible to develop a general-purpose drying simulation code. Such a multidimensional code would be particularly useful to analyze and understand the drying process of anisotropic materials, as studied by Ouelhazi et al. [143].

Well-controlled and carefully defined experimental studies are scarce in the literature. Lee et al. [144] conducted an experiment in an attempt to provide a database for drying packed beds of granular nonhygroscopic materials. Experimental results for drying rate, saturation distribution, temperature distribution, and surface saturation were reported for drying glass beads under various drying conditions. Their results revealed that, contrary to available model predictions, porous materials do not necessarily exhibit saturation gradients that always increase with distance from the drying surface. Under certain conditions, the capillary action may be sufficient to create an internal drying front. The data of Lee et al. [144] can be used to validate drying models applicable to different materials and drying scenarios.

3. Boiling of Multicomponent Liquids

Boiling of multicomponent liquids in porous materials is a topic closely related to many two-phase thermal devices such as heat pipes, capillary pumped loops, and porous media heat exchangers. In the past, these systems employed mostly single-component working fluids. However, it seems worthy of exploring a binary or multicomponent mixture as the working fluid in order to leapfrog the current thermal technologies for meeting future needs of higher heat load systems. This is based on several well-known attributes of binary mixture boiling without porous media:

1. Increase in critical heat fluxes
2. Creation of a passive control mechanism for device operation
3. Substantial decrease in the temperature overshoot typically associated with single-component liquid boiling.

Earlier studies on pool boiling of binary mixtures observed that the critical heat fluxes for water–alcohol mixtures at low alcohol concentrations were much higher than the corresponding values for pure water under comparable conditions [145]. Recently, Peterson et al. [146] reported that by using a binary mixture, the system pressure of a reflux thermosyphon can remain virtually constant with varying power input, thus achieving desirable passive control for sustainable device operation. This mechanism of passive control can be explained by the phase diagram of a binary mixture that requires evaporation to occur over a range of temperatures at a constant pressure. Normington et al. [147] performed extensive experiments to demonstrate that the use of mixtures of dielectric liquids can reduce or eliminate the temperature overshoot that occurs during boiling at high heat fluxes.

These unique features of binary mixture pool boiling can be extended to capillary systems. In addition, and perhaps more important, there exist particular merits of using binary mixtures in capillary structures. For instance, the addition of a more volatile component generates a larger amount of vapor in a porous wick, thus lowering the average liquid saturation and, hence, increasing the capillary pressure for feeding liquid into the system. This is because the capillary pressure increases markedly as the liquid saturation decreases (see Fig. 1). The augmented wicking effect may extend the capillary pumping limit substantially and increase the dryout heat flux of wicks. Another beneficial effect of binary mixtures is to improve the start-up transients during which vapor bubbles of the more-volatile component are first generated and serve as the "seeding vapor" to induce capillary forces.

The only work on boiling in porous wicks saturated with a binary fluid was performed by Pruzan et al. [148], who demonstrated that the maximum

heat flux with water–ethanol mixtures is 2.35 times larger than that for pure water. To date, these test data have not been supported and analyzed through corresponding fundamental studies, and none of the above-mentioned features of binary mixture boiling in porous structures has been explored.

4. *Nonaqueous Phase Liquids–Air Flow and Transport in the Unsaturated Zone*

In the category of liquid–gas systems, another important class of problems is concerned with groundwater contamination and remediation. Recently, groundwater contamination by nonaqueous phase liquids (NAPLs) such as hydrocarbon fuels and halogenated organic solvents has become a major environmental concern and, hence, has received intense research attention [149].

Figure 39 depicts a typical scenario of NAPL contamination. In the unsaturated zone near the ground surface, an organic liquid spilled from a leaky storage tank may migrate downward due to gravitational forces. Concurrently, the chemical volatilizes into the air in the pores, and the organic vapor advects laterally in the unsaturated zone, thereby greatly increasing the area of contamination. When the NAPL reaches a low-
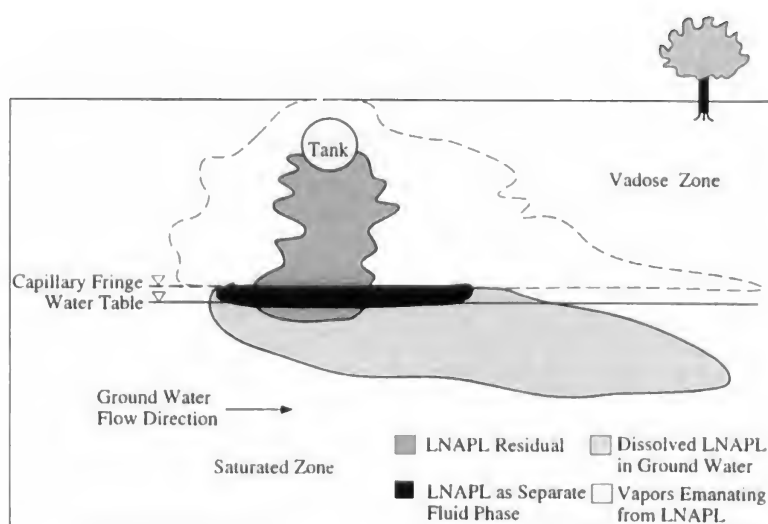
FIG. 39. Schematic illustration of LNAPL (lighter than water nonaqueous phase liquids) infiltration and redistribution in the vadose zone (after [149]).

permeability barrier or the saturated zone (in the case of a lighter than water NAPL), it spreads laterally, forming a pool or lens floating over the barrier or the water table. Clearly the most important NAPL contamination mechanisms in the unsaturated zone include NAPL transport as a separate phase and organic vapor transport via gas phase advection. The contaminant volatilized into the air in the soil pores may subsequently be dissolved into flowing groundwater or infiltrating recharge water, thereby contributing to contamination of the underlying groundwater. Modeling of these strongly coupled transport processes will ultimately determine the contaminant fate in the subsurface and subsequently define the task of locating and removing contaminants. A currently popular remediation technology involves injecting clean air into the contaminated site to recover contaminants. This method called soil vapor extraction (SVE) proves very effective for removing volatile organic compounds, which have high vapor pressures and large Henry constants at the ambient surface temperature. For semivolatile or low-volatile compounds, however, a thermally enhanced SVE would be necessary that injects heated air (instead of cold air) into the contaminated site to increase the subsurface temperature, thereby enhancing volatilization of contaminants and accelerating the rate of remediation.

To date, a good understanding and control of contaminant transport during thermal venting is absent. While the traditional soil vapor extraction has been studied both experimentally [150] and numerically [151], very little research has been performed for thermally enhanced SVE. Lingineni and Dhir [152] conducted 1D experiments of thermally enhanced SVE in a homogeneous sand column filled with gasoline at residual saturation. They also developed a nonisothermal mass transport model only for the gas phase. Figure 40 shows a favorable agreement between their experimental and numerical temperature profiles for normal and thermal venting, respectively, at an air flow rate of 234 L/min. It is also seen that temperature decreases occur due to evaporation of the contaminant in both normal (Fig. 40(a)) and thermal venting (Fig. 40(b)) cases. Moreover, the temperature decrease in the normal venting case is more severe than in that with thermal venting, because there is no external heat source in the former case to compensate for the latent heat of vaporization. Lingineni and Dhir [152] concluded that the effect of thermal energy on remediation of less-volatile contaminants is substantial, whereas the effect on high-volatile contaminants is minimal. In another recent study, Kaluarachchi and Islam [153] developed a nonisothermal model to describe gas flow, energy transport, and multicomponent mass transport and applied it to both 1D and 2D situations. The 1D results were favorably compared with the experimental data of Lingineni and Dhir [152], and hypothetical 2D

(a) normal venting
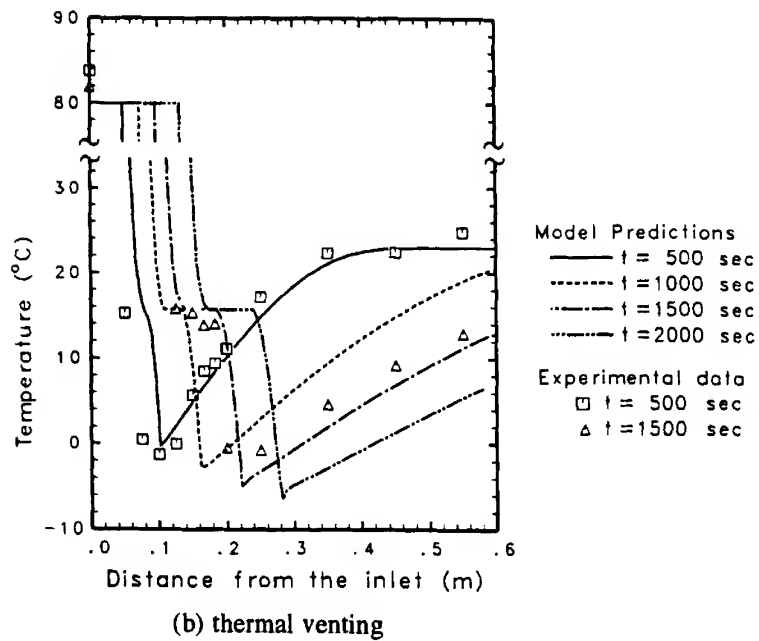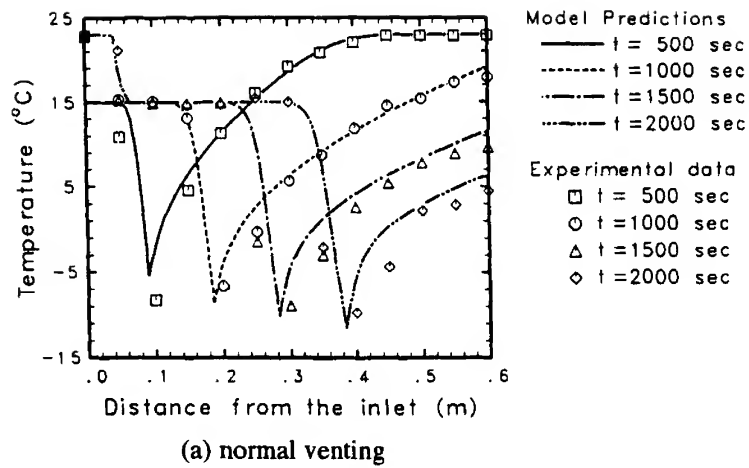
(b) thermal venting

FIG. 40. Comparison between the predicted and measured temperatures in a soil column for: (a) normal venting, and (b) thermal venting [152].

simulations provided considerable insight into thermally enhanced SVE for subsurface remediation. However, both studies have considered the gas phase flow only, and thus their applicability is limited to the vadose zone with immobile water and NAPL phases.

In an attempt to understand the SVE processes in cases of mobile NAPL, Cheng and Wang [47] considered infiltration and redistribution of a NAPL in a 2D homogeneous sand aquifer. The NAPL was introduced into the system through a small opening along the left boundary, which models a contaminant source resulting from a leaky underground tank. A constant NAPL saturation was assumed to prevail inside this region during the entire infiltration process. The aquifer initially contained air and water, while the water saturation was assumed to be uniform and at a residual value. In this numerical study, the water phase was excluded from the system for simplicity, because it is practically immobile ($k_{r_w} = 0$) during the NAPL transport; the problem was thus reduced to a two-phase (i.e., gas and NAPL), binary mixture system. As a first approximation, an isothermal system was also assumed.

Cheng and Wang's numerical study [47] was based on MMM, which fully accounts for the strong interactions between the two phases through the evaporation of the organic liquid into the gas phase. In the two-phase zone, the two-phase flow is driven by both capillary and gravitational forces, whereas in the pure gas phase region, the gas flow may be induced by the buoyancy forces due to concentration gradients. This solutal convection is important for the transport of chemical compounds through the gas phase. The vapor phase transport also represents a key mechanism for SVE. The rectangular domain shown in Figs. 41 to 43 was divided into a uniform 82 × 32 grid. The choice of this fine grid size was made possible due to the high computational efficiency of MMM. A typical transient simulation required only 2.7 hours of computation on a Hewlett Parkard 715/75 workstation. Such CPU time is on the same order of magnitude as for a single-phase problem with similar complexities [47]. Sample calculations were performed for three common contaminants: carbon tetrachloride (CCl_4), toluene, and trichloroethylene (TCE). Carbon tetrachloride is dense and more volatile, so that the resulting two-phase flow and gas phase advection are strong. Toluene represents an opposite case because its density is relatively low and its volatilization also is to a lesser extent. As an intermediate case, TCE is heavier and more volatile than is toluene, but is lighter and less volatile than CCl_4.

Figure 41 shows the composite plots of NAPL saturation distributions in the two-phase zone and contours of constant air concentration in the pure gas phase region at 3, 6, and 12 hours after the spill of CCl_4. The mass concentration of the organic vapor in the gas phase can be read from Fig.
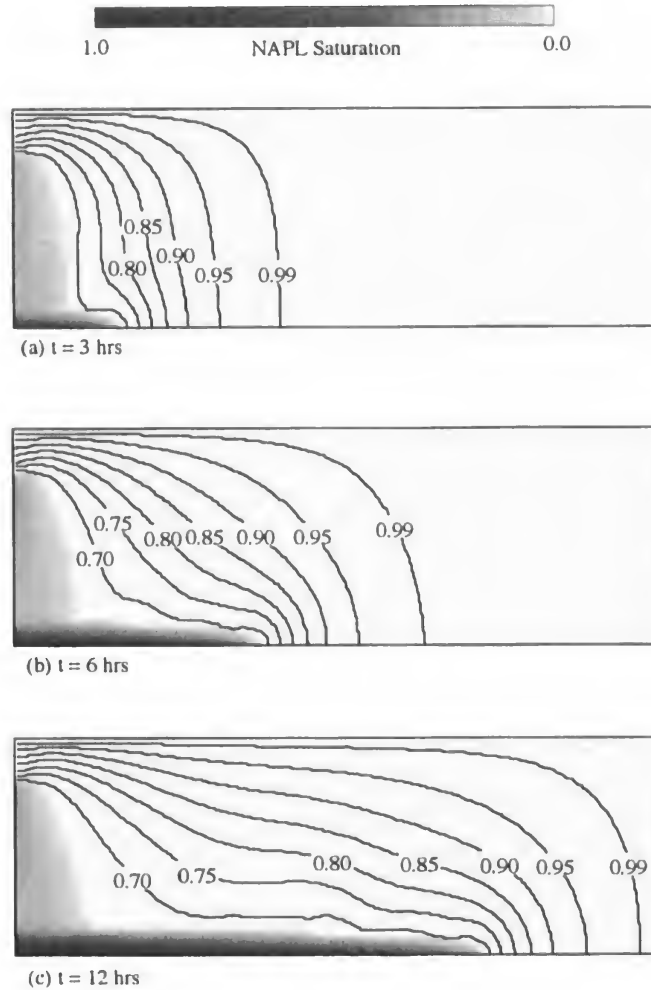
FIG. 41. Composite plots of carbon tetrachloride (CCl_4) saturation in the two-phase zone and air concentration in the gas phase for CCl_4, where $(1 - C_g)$ represents the organic vapor concentration [47]. NAPL, nonaqueous phase liquids.

41 using the conversion relation $C_v = (1 - C_g)$. Thus the 0.99 contours shown in Fig. 41 denote 1% of organic vapor present in the gas phase, a threshold value to define the contaminant front. The phase interface, which separates the two-phase zone from the all gas region, is also the evaporation front at which the air concentration is constant and equal to
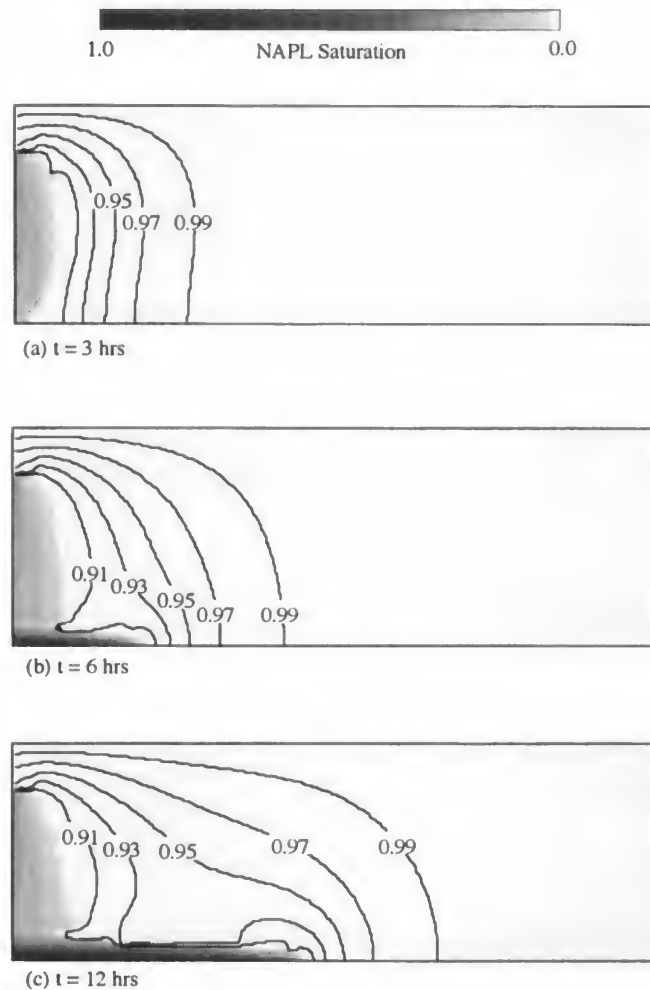
FIG. 42. Composite plots of toluene saturation in the two-phase zone and air concentration in the gas phase for toluene, where $(1 - C_g)$ represents the organic vapor concentration [47]. NAPL, nonaqueous phase liquids.

its equilibrium value (i.e., 0.513 in the case of CCl_4 at the ambient temperature).

At the very initial stages of NAPL invasion, a two-phase semicircular zone develops that covers the spill spot. This is expected because the initial infiltration is governed principally by isotropic capillary diffusion. At 3 h
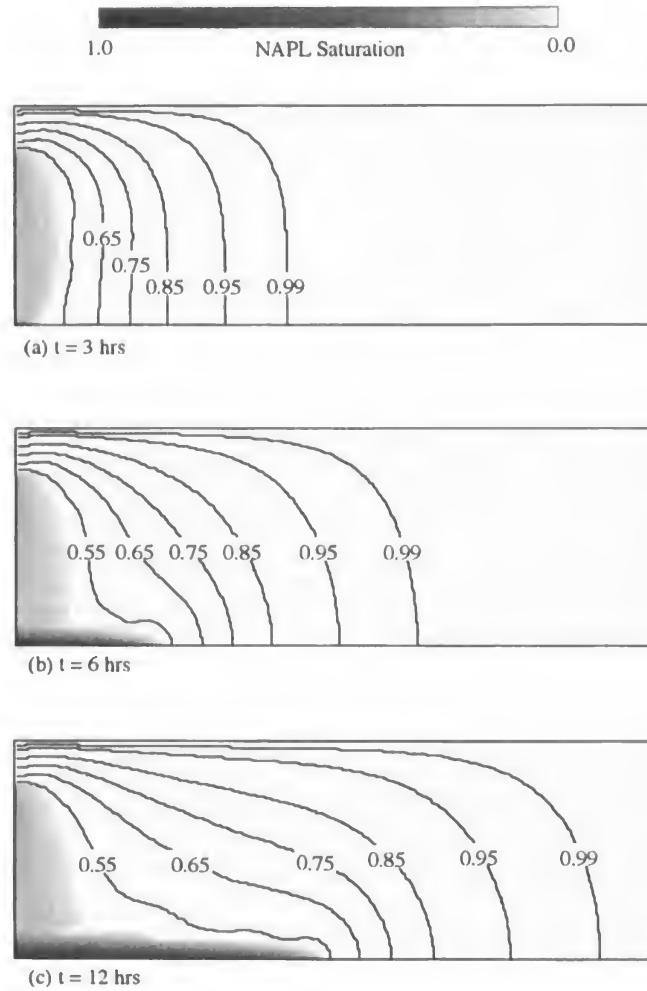
FIG. 43. Composite plots of trichloroethylene (TCE) saturation in the two-phase zone and air concentration in the gas phase for TCE, where $(1 - C_g)$ represents the organic vapor concentration [47]. NAPL, nonaqueous phase liquids.

after the spill (Fig. 41a), the NAPL infiltration front reaches the bottom water table. The gravitational forces due to the disparate density difference between the NAPL and gas has dominantly controlled the two-phase flow, resulting in preferential spreading in the vertical direction rather than in the lateral direction. This predicted shape of the NAPL infiltration front is reminiscent of those observed experimentally by Schwille [154] for

a dense NAPL, and by Pantanzidou and Sitar [155] and Geel and Sykes [156] for light NAPLs in the unsaturated zone. The gas phase advection induced by concentration gradients spreads the volatilized organic vapor far beyond the NAPL infiltration front (Fig. 41(a)). The contaminant front denoted by the 1% contour in the organic vapor concentration is seen to penetrate deeply into the aquifer away from the contaminant source. It should be noted that several single-phase studies [157, 158] also indicated the wide spreading of the organic vapor by solutally induced convection. However, in the conjugate single- and two-phase flow system, the displacement flow in the gas phase caused by the propagation of the phase interface overrides the density-driven flow [47]. This indicates a need for the consideration of NAPL movement in modeling gas flow and quantifying the vapor phase transport for remedial operations such as SVE.

At 6 h after the spill, the phase interface motion is characterized by the horizontal migration of the NAPL along the impermeable bottom. A NAPL lens is seen to float over the impermeable barrier (Fig. 41(b)). Greater lateral spreading occurs as a result of diminishing vertical movement of the NAPL and increasingly dominant capillary forces at the leading edge of the NAPL infiltration front. The volatilized vapor is spread farthest at the bottom because of combined density-driven downward flow and outward flow caused by the displacement of the infiltrating NAPL (Fig. 41(b)). By 12 h the zone of contamination has become so extensive that the contaminant front almost reaches the right boundary, which models an infinite boundary (Fig. 41(c)). It is also shown that the NAPL lens at the bottom of the aquifer becomes elongated and pancake-shaped, and higher NAPL saturations are found inside the lens because the NAPL is continually fed from the vertical infiltration. These predicted features are again in good agreement with the experimental observations by Pantanzidou and Sitar [155]. The NAPL saturation inside the lens can be significantly higher than that of the contaminant source due to the gravity-induced phase separation. The thickness of the NAPL lens depend on the equilibrium between the gravitational and capillary forces; therefore, the thin lens predicted implies that the gravitational forces override the capillary forces in the system under consideration.

Toluene has a lower density than does CCl_4, and therefore a lesser amount of the NAPL entering the subsurface is expected for the same saturation of the contaminant source. However, toluene is also less volatile, so that the amount of the chemical evaporated into the air in the soil pores decreases. The net effect of these counter factors results in a two-phase zone of almost the same extent, as shown in Fig. 42. Nonetheless, the all gas phase region contaminated by the organic vapor is minimal because of the low volatility of toluene. Therefore, the whole zone contaminated by

toluene is less extensive as compared with CCl_4, provided all other conditions are maintained the same. The air concentration isopleths in Fig. 42(c) indicate that the organic vapor concentrations are high near the water table. The gas of high organic vapor content combined with the direct dissolution of the NAPL lens into the water phase may cause serious contamination of the groundwater system underlying the water table.

Trichloroethylene is as dense as CCl_4, but less volatile. Moreover, TCE has an interfacial tension similar to CCl_4. Because the NAPL infiltration rate into the subsurface is determined mainly by the density difference between the phases and the interfacial tension, the rates for TCE and CCl_4 are expected to be about the same. The two chemicals differ only in volatility, which leads to a smaller two-phase zone in the case of CCl_4. This is indeed the case, as can be seen by comparing Fig. 43 with Fig. 41. However, the gas phase region contaminated by chemical vapor is less extensive for TCE than it is for CCl_4. Therefore, the whole zone of contamination remains almost the same for both TCE and CCl_4.

It is of practical interest to visualize all stages of groundwater contamination and remediation processes, starting from the NAPL spill, to the redistribution after the contaminant source is removed, and finally to the NAPL removal from the subsurface. MMM promises to provide a tool for such computationally intensive simulations [159]. Some illustrative results are presented below for a hypothetical 2D aquifer contaminated by CCl_4, as described earlier. The first phase of this simulation consisted of predicting the NAPL infiltration event for 3 h as described above. During the second phase, the leaking contaminant source was removed and the NAPL was allowed to redistribute in the aquifer due to gravity gradients and capillary forces. The last phase of the simulation considered a SVE remedial action by injecting clean air from a fully penetrated well along the right boundary. Figure 44 (in color section) presents selected results of the entire simulation, which include the NAPL saturation distribution (the color images), the iso-concentration contours in the gas phase (the color lines), and the gas phase velocity vectors (white arrows).

Figure 44(a) displays the composite plots at 3 h after the spill. The NAPL is seen to reach the impermeable bottom. At the same time, the organic vapor emanating from the NAPL-gas two-phase zone has widely spread into the aquifer due to a displacement flow in the gas phase caused by the infiltrating NAPL. It should be pointed out that in this figure the velocity scale has been chosen small enough to show the details of the velocity field in the all-gas region while omitting some large velocity vectors in the two-phase zone. It can be seen that the displacement stems mainly from the vicinity of the contaminant source at the left boundary as well as the leading infiltration front along the bottom impermeable bound-

Spill-Redistribution-Remediation

NAPL Saturation

0   0.6

ground surface

(a)

3 hrs after spill
(u_{gmax}=0.03 mm/s)

water table

(b)

9 hrs after
redistribution
(u_{gmax}=0.02 mm/s)

(c)

6 hrs after
remediation (recovery
well is fully screened;
u_{gmax}=0.28 mm/s;
injection u=0.1 mm/s)

NAPL recovery   Air injection

(d)

6 hrs after
remediation (recovery
well is half-screened;
u_{gmax}=0.78 mm/s;
injection u=0.1 mm/s)
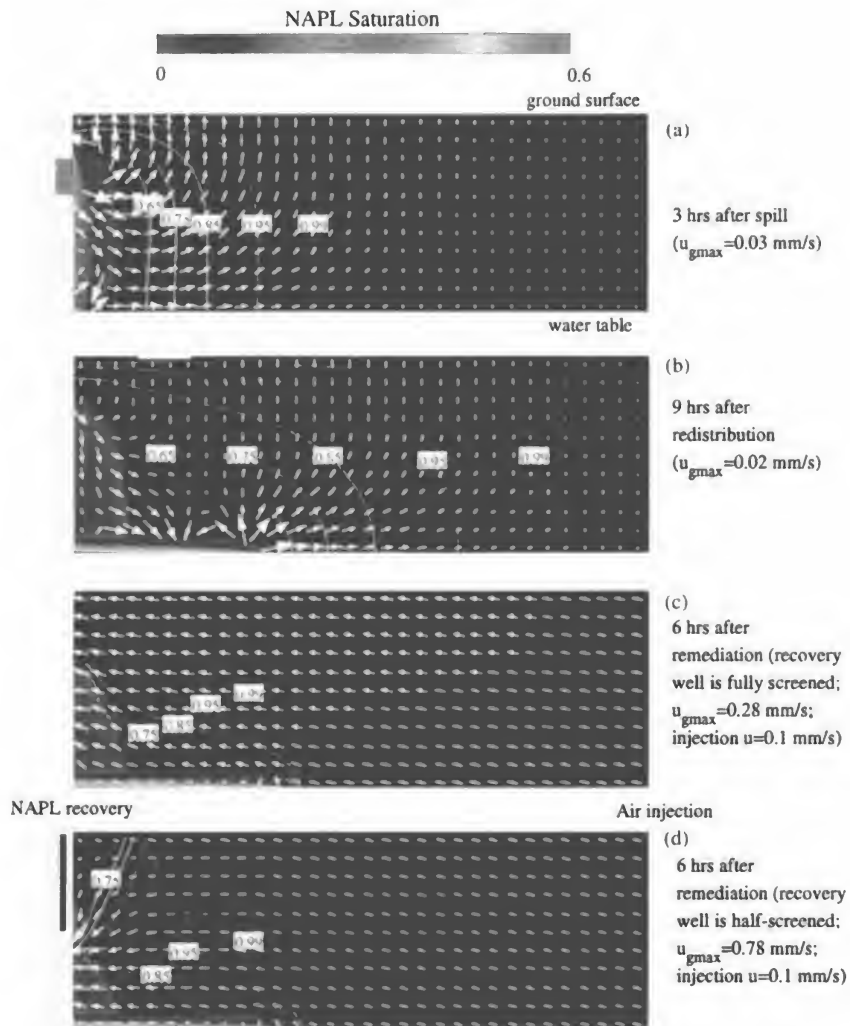
FIG. 44. Composite plots of carbon tetrachloride saturation, air concentration, and gas phase velocity for: (a) infiltration stage; (b) redistribution stage; (c) remediation stage by injecting air from right to left boundary with fully screened wells; and (d) remediation stage with a half-screened recovery well [159]. NAPL, nonaqueous phase liquids.

ary; both locations are characterized by rapid infiltration of the NAPL and hence significant displacement of the gas. The displaced gas exit through the permeable ground surface.

The plots displayed in Fig. 44(b) show the NAPL redistribution process after the contaminant source is removed. At 9 h of redistribution, the NAPL is seen to accumulate at the bottom because of the NAPL being much heavier than the gas. The maximum NAPL saturation is found therein, which may greatly endanger the underlying groundwater system. The NAPL saturation in the area adjacent to the original contaminant source is, however, decreasing so as to maintain the mass balance in the system. The gas phase in most of the aquifer has been contaminated by the organic vapor volatilized from the two-phase zone. Fast spreading of the contaminant is partly due to rapid infiltration of the NAPL along the bottom, and partly due to the displacement of the gas phase by the infiltrating NAPL.

Figure 44(c) displays results of the SVE process in which clean air is injected uniformly along the right boundary (i.e., the injection well) and the organic vapor is recovered through a production well sitting along the left boundary. Both injection and production wells were fully screened to the bottom of the aquifer. The ground surface is now covered to prevent the organic vapor from escaping to the atmosphere. The air velocity blown into the aquifer is 0.36 m/h. Comparing Fig. 44(b) and 44(c), it can be seen that the two-phase zone shrinks due to the evaporation of the organic liquid into the injected clean air, which is then removed. However, some portion of clean air bypasses the two-phase zone where the soil pores are partially occupied by the liquid contaminant and, hence, offer a higher resistance to air flow; only a portion of air actually penetrates through the two-phase zone and becomes saturated with the organic vapor. The bypassing phenomenon is also evident from the iso-concentration contours inclined toward the outlet at the top, which apparently limits the effectiveness of the remediation system. To alleviate this problem, a second SVE process is analyzed in which the production well is only half-screened from midheight to the bottom. All other conditions remain the same. The screened zone is designed to direct the injected air through the contamination zone to augment the recovery efficiency. Figure 44(d) shows that the two-phase zone indeed recedes more significantly than the first remediation system. The iso-concentration contours also demonstrate a nearly pistonlike displacement. Clearly, the two designs shown in Figs. 44(c) and 44(d) indicate the importance of a good understanding and control of the multidimensional distribution of the injected fluid in the subsurface. Herein lies the practical significance of a powerful and efficient analysis tool.

The previous simulation for all stages of infiltration, redistribution, and

remediation required approximately 3 CPU hours on a Hewlett Packard 715/75 workstation, and a total of 2700 grid blocks was used. Many fine-scale phenomena such as the island of residual NAPL (Fig. 44(d)) would not have been captured if coarser grids were used. Future research is to extend this numerical study to nonisothermal systems to allow for virtual remediation using thermal methods, thus providing a guide in designing actual field remedial systems.

C. THREE-PHASE SYSTEMS

The simultaneous presence of three phases such as water, gas, and an organic liquid immiscible with water in a porous medium significantly complicate transport processes. The scenarios are commonly encountered in the subsurface environment and petroleum reservoirs. Chemical components present in such systems may include water, air, and various hydrocarbons. Nonisothermal processes are of interest for thermally enhanced methods of recovering oil or contaminant. Typical thermal methods involve steam and hot water injection. In these complex multicomponent three-phase systems, a whole spectrum of transport phenomena is expected to occur and interact with one another. Examples are interphase solute partitioning, interfacial mass and heat transfer, evaporation, condensation, thermosolutal convection in the gas phase, phase migration driven by capillary forces, gravity-induced phase separation, and unstable immiscible displacement due to both density and viscosity contrasts. These complexities make numerical methods the only realistic choice in the pursuit of solutions for practical problems. For the same reason, explained in Part III, Section F, the following review excludes the petroleum engineering literature.

Very few experimental investigations on these systems existed in the open literature. Udell and coworkers [160, 161] conducted an extensive series of experiments using steam to displace various NAPLs such as xylene, diesel fuel, and perchlorolethylene (PCE). Visual observations of the contaminant front were made, and effluent concentrations of contaminants were measured as functions of the displacement time. No temperature and saturation distributions were presented, however, making it difficult to acquire a detailed understanding of the steam injection processes.

Numerical modeling of nonisothermal three-phase flow and transport in porous media was attempted only recently, and modeling issues essentially center on the treatment of phase appearance and disappearance. This issue is significant for the types of nonisothermal systems being considered, not only because it is inherent to MFM that has been used in all the

previous numerical work, but also because the practical goal of clean-up efforts is to completely remove NAPLs from the subsurface. Falta *et al.* [117] employed an integral finite difference method to discretize MFM, and proposed a variable substitution scheme that switches primary variables and governing equations whenever phase transitions occur at a location in the model domain. The variable switching criteria consist of minimum residual saturation requirements for gas and aqueous phases. Adenekan *et al.* [162] further refined the switching procedure, but did not demonstrate the performance of their improved algorithm. Forsyth [163] showed several sample calculations of steam injection in both Cartesian and axisymmetric geometries using a different technique to handle phase appearance and disappearance, which required the gas phase to always be present. Most recently, Panday *et al.* [40] categorized previous formulations and highlighted their respective advantages and disadvantages. In summary, all the previous numerical models were based on MFM and employed the procedure of switching variables and governing equations, which is inherently susceptible to poor convergence. In addition, because of intensive computational efforts associated with MFM, very coarse grids were used in numerical simulations. These grids certainly cannot capture the detailed behavior in the vicinities of moving evaporation and condensation fronts where large gradients occur over a rather short distance.

In conclusion, three-phase multicomponent systems remain largely unexplored and present very challenging numerical tasks. A robust and efficient model with three-phase multicomponent and nonisothermal capabilities is presently not available. Much more research, in particular on the fundamentals, is required to advance the development of various thermal technologies with application to environmental restoration.

D. SUMMARY

This section has exposed a full spectrum of fascinating physical phenomena involved in multiphase flow and multicomponent transport in porous media along with several emerging applications of great importance. Both fundamental and applied research in this area has been of recent origin. Much remains to be done in years to come. Whereas general applications of MMM to multiphase flow and multicomponent transport in porous media look promising, the capabilities of MMM need to be fully demonstrated. The following areas deserve immediate attention:

- Numerical modeling of three-phase systems. This is needed to provide a routine predictive tool for a wide variety of subsurface transport problems.

- Modeling of multicomponent transport. Although the application of MMM to single-component organic liquids has been demonstrated, many groundwater pollution problems involve multicomponent organic liquids, such as gasoline. When the gas phase is contaminated by multiple organic components with differing molecular diffusivities, the density-driven gas flow may become unstable, and thus enhance the transport of contaminants. Under these circumstances, multidiffusive convection occurs as a result of local buoyancy-driven instabilities formed by the difference in diffusivity of the various components.

- Effect of heterogeneities. Heterogeneities (e.g., zones of differing permeability) will contribute to contaminant spreading in a number of fundamental ways. For example, an NAPL tends to spread out horizontally when it encounters a low-permeability layer. In addition, the vapor phase transport is diffusion-dominated in low-permeability areas.

- Thermal effects in alternative remedial technologies. Such effects include thermally enhanced soil vapor extraction and hot water or steam injection.

V. Conclusions

This review has summarized the recent development in both theoretical and experimental studies of multiphase flow, heat transfer, and multicomponent transport in porous media. The available models were carefully compared and their respective merits pointed out. In particular, the recently developed multiphase mixture model (MMM) was reviewed in detail. This model was rigorously derived from the traditional multiphase flow model (MFM) without making further approximations. The new model views the multiple phases as constituents of a mixture, and thus consists only of the conservation equations for the whole multiphase mixture. All primary variables in this model are mixture properties; therefore, complex tasks to track phase interfaces separating various subregions and handle phase appearance or disappearance are avoided. In addition, explicit relations have been established to obtain the individual phase characteristics from the mixture variables in a postprocessing fashion. Finally, the new model strongly resembles the single-phase counterpart, thus offering an attractive alternative for the theoretical analysis and numerical simulation of multiphase transport phenomena in porous media. A number of successful applications of the model have been demonstrated and an efficient numerical methodology developed. It is expected that this

new model will provide a viable analysis and design tool in broad engineering fields involving multiphase flow and transport in porous media.

A large variety of fundamental topics have been covered in the present review, ranging from: (1) local thermal and chemical nonequilibrium among phases; (2) non-Darcian effects such as boundary and inertia effects; (3) 1D exact solutions for steady and transient flows; (4) onset of thermal instability in the presence of boiling; (5) interactive boiling and natural or forced convection; (6) boundary-layer multiphase flow with or without phase change; (7) dryout heat flux in porous medium systems; (8) propagation of evaporation and condensation fronts in steam injection; (9) effects of mass diffusion and heat transfer on multiphase flows; (10) thermosolutal convection in multiphase, multicomponent systems; and finally (11) effects of medium heterogeneity. There are many other fundamental issues present in multicomponent, multiphase systems that remain unexplored.

Practical applications involving multiphase flow and transport in porous media were also discussed. Particular emphasis was placed on multidisciplinary and emerging areas, such as novel capillary devices for cooling of high heat load electronics, enhancement of condensation heat transfer by the use of porous structures, environmental heat transfer, drying of porous materials, and remediation of contaminated soil and groundwater.

Future research areas have been identified in individual sections where appropriate. Overall, it can be said that a continuum approach of single-component, two-phase systems in porous media has been well established. The remaining issues lie only in the more accurate description of constitutive relationships through a proper account of microscopic phase distribution and dynamics on the pore level. This will require combined modeling and experimentation efforts. However, the studies of heat transfer in multicomponent porous media systems are only at the initial stage, and very extensive research is needed in this technologically important and fundamentally intricate subfield of heat transfer.

Nomenclature

c	specific heat	Ct_k	thermocapillary coefficient,
C	species concentration		$\sum_j \lambda_j \dfrac{\partial p_{cjk}}{\partial \sigma_{jk}} \dfrac{\partial \sigma_{jk}}{\partial T}$
Ca_{ik}	capillary coefficient,		
	$\sum_j \lambda_j \dfrac{\partial p_{cjk}}{\partial s_i}$	d_p	particle diameter
		D	diffusion coefficient
$Cs_{\alpha k}$	solutal-capillary coefficient,	$D(s)$	capillary diffusion coefficient
	$\sum_j \lambda_j \dfrac{\partial p_{cjk}}{\partial \sigma_{jk}} \dfrac{\partial \sigma_{jk}}{\partial C^\alpha}$	$f(s)$	hindrance function
		$\mathbf{g}$	gravitational acceleration

h	enthalpy or heat transfer coefficient	δ	boundary layer thickness
h_{fg}	latent heat of liquid–vapor phase change	ε	porosity
		η	similarity variable
$\mathbf{j}$	diffusive mass flux	λ	relative mobility
$J(s)$	capillary pressure function	μ	viscosity
Ja	dimensionless subcooling	ν	kinetic viscosity
k_r	relative permeability	ρ	density
k_{eff}	effective thermal conductivity	σ	interfacial tension
K	absolute permeability		
L	length		
$\dot{m}$	mass flux of multiphase mixture, ρu		

SUBSCRIPTS

Nu	Nusselt number		
p	pressure	c	capillary
Pe	Peclet number	dry	dryout
q	heat flux	g	gas phase
$\dot{q}$	volumetric heat generation rate	h	in vertical direction
Q	dimensionless heat flux	i	phase i
$\dot{Q}$	dimensionless heat generation rate	in	injection
Ra	Rayleigh number	k	phase k
s	phase saturation	kj	interface between phases k and j
Sh	dimensionless superheat	j	phase j
t	time	l	liquid phase
T	temperature	O	initial state
$\mathbf{u}$	superficial or Darcian velocity vector	out	outlet
u_{in}	inlet velocity	r	residual or irreducible
v_c	characteristic velocity	sat	saturated state
x	coordinate in horizontal direction	v	vapor phase
X	quality of steam	w	wall
y	coordinate in vertical direction or molar fraction of species	α	pertinent to species α
		κ	"kinetic" property
		2ϕ	two-phase
		∞	infinite

GREEK SYMBOLS

α	thermal diffusivity	SUPERSCRIPTS	
β	thermal expansion coefficient		
γ	multiphase correction coefficient	e	equilibrium
$\Delta\rho$	density difference, $\rho_l - \rho_v$.	$-$	interfacial

References

1. Boberg, T. (1988). *Thermal Methods of Oil Recovery*. Wiley, New York.
2. Abriola, L. M. (1988). *Multiphase Flow and Transport Models for Organic Chemicals: A Review and Assessment*, EA-5976, EPRI, Palo Alto, CA.
3. Faghri, A. (1995). *Heat Pipe Science and Technology*. Taylor & Francis, Washington, DC.
4. Whitaker, S. (1977). Simultaneous heat, mass, and momentum transfer in porous media: A theory of drying. In *Advances in Heat Transfer* (J. P. Hartnett and J. F. Irvine, Jr., eds.), Vol. 13, pp. 119–203, Academic Press, New York.

4a. Vafai, K., and Whitaker, S. (1986). Simultaneous heat and mass transfer accompanied by phase change in porous insulations. *J. Heat Transfer*, **108**, 132–140.

5. Shah, Y. T. (1979). *Gas-Liquid-Solid Reactor Design*. McGraw-Hill, New York.

6. Dhir, V. K. (1994). Boiling and two-phase flow in porous media. *Annu. Rev. Heat Transfer* **5**, 303–350.

7. Witherspoon, P. A., and Pruess, K. (1988). Environmental heat transfer in porous media. In *Collected Papers in Heat Transfer*, ASME HTD-Vol. **104**, Part 3, pp. 17–23. ASME, New York.

8. Cheng, P. (1978). Heat transfer in geothermal systems. In *Advances in Heat Transfer* (J. P. Hartnett and T. F. Irvine, Jr., eds.), Vol. 14, pp. 1–105, Academic Press, New York.

9. Wooding, R. A., and Morel-Seytoux, H. J. (1976). Multiphase fluid flow through porous media. *Annu. Rev. Fluid Mech.* **8**, 233–274.

10. Morel-Seytoux, H. J. (1973). Two-phase flows in porous media. *Adv. Hydrosci.* **9**, 119–202.

11. Adler, P. M., and Brenner, H. (1988). Multiphase flow in porous media. *Annu. Rev. Fluid Mech.* **20**, 35–59.

12. De Santos, J. M., Melli, T. R., and Scriven, L. E. (1991). Mechanics of gas-liquid flow in packed-bed contactors, *Annu. Rev. Fluid Mech.* **23**, 233–260.

13. Tien, C., and Vafai, K. (1990). Convective and radiactive heat transfer in porous media. *Adv. Appl. Mech.* **27**, 225–281.

13a. Vafai, K., and Sözen, M. (1990). A comparative analysis of multiphase transport in porous media. *Annu. Rev. Heat Transfer* **3**, 145–162.

14. Kaviany, M. (1991). *Principles of Heat Transfer in Porous Media*. Springer-Verlag, Berlin.

15. Catton, I., and Chung, M. (1994). Two-phase flow in porous media with phase change: Post dryout heat transfer and steam injection. *Nucl. Eng. Des.* **151**, 185–202.

16. Wang, C. Y., and Cheng, P. (1996). A multiphase mixture model for multiphase, multicomponent transport in capillary porous media. Part I: Model development. *Int. J. Heat Mass Transfer* **39**, 3607–3618.

17. Bear, J. (1972). *Dynamics of Fluids in Porous Media*. Elsevier, New York.

18. Scheidegger, A. E. (1974). *The Physics of Flow through Porous Media*. University of Toronto Press, Toronto.

19. Saez, A. E., and Carbonell, R. G. (1985). Hydrodynamic parameters for gas–liquid cocurrent flow in packed beds. *AIChE J.* **31**, 52.

20. Hassanizadeh, S. M., and Gray, W. G. (1980). General conservation equations for multiphase systems: 3. Constitutive theory for porous media. *Adv. Water Resour.* **3**, 25–41.

21. Whitaker, S. (1986). Flow in porous media II: The governing equations for immiscible, two-phase flow. *Transp. Porous Media* **1**, 105–125.

22. Brenner, H., and Edwards, D. A. (1993). *Macrotransport Processes*. Butterworth Heinemann, Boston.

23. Plumb, O. A., and Whitaker, S. (1988). Dispersion in heterogeneous porous media 1. Local volume averaging and large-scale averaging. *Water Resour. Res.* **24**, 913–926.

24. Quintard, M., and Whitaker, S. (1988). Two-phase flow in heterogeneous porous media: The method of large-scale averaging. *Transp. Porous Media* **3**, 357–413.

25. Wang, C. Y., and Beckermann, C. (1993). Single- vs. dual-scale volume averaging for heterogeneous multiphase systems. *Int. J. Multiphase Flow* **19**, 397–407.

26. Celia, M. A., Rajaram, H., and Ferrand, L. A. (1993). A multi-scale computational model for multiphase flow in porous media. *Adv. Water Resour.* **16**, 81–92.

27. Ferrand, L. A., Milly, P. C. D., and Pinder, G. F. (1989). Experimental determination of three-fluid saturation profiles in porous media. *J. Contam. Hydrol.* **4**, 373–395.

28. Wang, S. Y., Ayral, Y. S., and Gryte, C. C. (1984). Computer assisted tomography for the observation of oil displacement in porous media. *Annu. Meet. Soc. Pet. Eng.*, Dallas, TX, Pap. SPE 11758.

29. Zeev, P., Magaritz, M., and Bendel, P. (1990). Nuclear magnetic resonance imaging of miscible fingering in porous media. *Transp. Porous Media* 12, 107–123.

30. Montemango, C. D., and Gray, W. G. (1995). Photoluminescent volumetric imaging: A technique for the exploration of multiphase flow and transport in porous media. *Geophys. Res. Lett.* 22, 425–428.

31. Tidwell, V. C., and Glass, R. J. (1994). X ray and visible light transmission for laboratory measurement of two-dimensional saturation fields in thin-slab systems. *Water Resour. Res.* 30, 2873–2882.

32. Udell, K. S. (1985). Heat transfer in porous media considering phase change and capillarity—the heat pipe effect. *Int. J. Heat Mass Transfer* 28, 485–495.

33. Lenhard, R. J., and Parker, J. C. (1987). Measurement and prediction of saturation-pressure relationships in three phase porous media systems. *J. Contam. Hydrol.* 1, 407–424.

34. Parker, J. C., Lenhard, R. J., and Kuppusamy, T. (1987). A parametric model for constitutive properties governing multiphase flow in porous media. *Water Resour. Res.* 23, 618–624.

35. Faust, C. R. (1985). Transport of immiscible fluids within and below the unsaturated zone: a numerical model. *Water Resour. Res.* 21, 587–596.

36. Abriola, L. M., and Pinder, G. F. (1985). A multiphase approach to the modeling of porous media contamination by organic compounds 1. Equation development. *Water Resour. Res.* 21, 11–18.

37. McWhorster, D. B., and Sunada, D. K. (1990). Exact integration solutions for two-phase flow. *Water Resour. Res.* 26, 399–413.

38. Allen, M. B., III (1985). Numerical modeling of multiphase flow in porous media. *Adv. Water Resour.* 9, 162–187.

39. Ramesh, P. S., and Torrance, K. E. (1990). Numerical algorithm for problems involving boiling and natural convection in porous materials. *Numer. Heat Transfer B* 17, 1–24.

40. Panday, S., Forsyth, P. A., Falta, R. W., Wu, S. H., and Huyakorn, P. S. (1995). Considerations for robust compositional simulations of subsurface nonaqueous phase liquid contamination and remediation. *Water Resour. Res.* 31, 1273–1289.

41. Milly, P. C. D. (1988). Advances in modeling of water in the unsaturated zone. In *Groundwater Flow and Quality Modeling* (E. Custodio *et al.*, eds.), pp. 489–514. D. Reidel, Boston.

42. Shekarriz, A., and Plumb, O. A. (1986). A theoretical study of film condensation using porous fins. *Am. Soc. Mech. Eng. Pap.* 86-HT-31.

43. Majumdar, A., and Tien, C. L. (1990). Effects of surface tension on film condensation in a porous medium. *J. Heat Transfer* 112, 751–757.

44. Wang, C. Y., Beckermann, C., and Fan, C. (1994). Numerical study of boiling and natural convection in capillary porous media using the two-phase mixture model. *Numer. Heat Transfer A* 26, 375–398.

45. Wang, C. Y., Beckermann, C., and Fan, C. (1994). Transient natural convection and boiling in a porous layer heated from below. *Heat Transfer, Proc. Int. Heat Transfer Conf. 10th, 1994*, vol. 5, pp. 411–416.

46. Easterday, O. T., Wang, C. Y., and Cheng, P. (1995). A numerical and experimental study of two-phase flow and heat transfer in a porous formation with localized heating from below. In *ASME Heat Transfer and Flud Engineering Divisions*, HTD-Vol. 321, pp. 723–732. ASME, New York.

46a. Wang, C. Y. (1997). A fixed-grid numerical algorithm for two-phase flow and heat transfer in porous media. *Numerical Heat Transfer B*, in press.

47. Cheng, P., and Wang, C. Y. (1996). A multiphase mixture model for multiphase, multicomponent transport in capillary porous media. Part II: Numerical simulation of the transport of organic compounds in the subsurface. *Int. J. Heat Mass Transfer* **39**, 3619–3632.

48. Wang, C. Y. (1996). Multi-dimensional modeling of steam injection into porous media. *Proc. 2nd Euro. Therm. Sci., 14th UIT Natl. Heat Transfer Conf.*, Rome, Italy.

49. Chavent, G. (1976). A new formulation of diphasic incompressible flow in porous media. *Lect. Notes Math.* **503**.

50. Yortsos, Y. C. (1987). The relationship between immiscible and miscible displacement in porous media. *AIChE J.* **33**, 1912–1915.

51. Wang, C. Y., and Beckermann, C. (1993). A two-phase mixture model of liquid-gas flow and heat transfer in porous media. Part I: Formulation. *Int. J. Heat Mass Transfer* **36**, 2747–2758.

52. Whitaker, S. (1991). Improved constraints for the principle of local thermal equilibrium. *Ind. Eng. Chem. Res.* **30**, 983–997.

53. Quintard, M., and Whitaker, S. (1993). One and two-equation models for transient diffusion processes in two-phase systems. *Adv. Heat Transfer* **23**, 369–464.

54. Powers, S. E., Abriola, L. M., and Weber, W. J., Jr. (1992). An experimental investigation of NAPL dissolution in saturated subsurface system: Steady state mass transfer rates. *Water Resour. Res.* **28**, 2691–2706.

55. Hunt, J. R., Sitar, N., and Udell, K. S. (1988). Nonaqueous phase liquid transport and cleanup. *Water Resour. Res.* **24**, 1247–1269.

56. Geller, J. T., and Hunt, J. R. (1993). Mass transfer from nonaqueous phase organic liquids in water-saturated porous media. *Water Resour. Res.* **29**, 833–845.

57. Powers, S. E., Abriola, L. M., and Weber, W. J., Jr. (1994). An experimental investigation of nonaqueous phase liquid dissolution in saturated subsurface system: Transient mass transfer rates. *Water Resour. Res.* **30**, 321–332.

58. Wilkins, M. D., Abriola, L. M., and Pennell, K. D. (1995). An experimental investigation of rate-limited nonaqueous phase liquid volatilization in unsaturated porous media: Steady state mass transfer. *Water Resour. Res.* **31**, 2159.

59. Quintard, M., and Whitaker, S. (1994). Convection, dispersion, and interfacial transport of contaminants: homogeneous porous media. *Adv. Water Resour.* **17**, 221–239.

60. Nield, D. A., and Bejan, A. (1991). *Convection in Porous Media*. Springer-Verlag, New York.

61. Koch, D. L., and Brady, J. (1986). Dispersion in fixed beds. *J. Fluid Mech.* **154**, 399–427.

62. Hsu, C. T., and Cheng, P. (1990). Thermal dispersion in a porous medium. *Int. J. Heat Mass Transfer* **33**, 1587–1597.

63. Tung, V. X., and Dhir, V. K. (1988). A hydrodynamic model for two-phase flow through porous media. *Int. J. Multiphase Flow* **14**, 46–65.

64. Grosser, K. A., Carbonell, R. G., and Sundaresan, S. (1988). The onset of pulsing in two-phase cocurrent downflow through a packed bed. *AIChE J.* **34**, 1850–1860.

65. Dankworth, D. C., Kevrekidis, I. G., and Sundaresan, S. (1990). Dynamics of pulsing flow in trickle beds. *AIChE J.* **36**, 605–621.

66. Satik, C., Parlar, M., and Yortsos, Y. C. (1991). A study of steady-state steam-water counterflow in porous media. *Int. J. Heat Mass Transfer* **34**, 1755–1772.

67. Lipinski, R. J. (1984). A coolability model for postaccident nuclear reactor debris. *Nucl. Technol.* **65**, 53–66.

68. Bau, H. H., and Torrance, K. E. (1982). Boiling in low-permeability porous media. *Int. J. Heat Mass Transfer* **25**, 45–55.

69. McGuinness, M. J. (1996). Steady-solution selection and existence in geothermal heat pipes. I. The convective case. *Int. J. Heat Mass Transfer* **39**, 259–274.

70. Chuah, Y. K., and Carey, V. P. (1985). Analysis of boiling heat transfer and two-phase flow in porous media with non-uniform porosity. *Int. J. Heat Mass Transfer* **28**, 147–154.

71. Wang, C. Y., Groll, M., and Rosler, S. (1992). Dryout heat fluxes in composite porous layers heated from below. *Proc. Int. Heat Pipe Conf., 8th* (T. Z. Ma ed.), Int. Academic Publishers, Beijing.

72. Stubos, A. K., Satik, C., and Yortsos, Y. C. (1993). Effects of capillary heterogeneity on vapor-liquid counterflow in porous media. *Int. J. Heat Mass Transfer* **36**, 967–976.

73. Tsai, T. P., and Catton, I. (1987). The effect of flow from below on dryout heat flux. *J. Heat Transfer* **109**, 491–497.

74. Sheu, J. P., Torrance, K. E., and Turcotte, D. L. (1979). On the structure of two-phase hydrothermal flows in permeabale media. *J. Geophys. Res. B* **84**, 7524–7532.

75. Schubert, G., and Straus, J. M. (1979). Steam-water counterflow in porous media. *J. Geophys. Res. B* **84**, 1621–1628.

76. Morrison, F. A. Jr. (1973). Transient multiphase multicomponent flow in porous media. *Int. J. Heat Mass Transfer* **16**, 2331–2342.

77. Doughty, C., and Pruess, K. (1990). A similarity solution for two-phase fluid and heat flow near high-level nuclear waste packages emplaced in porous media. *Int. J. Heat Mass Transfer* **33**, 1205–1222.

78. Nilson, R. H., and Romero, L. A. (1980). Self-similar condensing flows in porous media. *Int. J. Heat Mass Transfer* **23**, 1461–1470.

79. Romero, L., and Nilson, R. H. (1981). Shock-like structure of phase-change flow in porous media. *J. Fluid Mech.* **104**, 467–482.

80. Nilson, R. H., and Montoya, P. C. (1980). Experiments on transient condensing flow through a porous medium. *J. Heat Transfer* **102**, 489–494.

81. Tsuruta, T., Narazaki, K., and Masuoka, T. (1988). Transient condensing two-phase flow through an initially subcooled porous medium. *JSME Int. J. Ser. II* **31**, 81–87.

82. Sleep, B. E., and Sykes, J. F. (1993). Compositional simulation of groundwater contamination by organic compounds. 1. Model development and verification. *Water Resour. Res.* **29**, 1697–1708.

83. Ambrose, J. H., Chow, L. C., and Beam, J. E. (1991). Detailed model for transient liquid flow in heat pipe wicks. *J. Thermophys. Heat Transfer* **5**, 532–538.

84. Sondergeld, C. K., and Turcotte, D. L. (1977). An experimental study for two-phase convection in a porous medium with applications to geological problems. *J. Geophys. Res.* **82**, 2045–2053.

85. Bau, H. H., and Torrance, K. E. (1982). Thermal convection and boiling in a porous medium. *Lett. Heat Mass Transfer* **9**, 431–441.

86. Ramesh, P. S., and Torrance, K. E. (1990). Stability of boiling in porous media. *Int. J. Heat Mass Transfer* **33**, 1895–1908.

87. Ramesh, P. S., and Torrance, K. E. (1993). Boiling in a porous layer heated from below: effects of natural convection and a moving liquid/two-phase interface. *J. Fluid Mech.* **257**, 289–309.

88. Schubert, G., and Straus, J. M. (1980). Gravitational instability of water over steam in vapor-dominated geothermal systems. *J. Geophys. Res. B* **85**, 6505–6512.

89. Tewari, P. K. (1982). A study of boiling and convection in fluid-saturated porous media. M.S. Thesis, Cornell University, Ithaca, NY.

90. Sondergeld, C. K., and Turcotte, D. L. (1978). Flow visualization studies of two-phase thermal convection in a porous layer. *Pure Appl. Geophys.* **117**, 321–330.

91. Hardee, H. C., and Nilson, R. H. (1977). Natural convection in porous media with heat generation. *Nucl. Sci. Eng.* **63**, 119–132.

92. Tung, V. X., and Dhir, V. K. (1990). Finite element solution of multi-dimensional two-phase flow through porous media with arbitrary heating conditions. *Int. J. Multiphase Flow* **16**, 985–1002.

93. Chung, M., and Catton, I. (1991). Post-dryout heat transfer in a multi-dimensional porous bed. *Nucl. Eng. Des.* **128**, 289–304.

94. Stubos, A. K., and Buchlin, J.-M. (1993). Analysis and numerical simulation of the thermohydraulic behaviour of a heat dissipating debris bed during power transients. *Int. J. Heat Mass Transfer* **36**, 1391–1401.

95. Stubos, A. K., Tassopoulos, M., and Kanellopoulos, N. (1994). Aspects of transient modeling of a volumetrically heated porous bed: A combination of microscopic and macroscopic approach. *Heat Transfer, Proc. Int. Heat Transfer Conf., 10th, 1994*, Vol. **5**, pp. 387–392.

96. Cioulachtjian, S., Tadrist, L., Occelli, R., Santini, R., and Pantaloni, J. (1992). Experimental analysis of heat transfer with phase change in porous media crossed by a fluid flow. *Exp. Therm. Fluid Sci.* **5**, 533–547.

97. Bodvarsson, G. S., Pruess, K., and Lippmann, M. J. (1986). Modeling of geothermal systems. *J. Pet. Technol.*, pp. 1007–1021.

98. Pruess, K. (1991). Grid orientation and capillary pressure effects in the simulation of water injection into depleted vapor zones. *Geothermics* **20**, 257–277.

99. Lai, C. H., Bodvarsson, G. S., and Truesdell, A. H. (1994). Modeling studies of heat transfer and phase distribution in two-phase geothermal reservoirs. *Geothermics* **23**, 3–20.

100. Cheng, P. (1981). Film condensation along an inclined surface in a porous medium. *Int. J. Heat Mass Transfer* **24**, 983–990.

101. Plumb, O. A. (1984). Capillary effects of film condensation in porous media. *AIAA Pap.* **84-1789**.

102. Chung, J. N., Plumb, O. A., and Lee, W. C. (1992). Condensation in a porous medium bounded by a cold vertical surface. *J. Heat Transfer* **114**, 1011–1018.

103. Nusselt, W. (1916). Die Oberflachen-Kondensation des Wasserdampfes. *VDI-Z* **60**, 541–575.

104. Schlichtling, H. (1968). *Boundary Layer Theory*, 6th ed. McGraw-Hill, New York.

105. Wang, C. Y., and Beckermann, C. (1993). A two-phase mixture model of liquid-gas flow and heat transfer in porous media. Part II: Application to pressure-driven boiling flow adjacent to a vertical heated plate. *Int. J. Heat Mass Transfer* **36**, 2759–2768.

106. Wang, C. Y., and Beckermann, C. (1995). Boundary-layer analysis of buoyancy-driven two-phase flow in capillary porous media. *J. Heat Transfer* **117**, 1082–1087.

107. White, S. M., and Tien, C. L. (1987). An experimental investigation of film condensation in porous structures. *Proc. Int. Heat Pipe Conf., 6th*, Grenoble, France.

108. Parmentier, E. M. (1979). Two-phase natural convection adjacent to a vertical heated surface in a permeable medium. *Int. J. Heat Mass Transfer* **22**, 849–855.

109. Cheng, P., and Verma, A. K. (1981). The effect of subcooled liquid on film boiling about a vertical heated surface in a porous medium. *Int. J. Heat Mass Transfer* **24**, 1151–1160.

110. Schrock, V. E., Fernandes, R. T., and Kesavan, K. (1970). Heat transfer from cylinders embedded in a liquid filled porous medium. *Heat Transfer, Proc. Int. Heat Transfer Conf., 4th, 1970*, Vol. 7, Pap. CT3.6.

111. Fukusako, S., Komoriya, T., and Seki, N. (1986). An experimental study of transition and film boiling heat transfer in liquid-saturated porous bed. *J. Heat Transfer* **108**, 117–124.

112. Tung, V. X., and Dhir, V. K. (1990). Experimental study of boiling heat transfer from a sphere embedded in a liquid-saturated porous medium. *J. Heat Transfer* **112**, 736–743.

113. Baker, P. E. (1973). Effect of pressure and rate on steam zone development in steamflooding. *SPE J.* **13**, 274–284.

114. Coats, K. H. (1976). Simulation of steamflooding with distillation and solution gas. *SPE J.* **16**, 235–247.

115. Coats, K. H. (1980). In-situ combustion model. *SPE J.* **20**, 533–554.

116. Basel, M. D. and Udell, K. S. (1989). Two-dimensional study of steam injection into porous media. In *Multiphase Transport in Porous Media—1989*, ASME HTD-217, pp. 39–46. ASME, New York.

117. Falta, R. W., Pruess, K., Javandel, I., and Witherspoon, P. A. (1992). Numerical modeling of steam injection for the removal of non-aqueous phase liquids from the subsurface; 1. Numerical formulation; 2. Code validation and application. *Water Resour. Res.* **28**, 433–465.

118. Menegus, D. K., and Udell, K. S. (1985). A study of steam injection into water saturated capillary porous media. In *Heat Transfer in Porous Media and Particulate Flows*, HTD-Vol. **46**, pp. 151–157. ASME, New York.

119. Stewart, L. D., Basel, M. D., and Udell, K. S. (1987). The effect of gravity on steam propagation in porous media. In *Heat Transfer in Porous Media and Particulate Flows*, HTD-Vol. **91**, pp. 31–42. ASME, New York.

120. Hanamura, K., and Kaviany, M. (1995). Propagation of condensation front in steam injection into dry porous media. *Int. J. Heat Mass Transfer* **38**, 1377–1386.

121. Basel, M. D., and Udell, K. S. (1991). Effect of heterogeneities on the shape of condensation fronts in porous media. In *Heat Transfer in Geophysical Media*, HTD-Vol. **172**, pp. 63–70. ASME, New York.

122. Chung, M., and Catton, I. (1993). Steam injection into a slow water flow through porous media. *J. Heat Transfer* **115**, 734–743.

123. Falta, R. W. (1990). Multiphase transport of organic chemical contaminants in the subsurface. Ph.D. Thesis, University of California at Berkeley.

124. Udell, K. S., and Fitch, J. S. (1985). Heat and mass transfer in capillary porous media considering evaporation, condensation and non-condensible gas effects. In *Heat Transfer in Porous Media and Particulate Flows*, ASME HTD-Vol. **46**, pp. 103–110. ASME, New York.

125. Yuan, Z. G., and Udell, K. S. (1993). Steam distillation of a single component hydrocarbon liquid in porous media. *Int. J. Heat Mass Transfer* **36**, 887–897.

126. Plumb, O. A. (1991). Heat Transfer during unsaturated flow in porous media. In *Convective Heat and Mass Transfer in Porous Media* (S. Kakac, B. Kikis, F. A. Kulacki, and F. Arinc, eds.), pp. 435–464. Kluwer Academic, Dordrecht, The Netherlands.

127. Plumb, O. A. (1983). Convective heat transfer from surfaces submerged in unsaturated porous media. In *ASME/JSME Thermal Engineering Joint Conference* (Y. Mori and W.-J. Yang, eds.), Vol. 2, pp. 327–332. ASME, New York.

128. Pollock, D. W. (1986). Simulation of fluid flow and energy transport processes associated with high-level radioactive waste disposal in unsaturated alluvium. *Water Resour. Res.* **22**, 765–775.

129. Chen, Y. T., and Boehm, R. F. (1995). An application of unsaturated flow and heat transfer in porous media—underground storage of high level radioactive waste. *Proc. Symp. Therm. Sci. Eng. Honor Chancellor Chang-Lin Tien*, pp. 59–65.

130. Weekman, V. W., Jr., and Myers, J. E. (1965). Heat transfer characteristics of concurrent gas-liquid flow in packed beds. *AIChE J.* **11**, 13–17.

131. Specchia, V., and Baldi, G. (1979). Heat transfer in trickle-bed reactors. *Chem. Eng. Commun.* **3**, 483–499.

132. Crine, M. (1982). Heat transfer phenomena in trickle-bed reactors. *Chem. Eng. Commun.* **19**, 99–114.

133. Krischer, O. (1963). *Die Wissenschaftlichen Groundlagen der Trockungstechnik.* Springer, Berlin.

134. Luikov, A. V. (1966). *Heat and Mass Transfer in Capillary-Porous Bodies.* Pergamon, Oxford.

135. Eckert, E. R. G., and Faghri, M. (1980). A general analysis of moisture migration caused by temperature differences in an unsaturated porous medium. *Int. J. Heat Mass Transfer* **23**, 1613–1623.

136. Plumb, O. A. (1991). Drying complex porous materials—modeling and experiments. In *Convective Heat and Mass Transfer in Porous Media* (S. Kakac, B. Kikis, F. A. Kulacki, and F. Arinc, eds.), pp. 963–984. Kluwer Academic, Dordrecht, The Netherlands.

137. Bories, S. A. (1991). Fundamentals of drying of capillary-porous bodies. In *Convective Heat and Mass Transfer in Porous Media* (S. Kakac, B. Kikis, F. A. Kulacki, and F. Arinc, eds.), pp. 391–434. Kluwer Academic, Dordrecht, The Netherlands.

138. Whitaker, S. (1980). Heat and mass transfer in granular porous media. In *Advances in Drying* (A. S. Mujumdar, ed.), Vol. 1, pp. 23–61. Hemisphere, Washington, DC.

139. Udell, K. S. (1985). An exact solution to high temperature drying of high permeability capillary porous media. *ASME 85-HT-66.* ASME, New York.

140. Rogers, J. A., and Kaviany, M. (1992). Funicular and evaporative-front regimes in convective drying of granular beds. *Int. J. Heat Mass Transfer* **35**, 469–480.

141. Perre, P., and Moyne, C. (1991). Processes related to drying: Part I. Theoretical model; Part II. Use of the same model to solve transfers both in saturated and unsaturated porous media. *Drying Technol.* **9**, 1135–1179.

142. Perre, P., Moser, M., and Martin, M. (1993). Advances in transport phenomena during convective drying with superheated steam and moist air. *Int. J. Heat Mass Transfer* **36**, 2725–2746.

143. Ouelhazi, N., Arnaud, G., and Fohr, J. P. (1992). A two-dimensional study of wood plank drying. The effect of gaseous pressure below boiling point. *Transp. Porous Media* **7**, 39–61.

144. Lee, W. C., Plumb, O. A., and Gong, L. (1992). An experimental study of heat and mass transfer during drying of packed beds. *J. Heat Transfer* **114**, 727–734.

145. Stralen, S. J. D. van (1966). The mechanism of nucleate boiling in pure liquids and in binary mixtures. *Int. J. Heat Mass Transfer* **9**, 995–1046.

146. Peterson, P. F., Hijikata, K., and Tien, C. L. (1990). Variable-conductance behavior in two-phase binary thermosyphons. *J. Thermophy. Heat Transfer* **4**, 325–331.

147. Normington, P. J. C., Mahalingam, M., and Lee, T. Y. (1992). Thermal management control without overshoot using combinations of boiling liquids. *IEEE Trans. Components, Hybrids, Manuf. Technol.* **15**, 806–814.

148. Pruzan, D. A., Torrance, K. E., and Avedisian, C. T. (1990). Two-phase flow and dryout in a screen wick saturated with a fluid mixture. *Int. J. Heat Mass Transfer* **33**, 673–681.

149. National Research Council (1994). *Alternatives for Ground Water Cleanup.* National Academy Press, Washington, DC.

150. Ho. C. K., and Udell, K. S. (1992). An experimental investigation of air venting of volatile liquid hydrocarbon mixtures from homogeneous and heterogeneous porous media. *J. Contam. Hydrol.* **11**, 291–316.

151. Forsyth, P. A., and Shao, B. Y. (1991). Numerical simulation of gas venting for NAPL site remediation. *Adv. Water Resour.* **14**, 354–367.

152. Lingineni, S., and Dhir, V. K. (1992). Modeling of soil venting processes to remediate unsaturated soils. *J. Environ. Eng. (N.Y.)* **118**, 135–152.

153. Kaluarachchi, J. J., and Islam, K. M. M. (1995). Thermal venting to recover less-volatile hydrocarbons from the unsaturated zone; 1. Theory; 2. Model applications. *J. Contam. Hydrol.* **17**, 293–331.

154. Schwille, F. (1988). *Dense Chlorinated Solvents in Porous and Fractured Media: Model Experiments.* Lewis Publishers, Ann Arbor, MI.

155. Pantanzidou, M., and Sitar, N. (1993). Emplacement of nonaqueous liquids in the vadose zone. *Water Resour. Res.* **29**, 705–722.

156. Geel, P. J. Van, and Sykes, J. F. (1994). Laboratory and model simulations of a LNAPL spill in a variably-saturated sand. 1. Laboratory experiment and image analysis techniques. *J. Contam. Hydrol.* **17**, 1–25.

157. Falta, R. W., Javandel, I., Pruess, K., and Witherspoon, P. A. (1989). Density-driven flow of gas in the unsaturated zone due to the evaporation of volatile organic compounds. *Water Resour. Res.* **25**, 2159–2169.

158. Mendoza, C. A., and Frind, E. O. (1990). Advective-dispersive transport of dense organic vapors in the unsaturated zone 2. Sensitivity analysis. *Water Resour. Res.* **26**, 388–398.

159. Wang, C. Y., Cheng, P., and Zhao, T. S. (1996). A novel approach to multiphase flow, heat and mass transfer in porous media. In press.

160. Basel, M. D. (1991). Two-dimensional propagation of steam through partially saturated porous media. Ph.D. Thesis, University of California, Berkeley.

161. Itamura, M. T., and Udell, K. S. (1993). Experimental clean-up of a dense non-aqueous phase liquid in the unsaturated zone of a porous medium using steam injection. In *Multiphase Transport in Porous Media*, ASME HTD-Vol. **265**, pp. 57–62. ASME, New York.

162. Adenekan, A. E., Patzek, T. W., and Pruess, K. (1993). Modeling of multiphase transport of multicomponent organic contaminants and heat in the subsurface: Numerical model formulation. *Water Resour. Res.* **29**, 3727–3740.

163. Forsyth, P. A. (1994). A positivity preserving method for simulation of steam injection for NAPL site remediation. *Adv. Water Resour.* **16**, 351–370.

Enhancement of Heat Transfer
and Fouling Mitigation

EUAN F. C. SOMERSCALES
ARTHUR E. BERGLES

Department of Mechanical Engineering, Rensselaer Polytechnic Institute
Troy, New York

I. Introduction

It is commonplace in discussions relating to the application of heat transfer enhancement techniques that concerns about their performance under fouling conditions are raised. This may have a basis in experience or may derive from imaginary concerns. It so happens that experience and imagination can be poor guides in this area. The wide variety of available heat transfer enhancement techniques means that how one method behaves under fouling conditions is no indicator of how another might behave. The conventional wisdom is that heat transfer enhancement techniques experience a decline in performance when they are exposed to fouling conditions. Furthermore, it is felt that the devices used to enhance heat transfer promote fouling by, for example, trapping foulant on the heat transfer surface. The truth, in fact, is rather different from the perception. While experience has indeed shown that some techniques do behave in this way, it also has demonstrated that the application of certain types of heat transfer enhancement can result in *less* fouling than is experienced with unenhanced heat transfer surfaces under the same general conditions of heat exchange, fluid flow, and fluid composition. In short, enhanced heat transfer devices may also be antifouling devices. This chapter reviews the empirical evidence and theoretical background of the performance of enhanced heat transfer devices that also mitigate fouling. We hope that the discussion here will lead to a wider appreciation of their role under

fouling conditions and promote research into their behavior. Ultimately, it may be possible to design *a priori* devices that both enhance heat transfer and mitigate fouling.

This chapter not only covers the scholarly literature on the fouling of heat transfer enhancement devices, but also considers the patent literature. Many of the enhancement techniques have been patented, and in some instances the inventors have claimed that their devices mitigate fouling as well as improve heat transfer.[1] Patents usually do not include the results of observations of the performance of the invention. Therefore, items in this literature cannot have the same standing as reports in the scholarly literature. Nevertheless, it is appropriate to consider patent claims in this review, because by doing so the scope of future research on the role of heat transfer enhancement devices in the mitigation of fouling is greatly widened.

The space available for this chapter does permit an extended discussion of heat transfer enhancement techniques. The reader is referred, in particular, to the monograph by Webb [71] for the appropriate details. In addition, in the preparation of this chapter extensive use has been made of the reviews by Bergles [4, 5], Webb [70], and Bergles *et al.* [8]. An additional and very important reference is the review of patents on the augmentation of the convective heat and mass transfer by Webb *et al.* [73].

It is appropriate to point out that the authors of this chapter have briefly reviewed the fouling behavior of enhanced heat transfer devices in two recent publications [6, 7]. The viewpoint of these publications was broader than is this chapter and touched not only on fouling mitigation, but also considered those situations where fouling increased.

Following a discussion in Part II and III of fundamental ideas on the fouling performance of heat transfer enhancement devices, those devices that have been identified as mitigating fouling are reviewed. As an aid to clarity, these are classified according to the scheme employed by Bergles [5]. The main headings of this classification are Extended Surfaces, Rough Surfaces, Displaced Enhancement Devices, Swirl Flow Devices, Surface Tension Devices, Treated and Untreated Surfaces, Additives, Mechanical Aids, Vibration, Electric and Electromagnetic Fields, and Injection and Suction. In certain instances two or more enhancement methods are

---

[1] We emphasize that only those patents that specifically claim the invented device both enhances heat transfer and mitigates fouling have been included in this chapter. To have done otherwise would have introduced an undesirable element of speculation. Readers interested in the patent literature on heat transfer enhancement in general, are referred to the references of Webb *et al.* [73] and Bergles *et al.* [8].

applied simultaneously, and these are considered under the heading Compound Enhancement. The chapter closes with a discussion of future prospects and a section that summarizes the chapter and draws appropriate conclusions.

II. Theoretical Ideas

A. INTRODUCTION

From the fouling point of view, Starner [57] and Epstein [17] have pointed out that it is important to distinguish between those techniques of heat transfer enhancement that *intensify* the heat transfer at a plain surface and those that represent an *enlargement* of a plain surface that increases the heat transfer area, usually by means of fins.

Heat transfer enhancement techniques that function by intensifying the heat transfer relative to that at a comparable plain surface are rough surfaces, displaced enhancement devices, surface tension devices, additives, mechanical aids, vibration, electric and electromagnetic fields, injection, and suction. Of the compound enhancement techniques discussed herein, the combination of rough surfaces and additives can be classified as heat transfer intensification.

Extended surfaces appear to be the only method of heat transfer enhancement that makes use of heat transfer area enlargement to achieve its purpose.

This paper considers a number of heat transfer enhancement methods that combine both mechanisms, namely, swirl flow devices, treated surfaces, and structured surfaces. In addition, the compound enhancement method using both swirl flow and additives can be assigned to this class. It is possible, of course, that in these various devices heat transfer intensification or surface enlargement may predominate.

B. HEAT TRANSFER INTENSIFICATION

1. Introduction

It can be anticipated that the surface average temperature on an enhanced heat transfer surface that uses heat transfer intensification will be lower than on a plain surface exposed to the same operating conditions. A mathematical expression that includes this effect can be obtained from an energy balance applied to a control volume at the heat transfer surface.

Thus,

$$\frac{T_{we}}{T_{wp}} = \frac{h_p}{h_e} + \frac{T_b}{T_{wp}}\left(1 - \frac{h_p}{h_e}\right),$$ (1a)

or in terms of the heat flux,

$$\frac{T_{we}}{T_{wp}} = 1 - \frac{q}{T_{wp}}\left(\frac{1}{h_p} - \frac{1}{h_e}\right).$$ (1b)

The reduction in surface temperature can be expected to affect fouling processes that are dependent on this quantity, such as *reactions* that incorporate the fouling precursor into the fouling deposit. A reduction in the rates of these processes would mitigate the effects of fouling.

In addition to heat transfer effects, it is to be expected that the surface average values of the coefficient of mass transfer will increase. This would be anticipated by the analogy between heat and mass transfer, which in this case can be written as that for comparable Schmidt and Prandtl numbers:

$$\frac{k_{m,e}}{k_{m,p}} = \frac{h_e}{h_p}.$$ (2)

The increased mass transfer coefficient should increase the rate at which the fouling precursor is transported to the surface, which would not contribute to the mitigation of fouling.

The shear stress at the enhanced heat transfer surface can be expected to be higher than it would be at the same Reynolds numbers in a plain tube [44]. This should affect the rate at which deposit is removed from the surface, and this might result in a mitigation in the rate of fouling.

Watkinson [66] has attempted to assess the effects on the fouling process, in plain tubes and in tubes with heat transfer intensification on the inner surface, of the differences in the thermal conditions noted previously. Calculations of this type provide an important indication of the extent to which an enhanced heat transfer surface of the intensification type might be expected to lead to the mitigation of fouling. Watkinson considered the following categories of fouling: chemical reaction fouling, precipitation fouling, and particulate fouling. He assumed that the fluid velocities and the heat fluxes were identical in the two types of tubes. The results of his analysis, and their implications as far as fouling mitigation is concerned, will be reviewed briefly.

2. Chemical Reaction Fouling

In the absence of deposit removal (i.e., a strong deposit) the rate of chemical reaction fouling is given by[2]

$$\frac{\dot{m}_f}{\rho_f k_f} = \frac{a_1 C_b}{v^n} \exp\left(-\frac{E}{RT_W}\right).$$

(3)

For the same fluid velocity and heat flux, the rates of formation of the fouling deposit for the plain and enhanced heat transfer surfaces are related by

$$\frac{\dot{m}_{fe}}{\dot{m}_{fp}} = \exp\left[-\frac{E}{R}\left(\frac{1}{T_{wc}} - \frac{1}{T_{wp}}\right)\right].$$

(4)

Watkinson [66] has plotted (Fig. 1) Eq. (4) as a function of the enhancement ratio h_e/h_p (from Eq. (1a)) for different values of the activation energy E that are representative of values of organic fluid fouling. This shows, for example, that an enhancement ratio of 1.5, the rate of formation of the fouling deposit would be reduced by 5% and 40% for $E = 50$ and $E = 150$ kJ/mole, respectively, compared with the comparable plain tube case. Clearly heat transfer intensification has an intrinsic tendency to mitigate the effects of chemical reaction fouling.

The validity of the conclusions resulting from Watkinson's analysis can be seen in Fig. 2, originally presented by Asomaning and Watkinson [2]. This shows quite clearly that an enhanced heat transfer surface delays the initiation of chemical reaction fouling and reduces the average rate at which the fouling thermal resistance increases. There also is satisfactory quantitative agreement between the theoretical and observed rates of fouling (see Table I).

3. Precipitation Fouling

Presumably to simplify the discussion, Watkinson restricts his analysis of the effects of heat transfer intensification on precipitation fouling to asymptotic conditions. He makes use of a result due to Epstein [18], who has shown that where the rate of deposit removal is as described by Kern

---

[2] In Eq. (3), the exponent n apparently [65] can take on values between 0 and 1. For $n = 0$, it is assumed that the fouling process is dominated by the reaction that incorporates the foulant into the fouling deposit. For $n = 1$, the fouling process appears to involve particle transport as well as chemical reactions.
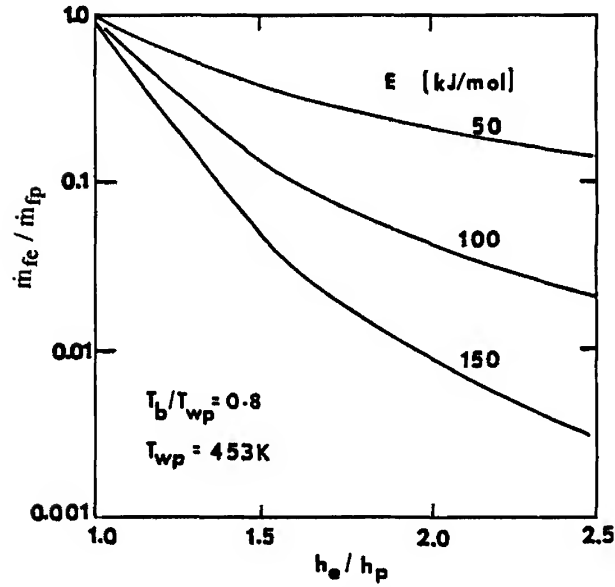
FIG. 1. The rates of formation of the fouling deposit for plain ($\dot{m}_{fp}$) and enhanced ($\dot{m}_{f_e}$) heat transfer surfaces as a function of the enhancement ratio h_e/h_p. The activation energy E values are representative of values for organic fluids. From Wilkinson [66].

and Seaton[3] [26], the asymptotic specific fouling thermal resistance (R_f^*) is given by

$$R_f^* \propto \frac{\psi \dot{m}_g}{\tau_w}.$$ (5)

Therefore,

$$\frac{R_{fe}^*}{R_{fp}^*} = \left(\frac{\psi_e}{\psi_p}\right)\left(\frac{\dot{m}_{ge}}{\dot{m}_{gp}}\right)\left(\frac{\tau_{wp}}{\tau_{we}}\right).$$ (6)

[3] Removal occurs by the deposit breaking at planes of weakness due to the shearing action of the fluid at the deposit-fluid interface. This model was subsequently modified by Taborek et al. [58] by the introduction of the bond resistance factor ψ shown in Eq. (5).
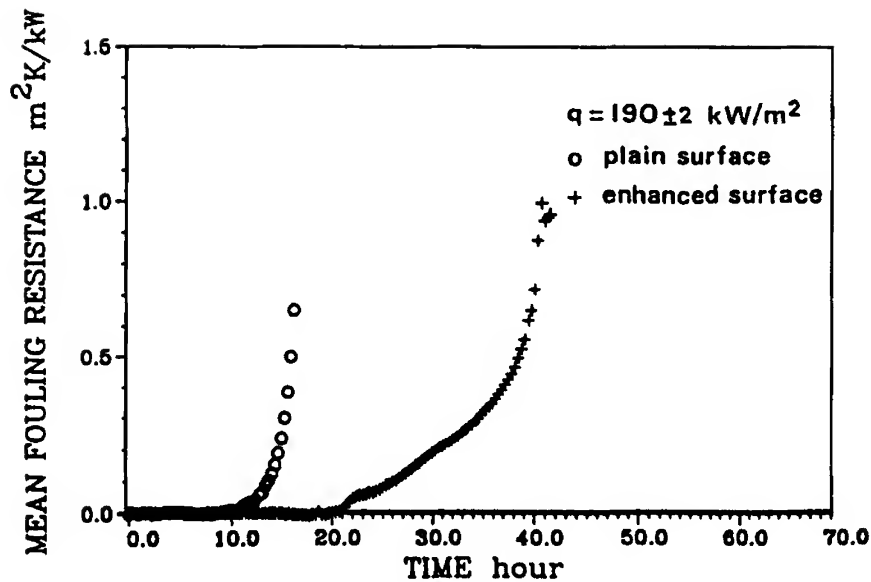
FIG. 2. Measured specific fouling thermal resistance on the inner surface of an electrically heated test section of the Heat Transfer Research Inc. type [29] exposed to kerosene containing 10% by weight of indene under air saturation at $p = 410$ kPa. The test fluid was supplied at constant velocity. Enhancement of the heat transfer was obtained by wrapping the test surface (10.74-mm diameter) with wire of 0.635-mm diameter at a pitch of about 6.4 mm. From Asomaning and Watkinson [2].

TABLE I

COMPARISON OF CHEMICAL REACTION FOULING RATE
ON PLAIN AND ENHANCED HEAT TRANSFER SURFACES

	$(\dot{m}_{fc} - \dot{m}_{fp})/\dot{m}_{fp}$	
	$q = 147$ kW/m^2	$q = 190$ kW/m^2
Predicted[a]	17%	13%
Observed[b]	25%	15%

Based on data in Watkinson [66]

[a] Watkinson [66] with $h_c/h_p = 2.1$, $E = 50$ kJ/mole.
[b] Asomaning and Watkinson [2].

Now Epstein [17] also has shown that the rate of growth $(\dot{m}_g)$ of a precipitation fouling deposit may be represented by[4]

$$\dot{m}_g = \frac{1}{\dfrac{1}{k_m} + \dfrac{1}{k_r(C_i - C_{sat})^{z-1}}}. \tag{7}$$

Equation (7) indicates that the rate of growth of a precipitation fouling deposit is controlled by two processes, namely, the rate of transport of the fouling material to the heat transfer surface and the incorporation reaction. The former is only weakly dependent on temperature, and for the purposes of this analysis, the effect is ignored. Conversely, the rate constant k_r for the surface incorporation reaction is temperature-dependent, and Watkinson assumes that it has an Arrhenius form:

$$k_r = k_{ro} \exp\left(-\frac{E}{RT_W}\right). \tag{8}$$

If for an enhancement ratio (h_e/h_p) greater than unity, there is a corresponding increase in the mass transfer coefficient (k_{me}) compared with that (k_{mp}) on the plain surface (see Eq. (2)), and if heat transfer enhancement leads to a reduction in surface temperature compared with the plain surface case, then Eq. (7) indicates that the ratio $\dot{m}_{ge}/\dot{m}_{gp}$ could be larger or smaller than unity, depending on which fundamental process has a dominating effect.

As an example, using the model of Hasson et al [23], Watkinson showed that for precipitation fouling by calcium carbonate $(CaCO_3)$ the increase in the rate of transport of the fouling precursor, as the enhancement ratio (h_e/h_p) increased, had a much greater effect than the rate of decrease of the wall temperature. This suggests that for precipitation fouling, enhancement of heat transfer by intensification cannot be expected to mitigate the rate of growth of the fouling. According to Watkinson [66], this is confirmed by empirical results due to Watkinson and Martinez [68] for the initial fouling rate $(\dot{m}_r \cong 0$, therefore, $\dot{m}_f \cong m_g)$.

---

[4] The effect of the difference in surface temperature between plain and enhanced heat transfer surfaces on the supersaturation (the term $(C_i - C_{sat})$ in Eq. (7)) is not considered by Watkinson. For inverse solubility salts (e.g., calcium carbonate) this should result in a smaller supersaturation at the enhanced heat transfer surface. If a normal solubility salt (e.g., silica in geothermal brine) is under consideration, the supersaturation should be greater at the enhanced heat transfer surface. This would seem to imply that Watkinson considers these effects to be small compared with the effect of surface temperature on the rate constant k_f, and therefore the analysis applies equally to precipitation fouling by normal and inverse solubility salts.

In Hasson's model for $CaCO_3$, fouling $\dot{m}_g$ depends directly on, among other things, the mass transfer coefficient k_m. Hence, if the strength factors ψ_e and ψ_p are about the same for enhanced and plain cases, we can write Eq. (6) as

$$\frac{R_{fe}^*}{R_{fp}^*} \propto \frac{h_e/h_p}{\tau_{we}/\tau_{wp}}.$$ (9)

The quantity on the right-hand side of this expression is related to the energy efficiency factor ε, a criterion of the thermal and hydraulic performance of enhanced heat transfer surfaces introduced by Rabas [44]. This quantity is defined as

$$\varepsilon = \frac{h_e/h_p}{f_e/f_p},$$ (10)

and therefore

$$\frac{R_{fe}^*}{R_{fp}^*} \propto \varepsilon.$$ (11)

An examination of the analysis of enhanced heat transfer surfaces carried out by Rabas [44] shows that generally ε is less than unity, although on occasion Rabas reported values greater than unity and in one case up to $\varepsilon = 1.36$. Accordingly, we would anticipate that $R_{fe}^* < R_{fp}^*$ for most types of heat transfer enhancement. This suggests that even if the rate of growth of precipitation fouling is not mitigated on an enhanced heat transfer surface, the removal processes are correspondingly enhanced such that the asymptotic fouling resistance is mitigated.

The available experimental data do not support this conclusion. The results of fouling tests due to Watkinson et al [69] and Watkinson and Martinez [68] with tubes enhanced on their inner surface are ambiguous; both the fluid velocity and the form of the heat transfer enhancement appear to have a role. For inner finned tubes (see the section entitled Extended Surfaces) subject to fouling by $CaCO_3$, according to Watkinson et al. [69], $R_{fe}^*/R_{fp}^* \geq 1$ for mean fluid velocities between about 0.75 m/sec and 2.0 m/sec. This is not in agreement with the preceding analysis. For spirally indented tubes (see the section entitled Rough Surfaces) exposed to fouling by $CaCO_3$, Watkinson et al. [68, 69] found that $R_{fe}^*/R_{fp}^* \leq 1$, if the mean fluid velocity exceeded about 1 m/sec. This observed mitigation of fouling is in agreement with the previous analysis. For mean fluid velocities below about 1 m/sec Watkinson et al. [69] found that $R_{fe}^*/R_{fp}^* > 1$, indicating that fouling was not mitigated by an enhanced heat transfer surface. Watkinson et al. [69] speculated that the fouling

mitigation observed with spirally indented tubes was due to the secondary fluid motion swirling induced by the form of heat transfer enhancement.

4. *Particulate Fouling*

Once again, apparently for simplicity, Watkinson only analyzes the case of asymptotic fouling using Eq. (5). He assumes that the rate of growth $\dot{m}_g$ is given by

$$\dot{m}_g = k_m S C_b. \tag{12}$$

In Eq. (12) it is assumed that the rate of deposit growth is controlled both by the mass transfer of particles (mass transfer coefficient k_m to the surfaces) and by the process that incorporates the particles into the deposit (sticking probability, S). The agglomerated particles attached to the surface are assumed to be, or are, in fact, different from the particles dispersed in the fluid. For this reason the rate of formation is taken as proportional to the bulk concentration C_b of the particles in the fluid.

According to Watkinson,

$$S = \frac{S_o}{\tau_w} \exp\left(-\frac{E_a}{RT_W}\right), \tag{13}$$

where E_a is the activation energy of the particle adhesion process.

For the same fluid velocity and heat flux, from Eqs. (1), (12), and (13) we have

$$\frac{\dot{m}_{ge}}{\dot{m}_{gp}} = \frac{k_{me}}{k_{mp}} \frac{\tau_{wp}}{\tau_{we}} \exp\left[-\frac{E_a}{R}\left(\frac{1}{T_{we}} - \frac{1}{T_{wp}}\right)\right]. \tag{14}$$

Assuming that the heat and mass transfer analogy applies,[5]

$$\frac{k_{me}/k_{mp}}{\tau_{we}/\tau_{wp}} = \frac{h_e/h_p}{\tau_{we}/\tau_{wp}} = \varepsilon. \tag{15}$$

Combining Eqs. (14) and (15), we have

$$\frac{\dot{m}_{ge}}{\dot{m}_{gp}} = \varepsilon \exp\left[-\frac{E_a}{R}\left(\frac{1}{T_{we}} - \frac{1}{T_{wp}}\right)\right]. \tag{16}$$

---

[5] A dubious assumption, as Watkinson points out, because the Schmidt number for particle mass transfer is many orders of magnitude larger than is the Prandtl number associated with the heat transfer process.

Using once more Epstein's [18] asymptotic fouling condition—Eq. (7)—we have

$$\frac{R_{fe}^*}{R_{fp}^*} = \frac{\varepsilon}{f_e/f_p} \exp\left[-\frac{E_a}{R}\left(\frac{1}{T_{we}} - \frac{1}{T_{wp}}\right)\right],$$ (17)

where the friction factor f has replaced the wall shear stress τ_w, and it has been assumed that the deposit strength factors ψ_e and ψ_p are about the same.

For small values of the activation energy E_a,

$$\frac{R_{fe}^*}{R_{fp}^*} = \frac{\varepsilon}{f_e/f_p}.$$ (18)

Since the probability that $f_e/f_p > 1$ and the energy efficiency factor ε is usually less than unity (see the discussion of Eq. (11) above), then

$$\frac{R_{fe}^*}{R_{fp}^*} < 1.$$ (19)

This result suggests that heat enhancement by intensification tends to mitigate particulate fouling.

The preceding conclusion is based on the implicit assumption that the sticking probability S is substantially less than unity. A surface for which the sticking probability is close to unity must also be considered.

From Eq. (12), with $S = 1$, we have

$$\frac{\dot{m}_{ge}}{\dot{m}_{gp}} = \frac{k_{me}}{k_{mp}}.$$ (20)

Again assuming that the heat and mass transfer analogy applies,

$$\frac{\dot{m}_{ge}}{\dot{m}_{gp}} = \frac{h_e}{h_p},$$ (21)

or in terms of the asymptotic fouling thermal resistance, with $\psi_e = \psi_p$,

$$\frac{R_{fe}^*}{R_{fp}^*} = \frac{h_e/h_p}{f_e/f_p} = \varepsilon.$$ (22)

Because typically $\varepsilon < 1$, then $R_{fe}^* < R_{fp}^*$; that is, even with an enhanced heat transfer surface to which most of the particles tend to stick, there is an intrinsic mitigating effect.

Data on the particulate fouling of enhanced heat transfer surfaces obtained by Somerscales et al. [55] indicated that, at sufficiently high fluid velocities, heat transfer surfaces enhanced by intensification mitigated the

effects of fouling. For certain surfaces, in which the enhancement was obtained by roughness of the surface together with a possible swirling motion of the fluid, Somerscales *et al.* [55] found that heat transfer enhancement mitigated fouling at all the fluid velocities used in their experiments.

5. Summary

Table II summarizes the results of the analysis by Watkinson [66] and other observations of the fouling performance of tubes with heat transfer surfaces enhanced by intensification and tubes with plain surfaces. As Watkinson emphasizes, this demonstrates the necessity of collecting data on the performance of both clean and fouled tubes if assessments of the type he has described are to be made.

TABLE II

RELATIVE FOULING PERFORMANCE OF PLAIN TUBES AND TUBES WITH IN-TUBE HEAT
TRANSFER ENHANCEMENT BY INTENSIFICATION

Category	According to Analysis [66]	Observation
Chemical reaction	Enhancement tends to mitigate fouling due to reduction in wall temperature	Enhancement mitigates the fouling effect [2]
Precipitation by inverse solubility salts	Enhancement does not mitigate the growth rate $(\dot{m}_g)$ of the fouling deposit	Enhancement does not mitigate the initial fouling rate (when $\dot{m}_f \cong \dot{m}_g$) [68]
	Enhancement mitigates asumptotic fouling	Enhancement may or may not mitigate asymptotic fouling; the mean fluid velocity and the form of heat transfer enhancement can affect fouling mitigation [68, 69]
Particulate	Enhancement tends to mitigate asymptotic fouling	Enhancement mitigates fouling at sufficiently high fluid velocities. In the presence of a strong swirling fluid motion enhancement mitigates fouling at all fluid velocities [55]

C. Heat Transfer Area Enlargement

1. *Introduction*

To investigate the effect of an enlarged heat transfer area on fouling mitigation, it is appropriate to compare the rate of heat transfer from a fouled surface Q_f with the rate from the same surface when it is clean, (Q_c):

$$Q_c = h[A - A_{\text{fin}}(1 - \eta_c)](T_w - T_b), \tag{23}$$

$$Q_f = \frac{[A - A_{\text{fin}}(1 - \eta_f)]}{(1/h) + R_f}(T_w - T_b). \tag{24}$$

The ratio of these two quantities for an enhanced heat transfer surface can be written as

$$\left.\frac{Q_c}{Q_f}\right)_e = \frac{(1 + H)[1 - (A_{\text{fin}}/A)(1 - \eta_c)]}{1 - (A_{\text{fin}}/A)(1 - \eta_f)}, \tag{25}$$

where H is the fouling Biot number given by

$$H = hR_f, \tag{26}$$

which is a measure of the *fouling level* on a heat transfer surface.

If an enlarged heat transfer surface mitigates the effects of fouling, it is expected that the ratio Q_c/Q_f would be less for an enlarged surface than for a plain surface carrying the same thickness of fouling deposit.

For the plain surface, with $A_{\text{fin}}/A = 0$, Eq. (25) becomes

$$\left.\frac{Q_c}{Q_f}\right)_p = 1 + H. \tag{27}$$

Therefore the enlarged heat transfer surface mitigates fouling if

$$\left.\frac{Q_c}{Q_f}\right)_e < \left.\frac{Q_c}{Q_f}\right)_p. \tag{28}$$

Equation (25) shows that the computation of the ratio $Q_i/Q_f)_e$ requires the determination of the efficiency η_f of the fouled fin.

2. *Two Models*

Epstein and Sandhu [19] have proposed two models for one-dimensional (1D) heat transfer to evaluate the efficiency η_f of a fouled fin. In the series model, the deposit is treated as a thermal resistance in series with the

convective resistance in the fluid in contact with the fin. In the parallel model, it is assumed that the fouling deposit acts as a thermal resistance in parallel to the resistance of the fin material. In both models, the fouling deposit on the prime (unfinned) surface is assumed to act as a thermal resistance in series with both the material below the prime surface and the convective resistance of the fluid. These models are in conflict, and therefore it is necessary to decide which is the most appropriate to use in a given situation. This requires a two-dimensional (2D) numerical analysis of heat transfer in the fin. Middis and Müller-Steinhagen [37] have carried out the necessary calculations in a situation typical of that encountered in practice. They found that the 1D series heat transfer model agreed more closely with the 2D model for their chosen heat transfer conditions. In these circumstances it is appropriate to concentrate attention on the series model.

3. Series Model

The analysis is applied to fins of uniform cross-sectional area parallel to the base at all distances from the base. That is, straight fins and pin fins. It is further assumed that the following conditions apply:

1. Steady heat flow
2. Homogeneous isotropic fin material with uniform conductivity
3. No heat sources in the fin
4. Uniform fin base temperature
5. Uniform fluid temperature surrounding the fin
6. Local heat transfer from the fin surface proportional to the local temperature difference between the fin surface temperature and the temperature of the surrounding fluid
7. Uniform coefficient of heat transfer over the entire fin surface
8. One-dimensional temperature distribution in the fin with the temperature gradient normal to the base
9. Negligible bond resistance between the fin and the base surface
10. Negligible heat transfer through the fin tip
11. Heat transfer coefficient on the prime surface (surface to which the fin is attached) uniform and the same as on the fin
12. Prime surface temperature uniform and the same as on the base of the fin.

Two additional assumptions are required for the fouling deposit:

13. Homogeneous and isotropic fouling deposit with a uniform thickness δ_f and thermal conductivity k_f over the entire heat transfer surface

14. Deposit sufficiently thin so that there is negligible change in fin perimeter, and in the solid-fluid interfacial area on both the fin and prime surface.

With these assumptions, the fin efficiency η_c of the clean fin is

$$\eta_c = \frac{\tanh(mL)}{mL}, \tag{29}$$

where L and m are the fin length and parameter, respectively, given by

$$m = \sqrt{\frac{hP}{kA'}}. \tag{30}$$

For the fouled fin

$$\eta_{fs} = \frac{\tanh(m_{fs}L)}{m_{fs}L}, \tag{31}$$

where the subscript s indicates the series model of Epstein and Sandhu. The effective fin parameter m_{fs} of the fouled fin, when using the series model, is given by

$$m_{fs} = \frac{m}{\sqrt{1 + H}}. \tag{32}$$

From Eq. (32) it is clear that the parameter m_{fs} is always less than m, from which it follows that the efficiency of the dirty fin η_{fs} is greater than that of the clean fin, η. This can be explained physically as a consequence of the fouling improving the temperature uniformity in the fin. Despite this, however, the fouling does reduce the heat transfer through the fin.

Combining the fin efficiencies given in Eqs. (29) and (31) with Eq. (25), Epstein and Sandhu obtained an expression for the heat transfer ratio Q_c/Q_f. This is plotted in Fig. 3, with the fouling Biot number[6] $H = 4$, as a function of the dimensionless fin length mL, and with the area ratio A_{fin}/A as a parameter. Figure 3 also shows the heat transfer ratio $(Q_c/Q_f)_p$ for a plain surface, when $A_{fin}/A = 0$. In Fig. 3, the curve associated with the upper limit of $A_{fin}/A = 1$ corresponds to the heat transfer ratio for the fin alone.

It is clear from Fig. 3, under the conditions of the model, that $Q_c/Q_{fs})_e < Q_c/Q_f)_p$ for all values of the parameter mL and A_{fin}/A. Therefore, for a case in which enhancement of the heat transfer is due to an enlargement of the surface, it is expected that the effects of fouling will

---

[6] Middis and Müller-Steinhagen [32] in their investigation of 2D heat transfer in a fouled fin also used $H = 4$, with $h = 2000$ W/(m^2 K), $\delta_f = 1.0$ mm, and $k_f = 0.5$ W/(m K). The value of k_f could, for example, represent fouling by a hard water salt.
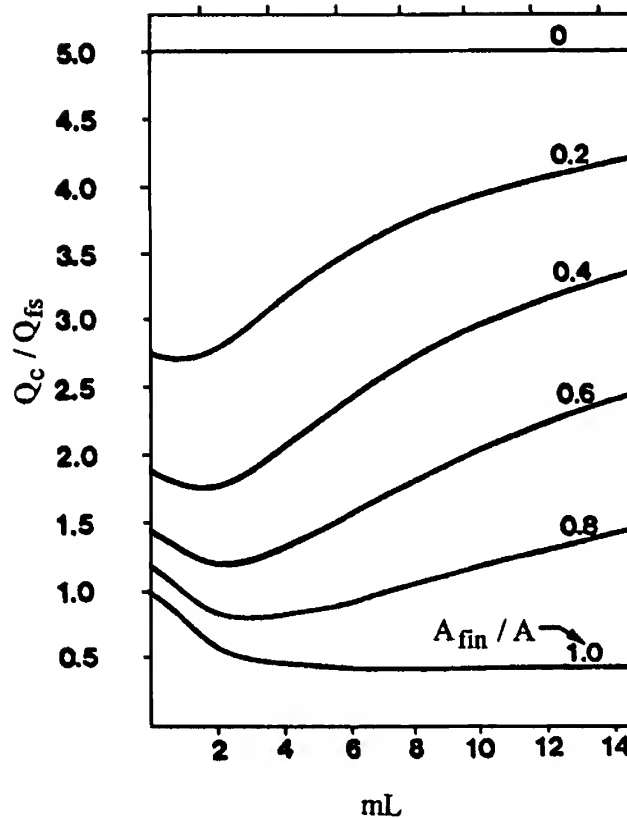
FIG. 3. The heat transfer ratio Q_c/Q_f on a finned heat transfer surface subject to fouling, with $H = 4$. From Epstein and Sandhu [19].

be mitigated. Alternatively, heat transfer is reduced by fouling on both the plain and enhanced surfaces; however, the reduction is greater in the case of the plain surface.

This conclusion about the mitigating effect on fouling of the enlarged surface is subject to three important caveats:

1. The deposit thicknesses on both the plain and enhanced surfaces are unlikely to be the same.
2. The thickness of the deposits in either case would probably not be uniform.[7]

[7] Note that Dreyster et al. [16] reported tests in which a uniform deposit thickness was observed on a rough surface (these tests are discussed further in the next section).

3. The comparison between the plain and enhanced heat transfer surfaces is made with the same thickness δ_f of fouling deposit on both the plain and enhanced surfaces. In practice, it is likely that the enhanced heat transfer surface will experience a heavier deposit than will the plain surface exposed to the same conditions.

Despite these cautions, the results of the analysis are suggestive and should encourage investigation of the fouling performance of heat transfer surfaces enhanced by surface enlargement.

Figure 3 shows that for values of A_{fin}/A lying between zero and unity, the heat transfer ratio passes through a minimum. At this point there is an optimum value of the dimensionless fin length (mL) for which the heat transfer ratio is affected least by the presence of the fouling deposit. That is, the mitigating effect of the enhanced heat transfer surface is a maximum.

The heat transfer ratio Q_c/Q_{fs} increases monotonically from unity at $H = 0$ (clean surface) to $(1 + H)\eta_f$ at high values of the fouling Biot number H. This indicates that the enlarged heat transfer surface mitigates fouling for all values of H.

Further discussion of the effects of fouling on the performance of enlarged heat transfer surfaces can be found in Epstein and Sandhu [19] and Middis and Müller-Steinhagen [37].

III. Assessment of Empirical Data

A. Electrically Heated Test Surfaces

Electrically heated test surfaces are used extensively in laboratory investigations of fouling and in field situations where a sensible heat exchanger is impractical. To determine the mitigating effects of fouling of an enhanced heat transfer surface, direct comparison of the measured specific fouling thermal resistance R_f is feasible. Knudsen [29] has reviewed devices of this type and details of the required calculations are provided.

B. Sensible Heat Exchangers

Owing to their intrinsic simplicity, electrically heated test surfaces are very attractive for fouling tests. However, practical heat transfer equipment is overwhelmingly of the type in which sensible heat is exchanged between two flowing streams. Heat exchangers of this type also are used as

fouling test sections. Observations on their performance usually are quite difficult to interpret; however, Watkinson [64] has demonstrated a method that allows the consistent evaluation of such data. The method applies to the case of a double-pipe heat exchanger, a common arrangement of the equipment used to obtain fouling data both in the field and laboratory. To formulate his criterion, Watkinson has examined the ratio Γ of the cleanliness factors in the heat exchanger using enhanced tubes (C_e) and plain tubes (C_p). Thus for the heat exchanger with an enhanced tube, the cleanliness factor is

$$C_e = \frac{U_{e,f}}{U_{e,c}}. \tag{33}$$

If the overall coefficients of heat transfer are based on the outer surface area A_o of the plain tube, then

$$\frac{1}{U_{e,c}} = \frac{A_o}{h_{e,o}A_{e,o}} + R_w + \frac{A_o}{h_{e,i}A_{e,i}}. \tag{34}$$

If the heat transfer coefficients $h_{e,o}, h_{e,i}$ are identical under clean and fouled conditions, that is $h_{e,o})_c = h_{e,o})_f$ and $h_{e,i})_c = h_{e,i})_f$, then[8]

$$\frac{1}{U_{e,f}} = \frac{1}{U_{e,c}} + R_{fe,o}\frac{A_o}{A_{e,o}} + R_{fe,i}\frac{A_o}{A_{e,u}}, \tag{35}$$

where $A_{e,i}$ and $A_{e,o}$ are the effective heat transfer areas for the inner and outer surfaces of the enhanced heat transfer tube, respectively. The exact forms of the mathematical expressions for these areas depend on the type of heat transfer enhancement.[9]

Substituting Eqs. (34) and (35) into Eq. (33), we have

$$C_e = \frac{1}{1 + U_{e,c}A_o[(R_{fe,o}/A_{e,o}) + (R_{fe,i}/A_{e,i})]}. \tag{36}$$

Similarly for the plain tube case, the cleanliness factor is

$$C_p = \frac{U_{p,f}}{U_{p,c}} + \frac{1}{1 + U_{p,c}A_o[(R_{fp,o}/A_o) + (R_{fp,i}/A_i)]}, \tag{37}$$

---

[8] Presumably, this implies that comparison between the performance of a heat exchanger under clean conditions and under fouled conditions should be made at the same fluid velocity in the tube. This, however, takes no account of the effects of the different roughnesses on the clean heat transfer surface and at the deposit–fluid interface.

where A_i and A_o are the heat transfer areas for the inner and outer surfaces of the plain tube, respectively. The ratio Γ of C_e and C_p is

$$\Gamma = \frac{C_e}{C_p} = \frac{1 + U_{p,c}A_o\left[(R_{fp,o}/A_o) + (R_{fp,i}/A_i)\right]}{1 + U_{e,c}A_o\left[(R_{fe,o}/A_{e,o}) + (R_{fe,i}/A_{e,i})\right]}. \qquad (38)$$

Special forms of this expression can be deduced for the different types of heat transfer enhancement. These will be discussed in the appropriate sections below. In all cases, if the value of Γ determined for a particular situation is at least equal to unity ($\Gamma \geq 1$), then the enhanced heat transfer surface has a better performance under fouling conditions than does the corresponding plain surface.

Because Eq. (38) is somewhat clumsy to use, Watkinson has shown that the equivalent criteria given in Table III can be employed.

It is important to note that in order to use the criteria represented by Eq. (38), or listed in Table III, it is necessary to have heat transfer data on both plain and enhanced surfaces. This means that tests of the fouling performance of enhanced heat transfer surfaces must be planned accordingly.

TABLE III

Simplified Criteria for the Fouling Performance of Enhanced (by Rough or Extended Surfaces) Heat Transfer Surfaces in a Double-Pipe Heat Exchanger [64]

Case		Fouling	Criterion for Fouling Mitigation
Inner	Outer		
Enhanced	Plain	Inner	$\left.\dfrac{R_{fe}}{R_{fp}}\right)_i \leq \left.\dfrac{A_e}{A_p}\right)_i \left.\dfrac{U_p}{U_e}\right)_c$
Plain	Enhanced	Outer	$\left.\dfrac{R_{fe}}{R_{fp}}\right)_o \leq \left.\dfrac{A_e}{A_p}\right)_o \left.\dfrac{U_p}{Ue}\right)_c$
Enhanced	Enhanced	Inner	$\left.\dfrac{R_{fe}}{R_{fp}}\right)_i \leq \left.\dfrac{A_e}{A_p}\right)_i \left.\dfrac{U_p}{Ue}\right)_c$

Based on the discussion of Watkinson [64].

Note. $A_{p,o} = A_o$, $A_{p,i} = A_i$.

IV. Extended Surfaces

A. INTRODUCTION

Increased rates of heat transfer can be attained by fins, which provide additional heat transfer area. The fins can be specially shaped or interrupted so that the heat transfer coefficient at the surface can be increased.

B. TEST DATA

Watkinson [64] used his criterion (discussed in the previous section) to analyze[9] a number of sets of experimental data on the fouling of heat transfer tubes with external fins and also with internal fins, when those two different types of tubes were installed in shell-and-tube or double-pipe heat exchangers. The results of the analysis are summarized in Table IV. With one exception,[10] the results of the tests are seen to conform to Watkinson's criteria ($\Gamma > 1$). Therefore, tubes with fin enhancement on either their inner or outer surfaces tend to mitigate the effects of fouling. This confirms the results of the earlier discussion.

The tests by Somerscales et al. [55] using an electrically heated test section studied the effects of particulate fouling on tubes with inside fins. These are not amenable to analysis by Watkinson's method, which only

---

[9] In Eqs. (34), (35), (36), and (38) the effective heat transfer areas are given by $A_e = A_{pr} + \eta A_{fin}$. The effective heat transfer area A_e is sometimes [25] written as $\eta'A$, where $A = A_{pr} + A_{fin}$ and η' is the area weighted fin efficiency.

[10] The exception was the data of Miller [38] in which the quantity Γ was found to be less than unity. Watkinson speculated that this may have been due to undetected fouling on the tube-side by oil leaking from the shell into the tubes.

TABLE IV

FOULING PERFORMANCE OF ENHANCED HEAT TRANSFER TUBES USING EITHER INTERNAL OR EXTERNAL FINS

Reference	Enhancement type	Foulant	$\Gamma = \dfrac{C_e}{C_p}$	Fouling Mitigation
Watkinson et al. [79]	Inner longitudinal fin	Calcium carbonate	> 1	Yes
Sheikholeslami and Watkinson [53]	Outer longitudinal fin	Artificial hard water	> 1	Yes
Katz et al. [24]	Outer radial fin	Fuel oil	> 1	Yes
Miller [38]	Outer radial fin	Asphaltic residuum	< 1	No

applies to heat exchange between two fluid streams. The results of the tests are shown in Figs. 4(a) to 4(c) and 4(e), together with the results from a plain surface exposed to the same conditions. Tests were carried out at two levels of velocity, and at the higher velocity (1.42 to 1.8 m/sec) all four types of surfaces had negligible fouling thermal resistances. At the lower fluid velocities (0.90 to 1.01 m/sec) only one of the finned surfaces had a lower fouling thermal resistance than did the plain tube for the full duration of exposure (15 h). The other two surfaces initially had higher fouling thermal resistances; however, after about 7 h of exposure their fouling resistances became less than that of the plain surface, which in fact had a fouling resistance that increased significantly in the latter part of the test. The results of the tests are inconclusive, but suggest that perhaps for certain geometries finned surfaces exposed to particulate fouling may mitigate the effects of fouling.

C. CONCLUDING REMARKS

Although theoretical analysis, admittedly under the unrealistic conditions of a uniform fouling deposit, suggests that enhanced heat transfer surfaces employing fins have the intrinsic property of mitigating fouling, the experimental data are not so clear. From these data it appears that finned surfaces mitigate fouling for precipitation or chemical reaction fouling conditions. On finned surfaces, particulate fouling may also be mitigated with certain fin geometries.

V. Rough Surfaces

A. INTRODUCTION

Rough surfaces can range from random and grain-type roughness to discrete structures. In the latter case machining and forging operations can be used to obtain protrusions or depressions in the surface. Protuberances also can be produced by inserts in a tube, such as wire coils that are maintained by their elasticity in close contact with the inner surface of the tube.

Enhancement by rough surfaces is intended to promote fluid turbulence rather than increase the heat transfer area by, for example, the fin effect (see the previous section entitled Extended Surfaces). They are used primarily in single-phase flow.
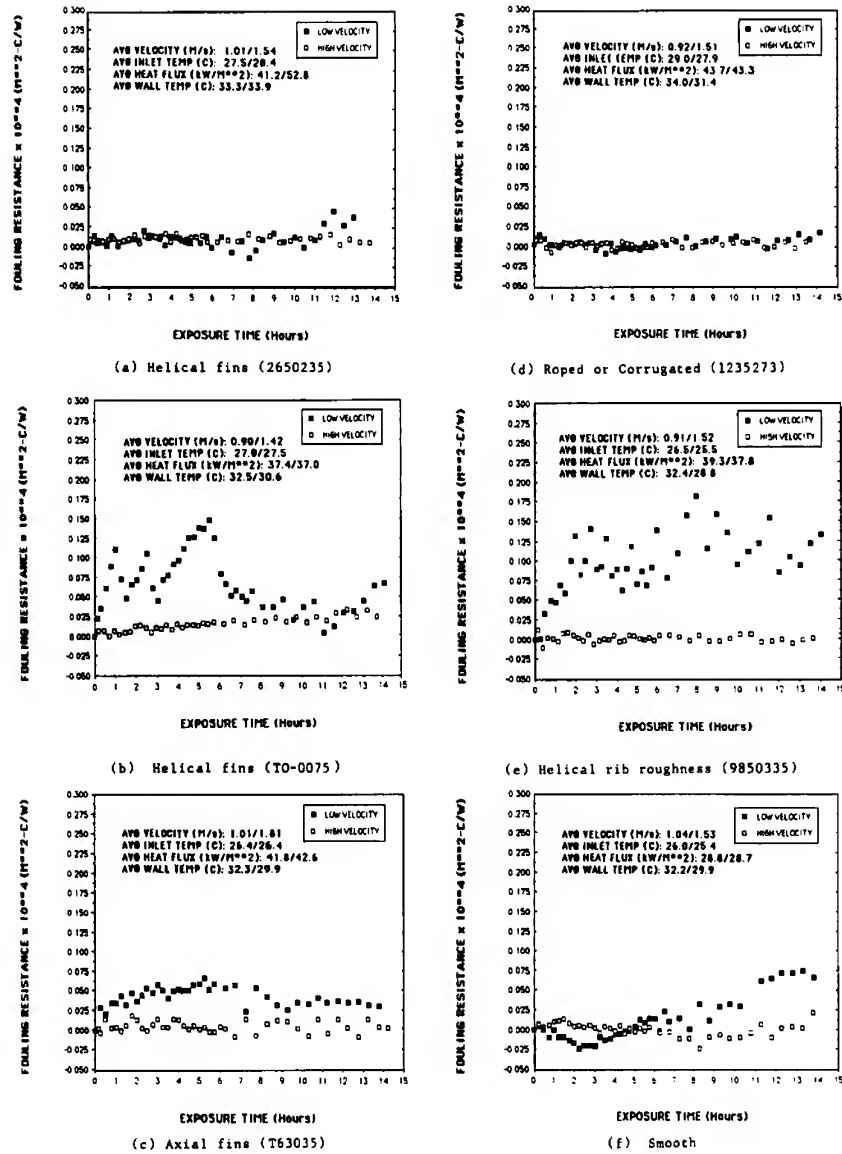
FIG. 4. Tube average specific fouling thermal resistance as a function of time of exposure for a plain tube and for various tubes with internal heat transfer enhancements when exposed to particulate fouling. From Somerscales *et al.* [55].

B. Patent Literature

Withers *et al.* [76], Withers [75], and Sartor [49] have described an enhanced heat transfer tube of a type that is variously called "roped," corrugated, or spirally indented (Fig. 5b). In his patent, Withers [75] claimed that roped-type tubes have a much lower fouling thermal resistance (43% less) than do plain tubes operating under comparable conditions. The particular category of fouling that this statement referred to was not described. Tubes of this type are sold by the Wolverine Co. (Decateur, AL) under the trademark Korodense®.

Tests under fouling conditions on the Wolverine Korodense® tube, both in the field and in the laboratory, have been reported by a number of investigators. These are discussed in more detail subsequently.
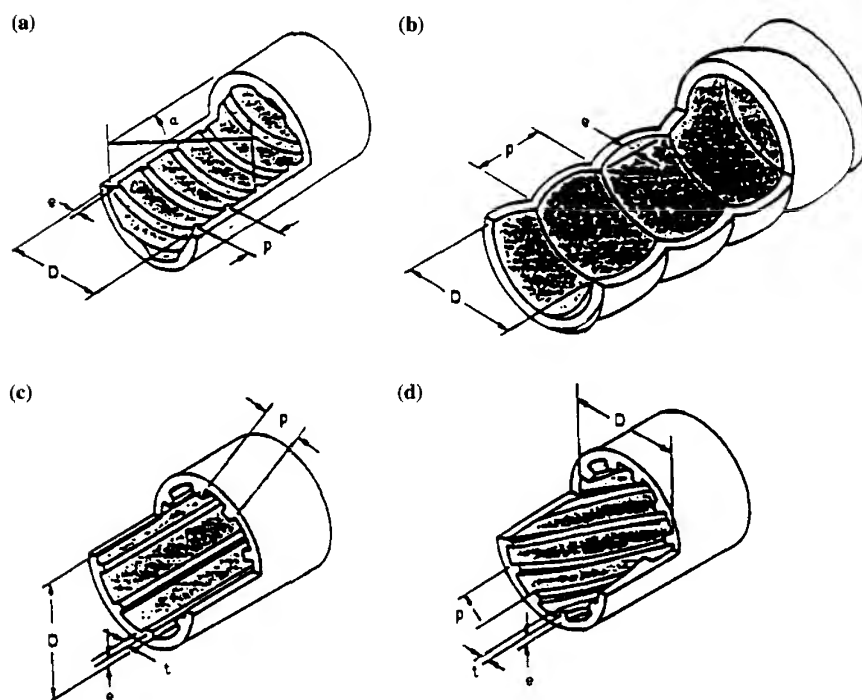
Fig. 5. Four types of in-tube heat transfer enhancements used in tests reported in the literature (see Tables 5(a) and 5(b)). (a) Helical rib roughness. (b) Corrugated or roped. (c) Axial fins. (d) Helical fins.

C. METHODOLOGY FOR ANALYZING TEST DATA

The Watkinson [64] criteria for evaluating empirical data on the fouling performance of heat transfer surfaces enhanced by surface roughness (using rough or extended surfaces) have been given previously (in particular, see Table 3). Application of these criteria is straightforward and will be illustrated below. It should be noted, however, that enhancement involving one particular type of surface roughness generates somewhat different criteria from those given previously. This involves situations in which the inner and outer heat transfer areas in a tube with enhanced heat transfer are almost the same. A particular example is the roped tube (Fig. 5b). In this case Eq. (38) becomes

$$\Gamma = \frac{1 + U_{p,c} A_o \left[(R_{fp,o}/A_o) + (R_{fp,i}/A_i) \right]}{1 + U_{e,c} A_o \left[(R_{fe,o}/A_o) + (R_{fe,i}/A_i) \right]} \tag{39}$$

with $A_{e,i} = A_i$ and $A_{e,o} = A_o$.

If fouling is restricted to the inner surface of the enhanced and plain tubes, then $R_{fp,o} = 0 = R_{fe,o}$. Further if fouling is mitigated by the enhanced surface, that is $\Gamma \geq 1$, then from Eq. (39)

$$\left. \frac{R_{fe}}{R_{fp}} \right)_i \leq \left. \frac{U_p}{U_e} \right)_c . \tag{40}$$

Further, if the fouling thermal resistances observed on the inner surfaces of the enhanced and plain tubes are about the same ($R_{f,pi} = R_{fe,i}$), then from Eq. (40) we have $U_p/U_e)_c \geq 1$, which is impossible. Because the result is a consequence of employing $\Gamma \geq 1$ as the criterion for fouling mitigation when an enhanced surface is used, then in this particular case the criterion must be $\Gamma < 1$.

D. RESULTS OF LABORATORY TESTS

The various laboratory tests that have been conducted on the fouling performance of rough surfaces are summarized in Table Va. The data of those tests that used a double-pipe heat exchanger have been analyzed according to the criterion proposed by Watkinson, and the results are shown in the findings column. Tubes of the roped type exposed to precipitation fouling appear to have a mitigating effect on fouling. However, rib-type roughness does not mitigate fouling, at least under the test conditions. It is noteworthy that in the tests on the latter type of enhancement, the performance under both particulate and precipitation fouling conditions were considered. Therefore, for these categories of foulant,

TABLE V(a)

FOULING OF TUBE-SIDE ENHANCED HEAT TRANSFER SURFACES. LABORATORY TESTS

Reference	Duration (h)	Tube Type	Foulant	Findings
Watkinson et al. [69]	8–12	Interior finned (Figs. 5(c) and 5(d)) Roped–corrugated (Fig. 5(b))	CaCO$_3$ solution	Coefficient of heat transfer higher than plain surface for both clean and fouled conditions *Interior finned* R_f of enhanced surface lower than plain surface. $\Gamma > 1$: fouling mitigated.[a] *Roped–corrugated:* R_f of enhanced surface lower than plain surface. $\Gamma < 1$: fouled mitigated[a]
Watkinson and Martinez [68]	5	Roped–corrugated (Fig. 5(b))	CaCO$_3$ solution	Enhanced tubes have lower R_f than plain tubes. $\Gamma < 1$: fouling mitigated.[a]
Dreyster et al. [16]	8	Rib roughness (Fig. 5(a)) with $\alpha = 90$ degrees)	Artificially hardened tap water	Heat transfer coefficient on the enhanced tube is higher than that of plain tube under fouled conditions. $\Gamma < 1$: fouling not mitigated.[b]
Webb and Kim [72]	12–17	Rib roughness (Fig. 5(a)) with $\alpha = 90$ degrees and interior finned (Figs. 5(c), 5(d))	Water and suspended Fe$_2$O$_3$ (0.64 μm) or Al$_2$O$_3$ (3 μm) particles	Fouling thermal resistance of enhanced tubes higher than plain tubes; however, at higher fluid velocities, values are almost identical. $\Gamma < 1$: fouling not mitigated.[b,c]
Somerscales et al. [55]	15	Helical rib roughness (Fig. 5(a)) Corrugated–roped (Fig. 5(b)) Axial internal fins (Fig. 5(c)) Helical internal fins (Fig. 5(d))	Water with suspended Al$_2$O$_3$ (0.3 μm) particles	Corrugated–roped and helical internal finned tubes showed no fouling effects. All surfaces showed no fouling effects at higher fluid velocity (1.5 m/sec).

[a] For cases where $A_{e,i} = A_i$, $A_{e,o} = A_o$, $R_{fp,i} = R_{fc,i}$.

[b] For cases where $A_{e,i} \neq A_i$, $A_{e,o} = A_o$, $R_{fp,i} \neq R_{fc,i}$.

[c] Low fluid velocity cases only. At higher fluid velocities the specific fouling thermal resistance on both plain and enhanced surfaces was very small ($R_f < 2.0 \times 10^{-5}$ m^2 K/W).

CaCO$_3$, calcium carbonate; Fe$_2$O$_3$, ferric oxide; Al$_2$O$_3$, aluminum oxide or alumina.

TABLE V(b)

FOULING OF TUBE-SIDE ENHANCED HEAT TRANSFER SURFACES. FIELD TESTS

Reference	Duration	Tube Type	Foulant	Findings
Boyd et al. [10]	12 months	Corrugated–roped (Fig. 5(b))	River water	Enhanced surface fouls more rapidly than plain surface. Overall heat transfer coefficient of the enhanced tube decays to the plain value in 2–4 months.
Kornbau et al. [30]	25–30 days	Corrugated–roped (Fig. 5(b))	Coastal seawater: biofouling	Smooth and enhanced tubes fouled approximately linearly and at the same rate. Increase in water velocity decreased the fouling rate.
Panchal [40]	40 days	Corrugated–roped (Fig. 5(b)) Helical internal fins (Fig. 5(d))	Coastal seawater: biofouling and corrosion	Fouling thermal resistance the same for both plain and enhanced tubes.
Panchal and Sasscer [41]	40 days	Helical internal fins (Fig. 5(d))	Coastal seawater: biofouling and corrosion	Fouling thermal resistance the same for both plain and enhanced tubes.
Rabas et al. [45–47]	10–15 months	Corrugated–roped (Fig. 5(b)) (between cleanings)[a]	River water	Enhanced tubes fouled at a higher rate and had higher fouling thermal resistances than plain tubes.[b]

[a] Data may be available over longer periods as indicated in parentheses, for the following TVA power plants: Gallatin Station, Unit 1 (10 years) and Shawnee Station, Unit 9 (2 years), but the relevant data are not given in the original reference.

[b] Authors do not discuss the possible presence of periodicities in the fouling thermal resistance data for enhanced heat transfer tubes, even though they note it in the case of plain tubes.

222

mitigation is more dependent on the type of rough surface enhancement than it is on the type of foulant.

The important effects of fluid velocity, as observed by Webb and Kim [72], also should be noted. Higher fluid velocities were associated with lower R_f values. In fact, with sufficiently high velocities, the fouling thermal resistances were negligible for both plain and enhanced heat transfer surfaces.

The particulate fouling tests using an electrically heated test section reported by Somerscales *et al.* [55], also employed tubes of the corrugated or roped type. The results showed that the tubes with the rib roughness, Figs. 4(a) to 4(c) and 4(e) had a much higher fouling thermal resistance than did either a plain tube (Fig. 4(f)) or a roped tube (Fig. 4(d)) (for which the fouling thermal resistance was actually negligible) at a velocity of 0.9 m/sec. At the higher velocity of 1.2 m/sec, all three tube types showed negligible fouling. At the lower fluid velocity of 0.9 m/sec it was interesting to note that whereas the fouling on the roped tube was immeasurably small, the plain tube exhibited appreciable fouling.

As a broad general conclusion from these laboratory tests it can be said that roped-type enhancement mitigates both precipitation and particulate fouling at all fluid velocities. The rib-type roughness does not mitigate particulate fouling at low fluid velocities, although it is not affected by fouling (nor is the plain surface) at higher fluid velocities.

These conclusions suggest that the fluid motion induced by the roped surface is an important contributor to the observed mitigation of fouling with this type of enhancement. The fluid flow in the vicinity of the ribs of the rib roughness type of enhancement probably causes the fouling deposit, due to particulate fouling, to be thicker upstream and downstream of the ribs. This is confirmed by photographs published by Kim and Webb [27]. This does not appear to be the case with precipitation fouling. Dreyster *et al.* [16] reported that the deposit formed by precipitation fouling was uniform over the whole heat transfer surface. In fact, the temperature of the heat transfer surface was found to be a significant variable with this type of fouling.

E. RESULTS OF FIELD TESTS

The field tests[11] (Table 5b) reported by Boyd *et al.* [10] and Rabas *et al* [45–47] concern the results of observations of the fouling performance made on condensers located at power plants of the Tennessee Valley Authority located on the Cumberland, Ohio, and Tennessee Rivers. Ob-

---

[11] These will involve combined categories of fouling, probably biological and particulate.

servations were made for durations of up to 10 years (in the case of Gallatin Station Unit 1), with condensers when they were operated with plain tubes and when they used enhanced tubes of the roped type (Fig. 5(b)). Conclusions that can be drawn from analysis of the results in the above noted references are

a. With both plain and enhanced tubes [46, 47], Fig. 6 shows that never in 10 years did the specific fouling thermal resistance exceed the value of 1.0×10^{-3} (h ft^2 °F)/BTU [1.8×10^{-4} (m^2 K)/W], which is the minimum value recommended by the Tubular Exchanger Manufacturers Association (TEMA) [11] for river water.

b. Plots (Fig. 7) of the average[12] cleanliness factor of condensers as observed immediately after cleaning showed that it was higher ($\Gamma > 1$) than when plain tubes were used in the condenser [45]. The values decreased with time after cleaning, with the enhanced tube declining faster, such that the two values were identical ($\Gamma = 1$) at 1.5 to 2 years after cleaning.

Field tests involving biofouling and corrosion fouling from seawater using an electrically heated test section (such as those of Somerscales *et al.* [55], noted previously—these are not amenable to analysis using Watkinson's criteria) have been reported by Panchal [40] and by Panchal and Sasscer [41]. The results are summarized in Figs. 8(a) and 8(b). Apart from the case of a plain surface made from aluminum alloy 5052 (Fig. 8(b)), the enhanced tubes demonstrated a lower fouling thermal resistance than the plain tubes. At least under the particular circumstances of the test, the enhanced heat transfer surfaces have a superior fouling performance.

The results reported from the various field tests suggest strongly that tubes of the roped type appear to mitigate fouling of the types encountered in freshwater rivers and ocean environments. Of course, tests involving a wide variety of natural waters would have to be conducted to provide a firm basis for such a conclusion.

F. CONCLUDING REMARKS

The tendency of a heat transfer surface, in which enhancement is supplied by surface roughness, to mitigate the effects of fouling depends

---

[12] The averaging procedure is not defined, but could refer to the method used to plot the data. This involved presenting a curve, which is an appropriate fit over the time (no more than 2 years) between cleaning, of the consolidated data gathered in the total duration of observation (in the case of the Gallatin Station Unit 1, this was 10 years). Because of the way they are presented, such data cannot provide information on the effects of fouling as a function of exposure time.
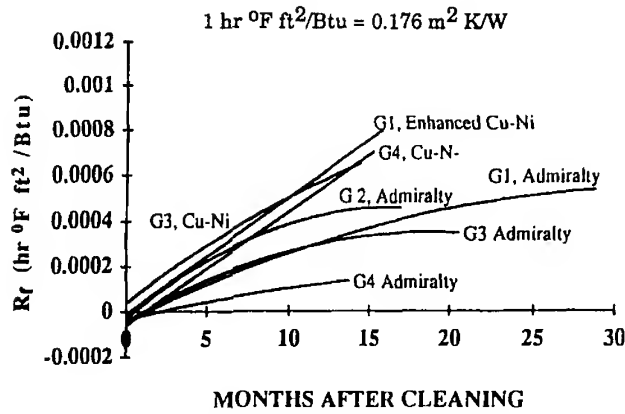
FIG. 6. Specific fouling thermal resistance as a function of time exposure for the condensers of the Gallatin Station. The curves show the trends of the data. Three groups of data are presented: Original tubes (plain, Admiralty brass), Units 1, 2, 3 and 4. Replacement tubes (Wolverine (Decateur, AL) Korodense®, copper–nickel), Unit 1. Replacement tubes (plain, Admiralty brass), Units 3 and 4. From Rabas et al [46].

particularly on

1. Category of fouling
2. Type of roughness
3. Mean fluid velocity; higher velocities favor fouling mitigation
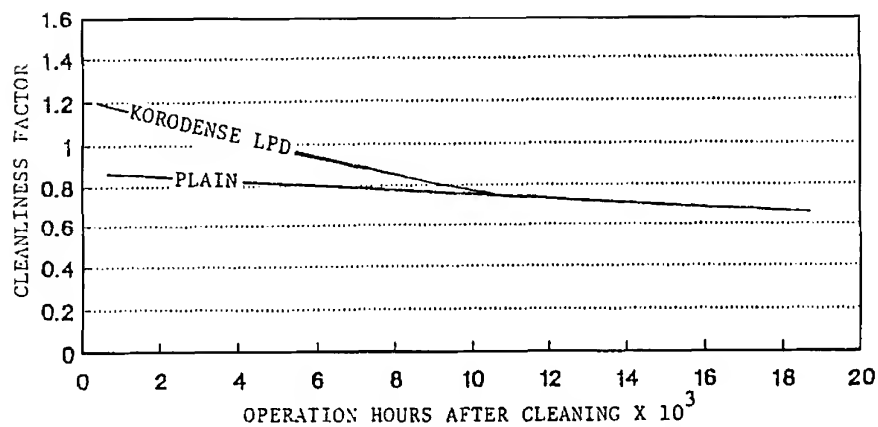
FIG. 7. Cleanliness factor as a function of time of exposure after tube-cleaning for Gallatin Station Unit 1 condenser. From Rabas et al. [45].
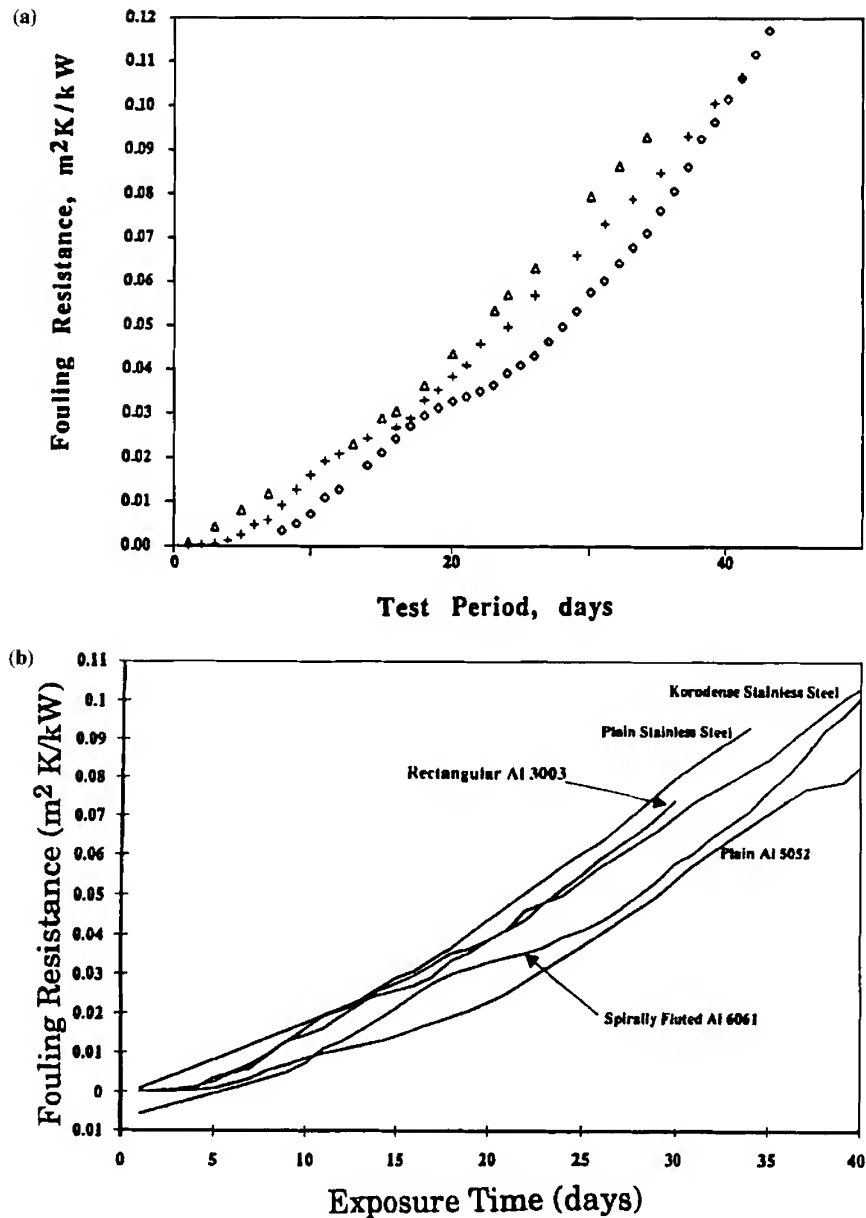
FIG. 8(a). Specific fouling thermal resistance as a function of time exposure for plain (titanium) (△), roped (Al-6XSS) (+), and spirally fluted (Al-6061) (◇) tubes exposed to seawater. From Panchal [40]. (b). Specific fouling thermal resistance as a function of time of exposure for plain (stainless steel), (Al-505) roped (stainless steel), spirally fluted (Al-6061), and rectangular cross-section (Al-3003) tubes exposed to seawater. From Panchal and Sasscer [41].

Long-term field tests show that the ability of the tube with roped-type enhancement to mitigate fouling is highest when the tube is first exposed to fouling conditions, and gradually declines until (after 1.5 to 2 years in the tests reported) there is no difference in the fouling performance between plain and enhanced tubes.

VI. Displaced Enhancement Devices

Bodies of various forms are inserted into the fouling stream to improve heat transfer by increasing the mixing between the fluid at the wall and the fluid in the free stream or bulk flow.

Devices of this type enhance heat transfer by intensification. According to Watkinson's [66] analysis, considered earlier, it can be anticipated that fouling should be mitigated in this case (with the possible exception of precipitation fouling). The test data, discussed below, support this expectation.

A. Hi Tran® Radial Mixing Elements

Hi Tran® radial mixing elements[13] are patented [21 inserts (Fig. 9), made from wire loops spaced radially and axially within the tube, supported by a central core. The dimensions of the insert are chosen such that the wire loops are in contact with the wall.

Hi Tran® elements are claimed to produce complete radial mixing of the fluid stream. This not only improves heat transfer by increasing the convective coefficient on the inner surface of the tube, but reduces the residence time of the fluid at the heat transfer surface.

Gough and Rogers [22] provide data on the performance of these elements in tubes when handling a fluid described as "tar"[14] in a steam-heated shell-and-tube heat exchanger. These data can be evaluated using Watkinson's criterion, Eq. (39). According to Gough and Rogers, the clean overall coefficients of heat transfer for a plain tube and a tube with an insert were 159.4 and 228.8 W/(m² K), respectively. Under fouling conditions, after two months of service, the fouling thermal resistances for a

---

[13] This device is manufactured and sold in Britain by Cal Gavin Ltd., Birmingham, England and in the United States by Norton Chemical Process Products, Akron, OH. It is described in a US patent obtained by Gough and Rogers [21].

[14] The original paper states that the analysis of the fouling fluid showed that it contained particles of various types. Therefore, rather than being chemical reaction fouling, as one would expect with a fluid described as "tar," this may in fact be a case of combined chemical reaction and particulate fouling.
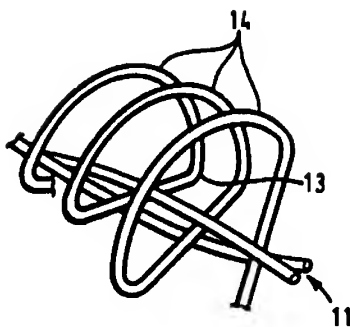
FIG. 9. Typical Hi-Tran® radial element (Gal Galvin Ltd., Birmingham, England; Norton Chemical Process Products Akron, OH). Key: 11, "core", a U-shaped length of wire that is aligned approximately along the tube axis to support the loops (14), 13, median line of the loops (14) that engages the core; 14, wire loops that lie on the inner surface of the tube. In the figure, the coils are shown separated for clarity; in practice, any appropriate spacing is used and the loops can abut if necessary. From Gough and Rogers [21].

plain tube and for a tube with an insert were 5.25×10^{-3} and 1.95×10^{-4} $(\text{m}^2 \text{ K})\text{W}$, respectively. The ratio of the fouling resistances is substantially smaller than the ratio of the clean overall coefficients of heat transfer, and therefore, according to Watkinson's criterion, the tube with the insert has mitigated fouling.

B. SPIRELF® SYSTEM

The Spirelf® system[15] is a displaced enhancement device consisting of a coiled spring attached to fixed supports, typically fins that lie radially across the mean fluid flow, at each end of the tube. The spring is installed, as far as can be gathered, with some initial tension; however, it is slack enough that it can be stretched sufficiently to allow the spring wire to contact the tube walls.

The fluid flowing through the tube is said to cause the insert to vibrate in various modes (Fig. 10). Repeated contact of the spring on the wall is supposed to keep the tube wall clean. The motion of the spring is said to increase the turbulence of the fluid in the vicinity of the tube wall. (A. W. Krueger, personal communication, July 10, 1991). Presumably this implies an increase in fluid mixing. No flow visualization data are available to the authors of this paper that would allow these claims to be substantiated.

Figure 11 shows data [31] that compare the measured fouling thermal resistance of two shell-and-tube heat exchangers exposed to the same

[15] This device is a patented element manufactured by Elf Aquitaine in France. It is sold in the United States by American European Consulting Co., Houston, TX.
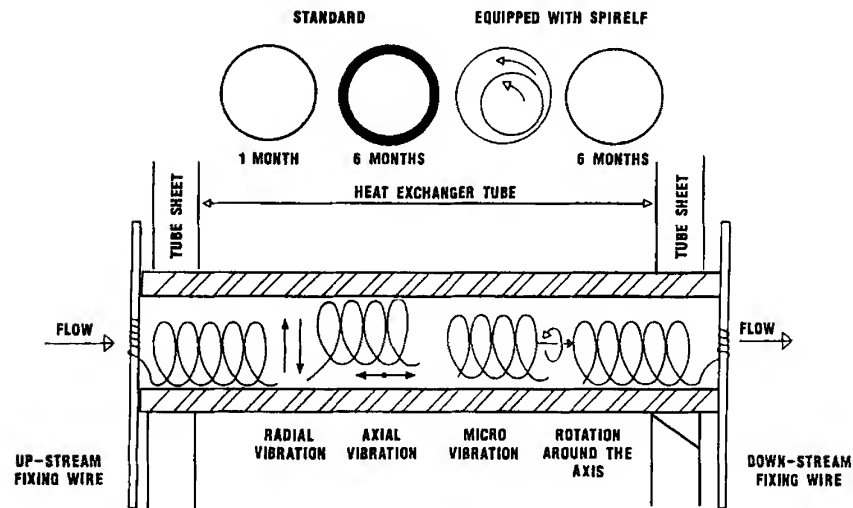
FIG. 10. Operation of Spirelf® element (Elf Aquitaine, France; American European Consultancy Co., Houston, TX). From Krueger [31].

Duration [days]
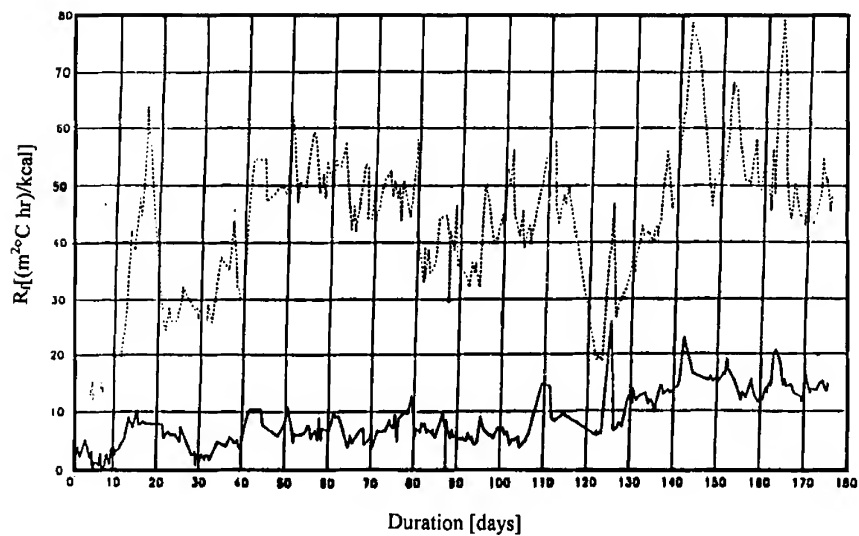
FIG. 11. The specific fouling thermal resistance R_f [(m^2 °C h)/kcal] as a function of time of exposure of heat exchangers handling crude oil. Key: — fitted with Spirelf® element; ---- not fitted with Spirelf® element. *Note*: the heat exchanger without the Spirelf® element was cleaned on days 76 to 78 and 115 to 125. To convert R_f to (m^2 K)/W, multiply by 0.860. From Krueger [31].

nominal conditions with the handling of crude oil on the tube-side. One exchanger is fitted with a Spirelf® element and one is not. After about 40 days of exposure the fouling thermal resistance of the unenhanced heat exchanger was about fire times that of the heat exchanger fitted with the Spirelf® elements. In addition, the heat exchanger not employing the Spirelf® element showed substantial variations in the fouling thermal resistance during the time of exposure. These variations were probably associated with the periodic spalling or sloughing of the fouling deposit. The consequent large variations in the thermal performance of the heat exchanger add to the difficulties of controlling associated processes.

VII. Swirl Flow Devices

Heat transfer in ducts can be improved by swirling the flow. This is accomplished by inserting devices into the duct, such as coiled wires, spiral fins, propellers, and twisted tapes. The swirl improves mixing of the fluid at the core and at the wall; however, there is no definite evidence concerning the role of swirling flow in the mitigation of fouling.

A. Rotating Twisted Tape

In a US patent, Penney [42] describes a twisted tape with its axis coincident with the axis of a heat transfer tube of circular cross section (Fig. 12). The tape is free to rotate under the action of the flowing fluid. The tape also is maintained in tension by the action of the fluid. According to the inventor, this is important because otherwise the tape will buckle under the force imposed by the flowing fluid and may bind against the inner surface of the tube. The clearance between the tape and the inner surface of the tube varies from 0.013 to 6.4 mm, depending on the fluid in the tube.

The inventor claims that the device enhances heat transfer and minimizes fouling because the layer of fluid adjacent to the tube wall is disturbed by the motion of the tape. No test data are provided to substantiate this claim.

VIII. Surface Tension Devices

Porous materials, such as wicking and grooves, can enhance heat transfer by promoting surface tensions forces as the physical process that controls heat transfer.
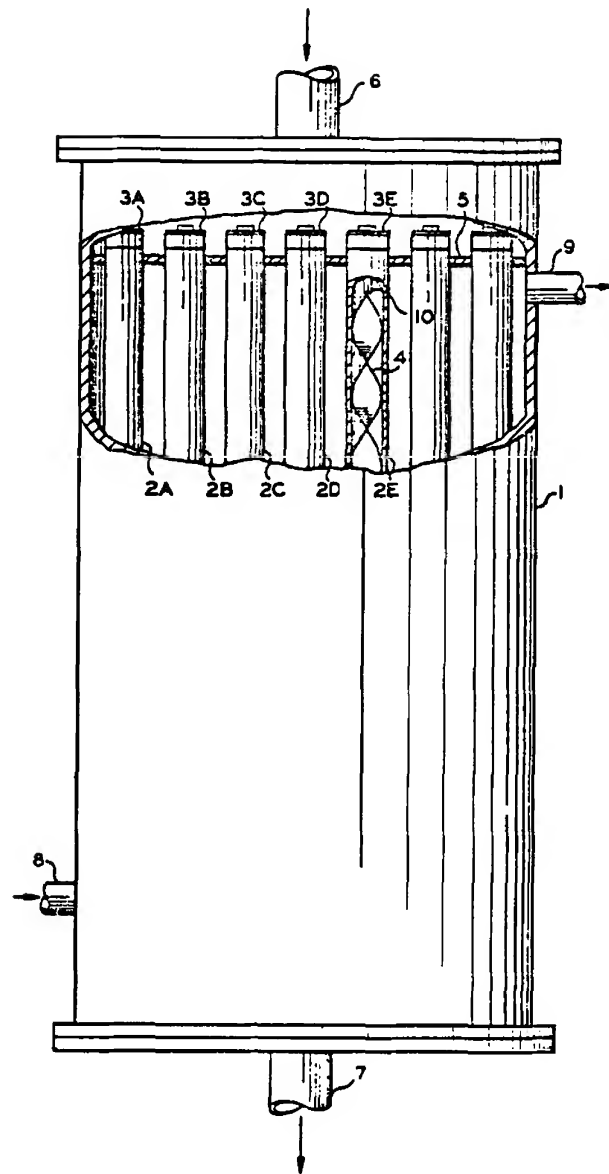
FIG. 12. Rotating twisted tape installed in a shell-and-tube heat exchanger. Key: 1, shell-2A-2E, tubes; 3A-3E, mounting plate for twisted tape; 4, twisted tape; 5, tube sheet; 6, tube-side fluid inlet; 7, tube-side fluid outlet; 8, shell-side fluid inlet; 9, shell-side fluid outlet; 10, support rod that connects the twisted tape (4) to the mounting plate (3E). From Penney [42].

No references were found concerning the effect of fouling on surface tension devices.

IX. Treated and Structured Surfaces

The finish of the heat transfer surface is subjected to fine scale alteration. Surfaces of this type are used for boiling and condensing; the roughness height is below that which affects single-phase heat transfer. Heat transfer tests [13] under nonfouling conditions show that surfaces of this type enhance heat transfer by increasing the number of active sites for bubble formation. This type of surface promoter therefore must operate by heat transfer intensification. Unpublished results obtained by McFarland [36] and Monthie [39], however, suggest that surfaces of this type also enhance heat transfer by area enlargement. In view of this situation it is appropriate to classify treated and structured surfaces, as far as their fouling behavior is concerned, as involving both area enlargement and heat transfer intensification.

A. POROUS LAYER ENHANCEMENT

Universal Oil Products (TSOP) (Tonawanda, NY) offers a surface, the High Flux® surface, in which heat transfer is enhanced by the application of a thin porous layer to a smooth surface. It is manufactured by sintering, at high temperature, fine metallic particles to a smooth metallic surface. The particles are sufficiently dense in number that the treated surface consists of a large number of minute cavities. Such a surface has the property of initiating nucleate boiling at a much smaller wall superheat than would be true for a plain surface at the same heat flux.

The fouling performance of this type of surface has been investigated by L. A. Curcio, Jr. [13], and this work has been reported briefly by Somerscales and Curcio [54], and more completely by Curcio and Somerscales [14]. In these experiments, two types of Praxair High Flux® surfaces and a plain surface were exposed to boiling heat transfer in a saturated solution of calcium sulfate ($CaSO_4$) for about 25 h. Tests were carried out at two levels of heat flux (10 and 80 kW/m^2). The results of some of these tests are shown in Fig. 13 for the plain surface, and Fig. 14 for one example of the Praxair High Flux® surface. The other sample of High Flux® surface demonstrated similar behavior. Figures 13 and 14 show the wall superheat $(\overline{T}_W - T_{sat})$ as a function of exposure time. A larger wall superheat is indicative of a larger fouling thermal resistance. By this measure the
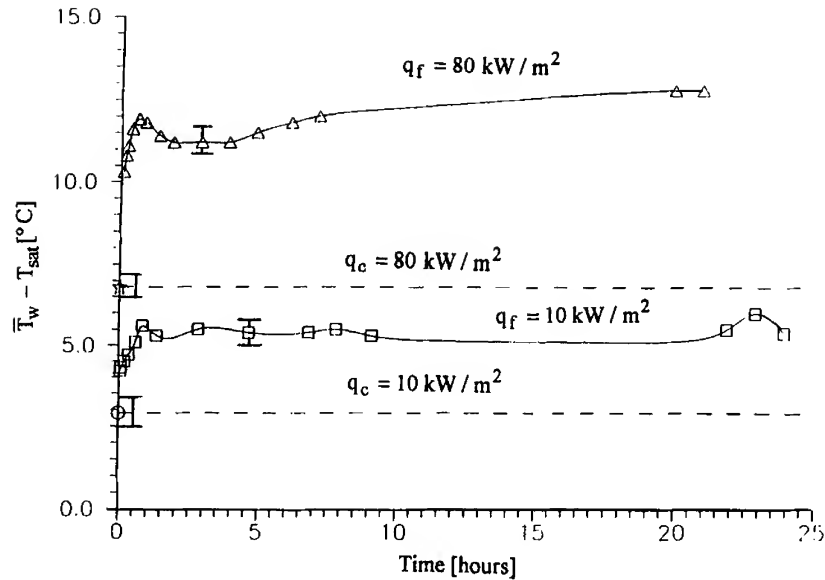
FIG. 13. The variation of wall superheat with time of a plain surface in a saturated aqueous calcium sufate solution at two boiling heat fluxes q. $\bar{T}_w$, spatial average surface temperature, °C; T_{sat}, saturation temperature, °C. From Curcio [13].

enhanced heat transfer surface exhibits a much smaller fouling effect than does the plain surface. Clearly in this case the enhanced heat transfer surface has a mitigating effect on fouling.

An examination of the surface with its large number of minute cavities suggests that it would be very sensitive to the effects of fouling. To explain this anomaly, an apparatus was constructed [12] in which the surface was modeled on a greatly enlarged scale. The model is immersed in saturated $CaSO_4$ solution, which is heated until it boils. The whole is arranged in an "ant farm" configuration so that events within the model cavities can be observed and recorded photographically. Preliminary results [39] obtained with this apparatus suggest that the fused particles act as fins (with a very irregular cross section normal to the mean heat flow direction, and with a very irregular surface in contact with the boiling liquid).

As noted earlier, Epstein and Sandhu [19] and Middis and Müller-Steinhagen [37] have demonstrated theoretically that a uniform fouling deposit on an extended surface can improve the fin efficiency. It is therefore plausible to explain the fouling behavior observed by Curcio with such a model. Tests are still underway with this apparatus.
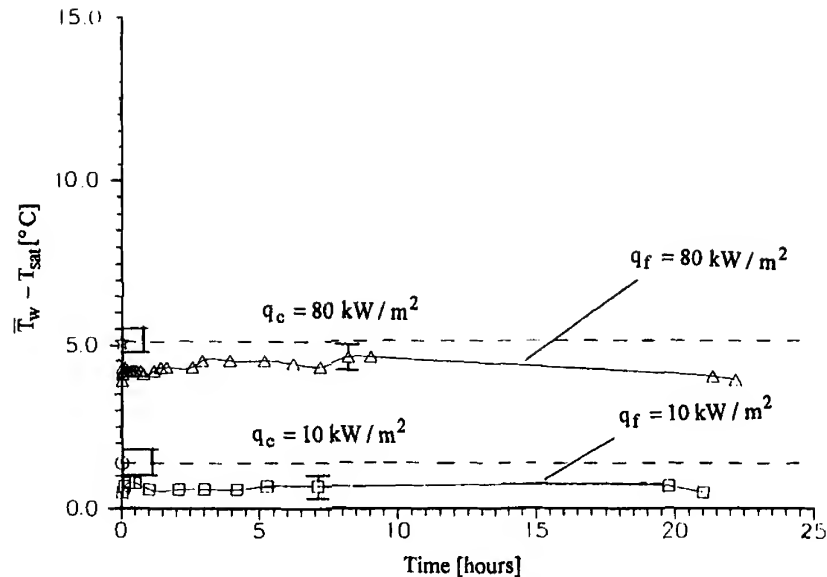
FIG. 14. The variation of wall superheat with time of a UOP, (Tonawando, NY) High Flux[®] small surface in a saturated aqueous calcium sulfate solution at two boiling heat fluxes q. $\bar{T}_w$, spatial average surface temperature, °C; T_{sat}, saturation temperature, °C. From Curcio [13].

B. STRUCTURED SURFACES

A number of commercially available heat transfer surfaces provide enhanced boiling heat transfer by employing re-entrant nucleation sites, which are interconnected below the surface [71]. The operation of these surfaces is presumably similar to the porous surfaces described in the previous section. The main difference between the porous and the structured surface is the much greater geometrical regularity of the cavities in the latter and their significantly lower area density.

Tests using the Turbo-B[®] structured surface manufactured by the Wolverine Co., (Decateur, AL) similar to those reported for the porous surface, have been described by Somerscales and Curcio [54] and Curcio and Somerscales [14]. The test results of one type of Turbo-B[®] surface are shown in Fig. 15. Comparison with the plain surface results, shown in Fig. 13, show that the enhanced surface mitigates the effects of fouling.

Tests similar to those described previously for the porous surface were conducted by McFarland [36] in which conditions in a very enlarged model of the Turbo-B[®] surface were examined. A fin model, such as that noted previously, has been proposed to account for the observed behavior of the experimental system. Tests involving detailed measurements of the temperature distribution in the model are continuing.
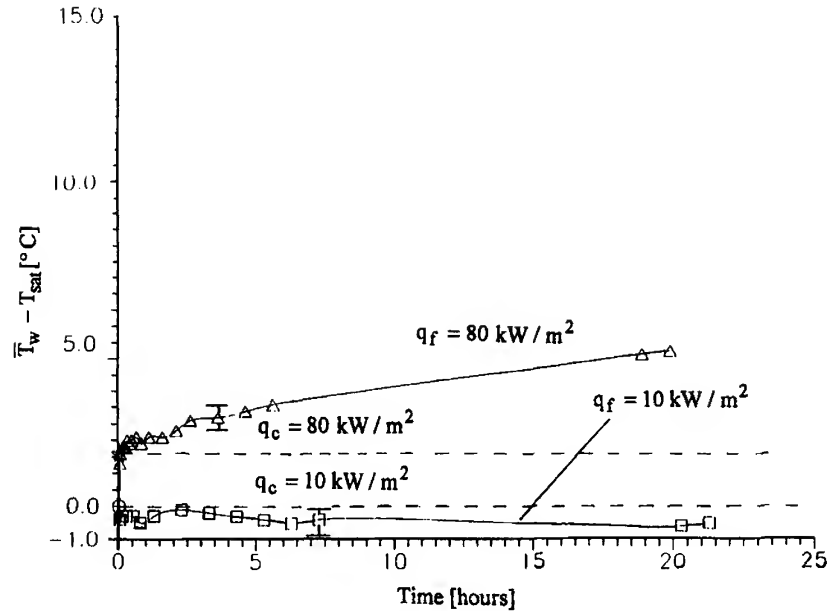
FIG. 15. The variation of wall superheat with time of a Wolverine (Decateur, AL) Turbo B® very open surface in a saturated aqueous calcium sulfate solution at two boiling heat fluxes q. $\bar{T}_w$, spatial average surface temperature, °C; T_{sat}, saturation temperature, °C. From Curcio [13].

C. Concluding Remarks

Structured surfaces that are used to enhance boiling heat transfer have a demonstrated capability to mitigate fouling. This appears to be a consequence of the finlike behavior of the structured elements; however, the results of on-going tests must be awaited for confirmation of this possible mechanism.

X. Additives

Additives for liquids include solid particles and gas bubbles in single-phase flows and liquid trace additives (e.g., surfactants) for boiling systems. Additives for gases are liquid droplets or solid particles, either dilute phase (gas–solid suspensions) or dense phase (fluidized beds).

A. INTRODUCTION

It should be noted that both particle size and fluid flow regime play important roles in the fouling performance of this class of flow-enhancing device. The fouling of heat transfer surfaces by graphite suspended in helium has been reported by Schluderberg et al. [50] and Abel et al. [1]. The former investigators proposed that the particles were transported to a surface at a lower temperature than the flowing gas-solid mixture as a consequence of Brownian motion associated with the temperature gradient normal to the mean flow direction. The latter investigators found that operating with high Reynolds numbers (2.2×10^4 to 6.5×10^4) reduced the fouling effect. Subsequently, Pfeffer et al. [43] reported that particles with diameters between 10 and 50 μm did not form fouling deposits. This is significantly smaller than the 2-mm diameter proposed for use in the fluid bed heat exchangers (Section X.B).

Abel et al [1] used larger particles in combination with smaller particles to try to minimize the fouling of heat transfer surfaces by the smaller particles. In the tests with graphite particles (1 to 10 μm, with an average size of 2 μm) in helium, particles of aluminum silicate of approximately 85 μm were added. Apparently these were effective in reducing fouling, but eroded the tube walls and abraded the pump impeller. The experience of Klaren [28] noted later, however, should be relevant in this connection, suggesting that the indicated modification of the additive method of enhancing heat transfer may yet have promise.

B. FLUID BED HEAT EXCHANGER

The fluid bed heat exchanger[16] consists of a number of parallel heat exchanger tubes in which small solid particles are kept in a fluidized condition by the liquid flowing through the tubes (Fig. 16). So that the particles are uniformly distributed in the section normal to the mean flow, the heat exchanger must be operated in the vertical position.

Stable operation of this type of heat exchanger requires equal distribution of particles and liquid inside the tubes. According to Klaren [28], this is achieved by dividing the inlet chamber in two by a horizontal distribution plate (Fig. 15) into which are drilled numerous holes of about half the diameter of the heat exchanger tubes. The portion of the chamber above the distribution plate is called the *particle distribution chamber*, which is designed to ensure that the particles are uniformly distributed over all the

---

[16] This heat exchanger is manufactured in the Netherlands by Eskla BV, Halfweg. It is sold in the United States by Scheffers of America, Inc., Houston, Texas.
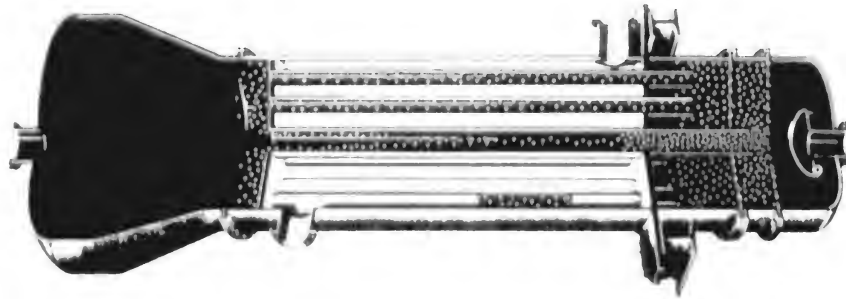
FIG. 16. Mode of operation of the fluid bed heat exchanger. (Illustration reproduced by courtesy of Eskla BV, Halfweg, the Netherlands.)

tubes. It should be noted that the tubes extend down into the particle distribution chamber, and according to Klaren [28] are provided with a side hole. The tube extension and side hole are apparently essential for stable operation of the fluid bed. The fluidizing liquid is supplied to the lower portion of the inlet chamber. In this chamber the fluid and particles are mixed before passing through the distribution plate.

The particles discharged into the outlet chamber separate from most of the fluidizing liquid, which leaves the outlet chamber and returns to the inlet chamber with some of the fluidizing liquid, by flowing down a large-diameter centrally located downcomer (Fig. 16).

According to Klaren [28] the fluid bed heat exchanger enhances heat transfer because the solid particles break through the boundary layer at the tube wall, resulting in a higher heat transfer coefficient than would be the case at the low liquid velocities employed. The continual contact of the particles with the walls of the heat transfer tubes removes any deposit that may form. This is clearly an example of heat transfer enhancement in which fouling is mitigated.

Klarent [28] provides a list of applications in which the fluidizing bed heat exchanger has demonstrated its ability to mitigate the effects of fouling. Examples from this list are shown in Table VI.

XI. Mechanical Aids

A. Stirring

Mechanical devices inserted into the bulk fluid or rotating surfaces stir the fluid. No examples were found that indicate that this type of heat transfer enhancement device mitigates fouling. Nevertheless, in many

TABLE VI

MITIGATION OF FOULING BY THE FLUIDIZED BED HEAT EXCHANGER

Application	Liquid on Fluid Bed Side	Temperature Range of Fouling Liquid (°C)	Fouling Behavior	
			Conventional Heat Exchanger	Fluidized Bed Heat Exchanger
Condenser	Seawater	45–85	U decreased from 2000 to 1200 W/(m² K) in 6 weeks	No fouling, $U = 3000$ W/(m² K)
Condenser	Highly polluted river water	25–45	U decreased from 1950 to 630 W/(m² K) in 3 months	No fouling, $U = 2580$ W/(m² K)
Condenser	Severely fouling cooling water	15–65	U decreased from 300 to 200 W/(m² K)	U constant at 960 W/(m² K)
Liquid–liquid heat exchanger	Geothermal brine	150–35	U decreased 50% in 5 weeks	No fouling observed

Based on information in Klaren [28].

cases an increase in the velocity of the fluid in contact with a heat transfer surface mitigates the effects of fouling. In some situations, stirring therefore might be expected not only to enhance heat transfer but also to mitigate fouling.

B. SURFACE SCRAPING

Mechanical devices in direct contact with the heat transfer surface are periodically wiped over the surface to remove, for example, stagnant fluid layers, layers of condensate, and fouling deposits.

Scraped surface heat exchangers are well known in the chemical and food-processing industries. They are used to minimize the required heat transfer surface in a double-pipe heat exchanger handling very viscous fluids that also are liable to form a deposit of crystalline material or polymerized substances on the heat transfer surface. Scrapers, powered externally, continually sweep over the inner annular surface. These enhance heat transfer by breaking up the boundary layer, and they mitigate fouling by removing deposits from the heat transfer surface.

The concept has been extended to gas heat transfer by Yeh (77), who describes an insert (Fig. 17) consisting of vanes that rotate under the action of the flowing gas, and therefore it is not externally powered. Brushes at the extremities of the vanes are claimed to break up the boundary layer adjacent to the tube wall and to sweep fouling material from the heat transfer surface.

In 1959, Lustenader et al. [35] described the application of a scraped surface heat transfer device to evaporation and condensation. The device is shown in Fig. 18. Tests were carried out with seawater, which showed
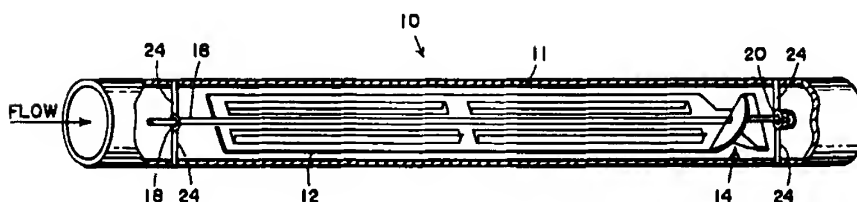
FIG. 17. In-tube surface scraper proposed by Yeh [77]. Key: 10, rotating surface scraper; 11, heat transfer tube; 12, strip; 14, impeller that uses the motion of the gas in the tube to rotate the strip (12); 16, shaft; 18, shaft bearing; 20, shaft bearing; 24, bearing support. From Yeh [77].
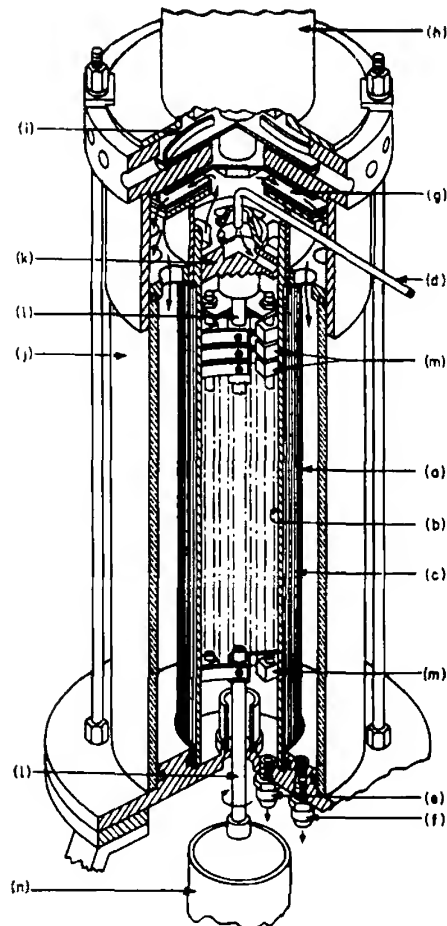
FIG. 18. Scraped surface heat exchanger tested by Lustenader *et al.* [35]. (a) Heat transfer tube; (b) surface for thin-film evaporation; (c) surface for thin-film condensation; (d) raw water inlet; (e) concentrate outlet; (f) condensate outlet; (g) vapor compressor; (h) vapor compressor drive motor; (i) drive motor cooling fan; (j) Pyrex® Corning Glass Works, (Corning, NY) glass jacket; (k) raw water distributor; (l) wiper; (m) spring-loaded carbon brushes; (n) wiper drive motor. From Lustenader *et al.* [35].

that for an exposure time of 50 h there was no degradation in the rate of heat transfer, such as might occur from a fouling deposit, nor was any visible deposit formed on the heat transfer surface. Similar experience was reported in a rotating flat-disk wiped film evaporator described by Tleimat [59].

C. Rotating Surfaces

Substantial increases in heat transfer coefficients have been reported for tubes rotating about their own axes, rotating about a parallel axis, in rotating circular tubes, and in rotating curved circular tubes. Rotating cylinders and discs in large bodies of fluid also have been shown to have much higher heat transfer coefficients that do stationary cylinders and discs.

A self-cleaning surface, which is described by Deck [15] in a US patent (Fig. 19), is intended for application to tube banks with radial fins and operating in cross flow with particulate fouling. The tubes are rotated at about one revolution per minute, so the enhancement in heat transfer
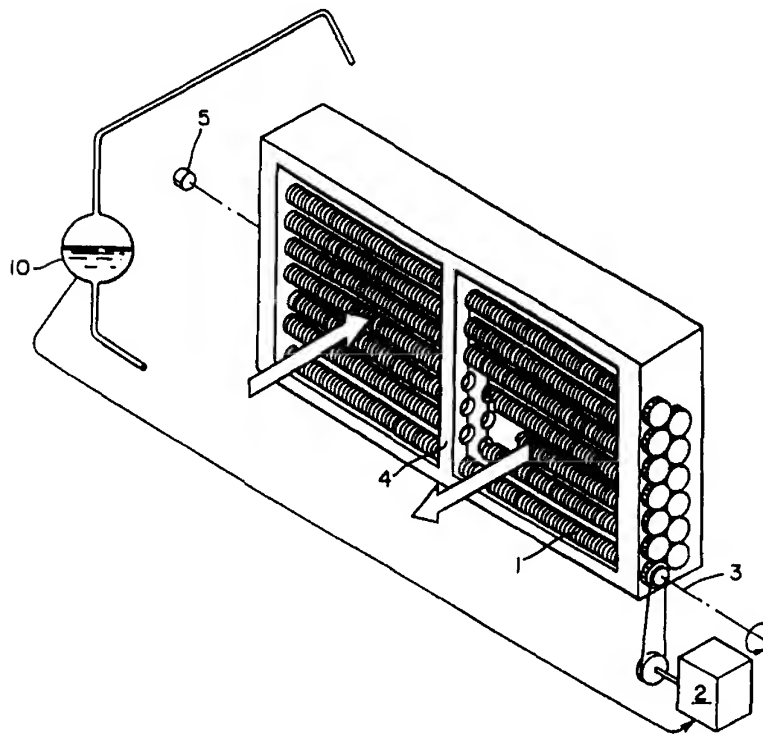
Fig. 19. Heat exchanger with rotating finned tubes proposed by Deck [15]. Direction of gas flow shown by the arrows. Key: 1, finned heat transfer tube; 2, drive motor; 3, axis of rotation of a tube; 4, bulkhead that carries bearings that support the rotating tubes; 5, sonic transducer for vibrating tubes to remove fouling deposit; 10, pressure sending switch that starts the motor (2) when the pressure drop across the tube bank reaches a preset value. From Deck [15].

from the rotation is probably quite small. Presumably there is no reason, other than mechanical limitations, that it should not be operated at higher rotational speeds. It is claimed that the continual movement of the heat transfer surface from the downstream location—which is a high fouling region—to the forward stagnation region—which is a low fouling region [34]—prevents the formation of a fouling deposit on the surface. The patent does not provide any performance data for this invention.

XII. Vibration

Transport processes are affected by oscillations either in the fluid or on the heat transfer surface. In general, sufficiently intense oscillations improve the rate of heat transfer, although cases of the opposite have been recorded. Good reviews of the effects of vibration on heat transfer have been published by Lemlich [32], Baird [3], and Richardson [48].

Surface vibration at either high or low frequency has been used mainly to improve single-phase heat transfer. The practicality of this technique is limited by the large mass of most heat transfer equipment and by considerations of mechanical reliability.

Fluid vibration is the more practical technique for heat transfer enhancement by vibration in most applications. The vibrations range from pulsations of about 1 Hz to ultrasonic vibrations. Pulsed combustion is an example of this technique that is used in domestic and small commercial heating and hot-water furnaces.

A. INTRODUCTION

The effect of fluid or heat transfer surface oscillations on fouling has been studied only sporadically. Lemlich [32] and Fand [20] describe cases in which oscillations are applied after deposit formation to remove a fouling deposit. Lemlich showed that oscillations of the fluid flowing through the tube of a steam-heated double-pipe heat exchanger can increase the rate of heat transfer. Fortuitously, he found that such oscillations also removed fouling that had formed on the heat transfer surface during extended periods of shutdown. Fand used high-frequency oscillations applied for a short duration to a precipitation fouling deposit formed during an extended exposure of a heated cylinder to the fouling liquid. Neither example demonstrates that either heat transfer enhancement by fluid or surface oscillation minimize fouling; however, there is every reason to believe this could be the case. The area is obviously open for investigation and exploration.

B. RESONATING PULSE REACTOR

In a US patent, Spence *et al.* [56] describe a resonating pulse reactor in which the reactants in liquid form are subjected to vibration. The objectives of the invention are to prevent fouling in the reactor, promote turbulent flow in the reactor fluids, and provide a continuous throughput.

The inventors demonstrate, by empirical evidence, that turbulent flow is obtained in their tubular reactor at Reynolds numbers as low as 700. They also demonstrate, by comparison of test results from conventional steady flow reactors and reactors with pulsating flow, that fouling in the latter case is negligible. Although the patent allows the application of heat transfer to the reactor, no evidence is quoted that would indicate that heat transfer was used in the described tests. It is clear, however, that heat transfer should be enhanced by this device because of the appearance of turbulent flow at a Reynolds number significantly lower than that for fluid flowing steadily in a pipe of circular cross section. Thus it is reasonable to conclude that the described invention will both enhance heat transfer and mitigate fouling.

XIII. Electric and Electromagnetic Fields

Electromagnetic fields (dc or ac) can be directed to cause greater bulk mixing in dielectric fluids in the vicinity of heat transfer surfaces. In addition, the motion of electrically conducting fluids can be influenced by the application of electromagnetic fields.

Many claims have been made, both by vendors and apparently disinterested parties, that electric and magnetic fields can mitigate fouling in liquids[17] [61]. These same claims have been rejected by others (see Welder and Partridge [74], for example). The confusion is undoubtedly a consequence of the lack of systematic and precise tests. Recent investigations, which also review the relevant literature, that meet these criteria have been reported by Limpert and Raber [33] and Bernardin and Chan [9]. Both of these studies indicate that devices that claim to use electric and magnetic fields to mitigate fouling in liquids are, in fact, ineffective.

In their research Bernardin and Chan found that small traces of iron (Fe^{+2}) reduced the polymerization rate of supersaturated silica solutions and, hence, the tendency of such solutions to foul a heat transfer surface (also noted by others; see Troup and Richardson [62]). Bernardin and

[17] No information was located on the effect of electric and magnetic fields on fouling in gases, although the action of electrostatic precipitators suggests that fields of this type should have important consequences for fouling.

Chan proposed that this may provide an indirect mechanism for fouling mitigation if a magnetic field promotes corrosion of iron surfaces and hence the release of Fe^{+2} into solution. As yet, this hypothesis has not been confirmed.

In summary, neither the results of careful experiments nor plausible hypotheses suggest that electric and magnetic fields could mitigate fouling in liquids, except possibly indirectly.

XIV. Injection and Suction

A. INJECTION

Heat transfer is augmented by supplying gas to a flowing liquid through a porous heat transfer surface or by injecting a similar fluid through holes in the heat transfer surface. In a US patent, Townsend [60] describes a device that injects an oxidizing or reducing gas through a porous tube sheet into the inlet plenum of a shell-and-tube heat exchanger. The gas reacts with the foulant to eliminate deposits on the tube sheet and at the inlets of the tubes. The foulant originates from high-temperature gases that pass from the inlet plenum to the tubes. The shell-side flow is typically water. It is not clear that such an arrangement would enhance heat transfer, and the inventor does not make such a claim. However, it is considered worthy of note and of investigation into its heat transfer characteristics.

B. SUCTION

In nucleate boiling, heat transfer vapor is removed through pores in the heat transfer surface or fluid is withdrawn by the same means in single-phase flow. No examples of devices of this type that might also mitigate fouling were found.

XV. Compound Enhancement

Two or more of the heat transfer enhancement techniques described in the previous sections can be used simultaneously to produce an enhancement larger than would be produced by only one technique. This simultaneous use is termed *compound enhancement.*

A. Swirl Flow and Additives

In a US patent, Schmidt [51] describes a heat transfer enhancement device that uses a twisted tape located axially in a tube (Fig. 20) to impart a swirl motion to the gas being pumped through the tube. In addition, solid particles may be injected continuously or intermittently into the gas to remove foulant from the duct walls. While Schmidt's objective in adding the particles is to minimize fouling, it is clear from the discussion on the fluid bed heat exchanger that these must also enhance the heat transfer, which Schmidt acknowledges. The swirl flow is said to aid the scouring of the walls by the particles, and can also be expected to enhance heat
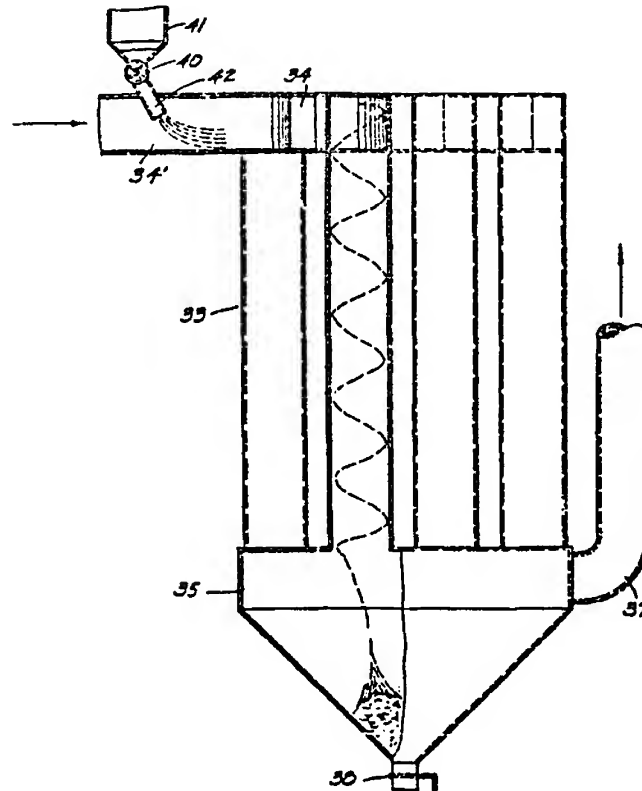
Fig. 20. Heat exchanger with swirl flow device and solid particle injection proposed by Schmidt [51]. Key: 33, heat exchanger; 34, inlet header; 34, tubeside fluid inlet; 35, particle collection bin; 37, tubeside fluid outlet; 38, gate for emptying particles from bin; 40, particle feed; 41, particle storage bin; 42, particle distribution chute. From Schmidt [51].

transfer. Schmidt also suggests that application of high voltage dc to electrodes suitably placed in the flow system can be expected to further increase the gas flow rate and, hence, the enhancement of heat transfer.

B. ROUGH SURFACE AND ADDITIVES

Enhancement of heat transfer and mitigation of fouling in seawater evaporators using spirally corrugated tubes and a surfactant has been reported by Sephton [52] and van der Mast et al. [63]. The first paper claims that the addition of a surfactant to the brine tends to keep the brine surfaces clean. It is not claimed that the surfactant enhances heat transfer; however, the second paper does make this claim for plain tubes. In the face of this somewhat contradicatory evidence, it is probably best to conclude that the use of the combined heat transfer enhancement techniques of a rough heat transfer surface and a surfactant added to the feedstock has promise for also mitigating fouling. However, further study is warranted.

XVI. Prospects for the Future

The possibility that devices which enhance heat transfer might also mitigate fouling is, perhaps, only just being realized among engineers who are concerned with heat transfer equipment. This recognition has come as a consequence of experimental studies of the fouling behavior of devices that enhance heat transfer. Our ability to predict the fouling performance of plain surfaces—never mind situations where the heat transfer is enhanced—is still limited. However, it is clear from this review that there is a need to develop methods for designing devices that both enhance heat transfer and minimize fouling.

Despite the desirability of basing design methods on analytical techniques, empirical data will play a large role, at least at first, in the development of minimum fouling enhanced heat transfer devices. In particular, very long term tests involving so-called real fluids, such as natural waters, must be conducted. Short-term laboratory tests, while useful for identifying important variables, are not likely to produce data that will be immediately useful to the designer and user of heat transfer equipment exposed to fouling conditions.

The manufacture and application of many devices that enhance heat transfer could involve substantial expenses over those incurred by the application of unenhanced heat transfer equipment under the same conditions. Fouling plays an important part in the economics of operating heat

transfer equipment, and therefore a clear need exists to include economic considerations in any program intending to develop design methods for minimum fouling enhanced heat transfer devices.

Because constraints on our use of energy and materials remain (unrecognized by the public and our political officials), the development of methods that enhance heat transfer and mitigate fouling should be a matter of very high priority in our future research agendas.

XVII. Conclusions

This review has demonstrated that, contrary to conventional wisdom, there are many devices that both enhance heat transfer and mitigate fouling.

Structured surfaces under boiling conditions

Some rough surfaces

Finned surfaces

Displaced enhancement devices

Fluid bed heat exchangers

A review of the patent literature has shown that the inventors of heat transfer enhancement devices also, on occasion, claim that their invention also mitigates fouling. Of the patents reviewed, no inventor provided test data that would substantiate their claims. There is clearly an opportunity to investigate the fouling characteristics of these inventions.

An important future task for engineers interested in fouling and heat transfer enhancement is the need to develop methods for designing *a priori* heat transfer enhancement devices that also mitigate fouling. Success in doing this will depend on three things:

1. Development of theories that adequately describe the fouling of heat transfer enhancement devices
2. Generation of substantial quantities of long-term in-plant data on the fouling performance of enhanced heat transfer devices
3. Painstaking program of investigation into the details of the interaction between the foulant and the hydrodynamic and thermal variables that control the fouling process.

As this paper demonstrates, a start has been made in these three areas, but much remains to be done.

Acknowledgments

Nomenclature

A heat transfer area, m^2 (for a finned surface, $A = A_{pr} + A_{fin}$)

A' cross-sectional area of fin normal to direction of heat flow, m^2

A_e effective heat transfer area of a finned surface $= A_{pr} + \eta' A_{fin}$, m^2

A_{fin} fin heat transfer area, m^2

A_{pr} prime (unfinned) heat transfer area, m^2

a_1 constant in Eq. (3), $(m^{5-n} \ K)/(kg \ W \ sec^{1-n})$

C cleanliness factor equal to U_f/U_c, dimensionless

C_b bulk concentration of fouling material, kg/m^3

C_i fluid–deposit interface concentration of fouling material, kg/m^3

C_{sat} saturation concentration of fouling material, kg/m^3

E activation energy for chemical reaction at deposit-fluid interface, $kJ/mole$

E_a activation energy for particle adhesion process, kJ/mol

f Fanning friction factor, dimensionless

H fouling Biot number equal to hR_f, dimensionless

h coefficient of heat transfer, $W/(m^2 \ K)$

k thermal conductivity, $W/(m \ K)$

k_f thermal conductivity of the fouling deposit, $W/(m \ K)$

k_m mass transfer coefficient for particulate fouling material, m/sec

k_r reaction rate constant for deposit incorporation reaction, $kg^{1-z}(m^{2-3z} \ sec)$

k_{ro} Arrhenius constant for k_r, $kg^{1-z}/(m^{2-3z} \ sec)$

L length of fin, m

m clean fin parameter equal to $\sqrt{hP/kA'}$, dimensionless

m_{fs} fouled fin parameter equal to $m/\sqrt{1+H}$, dimensionless

$\dot{m}_f$ rate of formation of the fouling deposit equal to $\dot{m}_g - \dot{m}_r$, $kg/(m^2 \ sec)$

$\dot{m}_g$ rate of growth of the fouling deposit, $kg/(m^2 \ sec)$

$\dot{m}_r$ rate of removal of the fouling deposit, $kg(m^2 \ sec)$

n exponent on velocity term in Eq. (3), dimensionless

P perimeter of fin, m

Q heat transfer rate, W

q heat flux, kW/m^2

R universal gas content equal to 8.314 $kJ/(kmole \ K)$

R_f specific fouling thermal resistance, $(m^2 \ K)/W$

R_f^* asymptotic specific fouling thermal resistance, $(m^2 \ K)/W$

R_w specific conductive resistance of tube wall, $(m^2 \ K)/W$

S sticking probability of Watkinson and Epstein [67], dimensionless: the mass of material permanently incorporated into the fouling deposit as a fraction of the mass of material transferred from the bulk of the fluid

S_o Arrhenius coefficient for the sticking probability, dimensionless

T_b bulk fluid temperature, °C or K

T_w wall temperature (if the wall has finite thermal resistance, this is the temperature at the wall surface exposed to the fouling fluid), °C or K

$\bar{T}_w$ average wall temperature measured by several sensors, °C or K

T_{sat} saturation temperature, °C or K

U overall coefficient of heat transfer in a double-pipe heat exchanger, referred to the outside surface area A_o of the inner tube W/(m² K)

v fluid velocity averaged over the duct cross section, m/sec

z order of fouling deposit incorporation reaction, dimensionless

δ_f thickness of fouling deposit, m

Γ Watkinson's [64] cleanliness factor ratio equal to C_e/C_p, dimensionless

ε energy efficiency factor, defined in Eq. (10), dimensionless

η fin efficiency, dimensionless

η' area weighted fin efficiency equal to

$(A_{pr} + \eta A_{fin})/(A_{pr} + A_{fin})$, dimensionless

ρ_f density of the fouling deposit, kg/m³

τ_w shear stress at the heat transfer surface N/m² (on a clean surface at the surface–fluid interface and on a fouled surface at the deposit–fluid interface)

ψ strength function for fouling deposit removal by spalling, $(N - s)/m^2$

SUBSCRIPTS

c clean

e enhanced

f fouled (note that k_f and ρ_f refer to the fouling deposit properties)

i inner tube surface

o outer tube surface

p plain

s series model of Epstein and Sandhu [19]

References

1. Abel, W. T., Bluman, D. E., and O'Leary, J. P. (1963). Gas-solids suspensions as heat carrying mediums. *Am. Soc. Mech. Eng. [Pap.]* **63-WA-210**.

2. Asomaning, S., and Watkinson, A. P. (1990). The role of olefins in fouling of heat exchangers. *AIChE Summer Meet.*, San Diego, CA, Paper 35d.

3. Baird, M. H. I. (1966). Vibrations and pulsations: Bane or blessing. *Br. Chem. Eng.* **22**, 20–24.

4. Bergles, A. E. (1969). Survey and evaluation of techniques to augment convective heat and mass transfer. *Prog. Heat Mass Transfer* **1**, 331–424.

5. Bergles, A. E. (1985). Techniques to augment heat transfer. In *Handbook of Heat Transfer Applications* (W. M. Rohsenew, J. P. Hartnett and E. N. Ganic, eds.), 2nd ed., pp. 3-1 to 3-80. McGraw-Hill, New York.

6. Bergles, A. E. (1996). The effect of fouling enhanced heat transfer equipment. In *New Developments in Heat Exchangers* (N. Afgan and M. G. Carvalho, eds.), pp. 73–92. Gordon and Breach/Overseas Publishers Association, Amsterdam, The Netherlands. 1993.

7. Bergles, A. E., and Somerscales, E. F. C. (1995). The effect of fouling on enhanced heat transfer equipment. *J. Enhanced Heat Transfer* **2**, 157–166.

8. Bergles, A. E., Jensen, M. K., Somerscales, E. F. C., and Manglik, R. M. (1991). *Literature Review of Heat Transfer Enhancement Technology for Heat Exchangers in Gas-Fired Application*, Top. Tech. Rep., GRI91-0146. Gas Research Institute, Chicago.

9. Bernardin, J. D., and Chan, S. H. (1991). Magnetic effects of simulated brine properties pertaining to magnetic water treatment. In *Fouling and Enhancement Interactions* (T. J. Rabas and J. M. Chenoweth, eds.), HTD-Vol. 164, pp. 109–117. ASME, New York.

10. Boyd, L. W., Harmon, J. C., Littrell, J. J., and Withers, J. G. (1983). Efficiency improvement at Gallatin Unit 1 with corrugated condenser tubes. *Am. Soc. Mech. Eng. [Pap.]* **83-JPGC-PWR-4**.

11. Chenoweth, J. M. (1990). Final report of the HTRI/TEMA Joint Committee to review the fouling section of the TEMA standards. *Heat Transfer Eng.* **11**(1), 73–107.

12. Coe, S. D. (1989). *Macroscopic Modeling of Enhanced Heat Transfer Surfaces*, Undergrad. Proj. Rep. Resselaer Polytechnic Institute, Troy, NY.

13. Curcio, L. A., Jr. (1989). Pool boiling of enhanced heat transfer surfaces in refrigerant-oil mixtures and aqueous calcium sulfate solutions. MS Thesis, Resselaer Polytechnic Institute, Troy, NY.

14. Curcio, L. A., Jr., and Somerscales, E. F. C. (1991). *Pool Boiling of Enhanced Heat Transfer Surfaces in Refrigerant-Oil Mixtures and Aqueous Calcium Sulfate Solutions*, Rep. No. HTL-5. Heat Transfer Laboratory, Department of Mechanical Engineering, Aeronautical Engineering and Mechanics, Rensselaer Polytechnic Institute, Troy, NY.

15. Deck, B. D. (1987). Heat exchanging with slowly rotating finned elements. U.S. Pat. 4,660,627.

16. Dreyster, G. A., Gorman, V. I., and Aronov, I. Z. (1983). Comparison of fouling in tubes with annular turbulence promoters and in smooth tubes of shell-and-tube heat exchangers. *Heat Transfer—Sov. Res.* **15**(1), 87–93.

17. Epstein, N. (1983). Fouling of heat exchangers. In *Heat Exchangers: Theory and Practice* (J. Taborek, G. F. Hewitt, and N. Afgan, eds.), pp. 795–815. Hemisphere, Washington, DC.

18. Epstein, N. (1988). General thermal fouling models. In *Fouling Science and Technology* (L. F. Melo, T. R. Bott, and C. A. Bernardo, eds.), pp. 15–30. Kluwer Academic, Dordrecht, The Netherlands.

19. Epstein, N., and Sandhu, K. (1978). Effect of uniform fouling deposit on total efficiency of extended heat transfer surfaces. *Heat Transfer, Int. Heat Transfer Conf., 6th, 1978*, Vol. 4, pp. 397–402.

20. Fand, R. M. (1969). The formation of calcium-sulfate scale on a heated cylinder in crossflow and its removal by acoustically induced cavitation. *J. Heat Transfer* **91**, 111–122.

21. Gough, M. J., and Rogers, J. V. (1984). Insert for placement in a vessel and method of forming the insert. U.S. Pat. 4,481,154.

22. Gough, M. J., and Rogers, J. V. (1987). Reduced fouling by enhanced heat transfer using wire matrix radial mixing elements. In *Heat Transfer-Pittsburgh 1987* (R. W. Lyczkowski, ed.) AIChE Symposium Series, Vol. 83, No 257, pp. 16–21. AIChE, New York.

23. Hasson, D., Sherman, H., and Biton, M. (1978). Prediction of calcium carbonate scaling rates. In *Proc. Int. Symp. Fresh Water Sea, 6th, 1978*, Vol. 2, pp. 193–199.

24. Katz, D. L., Knudsen, J. G., Balekjian, G., and Grover, S. S. (1954). Fouling of heat exchangers. *Pet. Refiner* **33**(8), 123–125.

25. Kern, D. Q., and Kraus, A. D. (1972). *Extended Surface Heat Transfer*, pp. 439–519. McGraw-Hill, New York.

26. Kern, D. Q., and Seaton, A. E. (1959). A theoretical analysis of thermal surface fouling. *Br. Chem. Eng.* **4**, 258–262.

27. Kim, N.-H., and Webb, R. L. (1990). Particulate fouling in tubes having arc-shaped two-dimensional roughness by a flowing suspension of aluminum oxide in water. *Heat Transfer, Proc. Int. Heat Transfer Conf., 9th, 1990*, Vol. 5, pp. 139–145.

28. Klaron, D. G. (1983). Fluid bed heat exchanger: A major improvement in severe fouling heat transfer. In *Heat Exchangers: Theory and Practice* (J. Taborek, G. F. Hewitt, and N. Afgan, eds.), pp. 885–896. Hemisphere, Washington, DC.

29. Knudsen, J. G. (1981). Apparatus and techniques for measurement of fouling of heat transfer surfaces. In *Fouling of Heat Transfer Equipment* (E. F. C. Somerscales and J. G. Knudsen, eds.), pp. 57–81. Hemisphere, Washington, DC.

30. Kornbau, R. W., Richard, C. C., and Lewis, R. O. (1983). Seawater biofouling counter-measures for spirally enhanced condenser tubes. *Inst. Chem. Eng. Symp. Ser.* No. 75, 200–212.

31. Krueger, A. W. (1991). *Improvement of the Heat Exchanger Efficiency by the Spirelf® System*. American European Consulting Co., Houston, TX.

32. Lemlich, R. (1961). Vibration and pulsation boost heat transfer. *Chem. Eng.* 68, May 15, 171–176.

33. Limpert, G. J. C., and Raber, J. L. (1985). Tests of nonchemical scale control devices in once through systems. *Mater. Perform.* 24(10), 40–45.

34. Lokshin, V. A., Furmina, A. A., Pavlov, N. V., Portyanko, A. A., and Skornyakova, L. G. (1980). Experimental investigation of the fouling of transversely finned bundles of tubes in a dust laden air flow. *Therm. Eng.* 27(6), 327–330.

35. Lustenader, E. L., Richter, R., and Neugebauer, F. J. (1959). The use of thin films for increasing evaporation and condensation rates in process equipment. *J. Heat Transfer* 81, 297–307.

36. McFarland, J. K. (1991). *Macroscopic Modeling and Photographic Analysis of the Effects of Fouling on Enhanced Heat Transfer Surfaces*, Undergrad. Proj. Rep. Rensselaer Polytechnic Institute, Troy, NY.

37. Middis, J., and Müller-Steinhagen, H. M. (1991). Heat transfer from finned surfaces with a uniform fouling deposit. *Can. J. Chem. Eng.* 69, 755–760.

38. Miller, E. R. (1982). Performance of low fin tubing in asphalt service. *Heat Transfer, Proc. Int. Heat Transfer Conf., 7th, 1982*, Vol. 6, pp. 409–414.

39. Monthie, A. (1992). *Macroscopic Modeling and Analysis of UOP High Flux® Heat Transfer Surface*, Undergrad. Proj. Rep. Rensselaer Polytechnic Institute, Troy, NY.

40. Panchal, C. B. (1989). Experimental investigation of seawater biofouling for enhanced surfaces. In *Heat Transfer Fundamentals, Design, Applications, and Operating Problems* (R. K. Shah, ed.), HTD-Vol. 108, pp. 231-238. ASME, New York.

41. Panchal, C. B., and Sasscer, D. S. (1991). Biofouling and corrosion fouling of plain and enhanced aluminum surfaces. In *Fouling and Enhancement Interactions* (T. J. Rabas and J. M. Chenoweth, eds.), HTD-Vol. 164, pp. 9–15. ASME, New York.

42. Penney, W. R. (1968). Heat exchanger. U.S. Pat. 3,407,871.

43. Pfeffer, R., Rossetti, S., and Lieblein, S. (1966). Analysis and correlation of heat transfer-coefficient and friction data for dilute gas–solid suspensions. *NASA Tech. Note* TN D-3603.

44. Rabas, T. J. (1989). Selection of the energy-efficient enhancement geometry for single phase turbulent flow inside tubes. In *Heat Transfer Equipment Fundamentals, Design, Applications and Operating Problems* (R. K. Shah, ed.), HTD-Vol. 103, pp. 231-238. ASME, New York.

45. Rabas, T. J., Merring, R., Schaefer, R., Lopez-Gomez, R., and Thors, P. (1990). Heat-rate improvements obtained with the use of enhanced tubes in surface condensers. *Proc. Elect. Power Res. Inst., Condens. Tech. Conf.*, Boston, 1990.

46. Rabas, T. J., Panchal, C. B., Sasscer, D. S., and Schaefer, R. (1991). Comparison of power-plant condenser cooling-water fouling rates for spirally-indented and plain tubes. In *Fouling and Enhancement Interactions* (T. J. Rabas and J. M. Cheneweth, eds.), HTD-Vol. 164, pp. 29–37. ASME, New York.

47. Rabas, T. J., Panchal, C. B., Sasscer, D. S., and Schaefer, R. (1993). Comparison of river-water fouling rates for spirally indented and plain tubes. *Heat Transfer Eng.* 14(4), 58–73.

48. Richardson, P. D. (1967). Effects of sound and vibrations on heat transfer. *Appl. Mech. Rev.* 20, 201–217.

49. Sartor, W. E. (1982). Extended and enhanced tube transfer surfaces to improve heat transfer. In *Second Symposium on Shell and Tube Heat Exchangers* (W. R. Apblett, Jr., ed.), pp. 411–418. American Society for Metals, Metals Park, OH.

50. Schluderberg, D. C., Whitelaw, R. L., and Carlson, R. W. (1961). Gaseous suspensions—A new reactor coolant. *Nucleonics* 19(8), 67–76.

51. Schmidt, W. A. (1933). Heat interchanging apparatus. U.S. Pat. 1,916,337.

52. Sephton, H. H. (1975). Upflow vertical tube evaporation of sea water with interface enhancement; process development by pilot plant testing. *Desalination* 16, 1–13.

53. Sheikholeslami, R., and Watkinson, A. P. (1986). Scaling of plain and externally finned heat exchanger tubes. *J. Heat Transfer* 108, 147–157.

54. Somerscales, E. F. C., and Curcio, L. A., Jr. (1990). Effect of calcium sulfate on pool boiling of enhanced heat transfer surfaces. *Am. Soc. Mech. Eng. [Pap.]* 90-WA/HT-2.

55. Somerscales, E. F. C., Ponteduro, A. F., and Bergles, A. E. (1991). Particulate fouling of heat transfer tubes enhanced on their inner surface. In *Fouling and Enhancement Interactions* (T. J. Rabas and J. M. Chenoweth, eds.), HTD-Vol. 164, pp. 17–28. ASME, New York.

56. Spence, S. P., Marshall, W. R., and Steen, H. W. (1965). Resonating pulse reactor. U.S. Pat. 3,167,395.

57. Starner, K. E. (1976). Effect of fouling factor on heat exchanger design. *Am. Soc. Heat. Refrig. Air Cond. Eng. J.* 18, 39–41.

58. Taborek, J., Knudsen, J. G., Aoki, T., Ritter, R. B., and Palen, J. W. (1972). Fouling—The major unresolved problem in heat transfer. Part II: Generalized predictive methods. *Chem. Eng. Prog.* 68(7), 69–78.

59. Tleimat, B. W. (1971). Performance of a rotating flat-disk wiped-film evaporator. *Am. Soc. Mech. Eng. [Pap.]* 71-HT-37.

60. Townsend, R. W. (1987). Minimizing coke buildup in transfer line heat exchangers. U.S. Pat. 4,703,793.

61. Troup, D. H., and Richardson, J. A. (1978). Scale nucleation on a heat transfer surface and its prevention. *Chem. Eng. Commun.* 2, 167–180.

62. Troup, D. H., and Richardson, J. A. (1978). The link between the corrosion and calcium carbonate scaling susceptibilities of heat transfer surfaces. *Werkst. Korros.* 29, 312–320.

63. van der Mast, V. C., Read, S. M., and Bromley, L. A. (1976). Boiling of natural seawater in falling film evaporators. *Desalination* 18, 71–94.

64. Watkinson, A. P. (1990). Fouling of augmented heat transfer tubes. *Heat Transfer Eng.* 11(3), 57–65.

65. Watkinson, A. P. (1990). Fouling of augmented and enhanced tubes—Experimental. In *Fouling von Warmeubertrangungsflachen—Fouling of Heat Exchanger Surfaces*, GVC-Diskussionstag., 1990, pp. 14–28. Gesellschaft Verfahrenstechnik und Chemieingenieurwesen, Munich, Germany.

66. Watkinson, A. P. (1991). Interactions of enhancement and fouling. In *Fouling and Enhancement Interactions* (T. J. Rabas and J. M. Chenoweth, eds.), HTD-Vol. 164, pp. 1–7. ASME, New York.

67. Watkinson, A. P., and Epstein, N. (1970). Particulate fouling of sensible heat exchangers. In *Heat Transfer, Inter. Heat Transfer Conf., 4th, 1970*, Vol. I, pp. 1–12.

68. Watkinson, A. P., and Martinez, O. (1975). Scaling of spirally indented heat exchanger tubes. *J. Heat Transfer* **97**, 490–492.

69. Watkinson, A. P., Louis, L., and Brent, R. (1974). Scaling of enhanced heat exchanger tubes. *Can. J. Chem. Eng.* **52**, 558–562.

70. Webb, R. L. (1987). Enhancement of single-phase heat transfer. In *Handbook of Single-Phase Convective Heat Transfer* (S. Kakaç, R. K. Shah, and W. Aung, eds.), Chapter 17. Wiley, New York.

71. Webb, R. L. (1994). *Principles of Enhanced Heat Transfer*. Wiley, New York.

72. Webb, R. L., and Kim, N.-H. (1989). Particulate fouling in enhanced tubes. In *Heat Transfer Equipment, Fundamentals and Design, Applications and Operating Problems* (R. K. Shah, ed.), HTD-Vol. 108, pp. 315–323. ASME, New York.

73. Webb, R. L., Bergles, A. E., and Junkhan, G. H. (1983). *Bibliography of U.S. Patents on Augmentation of Convective Heat and Mass Transfer*, Rep. No. HTL-32 (under DOE Contract No. DE-FG07-81 ID 12222). Iowa State University, Ames.

74. Welder, B. Q., and Partridge, E. P. (1954). Practical performance of water-conditioning gadgets. *Ind. Eng. Chem.* **46**, 954–960.

75. Withers, J. G., Jr. (1977). Heat exchange apparatus and method of controlling fouling therein. U.S. Pat. 4,007,779.

76. Withers, J. G., Jr., Habdas, E. P., and Jurmo, M. W. (1973). Internally ridged heat transfer tube. U.S. Pat. 3,779,312.

77. Yeh, H.-C. (1989). Device for producing high heat transfer in heat exchanger tubes. U.S. Pat. 4,832,114.

Laser Speckle Photography Technique Applied for Heat and Mass Transfer Problems

K. D. KIHM

Department of Mechanical Engineering
Texas A & M University, College Station, Texas

I. Introduction

Speckle photography technique [1] is an optical diagnostic method to measure nonintrusively the refractive index gradients of inhomogeneous medium, also called a phase object, based on light ray refraction and deflection. The measured refractive index gradients are converted into the medium temperature and density information using pertinent physical equations. The technique provides highly accurate and quantitative information on the temperature and density fields, with an excellent spatial resolution.

The encyclopedic definition of *optical speckle* is "a phenomenon in which the scattering of light from a highly coherent source, such as a laser, by a rough surface or inhomogeneous (refractive index) medium generates a random-intensity distribution of light that gives the surface or medium a granular appearance [2]." Here, the random-intensity distribution results from the randomly constructive or destructive interference of the scattered light rays.

Speckle photography is frequently confused with particle image velocimetry (PIV) under dense seeding particle concentration [3]. However, specklelike images of PIV are the result of overlapping of Mie scattering images from the physically seeded particles and not from optically created speckles. The dislocations of speckle images result from the flow–particle displacement in PIV. In this chapter, speckle photography refers to an

255

optical method that measures the refractive index gradients of a phase object based on the optically created and refractively dislocated speckle patterns.

Part II introduces the operating principle of the speckle photography technique and discusses its unique features compared with other competing optical methods.

In Part III, several different natural heat convection problems are presented for which speckle photography successfully measures the heat transfer coefficients without the need of corrections for the conduction and radiation losses. Speckle results provide data with high spatial resolution and make the experimental processes more reliable.

Part IV shows that speckle photography measures the statistical properties for turbulent flows with density and temperature fluctuations. Also discussed is tomographic reconstruction of a density field from multiple specklegrams.

The potential of speckle photography for high-temperature applications such as combusting flames is discussed in Part V. The viability of the technique emerges from its applications for premixed Bunsen flames of axisymmetric and laminar configuration.

Finally, Part VI brings an example application of speckle photography for a liquid flow with density variation where the refractive index behaves quite differently from that of air or other gases. Part VII closes with concluding remarks.

II. Speckle Photography Technique

Section A discusses the basic principle of laser speckle photography and its advantages over interferometry. In Sections B and C, two alternative data processing methods for specklegrams are presented. Section D discusses speckle interferometry as a variation of speckle photography. A brief comparison of speckle photography is given and speckle interferometry is discussed in Section E.

A. Operating Principle of Speckle Photography

The early stage of speckle photography attempted to use incoherent white light that allowed only a qualitative visualization of the medium index field [4]. The use of a laser for the system made speckle photography a truly quantitative and rigorous measurement tool [5, 6]. This section summarizes the basic principles of a modern laser speckle-photography system [7].

The randomly deflected and interfered light rays from spatially distributed optical speckles beyond the ground glass (optical deflector), as illustrated in Fig. 1(a). A bright optical speckle forms for coherent or constructive ray interference and a dark speckle results from incoherent or destructive interference. Diffraction laws [1, 8] give the size of an individual speckle as $d = 2.44\lambda \cdot H/D$, where λ is the wavelength of the laser radiation; H is the distance of the observation point from the deflector, that is, the ground glass surface; and D is the dimension on the grain size of the ground glass plate. Li and Chiang [9] presented a detailed analysis for calculating the fully three-dimensional (3D) dimension of laser speckle formation.

(a)   W/O TEST FIELD
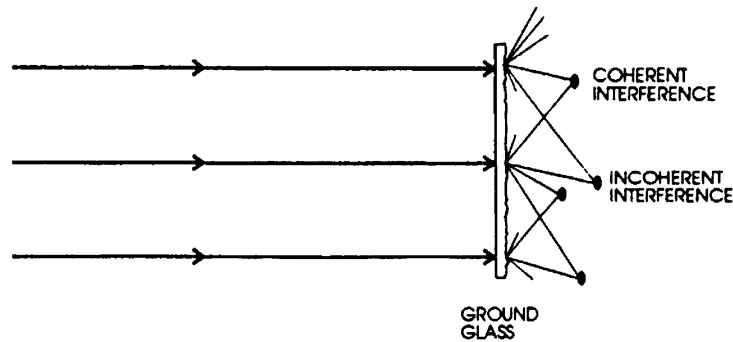
(b)   W/ TEST FIELD
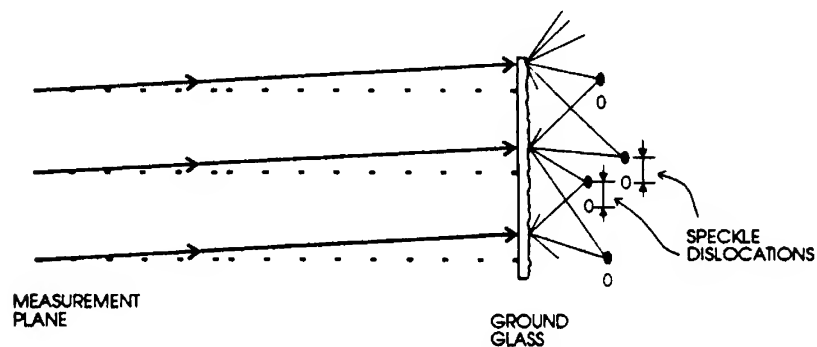
FIG. 1. Schematic illustration of formation of optial speckles and their dislocations (a) without test field and (b) with test field [55].

When a test section is presented, the light rays refract at a small angle because of the variable density or refractive index field, and the corresponding speckles form at different locations (Fig. 1(b)). A specklegram is taken by photographically overlapping the original speckles without a test section, and the dislocated speckles with a test section. The resulting speckle photograph, or specklegram, carries the information on both sizes of the speckle images and the amount of the speckle dislocations.

The optical layout of the speckle photography system closely resembles that of a Schlieren system [10]. Figure 2 shows the setup of the speckle photography system configured by Kastell et al. [11]. A helium–neon laser beam of λ = 632.8 nm expands to 120 mm in diameter and collimates via the first parabolic mirror to form parallel light rays throughout the test section. After passing through the test section, the light rays reflect from the second parabolic mirror and collimate its focal point. After the focal point, the light rays illuminate on the optical-grade ground glass plate (Fig. 3(a)) whose average grain size is on the order of one micron [12]. Commercial ground glass with coarser grains (Fig. 3(b)) does not generate speckles with acceptable resolution for optical measurement.

Laser speckles also can be generated by using a diffuser plate sprayed with an acrylic paint sealant [13]. However, the random phase of the diffuser plate is usually coarser than the sandblasted ground glass plate. Since the speckle resolution depends on the scale of the surface grains, the ground glass plate is preferred for its finer grain size.
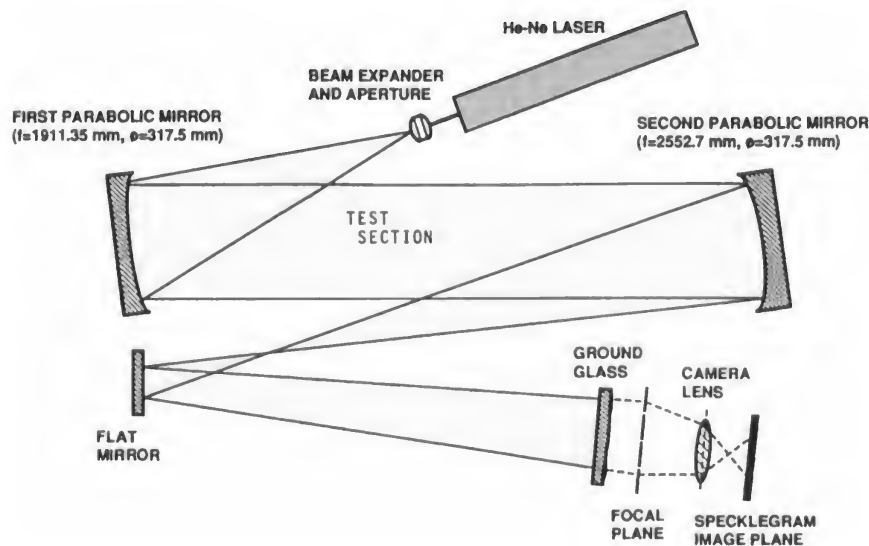
FIG. 2. Optical layout of speckle photography system [11]. He–Ne, helium–neon.
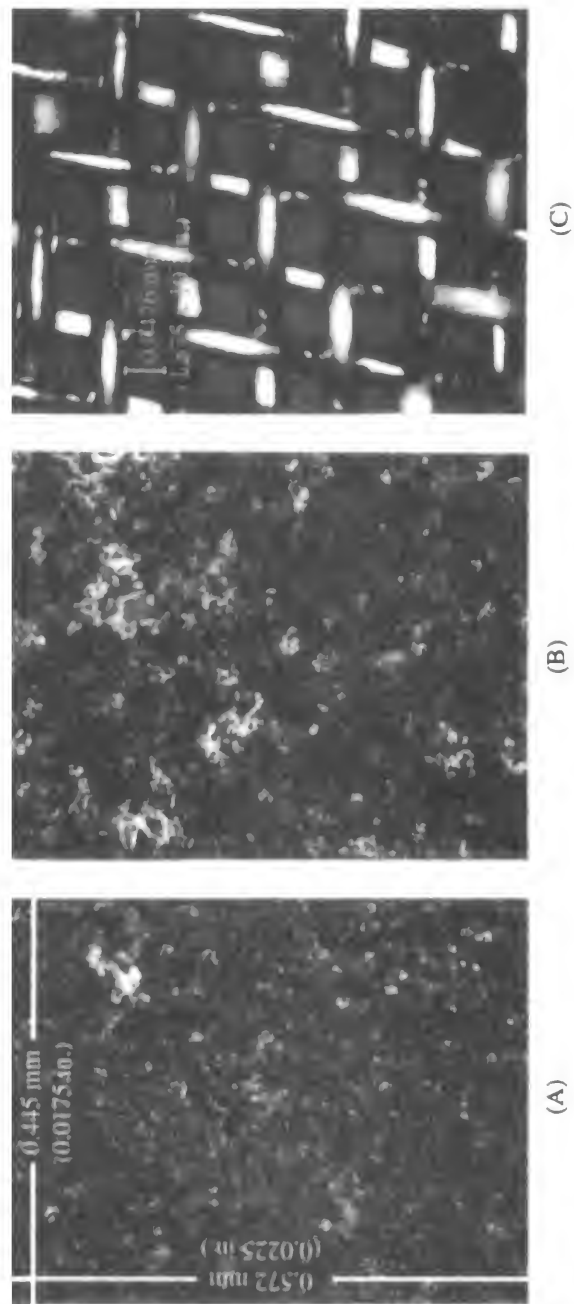
FIG. 3. Various diffracting surfaces under ×200 magnification. (a) Experimental grade ground glass; (b) commercial grade ground glass; (c) 500 × 500 copper wire mesh [12].

The speckle dislocation due to the presence of an inhomogeneous test field is schematically illustrated in Fig. 4. Without going through a test field, the light forms a speckle at the location I on the image plane. When the test field is present, the light ray refracts at a small angle α because of the density variation, and forms another speckle at I' on the specklegram. From the geometrical similarity, $\varepsilon = \alpha/m$ where the magnification of the second parabolic mirror m is equivalent to the ratio of the image distance to the object distance, that is, $m = b/a$. The speckle dislocation Δ is then expressed as

$$\Delta = m' \times \delta = m' \times c \times \varepsilon = \frac{m'}{m} \times c \times \alpha, \qquad (1)$$

where m' is the magnification of the camera lens, and δ the amount of speckle dislocation on the focusing plane for speckle imaging. The distance between the ground glass and the focal plane of the camera lens is denoted by c. This distance is called the *defocusing distance*.

The test section image is focused onto the ground glass. However, the camera focusing plane for the speckle image recording must be slightly away from the ground glass, because the speckle dislocations are not detectable on the ground glass itself (Fig. 1). The defocusing thus is inevitable to record a detectable dislocation of speckle images. Nevertheless, the defocusing distance must be minimized to reduce image blur. In estimating the optical defocusing distance, we must consider both optical parameters and test conditions. As a rule of thumb, however, about 2 cm of defocusing is recommended for the initial attempt at recording specklegrams [14]. The analysis for calculating the image blur in specklegram recording has been developed based on geometrical ray optics [15]. The
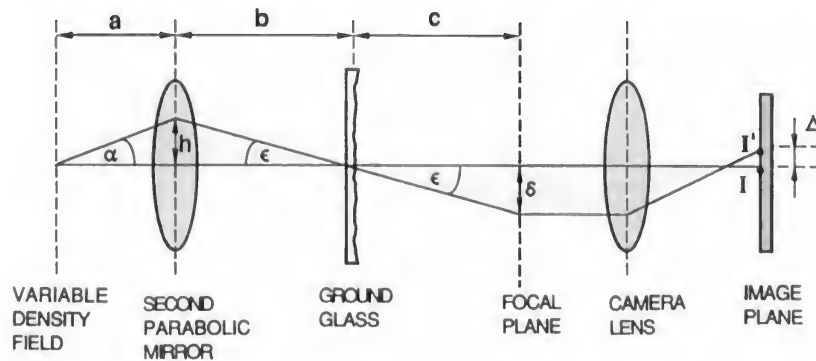
FIG. 4. Illustration of speckle dislocations by ray optics [11].

analysis suggests that the test object be placed near the optical axis to reduce the blur and that mirrors of larger diameters with longer focal lengths enhance the measurement sensitivity of the speckle photography system.

The main advantages of speckle photography over conventional optical methods relying on ray refraction, such as wave front interferometry, the Schlieren method, and holography, can be summarized as follows [16]:

1. The optical setup is simple because of the single beam path that needs no reference beam
2. Requirements concerning mechanical stability against the external disturbance are less stringent
3. Specklegrams have higher spatial resolution of information density than do interferograms
4. Speckle photography using a short pulsed laser can effectively record turbulence flow properties, whereas interferometry fails to construct any stable fringes for turbulent flows.

The most striking advantage of speckle photography over conventional methods is that quantitative information on the refractive index (or its gradient) is obtained along each beam trajectory, independent of one another, without the need to know the values of adjacent beams. This important feature of the speckle method makes it suitable for turbulent flow studies, whereas conventional methods fail because they must be interpreted simultaneously over the entire field.

B. Point-by-Point Interrogation of a Specklegram

The point-by-point interrogation [17] of a specklegram determines the distance of the speckle dislocation Δ from the spacing of Young's fringes that are generated by illuminating the specklegram with a low-power laser (Fig. 5). The principle of Young's fringes [18] states that the fringe spacing s decreases with an increase of the speckle dislocation Δ; that is,

$$s = (s_y, s_z) = \frac{\lambda \times d}{\Delta}, \tag{2}$$

where $s_y = s \cos \theta$ and $s_z = s \sin \theta$, with θ being the tilt angle of the fringe orientation on the y-z recording plane; λ is the wavelength of the interrogating laser beam ($\lambda = 632.8$ nm for a helium–neon laser); and d is the distance between the interrogating specklegram and the imaging screen.

A charge-coupled device (CCD) camera digitizes the fringe images for a computerized evaluation of the fringe characteristics [19]. The uncertain-
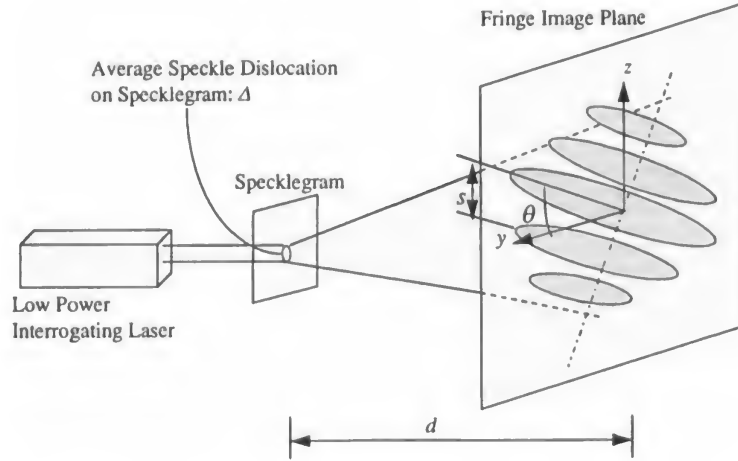
FIG. 5. Point-by-point data analysis by measuring Young's fringes generated from specklegram.

ties associated with manually reading fringe spacings have been reported to be as high as $\pm15\%$ in some cases [20]. Erbeck [21] has developed a more sophisticated specklegram processing system that uses a rotating ground glass screen to enhance the signal-to-noise ratio (SNR) in reading fringe spacings (Fig. 6). The rotating ground glass screen reduces the fluctuating small-scale speckle noise. The computerized analysis, using an advanced fringe reading software, is able to reduce the uncertainties below $\pm3\%$. Less popular alternative techniques for interrogating specklegrams are presented elsewhere [22–24].

Within the context of geometrical optics, Fermat's principle describes the propagation of a single light ray through a medium and states that the light wave takes a path that involves the least travel time. The use of a paraxial approximation, that is, the amount of ray diffraction in the medium being very small and the light ray remaining nearly straight (Fig. 7), the diffraction angle components ε_y and ε_z are expressed as the path integral along the optical axis [25]:

$$\tan \varepsilon_y \cong \varepsilon_y(y, z = z_k) = \int_{\zeta_1}^{\zeta_2} \frac{1}{n(x,y)} \frac{\partial n(x,y)}{\partial y} dx, \qquad (3a)$$

$$\tan \varepsilon_z \cong \varepsilon_z(y, z = z_k) = \int_{\zeta_1}^{\zeta_2} \frac{1}{n(x,y)} \frac{\partial n(x,y)}{\partial z} dx. \qquad (3b)$$
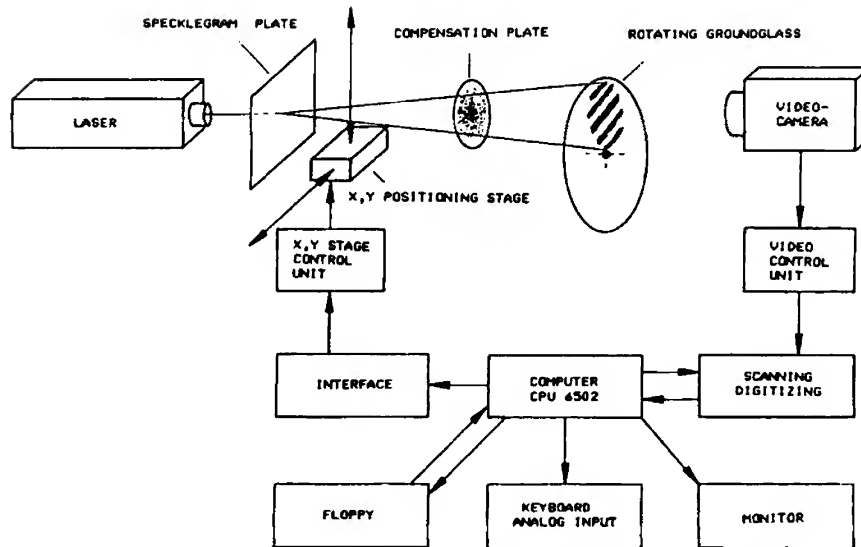
FIG. 6. Setup for automatic point-by-point evaluation of specklegram [21].

Equations (3a) and (3b) describe the x-y cross section at $z = z_k$. Repeated slicings at different z coordinates describe the whole 3D field. The y-z recording plane is perpendicular to the optical axis x, and the light ray occupies the test field between ζ_1 and ζ_2 along the optical axis.

Substituting Eqs. (1) and (2) into Eqs. (3a) and (3b) constitutes the basic relations between the measured fringe spacing and the medium refractive
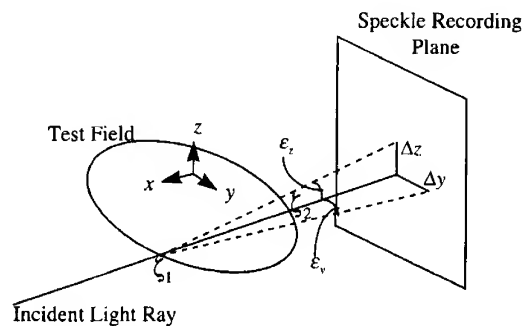
FIG. 7. Ray diffractions due to a phase object (test field) and their deflection angles.

index field:

$$s_y(y, z_k) = \frac{m}{m'} \frac{\lambda d}{c} \left[\int_{\zeta_1}^{\zeta_2} \frac{1}{n} \frac{\partial n}{\partial y} dx \right]^{-1}, \tag{4a}$$

$$s_z(y, z_k) = \frac{m}{m'} \frac{\lambda d}{c} \left[\int_{\zeta_1}^{\zeta_2} \frac{1}{n} \frac{\partial n}{\partial z} dx \right]^{-1}, \tag{4b}$$

which depict that the fringe spacing reflects the line-of-sight effect from an integrated contribution of the refractive index field along the occupied laser ray. The integral expressions of Eqs. (4a) and (4b) must be inverted to determine the refractive index field distribution on the tomographic interrogating plane.

C. FULL-VIEW INTERROGATION OF A SPECKLEGRAM

An alternative reconstruction method is a full-view semiquantitative decoding by spatial filtering of a specklegram [26]. Figure 8 shows an optical arrangement for spatial filtering where the specklegram is illuminated with an expanded collimated beam. A Fourier transforming lens (the second lens) produces the spatial Fourier transform of the speckle patterns in the back focal plane of the lens. A small and eccentric filtering aperture placed at the focal plane selects the diffraction order and direction of speckle displacement. A fringelike pattern can be reconstructed on the imaging screen, as shown for the isothermal vertical wall in Fig. 9 [27]. The visible patterns indicate constant density or temperature gradient contours, and these patterns are analogous to the conventional interferometric fringes in the infinite fringe width mode [28]. Although the resolution and accuracy are low for accurate quantitative information, the spatial filtering method is useful for a quick qualitative check of the recorded flow situation prior to the more time-consuming point-by-point evaluation of Young's fringes.
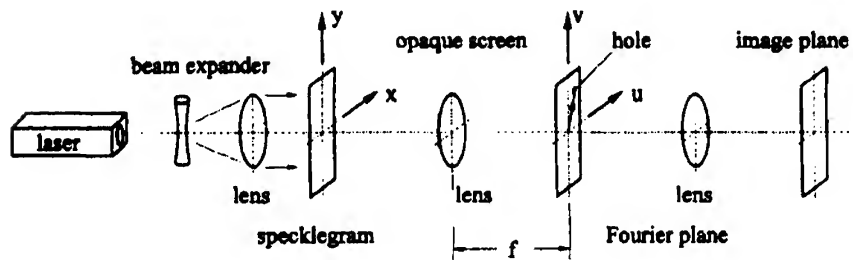
FIG. 8. Optical spatial filtering of a specklegram: The range of visible spatial frequencies is determined by the position of the hole [26].
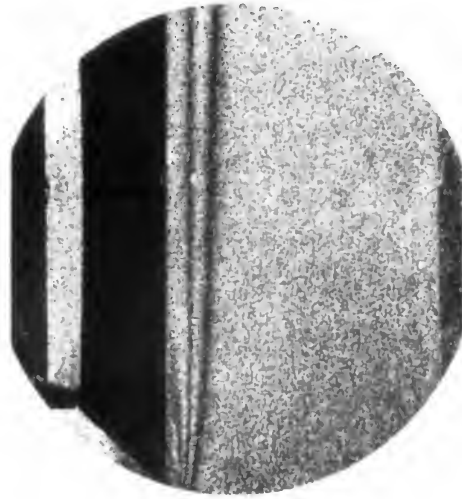
FIG. 9. Whole-field reconstruction of a laminar, natural convection flow along an isothermal vertical wall [27].

D. SPECKLE INTERFEROMETRY

Speckle interferometry [29], an alternative visualization method using optical speckles and their dislocations, is a hybrid system of speckle photography and interferometry, as schematically shown in Fig. 10. Optical speckles are essentially generated by passing the object beam through a ground glass, as in speckle photography. However, speckle interferometry devises an additional reference beam that eventually merges with the
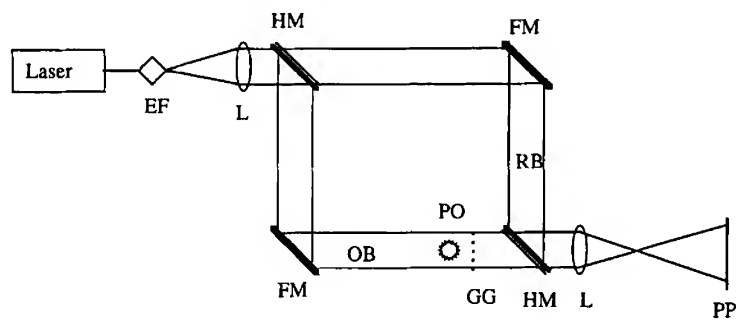
FIG. 10. Schematic illustration of speckle interferometry. EF, expander–filter; FM, full-reflecting mirror; GG, ground glass; HM, half-reflecting mirror; L, lens; OB, object beam; PO, phase object; PP, photographic plate; RB, reference beam.

object beam via the half-reflecting mirror. A slight variation of speckle interferometry is a double-hole aperture that can substitute for the reference beam (Fig. 11). This optical arrangement is called speckle shearing interferometry, where the speckle images constructed by the two holes are separated, sheared, and eventually imaged together on the recording plane [30]. This is analogous to the beam separation and merging of interferometry. Speckle shearing interferometry generates interferograms similar to those generated by speckle interferometry. Therefore, these fringes can be read in the same way as for interferometry, with alternate dark fringes indicating a 2π phase shift equivalent to a single wavelength differential in the optical path.

Both speckle interferometry and speckle shearing interferometry are double-exposure techniques, one with and one without the presence of a test field. The local brightness of speckles depends on whether the combination of the two speckles are coherent or incoherent. The combination of the two speckle patterns results in a fringe pattern on the photographic negative. Thus, by evaluating the fringe pattern, information regarding the changes in the refractive index between the two exposures is obtained.

Viewing these fringes with a higher SNR can be achieved by the whole-field filtering of the speckle interferogram, which is similar to the whole-field filtering of speckle photography (Fig. 8). Figure 12 shows a typical shearing interferogram of gaseous Bunsen flame obtained after the whole-field filtering [31].
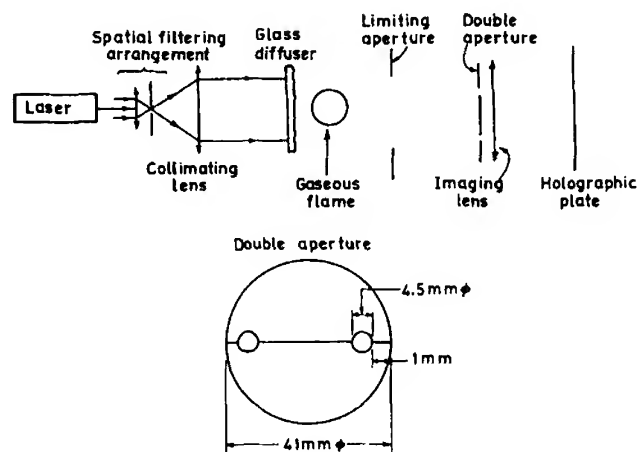
FIG. 11. Schematic of experimental setup for recording a speckle shearing interferogram of the temperature field of gaseous flame [30].
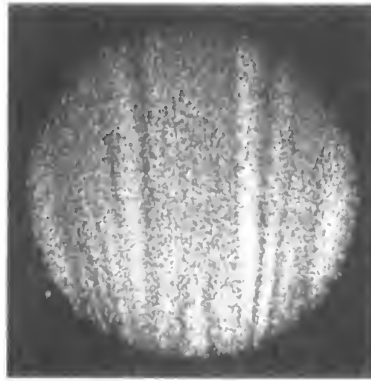
FIG. 12. Speckle shearing interferogram of gaseous flame obtained after whole-field filtering [31].

E. COMPARISON OF SPECKLE PHOTOGRAPHY VERSUS SPECKLE INTERFEROMETRY

Speckle interferometry and speckle shearing interferometry provide information regarding the refractive index itself, while speckle photography provides the gradient of refractive index. Although speckle (or speckle shearing) interferometry offers the convenience of providing a full-field fringe pattern that allows both a qualitative inspection and semiquantitative results, the technique has all the disadvantages of interferometry (Section A). Speckle interferometry was found to be easier than speckle photography in some applications for direct temperature measurements [32]. Nevertheless, speckle interferometry needs *a priori* information on the direction of temperature gradient to complete the quantitative data analysis. It also requires a photographic film with higher resolution compared with speckle photography. For these reasons, speckle photography is more popular for thermal and fluid applications. The subsequent chapters will primarily discuss the applications of speckle photography.

III. Applications to Natural Convection Problems

Laser speckle photography has been applied for natural convection problems where the refractive index gradient is strong only in a single direction, for example, in the y-direction in Fig. 7. The refractive index gradient is zero along the ray parallel to the x-direction. A typical example that satisfies these two conditions is a vertical isothermal wall aligned parallel to the x-z plane.

Section A presents a speckle data analysis for one-dimensional (1D) ray refraction, while Section B discusses the application of speckle photography for a natural convection heat transfer coefficient. Section C shows applications for natural convection flows along an isothermal vertical wall, Section D for thermal boundaries along an isothermal vertical channel, and Section E for a horizontal isothermal plate. Finally, Section F discusses the heat transfer and boundary layers for converging channels with different inclination angles.

A. SIMPLIFIED DATA REDUCTION FOR ONE-DIMENSIONAL REFRACTION

For such a simple geometry allowing 1D refraction, such as a vertical isothermal wall, Eq. (4b) is zero and Eq. (4a) reduces to

$$\frac{\partial n}{\partial y} = \frac{m}{m'} \cdot \frac{\lambda d}{cL} \cdot \frac{1}{s_y},\tag{5}$$

where L denotes the dimension of the test field measured along the optical axis. The chain rule of differentiation converts Eq. (5) into an expression for a temperature gradient as

$$\frac{\partial T}{\partial y} = \frac{m}{m'} \cdot \frac{\lambda d}{cL} \cdot \frac{1}{s_y} \cdot \left(\frac{\partial n}{\partial T}\right)^{-1},\tag{6}$$

where the refractive index change per unit temperature, $\partial n/\partial T$, for air at the 632.8 nm wavelength of a helium−neon laser, is [28]

$$\frac{\partial n}{\partial T} = -\frac{1.075 \times 10^{-6}}{(1 + 0.003681847)^2},\tag{7}$$

where T is in degrees Centigrade. The use of the ideal gas equation of state, together with the Gladstone-Dale relationship [33], $n = 1 + K \cdot \rho$, with K being the Gladstone-Dale constant (for air 0.2257×10^{-3} m^3/kg at $\lambda = 632.8$ nm), converts Eq. (5) into an expression for the density gradient, that is,

$$\frac{\partial \rho}{\partial y} = \frac{m}{m'} \cdot \frac{\lambda d}{cL} \cdot \frac{1}{s_y} \cdot \frac{1}{K}.\tag{8}$$

A high refractive index gradient increases the speckle dislocations and decreases the fringe spacing s_y (Eq. (5)). A small fringe spacing reflects a large temperature or density gradients (Eq. (6) or (8)). Another point is that the fringes are perpendicular to the average direction of the speckle dislocations, which is parallel to the primary direction of the refractive index, temperature, and density gradients.

Figure 13 shows the fringe patterns at five locations inside and outside the thermal layer of an isothermal vertical wall [11]. Near the wall where the temperature gradient is very steep, the fringes are very definite and the spacings are narrow (inset photograph (d)). The fringe spacing becomes wider as the edge of the boundary layer is approached (inset photograph (e). The fringes disappear outside the thermal layer where there is no detectable dislocation of speckles (inset photograph (b)). The orientation of the fringes around the leading edge is altered because the fringes (or the primary direction of speckle dislocation) must appear perpendicular to a local temperature gradient (inset photographs (a) and (c)).

B. DETERMINATION OF THE HEAT TRANSFER COEFFICIENT USING SPECKLEGRAM DATA

The heat transfer to or from a solid surface can simulate many popular engineering problems, for example: cooling in electronic packaging, turbine blade cooling, and a variety of heat exchangers. Assuming a steady problem with uniformly distributed heat sources, such as a plate heater affixed to the solid base shown in Fig. 14, the energy balance yields

$$q''_{total} = q''_{radiation} + q''_{conduction} + q''_{convection} . \qquad (9)$$

One traditional measurement technique for heat convection involves setting the total heat generation q''_{total} and then determining the heat radiation $q''_{radiation}$, and the conduction losses $q''_{conduction}$. These last two terms are subtracted from q''_{total} to determine $q''_{convection}$ and h; that is,

$$h = \frac{\left(q''_{convection} \equiv q''_{total} - q''_{radiation} - q''_{conduction} \right)}{T_w - T_x} . \qquad (10)$$

This method requires that the whole experimental apparatus—other than the test surface—be wrapped with bulky insulation material to reduce the losses to the environment, which are not easy to estimate accurately. The uncertainties in determining the radiation heat losses are equally difficult to quantify. Incorrect evaluation of these heat losses can significantly affect the measurement accuracy and uncertainties, especially for natural convection problems for which the heat loss amounts can compare with the amount of convection heat transfer itself.

Such difficulties are alleviated by directly measuring the heat transfer coefficient h, without involving the total heat generation rate. At the wall, the velocity is zero and the heat transfer into the fluid takes place by radiation and conduction; that is,

$$q''_{total} = q''_{radiation} + q''_{conduction} . \qquad (11)$$
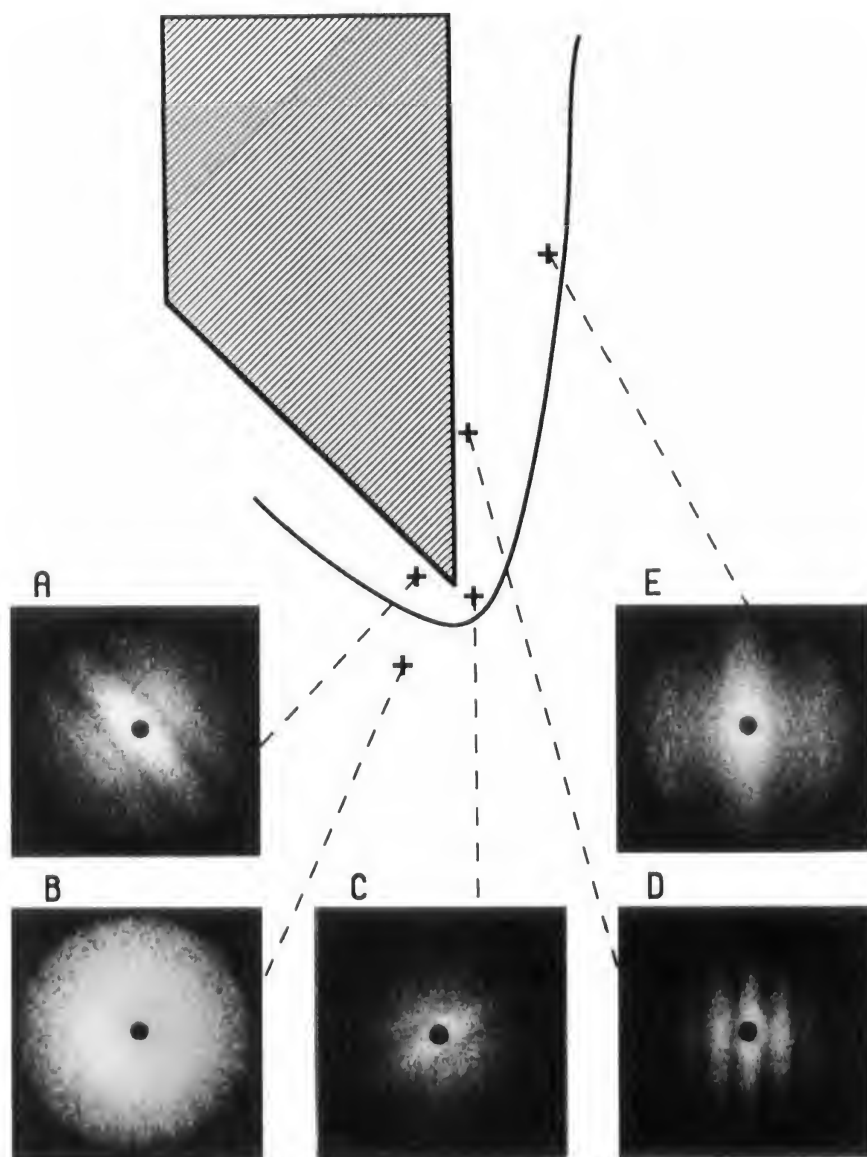
FIG. 13. Fringe spacings and orientations at five different locations (a)-(d) around the leading edge of an isothermal vertical wall at $T_w = 86.2°C$ [11].
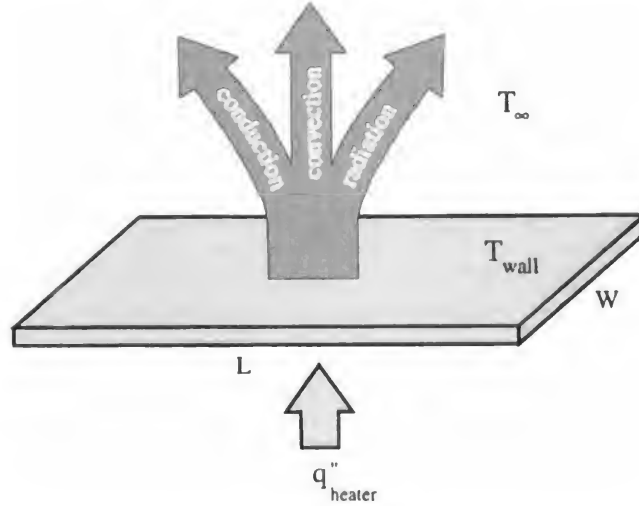
Fig. 14. Heat transfer modes of a plate heated by means of surface heating [12].

The heat transfer into the fluid away from the wall can be expressed as

$$\dot{q}''_{total} = \dot{q}''_{radiation} + \dot{q}''_{convection} \,. \tag{12}$$

Combining Eqs. (11) and (12) with Newton's law of cooling [34], the convection heat transfer coefficient is given as

$$h = -\frac{k(\partial T/\partial y)_{wall}}{T_w - T_\infty}, \tag{13}$$

where the y-coordinate is normal to the heater surface. The heat transfer coefficient can be determined once the wall temperature gradient $(\partial T/\partial y)_{wall}$ is provided from the measurement.

The laser speckle photography technique makes it possible to find the heat transfer coefficient by evaluating the temperature gradient at the solid surface from the measured fringe spacing data (Eq. (6)). The wall temperature and ambient temperature are measured by a traditional means such as a thermocouple probe. Use of the laser speckle photography technique significantly reduces the experimental uncertainties associated with the heat loss corrections and provides a noticeably improved convenience in performing experiments [35].

C. Isothermal Single Vertical Wall

The vertical heated plate has been the standard for comparing different optical methods, particularly since its well-established analytical and numerical solutions are available for the temperature profile [36–40]. The viability of laser speckle photography has been examined by applying it to the isothermal vertical wall shown in Fig. 13. Using Simpson's rule [41], the temperature profiles were calculated by numerically integrating the temperature gradient data obtained from the fringe spacing results (Eq. (6)).

Temperature data at $x = 14.2$ mm and $x = 50.0$ mm are presented in Fig. 15 for several different wall temperature conditions. In this presentation, the kinematic viscosity of air was evaluated at the reference temperature $T_r = T_w - 0.38(T_w - T_\infty)$, as suggested by Sparrow and Gregg [42]. The similarity solution by Ostrach [43] assumed an ideal thermal boundary layer starting exactly at the leading edge, while the practical boundary layer starts before the leading edge and grows thicker than the ideal one [44]. This thicker boundary layer makes the measured temperature data higher than the theoretical predictions, particularly in the region near the leading edge at $x = 14.2$ mm.
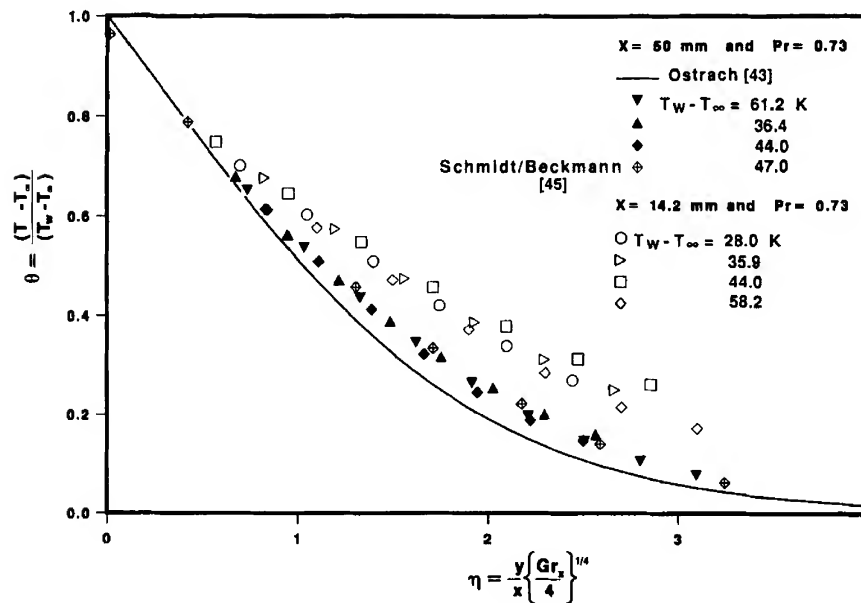
Fig. 15. Dimensionless temperature profiles as a function of dimensionless similarity variables measured at $x = 14.2$ mm and $x = 50.0$ mm for different wall temperatures [11]. Pr, Prandtl; Gr, Grasof.

The solid symbols in Fig. 15 represent developed temperature profiles away from the leading edge at x = 50.0 mm, where the leading edge effect has been diminished. Also presented is a set of data obtained at the same x location by Schmidt and Beckmann [45], who used a miniature thermocouple sensor probe to measure temperature. The speckle data provide higher measurement resolution than does the thermocouple probe and show good agreement with the theory.

Shu and Li [27] used an optical system to record a specklegram and a shearing interferogram (Fig. 16) simultaneously to visualize an isothermal vertical wall. This combined system used a pulsed ruby laser as the light source for high-speed data recording. The interferogram gives a qualitative examination of the field, and the fringe analysis [28] of the interferogram provides temperature data. The two measurements showed close agreement in the temperature profile for the region away from the leading edge.

Wernekinck and Merzkirch [46] conducted a more rigorous comparison. Figure 17 shows an excellent comparison of data obtained by the speckle photography technique, a shearing interferometer using a Wollaston prism, a Mach-Zehnder interferometer, and Schlichting's similarity results [47]. The results are plotted as dimensionless temperature $\theta \equiv (T - T_x)/(T_w - T_x)$ versus normalized y-distance from the wall, $\eta = y/\delta$, with δ being the boundary layer thickness. The data for the three methods were taken at the region away from the leading edge, where the flow similarity was satisfied. The data showed good agreement with the similarity solutions.
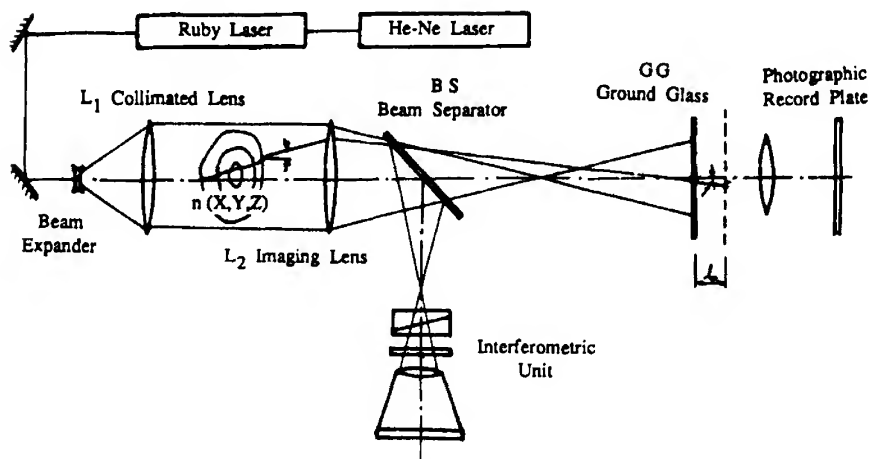
FIG. 16. Optical system for simultaneous recording of a specklegram and a shearing interferogram of a phase object [27]. He–Ne, helium–neon.
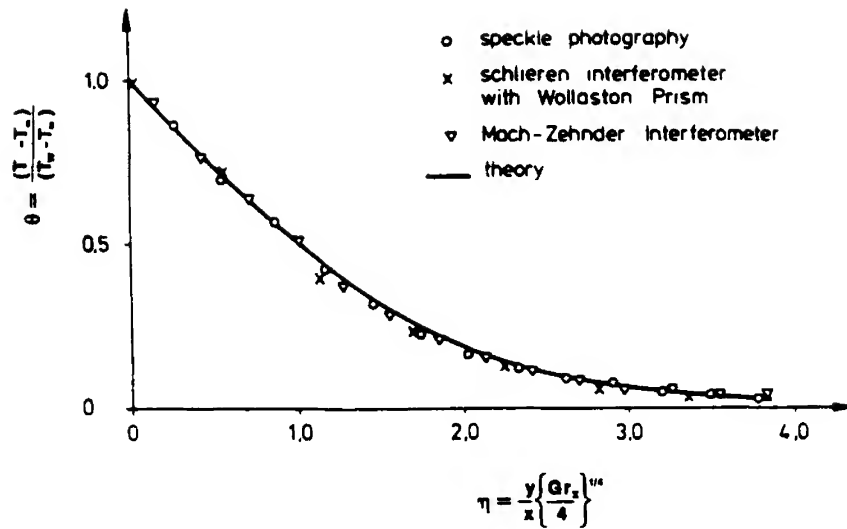
FIG. 17. Nondimensional temperature θ in the laminar, free-convective flow along a vertical, heated plate, plotted against the nondimensional distance from the wall η [46].

D. ISOTHERMAL VERTICAL CHANNEL FLOWS

Speckle photography can visually determine the length of the developing region of the thermal boundary layers growing along the isothermal vertical channel walls [48]. Figure 18 shows the Young's fringe pattern along the channel surface created from the specklegram taken for a 3-mm spaced vertical isothermal channel. The location X_f where Young's fringes completely disappear can be defined as the point of merging of the two separate boundary layers into a fully developed laminar convection channel flow. This is because the temperature gradient at the wall surface reduces to nearly zero once the flow is fully developed. Measurements showed that X_f first increased with the surface-to-ambient temperature ΔT and then decreased with ΔT (Fig. 19). This phenomenon is the well-known *thermal choking* and can be predicted when the concept of thermal drag is introduced. The induced mass flow rate and heat transfer increase with an increasing channel wall temperature. However, once the wall temperature exceeds a critical temperature the induced mass flow rate and heat transfer decrease with increasing wall temperature [49].

The flow reversal occurring in the vertical channel flows can describe the nature of thermal choking. Figure 20 shows the numerically calculated streamlines and isotherms for the aspect ratio $L/b = 8$, where L is the vertical channel length and b is half the channel width [50]. The modified
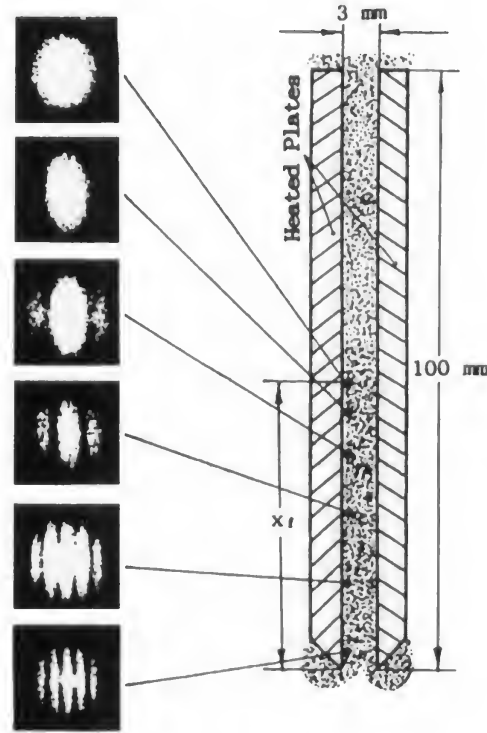
FIG. 18. Experimental determination of the length X_f of the developing region by the changes in Young's fringes [48].

Rayleigh number is [51]

$$\text{Ra}^* \equiv \text{Gr}_b \cdot \frac{\nu}{\alpha} \cdot \frac{b}{L} \equiv \text{Ra} \cdot \frac{b}{L} \equiv \frac{g\beta \cos \gamma (T_w - T_\infty) b^3}{\nu^2} \cdot \frac{\nu}{\alpha} \cdot \frac{b}{L}.$$

With increasing Ra^*, the flow in the channel progresses to deplete streamlines from the channel center, showing the separate boundary layer development. The more concentrated streamlines appearing near the wall suggest increased buoyancy-driven air flow. This increased convection also reduces the penetration of the conduction effect at the inlet, as seen in the isotherm distributions.

When $\text{Ra}^* = 500$, exceeding the critical Rayleigh number of 146 (Fig. 21), the pocketlike streamlines show the formation of recirculating flows. Vena-contracta-like streamlines at the entrance appear to reduce the effective opening. This effectively narrowed opening reduces the incoming air, whereas the increased thermal driving force requires more air flow.
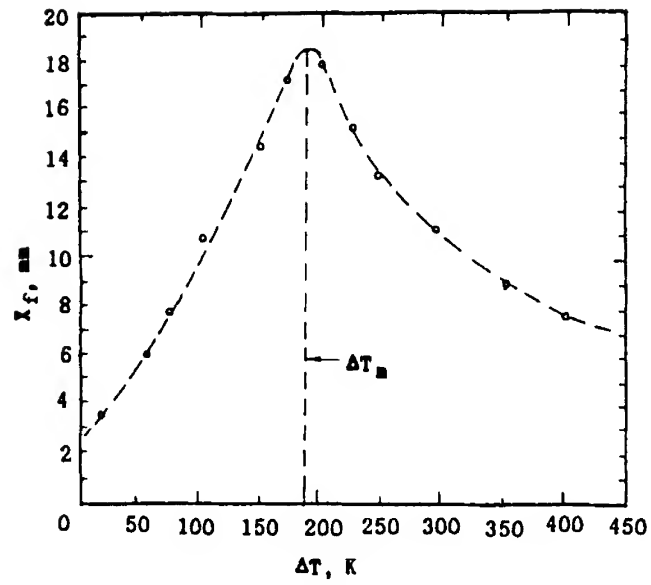
FIG. 19. The length X_f versus the surface-to-ambient temperature difference $\Delta T = T_w - T_\infty$ [48].
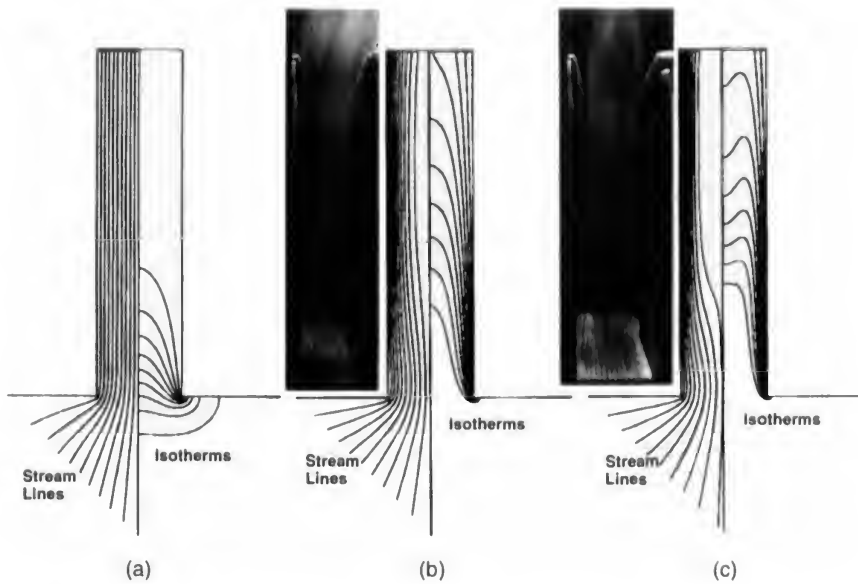
FIG. 20. Calculated flow streamlines and isotherms of convective air (Pr = 0.7) for $L/b = 8$: (a) Ra* = 1.0; (b) Ra* = 100; and (c) Ra* = 500. The photographs indicate smoke stream visualization at Ra* = 130.2 and 501.8, respectively [50].
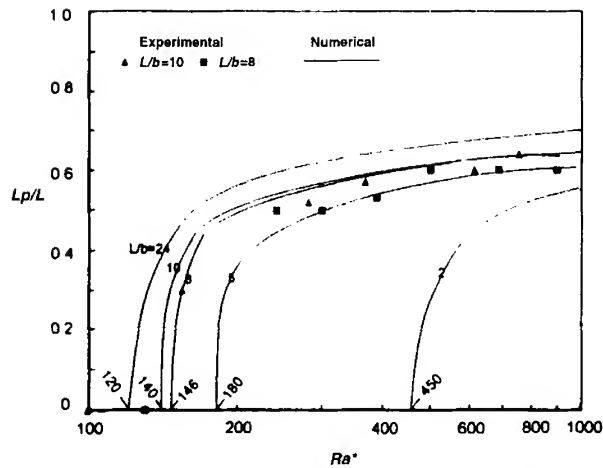
Fig. 21. Experimental and numerical results of the penetration length versus Ra* and numerically predicted onset Rayleigh numbers for flow reversal [50].

When a critical point is reached, the incoming air flow through the inlet is insufficient and additional air is drawn in through the central portion of the channel exit, resulting in flow reversal. The isotherms show that the temperature in the recirculation region is much lower than it is in the convecting flow. This suggests that the convection heat transfer to the recirculating air from the wall is limited and that the presence of the flow reversal decreases the overall heat transfer.

Figure 22 shows the laser speckle data of the local Nusselt numbers for vertical channel flows of different aspect ratios of b/L, where b is the channel width, and L the channel length [52]. For opening ratios down to 0.1, where each wall acts as an independently developing separate boundary layer, the results showed good agreement with the well-established theory of a single vertical isothermal wall of Ostrach, $Nu_x = 0.5046(Gr_x/4)^{0.25}$ [43]. For $b/L = 0.05$, however, the data began to deviate from the theory when the local Grashof number exceeded 5×10^4. The two thermal boundary layers began interfering with each other, which resulted in a decrease in the wall temperature gradients and Nusselt numbers because of thermal choking. When the local Grashof number was larger than 10^5, as in $b/L = 0.05$, the merged flows prevail over uniform temperature profiles across the channel giving no measurable fringes.

Given the condition in Fig. 22, the minimum channel opening for separate layer development was estimated to be $(b/L)_{min} = 0.0584$ using the experimental correlation of Bar-Cohen and Rohsenow [53]. This is consistent with the experimental finding of $b/L = 0.05$, where the thermal boundary layers are expected to merge and interact.
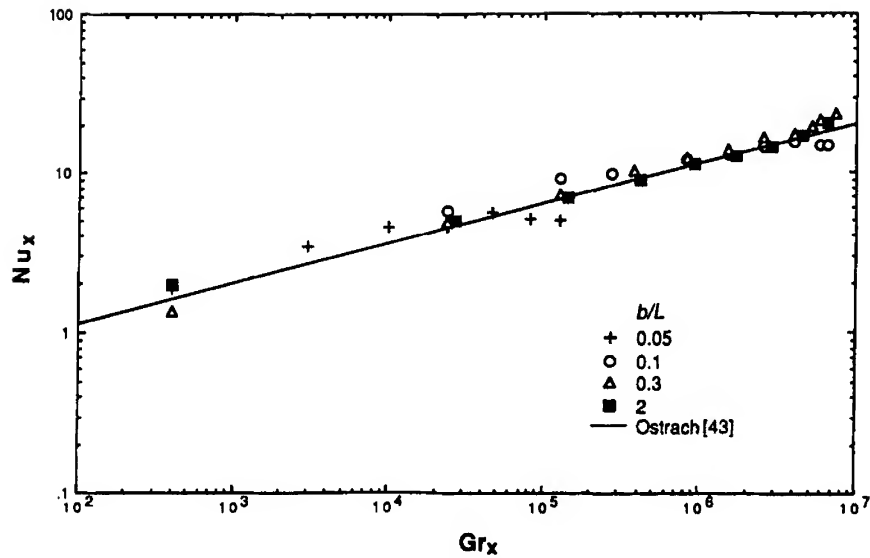
FIG. 22. Local Nusselt number versus local Grashof number for an isothermal vertical channel flow for different aspect ratios [52].

E. UPWARD-FACING ISOTHERMAL SURFACES

The upward-facing isothermal plate (Fig. 23) has been studied in many different ways, but is still under dispute, showing the widely scattering results of heat transfer correlation coefficients [54]. The laser speckle
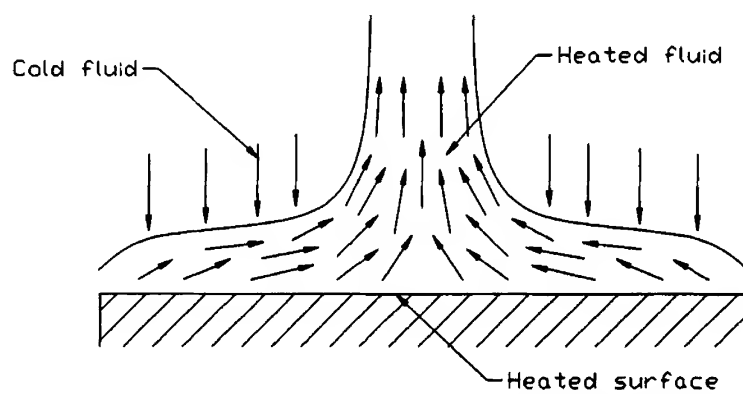
FIG. 23. Thermal flow of natural convection from an upward-facing heated plate [55].

technique has measured the heat transfer coefficients for upward isothermal plates of different aspect ratios [55, 56]. The measured local heat transfer coefficient data were integrated along the plate to evaluate the average or global heat transfer coefficient because most existing data are available only for the average values.

Figure 24 presents the global Nusselt number data for two rectangular isothermal plates with aspect ratios of 1.75 and 15, respectively. The speckle results fall in the band between the one-fourth power-law, an experimental correlation using an electrochemical method for a square plate [57], and the one-fifth power-law prediction, based on the similarity solution for an infinite plate using a mass transfer analogy [58]. The length scale used was traditionally accepted, that is, $x = A/P$ where A is the total surface area and P is the perimeter along the plate edges. The band between one-fourth and one-fifth power consists of the data and predictions of aspect ratios, ranging from 1.0 to infinity, showing a gradual decrease in Nusselt number with increasing aspect ratio.

The local Nusselt number along the perimeter is usually higher than is the average value because the cold-induced flow creates a large tempera-
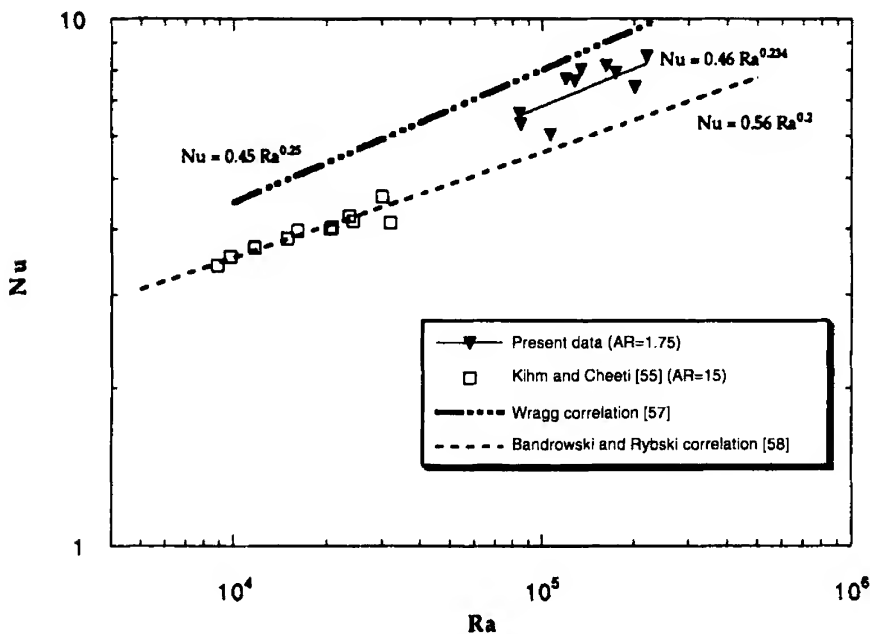
FIG. 24. Speckle results of average Nusselt number for a horizontal isothermal plate compared with other experimental and numerical results [56]. Ra, Rayleigh; AR, aspect ratio.

ture difference with the isothermal surface temperature. The specific perimeter, total perimeter length divided by total heated surface area, increases with decreasing aspect ratio (AR), and the maximum specific perimeter is given for a square surface (AR = 1). Thus, a surface of a smaller AR gives a higher average Nusselt number because of its relatively larger specific perimeter. This is attributed to the gradual increase in the Nusselt number toward the square surface of AR equal to one, as shown in Fig. 25. It is conjectured that the Nusselt number decreases because of the decrease in the specific perimeter per unit heated area with an increase in the AR.
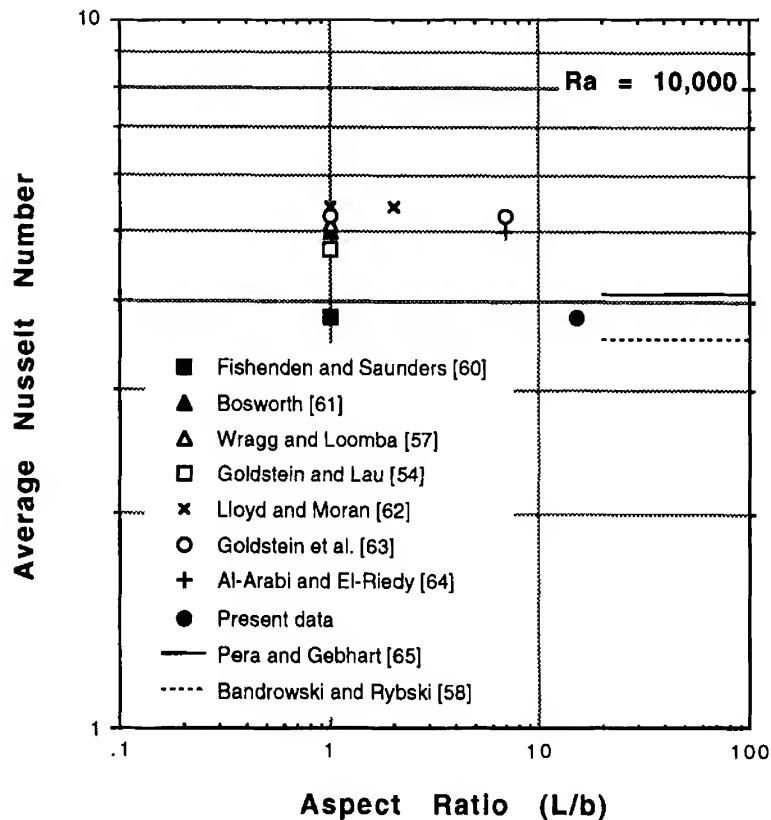
FIG. 25. Average Nusselt number versus aspect ratio of a horizontal heated plate for $Ra = 10^4$ [55]. Ra, Rayleigh.

F. Converging Channel Flows

Natural convection heat transfer characteristics for a unique geometry of vertically converging isothermal channel walls (Fig. 26) were studied using the laser speckle technique [52, 59]. Unlike a closed triangular enclosure with no openings [66, 67], the natural convection boundary layers along the inclined heated surface induce air flow from the lower openings. Enough top openings ventilate the induced flow (Fig. 26(a)) and

(a)

ISOTHERMAL HEATING   ISOTHERMAL HEATING

ADIABATIC BOTTOM

(b)
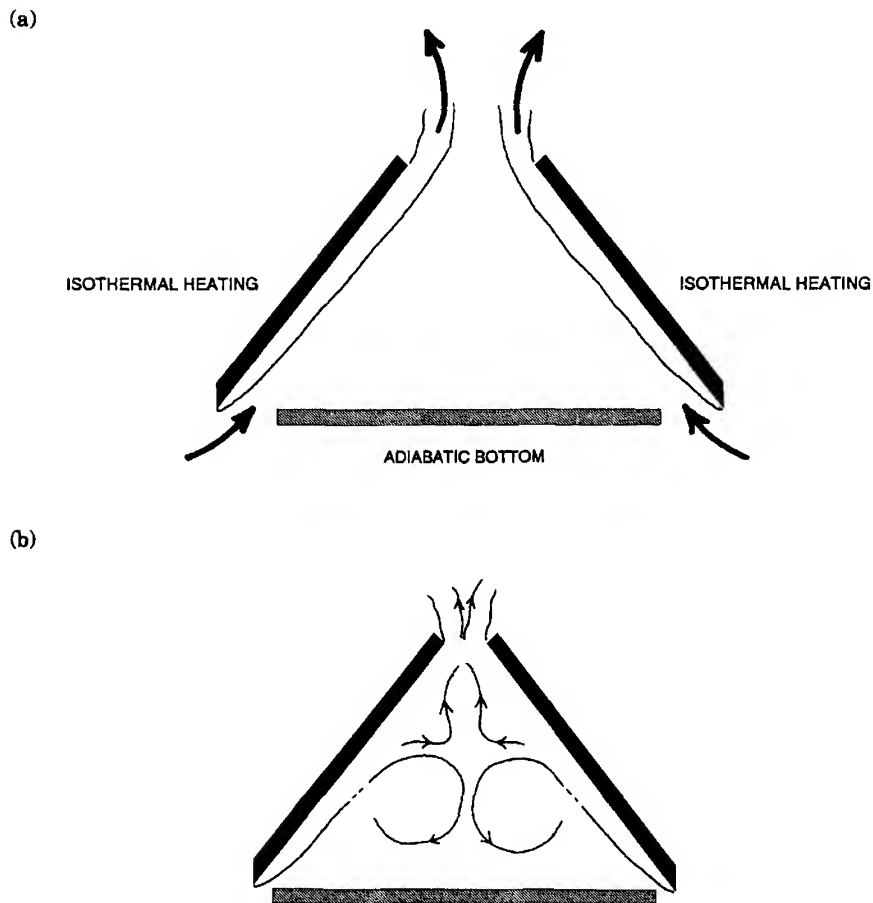
Fig. 26. Schematic illustrations of thermal boundary layers in a triangular enclosure: (a) complete ventilation with separate boundary layer development for $b/L > (b/L)_{opt}$ and (b) heated air recirculation with merging of two thermal layers for $b/L < (b/L)_{opt}$ [59].

enable the bottom plate (the ceiling in a building) to be effectively insulated from the heated inclined surfaces (the roof). However, when the top opening is too small (Fig. 26(b)), the two boundary layers merge inside and the heat and mass transfer of the convective air can significantly decrease, because some of the induced and heated air must recirculate within the enclosure. The phenomenon can be considered analogous to the thermal choking for a parallel channel, discussed in Section D.

Figure 27 presents results of the local Nusselt number versus the Grashof number for a 30-degree inclination from the vertical. The solid line represents Ostrach's theory [43], which accounted for the decreased gravitational effect due to the inclination. For the wide opening of b/L = 0.2 or larger, which allowed an uninterrupted boundary layer to grow along each plate, the data are well predicted by the single plate theory. As the top opening decreased, however, the thermal boundary layers merged inside the channel and the heat transfer along the plate significantly decreased after that. The data began deviating from the single plate theory at a critical Grashof number, and the local Nusselt number remained
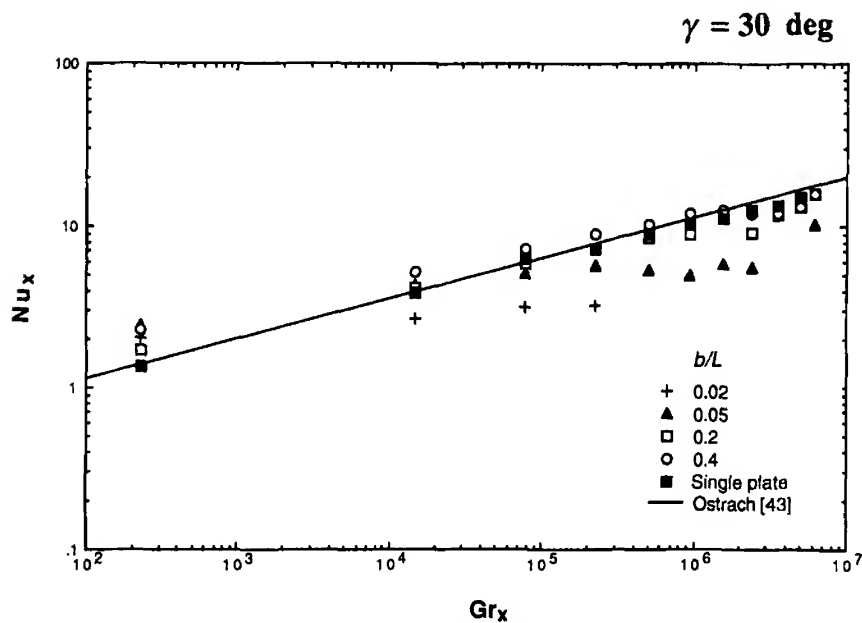
FIG. 27. Local Nusselt number versus local Grashof number for the converging flow with an inclination angle $\gamma = 30$ degrees measured from vertical [52].

nearly flat. With a decrease in b/L, the deviation started at a smaller Grashof number because the merging of the thermal boundary layers occurred nearer the leading edge. With a decrease in the slope, the degree of data deviations from the single plate theory became larger and the deviation started at a smaller Grashof number.

Figure 28 shows the speckle data of the average Nusselt number versus the top opening ratio b/L for the range of the inclination angle γ *measured from the vertical*. When b/L was large, the average Nusselt number $\overline{Nu}_L$ approached the analysis for an inclined single plate [43], despite the inclination angle. As b/L decreased, a slight increase in $\overline{Nu}_L$ was observed until the gradual ridge was reached. This maximum heat transfer occurred at an optimum opening ratio $(b/L)_{opt}$, which maximizes the so-called *chimney effect*. The vertically parallel channel of $\gamma = 0$ showed the smallest optimum opening ratio of $(b/L)_{opt} = 0.07$ (compared with $(b/L)_{min} = 0.0584$ estimated by Bar-Cohen and Rohsenow [53]). The optimum opening ratio increased with an increasing inclination angle or decreasing slope. When the top opening decreased beyond the optimum value, the average Nusselt number began decreasing and eventually became far smaller than the corresponding single plate limit because of the more prevailing thermal choking and recirculation of heated air inside.

The average Nusselt numbers and optimum top openings are summarized in Table I. The optimum opening increases with an increase in the inclination angle or decreasing slope with an approximately linear relationship. The buoyancy driving force decreases with a decrease in the slope (increasing inclination angle), and the average Nusselt number decreases with the inclination angle for each opening.

IV. Applications for Turbulent Flows with Density Fluctuation

Speckle photography can provide a full-field measurement of turbulence properties for a fluctuating density field [68]. For example, an axisymmetric helium jet exhausted at a high Reynolds number into the ambient air (Fig. 29) can generate a completely turbulent flow with a fluctuating density field [69]. The use of a pulsed ruby laser allowed freezing of the flow within its pulse duration, which was adjusted to be shorter than the density fluctuating time scale and reduced the blurring of speckle images. The inset photographs show Young's fringes generated at the respective locations on the specklegram. The different spacings and orientations of the fringes show that the angle of light deflection is irregularly distributed in the turbulent jet.
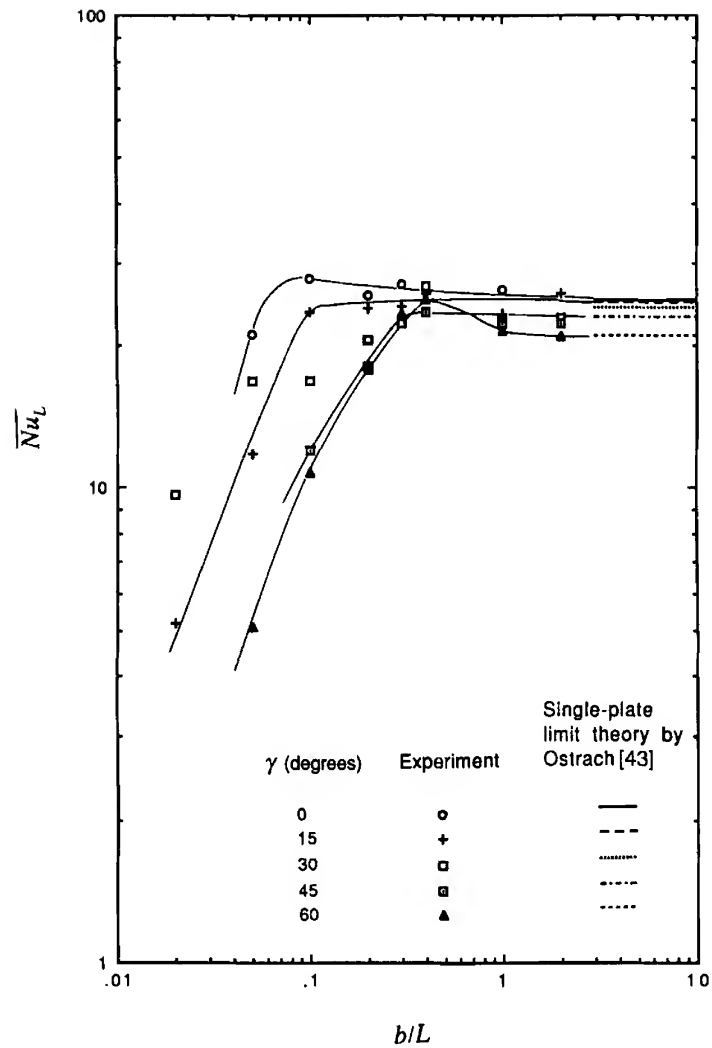
FIG. 28. Average Nusselt number based on the plate length versus the opening ratio for five different inclination angles: $\gamma = 0$ (vertical channel), 15, 30, 45, and 60 degrees; Grashof number $[g\beta \cos \gamma(T_w - T_x)L^3/\nu^2]$ ranged from 3.58×10^6 ($\gamma = 60$ degrees) to 7.16×10^6 ($\gamma = 0$) [52].

TABLE I

AVERAGE NUSSELT NUMBER, $\overline{Nu}_L = \overline{h}L/k$ FOR $Pr = 0.71$; $Gr_L(\equiv g\beta\cos\gamma(T_w - T_c)L^3/\nu_r^2)$
RANGED FROM 3.58×10^6 ($\gamma = 60$ DEGREES) TO 7.16×10^6 ($\gamma = 0$) [52].

γ (degrees) b/L	0	15	30	45	60
0.02	—	5.17	9.72	—	2.78
0.05	21.21	11.798	16.876	—	5.08
0.1	27.867	23.554	16.926	12.06	10.8
0.2	25.65	24.028	20.667	18.187	17.75
0.3	27.122	24.168	22.309	—	23.37
0.4	—	25.816	26.857	23.64	25.25
1.0	26.258	23.35	22.791	22.28	21.53
2.0	—	25.933	23.029	22.44	20.91
∞: single-plate limit (Ostrach [43])	24.952	24.736	24.07	22.88	20.98
$(b/L)_{min}$	0.07	0.1	0.3	0.35	0.4

Section A discussed a laminar flow of inhomogeneous density field and
Section B presents a measurement of the spatial correlation functions and
other statistical turbulence properties for fluctuating density and tempera-
ture fields. Section C presents a single-exposure speckle photography that
measures the turbulence root mean square (rms) intensities and anisotropy
characteristics for turbulent flames.

A. LAMINAR AND INHOMOGENEOUS DENSITY FIELDS

Equations (3a) and (3b), with the Gladstone-Dale relationship $n = K \cdot \rho + 1$, give expressions for the deflection angles measured for an
unknown density field at a sliced cross section $z = z_k$ (see Fig. 7 for the
coordinate system):

$$\varepsilon_y(y, z_k) = K \int_0^L \frac{\partial \rho(x, y, z_k)}{\partial y} dx \qquad \varepsilon_z(y, z_k) = K \int_0^L \frac{\partial \rho(x, y, z_k)}{\partial z} dx,$$

$$(14)$$

where K is the Gladstone-Dale constant and L is the light path length
occupied by the test field in the line-of-sight x-direction. The two compo-
nents of instantaneous deflection angle ε_y, ε_z represent the path integral
of a density gradient in each direction. Tomographic inversion of Eq. (14)
gives the density distribution in the x-y plane at $z = z_k$. This inversion is
repeated at different z locations to complete the reconstruction of the
whole density field.

An axisymmetric field can be reconstructed from a single projected
image at any arbitrary projection angle [70]. After expressing Eq. (14) for a
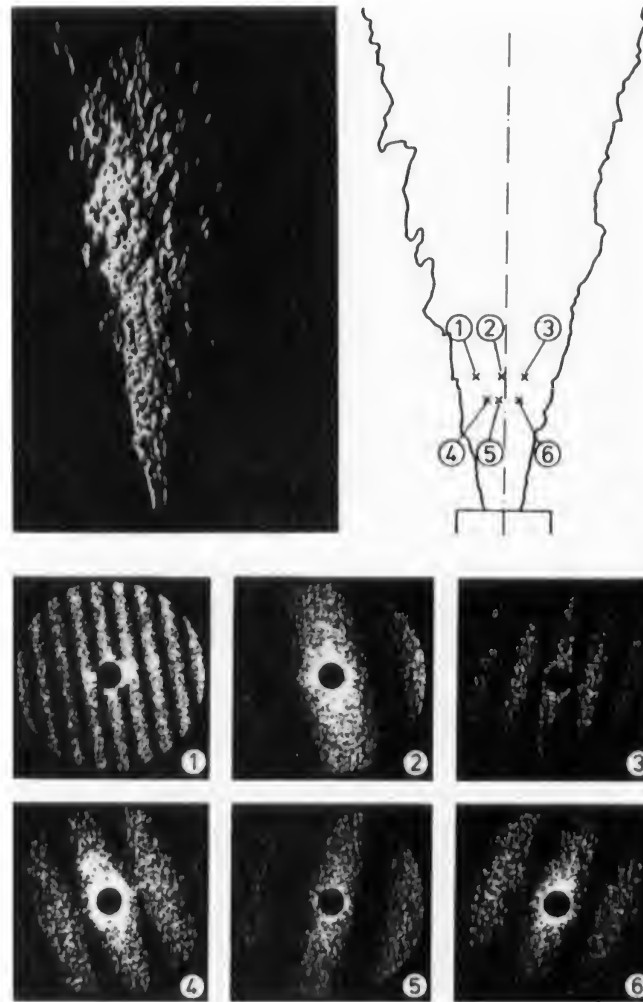
FIG. 29. Schlieren photograph of the turbulent jet. Six positions in the field of view are designed for which the respective systems of Young's fringes are shown [69].

cylindrical coordinate system, the use of the Abel transform gives an analytical inversion of Eq. (14) [71]:

$$\frac{\rho(r, z)}{\rho_o} = 1 - \left(\frac{1 + K\rho_o}{K\rho_o\pi}\right) \cdot \int_r^\infty \frac{\varepsilon_y(y, z)}{\sqrt{y^2 - r^2}} \, dy, \qquad (15)$$

where ρ_o is the ambient density and $r^2 = x^2 + y^2$. The derivation of Eq. (15) assumes a paraxial ray refraction with very small deflection angles and

the primary ray refraction occurring only within the x-y plane; that is, all fringes are formed perpendicular to the x-y plane. Another assumption used in Eq. (15) is a constant value for the Gladstone-Dale constant K through the whole field.

Tomographic reconstruction requires multiple projections for a non-axisymmetric field. In Fig. 30, the nonrotating x-y coordinate is fixed on the cross-sectional plane. The s-t coordinate rotates with the projection angle θ_j, where the s-coordinate is parallel to the speckle image plane at a given projection angle θ_j and the t-coordinate is parallel to the ray direction. The z-direction is aligned with the flow perpendicular to the s-t plane. Assuming that several projections are available at equal angular intervals, the field reconstruction can be achieved by a direct mathematical inversion calculated simultaneously from the projected images. This is typically possible by using Fourier convolutions (FCs) based on the Fourier slice theorem [72, 73].

For a laminar helium jet into ambient air, for example, the reconstruction equation for the relative helium density was derived as a discretized form [74]. When specklegrams are taken in N different viewing directions with equal angular intervals $\Delta \theta$, and evaluated along the s-direction at M discrete points of equal spacing Δs on the imaging plane, the result is

$$\rho^*(x_i, y_j) = \frac{\rho_{He}}{\rho_{He_o}}$$

$$= \frac{1}{N\pi} \sum_{n=0}^{N-1} \sum_{m'=-(M-1)/2}^{(M-1)/2} \varepsilon(m' \Delta s, n \Delta \theta) \cdot q(m - m'), \quad (16)$$

Line-of-sight direction
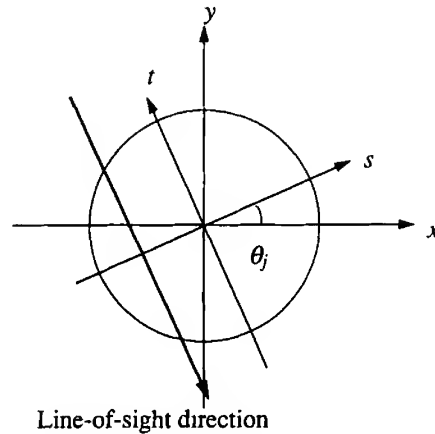
FIG. 30. Coordinate system of an arbitrary cross section of test field.

where i, j, m, m', and n are integers, and ρ_{He} and ρ_{He_o} are the partial density of helium in the jet and the density of pure helium, respectively. The discretized filter function [75, 76] is given as $q(m) = 1/m$ for odd m, and $q(m) = 0$ for even m.

Figure 31 shows the tomographic reconstruction of the helium jet at a cross section 5 mm above the elliptic nozzle exit. The nozzle was mounted

(a)

(b)

(c)

(d)
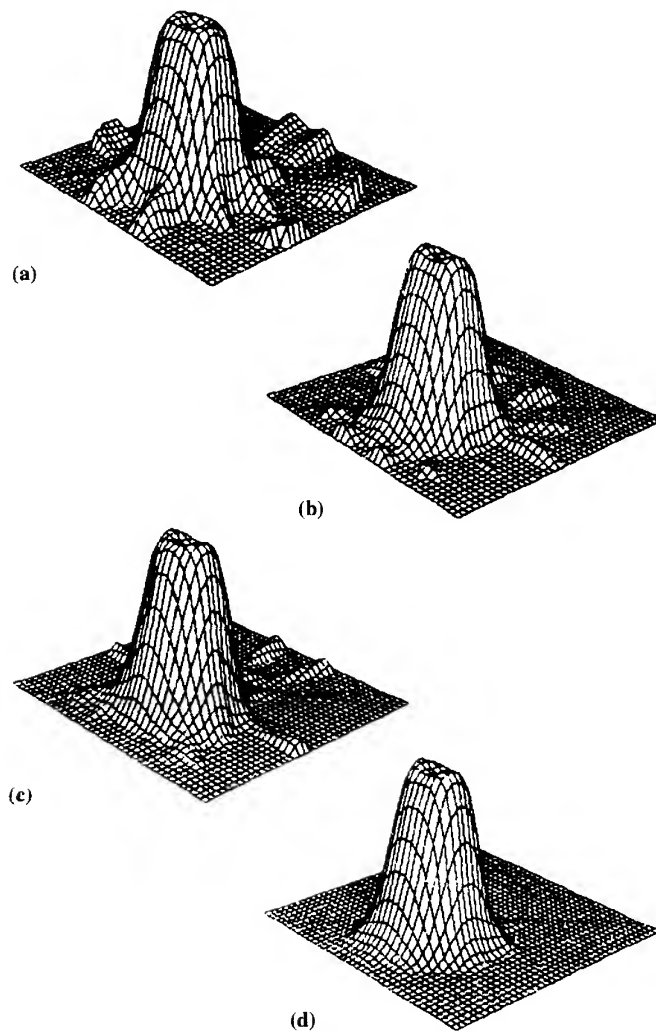
FIG. 31. Tomograms of the helium density distribution in a jet of elliptic cross section; reconstructed with (a) 4, (b) 6, (c) 8, and (d) 12 speckle projection [74].

on a turning plate and specklegrams of up to 12 viewing angles were taken with 20 × 20 mm projected image size. Each specklegram was processed by the point-by-point analysis measuring the Young's fringe spacings and the ray deflection angles so that the relative helium density could be determined from Eq. (16). The results show that speckle photography extends its applicability to optical tomography for measuring 3D density fields. Reconstructions with less than 12 angular samplings show artifacts of the aliasing effects. For more arbitrary fields, such as the human body or brain, the FCs commonly require hundreds of equal-angled projections for acceptable reconstruction with minimal aliasing effects [77].

B. FLUCTUATING DENSITY AND TEMPERATURE FIELDS

Certain statistical properties describe turbulent flow characteristics rather than spatially and temporally resolved quantities [78]. Uberoi and Kovasznay [79] found a way to derive the statistical properties of a turbulent density field once spatial correlations of an integrated optical quantity, here the light deflection angle, are obtained. The spatial correlation function R_{ε_y} of the component ε_y, for example, between the points (x, y) and $(x + \xi, y + \eta)$, is expressed as

$$R_{\varepsilon_y}(\xi, \eta) = \langle \varepsilon_y(x, y) \cdot \varepsilon_y(x + \xi, y + \eta) \rangle, \tag{17}$$

where $\langle \dots \rangle$ denotes an integral and averaging operation over the whole field. The spatial correlation of ε_y in the x-direction is calculated by $R_{\varepsilon_y}(\xi, \eta = 0)$, and the spatial correlation of ε_y in the y-direction is calculated by $R_{\varepsilon_y}(\xi = 0, \eta)$. To perform the correlation integration in Eq. (17) with proper statistics satisfied, thousands of point-by-point analysis for a single specklegram are required. This requires the automatic scanning and computerized fringe analysis.

For the axisymmetric and isentropic turbulent flow field, the spatial density correlation function of the radial coordinate $R_\rho(r)$ can be derived from the spatial correlation [80]

$$R_\rho(r) = \frac{1}{\pi L K^2} \int_r^\infty \frac{\xi}{\sqrt{\xi^2 - r^2}} R_{\varepsilon_y}(\xi, \eta = 0) \, d\xi, \tag{18}$$

where L is the length of the beam path occupied by the test field, and K the Gladstone-Dale constant. The density correlation can be determined strictly from the measured deflection angles. Using the equation of state and assuming constant pressure, the correlation function for the density $R_\rho(r)$ can be converted into the correlation function for the temperature $R_T(r)$.
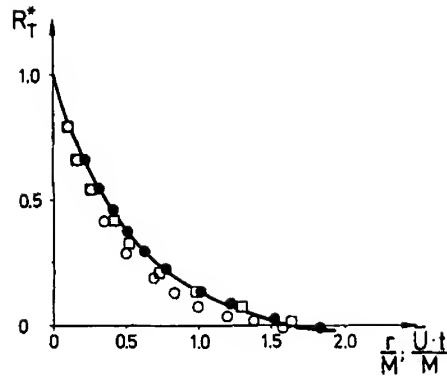
FIG. 32. Normalized correlation function of the temperature R_T^* as function of the nondimensional radial distance; speckle measurement taken at the axial position $x/M = 18$: —; referred data were taken for x/M positions of 17 [81: $\bigcirc$], 35 [83: $\bullet$], and 40 [82: $\square$] [75]. M, MESH size.

Figure 32 shows the normalized correlation function of the temperature based on Eqs. (17) and (18). The deflection angle measurement was made for an axisymmetric isotropic turbulent flow parallel to the x-direction and the temperature fluctuation was generated by electrically heated wires with an approximate 800°C surface temperature [80]. A wire mesh ($M = 41$ mm) was used both to heat and to generate density and temperature fluctuations. The results of the spatial correlation were compared with others using a cold-wire probe [81–83]. Good agreement was found.

The spatial correlation of the cold-wire results is referred to an equivalent radial distance $\bar{U} \cdot t$, because the point-by-point cold-wire data have been taken as a function of time under a mean velocity $\bar{U}$. This determination of the spatial correlation function from the temporally measured cold-wire data is accepted under Taylor's hypothesis [84]. Laser speckle photography allows nonintrusive and full-field measurement of a spatial correlation without the Taylor hypothesis, because the correlation function from the speckle measurement was carried out simultaneously. Another feature of the speckle measurement is its higher data resolution. The speckle interrogation for Fig. 32 was made at 0.4-mm increments, which conforms to a nearly continuous data curve.

Fourier analysis of the spatial correlation function allows for determining the turbulence energy spectrum, and the differentiation and integration of the spatial correlation curve provides micro- and macro-length scales for temperature and density fluctuations. A study has been done to determine these turbulent statistical properties from the spatial correla-

tion function for hot air flows generated by a combination of a turbulence grid and flat flame burner [85]. The measured properties showed good agreement with the existing theoretical models and experimental data obtained by an intrusive means such as a hot-wire probe. A shock tube experiment was also performed to study a compressible turbulent flow using laser speckle photography. An amplification of the turbulence intensity by the shock-grid interaction process was observed quantitatively [86].

C. Single-Exposure Speckle Photography

Regular double-exposed speckle photography for turbulence measurements requires a short exposure time to freeze the turbulence structure. This is usually achieved with a short-pulsed ($\ll 1$ μsec) laser. The single-exposure speckle photography technique [87] records speckles only with the test section present, and the exposure time is set much longer than the turbulent fluctuating time scale. Analysis of the smeared speckle images, which result from the beam steering by the fluctuating field during the lengthy exposure period, can provide information on the turbulence characteristics.

The interrogating laser light ray is diffracted by the speckle images recorded on a single-exposed specklegram and a diffraction halo [88] forms on the imaging screen (Fig. 33). When the turbulence fluctuation is uniformly distributed, as in isotropic turbulence, the smeared speckle images and their halo are both of circular cross section (dashed circles in Fig. 34). The higher the flow fluctuation is, the larger the diffraction halo
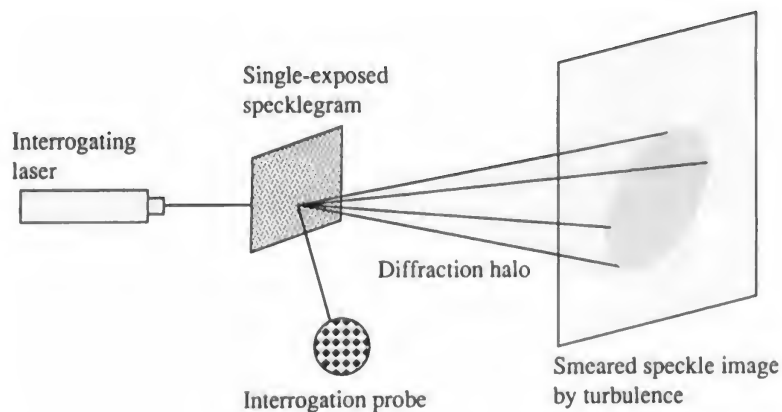
FIG. 33. Formation of diffraction halo by illuminating a specklegram with a low-power interrogating laser.

Speckle plane   Diffraction plane
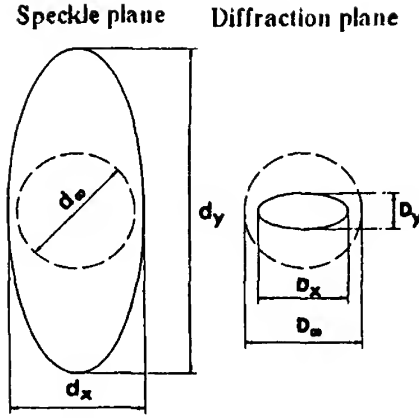
FIG. 34. Schematic of averaged speckle form obtained by single-exposure speckle photography, and diffraction halo cross section: undisturbed or isotropic turbulence (dashed circles); and disturbed or anisotropic turbulence (solid ellipses) [87].

image that is recorded because of the more significant beam steering. With anisotropic turbulence, the speckles become elongated in the preferential direction of the turbulent fluctuations. The halo then has an elliptic cross section with its major axis perpendicular to the major axis of the smeared speckle image (solid ellipses in Fig. 34).

The geometric correlation between the speckle and halo images gives an expression for a quantity A that describes the deviation of the halo cross section from circular form, or asphericity, as [89]

$$A = \sqrt{\langle (\Delta d_x)^2 \rangle / \langle (\Delta d_y)^2 \rangle} \cong \frac{D_y}{D_x} \approx \sqrt{\langle \Delta T_y^2 \rangle / \langle \Delta T_x^2 \rangle}, \qquad (19)$$

where Δd_x and Δd_y denote the deformation of the speckle image in its minor, or shorter, and major, or longer, axis directions, respectively. The average $\langle \ldots \rangle$ must be taken over all speckles inside the area of the interrogating laser beam cross section. The asphericity of halo image A measures the anisotropy of the temperature fluctuation on the x-y recording plane. The rms temperature fluctuation is given as

$$\sqrt{\langle \Delta T^2 \rangle / T_x^2} \approx \frac{D_x}{D} - 1, \qquad (20)$$

where D_x is the halo image size for isotropic turbulence.

Example results obtained from a turbulent flame are shown in Fig. 35 as contour maps, using the false gray levels for different quantities. At the

A   B
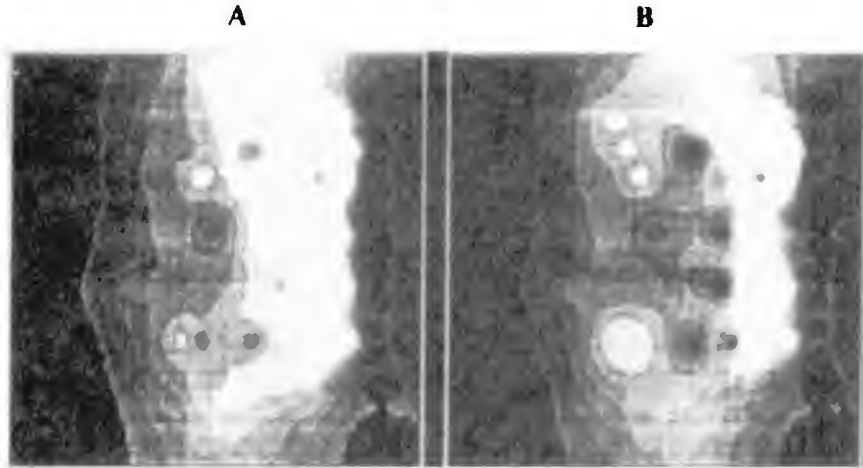
FIG. 35. RMS values of temperature fluctuations in turbulent flame (a) and anisotropy of turbulence in flame (b), visualized by different gray scales and reconstructed from a single-exposure specklegram [87].

instant when the specklegram was recorded, the right side of the flame showed a higher rms turbulence level and larger anisotropy of the temperature fluctuation then did the left side.

V. Applications for Flame Temperature Measurements

Speckle photography can nonintrusively measure temperature distributions for inhomogeneous gas fields, such as combusting flames, and is considered a potentially promising tool for the analyses of inhomogeneous flows of liquids or plasmas [90]. Part V discusses temperature measurements of axisymmetric and laminar gas flames. (Part VI will then present an application for a liquid jet flow). Section A discusses the tomographic reconstruction of the temperature field from the deflection angles recorded on the specklegrams. Section B and C discuss the temperature fields for axisymmetric candle flames and other gaseous flames, respectively.

A. TOMOGRAPHIC RECONSTRUCTION OF TEMPERATURE FIELD

Refractive indices of most gas species gradually decrease with an increase in temperature. All of these refractive index values are extremely close to that of air, that is, nearly unity [91]. The Gladstone-Dale relation-

ship [7] provides an expression for the index of refraction of air at 1 atm as

$$n(T) = 1 + K \cdot \rho = 1 + K \cdot \frac{p}{RT} = 1 + \frac{0.07966}{T}, \qquad (21)$$

where T is in K and the Gladstone-Dale constant $K = 0.2257 \times 10^{-3}$ m^3/kg at $\lambda = 632.8$ nm of a helium–neon laser. At high-temperature environments, such as a combusting flame, the refractive index itself is low; however, more noticeably, the absolute magnitude of its gradient, dn/dT (Eq. (7)), approaches zero (Fig. 36). This means that the change of refractive index per unit temperature change dramatically decreases with an increase in temperature and reduces the sensitivity of any optical technique, including laser speckle photography, relying on the refractive index variation. Henceforth, the application of the speckle technique for flame temperature measurements inherently enlarges the measurement uncertainties compared with applications for flows at moderate temperature range, such as an application to natural convection.

The polar coordinate transformation of Eq. (3a) for an axisymmetric field gives the measured deflection angle $\varepsilon(y)$ as an integral function of the radially distributing index of refraction $n(r)$ as [12]

$$\varepsilon(y) = 2y \int_y^\infty \frac{\partial}{\partial r}\left[\frac{n(r)}{n_o}\right] \frac{dr}{\sqrt{r^2 - y^2}}, \qquad (22)$$
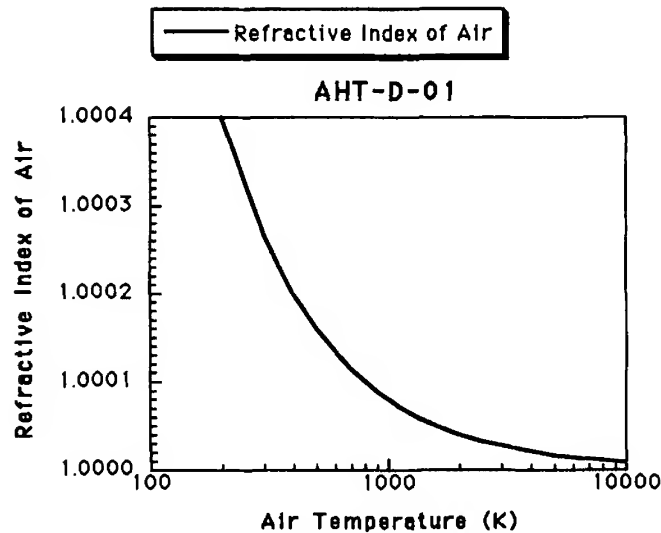
Fig. 36. Refractive index of air 1 atm versus air temperature.

where the y-z imaging plane lies perpendicular to the optical axis x (Fig. 7). Equation (22) represents an integral transform of the Abel type. Thus, the inverse Abel transform of Eq. (22) is given as

$$\frac{n(r)}{n_o} = 1 - \frac{1}{\pi} \int_r^\infty \frac{\varepsilon(y)}{\sqrt{y^2 - r^2}} \, dy, \tag{23}$$

which also is called Radon transform and allows the reconstruction of the refractive index field from the line-of-sight deflection angle data $\varepsilon(y)$ [70].

The reconstructed radial refractive index profile can be converted to the temperature field once the species concentration are known in the flame. When the deviation of index of refraction in the flame is small, the effect of combustion species can be neglected and the flame field can be approximated and represented by air. Applying the Gladstone-Dale relation $n = 1 + K \cdot \rho$ once for a reference point denoted by a subscript o and for any arbitrary radial point, and then combining the two equations with an ideal gas assumption gives [12]

$$\frac{T(r)}{T_o} = \left[\left(\frac{n(r)}{n_o} - 1 \right) \left(\frac{RT_o}{K\rho_o} + 1 \right) + 1 \right]^{-1}, \tag{24}$$

where the pressure is assumed constant in the whole recorded field.

An alternative conversion is possible by using the Lorenz-Lorenz relation [92], $A \cdot \rho = (n^2 - 1)/(n^2 + 2)$, where A and ρ are the molar refractivity and molar density, respectively. An ideal gas assumption with an index of refraction $n \cong 1.0$ gives an expression for local temperature as [93]

$$\frac{T(r)}{T_o} = \left[\left(\frac{n(r)}{n_o} - 1 \right) \left(\frac{3p_o A + 2RT_o}{3p_o A} \right) + 1 \right]^{-1}, \tag{25}$$

where a constant pressure p_o is assumed to prevail in the test field. An extensive tabulation of the Gladstone-Dale constant and molar refractivity as functions of light wavelength for different species is available from Gardiner et al. [94]. To complete the temperature conversion, either by Eq. (24) or Eq. (25), the temperature and index of refraction at one reference point, T_o and n_o, must be given a priori.

The use of speckle interferometry [29] can also determine the temperature field by analyzing the fringes appearing in a speckle interferogram. The analysis method is identical to that for wave front interferometric techniques such as Mach-Zehnder interferometry [95]. For an axisymmetric field with $n \cong 1.0$, the index of refraction can be given as the fringe

data N_f, which is equivalent to the number of crossing fringes [96]:

$$\frac{n(r)}{n_o} = 1 - \frac{\lambda}{\pi} \int_r^\infty \frac{(dN_f/dy)}{\sqrt{y^2 - r^2}} \, dy. \tag{26}$$

Using the Lorenz-Lorenz equation and the assumption of an ideal gas, an equation for temperature conversion is

$$\frac{T(r)}{T_o} = \left[\frac{C}{T_o} \cdot \left(\frac{n(r)}{n_o} - 1 \right) \right]^{-1}, \tag{27}$$

where C is an optical constant and is equal to 0.083928 K for a helium-neon laser. The temperature of the ambient air is T_o where the refractive index is n_o.

B. Axisymmetric Candle Flames

Free candle flame in a quiescent environment generates a laminar steady flame and maintains its degree of asymmetry by 10% to 15% [97]. Because of this simplicity candle flames are a popular example, not only for laser speckle photography but also for other optical techniques and theoretical interpretations [98]. Figure 37 shows Young's fringe patterns constructed at different axial (z) and transverse (y) locations on a speckle-gram taken for a diffusive candle flame [56]. A narrower fringe pattern represents a larger refraction angle resulting from a higher temperature gradient, and vice versa for fringes with wider spacing. A zero temperature gradient of symmetry condition along the centerline does not dislocate speckles in either direction and generates infinite fringe spacing. The temperature gradient becomes zero at larger r as the undisturbed ambient condition is approached.

Work was done on a candle flame simultaneously projected in four directions with the multiple speckle system, shown schematically in Fig. 38 [99]. The system used two pulsed ruby lasers having a wavelength of $\lambda = 690$ nm, a pulse energy of 0.5 J, and a pulse duration of approximately 0.5 msec. The candle flame was positioned at an approximately equal (defocusing) distance of 50 mm from all four ground glass scattering plates.

The reconstruction results of Fig. 39 were obtained from the four-angle speckle photographs by means of Radon transform in association with the Gladstone-Dale type conversion with an assumption of Eq. (24). The error associated in the mathematical reconstruction procedure for local temperatures did not exceed 10%. An error of an additional 10% to 15% was estimated to account for the combustion products of paraffin involving
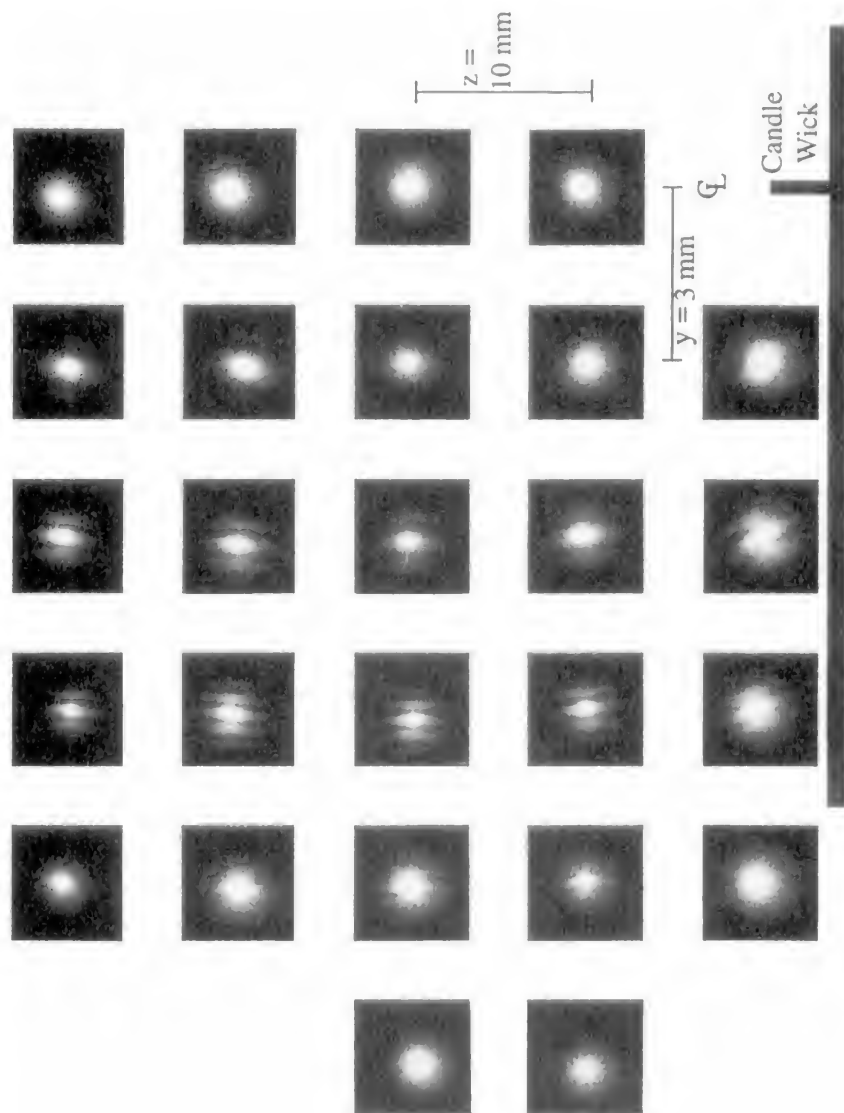
Fig. 37. Spatial distribution of Young's fringes generated from a laser specklegram recorded for an axisymmetric paraffin candle flame [56].

297
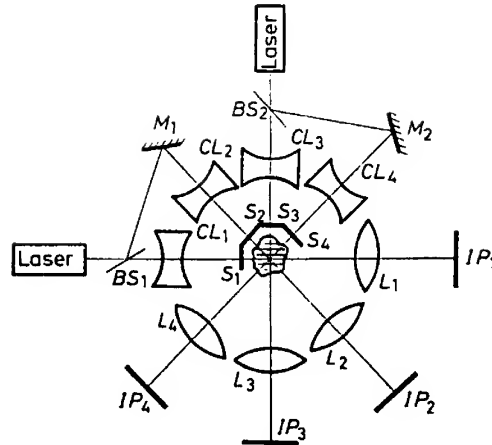
FIG. 38. Scheme for obtaining specklegrams simultaneously in four directions: $S_1, \ldots, S_4$, scattering plates; $L_1, \ldots, L_4$, lenses; $CL_1, \ldots, CL_4$, collimated lenses; BS_1, BS_2, beam splitters; M_1, M_2, mirrors; $IP_1, \ldots, IP_4$, image planes [99].
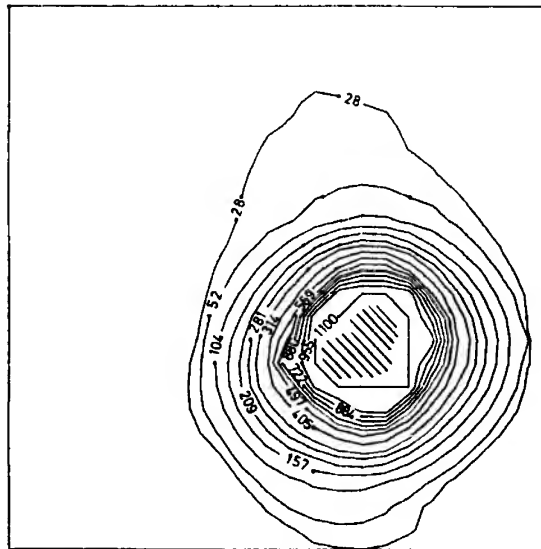
FIG. 39. Results on reconstructed two-dimensional temperature distribution in a candle flame [99].

carbon dioxide and water that would alter the Gladstone-Dale constant. The isotherms show that most of the section develops an axisymmetric flame. The reconstructed temperature field oscillated in the boundary of the region surrounded by an isotherm corresponding to $T - T_x = 1100$ K.

Isotherms for the whole field of view were created (Fig. 40) by repeating the temperature reconstruction process for different cross-sectional fields at different axial locations in a single specklegram. The isotherms ensure the approximate symmetry of a paraffin flame.

C. Premixed Gaseous Flames

Figure 41 demonstrates an unstable and fluctuating Bunsen burner flame where the central interferogram gives an overall view of the fringe distortion occurring due to the flame at a particular instant of time [100]. Young's fringes were generated at 16 different positions from a single specklegram. Quantitative analysis of such a sophisticated flame would need multiple projections of specklegrams at many different angles. The recovery of the cross-sectional field requires a rigorous reconstruction algorithm for the asymmetric field, using a regression method [101] or a mathematical inversion [75].

The viability of laser speckle photography for flame temperature measurement has been examined with the Lorenz-Lorenz conversion (Eq. (25)) for a propane gas burner [93]. Similar investigation of flame temperature measurement have been performed using speckle shearing interferometry.
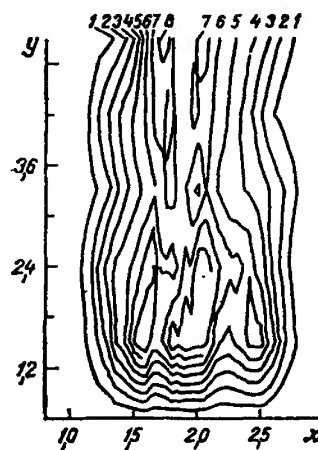
FIG. 40. Temperature isolines in one of the vertical cross-sections of the axisymmetric candle flame: curves 1 to 8 correspond to temperatures of 400 to 1250 K; x and y in cm [97].
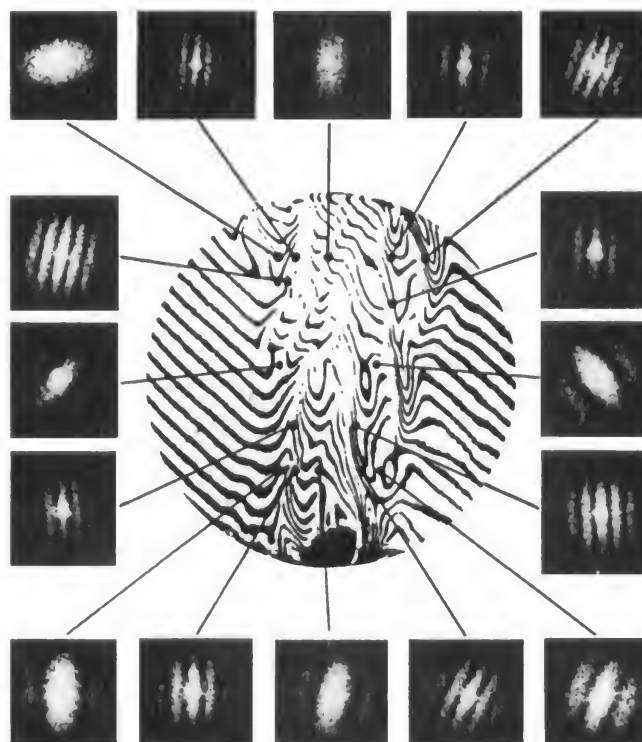
FIG. 41. Shearing interferogram of the Bunsen burner flame (center), and patterns of Young's fringes obtained by the point-by-point analysis of the specklegram at 16 different positions in the field of view [100].

They showed close agreement with their thermocouple data [30]. Verhoeven and Farrell [96] used speckle interferometry to reconstruct radially distributing flame temperature data based on the conversion in Eq. (27).

Figure 42 shows the radial temperature distribution of a premixed propane Bunsen flame 50 mm downstream of the 8-mm diameter nozzle [71]. The temperature field was reconstructed from the index of refraction using the Gladstone-Dale based formula of Eq. (24). The solid curve shows a temperature profile calculated based on the specklegram data, with the centerline as a reference point and assuming the gas constant for air and the Gladstone-Dale constant in air. The speckle data shows fairly good consistency with the thermocouple (platinum–rhodium B-type) data, except for the region near the flame boundary where the speckle data underpredicts the ambient temperature. The thermocouple data, however,

Propane Flame Temperature Profiles
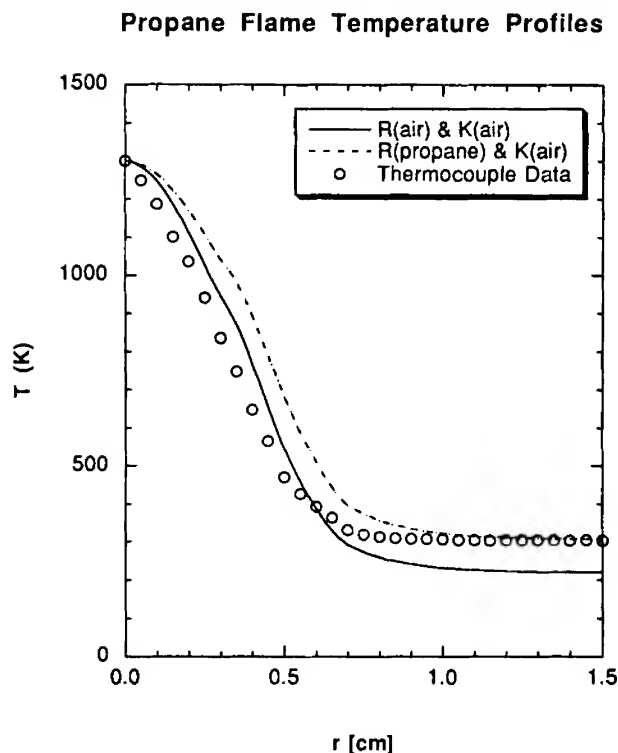
FIG. 42. Comparison of temperature profile obtained from deconvolved refractive index with thermocouple-measured temperature data for the axisymmetric propane Bunsen flame [71].

has not been attempted for any corrections of the radiation loss from the probe surface nor for the conduction heat loss through the probe stem [102]. The probe corrections must know the emissivity of the probe surface, the time constant of the probe material, and the flow Reynolds number. The temperature correction for the heat losses could upshift the thermocouple data as much as 20% near the flame center [103].

The specific gas constant and the Gladstone-Dale constant must be estimated for the mixture of gases presented in the flame when the mass fractions of the product gases are known or measured for the flame [104]. Since it is a primary function of the wavelength, the Gladstone-Dale constant K for air is expected to be a fairly acceptable approximation for the propane flame. However, the gas constant R varies rather significantly for gas species. The dashed curve represents a temperature profile calcu-

lated by assuming a gas constant for 100% propane, while keeping the Gladstone-Dale constant for air. The discrepancy in the ambient region has been significantly diminished in this limit, whereas the midrange temperature profile shows more deviations from the thermocouple data.

The nature of the refractive index dependence on temperature increases the measurement uncertainties in applications for high-temperature flames (Eq. (21)). Additionally, some improvements can reduce the measurement uncertainties:

1. The thermocouple probe corrections would raise the thermocouple data near the center to a noticeable degree, and this increase in the reference temperature T_o would also increase the speckle temperature data approaching the flame boundary.
2. The corrections for the nonradial angular refraction (occurring up to 20% at some locations [12]) would lower the specklegram temperature data and reduce the deviations from the thermocouple data in the midrange of the flame.
3. The discrepancy also can be attributed to the asymmetry of the flame, although is expected to be less than 5%.

VI. Applications for Liquid Temperature Measurements

Water is a dramatically different optical medium compared with air in view of light ray refraction. The index of refraction is related to temperature through the experimental correlation given in Radulović [105]:

$$n(T) = 1.3331733 - 0.00001 \cdot (1.936 + 0.1699T)T, \qquad (28)$$

where T is in degrees Centigrade assuming a constant pressure of 1 atm. Figure 43 shows $n(T)$ in the range between the freezing and condensing points at 1 atm. Compared with the refractive index of air (Fig. 36), the refractive index of water not only has higher values, but the rate of its change per unit temperature dn/dT is roughly three orders of magnitude higher than its counterpart for air. Expressions for dn/dT are

$$\frac{dn(T)}{dT} = -0.00001 \cdot (1.936 + 2 \times 0.1699T) \quad \text{for water [105]}, \qquad (29)$$

$$\frac{dn(T)}{dT} = -\frac{1.075 \times 10^{-6}}{(1 + 0.003681847T)^2} \quad \text{for air [28]}, \qquad (30)$$

where, for example, $dn/dT = 1.111 \times 10^{-4}$ for water at 27°C, and $dn/dT = 2.427 \times 10^{-7}$ for air at 300 K.
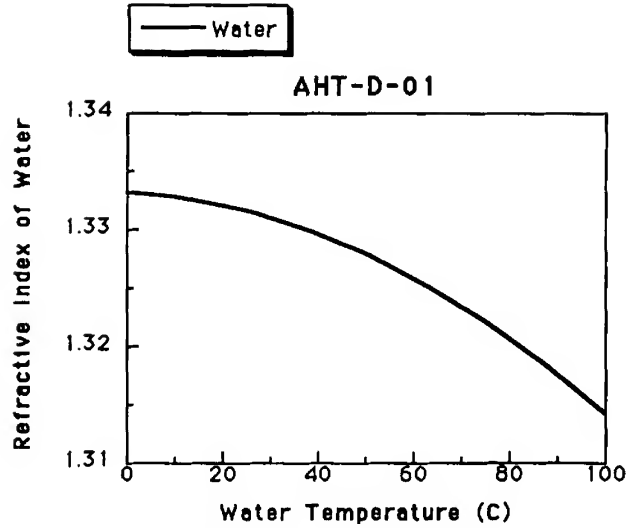
Fig. 43. Refractive index of water at 1 atm versus water temperature.

The paraxial approximation, which has been the basic assumption for the speckle analyses of air and other gases previously herein, assumes that the ray defraction angle is negligibly small due to a small dn/dT. Thus the Abel conversion formula for air (Eq. (23)) is derived based on a straight ray of a negligible ray bending in the gaseous phase object. However, the paraxial assumption may not be applicable to a water flow field because of its large values of dn/dT. For a strong refraction, such as that in water, Lira [106] developed an analysis for the reconstruction of a refractive index field from the deflection angle data for the case of the axisymmetric situation assuming nonnegligible ray bendings:

$$\frac{n(r)}{n_o} = \exp\left(-\frac{1}{\pi}\int_\chi^\infty \frac{\varepsilon(y)}{\sqrt{y^2 - \chi^2}}\,dy\right),\tag{31}$$

where $\chi = rn(r)$ and $n_o \cong 1.0$.

Speckle photography was examined to demonstrate the viability of its full-field temperature measurement capabilities for a transparent liquid medium [107]. The experiment was carried out for an axisymmetric hot water jet discharging vertically upward from a 5.9-mm diameter tube, as shown in Fig. 44. The measured deflection angle data were converted to the radial profile of the refractive index using Eq. (31), and the temperature was recovered by solving Eq. (28). Figures 45(a) to 45(c), respectively,
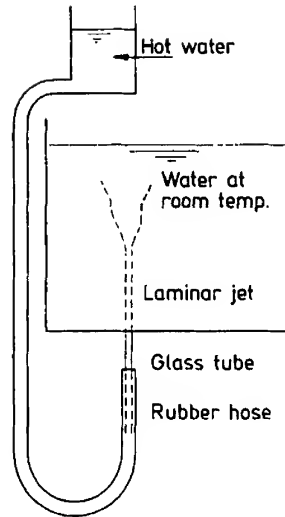
FIG. 44. A hot water laminar jet discharging into water at room temperature [107].

show the fringe spacing, deflection angle, and water temperature measured at 22 mm above the discharge point.

VII. Concluding Remarks

Speckle photography shows promising potential for nonintrusively studying thermal flow behaviors of both laminar and turbulent gas flows, flames, and liquid flows. The speckle technique extends its scope by employing a tomographic scheme to reconstruct the cross-sectional properties from the line-of-sight speckle data.

Laser speckle photography accurately determines the heat transfer correlation coefficients for natural convection problems. In addition, Young's fringes generated by the point-by-point analysis of the specklegram provide full-view qualitative information on the primary direction and intensity of heat transfer. The speckle system with a pulsed laser measures the statistical turbulence properties by detecting the density and temperature fluctuations. A unique single-exposure speckle system measures turbulence rms and anisotropy using a continuous wave (CW) laser. Another important application of speckle photography is for temperature measurement of high-temperature gas flows such as flames, where the sensitivity of the speckle photography technique is inherently poor with
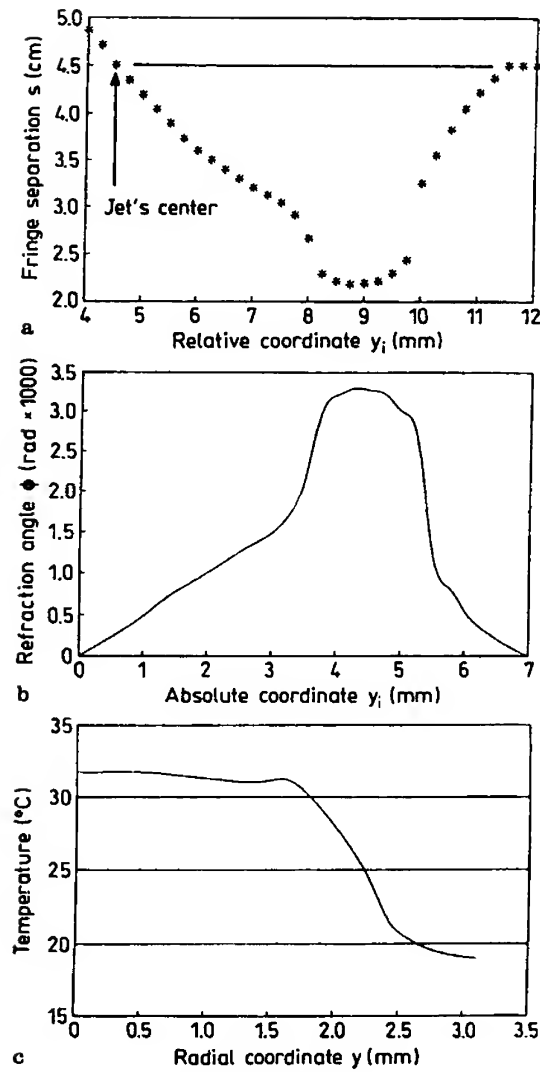
FIG. 45. (a) Fringe spacing as a function of relative coordinate y_i measured directly in the specklegram; (b) refraction angle ϕ as a function of absolute coordinate y_t measured with respect to the center of the jet; and (c) temperature profile as a function of radial coordinate y [107].

large uncertainties. The tomographic deconvolution allowed reconstruction of the flame temperature field for the flame cross section from multiple specklegrams. Finally, the technique shows its extended capability in measuring liquid temperature where the refractive index variation is more pronounced by a factor of approximately one thousand times.

Nomenclature

A heated surface area, or asphericity of a deflection halo image

a object distance

b image distance, or the channel width

c defocusing distance

D grain size of optical deflector or ground glass, or the diffraction halo dimension

d distance measured from a specklegram to the fringe imaging plane, or speckle dimension imaged on specklegram

Gr_b Grahsof number,
$$\frac{g\beta \cos \gamma(T_w - T_x)b^3}{\nu^2}$$

g gravitational acceleration

H distance measured from optical deflector to an observer

h convection heat transfer coefficient

K Gladstone-Dale constant (for air, $K = 0.2257 \times 10^{-3}$ m^3/kg at $\lambda = 632.8$ nm)

k thermal conductivity

L test field dimension parallel to the optical axis, or the channel length measured parallel to the convective flow direction

M number of data realization points in the s-direction on specklegram

m magnification of the second parabolic mirror

m' magnification of camera

N number of viewing or projecting angles

n refractive index of medium

N_f fringe reading from interferogram

Nu_x Nusselt number, hx/k

$\overline{Nu}_L$ average Nusselt number, $\overline{h}L/k$

P edge perimeter of heated surface

p pressure

$\dot{q}''$ heat flux, amount of heat transfer per unit time per unit area

R gas constant, or spatial correlation function

Ra Rayleigh number,
$$\frac{g\beta \cos \gamma(T_w - T_x)b^3}{\nu\alpha}$$

Ra^* modified Rayleigh number, $Ra \cdot b/L$

r, θ, z cylindrical coordinate system

s fringe spacing

s, t coordinate rotating on the x-y plane

T temperature

t time

$\overline{U}$ average flow velocity

X_f merging location of two boundary layers in vertical isothermal channel

x, y, z rectangular coordinate system

Greek Symbols

α ray deflection angle measured before the second parabolic mirror, or thermal diffusivity, $k/\rho c_p$

β volumetric coefficient of expansion

γ inclination angle measured from vertical

Δ amount of speckle dislocation on the recording plane

δ amount of speckle dislocation on the defocusing plane, or boundary layer thickness

ε ray deflection angle measured after the second parabolic mirror

ζ_1, ζ_2 ray entering and exiting points of test section boundary

η	dimensionless distance, y/δ, or arbitrary length scale in the y-direction with δ being boundary layer thickness	ρ	medium density
		ρ^*	relative helium density, Eq. (16)
		χ	length scale, $r \cdot n(r)$
θ	fringe orientation angle measured from horizon, or dimensionless temperature, $(T - T_x)/(T_w - T_x)$, or projection angle	Subscripts	
		min	minimum
		o	ambient condition
λ	laser wave length (λ = 632.8 nm for helium–neon laser)	opt	optimum
		r	reference point
ν	kinematic viscosity	w	wall
ξ	arbitrary length scale in the x-direction	∞	ambient condition away from the heated wall

References

1. Françon, M. (1979). *Laser Speckle and Applications in Optics*. Academic Press, New York.
2. Parker, S. P. (Editor-in-Chief) (1984). *McGraw-Hill Dictionary of Scientific and Technical Terms*, 3rd. ed. McGraw-Hill, New York.
3. Adrian, R. J. (1984). Scattering particle characteristics and their effect on pulsed laser measurements of fluid flow: Speckle velocimetry vs particle image velocimetry. *Appl. Opt.* 23, 1690–1691.
4. Debrus, S., Françon, M., Grover, G. P., May, M., and Roblin, M. L. (1972). Ground glass differential interferometer. *Appl. Opt.* 11, 853–857.
5. Köpf, U. (1972). Application of speckling for measuring the deflection of laser light by phase objects. *Opt. Commun.* 5, 347–350.
6. Debrus, S., and Grover, C. P. (1971). Correlation of light beams scattered at different angles by a ground glass. *Opt. Commun.* 3, 340–342.
7. Merzkirch, W. (1987). *Flow Visualization*, 2nd ed. Academic Press, New York.
8. van de Hulst, H. C. (1957). *Light Scattering by Small Particles*. Dover, New York.
9. Li, Q. B., and Chiang, F. P. (1992). Three-dimensional dimension of laser speckle. *Appl. Opt.* 31, 6287–6291.
10. Goldstein, R. J. (1983). *Fluid Mechanics Measurements*. Hemisphere, New York.
11. Kastell, D., Kihm, K. D., and Fletcher, L. S. (1992). Study of laminar theory boundary layers occurring around the leading edge of a vertical isothermal wall using a specklegram technique. *Exp. Fluids* 13, 249–256.
12. Walsh, T. E. (1996). A comparative study of laser speckle photography and laser interferometry for optical tomography. Ph.D. Dissertation, Department of Mechanical Engineering, Texas A & M University, College Station.
13. Bonin, K. D., and Kadar-Kallen, M. A. (1989). Simple diffuser for production of laser speckle. *Appl. Opt.* 28, 5293–5297.
14. Kim, J. H. (1993). Investigation of heat transfer characteristics and flow reversal phenomena in naturally convecting parallel/converging vertical channel flow. Ph.D. Dissertation, Department of Mechanical Engineering, Texas A & M University, College Station.
15. Kihm, K. D. (1992). Image blurring of test section boundary in a specklegram technique for temperature gradient measurements. *Appl. Opt.* 31, 5907–5910.

16. Mewes, D. (1992). Advances in optical methods for visualizing and measuring transport phenomena. *Proc. Int. Symp. Transp. Phenom. 2nd*, Beijing, China, pp. 1-16.

17. Archbold, E., Burch, J. M., and Ennos, A. E. (1970). Recording of inplane surface displacement by double-exposure speckle photography. *Opt. Acta* **17**, 883-893.

18. Hecht, E. (1974). *Optics*. Addison-Wesley, New York.

19. Chitsaz, B., and Moslehy, F. A. (1989). A computerized displacement data analysis in laser speckle photography. *Exp. Tech.*, pp. 21-24.

20. Sivasubramanian, M. S., Cole, R., and Sukanek, P. C. (1984). Optical temperature gradient measurements using speckle photography. *Int. J. Heat Mass Transfer* **27**, 773-780.

21. Erbeck, R. (1985). Fast image processing with a microcomputer applied to speckle photography. *Appl. Opt.* **24**, 3838-3841.

22. Huntley, J. M. (1989). Speckle photography fringe analysis: Assessment of current algorithms. *Appl. Opt.* **28**, 4316-4321.

23. Rösgen, T., Wozniak, K., and Wozniak, G. (1990). Image processing for laser speckle velocimetry using the 2-D fast fourier transform. *Appl. Opt.* **29**, 5298-5302.

24. Pei, W., and Song, F. (1992). Automatic specklegram fringe analysis by using symmetry evaluation of the Θ-scanning function. *Appl. Opt.* **31**, 665-669.

25. Weyl, F. J. (1954). Analysis of optical methods. In *Physical Measurements in Gas Dynamics and Combustion* (R. W. Ladenburg, ed.), pp. 3-25. Princeton University Press, Princeton, NJ.

26. Merzkirch, W. (1995). Density-sensitive whole-field flow measurement by optical speckle photography. *Exp. Therm. Fluid Sci.* **10**, 435-443.

27. Shu, J. Z., and Li, J. Y. (1993). A laser Schlieren-speckle interferometry system for measurement of phase objects. *J. Flow Visual. Image Process.* **1**, 63-68.

28. Vest, C. M. (1979). *Holographic Interferometry*. Wiley, New York.

29. Goodman, J. W. (1975). Speckle interferometry. In *Laser Speckle and Related Phenomena* (J. C. Dainty, ed.). Springer-Verlag, Berlin.

30. Shakher, C., Daniel, A. J. P., and Nirala, A. K. (1994). Temperature profile measurement of axisymmetric gaseous flames using speckle photography, speckle shearing interferometry, and Talbot interferometry. *Opt. Eng.* **33**, 1983-1988.

31. Shakher, C., and Nirala, A. K. (1994). Measurement of temperature using speckle shearing interferometry. *Appl. Opt.* **33**, 2125-2127.

32. Shakher, C., and Nirala, A. K. (1994). A comparative study of speckle shearing interferometry and speckle photography for measurement of temperature of an axisymmetric flame. *Optik* **97**, 43-46.

33. Partington, J. R. (1953). *An Advanced Treatise on Physical Chemistry, Physico-Chemical Optics*, Vol. IV. Longmans, Green, London.

34. Holman, J. P. (1963). *Heat Transfer*. McGraw-Hill, New York.

35. Kihm, K. D. (1993). On the application of a laser specklegram technique for convective heat transfer problems. *Proc. Int. Symp. Transp. Phenom. Therm Eng., 6th*, Seoul, Korea, pp. 1211-1217.

36. Elenbaas, W. (1942). Heat dissipation of parallel plates by free convection. *Physica* **9**, 1-28.

37. Eckert, E. R., and Carlson, O. (1961). Natural convection in an air layer enclosed between two vertical plates with different temperatures. *Int. J. Heat Mass Transfer* **2**, 106-120.

38. Levy, E. K. (1972). Optimum plate spacing for laminar natural convection heat transfer from parallel vertical isothermal flat plates. *J. Heat Transfer* **93**, 463-465.

39. Wirtz, R. A., and Stutzman, R. J. (1982). Experiments on free convection between vertical plates with symmetric heating. *J. Heat Transfer* **104**, 501-507.

40. Anand, N. K., Kim, S. H., and Fletcher, L. S. (1991). The effect of plate spacing on free convection between heated parallel plates. *Proc. ASME Winter Ann. Meet.*, HTD-153, pp. 81–87.

41. Carnahan, B., Luther, H. A., and Wilke, J. O. (1969). *Applied Numerical Methods*. Wiley, New York.

42. Sparrow, E. M., and Gregg, J. L. (1958). The variable fluid problem in free convection. *Int. J. Heat Mass Transfer* **78**, 1823–1828.

43. Ostrach, S. (1952). An analysis of laminar free-convection flow and heat transfer about a flat plate parallel to the direction of the generating body force. *Natl. Advis. Comm. Aeronaut., Tech. Note* **2635**.

44. Brodowicz, K. (1968). An analysis of laminar free convection around isothermal vertical plate. *Int. J. Heat Mass Transfer* **11**, 201–209.

45. Schmidt, E., and Beckmann, W. (1930). Das Temperatur und Geschwindigkeitsfeld von einer Warme abgebenden senkrechten Platte bei naturlicher Konvektion. *Tech. Mech. Thermodyn.* **1**, 341–349, 391–406.

46. Wernekinck, U., and Merzkirch, W. (1986). Measurement of natural convection by speckle photography. *Heat Transfer, Proc. Int. Heat Transfer Conf., 8th, 1986*, pp. 531–535.

47. Schlichting, H. (1968). *Boundary Layer Theory*. McGraw-Hill, New York.

48. Guo, Z.-Y., Song, Y.-Z., and Zhao, X.-W. (1991). Experimental investigation on natural convection in channel by laser speckle photography. *Exp. Therm. Fluid Sci.* **4**, 594–600.

49. Guo, Z.-Y. (1986). Thermal drag and thermal roundabout flow in convection problems. *Heat Transfer, Proc. Int. Heat Transfer Conf., 8th, 1986*, pp. 59–68.

50. Kihm, K. D., Kim, J. H., and Fletcher, L. S. (1995). Onset of flow reversal and penetration length of natural convective flow between isothermal vertical walls. *J. Heat Transfer* **117**, 776–779.

51. Elenbaas, W. (1942). Heat dissipation of parallel plates by free convection. *Physica* **9**, 1–28.

52. Kihm, K. D., Kim, J. H., and Fletcher, L. S. (1993). Investigation of natural convection heat transfer in converging channel flows using a specklegram technique. *J. Heat Transfer* **115**, 140–148.

53. Bar-Cohen, A., and Rohsenow, W. M. (1984). Thermally optimum spacing of vertical, natural convection cooled, parallel plates, *J. Heat Transfer* **106**, 116–123.

54. Goldstein, R. J., and Lau, K. S. (1983). Laminar natural convection from a horizontal plate and influence of plate-edge extensions. *J. Fluid Mech.* **129**, 55–75.

55. Kihm, K. D., and Cheeti, S. K. R. (1994). Study of thermal flows from two-dimensional, upward-facing isothermal surfaces using a laser speckle photography technique. *Exp. Fluids* **17**, 246–252.

56. Walsh, T. E., and Kihm, K. D. (1995). Tomographic deconvolution of laser speckle photography for axisymmetric flame temperature measurement. *J. Flow Visual. Image Process.* **2**, 299–310.

57. Wragg, A. A., and Loomba, R. P. (1970). Free convection flow patterns at horizontal surfaces with ionic mass transfer. *Int. J. Heat Mass Transfer* **13**, 439–442.

58. Bandrowski, J., and Rybski, W. (1976). Free convection mass transfer frorm horizontal plates. *Int. J. Heat Mass Transfer* **19**, 827–838.

59. Kihm, K. D., Kim, J. H., and Fletcher, L. S. (1991). Effects of partial openings on natural convection heat transfer in triangular enclosures. *Proc. ASME, Winter Ann. Meet.*, HTD-177, pp. 51–57.

60. Fishenden, M., and Saunders, O. A. (1950). *An Introduction to Heat Transfer*. pp. 95–97. Oxford Univ. Press, London.

61. Bosworth, R. L. C. (1952). *Heat Transfer Phenomena*, pp. 102–104, John Wiley, New York.

62. Lloyd, J. R., and Moran, W. R. (1974). Natural convection adjacent to horizontal surface of various planforms. *J. Heat Transfer* **96**, 443–447.

63. Goldstein, R. J., Sparrow, E. M., and Jones, D. C. (1973). Natural convection mass transfer adjacent to horizontal plates. *Int. J. Heat Mass Transfer* **16**, 1025–1035.

64. Al-Arabi, A., and El-Riedy, M. K. (1976). Natural convection heat transfer from isothermal horizontal plates of different shapes. *Int. J. Heat Mass Transfer* **19**, 1399–1404.

65. Pera, L., and Gebhart, B. (1973). Natural convection boundary flow over horizontal and slightly inclined surfaces. *Int. J. of Heat Mass Transfer* **16**, 1131–1146.

66. Flack, R. D., Konopnicki, T. T., and Rooke, J. H. (1979). The measurement of natural convective heat transfer in triangular enclosures. *J. Heat Transfer* **101**, 648–654.

67. Flack, R. D. (1980). The experimental measurement of natural convection heat transfer in triangular enclosures heated or cooled from below. *J. Heat Transfer* **102**, 770–772.

68. Merzkirch, W. (1993). Density-sensitive whole-field flow measurement by optical speckle photography. *Proc. Int. Conf. Exp. Heat Transfer, Fluid Mech. Thermodyn. 3rd*, Honolulu, Hawaii, pp. 1–11.

69. Wernekinck, U., Merzkirch, W., and Fomin, N. A. (1985). Measurement of light deflection in a turbulence density field. *Exp. Fluids* **3**, 206–208.

70. Deans, S. R. (1983). *The Radon Transform and Some of its Applications*. Wiley, New York.

71. Walsh, T. E., and Kihm, K. D. (1995). Tomographic deconvolution of laser speckle photography applied for flame temperature measurement. *Proc. Int. Symp. Flow Visual., 7th*, Seattle, pp. 898–903.

72. Bracewell, R. (1978). *The Fourier Transform and its Applications*. McGraw-Hill, New York.

73. Kak, A. C., and Slaney, M. (1987). *Principles of Computerized Tomographic Imaging*. IEEE Press, New York.

74. Liu, T. C., Merzkirch, W., and Oberste-Lehn, K. (1989). Optical tomography applied to speckle photographic measurement of asymmetric flows with variable density. *Exp. Fluids* **7**, 157–163.

75. Goulard, R., and Emmerman, P. J. (1980). Combustion diagnostics by multiangular absorption. In *Inverse Scattering Problems in Optics*, pp. 215–235. Springer-Verlag, Berlin.

76. Shepp, L. A., and Logan, B. F. (1974). Reconstruction interior head tissue from X-ray transmissions. *IEEE Trans. Nucl. Sci.* **NS-21**, 21–43.

77. Swindell, W., and Barrett, H. H. (1977). Computerized tomography: Taking sectional X-rays. *Phys. Today* pp. 32–41.

78. Tennekes, H., and Lumley, J. L. (1972). *A First Course in Turbulence*. MIT Press, Cambridge, MA.

79. Uberoi, M. S., and Kovasznay, L. S. G. (1955). Analysis of turbulent density fluctuations by the shadow method. *J. Appl. Phys.* **26**, 19–24.

80. Erbeck, R., and Merzkirch, W. (1988). Speckle photographic measurement of turbulence in an air stream with fluctuating temperature. *Exp. Fluids* **6**, 89–93.

81. Mills, R., Kistler, A. L., O'Brien, V., and Corrsin, S. (1958). Turbulence and temperature fluctuations behind a heated grid. *Natl. Advis. Comm. Aeronaut., Tech. Note* **4288**.

82. Sepri, P. (1976). Two-point turbulence measurements downstream of a heated grid. *Phys. Fluids* **19**, 1876–1884.

83. Van Atta, C. W., and Yeh, T. T. (1972). Spectral transfer of scalar and velocity fields in heated grid turbulence. *J. Fluid Mech.* **58**, 233–261.

84. Hintze, J. O. (1959). *Turbulence*. McGraw-Hill, New York.

85. Oberste-Lehn, K., and Merzkirch, W. (1993). Speckle optical measurement of a turbulent scalar field with high fluctuation amplitudes. *Exp. Fluids* 14, 217-223.

86. Keller, J., and Merzkirch, W. (1990). Interaction of a normal shock wave with a compressible turbulent flow. *Exp. Fluids* 8, 241-248.

87. Fomin, N., Merzkirch, W., Vitkin, D., and Wintrich, H. (1995). Speckle photography of temperature field microstructure in a turbulent flame. *Proc. Int. Symp. Flow Visual., 7th*, Seattle, pp. 904-909.

88. Meynart, R. (1984). Diffraction halo in speckle photography. *Appl. Opt.* 23, 2235-2236.

89. Fomin, N., Merzkirch, W., Vitkin, D., and Wintrich, H. (1997). Visualization of turbulence anisotropy by single exposure speckle photography. *Exp. Fluids* (to be published).

90. Blinkov, G. N., Soloukhin, R. I., and Fomin, N. A. (1987). Speckle photography of density gradients in a free flame. Translated from *Fiz. Goreniya Vzryva* 23, 40-46.

91. Chemical Rubber Company (1988). *CRC Handbook of Chemistry and Physics*, 69th ed. CRC Press, Boca Raton, FL.

92. Born, M., and Wolf, E. (1980). *Principles of Optics*. Pergamon, Oxford.

93. Farrell, P. V., and Hofeldt, D. L. (1984). Temperature measurement in gases using speckle photography. *Appl. Opt.* 23, 1055-1059.

94. Gardiner, W. C., Hidaka, Y., and Tanzawa, T. (1981). Refractivity of combustion gases. *Combust. Flame* 40, 213-219.

95. Michael, Y. C. (1991). Three-dimensional temperature reconstruction using Mach-Zehnder interferometric tomography. Ph.D. Dissertation, Dept. of Aerospace and Mechanical Engineering, University of Notre Dame, South Bend.

96. Verhoeven, D. D., and Farrell, P. V. (1986). Speckle interferometry in transparent media. *Appl. Opt.* 25, 903-906.

97. Fomin, N. A. (1989). Multidirectional speckle photography of density fields in gasdynamics flows. *Inzh.-Fiz. Zh.* 56, 540-547.

98. Barakat, N., El-Ghandoor, H., Hamed, A. M., and Diab, S. (1993). Refractive index profiling across a candle flame using speckle techniques. *Exp. Fluids* 16, 42-45.

99. Blinkov, G. N., Fomin, N. A., Rolin, M. N., Soloukhin, R. I., Vitkin, D. E., and Yadrevskaya, N. L. (1989). Speckle tomography of a gas flame. *Exp. Fluids* 8, 72-76.

100. Shu, J.-Z., and Li, J.-Y. (1987). Speckle photography applied to the density field of a flame. *Exp. Fluids* 5, 422-424.

101. Gordon, R. (1974). A tutorial on ART. *IEEE Trans. Nucl. Sci.* Ns-21, 78-92.

102. ASTM (1993). Manual on the Use of Thermocouples in Temperature Measurement, 4th ed. ASTM Press, Philadelphia.

103. Moffat, R. J. (1962). The gradient approach to thermocouple circuitry. *Meas. Control Sci. Ind.* 3, 33-37.

104. Weinberg, F. J. (1963). *Optics of Flames*. Butterworth, Washington, DC.

105. Radulovič, P. T. (1977). Holographic interferometry of three-dimensional temperature or density fields. Ph.D. Dissertation, Dept. of Mechanical Engineering and Applied Mechanics, University of Michigan, Ann Arbor.

106. Lira, I. H. (1994). Reconstruction of an axisymmetric refractive index distribution with non-negligible refraction. *Meas. Sci. Technol.* 5, 226-232.

107. Lira, I. (1995). Measurement of an axisymmetric temperature fields by speckle photography methods. *Exp. Fluids* 20, 100-105.

Transport Phenomena in Czochralski Crystal Growth Processes

V. PRASAD
H. ZHANG

Department of Mechanical Engineering, State University of New York, Stony Brook, New York

A. P. ANSELMO

USAF Rome Laboratory, Hanscom Air Force Base, Massachusetts

I. Introduction

A. GROWTH OF ELEMENTAL SEMICONDUCTORS

The growth of silicon (Si) single crystals and other electronic semiconductor materials is the basis for electronic device fabrication. Although several methods have been devised to manufacture Si single crystals, the Czochralski (Cz) method [1] has virtually dominated the entire production of single crystals for the microelectronics industry [2, 3]. The popularity of this method comes from its ability to meet the stringent requirements for purity, doping, electrical and mechanical properties, and crystallographic perfection. Fundamentally, the Cz process consists of freezing material from a molten pool contained in a quartz crucible, onto the end of a single-crystal "seed" of the same material. The material thus frozen replicates the single-crystal structure of the seed, and consequently, a small seed becomes a large crystal. A detailed discussion on growing semiconductor crystals using the Cz method may be found in several books and review articles [2-8].

Using the Cz method, in 1950, Teal and Little [9] were the first to grow single crystals of germanium (Ge), 203-mm long and 19 mm in diameter. Subsequently, they succeeded in growing Si crystals with a high degree of

313

lattice perfection and chemical purity [10]. Interestingly, the basic technique to grow single-silicon crystals has not changed since then. Today, single crystals of 100 to 200 mm (4 to 8 in.) in diameter are grown from a 356 to 457-mm (14 to 18 in.) diameter crucible and an initial charge of 30 to 60 kg. The crystal pull rate may vary from 12.7 to 50.8 mm (0.5 to 2 in.) per hour, and it takes about 24 h to grow a crystal of industrial size. The current industry standard for Si growth is 200 mm diameter. Commercial development of pullers that can produce crystals with larger diameters—up to 300 mm from a crucible to 560 mm in diameter—is in progress.

New VLSI-ULSI (very large scale integration-ultra large scale integration) technology places ever-increasing demands on crystal perfection and ensuing electrical properties. Therefore, it is important to control and regulate the physical phenomena occurring during the growth of the crystal. The conventional Cz method is a "batch process" in which a single crystal is grown from the melt in a crucible. When the source of melt (known as the *charge*) is depleted, the growth process is ended, and the entire procedure must be restarted. A schematic of the Cz process is given in Fig. 1, illustrating the various steps in Cz growth, from charging to crystal removal. A silicon crystal being grown from the Cz melt is shown in Fig. 2, while Figs. 3 and 4 present outside and inside views, respectively, of an industrial Cz system for Si growth.
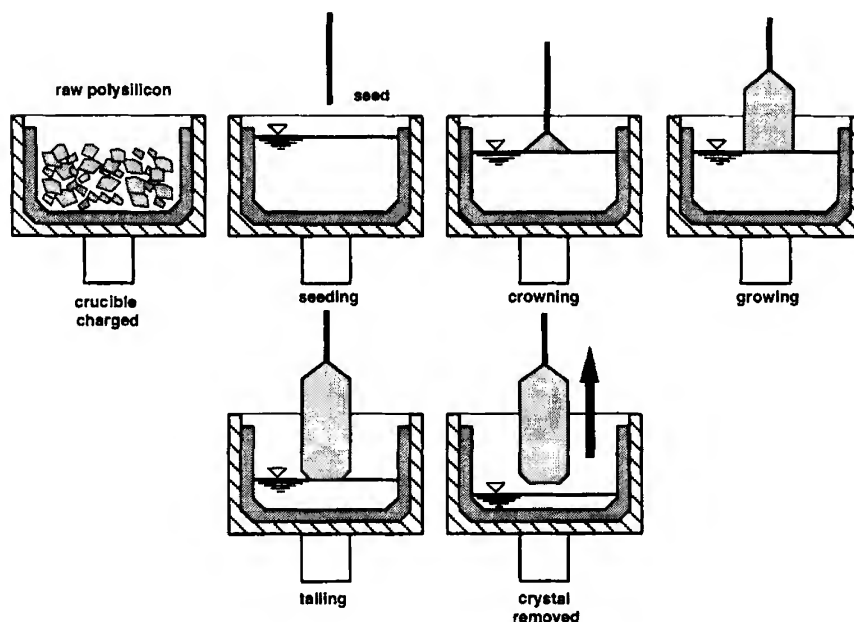
FIG. 1. Various steps in a Czochralski process.
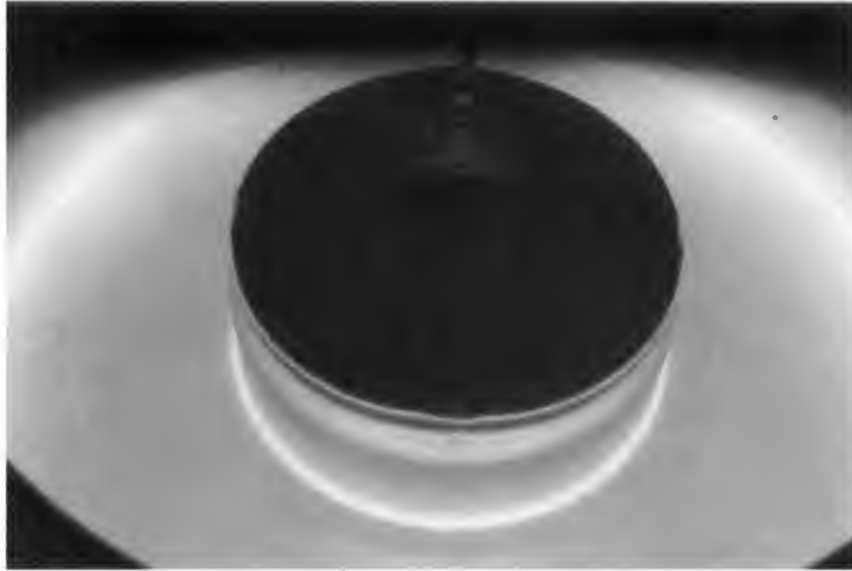
FIG. 2. A silicon crystal being grown from the Czochralski melt. (Courtesy of Ferrofluidics Corporation Nashua, New Hampshire.)

Many of the inhomogeneities in crystals grown by the conventional Cz batch technique are primarily a result of the nonsteady nature of the growth kinetics due to the initial size of the melt volume, and its change from start to finish [2]. This change in volume is reflected in the melt height, which is one of the length scales of the process. Since buoyancy and surface tension forces are very strong and produce convective rolls of complex nature that may be oscillatory, turbulent, or both in the case of large melt volumes, forced convective effects are superimposed by rotating the crucible. Crystal is also rotated to produce homogeneity near the melt–crystal interface. The convective flow and temperature fields therefore depend on each other as well as on the length scale of the melt in a highly complex manner. Due to the variation in melt height from start to finish, the flow changes radically in time.

The recirculating flow in the melt therefore is caused by a combination of five basic modes of convection [3, 4, 11, 12]:

1. Natural convection due to buoyancy forces produced by complex thermal boundary conditions, which include heating on side walls, radiative cooling at the free surface, and phase change at the crystal–melt interface

FIG. 3. A Czochralski furnace for silicon growth. (Courtesy of Ferrofluidics Corporation.)

2. Marangoni convection due to the variation in surface tension with temperature and impurity concentration
3. Forced convection due to crystal rotation
4. Forced convection due to crucible rotation
5. Forced convection due to crystal pulling and drop in the melt height

Convection due to crystal pulling is much weaker since the pull rate is generally very small and therefore is neglected in theoretical studies and simulation experiments. However, its contribution in comparison with that
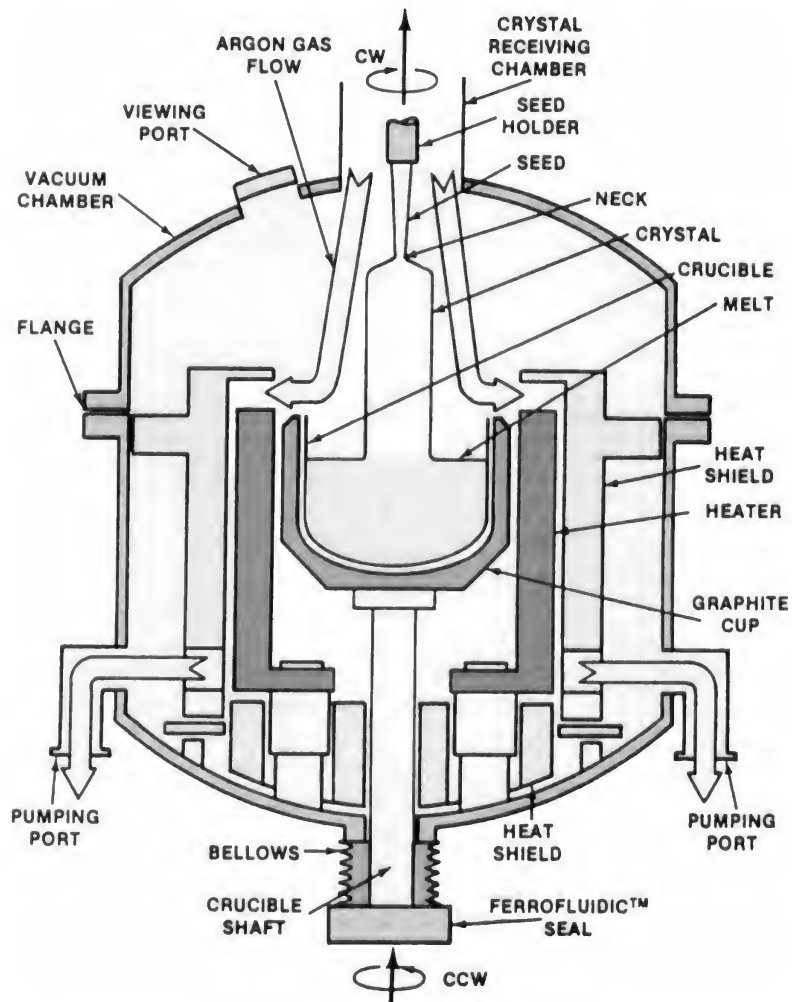
FIG. 4. Inside view of a Czochralski Si growth system. CW, clockwise; CCW, counter clockwise; (Courtesy of Ferrofluidics Corporation.)

of the other modes of convection may be appreciable under certain growth conditions, for example, during the formation of the crown of the crystal when the pull rate is high and for magnetic Cz growth when flow in the melt due to other modes of convection is weak.

Convective transport in the melt is closely coupled with the radiation in a Cz system. For example, the melt surface in the case of Si growth is maintained at a temperature above 1410°C, while the walls of the Cz

furnace are cooled by recirculating water at around room temperature. The crystal and other components of the furnace also participate in radiation exchange, making the transport phenomena in a Cz system further complex.

Transport of impurities and dopants[1] are also important to the quality of the crystal grown by Cz processes. In Si crystal growth, the quartz crucible releases oxygen due to the decomposition of silicon dioxide (SiO_2) at melt temperature. Most of this oxygen evaporates from the melt surface in the form of volatile SiO, through the reaction [13-15]:

$$SiO_2 + Si \rightarrow 2SiO$$

$$2SiO_2 \rightarrow 2SiO + O_2$$
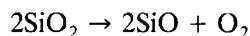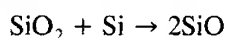
However, some of these oxygen atoms are incorporated into the crystal through the solid-liquid interface, which is highly undesirable. Under most typical Cz conditions, the flow is unsteady and periodic. For 250 to 300-mm diameter Si crystal growth, the melt flow is indeed turbulent. The fluctuations that the convective mechanisms impart to the flow have been shown to directly produce the inhomogeneity of oxygen incorporation within the grown crystal, and other microscopic defects. Flow within the melt therefore is of great importance to Cz growth. The solidification and remelting at the solid-liquid interface induced by the flow oscillations and other phenomena and dopant and impurity segregation can cause striations and inhomogeneities within the crystal.

The scaling up of the process (especially with regard to the natural convection effect, which magnifies as the cube of the length scale) is also a major concern, since these flows may become chaotic and turbulent, resulting in crystals with greater impurities and inhomogeneities [16]. Magnetic fields, in both the axial and radial directions have been used to dampen these effects; however, this results in added capital and operational costs. This also adds another control parameter to be varied within the system. The reductions in convective flows also can increase the amount of oxygen incorporated into the melt when local temperatures near the crucible wall becomes high as the fluid motion is reduced. Magnetic Cz (MCz) growth of larger Si crystals therefore is not an industry norm, as yet.

The Czochralski process also has been used to grow single crystals of many other materials, for example, Ge. Crystals of other elements are less commonly used and have a very small market compared with that of Si. As a result, theoretical and experimental research on Cz growth has focused

---

[1] Various kinds of dopants are added to the melt to modify the electrical, mechanical, optical, and magnetic properties of the crystals for different applications.

largely on Si. The size of the melt in the case of Si growth also is much larger and the quality constraints much more stringent. Research into Si growth therefore has been quite extensive and forms a basis for Cz growth of other elemental crystals.

B. Growth of Oxide Crystals

The importance of single crystals of oxides for technological applications was recognized after the discovery of pulsed laser action in ruby in 1960 [17] and both pulsed and continuous wave laser emission in Neodymium-doped Calcium Tungstate in the following two years [18]. Since then, oxides have found important applications in many fields including lasers, substrates, shock-proof transparent windows, and small-diameter crystal fibers. Rare earth gallates and aluminates, such as $LaAlO_3$, $NdGaO_3$, $LaGaO_3$, and perovskites are excellent substrates for superconducting thin films. Widespread use of oxide crystals has stemmed from their special optical, fluorescent, electrical, and mechanical properties, and these crystals are finding new applications in a vast field of ferroelectric, pyroelectric, piezoelectric, acoustic, magnetic, and opto-magnetic devices. Most of these applications require a high level of microstructural and chemical perfection that only can be exhibited by single crystals. Table I presents a short list of oxides with their melting temperatures, pulling rates, and the gas environment under which they can be grown by the Cz process. The oxides listed in Table I are of great interest for use in optical and electronic devices. A comprehensive list of oxides that can be grown by the Cz method can be found in Pressley [19], and Cockayne [20]. Hurle and Cockayne [3] have presented an excellent review of the conditions for Cz growth of oxides, quality of the oxide crystals grown thus far, and major difficulties in growing these materials.

Defects in oxide crystals can be categorized into two groups: stress and chemical effects, although both are interrelated. They lead to various kinds of inhomogeneities and defects in the crystal, such as color centers, facets, growth striations, dislocations, twins, voids, cellular structures, solid state precipitates, inclusions, and cracks. As in the case of semiconductor materials, thermal conditions during the growth are major factors behind these chemical and stress-related defects.

C. Growth of III-V Compounds

Many compounds possess structural and electrical characteristics similar to those of the elemental semiconductors Si, Ge. Many of these are covalent compounds formed between elements of group III (boron, alu-

TABLE I

TYPICAL CONDITIONS FOR THE CZOCHRALSKI GROWTH OF
OXIDE SINGLE CRYSTALS

Oxides	Melting Point (°C)	Environment	Pulling Rate (mmh^{-1})
$Pb_5Ge_3O_{11}$	738	O_2	1–10
$Bi_{12}GeO_{20}$	930	O_2	5–15
$PbMoO_4$	1070	O_2	1–10
$ZnWO_4$	1200	Air	5–15
$LiNbO_3$	1250	O_2	5–10
$Sr_xBa_{1-x}Nb_2O_6$	1400	O_2	1–10
$Ba_2NaNb_5O_{15}$	1450	O_2	1–10
$CaWO_4$	1600	A/O_2 or N_2/O_2	1–10
Lithium tantalate			
$(LiTaO_3)$	1650	A/O_2 or N_2/O_2	5–10
$Gd_3Ga_5O_{12}$	1825	A/O_2 or N_2/O_2	1–10
$YALO_3$	1870	A/O_2 or N_2/O_2	1–10
$Gd_2Sc_2Ga_5O_{12}$	1875	A/O_2 or N_2/O_2	1–10
$Y_3Al_5O_{12}$	1970	A/O_2 or N_2/O_2	1–10
Al_2O_3	2105	A or N_2	1–10
$MgAl_2O_4$	2150	A or N_2	1–10

A, atmosphere; N_2, nitrogen; O_2, oxygen.
Reprinted with permission by Hurle and Cockayne [3].

minum, gallium, indium, thallium) and group V (neon, phosphorus, arsenic, antimony, bismuth) of the periodic table. The general decrease in energy gap with increasing atomic number of group IV semiconductors and group III-V compounds is a result of an increasing tendency toward ionic bonding. General reviews describing their properties are available in the literature, and some relevant properties are listed in Table II. Crystal growth by solidification has been successfully employed for indium antimonide (InSb), gallium antimonide (GaSb), aluminum antimonide (AlSb), indium arsenide (InAs), gallium arsenide (GaAs), indium phosphide (InP), and gallium phosphide (GaP). Large crystals have been grown for most of these compounds [21–24].

The electronic and opto-electronic applications of III-V semiconductors have rapidly expanded with the availability of bulk single crystals of GaAs and InP. These compounds are playing an increasingly important role in microwave devices, millimeter-wave devices, and circuit technology. In the area of electro-optics, the direct bandgap of GaAs and InP has made these materials all the more useful. To a large extent, promising developments in high-speed electronic and photonic technologies have motivated the progress in improving the quality of GaAs and InP substrates.

TABLE II

SELECTED PROPERTIES OF III-V COMPOUNDS

Material	Lattice Constant a_o (Å)	Energy Gap E_g (eV)	Melting Point, T_m (°C)	Vapor Pressure (atm)	Mobility at 300 K (cm²/Vsec)	
					Electrons	Holes
Boron nitride (BN)		4.6	>2700	High		
Aluminum nitride (AlN)		5	>2900	>80		
Gallium nitride (GaN)		3.25	>1700	>200		
Indium nitride (InN)		3.5		High		
Boron phosphide (BP)		5.9	>1300	>24		
Aluminum phosphide (AlP)		2.42	>2000	High		
Gallium phosphide (GaP)	5.451	2.26	1467	35	110	75
Indium phosphide (InP)	5.869	1.35	1060	25	5000	150
Boron arsenide (BAs)		2.6	>1000	High		
Aluminum arsenide (AlAs)	5.661	2.17	>1700	High	280	
Gallium arsenide (GaAs)	5.654	1.40	1238	0.9	8500	400
Indium arsenide (InAs)	6.058	0.36	943	0.33	33000	460
Aluminum antimonide (AlSb)		1.58	1050	<0.02		
Gallium antimonide (GaSb)	6.095	0.72	706	$<4 \times 10^{-4}$	5000	850
Indium antimonide (InSb)	6.479	0.17	525	$<10^{-5}$	80000	1250
Indium bismide (InBi)		Metallic	107	Very low		
Thallium bismide (TlBi)		Metallic	230	Very low		
Zinc (ZnSe)	5.668	2.80			530	
Zinc telluride (ZnTe)	6.088	2.20			530	
Cadmium telluride (CdTe)	6.482	1.49			700	60

For silicon, lattice constant = 5.431 Å, energy gap = 1.11 eV, melting point = 1420°C, vapor pressure = 10^{-6}, mobility of electrons = 1400 cm²/Vsec, mobility of holes = 470 cm²/Vsec. For germanium, lattice constant = 5.646 Å, energy gap = 0.67 eV, melting point = 936°C, vapor pressure = 10^{-9}, mobility of electrons = 3900 cm²/Vsec, mobility of holes = 1900 cm²/Vsec.

321

In particular, GaAs has attractive photovoltaic (PV) properties, and its surface is readily passivated with wide bandgap, lattice-matched layers. Its bandgap is nearly optimum for the solar spectrum. GaAs wafers are used in microwave low noise and power fast field-effect transistors (FETs), analog integrated circuits for lightwave transmitters and receivers, and digital integrated circuits. In addition, for over a decade, n-type GaAs substrates have been utilized in high power lasers emitting at 0.87 μm and light-emitting diodes (LEDs).

Group III-V compound-based commercial products are now advancing beyond the use of microwave to millimeter-wave communications systems. Consequently, the substrate requirements are changing from GaAs wafers (grown at a low or moderate pressure) to InP wafers, which require high-pressure growth. In the field of photonics, the trend toward greater bandwidth, requires a shift from solid-state infrared lasers to visible blue lasers, which can operate at room temperature and above. Substrate technology likewise is moving to grow crystals such as gallium nitride (GaN) and zinc oxide (ZnO), which require even higher pressures for growth. Large crystals of nitrides have not yet been prepared by conventional Cz techniques due to the requirement of ultrahigh pressures, and usually are produced by other techniques, including thin film deposition.

D. TECHNOLOGICAL CHALLENGES IN GROWTH OF III-V COMPOUNDS

In the case of III-V compounds, an encapsulant layer of a highly viscous melt (generally boric oxide, B_2O_3) is placed over the compound melt to prohibit the escape of the volatile component, for example, as in the case of GaAs. This growth technique is referred to as the liquid-encapsulated Czochralski (LEC) process (Fig. 5). Crystals of GaAs can be grown at about atmospheric pressure (as opposed to a very low pressure in the case of Si), because the equilibrium vapor pressure at its melting temperature is about 0.9 atm. When the equilibrium vapor pressure of the volatile component in the melt is high (e.g., about 27.5 atm for phosphorus in the InP melt), the LEC growth becomes further complex [3] because of the presence of an inert gas in the crystal growth furnace. Figure 6 shows a schematic of the high-pressure system being used for "one-step" *in situ* synthesis and growth of InP crystals at the US Air Force Rome Laboratory.

Even though the LEC technique is advantageous for growing large-diameter single crystals with high yield, twinning is a major problem in the case of InP and other materials. Indium phosphide has a very small stacking fault energy so that twin boundaries are easily formed when ⟨100⟩-oriented crystals are grown. There are many factors that could be
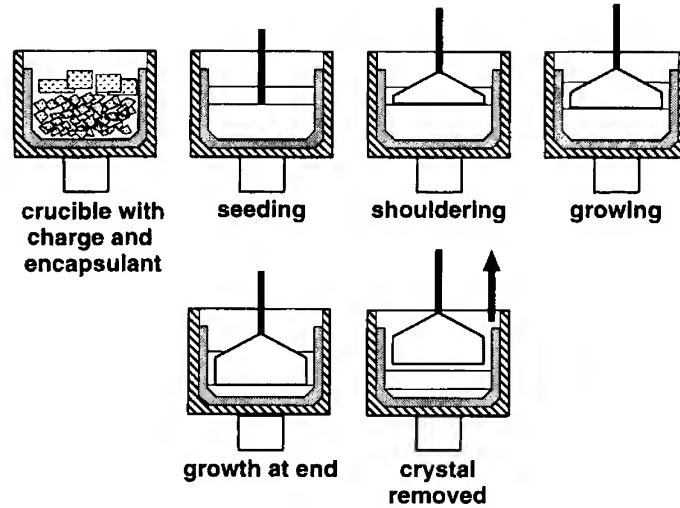
FIG. 5. Various steps in a liquid-encapsulated Czochralski (LEC) process.

responsible for twinning: B_2O_3 purity, melt composition, crystal shape, crystal and crucible rotation rates, radial and axial temperature distributions, temperature fluctuations, and growth rate. Dislocation generation and propagation resulting from thermal stresses, native defects, non-stoichiometry, and dislocations in the seed also affect crystal quality. Akai et al. [25] have noted that the dislocation densities can be reduced by

- Reduction of thermal stresses by decreasing the radial and axial temperature gradients
- Increase of the critical shear stress by doping the crystal with specific impurities (impurity hardening effect)

Some success has been achieved in improving the quality of InP crystals by applying a magnetic field during the growth process. Note that the mechanisms of energy transport in a high-pressure liquid-encapsulated Czochralski (HPLEC) system are very different from that in a low-pressure Cz furnace for Si crystals [26]. For example, in a low-pressure system the energy is transferred to and from the melt surface and the crystal by conduction and radiation only, while gas convection plays an important role in a HPLEC furnace. The recirculating gas flow pattern is a strong function of the geometric configuration, temperatures of the heater, susceptor, melt, crystal and furnace walls, and the gas properties. In addition, convection in a HPLEC melt is strongly coupled with conduction in various components of the furnace as well as with the radiation heat

● Thermocouples A,B,C,D,E
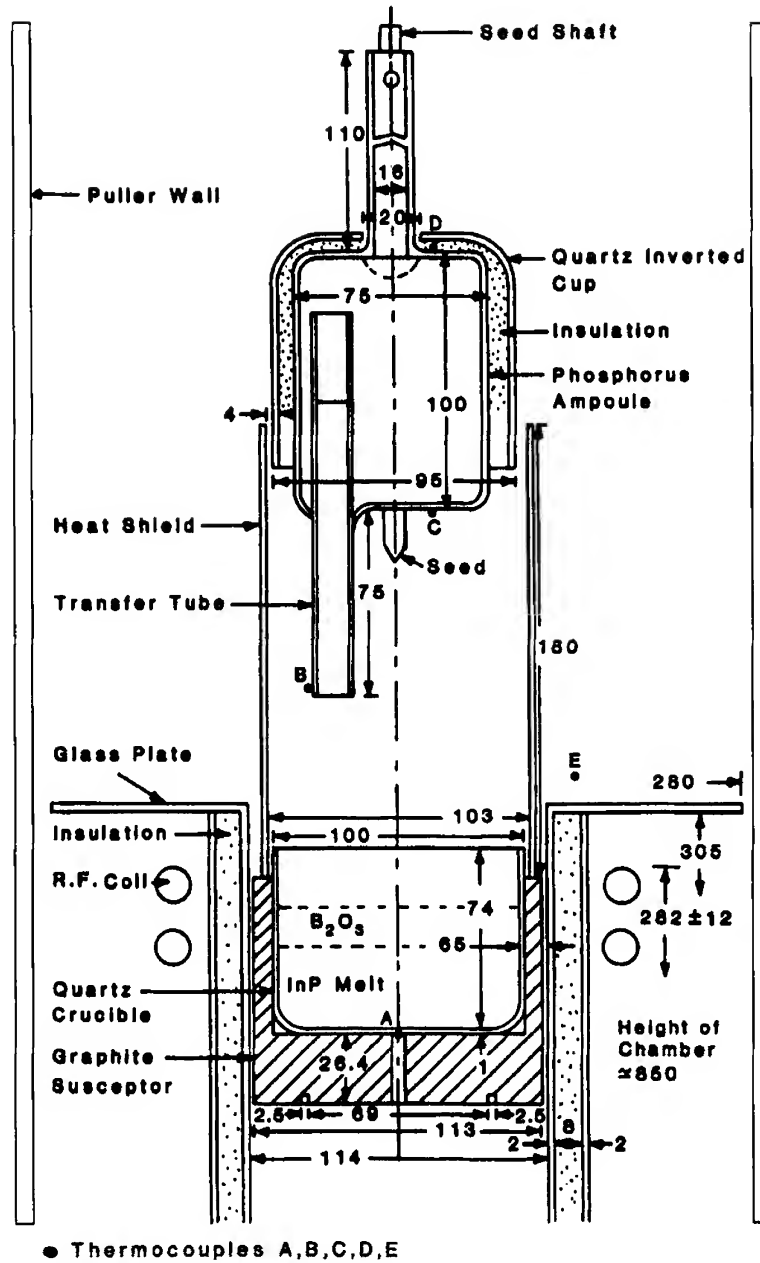
FIG. 6. A schematic of a high-pressure furnace for "one-step" *in situ* synthesis and growth of indium phosphide (InP) crystals. R.F., radio frequency. (Courtesy of USAF Rome Laboratory, Hanscom Air Force Box, Massachusetts.)
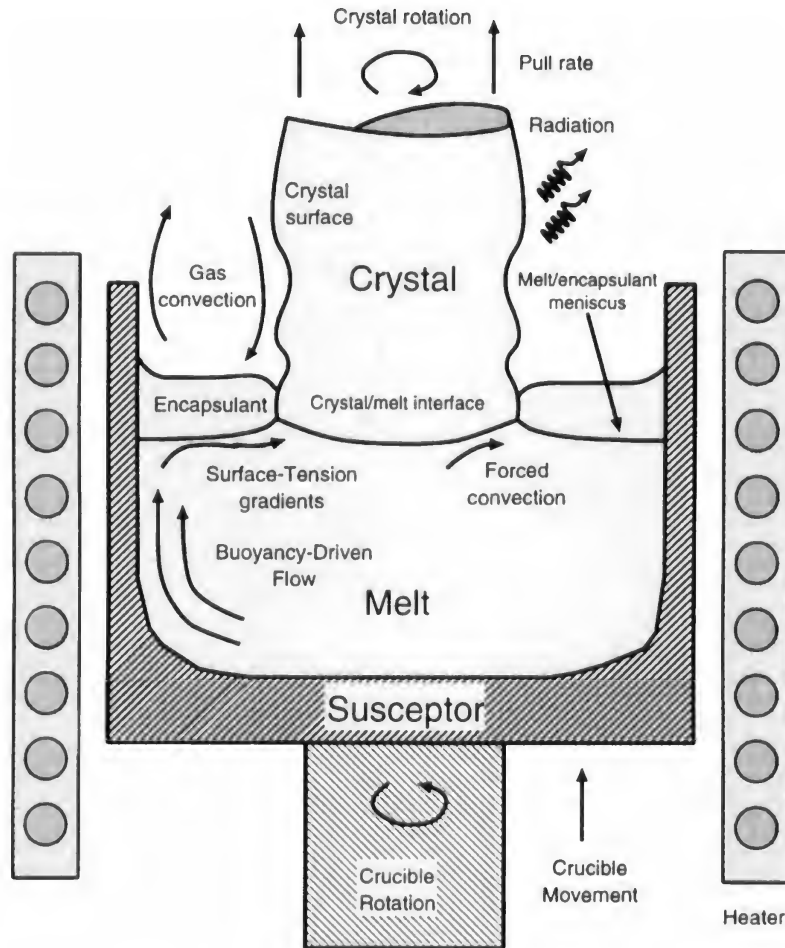
FIG. 7. A schematic of the modes of heat transfer in a HPLEC system, after Brown [71].

transfer. A highly instructive schematic of the modes of heat transfer in various regions of a HPLEC furnace is presented in Fig. 7. (The buoyancy-induced gas flows in a HPLEC system are oscillatory and turbulent [26].) Figure 8 demonstrates the transport mechanisms in a LEC system and their influence on crystal inhomogeneities and defects.

E. CHAPTER ORGANIZATION

This chapter presents a brief review of transport phenomena associated with Cz growth of semiconductor materials. Most of the discussions are restricted to the growth of Si, GaAs, and InP crystals. However, the growth
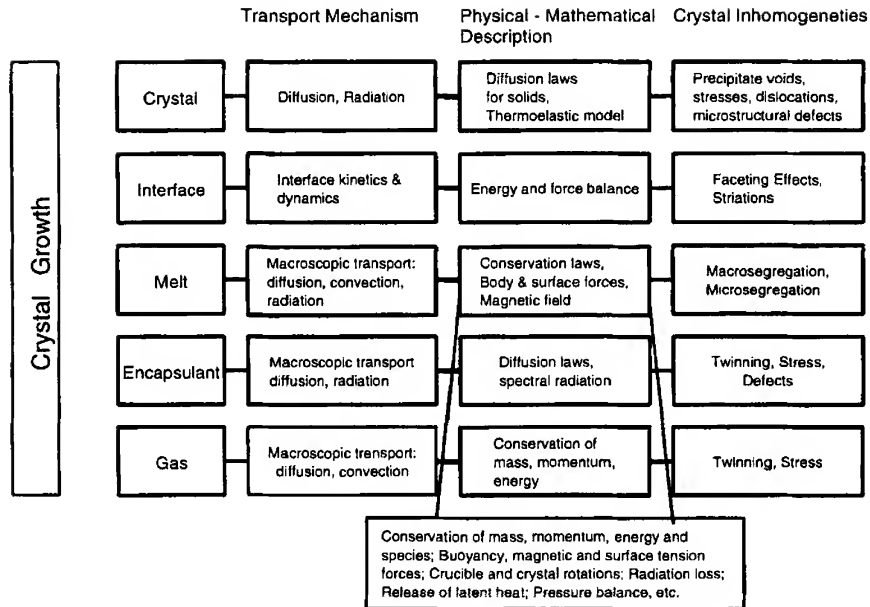
Fig. 8. Transport mechanism and inhomogeneities associated with crystal growth processes, after Müller [6].

of these material spans a pressure range of few millitorrs to about 4 MPa, and thereby reveals a high level of complexity in transport phenomena. Indeed, these processes form a class of most challenging problems for theoretical, experimental, and industrial research.

Section II presents a description of the theoretical model and the numerical techniques used to solve them. A brief analysis of the melt flow mechanisms is presented in Section III. Section IV focuses on low pressure Cz growth of Si crystals, while Section V describes the research on high-pressure growth of III-V compounds. The chapter focuses on fluid flow and heat transfer, although their effects on impurity and dopant transport and stresses in the grown crystals have been discussed in some details wherever relevant.

II. Theoretical Model

It is evident that crystal growth is a physically complex and mathematically rich process. The quality of the grown crystal depends on many macroscopic and microscopic physical effects (Fig. 8). Description of all of

these physical phenomena and their incorporation into a mathematical model are not easy tasks. One therefore must make judicious choices and first consider all the primary effects that influence the growth process, and then examine the effects of the secondary parameters. Here, we present the physical–mathematical model that allows consideration of as many effects as the problem demands and is believed crucial for the modeling of the process. Less important effects easily can be dropped from this model as and when desired.

A. MATHEMATICAL MODEL

1. Governing Equations

Conservative equations for transport processes in the melt, encapsulant, ambient gas, and solid can be written as follows [27, 28]:

Continuity:

$$\frac{\partial}{\partial t}(r\bar{\rho}) + \frac{\partial}{\partial x}(r\bar{\rho}u) + \frac{\partial}{\partial r}(r\bar{\rho}v) + \frac{1}{r}\frac{\partial}{\partial \theta}(r\bar{\rho}w) = 0. \tag{1}$$

Conservation of momentum:

$$\frac{\partial}{\partial t}(r\bar{\rho}u) + \frac{\partial}{\partial x}(r\bar{\rho}uu) + \frac{\partial}{\partial r}(r\bar{\rho}vu) + \frac{1}{r}\frac{\partial}{\partial \theta}(r\bar{\rho}wu)$$

$$= \frac{\partial}{\partial x}\left(r\bar{\mu}_{\text{eff}}\frac{\partial u}{\partial x}\right) + \frac{\partial}{\partial r}\left(r\bar{\mu}_{\text{eff}}\frac{\partial u}{\partial r}\right) + \frac{1}{r^2}\frac{\partial}{\partial \theta}\left(r\bar{\mu}_{\text{eff}}\frac{\partial u}{\partial \theta}\right)$$

$$+ r\left[-\frac{\partial p}{\partial z} + \text{Gr}\,\bar{\beta}\bar{\rho}\theta + S_{\text{turb}} + S_{\text{mag}}\right]. \tag{2}$$

$$\frac{\partial}{\partial t}(r\bar{\rho}v) + \frac{\partial}{\partial x}(r\bar{\rho}uv) + \frac{\partial}{\partial r}(r\bar{\rho}vv) + \frac{1}{r}\frac{\partial}{\partial \theta}(r\bar{\rho}wv)$$

$$= \frac{\partial}{\partial x}\left(r\bar{\mu}_{\text{eff}}\frac{\partial v}{\partial x}\right) + \frac{\partial}{\partial r}\left(r\bar{\mu}_{\text{eff}}\frac{\partial v}{\partial r}\right) + \frac{1}{r^2}\frac{\partial}{\partial \theta}\left(r\bar{\mu}_{\text{eff}}\frac{\partial v}{\partial \theta}\right)$$

$$+ r\left[-\frac{\partial p}{\partial r} - \frac{v}{r^2} + \frac{w^2}{r} - \frac{2}{r^2}\frac{\partial w}{\partial \theta} + S_{\text{turb}} + S_{\text{mag}}\right]. \tag{3}$$

$$\frac{\partial}{\partial t}(r\bar{\rho}\Omega) + \frac{\partial}{\partial x}(r\bar{\rho}u\Omega) + \frac{\partial}{\partial r}(r\bar{\rho}v\Omega) + \frac{1}{r}\frac{\partial}{\partial \theta}(r\bar{\rho}w\Omega)$$

$$= \frac{\partial}{\partial x}\left(r\bar{\mu}_{\text{eff}}\frac{\partial \Omega}{\partial x}\right) + \frac{\partial}{\partial r}\left(r\bar{\mu}_{\text{eff}}\frac{\partial \Omega}{\partial r}\right) + \frac{1}{r^2}\frac{\partial}{\partial \theta}\left(\bar{\mu}_{\text{eff}}\frac{\partial \Omega}{\partial \theta}\right)$$

$$+ r\left[-\frac{2}{r}\frac{\partial \Omega}{\partial r} + \frac{\partial p}{\partial \theta} + \frac{2}{r}\frac{\partial v}{\partial \theta} + S_{\text{turb}} + S_{\text{mag}}\right]. \tag{4}$$

Conservation of energy:

$$\frac{\partial}{\partial t}\left(r\bar{\rho}\bar{C}_p\Theta\right) + \frac{\partial}{\partial x}\left(r\bar{\rho}\bar{C}_p u\Theta\right) + \frac{\partial}{\partial r}\left(r\bar{\rho}\bar{C}_p v\Theta\right) + \frac{1}{r}\frac{\partial}{\partial\theta}\left(r\bar{\rho}\bar{C}_p w\Theta\right)$$

$$= \frac{\partial}{\partial x}\left(r\frac{\bar{k}_{eff}}{Pr}\frac{\partial\Theta}{\partial x}\right) + \frac{\partial}{\partial r}\left(r\frac{\bar{k}_{eff}}{Pr}\frac{\partial\bar{C}_p\Theta}{\partial r}\right)$$

$$+ \frac{1}{r^2}\frac{\partial}{\partial\theta}\left(r\frac{\bar{k}_{eff}}{Pr}\frac{\partial\bar{C}_p\Theta}{\partial\theta}\right) + r[-\nabla\cdot\mathbf{q}'' + q''' + S_{turb}]. \qquad (5)$$

Conservation of species:

$$\frac{\partial}{\partial t}(r\bar{\rho}C_i) + \frac{\partial}{\partial x}(r\bar{\rho}uC_i) + \frac{\partial}{\partial r}(r\bar{\rho}vC_i) + \frac{1}{r}\frac{\partial}{\partial\theta}(r\bar{\rho}wC_i)$$

$$= \frac{\partial}{\partial x}\left(r\frac{D_{eff}}{Sc_i}\frac{\partial C_i}{\partial x}\right) + \frac{\partial}{\partial r}\left(r\frac{D_{eff}}{Sc_i}\frac{\partial C_i}{\partial r}\right)$$

$$+ \frac{1}{r^2}\frac{\partial}{\partial\theta}\left(r\frac{D_{eff}}{Sc_i}\frac{\partial C_i}{\partial\theta}\right) + rS_i. \qquad (6)$$

where S_{turb} and S_{mag} are the source terms for turbulence and magnetic forces, respectively, Ω ($= rw$) is the swirl in the θ direction for rotating systems, C_i is the concentration of impurity or dopant i, $\bar{D}_{eff,i}$ is the diffusion coefficient of species i into the melt, V_p is the pulling velocity of the crystal, $\bar{\mu}_{eff}$ is the effective dimensionless viscosity, and so on. The quantities with overbars in Eqs. (1) to (6) represent dimensionless properties.

In Eq. (5), q'' represents the heat flux and can be used to account for radiation heat exchange at the melt and crystal surfaces [29]. This is the term that couples radiation equations with convection-diffusion equations (1) to (6). In Eq. (5), q''' accounts for the volumetric energy source or sink [30]. This term can help in analyzing the melt flows for continuous Cz growth process where solid polysilicon pellets are added to the replenishing melt as the crystal is grown (see Part IV, Section H). In Eq. (6), S_i is the volumetric source of the species i. Note that a buoyant term due to the concentration gradient is not included in Eq. (2) because the concentration of impurities and dopants in a Cz melt is generally low and the melt can be considered a dilute solution. Equations (1) to (6) can be used for the entire multiphase, multicomponent domain, with the provision to account for local properties and abrupt changes in transport properties across the zone boundaries and their possible movements.

The following scales have been used to nondimensionalize the governing equations, Eqs. (1) to (6): length, b; velocity, v_o/b; pressure, $\rho_o v_o^2/b^2$; time, b_2/v_o; density, ρ_o; dynamic viscosity, μ_o; conductivity, k_o; specific heat, C_{po}; and temperature, $\theta = (T - T_x)/(T_h - T_x)$, where the subscript o refers to the melt properties at ambient temperature T_x.

The dimensionless turbulent kinetic energy k and its dissipation rate ε are obtained from the following conservation equations [31]:

$$\frac{\partial \bar{\rho}k}{\partial t} + \nabla \cdot (\bar{\rho}\mathbf{u}k) = \nabla \cdot \left(\frac{\bar{\mu}_{\text{eff}}}{\sigma_k} \nabla k \right) + G - \bar{\rho}\varepsilon, \tag{7}$$

$$\frac{\partial \bar{\rho}\varepsilon}{\partial t} + \nabla \cdot (\bar{\rho}_i\mathbf{u}\varepsilon) = \nabla \cdot \left(\frac{\bar{\mu}_{\text{eff}}}{\sigma_\varepsilon} \nabla\varepsilon \right) + C_1 f_1 G \frac{\varepsilon}{k} - C_2 f_2 \bar{\rho} \frac{\varepsilon^2}{k}, \tag{8}$$

where

$$\bar{\mu}_{\text{eff}} = \bar{\mu} + f_\mu C_\mu \bar{\rho}k^2/\varepsilon, \tag{9}$$

$$\bar{k}_{\text{eff}} = \bar{k} + f_\mu C_\mu \bar{\rho}k^2/\varepsilon \cdot \text{Pr}_m/\text{Pr}_{\text{turb}}, \tag{10}$$

with Pr_{turb} being the turbulent Prandtl number. For laminar flows, $\bar{\mu}_{\text{eff}} = \bar{\mu}$ and $\bar{k}_{\text{eff}} = \bar{k}$. Scale to nondimensionalize turbulence equations are: (1) kinetic energy, k, v^2/b^2; and (2) dissipation, ε, v^3/b^4. The constants and variables (f_u, f_1, and f_2) in Eqs. (8) to (10) can be obtained from literature [32]. The suitability of the k-ε turbulence model for buoyancy-driven flows is always in question and several turbulence models have been tested in recent years to examine their appropriateness for enclosure and other problems [32]. Further discussions on turbulence models for Cz flows can be found in Kobayashi et al. [33], Ristorcelli and Lumley [16], Kinney et al. [34, 35], and Zhang et al. [36].

2. Impurity, Doping and Segregation

It is well known that the electrical, mechanical, and optical properties of crystals are very sensitive to impurities and dopants [37-39]. At the melt–crystal interface, when the crystal is pulled, there is a tendency for some solutes to remain in the liquid and for the others to prefer the solid because of segregation. This causes the concentration of the solutes to accumulate or decrease. However, convection in the melt produces mixing and alters the characteristics of the diffusion layer adjacent to the interface. The spatial structure and intensity of the flow determine the axial and lateral (perpendicular to the growth direction) profiles of the solute concentration in the crystal. Since segregation is coupled with melt convection, solidification, species diffusion, and the physical and chemical proper-

ties of the impurities in the melt and the solid, an accurate simulation of segregation remains a difficult task. The major challenge in predicting the dopant distribution in the crystal stems from the fact that truly it is a transient problem. Thus dopant distribution cannot be treated as quasi-static-like flow and temperature fields, which do not change much in a small time interval since the growth rates are generally very small.

The dopant is added in the beginning of the process, and its concentration changes continuously with the growth.[2] Incorporation of the dopant (and also the impurity) in the crystal is governed by many physical phenomena, as noted earlier, whose time scales are much smaller. The calculations for dopant and impurity distribution therefore need to be carried out from the beginning to the end of the crystal growth using a very small timestep. This is a formidable task, and no success has been reported thus far. Steady-state calculations for dopant and impurity distributions, although performed by some investigators [40, 41], cannot employ realistic boundary conditions and therefore can lead to misleading results. The prediction of impurity incorporation into the crystal is further complicated by the lack of information on kinetics of chemical decomposition of SiO_2 (quartz), volatility of SiO and O_2, and segregation behavior of O_2 atoms at the crystal–melt interface.

In general, the impurity concentration of the solid phase is different from that of the liquid phase due to segregation. The equilibrium segregation during solidification of a binary system can be determined from the corresponding phase diagram. In many cases, for low impurity concentrations the solidus and liquidus curves on a phase diagram can be considered as straight lines in the vicinity of the melting temperature [2]. This implies that the ratio of the solubility of an impurity or dopant in the solid C_s, to that in the melt C_l, remains constant over a concentration range. This ratio is referred to as the equilibrium segregation coefficient:

$$k_o = C_s/C_l. \tag{11}$$

When the impurity solubility in liquid is higher than that in the solid, $k_o < 1$; otherwise $k_o > 1$. For example, k_o for most of the dopants in Si is less than unity; however, k_o is greater than unity for oxygen impurity ($k_o = 1.25 \pm 0.17$). Equilibrium segregation coefficients for several dopants and impurities in various elements of the periodic table have been listed by Shimura [2].

---

[2] With the availability of a precise feed system developed for solid pellets-feed continuous Cz Si growth, it is now possible to add dopants intermittently in some cases (see Part IV, Section H).

The equilibrium segregation coefficient k_o is applicable only for negligibly slow growth rates. For finite or higher solidification rates, impurity atoms with $k_o < 1$ are rejected by the advancing solid at a greater rate than they can diffuse into the melt. Many attempts therefore have been made to obtain appropriate values of the effective segregation coefficient. For 1D (longitudinal) steady-state diffusion of an impurity, we can obtain

$$k_{\text{eff}} = \frac{k_o}{\left[1 - (1 - k_o)J\right]},$$ (12)

where

$$J = \left[\frac{V_P(\nu/\omega_s)^{1/2}}{D}\right]\int \exp\left[Sc - \int_0^x H(z)\,dz\right]dz.$$ (13)

Here, ω_s is the rotation rate for the crystal and H is a rotational parameter [40].

Burton et al. [42, 43] assumed that the impurity distribution varies within a thin layer of thickness δ adjacent to the solid–melt interface. A complete mixing caused by convection is assumed outside this boundary layer. The parameter J is then related to boundary layer thickness δ by [42]

$$\frac{V_P\delta}{D} = -\ln(1 - J).$$ (14)

This approach, however, has been criticized by Wilson [44, 45], who has demonstrated that the relationship should be

$$\frac{V_P\delta}{D} = J.$$ (15)

These two definitions (Eqs. (14) and (15)) approach each other as J becomes very small compared with unity. An evaluation of integral in Eq. (13) then yields

$$\delta = 1.6Sc^{-1/3}\left(\frac{\nu}{\omega}\right)^{1/2}.$$ (16)

This gives the famous BPS model as

$$k_{\text{eff}} = \frac{k_o}{\left[k_o + (1 + k_o)\exp(-V_P\delta/D)\right]},$$ (17)

where it has been assumed that $\rho_l = \rho_s$.

In the limit when $\delta \to 0$, k_{eff} becomes equal to k_o; that is, the boundary layer vanishes due to very strong convective flows in the melt. When $\delta \to \infty$, the effective segregation approaches unity, that is, the incorporation of impurity in the solid is equal to that in the melt.

The impurity concentration in the solid C_s as a function of the fraction solidified g is given by [46]

$$C_s = k_{eff}[C](1 - g)^{k_{eff} - 1},\qquad(18)$$

where $[C_i]_o$ is the initial impurity concentration in the melt. Here, it is assumed that the diffusion in the solid is negligible, impurity concentration in the liquid is uniform, k_{eff} is constant, a steady growth rate is employed, and the crystal–melt interface is planar and normal to the macroscopic direction of solidification.

Using an integral control-volume analysis of convective solute transfer, Ostrogorsky and Müller have derived a model that relates the effective distribution coefficient k_{eff} with the convective velocity at the edge of the solute boundary layer and the actual physical thickness of the solute layer [47].

A detailed discussion on microsegregation in the formalism of the boundary layer model has been presented by Favier et al. [48, 49]. They have decoupled the convective and diffusive material transport and have assumed convection to be steady and diffusion to be time-dependent. This assumption is interesting and questionable since it has been observed that the unsteady convection is the cause of change of the crystal radius.

A fundamental treatment of microsegregation based on the solution of basic transport equations without a boundary layer assumption was presented by Wilson [44, 45]. A fully time-dependent analysis was carried out, assuming an interface velocity of the form

$$V(t) = \bar{V}[1 + A\sin(\omega t)],\qquad(19)$$

where ω is the angular velocity of crystal rotation. In their simulation, (a) the crystal is assumed to be a rotating disc of infinite radius, (b) the crystal growth is considered as a flow of the melt through the phase boundary, and (c) the solute concentration in the melt is allowed to depend only on the axial coordinate and time. As demonstrated by Garandet et al. [49], the results of Favier's and Wilson's models are quite close, and also are in agreement with the theoretical model of Hurle et al. [37]. The simulation results obtained from the steady state are far from the transient solutions obtained by Favier [48, 49] and Wilson [44, 45].

The segregation in the lateral direction cannot be treated by a 1D model. Experimental results clearly demonstrate that the impurity concentration is a strong function of radial and angular directions because of strong convective effects in the melt and nonplanar crystal–melt interface.

Impurity and doping concentrations based on dynamic simulations from beginning of the growth until the end have never been reported. Several researchers, however, have solved the full Navier-Stokes equations based

on steady-state assumptions [50–52]. Ono *et al.* [52] have studied the oxygen distribution in a .double-crucible growth with a k-ε turbulence model. These authors compared their results with the single-crucible prediction. This has allowed a better understanding of oxygen concentration in the crystal for the double-crucible process. Langlois *et al.* [51] have studied the distribution of boron and Ga as dopants, and also oxygen impurity distribution in the Cz growth. Bulk flow approximations have been employed and numerical results are shown to be in agreement with the experimental data for MCz growth under various magnetic fields.

3. *Magnetohydrodynamic* (*MHD*) *Model*

Without an externally applied magnetic field, the melt motion in many Cz processes may be turbulent and can involve large-scale periodic motions. The heat flux fluctuations from the melt to the crystal produce a cycle of solidification and remelting at the interface, resulting in dislocations and other microscopic defects in the crystal. Periodic melt motions also produce microscopic variations of dopant and impurity concentrations in the crystal. Semiconductor materials such as Si, GaAs, and InP, behave as liquid metals with large electrical conductivities. Even a relatively weak, externally applied magnetic field produces an electromagnetic (EM) body force in their melts. Experiments on MCz and MLEC processes have shown that the temperature fluctuations and erratic doping striations can be greatly suppressed by the application of a magnetic field. The most important advantage of a magnetic field is that it controls impurities and inhomogeneities at microscopic level by producing better conditions in the vicinity of the melt–crystal interface.

The relevant magnetohydrodynamic (MHD) equations result from the combination of Maxwell's equations coupled with the appropriately extended Navier–Stokes equations. The former can be written as [53–57]

$$\mathbf{j} = \sigma(\mathbf{E} + \mathbf{u} \times \mathbf{B}), \tag{20}$$

$$\nabla \times \mathbf{B} = \mu_c \mathbf{j}, \tag{21}$$

$$\nabla \cdot \mathbf{B} = 0, \tag{22}$$

$$\nabla \times \mathbf{E} = -\frac{\partial \mathbf{B}}{\partial t}, \tag{23}$$

where $\mathbf{j}$ is the induced current density, μ_e and σ are the magnetic permeability and electrical conductivity of the melt, and $\mathbf{B}$ and $\mathbf{E}$ are the magnetic and current field vectors, respectively.

Using the dimensionless variables, the magnetic field can be represented by

$$\frac{\partial \mathbf{B}}{\partial t} = \frac{1}{\mathrm{Re}_m} \nabla^2 \mathbf{B} + \nabla \times (\mathbf{u} \times \mathbf{B}),$$ (24)

where the magnetic Reynolds number $\mathrm{Re}_m = \mu_o \sigma b U$. For large flow velocities or a large Re_m, the first term on right-hand side of Eq. (24) can be neglected. When Re_m is very small, the second term is small, and therefore the flow does not distort the magnetic flux lines significantly—a diffusion-dominated magnetic effect.

To fully exploit the missing azimuthal θ dependence, rotationally symmetric Cz flows are generally computed using the electric current streamfunction. The Lorentz force can be introduced into the momentum equation as a body force [53, 58–60]:

$$F_x = -\frac{\mathrm{Ha}^2 \sigma}{\sigma_m} b_r(b_r u - b_x v),$$

$$F_r = \frac{\mathrm{Ha}^2 \sigma}{\sigma_m} b_x(b_r u - b_x v),$$

$$F_\theta = -\mathrm{Ha}^2 \left(b_x \frac{\partial \Psi_J}{\partial x} + b_r \frac{\partial \Psi_J}{\partial r} \right),$$ (25)

where F_x and F_r are the Lorentz forces in x and r directions, respectively, and F_θ is the force in the θ direction due to swirl velocity Ω. In Eq. (12),

$$\mathrm{Ha} = Bb(\sigma/\rho\nu)^{1/2}$$ (26)

is the Hartmann number, $b_x = 1$ and $b_r = 0$ for an axial magnetic field and $b_x = 0$ and $b_r = 1$ for a horizontal magnetic field [61].

The electric current streamfunction equation then can be written as [60, 61]

$$\frac{\partial}{\partial x}\left(\frac{\sigma_m}{\sigma} \frac{1}{r} \frac{\partial \Psi_J}{\partial x} \right) + \frac{\partial}{\partial r}\left(\frac{\sigma_m}{\sigma} \frac{1}{r} \frac{\partial \Psi_J}{\partial r} \right) = b_x \frac{\partial w}{\partial x} + b_r r \frac{\partial}{\partial r}\left(\frac{w}{r} \right).$$ (27)

In the case of 3D dimensional MHD flows, the electric potential replaces the electric streamfunction. Equations for 3D flows can be found in Langlois et al. [51] and Ozoe et al. [62, 63], and they are difficult to solve.

4. Interface and Boundary Conditions

The simplest Cz growth system consists of two uniform phases, separated by an interface. The interface region in such a case can be assumed as an infinitesimally thin layer. Theoretical models for crystal growth

always employ this approximation. However, the dynamics of melt–crystal interface depends on the topology at an atomic level (absorption, surface steps, atomic roughness, etc.). The readers should refer to van der Eerden [64] for a detailed discussion on structural and dynamical properties of the interface. It has generally been assumed that the phase transformations in Cz and LEC processes occur under equilibrium conditions. The melt–crystal interface therefore is governed by an energy balance that must account for the latent heat, pull rate, rate of change in the melt height, heat gain–loss, crystal rotation, and crucible rotation. Solidification of a pure substance is modeled with a definite fusion temperature T_f, implying that the solid and liquid phases are separated by a sharp interface.

At the free surface, the required hydrodynamic conditions are: (1) fluid particles at the surface must remain attached (kinematic condition), (2) stress tangential to the surface is zero, and (3) stress normal to the surface must be exactly balanced by the externally applied normal stress [65]. Denoting the free surface position as $x = H_2(r, t)$, and enforcing orthogonality at the free surface, these conditions reduce to [66, 67]

$$u = \frac{\partial H_2}{\partial t} + v\frac{\partial H_2}{\partial r}, \tag{28}$$

$$\frac{\partial v}{\partial n} - \frac{\partial u}{\partial \tau} = \frac{Ma}{Pr}\frac{\partial \theta}{\partial n}, \tag{29}$$

where n and τ are the unit normal and tangential direction.

For a LEC growth (Fig. 6), the shapes of the melt–encapsulant and encapsulant–ambient gas are determined by solving the following equations simultaneously with equations (1) to (5) [27, 28, 68, 69]:

$$\frac{\partial^2 H_2/\partial r^2}{\left[1 + (\partial H_2/\partial r)^2\right]^{3/2}} + \frac{\partial H_2/\partial r}{r\left[1 + (\partial H_2/\partial r)^2\right]^{1/2}}$$

$$= Bo(H_2 - \Delta\rho \cdot Fr + 2\partial u/\partial n \cdot Fr), \tag{30}$$

$$\frac{\partial H_{2,ls}}{\partial r} = \tan(\phi_{ls} - 90°), \qquad \frac{\partial H_{2,lc}}{\partial r} = \tan(\phi_{lc} - 90°), \tag{31}$$

$$\int_{Rr_s}^{1}(H_3 - H_2)\, r\, dr = Constant, \tag{32}$$

where H_2 and H_3 are the height of the melt–encapsulant and the encapsulant–ambient gas interfaces, respectively. The interface of the encapsulant–ambient gas is assumed to be flat since the viscosity B_2O_3 is very high. In the previous equations Ma is considered to be zero while considering the high-pressure growth.

It should be noted that the accuracy of the solutions strongly depends on orthogonality at the interface and free surface. Much more complex expressions will be required to impose the interface and boundary conditions if the grids are nonorthogonal. The melt meniscus connects to the edge of the growing crystal at the junction between melt, solid, and ambient gases or encapsulant. At the triphase point, the meniscus pins to the edge of the crystal and wets its own solid at a specified angle. Some of the important conditions are [27, 28, 68, 69]

Melt–crystal interface:

$$u = v = 0, \quad w = \mathrm{Re}_s r, \quad \theta = 0. \tag{33}$$

Melt–encapsulant interface:

$$u = \frac{\partial H_2}{\partial t} + v \frac{\partial H_2}{\partial r}, \quad \frac{\partial v}{\partial x} = 0, \quad \frac{\partial w}{\partial x} = 0, \tag{34}$$

$$-\kappa_l \frac{\partial \theta_l}{\partial x} + \kappa_e \frac{\partial \theta_e}{\partial x} = \mathrm{Bi}_{r,le}(\theta_{le} - \theta_\infty). \tag{35}$$

Free surface of encapsulant:

$$\frac{\partial w}{\partial x} = 0, \quad -\kappa_e \frac{\partial \theta_e}{\partial x} + \kappa_g \frac{\partial \theta_g}{\partial x} = \mathrm{Bi}_{r,eg}(\theta_{eg} - \theta_\infty). \tag{36}$$

Top and side wall of crystal:

$$u = U_s, \quad v = 0, \quad w = \mathrm{Re}_s r, \quad -\kappa_s \frac{\partial \theta_s}{\partial r} + \kappa_g \frac{\partial \theta_g}{\partial r} = \mathrm{Bi}_{r,s}(\theta_s - \theta_\infty). \tag{37}$$

Bottom and side wall of crucible:

$$u = v = 0, \quad w = \mathrm{Re}_c r, \quad \theta = 1. \tag{38}$$

Solidification of a pure substance is modeled with a fixed fusion temperature T_f, implying that the solid and liquid phases are separated by a sharp interface, $s(x, r, t) = H_1(r, t) - x = 0$, where H_1 is the dimensionless height of the melt–crystal interface. The energy balance at the interface defines its position and motion, and can be derived as

$$\rho_s h_{sl}(U_{\mathrm{int},n} - U_s(t)\mathbf{e}_x \cdot \mathbf{n}) = k_s \frac{\partial T_s}{\partial n} - k_l \frac{\partial T_l}{\partial n}, \tag{39}$$

where the densities of the crystal and melt phases are assumed to be equal, $\mathbf{n}$ is the unit normal vector from solid to melt, $\mathbf{e}_x$ is the unit vector in the x direction, $U_{\mathrm{int}} = \partial H_1/\partial t \; \mathbf{e}_x$ is the velocity of the crystal–melt interface movement in its normal direction, and $U_s(t)$ is the pull velocity. An

expression for the movement of melt–crystal interface can be obtained as follows [27, 70]:

$$\frac{\partial H_1}{\partial t} - U_s(t) = \frac{Ste_l}{Pr_l}\left(\kappa_s \frac{\partial \theta_s}{\partial n} - \kappa_l \frac{\partial \theta_l}{\partial n}\right)\left[1 + \left(\frac{\partial H_1}{\partial r}\right)^2\right], \qquad (40)$$

and the pull rate $U_s(t)$ can be calculated from

$$U_s(t) = -(1 - Rr^2)\left\{\frac{Ste_l}{Pr_l}\left(\kappa_s \frac{\partial \theta_s}{\partial n} - \kappa_l\frac{\partial \theta_l}{\partial n}\right)\left[1 + \left(\frac{\partial H_1}{\partial r}\right)^2\right]\right\}\Bigg|_{r=Rr}, \qquad (41)$$

where Rr is the radius ratio (crystal-to-crucible radii). This equation is based on the assumption that the crystal and melt are not separated at the trijunction. Detailed equations for interface movement can be found in Kopetsch [70] and Zhang and Prasad [27].

To obtain conditions at the melt–encapsulant and encapsulant–gas interfaces in the case of the LEC growth system, we can assume that the tangential stresses at these interfaces are balanced in relation to each other and that the normal stress are exactly balanced by the externally applied stresses in the normal direction. This leads to

$$[(-p\mathbf{I} + \tau)_i \cdot \mathbf{n}] \cdot \mathbf{n} - [(-p\mathbf{I} + \tau)_{i+1} \cdot \mathbf{n}] \cdot \mathbf{n} = \frac{2H}{Bo\,Fr}\,\mathbf{n}, \qquad (42)$$

where $\mathbf{t}$ and $\mathbf{n}$ are tangential and normal unit vectors, τ is the dimensionless stress tensor, H is the mean interface curvature, $\mathbf{I}$ is the unit tensor, and Bo and Fr are the dimensionless Bond and Foude numbers, respectively. Further discussions on these boundary conditions can be found in Zhang et al. [27, 66].

For the concentration field C, two conditions must be satisfied at the solid–melt interface. First, the kinetics of the solidification involves a relation between the growth speed, interface temperature, and local concentrations C_l and C_s in the liquid and solid phases as given by Eq. (11) or an improved form of this equation. The second condition for the concentration field at the solidification front is obtained from species conservation [71]

$$-\rho_l D\,\nabla C_l \cdot \mathbf{n} + \rho_s C_l v_g = \rho_s C_s v_g, \qquad (43)$$

where D is the diffusion coefficient. In writing Eq. (43), the diffusion in the solid phase has been neglected. These conditions can be used for both impurity and dopant with appropriate values of the coefficients. For dopants, adiabatic conditions exist on crucible walls and the free surface. The boundary conditions, however, are not straightforward for oxygen and other impurities. Since the solutions are very dilute, the transport of impurity and dopant can be considered independent of each other.

The conditions on the crucible wall are the most difficult to define. The most popular heating system consists of an inductor (r.f. coil), which is made of a water-cooled copper coil to which a high alternating current is applied, and a conducting susceptor (generally made of graphite), where electric current is induced and generates power by Ohmic dissipation. However, resistance heaters are becoming more and more popular. Modeling of induction heating is a difficult problem. Energy distribution in various components of the furnace is a function of the total power supply and the geometry of the system, as represented by the vertical position of the susceptor, melt height, and the actual shapes of the crystal. The functional dependence of energy supply with respect to the total power is also complex, since it involves the solution of Maxwell equations on a domain with deforming boundaries. Most of the studies therefore have assumed either a constant temperature or uniform heat flux on the walls of the crucible. In some studies, experimental data have been employed to determine temperature distribution on the crucible wall. In this approach, coupled electromagnetic and radiation heat transfer equations are solved over the entire domain using a global transport model to obtain temperature boundary conditions of the crucible and the crystal. However, a large number of assumptions need to be made to solve the governing equations. Elaborate discussions on this approach are presented by Brown [71] and Dupret and van den Bogaert [7].

5. Radiation Heat Transfer

Heat transfer in Cz and LEC systems is dominated by radiation exchange between the surfaces separated by thermally transparent media as well as radiative transfer through semitransparent media (see Table IV), for example, radiative emission, absorption, and transmission through the B_2O_3 layer and optically transparent or semitransparent crystals. Both surface and volumetric radiation are important for accurate simulations in these cases. Due to the difficulty in solving highly nonlinear radiation equations and lack of experimental data on thermophysical properties, only radiation exchange between surfaces [72–74] could be considered for crystal growth modeling. Only recently, the spectral radiations have been considered in crystal growth [29, 75].

The best choice for calculation of surface radiation may be the Monte Carlo method, which uses a statistical approach [76–78]. Such methods are well suited for solving complex problems, but have not been used due to the prohibitively high computational costs for reasonable accuracy. The second approach is obviously the radiation heat transfer models.

In previous works, various approaches have been taken to model the radiative exchange of heat among participating surfaces in the crystal growth furnace. Ramachandran and Dudukovič [79] treated the melt-free surface and the exposed portions of the crucible wall as isothermal and divided the cylindrical crystal into a number of isothermal axisymmetric ring elements. The radiative boundary condition was linearized using the Gebhart factor methodology to define an effective ambient temperature and radiation heat transfer coefficient. This approximation is computationally effective when dealing with finite-element schemes. Following a similar method, Motakef and Witt [80] established an average radiative sink temperature (RST), ignoring reflection of energy at all surfaces in the Cz enclosure other than the crystal, to compute the axial temperature profile along the crystal.

Atherton et al. [73] have modified the computer program FACET [72], developed at Lawrence Livermore Laboratory (Berkeley, California) to evaluate the view factors between azimuthally partitioned axisymmetric strips. The original algorithm only computes view factors between arbitrary axisymmetric surfaces. FACET accounts for shadowing effects produced by the crystal. View factors between axisymmetric ring elements are computed by summing the contributions of constituent elements of the strip, from which the Gebhart factors [77, 78] are calculated. This surface-to-surface radiative exchange scheme was combined with the thermal-capillary model (TCM), based on the finite-element method. The TCM allows the calculation of interface and meniscus shapes by considering conduction and steady-state laminar convection in the melt.

Most of the surface-to-surface thermal radiation modeling of the Cz process considers the optical properties of the crystal to be invariant or nonspectral. However, it is well-established that for many types of crystals, there exist two spectral bands, where the crystal is approximated as opaque and transparent (Table III) [78]. In an effort to approximate the effects of internal radiative transport within yttrium–aluminum–garnet (YAG) and gadolinium–gallium–garnet (GGG) crystals, Xiao and Derby [75] considered the interior of the crystal as a radiative enclosure, bounded by vanishingly thin opaque surfaces. Radiative heat fluxes were computed using a method similar to that of Ramachandran and Dudukovič [79]. This simplified treatment of opaque surfaces is valid for real systems where surfaces are often coated with impurities deposited by vapor-phase transport.

Here, we present the formation developed by Nunes et al. [29]. A surface-to-surface radiation model based on the method of discrete exchange factor (DEF) has been developed and applied to Cz and LEC modeling by these authors [81–83]. It has been demonstrated that the DEF

TABLE III

TRANSITION TEMPERATURES TO TRANSPARENCY, $T(x)$

Material	n^a	Melting Point, K	$T(x)$ K	$T(x)/T_m$
Silicon (Si)	3.4	1693	850	0.5
Germanium (Ge)	4.0	1210	450	0.37
Gallium arsenide (GaAs)	3.2	1553	1125	0.72
Indium phosphide (InP)	3.0	1343	1015	0.76
Cadmium telluride (CdTe)		1372	1235	0.9

Reprinted with permission by Hurle [40].

method provides more accurate results and requires less computational time than do the zone method and P-N approximation for both surface and volumetric radiations. The DEF method is powerful and robust for solving geometrically complex radiation problems.

The first step in the implementation of the DEF method is to evaluate direct exchange factors between two surface nodes for each wave number. The configuration factor between two arbitrarily oriented differential ring elements, illustrated in Fig. 9, may be evaluated using the formulation developed by Modest [84]. The differential view factor expression is given by

$$dF_{d1 \to d2} = \frac{2}{\pi} \int_{\psi_{min}}^{\psi_{max}} \frac{\cos(\beta_1)\cos(\beta_2)}{S^2} \, d\psi \, r_2 \, ds_2, \qquad (44)$$

where the subscripts, 1 and 2, denote the outer and inner axisymmetric ring elements respectively. The angle ψ is the azimuthal angle in the plane perpendicular to the z-axis, with limiting values of ψ_{min} and ψ_{max} between which a point on the outer element can see the inner element. The values of ψ_{min} and η_{max} are constrained by geometric consideration of the element pair. The symbol S is defined as the magnitude of the vector connecting two points situated on a pair of differential ring elements. The angle β represents the angle between the surface normal of the element and the segment S. By considering the geometry of the ring elements, the differential view factor between the axisymmetric elements may be expressed in terms of φ, the angle in the r-z plain from the z-axis, going in the direction of increasing radius, onto the backside of the element [29, 84]:

$$\frac{dF_{d1 \to d2}}{2\pi r_2 \, ds_2} = \frac{\cos(\varphi_1)\cos(\varphi_2)}{4\pi^2 r_1 r_2} \int_{\psi_{min}}^{\psi_{max}} \frac{(\phi_1 - \cos(\psi))(\phi_2 - \cos(\psi))}{(\alpha_{12} - \cos(\psi))^2} \, d\psi,$$

$$(45)$$
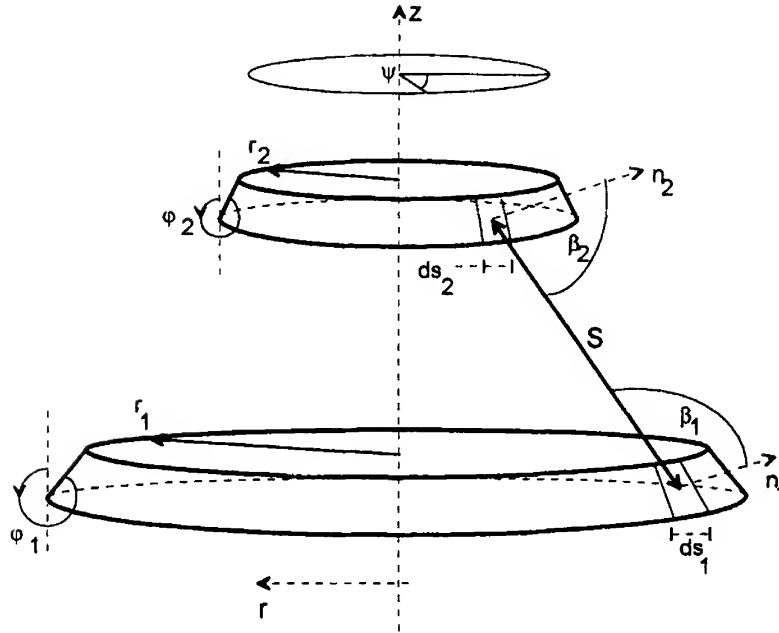
FIG. 9. Configuration of axisymmetric ring elements for radiation calculations [29].

where

$$\phi_i = \frac{r_i}{r_j} + \frac{z_j - z_i}{r_j}\tan(\varphi_i), \qquad \text{or} \quad \begin{array}{l} i = 1, j = 2 \\ i = 2, j = 1 \end{array} \qquad (46)$$

$$\alpha_{12} = \frac{1}{2}\left(\frac{r_1}{r_2} + \frac{r_2}{r_1}\right) + \frac{(z_2 - z_1)^2}{2r_1 r_2}. \qquad (47)$$

An integration of Eq. (45) yields

$$\frac{dF_{d1 \to d2}}{2\pi r_2 \, ds_2} = \frac{\cos(\varphi_1)\cos(\varphi_2)}{4\pi^2 r_1 r_2} - B\big[(\alpha_{12}, \phi_1, \phi_2, \cos(\psi_{\min}))\big], \qquad (48)$$

where

$$B(\alpha, \phi_1, \phi_2, \phi_e) = \cos^{-1}(\phi_e) + \frac{(\alpha - \phi_1)(\alpha - \phi_2)\sqrt{1 - \phi_e^2}}{(\alpha^2 - 1)(\alpha - \phi_e)} + \cdots$$

$$+ 2 \cdot \frac{2\alpha - \phi_1 - \phi_2 - \alpha(\alpha^2 - \phi_1\phi_2)}{(\alpha^2 - 1)^{3/2}}$$

$$\cdot \tan^{-1}\left[\left(\frac{\alpha + 1}{\alpha - 1}\frac{1 - \phi_e}{1 + \phi_e}\right)^{1/2}\right], \qquad \alpha \neq 1, \qquad (49)$$

$$B(\alpha, \phi_1, \phi_2, \phi_e) = \cos^{-1}(\phi_e), \qquad \alpha = 1. \tag{50}$$

There exists a problem with defining Eq. (49) in terms of ϕ_1 and ϕ_2. The angles φ for ring elements lying in the r-ψ plane with normals in the positive or negative z directions are, respectively, 270 and 90 degrees. Such values of φ yield $\pm\infty$ for ϕ_1 and/or ϕ_2, resulting in a view factor of $\pm\infty$ between the elements. Thus, the $\cos(\psi_1)$ and $\cos(\psi_2)$ terms in Eq. (49) are combined with the expressions for ϕ_1 and ϕ_2 to resolve this complication. The limiting values of ψ, ψ_{min}, and ψ_{max}, are determined by the geometric configuration of the ring elements and the obstruction of view between the elements by the inner or outer axisymmetric concentric bodies. The cosines of the minimum and maximum azimuthal angles from a point on the outer element to the inner element with interference produced by the inner or outer concentric bodies, or both, Γ_i and Γ_o, are found by means of the following relations [84]:

$$\Gamma_i = \max\left(\frac{W \cdot R_i^2(z) - X(z) - Y(z)}{Z(z)}\right)_{z \in (z_1, z_2)} \tag{51}$$

$$\Gamma_o = \min\left(\frac{W \cdot R_i^2(z) - X(z) - Y(z)}{Z(z)}\right)_{z \in (z_1, z_2)} \tag{52}$$

where $W = (z_2 - z_1)^2$; $X(z) = r_1^2(z_2 - z)^2$; $Y(z) = r_2^2(z - z_1)^2$; $Z(z) = 2r_1r_2(z - z_1)(z_2 - z)$; and $R_i(z)$ and $R_o(z)$ are the local radii of the inner and outer bodies. The crystal grown during the Cz process is assumed, at this level, to be cylindrical. Equation (51) may be further simplified for an inner cylindrical body, accounting for the shadowing effects produced by the crystal:

$$\Gamma_i = \frac{R_i^2}{r_1 \cdot r_2} - \left[\left(1 - \frac{R_i^2}{r_1^2}\right) \cdot \left(1 - \frac{R_i^2}{r_2^2}\right)\right]^{1/2}. \tag{53}$$

Table IV summarizes the allowable azimuthal angle range for all possible configurations of the ring elements.

For a cylindrical crucible wall, as is the case, Γ_o has no influence on azimuthal angle range. For ring elements in the r-ψ plane, infinite ϕ values are not considered when determining the limits of ψ. If the cosines

TABLE IV

LIMITING VALUES FOR COSINES OF AZIMUTHAL ANGLES

	$\cos(\theta_1) \geq 0$	$\cos(\theta_1) \leq 0$
$\cos(\theta_2) \geq 0$	$\cos(\psi_{min}) = \min(\Gamma_o, 1)$ $\cos(\psi_{max}) = \max(\phi_1, \phi_2, \Gamma_i, -1)$	$\cos(\psi_{min}) = \min(\phi_1, \Gamma_o, 1)$ $\cos(\psi_{max}) = \max(\phi_2, \Gamma_i, -1)$
$\cos(\theta_2) \leq 0$	$\cos(\psi_{min}) = \min(\phi_2, \Gamma_o, 1)$ $\cos(\psi_{max}) = \max(\phi_1, \Gamma_i, -1)$	$\cos(\psi_{min}) = \min(\phi_1, \phi_2, \Gamma_o, 1)$ $\cos(\psi_{max}) = \max(\Gamma_i, -1)$

of the minimum azimuthal angle are less than that of the maximum azimuthal angle, the view factor between the ring elements is taken to be zero.

The previous view factor formulations is repeated for all possible combinations of axisymmetric ring element pairs. Naraghi and Chung [85] have devised a method for determining exchange factors between diffusely reflective surfaces using Markov chain techniques. The view factor matrix, also known as the transition probability matrix, is denoted as $\mathbf{F} = [F_{i,j}]$, where $F_{i,j}$ is the probability that radiation is transferred from surface i directly to surface j. The absorptivities and reflectivities of all surfaces are represented by the diagonal matrices $\mathbf{A} = [\alpha_i \delta_{i,j}]$ and $\mathbf{R} = [\rho_i \delta_{i,j}]$, respectively. The total exchange factor (absorption factor) matrix $\mathbf{B}$ is evaluated from [85]

$$\mathbf{B} = [\mathbf{I} - \mathbf{FR}]^{-1}\mathbf{FA}. \tag{54}$$

Once the absorption factors are determined, the radiative heat flux for surface j can be determined from radiant energy considerations. For radiation exchange between gray surfaces, the energy balance is [78]

$$q''_{r,j} = \varepsilon_j \sigma T_j^4 - \sum_{i=1}^{n_{tot}} \varepsilon_i \sigma B_{i,j} T_i^4. \tag{55}$$

For radiation exchange between spectrally emitting surfaces, the emissive power in Eq. (55) is obtained from Planck's distribution, which yields the following expression for net radiative heat flux:

$$q''_{r,j} = \varepsilon_j \big[g(\lambda_2 T_j) - g(\lambda_1 T_j) \big] + \cdots - \sum_{i=1}^{n_{tot}} \varepsilon_i B_{i,j} \big[g(\lambda_2 T_i) - g(\lambda_1 T_i) \big], \tag{56}$$

where

$$g(\lambda_2 T_i) - g(\lambda_1 T_i) = \frac{C_1}{n_f^2} \int_{\lambda_1}^{\lambda_2} \frac{d\lambda}{\lambda^5 \big[\exp(C_2/n_f \lambda T_i) - 1 \big]}. \tag{57}$$

Volumetric radiation must be considered in order to analyze the effect of the encapsulant B_2O_3 layer, high-pressure inert gas, and optical behavior of crystal materials (Table III). A volumetric formulation for DEF has been developed by Nunes et al. [29] and is being applied to HPLEC growth of III-V compounds. They have also considered the spectral volumetric radiation through oxide crystals. However, the combined radiative–convective analysis of a crystal growth system is computationally intensive and still is in its early stages.

6. Thermophysical Properties and Governing Parameters

Low- and high-pressure Cz processes are governed by a large number of parameters such as Grashof and Prandtl numbers for melt and gas flows; crystal and crucible Reynolds numbers; the Stark number for radiation heat transfer; Weber and Froude numbers for surface tension; density, thermal conductivity, and specific heat ratios for solid and melt phases; thermophysical property variation in gas; geometric variables, and so on (Table V). Thermophysical properties of selected semiconductors, metals, oxides, salts, and model fluids are shown on Table VI.

These parameters vary greatly with a change in phase–zone i, as well as in the surface j. Suitable values of these numbers need to be selected for realistic growth conditions. Generally, the researchers have performed calculations for dimensionless parameters at least one or two orders of magnitude lower than that encountered in the industrial systems. Only recently have researchers succeeded in performing simulations for conditions close to that of industrial growth.

The range of nondimensional parameters even in the case of low-pressure growth of Si, for a crystal diameter of 100 to 200 mm (4 to 8 in.), a crucible diameter of 356 to 467 mm (14 to 18 in.), a temperature difference of 25 to 50 K, and using the standard properties for liquid Si are very broad, due to the indeterminacy of some of the physical properties of liquid Si,[3] and the wide span of operating conditions for crystal pullers. Other effects, such as contamination of the melt, may also affect the property values. For example, thermocapillary-driven convection may be reduced or eliminated if the melt surface is covered by a viscous liquid or with solid Si pellets; pure liquid Si also has a surface tension coefficient that decreases with increasing oxygen contamination. The variations in the parameters Rr, Ar, and so on, in Table 5 can be obtained in industrial Cz pullers by changing the puller geometry, and the crucible and crystal

---

[3] Kimura and co-workers have conducted extensive experiments to measure the liquid Si properties and have published a series of papers on these studies [86].

TABLE V

LIST OF DIMENSIONLESS PARAMETERS AND THEIR COMMON VALUES

Parameter	Definition	Value[a]
i-phase		
Grashof number	$\mathrm{Gr}_i = g\beta_i b^3(T_w - T_f)/\nu_i^2$	10^7–10^{12}
Solutal Grashof number	$\mathrm{Gr}_s = g\beta_s b^3(T_w - T_f)/\nu_i^2$	10^5–10^8
Prandtl number	$\mathrm{Pr}_i = \nu_i/\alpha_i$	0.01–0.07
Schmidt number	$\mathrm{Sc}_i = \nu_i/D_i$	$\approx 10^3$
Density ratio	$\bar{\rho} = \rho_i/\rho_l$	0.001–1.0
Conductivity ratio	$\bar{k}_i = k_i/k_l$	0.001–1.0
Specific heat ratio	$\bar{C}_{p,i} = C_{pi}/C_{pl}$	0.001–1.0
Viscosity ratio	$\bar{\mu}_{\mathrm{eff},i} = \mu_i/\mu_l$	0.01–10^3
Stefan number	$\mathrm{Ste}_l = C_{pl}(T_l - T_f)/h_{sl}$	0.05–0.5
Marangoni number	$\mathrm{Ma}_l = (d\sigma_l/dT)(T_h - T_f)b/\nu_l\alpha_l$	10^3–10^5
Solutal Maragoni number	$\mathrm{Ma}_s = (d\sigma_l/dS)(T_h - T_f)b/\nu_l\alpha_l$	10^4–10^5
Froude number	$\mathrm{Fr}_i = \nu_i^2/gb^3$	10^{-9}–10^{-10}
Bond number	$\mathrm{Bo}_l = \rho_L gb^2/\sigma_l$	10^2–10^3
Hartmann number	$\mathrm{Ha} = Bb(\sigma_e(\rho_l\nu_l)^{1/2}$	10^2–10^3
Geometric parameter (j-surface)		
Reynolds number	$\mathrm{Re}_j = \omega_j b^2/\nu_l$	10^4–10^5
Stark number	$N_i = k_i b/4\sigma T_i^3$	0–∞
Aspect ratio	$\mathrm{Ar}_j = h_j/b$	0.01–1.0
Radius ratio	$\mathrm{Rr}_j = R_j/b$	0.01–1.0

[a] Values quoted here provide approximate range of process parameters in various zones.

rotation rates. A variation in aspect ratio Ar stems from the change in the melt height as crystal is pulled. At the beginning of a typical Cz growth run, Ar can be as high as 2.0; at the end, it can be as low as 0.25, when the melt is almost entirely depleted. A change in radius ratio Rr can be obtained by growing a larger crystal in a smaller crucible, and may vary between 0.3 and 0.5. Many unsteady simulations reported in the literature are conducted with parameters that are lower by at least one or two orders of magnitude, especially with regard to the Grashof number, because of the computational difficulty as flows become oscillatory and possibly chaotic at high Grashof numbers.

The range of nondimensional parameters in the case of LEC growth of III-V compound crystal is much more complex than that of Si crystal growth. The Grashof number for melt convection ranges from 10^8 to 10^9, whereas the Gr for gas is generally greater than 10^{10} [26].

TABLE VI
MATERIAL PROPERTIES OF SELECTED MATERIALS NEAR MELTING POINT [47, 87, 88]

Material	ρ_s kg/m³	ρ_l kg/m³	k_s W/(mK)	k_l W/(mK)	c_s J/(kgK)	c_l J/(kgK)
Si	2300	2420	22	64	1059	1000
GaAs	5170	5700	7.12	17.8	420	434
InP	4710	5050	9.11	22.8	378	424
GGG	7200	5700	20	5	586	586
GaSb	5619	6030	7.81	17.1	290	328
Ge	5600	5600	16	17	395	390
YAG	4300	3600	8	4	800	800
H₂O	917	1000	2.2	0.598	2060	4184

Material	α_s m²/s	α_l m²/s	μ kg/(m·s)	ν m²/s	Pr	T_m K
Si	9.03×10^{-6}	2.64×10^{-5}	7.0×10^{-4}	2.89×10^{-7}	0.01	1683
GaAs	3.27×10^{-6}	7.18×10^{-6}	2.79×10^{-3}	4.88×10^{-7}	0.068	1511
InP	3.99×10^{-6}	1.06×10^{-5}	8.19×10^{-4}	1.62×10^{-7}	0.015	1335
GGG	4.7×10^{-6}	1.5×10^{-6}	4.0×10^{-2}	7.01×10^{-6}	4.67	2023
GaSb	4.8×10^{-6}	8.64×10^{-6}	2.31×10^{-3}	3.83×10^{-7}	0.044	985
Ge	7.2×10^{-6}	7.8×10^{-6}	7.28×10^{-4}	1.3×10^{-7}	0.016	1231
YAG	2.3×10^{-6}	1.4×10^{-6}	4.6×10^{-2}	1.3×10^{-5}	9.1	2243
H₂O	1.16×10^{-6}	1.42×10^{-7}	1.79×10^{-3}	1.79×10^{-6}	12.5	273

Material	ε_s	ε_l	β K⁻¹	L J/kg	σ (dyne/cm)	$\partial\sigma/\partial T$ -(dyne/cmK)
Si	0.7	0.05-0.318	$0.141-1.4 \times 10^{-4}$	1800	720	0.1-0.43
GaAs	0.75	0.75	1.87×10^{-4}	726	530	0.25
InP	0.5-0.6	0.5-0.6	4.44×10^{-4}	436		
GGG	0.3	0.3	$0-2.7 \times 10^{-5}$	455	700	0
GaSb			9.58×10^{-5}			
Ge	0.3	0.3	1.8×10^{-5}	455	781	0
YAG	0.5-0.7	0.5-0.7	2.5×10^{-4}	478	650	0.6
H₂O	0.98	0.96	0.205×10^{-4}	333	73	0.16

Si, silicon; GaAs, gallium arsenide; InP, indium phosphide; GGG, gadolinium-gallium-garnet; GaSb, gallium antimonide; GE, germanium; YAG, yttrium-aluminum-garnet; H₂O, water.

346

B. TRANSPORT SIMULATIONS

Since 1975, numerical simulations of transport phenomena in Cz crystal growth have been performed by many investigators, as shown in Table VII. These simulations vary from bulk flow approximations that only simulate 2D cavity flows to models that use global models and incorporate crystal, melt, heater, shield, and many other characteristics. Both finite difference methods (FDM) and finite-element methods (FEM) have been used to simulate the 2D axisymmetric or 3D melt flows. Excellent discussions on modeling and simulation are presented in the state-of-the-art reviews written by Chan et al. [69], Brown [71], Müller [6], and more recently, by Hurle [3] and Prasad and Zhang [8].

Extensive investigations have been carried out on convective flows due to buoyancy and surface tension forces, crystal and crucible rotations, and radiation effects, most of them restricted to either the Cz Si growth or LEC growth without gas convection. Since the melt flow patterns and temperature fields are quite sensitive to the boundary conditions, many different kinds of conditions on the walls of the crucible, crystal–melt interface, and free surface have been considered. Although FEMs have used more complex boundary conditions, the convective flow in the melt has been neglected except for some recent studies. Conversely, although the FDM and the finite volume model (FVM) have routinely included the melt convection, the irregularity of the domain has remained a problem with these models. Indeed, a regular cylindrical geometry and a flat melt–crystal interface have been assumed in most of the Cz simulations. Limited studies also have been performed to account for the crucible bottom curvature by approximating the irregular boundary by a zigzag line. This approximation affects the accuracy of the simulation, and is it not adequate for flow calculations at high Grashof numbers, where the velocity gradients in the near wall regions are strong. Another serious problem with many of these models is that the melt flow is generally isolated from the crystal, making it impossible to couple them with stress calculations.

The primary difficulty in modeling Cz flows arises from the fact that the positions of the crystal–melt interface and melt–gas meniscus are neither known a priori nor planar. The crystal–melt interface coincides with the freezing point isotherm in the system, and the melt meniscus results from a force balance between the surface tension, pressure forces, and viscosity stresses. To complicate this further, the flow and temperature fields used to determined the shapes and locations of the interface and meniscus are frequently oscillatory in nature. This creates difficulties with both the FEM and FDM because the accuracy of the simulations is closely related to grid resolution near the crystal–melt interface. To overcome these difficulties, iterative methods have been devised for both field variables and grid distribution near the interface.

TABLE VII

SELECTED SIMULATION STUDIES ON CZOCHRALSKI (Cz), CONTINUOUS Cz (CCz) AND LIQUID-ENCAPSULATED Cz (LEC) GROWTH WITH THE RANGE OF IMPORTANT NON-DIMENSIONAL PARAMETERS AND PHYSICAL PHENOMENA EMPLOYED

Author	Method	Convection		Free Surface	Rad. H.T. (ε)	Magn. (Ha)
		Forced (Re)	Free (Gr)			
Czochralski process						
Kobayashi (1975)	FDM, 2D	<125	—	Planar	—	—
Langlois (1977)	FDM, 2D	6.4×10^3	$<4 \times 10^6$	Planar	0.31	—
Kobayashi (77–81)	FDM, 2D	4×10^3	2.5×10^4	Planar	0.318	—
Langlois (79,82)	FDM, 2D	3×10^4	2×10^7	Planar	0.318	—
Langlois (83,84)	FEM, 2D	—	—	Planar	—	yes
Crochet [140]	FDM, 2D	10^3	10^7	Planar	—	—
Mihelčić [84, 151]	FDM, 3D	4×10^3	5×10^6	Planar	0.318	—
Mihelčić [153]	FDM, 2D	—	—	Planar	—	high
Hjellming (86–93)	FDM, 3D	—	—	Planar	—	1600
Bottaro (1987)	FDM, 2D	—	6.6×10^5	Planar	—	—
Bottaro (1988)	FDM, 2D	—	10^7	Planar	—	—
Kopetsch (88–91)	FVM, 2D	4.4×10^5	5.8×10^6	Meniscus	0.3	—
Derby (85–89)[a]	FEM,[b] 2D	—	—	Meniscus	—	—
Brown (1989)[a]	FEM,[b] 2D	—	10^8	Meniscus	—	620
Roux (1989)	FDM, 3D	—	5×10^4	Planar	—	—
Sackinger (1989)[a]	FDM,[b] 2D	10^5	10^8	Meniscus	0.05–0.3	—
Baumgartl (89–93)	FVM, 3D	—	2×10^7	Planar	—	1000[c]
Kakimoto (90–93)[a]	FEM,[b] 3D	—	3×10^7	Meniscus	0.3	—
Virzi (1991)[a]	FEM,[b] 2D	—	—	Meniscus	0.90	—
Araki (1991)[a]	FDM, 2D	3×10^5	10^9	Planar	—	—
Kobayashi (1991)	FDM, 2D	turb	turb	Planar	0.318	—
Williams (1992)	FDM, 2D	turb	—	Planar	0.5	620[c]
Kinney (1992)[a]	FEM,[b] 2D	turb	turb	Meniscus	—	—
Bückle (1993)[a]	FDM, 2D	10^4	10^6	Planar	fixed	—
Maruyama (1994)[a]	FEM,[b] 3D	—	—	Meniscus	—	—
Zhou (1994)[a]	FEM,[b] 2D	—	—	Meniscus	—	—

TABLE VII
(Continued)

Author	Method	Convection		Free Surface	Rad. H.T. (ϵ)	Magn. (Ha)
		Forced (Re)	Free (Gr)			
Kakimoto (1994)[a]	FEM,[b] 3D	78	3.56×10^7	Meniscus	0.3	—
Ozoe [63]	FDM, 3D	3240	10^7	Planar	—	1000
Oshima [155]	FEM, 3D	1154	1.4×10^6	Meniscus	—	50
Khine (1995)	FDM, 2D	—	—	Planar	—	1600
Xiao (1995)	FEM, 3D	2×10^3	2.54×10^5	Planar	—	—
Togawa (1995)[a]	FDM, 2D	3×10^6	5×10^9	Meniscus	0.318	—
Continuous Czochralski process						
Ono [52, 101]	FDM, 2D	turb	turb	Planar	0.3	—
Anselmo (1994–96)[a]	FDM, 3D	10^5	10^8	Planar	0.25	—
Jafri (1995)[a]	FDM, 2D	10^4	10^8	Planar	0.25	—
Liquid encapsulated Czochralski process (without gas convection)						
Derby (1985–92)[a]	FEM, 2D	—	—	Meniscus	0.3–0.6	—
Chan (87,88)	FDM, 3D	4000	6×10^6	Meniscus	0.2	—
Nicodeme (1988)	FEM,[b] 2D	—	3×10^7	Meniscus	—	—
Sabhapathy (88–90)	FDM, 2D	2400	5.2×10^6	Planar	0.75	950
Fontaine (89–94)	FEM, 2D	1.5×10^4	2×10^7	Planar	—	—
Crowley (1989)[a]	FDM,[b] 2D	—	—	Meniscus	0.5	—
Dupret (89,90)	FEM,[b] 2D	—	—	Meniscus	0.2, 0.36	—
Ryckmans (1990)	FEM,[b] 2D	10^4	5×10^7	Meniscus	—	—
Baumgartl [58][a]	FEM/FVM. 2D	—	—	Meniscus	—	—
Koai [95][a]	FEM,[b] 2D	—	—	Meniscus	—	—
High pressure Czochralski process (with gas convection)						
Zhang and Prasad*[a]	FVM, 2D	10^4	10^{10}	Meniscus	0.05–0.4	200

[a] Curved crucible.
[b] Detailed radiation heat transfer model.
[c] Horizontal magnetic field.
FDM, finite difference method; FVM, finite volume method; FEM, finite-element method; 2D, two-dimensional; 3D, three-dimensional.

349

Earlier studies in the area of FEM were performed by Brown *et al.* [89–92]. They developed an integrated hydrodynamic thermocapillary (IHTCM) model, which allowed for the calculation of both the interface and the meniscus shapes. The IHTCM assumes heat transfer by conduction, diffuse gray radiation between all components within the Cz apparatus, and axisymmetric steady-state laminar convection in the melt. The radius of the crystal is computed simultaneously and self-consistently with the heat transfer throughout the system. Recently, they also have incorporated the k-ε model into the IHTCM to account for turbulent melt convection.

Other important studies were performed by Crowley *et al.* [93]. These authors treated all the interfaces—that is, the solidification front, the meniscus, and crystal wall—as unknowns in the problem in order to perform time-dependent simulations and to analyze the dynamics of the system. However, these studies neglected convection in the melt, which is crucial to the modeling of crystal growth. (No doubly-curved or other complex shapes of the crystal–melt interface, as observed in the experiments, could be predicted by a conduction-dominated model.) A more general global model is introduced by Dupret *et al.* [7, 74] where heat transfer is simultaneously calculated in all components of the furnace. Coupling of flow and temperature calculations in quasi-steady global models have been considered by Dupret *et al.* [7], Sackinger [94], and Derby *et al.* [91]. Time-dependent global models also have been developed by some investigators.

Efforts also have been made to consider convective flows in the melt, to allow an interaction between the global heat transfer and melt convection, and to update the crystal–melt interface based on this interaction [95]. This external iteration is considered to be a weak link between the melt flows and the global temperature field. This kind of iterative algorithm is easier to formulate and can provide satisfactory results for Cz growth at low pressures, for example, Si, due to the radiation-dominance in the system. (The radiation heat transfer is changed very little when convection in the melt is updated.) However, the approach is not suitable when gas convection is strong, as in the case of moderate- or high-pressure systems for the growth of GaAs, InP, and other compounds. In these systems, the gas convection strongly couples with the radiation and melt convection. The iterative schemes between the global and local fields are very expensive, and many times it is impossible to obtain converged solutions. This is particularly true when the gas flow is turbulent [26].

In the area of the FDM and FVM, the applicability of these methods for complex geometrical domains has been greatly enhanced by numerical grid generation with body-fitted coordinate systems. Although this technique is

not new and is widely used in the field of aerodynamics, Kopetsch [70] was the first to use coordinate transformation to include the deformable shapes of the melt–crystal interface and melt meniscus in the simulation of the Cz growth. He used an algebraic transformation for the domain of the crystal and a numerical transformation for the domain of the melt. One of the major advantages of this scheme is that it attaches the grid coordinate axes with the boundaries, making it easier to implement the boundary conditions. Kopetsch considered several cases of combined buoyancy, forced convection, and thermocapillary flows, and compared them with the corresponding solutions to the "bulk flow approximation." The deflection of crystal–melt interface was well demonstrated by his results.

Baumgartl et al. [96] recently have developed a hybrid method that uses a global conduction-radiation model based on a commercial FEM code, called ABAQUS (Habbitt, Karlson & Sorensen, Inc., Pawtucket, Rhode Island), and thermal radiation model, combined with STAR-CD (Analysis & Design Co., Ltd., Melville, New York) or a 3D Navier-Stokes solver based on a FVM for the flow field.

Most recently, a multizone adaptive grid generation combined with a curvilinear coordinate FVM developed by Zhang et al. [97–99] has been implemented to simulate the low- and high-pressure crystal growth processes [27, 28, 68]. A short description of this algorithm will be presented in the next section. The influence of gas convection on high-pressure crystal growth is well demonstrated by their calculations. These authors also have shown the importance of grid adaptivity and grid resolution, particularly with respect to the dynamics of the crystal–melt interface, free surfaces, and melt meniscus.

Several studies also have been conducted to examine the effect of magnetic field on Cz growth by employing the MHD equations [68]. The theory of hydromagnetic crystal growth is greatly simplified by the liquid metal approximations. Important studies in this area have been performed by Hjellming and Walker [54], Müller [6], and Sabhapathy and Salcudean [100] for both the vertical and horizontal magnetic fields. The effect of magnetic field on HPLEC growth has been studied for the first time by Zhang and Prasad [27]. These authors have found that oscillations in the gas can influence the temperature field in the encapsulant and the melt, and consequently, make the crystal–melt interface oscillate. The stabilization effect of magnetic field in a high-pressure system is therefore weakened by this phenomenon.

The turbulent flow in the melt phase was first studied by Ristorcelli and Lumley [16], and later by Ono et al. [101], Kinney [34, 35], Brown [17], and Zhang et al. [36]. This area of research has not been given serious attention due to the continuing argument on whether the Cz melt flow is

laminar, oscillatory, or turbulent. However, in the case of industrial Si melt for large-diameter crystals and high-pressure growth, it is crucial that an accurate turbulence model be employed and the turbulent flows in the melt and the gas be fully understood. Further work in this direction is underway by Zhang *et al.* [36].

C. MULTIZONE ADAPTIVE CURVILINEAR FINITE VOLUME SCHEME

Zhang and Prasad [27, 98, 99] have developed a high-resolution computer model based on 3D multizone adaptive grid generation (MAGG) and curvilinear finite volume (CFV) discretization to simulate the transport phenomena associated with crystal growth processes. The computational domain is permitted to consist of various materials in different phases with significantly different thermophysical and transport properties. The model uses a generalized governing equation for 3D transient processes involving diffusion and convection, thereby allowing a single formulation for both low- and high-pressure crystal growth and other kinds of materials processes with or without phase change. An efficient scheme is devised for fast and accurate interface movement with respect to the phase change rate and flow oscillations, as well as for clustering of grids in interface regions as the solutions progress.

1. *Multizone Adaptive Grid Generation* (*MAGG*)

The MAGG scheme is based on constrained adaptive optimization of grid characteristics. One of the major advantages of this scheme is that it preserves internal interfaces separating various zones and always makes them coincide with some grid lines. The scheme allows grids to move adaptively as the solutions progress, domains change, or both. By selecting appropriate weighting functions, the grid nodes can be concentrated in regions of large variations in field variables, and by using appropriate grid inertia, the rate of grid movement can be adjusted selectively. The generated grids are always smooth and orthogonal, maintain slope continuity, and cluster in the regions of interfaces-free surfaces and large gradients. If general curvilinear coordinates are denoted by ξ^j ($j = 1, 2, 3$), and Cartesian coordinates are denoted as x_i ($i = 1, 2, 3$). The grid generation system is then obtained as the Euler-Lagrange equations by minimizing a linear combustion I of the smoothness, orthogonality, and concentration integrals given by [97–99]

$$I = I_s + \lambda_w I_w + \lambda_o I_o + \lambda_v I_v = \iiint F d\xi^1 \, d\xi^2 \, d\xi^3, \qquad (58)$$

where F is the kernel of the functional that also is referred to as the overall *performance function* of the optimization problem. It is a linear function of

$$F_s = \frac{1}{\sqrt{g}} \sum_i \left(g_{jj}g_{kk} - g_{jk}^2 \right),$$

$$F_w = wg,$$

$$F_o = \sum_i G(\mathbf{x})(g_{ij}g_{ik} - g_{ii}g_{jk})^2,$$

$$F_l = V(\xi)(\mathbf{x} - \mathbf{r})^2.$$

Here, F_s considers smoothness, F_o is the orthogonality function, F_w is the weighting volume of the grids, F_l considers the inertia of the grids, w and G are weight functions that control grid volume and orthogonality, respectively, and $\mathbf{r}$ is the mesh at the previous timestep. The g_{ij}'s are the elements of the covariant metric tensor and g is the square of the Jacobian. The Euler-Lagrange equations in the transformation space are [102]

$$\sum_{j=1}^{3} \frac{\partial}{\partial \xi^j} \frac{\partial F}{\partial (x_i)_{\xi^j}} - \frac{\partial F}{\partial x_i} = 0, \qquad i = 1,2,3, \tag{59}$$

where $(x_i)_{\xi^j}$ denotes the partial derivative of a Cartesian coordinate x_i with respect to a curvilinear coordinate ξ^j.

A grid generator is an integral part of the algorithm that enables the grid distribution to adapt to the solution of the finite difference equations. Grid control is employed by using an appropriate weight function w (e.g., some measure of the solution variation or error) that results in a finer grid, where w is large. The choices of the weighting functions w and G are generally problem-dependent. This grid generation routine can be formulated for the entire domain, with the exception of the zonal interfaces where a grid distribution is obtained by the same variational problem subject to constraints of the form

$$f_{\text{int},k} = f_{\text{int}}(x_i), \tag{60}$$

where $f_{\text{int},k}$'s are known real-valued functions with respect to arguments x_i, which are implicit functions of ξ^j. They define the interfaces for constant ζ_k values, with k representing the interface at difference locations. The previous constrained optimization problems are converted to unconstrained ones by introducing Lagrange multipliers Λ_k to form an

augmented functional [102]:

$$I = \iint (F + \Lambda_k g_k)\, d\xi\, d\eta. \tag{61}$$

The Euler-Lagrange equations derived from Eq. (59) along with the constraint in Eq. (60) provide necessary conditions for obtaining grid distribution $(x(\xi, \eta, \zeta_k),\ y(\xi, \eta, \zeta_k),\ z(\xi, \eta, \zeta_k))$ and Lagrange multipliers, Λ_k. The interface position function and its derivatives are determined from an accurate curve fitting procedure in order to preserve its shape, while the gridpoints move along the interface.

The MAGG technique is more efficient and has better characteristics than do the previous methods [99]. This is due primarily to a direct and dynamic link between the zonal and interfacial grid generation routines that is provided by the presence of second-order derivatives in the formulation. The finite difference approximation of the Euler-Lagrange equations are formed and solved by the successive overrelaxation (SOR) method to determine the coordinates of the gridpoints.

2. Nonorthogonal Curvilinear Finite Volume Solution Technique

Zhang et al. [27, 98, 99] have used a nonorthogonal CFV scheme to obtain finite difference equations. Equations for

Mass conservation:

$$\frac{\partial \rho}{\partial t} + \frac{\partial (\rho u_i)}{\partial x_i} = 0, \tag{62}$$

Generalized convection-diffusion:

$$\frac{\partial (\rho \Phi)}{\partial t} + \frac{\partial (\rho u_i \Phi)}{\partial x_i} = \frac{\partial}{\partial x_i}\left(\Gamma \frac{\partial \Phi}{\partial x_i} \right) + S_\Phi \tag{63}$$

in a 3D generalized coordinate system (ξ, η, ζ) can be expressed as

$$\frac{\partial \rho\, \mathrm{Ja}}{\partial t} + \frac{\partial (\rho U)}{\partial \xi} + \frac{\partial (\rho V)}{\partial \eta} + \frac{\partial (\rho W)}{\partial \zeta} = 0 \tag{64}$$

and

$$\frac{\partial (\rho \Phi\, \mathrm{Ja})}{\partial t} + \frac{\partial (\rho U \Phi)}{\partial \xi} + \frac{\partial (\rho V \Phi)}{\partial \eta} + \frac{\partial (\rho W \Phi)}{\partial \zeta}$$

$$= \frac{\partial}{\partial \xi}\left[\Gamma\, \mathrm{Ja}(q_{11}\Phi_\xi + q_{12}\Phi_\eta + q_{13}\Phi_\zeta) \right]$$

$$+ \frac{\partial}{\partial \eta} \left[\Gamma \, \mathrm{Ja} \left(q_{21} \Phi_\xi + q_{22} \Phi_\eta + q_{23} \Phi_\zeta \right) \right]$$

$$+ \frac{\partial}{\partial \zeta} \left[\Gamma \, \mathrm{Ja} \left(q_{31} \Phi_\xi + q_{32} \Phi_\eta + q_{33} \Phi_\zeta \right) \right] + \mathrm{Ja} \, S_\Phi, \tag{65}$$

where q_{ij} is the metrics of transformation and U, V, and W are the contravariant velocity components given by

$$U = \left(\xi_x u + \xi_y v + \xi_z w \right) \mathrm{Ja},$$

$$V = \left(\eta_x u + \eta_y v + \eta_z w \right) \mathrm{Ja},$$

$$W = \left(\zeta_x u + \zeta_y v + \zeta_z w \right) \mathrm{Ja}. \tag{66}$$

The generalized equations can be integrated over each finite volume in the computational domain. For a typical primary point P, the integrated equation with $\Delta \xi = \Delta \eta = \Delta \zeta = 1$, yields

$$\frac{\left(\mathrm{Ja} \, \rho \Phi - \mathrm{Ja}^o \, \rho^o \Phi^o \right)_P \Delta \xi \Delta \eta \Delta \zeta}{\Delta t} + \left(\alpha_\xi J_\xi + \beta_\xi J_\eta + \gamma_\xi J_\zeta \right)_e \Delta \eta \Delta \zeta$$

$$- \left(\alpha_\xi J_\xi + \beta_\xi J_\eta + \gamma_\xi J_\zeta \right)_w \Delta \eta \Delta \zeta + \left(\alpha_\eta J_\eta + \beta_\eta J_\zeta + \gamma_\eta J_\xi \right)_n \Delta \xi \Delta \zeta$$

$$- \left(\alpha_\eta J_\eta + \beta_\eta J_\xi + \gamma_\eta J_\zeta \right)_s \Delta \xi \Delta \zeta + \left(\alpha_\zeta J_\zeta + \beta_\zeta J_\xi + \gamma_\zeta J_\eta \right)_t \Delta \xi \Delta \eta$$

$$- \left(\alpha_\zeta J_\zeta + \beta_\zeta J_\xi + \gamma_\zeta J_\zeta \right)_b \Delta \zeta \Delta \eta = \left(\mathrm{Ja} \, \hat{S} \right)_P \Delta \xi \Delta \eta \Delta \zeta, \tag{67}$$

where the superscript o denotes values from the previous timestep; α, β, and γ are the geometrical coefficients; and J denotes the fluxes of the control volume.

The governing equation, Eq. (67), then can be written as

$$a_P \Phi_P = \sum_{nb} a_{nb} \Phi_{nb} + b, \tag{68}$$

where Φ represents the velocities, pressure, and other scalar variables. All equations are discretized in the same control volume in finite volume structure.

3. Solution Method

Staggered grids commonly have been used for computational fluid flow and heat transfer problems, and are considered to be more appropriate for velocity-pressure coupling. However, there are many advantages of using a nonstaggered grid system. For example, if the velocity components and other dependent variables are stored at nodal points, the geometric parameters and the coefficients of discretized momentum equations re-

main identical. The main fluxes also are the same for all variables. Furthermore, in the case of multiphase systems, one important requirement is the imposition of interfacial boundary conditions, and for this purpose a nonstaggered grid is more appropriate. The only drawback to this approach is that it requires a higher-order interpolation to calculate the fluxes and handle the velocity-pressure coupling. The general equations can be integrated over each finite volume in the computational domain.

The solution algorithm for fluid flow calculations in a generalized curvilinear coordinate system is basically similar to the SIMPLER algorithm [103], which consists of solving a pressure equation to obtain the pressure field and solving a pressure-correction equation to correct predicted velocities. However the scheme is much more complicated because the velocity directions continually change along the coordinate lines. The detail of this scheme MASTRAPP (Multizone Adaptive Scheme for Transport and Phase change Processes) for low- and high-pressure crystal growth processes is presented in Zhang *et al.* [27, 98, 99].

4. Parallel Computation

In crystal growth modeling, further progress will depend on realistic large-scale numerical simulations. For example, very fine grids are needed to resolve the various temporal and spatial scales involved in an unsteady, often turbulent, flow field. Moreover, in many cases, 3D simulations are necessary to yield a reliable description of the flow behavior. Furthermore, a large number of calculations are required in parametric studies to explore the solution dependence on process parameters. These simulations, which require extensive computer resources such as computational speed and processor memory, pose many challenges both in terms of computing hardware and software. Recent advances in computer architecture and algorithm development for massively parallel systems make parallel computation an attractive approach to perform simulations for crystal growth.

Chui *et al* [104] have presented a parallel algorithm that is an extension of the sequential algorithm MASTRAPP [27]. Xiao and Derby [105] also have used parallel computations for crystal growth modeling. The parallel algorithm of Chui *et al.* [104] is based on the overlapping domain decomposition approach [106]. The computational domain is divided into a number of rectangular subdomains. Each subdomain is assigned to one processor. The subdomains have approximately the same size to ensure load balancing. Each processor computes and stores only variable values within its own subdomain. In order to carry out the calculations within a

subdomain, each processor requires some variable values on the subdo-main boundaries. These values are computed by other processors to which neighboring subdomains are assigned. Communication between processors is required to update these values on subdomain boundaries. In this approach, communication is restricted to data on subdomain boundaries and communication cost is proportional to the size of those boundaries. This strategy ensures a relatively low communication cost in comparison with the computational cost.

Two levels of iterations are required at every timestep. The outer iteration loop provides for the update of the equation coefficients, grid coordinates, and source terms to take into account for nonlinearity and coupling of the equations for the physical variables. In the inner iterations, large linear equation systems, which result from the discretization of the governing equations, are solved. The outer iterations are explicit in nature, since the update only requires the variable values from the previous iteration. This part of the parallelization is straightforward. The inner iterations are implicit and pose special challenges in the parallel imple-mentation. The MASTRAPP-based parallel algorithm is designed for MIMD (multiple instructions multiple data) architectures [106], and the parallel code is portable to a variety of computer architectures, including massively parallel computers and clusters of workstations. It is hoped that high-performance parallel computing may ultimately facilitate 3D tran-sient calculations for fluid flow heat transfer, mass transport of impurity and dopants, and stress distributions during the Cz growth processes. It also may make it possible to simulate the entire growth process—from seeding to the end of the growth—in the near future.

D. THERMOMECHANICAL MODELS

Once the shape of the crystal and its temperature distribution are known, it is possible to calculate thermal stresses in the crystal. If the stress model assumes that the material is linearly elastic and isotropic, its properties remain unchanged and the crystal is free of surface traction. The constitutive equation for a linear elastic material in an axisymmetric system is expressed as follows:

$$\sigma = D(\varepsilon - \varepsilon^0), \tag{69}$$

where D is the coefficient matrix and ε^0 is the initial strain corresponding to the free expansion or contraction due to temperature variations. A fully coupled calculation can predict an accurate temperature field and the shape of the melt–solid interface during the growth. The stress field then can be calculated without any arbitrary simplifying assumptions on the shape of the crystal and the temperature field [107, 108].

A direct correlation between the transport phenomena in a crystal growth system and stresses and defects–dislocations in grown crystals has been well recognized by researchers in crystal growth. As early as 1980, Jordan et al. [109] pioneered the idea of theoretically explaining the dislocation formation in crystal growth by proposing that the formation of dislocations is caused by the presence of thermoelastic stresses in the material. When the thermal stress exceeds the critical resolved shear stress (CRSS), the dislocations begin to form and multiply by gliding in the preferred slip directions. These authors treated the pulled crystal as a long cylindrical rod, calculated the conduction temperature distribution and thermal stress components, and used the excess of resolved shear stresses for slip over the estimated CRSS as a measure of the dislocation density. The density distribution showed a good qualitative agreement with that observed on sections taken from the cylindrical part of the real crystals. Following the work of Jordan et al. [109, 110], thermal stress calculations have been performed by many investigators since 1980. Table VIII lists a summary of the important work on this topic.

In the early calculations, the crystal was isolated and the melt–crystal interface was simplified either as planar or a known shape, and the effect of the melt was not taken into account. Further improvements were made by Kelly et al. [111, 112] and Dupret and van den Bogaert [7] by using global radiation and conduction thermal models that included both the melt and the crystal. The model neglected convection in the melt, but the melt–crystal interface shape was obtained simultaneously. The sensitivity of stress distribution to radiation heat exchange was well demonstrated by these simulations. Most recently, Kinney et al. [34, 35, 113, 114] have investigated the sensitivity of interface dynamics and melt convection to stress distribution by using the IHTCM code. However, they needed to use an artificial viscosity to obtain converged solutions when the convective flows were strong. Imaishi et al. [115] used a FEM model to predict melt convection and stresses in the growth of oxide single crystals where the Prandtl number is much larger than that of the Si and III-V compounds. All of these investigators used FEM for both thermal and stress calculations in the crystal and assumed that the grown crystal is elastic (Table VIII).

The experimental evidence suggests that the crystal goes through a plastic deformation while it is grown. An alternative description of dislocation formation therefore relies on microscopic modeling of dislocation and multiplication, and introduces the notion of stress relief caused by plastic strain in the crystal. Völkl and Müller [116, 117] have proposed a plastic deformation calculation based on the Alexander and Hassen (AH) model [118]. The model gives a relationship between the macroscopic strain ε_{pl} and the microscopic process of dislocation motion or the mobile disloca-

TABLE VIII
A Selected List of Stress Calculations for Czochralski Processes

Author	Method	Stress Model		Transport Model		Interface	Gas Convection	Crystal
		Elastic	Plastic	Crystal	System			
Jordan (80–85)	Analytical	Yes	—	Only	—	Planar	Given h	InP, GaAs
Duseaux (85)	FEM (2D)	Yes	—	Only	—	Planar	Given h	GaAs
Kobayashi (85)	Analytical	Yes	—	Only	—	Planar	—	—
Szabo (85)	Analytical	Yes	—	Only	—	Planar	—	—
Lambropoulos (87)	FEM (2D)	Yes	Yes	Only	—	Sin	Given h	InP, GaAs
Motakef (87–91)	FEM (2D)	Yes	—		G*Cd/R	Cal.	Given h	GaAs
Völkl (87–94)	FEM (2D)	—	A–H		Cd/R	Given	Given h	InP
Meduoye (89–91)	FEM (2D)	Yes	—	Only		Given	Given h	GaAs
Schvezov (89)	FEM (2D)	Yes	—	Only		Given	Given h	GaAs
Dupret (89–90)	FEM (2D)	Yes	—		G*Cd/R	Cal.	Given h	Ge, GaAs
Ishida [123]	FEM (2D)	Yes	—		G*Cv/R	Cal.	—	GaAs
Imaishi (90)	FEM (2D)	Yes	—		Cv/R	Cal.	Negl	Oxide
Koai (90–94)	FEM (2D)	Yes	—		G*Cd/R	Cal.	Given h	GaAs
Bornside (91)	FEM (2D)	Yes	—		G*Cd/R	Cal.	Given h	Si
Kinney (91–94)	FEM (2D)	Yes	—		G*Cv/R	Cal.	Given h	Si
Miyazaki (91–92)	FEM (3D)	Yes	—		G*Cd/R	Cal.	Given h	Si
Huang (93)	Analytical	Yes	—	Only		Given	—	—
Zou (95–96)	FEM (2D)	Yes	—		Cv/R	Cal.	Cal.	InP

G*, global model that considers the entire puller; Cd, conduction; Cv, convection; R, Radiation; Cal, calculated; Sin, sine function; FEM, finite-element method; 2D, two-dimensional; InP, indium phosphide; GaAs, gallium arsenide; Ge, germanium; Si, silicon.

359

tion density N moving a distance dx in the crystal,

$$d\varepsilon_{pl} = \Phi bN\,dx,\qquad(70)$$

the integration of which results in the strain rate

$$d\varepsilon_{pl}/dt = \Phi bN v,\qquad(71)$$

where N is the mean mobile dislocation length per unit volume m/m^3, b is the Burgers vector, x is the mean free surface distance passed by the dislocations, v is the mean velocity of the dislocations, and Φ is a geometrical factor relating the direction of true shear strain within the slip system to the direction of the strain generated by a load. The difficulties in solving the previous equations arise from the interaction between N and v and their dependence on parameters such as shear stress τ and temperature T. The relationship equations have been given by Völkl and Müller [116]:

$$d\varepsilon/dt = \Phi bNB_o \exp(-E/kT)(\tau - A\sqrt{N})^{m},\qquad(72)$$

$$dN/dt = KNB_o \exp(-E/kT)(\tau - A\sqrt{N})^{m+1},\qquad(73)$$

where K is obtained from the degree of deformation at the inflection point of the creep curves [118], E is the active energy, and m is the stress exponent.

Experimental data and numerical calculations by Völkl and Müller [116, 117] show that the dislocation dynamics predicted by the AH model is appropriate for LEC growth of InP, where large dislocation densities are reported. Maroudas and Brown [119] have used the AH model to analyze dislocation dynamics in Si and III-V compounds. At the same time, Motakef et al. [80, 120, 121] have reported that the CRSS-based thermo-elastic calculations, as well as quantitative approaches to reduce density identified by this formulation, are consistent with the AH model. Evidently, more experiments are needed before the model predictions can be quantitatively compared with the experimental data. In addition, if a consistent theory is developed, the theory applicable to one material also should work for other materials. A precise methodology to correlate the level of thermal stress with the formation of defects in the crystal is not fully understood.

Both of the previous viewpoints (Jordan's approach and the AH model) focus on the importance of thermal stress to dislocation formation in the crystal and start with a stress calculation; however, they do not account for the mechanism of dislocation generation. The AH model, however, requires complex simulations and vast computing resources, whereas the earlier CRSS model uses linear elastic assumptions and is computationally less expensive.

An accurate prediction of stress field therefore requires precise calculations of temperature field and solid–liquid interface shape and dynamics. However, as noted earlier, most of the studies use a relatively simplified thermal model to calculate these quantities. In fact, many of the reported stress fields are based on either a planar or a parabolic-shaped interface, with the temperature field obtained either from the conduction model or from the experiment. The convection flows in both the melt and the gas have been either simplified or completely neglected until recently. It is also interesting to note that while a FEM has been used to predict stresses in the crystal, most of the simulations for melt flows are carried out by either the FVM or the FDM, and they are presented independently of each other.

In addition, under the HPLEC conditions such as in the case of InP growth or commercial growth of GaAs crystals, convection in the inert gas become quite important and must be taken into account. Very little is reported on stress field in the HPLEC grown crystals. Völkl and Müller [122] published their analysis of InP growth in 1987. Their calculation is partially based on some experimental data and this limits the applicability of their model. Ishida et al. [123] have presented simulations for high-pressure growth of GaAs crystals, but no detailed description of the model is given.

Since the crystal quality strongly depends on thermal stresses that arise during the growth, it is important to have a realistic model for the growth of the single crystal under the thermomechanical conditions. Zou et al. [107, 108] have shown that after the melt–crystal interface profile and temperature distribution in the crystal have been obtained from MASTRAPP, a finite-element code can be coupled as a postprocessor to predict the thermal elastic stress in the crystal. Their model assumes that the material is linear elastic and isotropic; the crystal is stress-free under uniform temperature; the material properties are constant and the gas pressure on crystal side is the same as the melt pressure at the melt–crystal interface, and remains unchanged. In addition any fluctuations in the pressure due to flow oscillations are considered to be small and are neglected. They have obtained von Mises stress for the plastic deformation threshold in an isotropic material using the theory of plastic deformation

$$\sigma_{VM} = \left\{ \tfrac{1}{2} \left[(\sigma_1 - \sigma_2)^2 + (\sigma_2 - \sigma_3)^2 + (\sigma_3 - \sigma_1)^2 \right] \right\}^{1/2}, \qquad (74)$$

where σ_{VM} is the von Mises stress, and σ_1, σ_2, and σ_3 are the principle stresses. The solution of thermomechanical equations in the solid domain is divided into two parts, the solution of the equilibrium boundary value problem for the displacement field and the integration of the constitutive

equations to update the material state over each time increment. Since these two parts are tightly coupled, an iterative procedure has been implemented.

III. Analysis of Melt Flow Mechanisms

Current Cz systems for Si growth have melt flows that may be characterized as either oscillatory, in transition to turbulence, or turbulent, depending on the geometry and operating conditions of the furnace. Steady flow is defined by its invariability with time. Oscillatory flows are unsteady flows that show a regular and periodic flow pattern, and a Fourier transform of any flow variable will show one or more well-defined frequencies that exist in the flow. Flows in transition to turbulence are unsteady flows that show only a few important frequencies in the power spectrum (but with less definition than oscillatory flows), while turbulent flows are marked by random fluctuations in the flow and a power spectrum that is broad-banded and featureless [16]. For Cz growth, a wide variation in Ar, Gr, Re_c, Re_s, and Ma can produce flows that are strikingly different for different realistic flow situations. The limiting regimes for nonturbulent flow (which are generally obtained experimentally) for natural convection, rotation, and surface tension in Cz flow are discussed here.

A. Natural Convection

Natural convection is an ever-present phenomenon in the flow of any liquid whose density changes with temperature while in a gravitational field. Based on the characteristic length of the fluid and the thermal boundary conditions, flow may be nonexistent, or if flow exists, it may be steady, oscillatory, or turbulent.

For convection between two rigid horizontal plates, bottom-heated and top-cooled (the Bénard convection), with moderate Prandtl number fluids (Pr ≈ 1), flow initiates at $Ra_h = 1708$, starts oscillating when $Ra_h > 10^5$, and then becomes turbulent at $Ra_h > 10^6$ [124]; whereas for a vertical enclosure heated on the side wall, fluid motion starts at $Ra_h > 0$, and turbulent convection begins at $Ra_h \approx 10^9$ [125]. For low Pr fluids, the critical Rayleigh number for the onset of flow remains the same ($Ra_h = 1708$), but the limiting values for the initiation of oscillatory and turbulent flow are closer together. As noted by Krishnamurthi [126] in experiments for pure Bénard systems with mercury (Pr = 0.025), flow is steady in two-dimensions up to $Ra_h = 2.4 \times 10^3$, and bypasses the transition to steady 3D flow, becoming time-dependent and 3D when $Ra_h > 2.4 \times 10^3$.

Krishnamurthi also finds multiple frequencies in this system at $Ra_h = 3.1 \times 10^3$, which Ristorcelli and Lumley [16] interpret as low-dimensional turbulence. Although many natural convection results are reported using Ra (where $Ra = GrPr$), for low Pr fluids, some researchers point out that Gr is a more relevant parameter, since the viscous boundary layer scales as $\delta/h = Gr_h^{-1/4}$ [127].

To avoid microscopic and macroscopic inhomogeneities due to the oscillations in natural convection-driven flow, boundary conditions are modified to yield steady flow or suppress oscillations as much as possible. It is impossible to achieve the no-flow situation in a conventional Cz geometry, since the thermal boundary conditions will always initiate fluid motion. For a pure Bénard flow, this limitation would impose a melt height of about 2 cm for a temperature difference of 10 K. This would prove difficult to achieve in a real crystal puller, since a certain thermal mass of melt is required in order to dampen any fluctuations in heater input. Small temperature variations in the heater, due to large losses and inefficiencies in typical Cz pullers, also can cause rapid cooling of the melt and can result in an end to the crystal growing process. Since the addition of other effects such as rotation, surface tension, and magnetic fields can significantly enhance or reduce the stability of such flows, a very low melt height may not be the ultimate factor in generating the best conditions for nonoscillatory flows.

In examining the scales of natural convection, we should always recognize that low Prandtl number fluids such as liquid Si have unique properties. Low Pr fluids have thermal boundary layers much larger than viscous boundary layers, which has motivated many investigators to model Cz heat transfer as conduction-dominated, particularly those who have studied global heat transfer in the Cz system. Based on Jones' [128] scale analysis of the Cz melt, advection may be ignored in the interior region when

$$0.5\varepsilon^{1/2} Ar^{5/2} Gr^{1/2} Pr \ll 1, \tag{75}$$

where ε is the fraction of the temperature at the center of the melt in relation to the overall temperature difference in the system between the crucible and crystal $(T_c - T_{center})/(T_c - T_s)$. For the purpose of this analysis, with a low Pr fluid, the temperature field can be *roughly* approximated by a conduction solution, and therefore this may be estimated to be 0.5. When $Ar = 0.25$, $Gr = 10^8$, and $\varepsilon = 0.5$, the left-hand side of Eq. (75) is 0.59, indicating that convective effects may not be negligible. Evidently, at high aspect ratios ($Ar > 0.25$), this criterion can never be satisfied for the industrial range of parameters, which severely limits applicability of the conduction solutions.

Strictly speaking, purely buoyancy-driven flows will only exist if the melt is contained by a system with rigid walls. In the case of Cz growth, the upper surface of the melt is free, and hence the effect of surface tension must be considered when analyzing the melt flow even if the crystal and crucible are not rotated.

B. SURFACE TENSION

The effect of surface tension in Si crystal growth systems is large due to a significant variation in surface tension with temperature, which is embedded in the Marangoni number, Ma. Some investigators prefer to consider a surface tension Reynolds number, $Re_\sigma = Ma/Pr$, very similar to $Gr = Ra/Pr$ for natural convection. Very little information is available on under what conditions surface tension-driven liquid metal (low Pr) flows become oscillatory and turbulent. Oscillatory flows in rectangular cavities have been tentatively identified as beginning at about $Ma = 10^4$ [16].

The boundary layer thickness for surface tension flow was obtained by Balasubramaniam and Ostrach [129] as

$$\frac{\delta}{h} = \frac{1}{Ar}\left(\frac{Ma}{Pr}\right)^{-1/3} = \frac{Re_\sigma^{-1/3}}{Ar}.\tag{76}$$

For a typical value of $Re_\sigma = 10^7$ in a Cz melt with $b = 17.54$ cm, $Ar = 0.5$, this yields a boundary layer thickness, $\delta/h = 0.009$ of 0.04 cm.

C. ROTATION

The effect of rotation in a melt system is to eliminate azimuthal variations in the thermal boundary conditions of the crucible and crystal that are inherent in the system due to manufacturing limitations and process requirements. These rotations provide a more uniform mixed flow for crystal growth, and can dampen the effects of surface tension and buoyancy. With higher rotation rates, the flow gets stratified, and these effects are suppressed to some extent. However, there are practical and theoretical limitations on how large these rotation rates can be.

One practical limit is that the melt surface depresses in the center of the melt as centrifugal force becomes large. The difference in height between the center of the melt and the outside of the melt is given by [130]

$$\Delta h = \frac{\Omega^2 b^2}{2g}.\tag{77}$$

When Δh becomes sufficiently large (≈ 1 cm in a real melt), it becomes difficult to grow a crystal. For 17.78-cm (7-in.) radius melt at 10 rpm, this

difference in height is 0.176 cm; at 30 rpm, it is 0.704 cm. Crystal growers in industry have found experimentally that crucible rotations of about 5 to 6 rpm minimize the amount of oxygen incorporated into the crucible, and that rotation rates of about 10 rpm are optimal for the best crystal structure.

In addition, if a crystal supported by a pulling wire is rotated at high speeds, the axis of the crystal can orbit about the center of the crucible, creating waves in the flow and making the system highly asymmetric and unsuitable for the growth of good crystals. This is found to happen at about 20 to 30 rpm in industrial systems.

The flow near a rotating disk has been studied extensively. Cochran has shown that the boundary layer for the radial flow ejected from a rotating disk is [131]

$$\frac{\delta}{h} \approx \frac{4}{Ar} Re_s^{-1/2}. \tag{78}$$

For a crystal in a typical Cz system ($Re_s = 10^5$, $Ar = 0.5$, $b = 17.54$ cm), this will yield a boundary layer thickness of about 0.11 cm. Experimental work has found that instabilities for perfectly flat rotating disks occur at $Re = 8 \times 10^4$, and that the flow can become turbulent at $Re = 2 \times 10^5$ [132] (where Re is based on disk radius; therefore, $Re = Rr^2 Re_s$). When the flow becomes turbulent due to crystal rotation in the Cz system, impurities are incorporated more readily in the growing crystal; it is for this reason that impurity variation can be greatest at the edges of large-diameter crystals, since the flow at the edges is in transition to turbulence. This transition probably occurs at a lower Re in the Cz system since the crystal-melt interface in a Cz geometry is not always flat, and the rest of the flow is not quiescent. In the industrial Cz process, where the crystal diameter is large, this transition to turbulence occurs at the edge of the crystal (where flow is the fastest) and results in larger radial impurity variations and inhomogeneities.

D. NATURAL CONVECTION AND SURFACE TENSION

When the melt height is low, buoyancy effects can be reduced while surface tension effects may remain unchanged. Therefore, care must be taken in determining the dominating effects in the boundary layers close to the surface and in the interior of the domain, since surface tension only acts at the surface and buoyancy acts everywhere in the flow. An analytical solution to the problem of surface tension and natural convection in a shallow rectangular cavity heated at one end and cooled at the other was

made by Birikh [133], which gives the ratio of surface tension to buoyancy forces as

$$N_\sigma = \frac{12}{\rho g \beta h^2} \left(-\frac{d\sigma}{dT} \right). \tag{79}$$

For a low aspect ratio melt, with Ar = 0.25, b = 17.78 cm and h = 4.45 cm, yielding N_σ = 11.4. This would mean that the flow in the melt would be induced mainly by surface tension forces. However, the assumptions made in the analysis by Birikh do not pertain entirely to the Cz melt, since he considered the temperature gradient only in the horizontal direction. There also are significant geometric variations between his model and the Cz melt; for example, the crystal occupies a significant portion of the melt, and the melt is not extremely shallow.

Balasubramaniam and Ostrach [129] also have attempted to examine this problem. However, Sackinger [94] is of the view that the value of Gr defined in this work is in error (Gr was erroneously defined as Gr = $g\beta\Delta T b^3/\nu$, instead of the correct Gr = $g\beta\Delta T b^3/\nu^2$.) They define the influence of surface tension in the boundary layer as compared with buoyancy in the parameter N_σ, where

$$N_\sigma = \mathrm{Gr}\,\mathrm{Ma}^{-5/3}\,\mathrm{Pr}^{5/3} = \frac{\mathrm{Gr}}{\mathrm{Re}_\sigma^{5/3}}. \tag{80}$$

Using this criteria, $N_\sigma = 5 \times 10^{-4}$ in a typical Cz system. These authors have concluded that the flow in the Cz system is dominated by surface tension forces, and not buoyancy forces.

The scaling analysis of Balasubramaniam and Ostrach has been challenged by Jones [128]. Jones argues that surface tension effects are confined to the upper boundary layers, whereas buoyancy is a body force that acts over the entire fluid. By scaling the system based on the strength of the streamfunction induced by these effects, a ratio of buoyancy-to-surface tension streamfunction may be obtained as

$$\frac{\psi_b}{\psi_s} = 0.25\varepsilon^{1/2}\,\mathrm{Gr}^{1/2}\mathrm{Ar}^{3/2}\,\mathrm{Ma}^{-1/3}\,\mathrm{Pr}^{1/3}. \tag{81}$$

The streamfunction ratio ψ_b/ψ_s is plotted in Fig. 10 for Ar = 0.25 and in Fig. 11 for Ar = 0.50 as a function of Gr and Ma, with ε = 0.5, Pr = 0.015. One advantage of this type of analysis is that the stream function gives the impact of the driving forces of the flow over the entire domain. These plots demonstrate that for realistic values of Ma and Gr, both of these effects are of equal magnitude at Ar = 0.25, and that buoyancy is more dominant when Ar = 0.5 and higher.
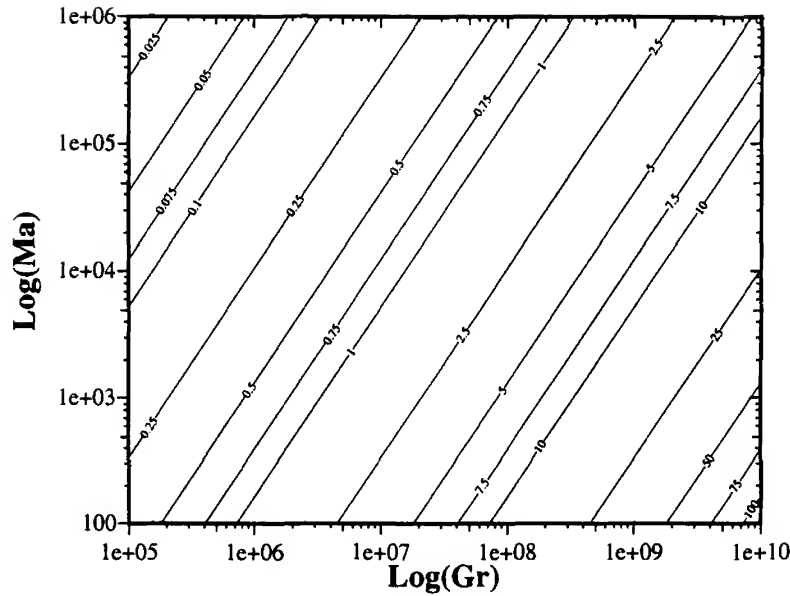
FIG. 10. The ratio of buoyancy-driven to surface tension-driven streamfunctions ψ_b/ψ_s, as a function of Gr and Ma, with $\varepsilon = 0.5$, Pr = 0.015, and Ar = 0.25 [145].

E. NATURAL CONVECTION AND ROTATION

Natural convection in Cz melts is known to cause regular and irregular striations in the grown crystal due to oscillatory, chaotic, or turbulent flow. Crystal and crucible rotations have been used to ameliorate such effects by suppressing natural convection. The large variation in possible crystal–crucible rotation rates has been well mapped out in the experimental work by Carruthers and Nassau [134] and Jones [128]. The body of analytical and numerical work investigating the interaction between natural convection and forced convection due to rotation also is large.

Carruthers [135] analyzed the effect of crystal rotation on natural convection to explain the interface inversion in crystals grown by the Cz method from oxide melts (Pr = 1). Since the interaction of thermal convection and forced convection is one that involves viscous effects, the convective forces are compared by normalizing convective velocities with viscosity. The effects of natural and forced convection are equal when $Gr/Re^2 \approx 1$; when $Gr/Re^2 \gg 1$, natural convection flows are dominant, and vice versa when $Gr/Re^2 \ll 1$. Other analyses and numerical results show similar results, but with $Re^{2.5}$, since the direction of the motive force of forced convection is perpendicular to that of free convection. Kobayashi
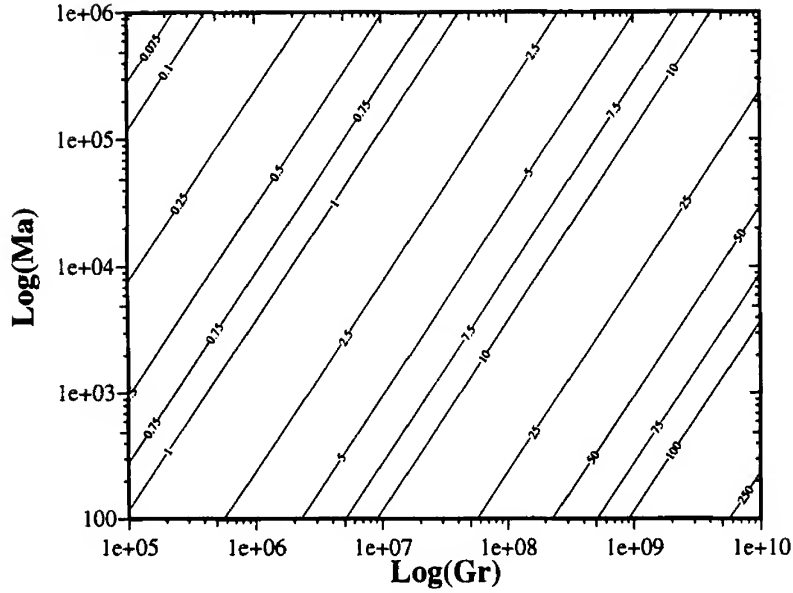
FIG. 11. The ratio of buoyancy-driven to surface tension-driven streamfunctions ψ_b/ψ_s, as a function of Gr and Ma, with $\varepsilon = 0.5$, Pr $= 0.015$, and Ar $= 0.50$ [145].

[136] arrived at the relation $Gr/Re^{2.5} = 0.1$ and Chan *et al.* [137], analyzing flow in counterrotating melt, arrived at the nondimensional ratio of $Gr/Re^{2.5} = 0.2$ to denote the medial case when natural convection and forced convection flows play an equal role in the system.

For rotation of the crucible, many other numerical simulations and experiments show that a solid body flow exists in the crucible, except under crystal when rotation rates are dissimilar, resulting in large shear forces. Scaling of crystal and crucible rotations with natural convection shows that crystal rotation does not affect the bulk flow, but only the local flows near the crystal. This is still important, since the flow near the crystal is responsible for how inhomogeneities are incorporated into the crystal. In general, when rotation is added to a Bénard system, the critical Ra where oscillations begin is increased (as a function of $Ta^{2/3}$), based on the value of the Taylor number Ta, where $Ta = (2\Omega h^2/\nu)^2 = 4Re^2 Ar^4$. The mechanism for the stabilizing effects of rotation are due to the Coriolis force and the physics expressed in the Taylor-Proudman theorem, which restricts disturbances to the flow (components along the axis of rotation are suppressed).

For a lower limit of melt height h = 44.45 mm and rotation rate of 1 rpm, Ta = 1.87 × 10⁶. For moderate Prandtl number flow, this increase in stability as shown by Chandrasekhar [138], also can increase the critical Ra for onset of oscillations, and the transition to turbulence. For low Pr flows, rotation of a system with natural convection only stabilizes the flow until a critical value Ta_c is reached. Beyond Ta_c, the flow is considered "overstable," and 3D effects manifest themselves. The critical value of Ta is about 2300 when Pr → ∞, and is reduced when Pr is lowered.

Likewise, for systems with horizontal temperature gradients, the flow also can become 3D with the addition of rotation. For example, in a rotating annulus with heating on the outer wall (radius, b) and cooling on the inner wall (radius, a), when Ro < 1, the flow becomes time-dependent and oscillatory. The governing parameter here is the Rossby number, Ro = $g\beta\Delta Th/(\Omega^2(b - a)^2)$ (Ro is similar to Gr Ar/Re², with b replaced by ($b - a$)). For the base Cz flow, Ro = 1.77 for a crucible rotation rate of 1 rpm, with Ar = 0.25. Ristorcelli and Lumley [16] have presented a more in-depth review of these effects and conclude that Cz flows may be asymmetric and time-dependent at higher rotation rates. They do, however, make the proviso that the Cz geometry is significantly different from both the Bénard and the annular systems, and that any firm conclusions are difficult.

F. Surface Tension and Rotation

Surface tension flows may also be restricted by the rotation of the crucible and crystal. Adapting Carruthers' [135] relation of viscous scales for natural and forced convection, a similar relation of viscosity for forced convection in either the crucible or crystal and Marangoni flow may be given by

$$N_{\sigma_2} = \frac{\text{Ma}}{\text{Re}^2\,\text{Pr}} = \frac{\text{Re}_\sigma}{\text{Re}^2}. \tag{82}$$

When N_{σ_2} > 1, surface tension flows predominate, and vice versa. The competition between these effects may be less important for regular Cz melts, since natural convection generally has an equal or greater impact on the flow than does surface tension. For very low aspect ratio melts where Marangoni effects may be pronounced, or for crystal growth systems where natural convection is absent (such as in microgravity), this relation will be important.

G. Summary of Flow Effects

Because of the broad range of operating parameters in Cz pullers, the uncertainty in property variations, and the nonlinearity of the various flow effects, it cannot be stated with certainty that any one effect is much more important than another. Langlois [139] has commented that although certain effects may dominate in specific regions of the melt, (e.g., crystal rotation effects near the crystal, or Marangoni effects near the free surface), the interaction of these effects can significantly affect the ultimate flow field, since each of these phenomena can influence the melt flow structure. Small changes in the value of material properties or in parameters such as the crucible or crystal rotation rate have been found to radically change the overall flow. Hence, only very broad generalizations can be made about the flow regimes. For example, in comparing the effects of crucible and crystal rotation to natural convection, the criteria $Gr/Re^2 \approx 1$ can only be used as a *rough* estimate of the strengths of free and forced convection. Likewise, although scaling analysis shows that both natural convection and surface tension play important roles in the Cz system at moderate aspect ratios, no single effect can be shown to have an absolutely overwhelming influence on the flow. The suggestion that the Cz melt flow in the current generation of industrial pullers is oscillatory also complicates the resolution of these questions. With the addition of the irregular geometrical and thermal boundary conditions present in the Cz system, and the uncertainties for even the most basic thermophysical properties, there are no simple guidelines that can be followed for discovering the true flow in a Cz system.

IV. Convection in Czochralski Melt Systems

Convective flows and heat transfer in moderate and large Cz melts and their implication on growth conditions are discussed here. The effects of buoyancy forces, melt height, rotation rates, surface tension, and shape of the crucible bottom on temperature field, flow structure bifurcation to oscillatory flow, modes of convection in oscillatory regimes, and heat flux oscillations are presented through numerical and experimental results.

A. Natural Convection

As noted earlier, buoyancy-induced flows are inherent in Cz melt systems due to heating at the crucible walls, cooling at the melt surface, and enthalpy change at crystal–melt interface. The numerical studies have

generally neglected the latent heat release due to solidification and have considered the crystal–melt interface maintained at a constant freezing temperature. This is not an unrealistic assumption since the growth rate is very small. The crucible wall is generally considered to be isothermally heated, although some variation in the wall condition—for example, varying heat flux or linear temperature variation on the side wall—has also been considered.

In most of the previous Cz simulations the free surface thermal boundary condition has been considered to be adiabatic, $\partial \Theta / \partial z = 0$ [11, 140]; a linearly varying temperature variation, $\Theta = (r - a)/(b - a)$; or radiatively cooled, $k(\partial T/\partial x) = \varepsilon \sigma (T_{surf}^4 - T_x^4)$ [141]. However, in these simulations, seemingly minor efforts have been made to study the impact of a variation in the free surface thermal boundary condition, although Langlois [142] has conducted a varying emissivity study in order to obtain a better estimate for ε_{S_i}. Kobayashi [136] also has obtained a few numerical results with a simple radiative boundary condition; however the Grashof number was low (Gr = 7.8 × 10³) and the Prandtl number was unity. Sackinger [94] has made some calculations with varying surface emissivity, but with T_x close to Si melting temperature. In all likelihood, the radiation boundary condition has not been considered to be important, because of the nature of the flow at high aspect ratios. In Cz geometries with Ar ≈ 2.0, for example, the flow is more dependent on the heating at the vertical wall, because of the greater area this surface presents to the flow. Therefore, flow patterns when the free surface is insulated and those when it is radiatively cooled are relatively similar [141]. As a result, the onset of instabilities is not affected significantly by a change in the free surface condition. However, as the aspect ratio is lowered, the influence of the side walls may be overshadowed by direct interactions between the bottom of the crucible, the crystal, and the free surface of the melt. The present industrial configuration for Cz growth of Si crystals has resulted in a melt pool that is much shallower than that used a few years ago. Indeed, over the years, the melt aspect ratio (at the start of the process) has decreased from two to a value close to unity. This aspect ratio is further reduced as the crystal is grown. Therefore, it is important to analyze the melt behavior at various aspect ratios.

To examine the basic structure of convective flows in Cz melts, we shall first consider a 2D system, as shown in Fig. 12. As first reported by Crochet et al. [140], and later confirmed by Bottaro and Zebib [143, 144], Anselmo et al. [141, 145] and others, the flow in an axisymmetric system oscillates with a single dominant frequency when Ar = 2.0 and Gr = 10⁷, whether the free surface is insulated or loses heat by radiation. The flow at this aspect ratio is characterized by fluid that moves up along the crucible wall
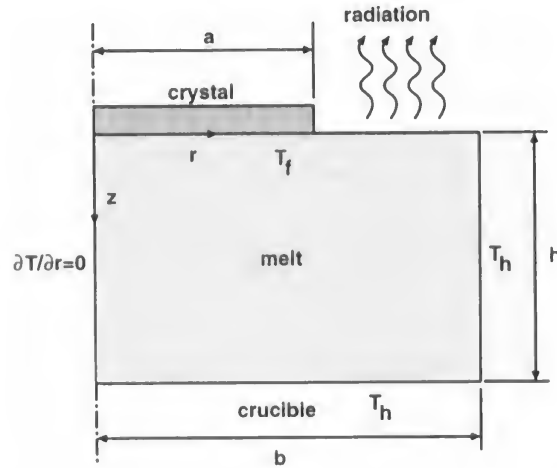
Fig. 12. Two-dimensional axisymmetric computational domain for Czochralski (Cz) flow simulations.

due to natural convection, then buckles and breaks away from the wall, producing one or more counterrotating cells in the process. (Fig. 13). The total amount and overall variation in heat flux (Fig. 14) passing through the system, however, is much lower when the radiation loss is neglected [141, 145].

Interestingly, if the Grashof number is kept constant and the melt height is lowered, the flow oscillations are suppressed and there exists a critical aspect ratio at which the flow can become steady. Figure 15 shows the melt flow at Ar = 0.5. The variation in flow structure between Figs. 13 and 15 is noticeable. The effect of the bottom wall boundary condition vis-à-vis that of the vertical wall is further strengthened as the aspect ratio is reduced to 0.25 (Fig. 16). When the aspect ratio is reduced to Ar = 0.25, and the free surface is allowed to radiate, the boundary conditions for the system closely approximate that of a Bénard configuration, where the bottom surface is heated and the top surface is cooled. When the top surface radiates, a destabilizing temperature gradient will always exist, even without a low temperature at the melt-crystal interface. This can be seen in Fig. 16, where the stream functions still vary in time. In this case, although oscillations are present, they are strongly concentrated in the region under the free surface. The cell that forms under the crystal does not travel towards the outside wall as it does at higher aspect ratios. This may be a desirable occurrence, since the lack of interaction between the outer and inner regions may reduce the amount of impurities that can be transferred by convective means from the crucible wall to the crystal.
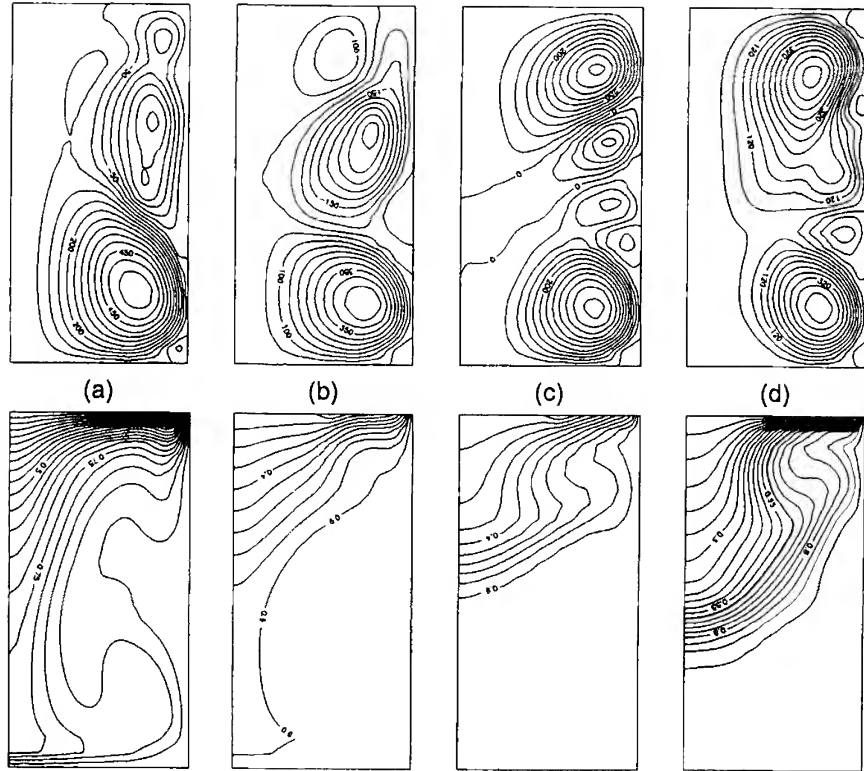
FIG. 13. Streamfunctions and isotherms for a radiative-free surface when Ar = 2.0 and Gr = 10^7 [141].

1. Effect of Crucible Bottom Curvature

Crucibles are generally made of quartz,[4] and have a well-defined curved bottom, due to limitations of the manufacturing process, which make the creation of large right circular cylinders extremely difficult. Also, at the temperatures required for Si growth, quartz tends to soften and distort under load. A curved crucible bottom eases the stress upon the lower half of the container, enabling the crucible to maintain its shape. In addition, a curved crucible allows the remaining silicon melt at the end of growth cycle to pool at the center of the crucible, where it may be pulled up by the tail end of the finished crystal. This reduces the waste of silicon which gets frozen as the system is cooled down and the crucible is replaced. As the

[4] Crucibles made of PBN (boron nitride) are sometimes used in smaller Cz and LEC systems. However, industrial systems for Si growth invariably use quartz crucibles.
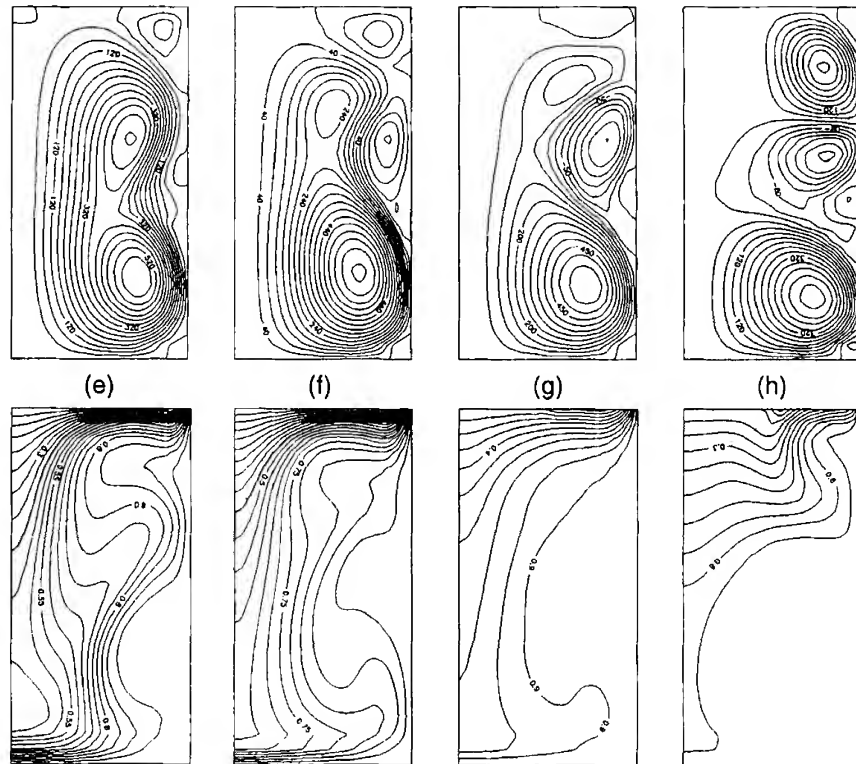
Fig. 13—(Continued)

melt volume is reduced, models of the bulk flow using a right circular cylinder may lose validity. This influence may be less significant at higher aspect ratios, but more pronounced when the aspect ratio is lowered. In order to investigate this effect, Anselmo et al. [141] have performed simulations for both curved and rectangular domains at $Ar = 0.5$, 0.375 and 0.25, and $Gr = 10^7$. The curved bottom of the crucible used in their simulations was based on the shape of a standard General Electric No. 18141F (457 mm in diameter) crucible used in industry. The curve of the crucible bottom was limited to an aspect ratio of 0.25; above this, the crucible was considered to be of constant diameter.

When $Ar = 0.5$, the impact of the bottom curvature on flow pattern, heat flux, and flow oscillations was not found to be pronounced [141, 145]. For example, the variation in the heat flux passing through the system (measured at the top surface of the computational domain) is generally of
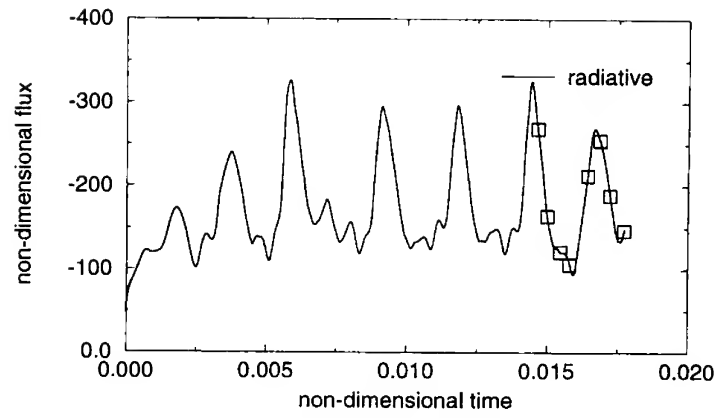
FIG. 14. Heat flux variation for a radiative-free surface when $Ar = 2.0$ and $Gr = 10^7$ [141].

(a)

(d)

(b)

(e)

(c)

(f)
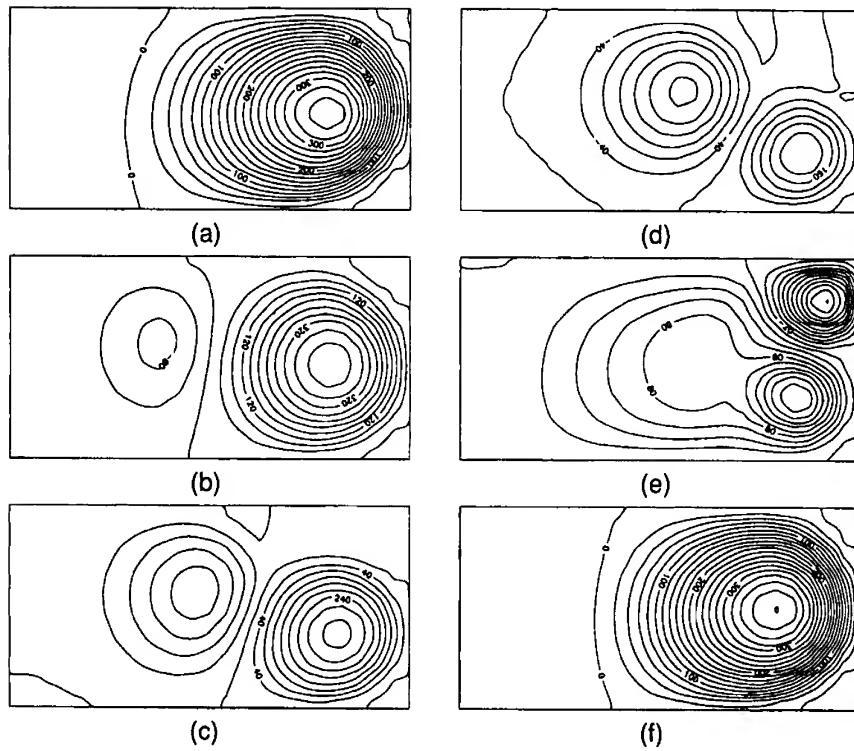
FIG. 15. Streamfunction in time for $Ar = 0.5$ and $Gr = 10^7$ [141].
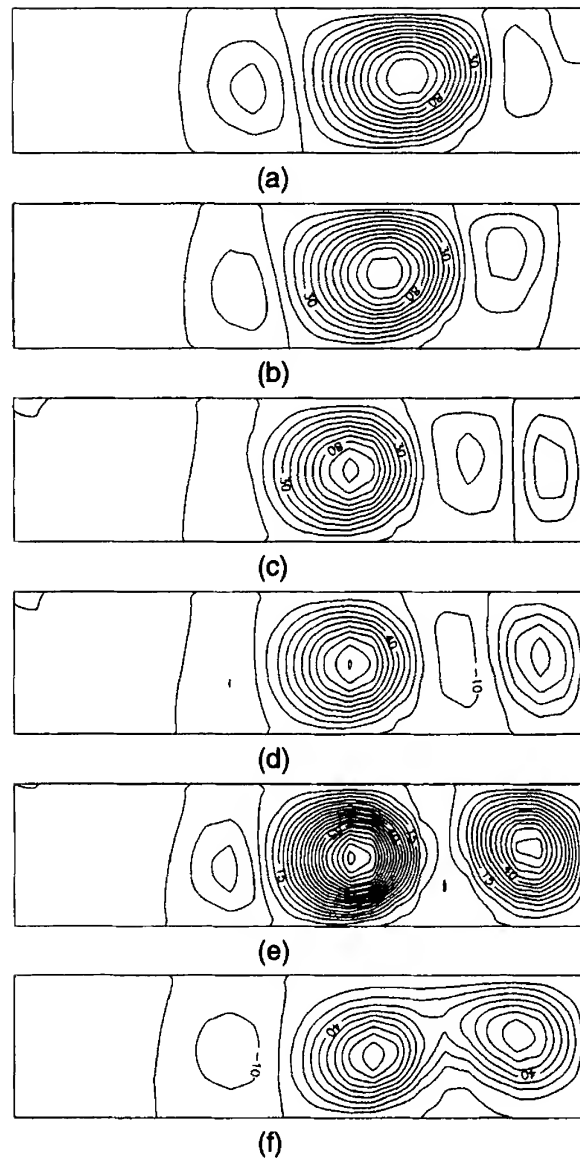
FIG. 16. Streamfunction variations in a rectangular domain with radiative cooling for $Ar = 0.25$ and $Gr = 10^7$ [141].

(g)

(h)
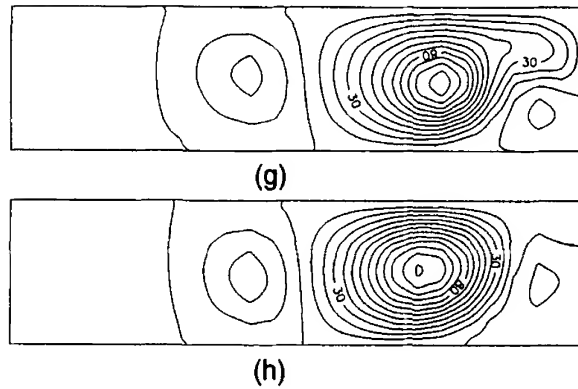
FIG. 16—(*Continued*)

the same frequency and magnitude. However, the effect of the aspect ratio becomes appreciable at Ar = 0.375. Although the frequencies of heat flux oscillations between the rectangular and curved bottom cases were almost the same for Ar = 0.375, the variation in magnitudes was measurable [141].

The combined effect of aspect ratio and crucible bottom curvature becomes much more pronounced when Ar is reduced to 0.25 (Fig. 17). At this aspect ratio, in the curved crucible simulation, the shape of the bottom changes the flow structure to such a degree that the magnitude in flux variation becomes zero and the flow remains steady (Fig. 18). In the right rectangular cylinder model, the flow is still oscillating (as noted before), although the magnitude of this variation also is reduced. As shown in Fig. 17(a), the weak cell formed under the crystal cannot move to the outer region of the crucible, and one strong and one weak counterclockwise cell are maintained under the free surface. Since the curved crucible has a reduced melt height near the edge of the crucible, there is less room for the clockwise cell under the crystal to rise up over the predominating cell located under the free surface. Even in the rectangular case (Fig. 16), the traveling wave pattern has been broken and the oscillations are confined to the region under the crystal. This explains why the oscillations are suppressed, eliminated, or both, at low aspect ratios.

From these natural convection-only results, it is evident that low aspect ratio melts exhibit very interesting flow characteristics, and are strongly influenced by the thermal boundary conditions and the shape of the crucible. It is found that the oscillations in heat flux may be suppressed when the melt height is low and the curved crucible is used. This shows

(a)

(b)
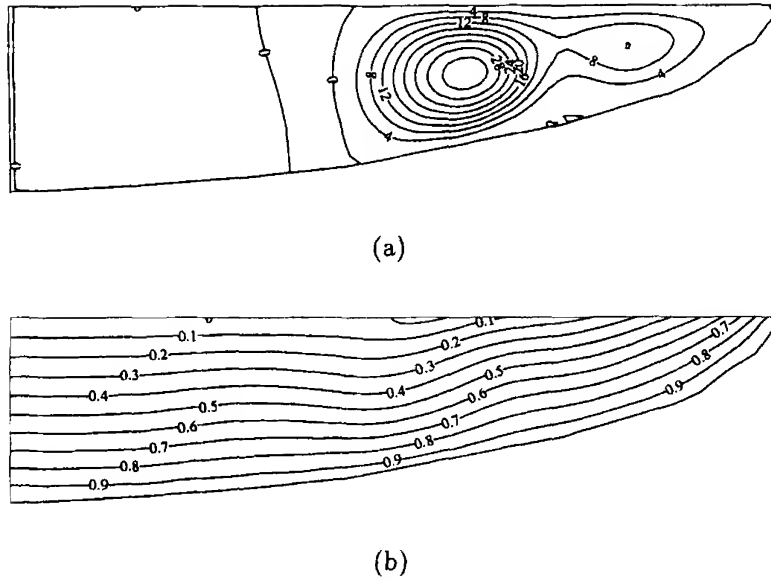
Fig. 17. Steady streamfunction (a) and isotherms (b) in a curved crucible with radiation cooling when Ar = 0.25 and Gr = 10^7 [141].

that a continuous Czochralski (CCz) process with a low melt height may be able to suppress buoyancy-induced flow oscillations. Several schemes for continuous replenishment of melt and Cz growth have been presented in crystal growth literature [2, 30, 101, 141, 145, 146]. A brief discussion on CCz growth is presented later.
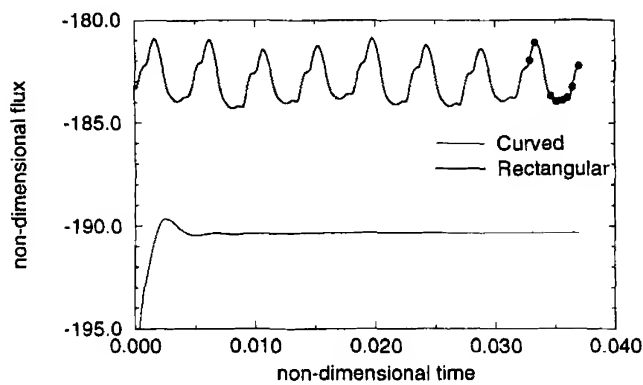
Fig. 18. Flux variations with time for rectangular and curved systems with radiatively cooled free surface when Ar = 0.25 and Gr = 10^7 [141].

2. High Grashof Number Flows

The Grashof number in an industrial Cz Si system is estimated to range from 10^8 to 10^9. Simulations for Gr $= 10^8$ (Figs. 19 and 20) show that the buoyancy-induced flow becomes oscillatory even in the case of curved crucible bottom and Ar $= 0.25$ [141]. In comparison with the Gr $= 10^7$, Ar $= 0.25$ case, the flow structure has changed remarkably. One major difference is that two cells of equal strength may exist under the crystal at a given time, whereas at Gr $= 10^7$, only one strong cell would exist under the crystal at any given time (Fig. 16). The higher value of Gr reinforces the Bénard condition under the crystal and therefore the rolls created in this zone can be stronger. Both the rectangular and curved systems are punctuated by large variations in flux, but the minor variations (secondary frequency) in the rectangular system are much greater, and the overall flux and flow oscillations also are greater.

It is worth mentioning here that Sackinger's global model [94] predicted two steady convective cells in a rectangular domain of Ar $= 0.23$ when Gr $\approx 10^8$, using a melt surface emissivity of 0.05. When Gr $> 10^8$, flow is difficult to simulate, since low Pr flow begins to become chaotic or turbulent. The multiple frequencies found in the Gr $= 10^8$ example support this hypothesis, since the appearance of many frequencies in the flow means that the system is close in parameter space to these regimes. Raising Gr to 10^9, or Gr $= 10^8$ when Ar $= 0.5$ causes computational difficulties, as extremely small timesteps and grids are required to model the flow. Simulations by Araki and Matsuura [147] using a curved crucible have considered higher Grashof numbers at Ar $= 0.5$; however, an up-winding scheme was used for these simulations, and no flow oscillations were presented.

3. General Discussions

From the natural convection-only results, it is evident that large Cz melts exhibit very interesting flow characteristics, and are strongly influenced by aspect ratio, thermal boundary conditions, and shape of the crucible. Although it is a fortunate finding that the oscillations in heat flux (and hence flow, that cause inhomogeneities in the grown crystal) may be suppressed when the melt height is low and a curved crucible is used.

In Fig. 20, the fluxes passing through the various boundaries of a rectangular domain are presented for Ar $= 0.25$, Gr $= 10^8$. One important fact gleaned from Fig. 20 is that the fluxes passing through the system has a detectable phase lag. This lag in heat flux is well known to the industrial crystal growers because heating must be continually adjusted so as not to overheat or undercool the system.

(a)

(b)

(c)

(d)

(e)

(f)
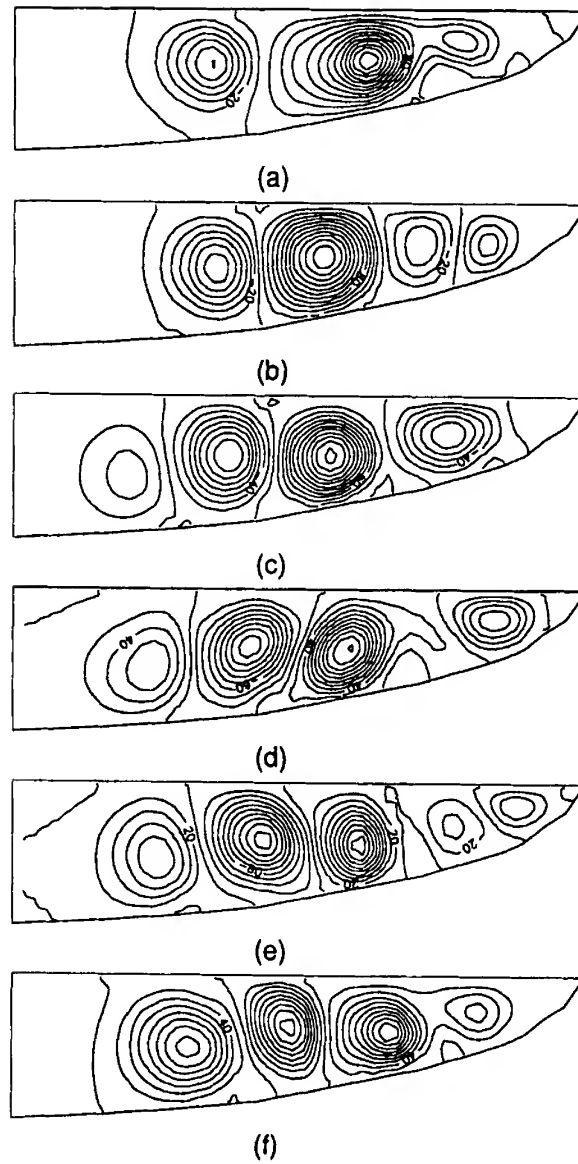
FIG. 19. Streamfunction with time for a curved bottom crucible with radiative cooling when Ar = 0.25 and Gr = 10^8 [141].

(g)

(h)
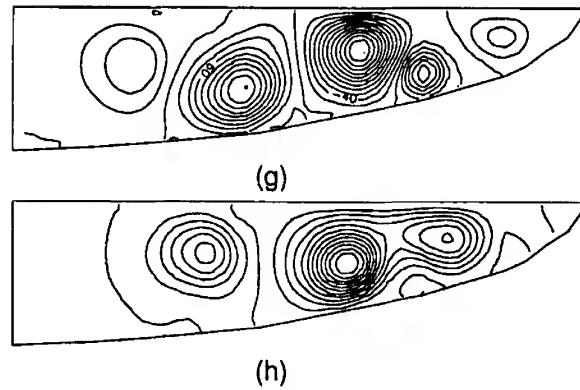
FIG. 19—(Continued)
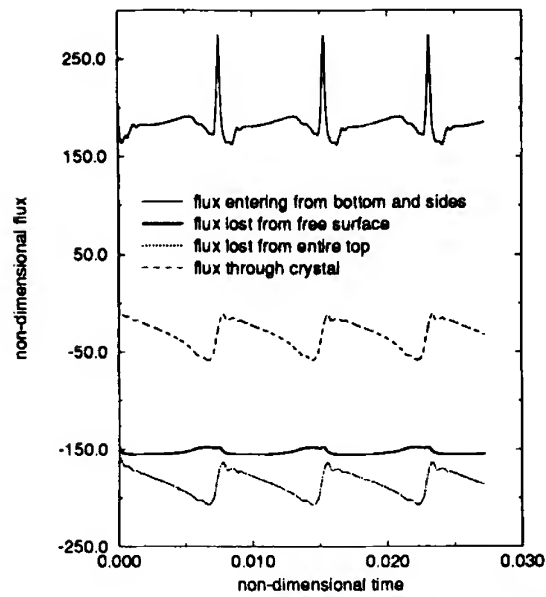
FIG. 20. Flux variations from the bottom and sides, compared with the flux variation from the top surface (crystal, free surface, and combined) for the case of a radiatively cooled free surface in a rectangular crucible, when Ar = 0.25 and Gr = 10^8 [141].

The second point to be noted is that most of the energy passing through the system is due to losses from the free surface, although the variation here is minimal. Instead, the heat rejected at the crystal–melt interface varies widely, due to the generation, strengthening, and disappearance of a convective roll(s) under the crystal; however, the magnitude of the energy lost is much lower than at the free surface. This observation also has been made by Virzi [148] in his global heat transfer model, where only 25% of the heat flux passing through the crucible exits from the melt–crystal interface. This is not unexpected, because a small change in surface temperature caused by flow oscillations does not significantly influence the radiation loss due to the 4th power law. This issue can be expected to pose problems for crystal growth, since variations in heat transfer and flow near the crystal may be more influential than the same variations at the free surface. The variation in heat flux in the crystal zone may be related to the reported phenomena of melt–interface oscillation and remelting–solidification [2].

Müller and coworkers [6, 149, 150] have performed both numerical and laboratory experiments in cylindrical enclosures with Bénard-type boundary conditions, as well as experiments with Bénard geometries having isothermal walls. Although the impetus for their work was the vertical Bridgman configuration, their results may shed some light on the critical value of Gr for onset of oscillations in Cz melts as well. A map of these flow regimes distilled from a series of experiments in Ga (Pr = 0.02) and at aspect ratios $1 < Ar < 10$ is presented in Fig. 21. For a system with Ar = 2.0, Gr = 10^7 (Gr$_h$ = 8 × 10^7), with Pr = 0.02, this map predicts an unsteady turbulent flow, although this is not borne out by Crochet et al. [140], Bottaro and Zebib [143], and the results presented here. This is most likely due to the contribution of wall heating, which also has been investigated by Müller. The Müller regime map (Fig. 21) extends to only an aspect ratio of unity and does not consider Ar in the lower range. The slopes of the critical Rayleigh number-versus-aspect ratio curves for unsteady periodic and turbulent flows in the low aspect ratio regime are such that the extensions of these curves will result in values of Ra$_c$ very close to the critical value Ra for onset of convection. In the present case, Ra$_h$ is only 2.3 × 10^4 when Gr = 10^8 and Ar = 0.25. Although the present boundary conditions are not so simple, the flow at Ar = 0.25 and Gr = 10^8 cannot be expected to be turbulent, since the system is not a pure Bénard system. It is also important to make a distinction between random oscillatory and turbulent convection. Anselmo's model, as well as that considered by Müller and others, can predict flows and heat transfer in stable, periodic, and random oscillatory convection regimes, but is not valid for turbulent flows.
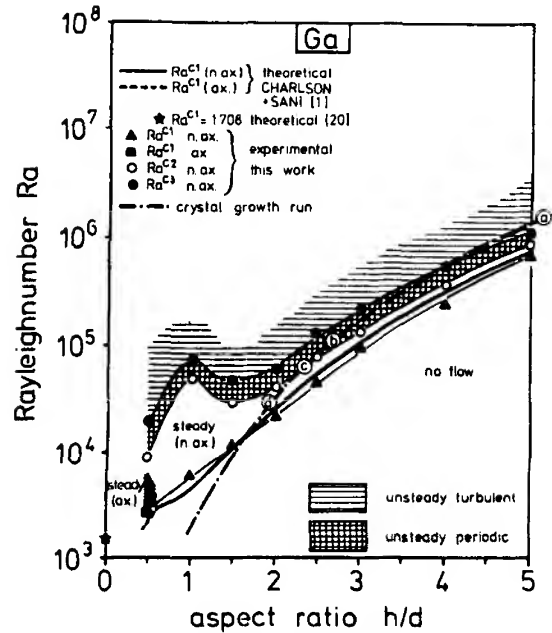
FIG. 21. Regime map, from Müller, for Bénard flow in cylinders with insulated sides for gallium (Pr = 0.02), where Ra = $g\beta \Delta Th^3/\nu\alpha$ [6].

In addition, the possibility of nonaxisymmetric (hence 3D) flow as found by Müller in his simulations and experiments should not dissuade us from drawing any conclusions, since simulations by Mihelčić and Wingerath [151] show that at lower aspect ratios, flows may still remain axisymmetric. With regard to the steady flow in a curved crucible when Ar = 0.25, Gr = 10^7, this may be attributed to the reduced height in the outer regions of the flow field, lowering the local Ra_h below $Ra_{h,c}$. The extension of the model, however, to include the effects of rotation, surface tension, and a variation in bottom surface boundary condition will add to the complexity of the flow.

B. FLOWS DRIVEN BY BUOYANCY, SURFACE TENSION, AND ROTATION

As noted in Section IV, the superposition of crystal and crucible rotations and surface tension on buoyancy-driven flows can be quite influential in the case of Cz growth. Extensive numerical and experimental studies have been performed to examine the combined effects of various process parameters.

1. *Effects of Surface Tension and Buoyancy Forces*

As demonstrated by the scaling analysis, the effects of surface tension on natural convection can be strong for low-height melts. Anselmo *et al.* [141, 145] have shown that the flow remains steady at $Gr = 10^7$ and $Ma = 10^3$, when $Ar = 0.25$. However, the flow strength is doubled compared with that presented in Fig. 18 because of the strong velocities toward the crystal in the melt surface region. For $Gr = 10^8$ and $Ma = 10^4$, the flow is equally driven by both natural and Marangoni convection (Fig. 22)

(a)

(b)

(c)

(d)

(●)
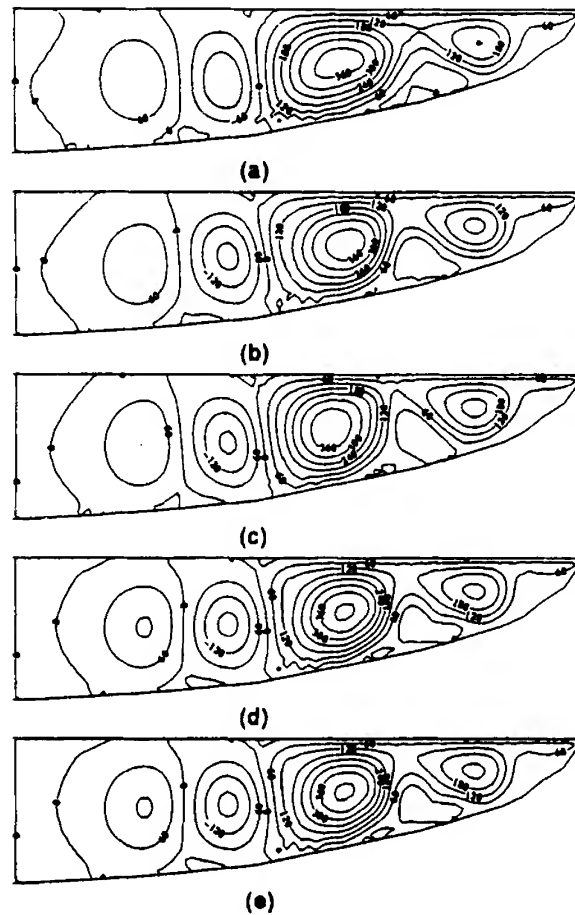
FIG. 22. Streamlines in time for $Ar = 0.25$, $Gr = 10^8$, and $Ma = 10^4$, with curved bottom [145].

and is oscillatory. It is interesting to note that under the crystal, buoyancy forces still dominate, and the flow is of similar strength as observed for $Gr = 10^8$, $Ma = 0$ (Fig. 19). The strength of the convective rolls under the free surface, however, has increased significantly. Although the effect of surface tension decreases as the aspect ratio is increased, it cannot be neglected in the case of semiconductor growth, since the Marangoni number can be as large as 10^5.

2. Natural Convection in a Rotating System

The flow patterns due to crucible rotation are similar to one exhibited by wind patterns on earth. Convective cells in the atmosphere initiate a wind movement from the poles toward the equator. These linear flows under the influence of the earth's rotation, however, develop an orthogonal component of motion. This component changes the orientation of the wind from north-south to east-west, thus giving rise to east-west Trade Winds. This phenomenon has been well demonstrated by liquid crystal thermography (Fig. 23) in a recent article by Mukherjee et al. [152]. Although crucible rotation helps to homogenize the melt [5, 71, 152], an optimum rotation rate exists whereby the increased homogeneity of the cold zone at the surface helps weaken the radial temperature gradient that is characteristic of buoyancy-induced flows. The existence of an optimum rotation rate is well known to crystal growers.

Figure 24 shows the salient features of crystal rotation ($Ra = 1.12 \times 10^5$, $Pr = Gr/Re_s^2 = 6.4$). The complex physics of the flow in the vicinity of the Ekman layer (the boundary layer on the rotating disc) is evident. The three distinct cells representing three different phenomena arise from rotation of the crystal. The strongest cell is induced by buoyancy along the side wall and augmented by surface tension at the free surface region. Near the crystal periphery, the centrifugally driven flow conjugates with the buoyancy-driven and surface tension-driven flows and the resultant shear drives the fluid to the bottom of the simulated melt. The fluid that flows toward the central axis gains heat from the bottom wall and rises up in the middle with finite velocity. This rising column of fluid encounters the gravitationally accelerated fluid descending from the central region of the crystal, and bifurcates. At the crystal–melt interface, the dominant driving forces are centrifugal and gravitational. The effect of Coriolis force is minimal since viscous diffusion of momentum outweighs Coriolis acceleration. The only retarding force is viscous friction. The centrifugal acceleration, $\omega_s^2 r$ (where ω_s is the rotation rate of the crystal and r the radial distance along the surface of the crystal) increases with r for a constant ω_s. Therefore for

small radial distances, the effects of gravitational acceleration outweigh those due to centrifugal acceleration (as also shown by the low Froude number). Part of the fluid at the solid–liquid interface is driven by the centrifugal force toward the crucible wall; the rest of the cold descending fluid acts perpendicularly on the radial temperature gradient-induced flow, producing a gravitational torque ($g\beta \times \nabla T$) that feeds energy into the secondary cell established due to interaction of the previously mentioned forces. The diverging streamlines indicate regions of high pressure and stagnation. The competition between centrifugal and free convection effects is inherently unstable as manifested by the periodicity of flow structures.

The combined effect of crucible and crystal rotations produces very complex temperature and flow fields in the Cz systems. At higher rotation rates, the flow may become three-dimensional as the transition to oscillatory flows and turbulence takes place. These upper limits of rotational flow cannot be captured by a 2D formulation; however, the influence of rotation should still be accurate in a 2D model when the Reynolds number is low. Figure 25 demonstrates the impact of increasing counterrotation on buoyancy-induced flow in a curved crucible at Gr = 10^7, Ar = 0.25.

Using Chan's and Kobayashi's criteria for the equality of forced and free convection in a Cz system (Gr/Re$^{2.5}$ = 0.2 and Gr/Re^2 = 0.1, respectively), the transition between the two flows should occur at 1.2 × 10^3 < Re < 10^4. As borne out by Figs. 25(b) and 25(c), this transition in the present case is initiated at a Reynolds number between 10^3 and 5 × 10^3. The buoyance-driven flow is characterized by a single counterclockwise cell under the free surface, whereas the rotational flow is marked by a Taylor-Proudman column under the crystal. This is composed of two cells; one cell that has a clockwise flow near the crystal, driven by melt ejected from the periphery of the crystal, and a corresponding counterclockwise cell that penetrates to the bottom of the crucible. As Re is increased from 5 × 10^4 to 10^5, the system starts to show oscillatory behavior, and becomes more difficult to simulate since the boundary layers near the crystal become very thin. The overall flows at these high Reynolds numbers are very similar to those obtained for Re = 10^4, except that the thin cells underneath the crystal change character with time.

3. Combined Effects of Buoyancy, Surface Tension, and Rotation

Figure 26 shows the oscillatory behavior of the flow field and the melt–crystal interface when the surface tension and the crystal and crucible rotations are included in the model, Gr = 10^7, Re$_s$ = $-$Re$_c$ = 10^3, Ma = 10^3, Fr = 10^{-9}, Bo = 10^3, and the crystal is allowed to cool by
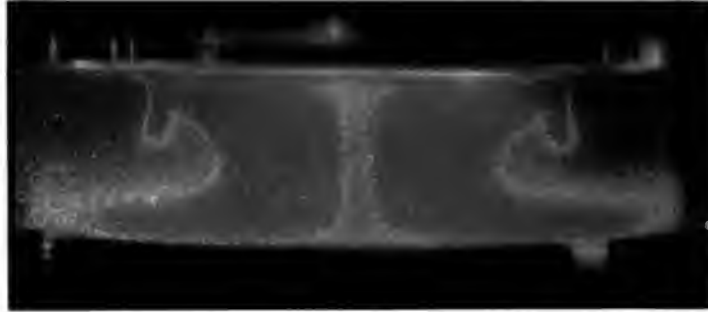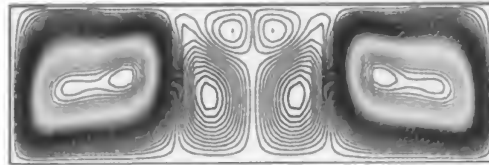
FIG. 23. (a) Temperature field for crystal rotation at 8.5 rpm; (b) temperature field at 2.5 min; (c) predicted streamlines; and (d) temperature field using MASTRAPP2d [152].
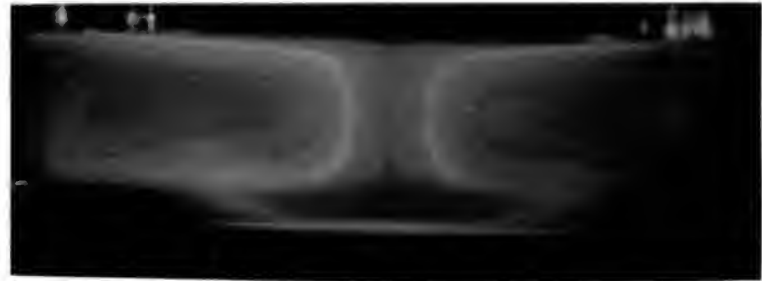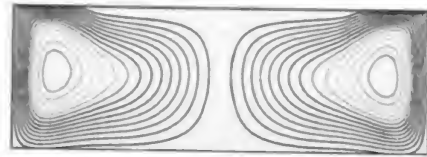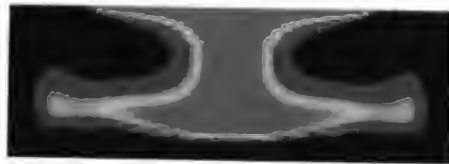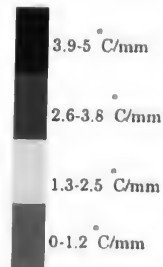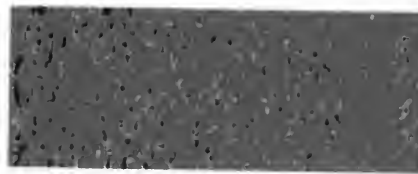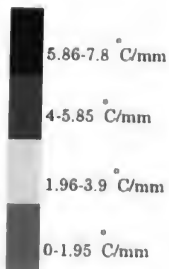
FIG. 24. (a) Temperature field for crucible rotation at 11.26 rpm, where $Re_c = 13.74$ and $Ra = 1.5 \times 10^5$. MASTRAPP2d simulation of a 11.26-rpm rotation. (b) Streamlines; (c) isotherms; (d) radial temperature gradient map; and (e) axial temperature gradient map [152].
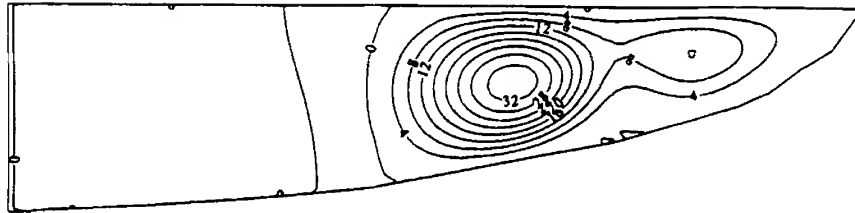
(a)
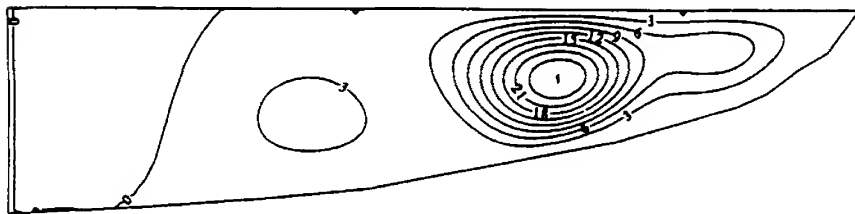
(b)
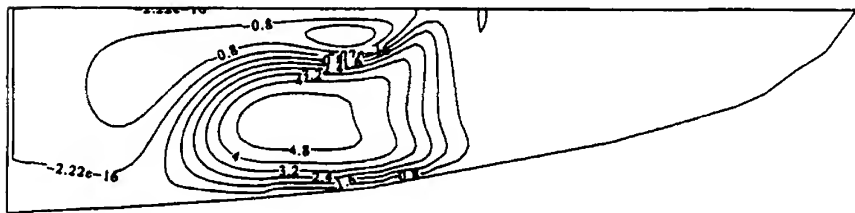
(c)
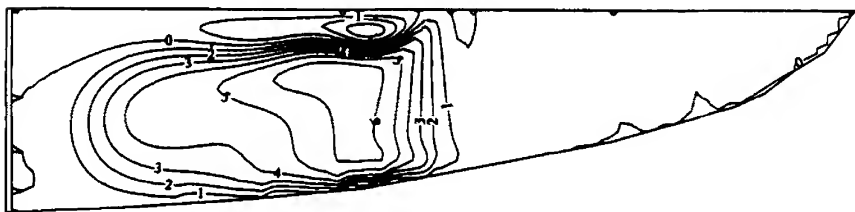
(d)

Fig. 25. Steady streamfunction for Ar = 0.25 and Gr = 10^7, with curved bottom, where
$\mathrm{Re}_c = -\mathrm{Re}_s$ equal to (a) 10^2, (b) 10^3, (c) 5×10^3, and (d) 10^4 [145].

(a)

(b)

(c)
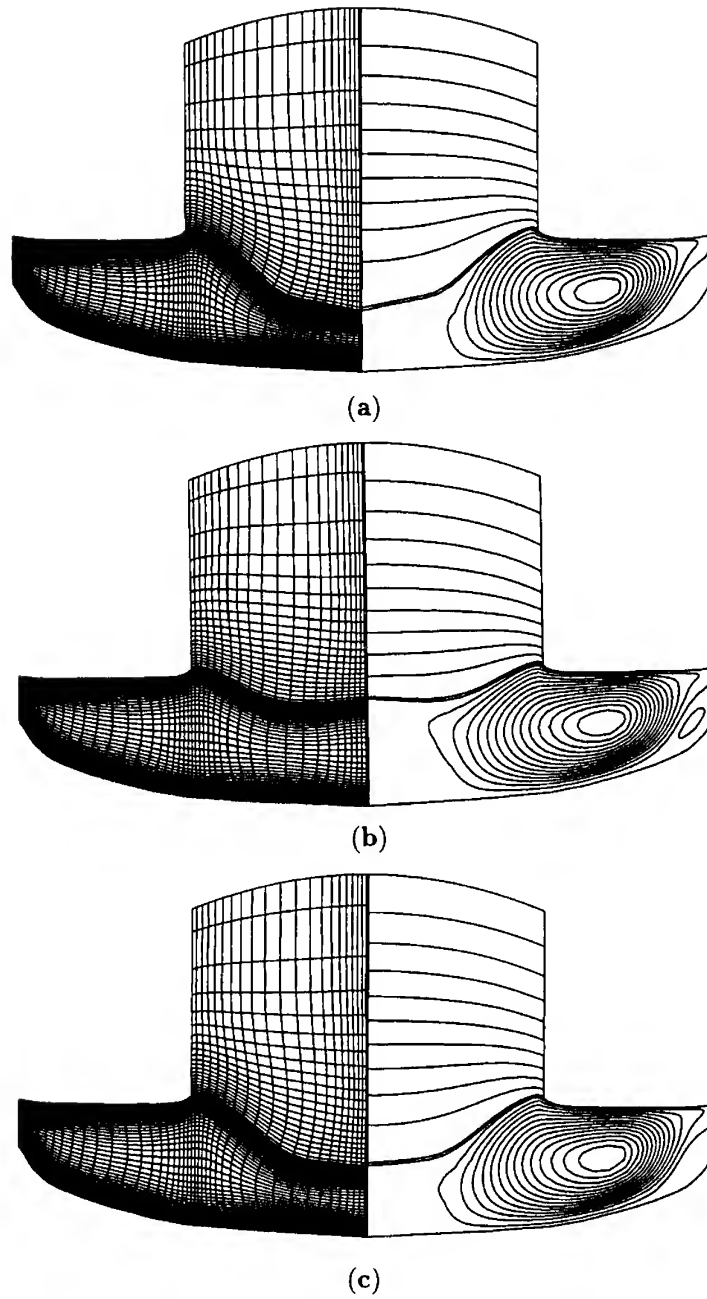
Fig. 26. Grid distribution, flow field, and melt–crystal interface at three instants of time for Ar = 0.375, Gr = 10^7, Fr = 10^{-9}, and Bo = 10^3 [27].

radiation. The primary cell in the present case starts in the outer region and flows deep into the region under the crystal because of radiation cooling on the free surface and Marangoni effects. Oscillations initially are strong, become weak at $\tau > 0.2$, and finally dampen out. As the crystal and crucible rotations are increased, Re from 10^3 to 10^4, the system becomes difficult to simulate because the boundary layers near the crystal and side wall of the crucible become very thin (Fig. 27). Several cells emerge beneath the crystal and in the region near the crucible and free surface. Strong temperature gradients exist in the regions close to the free surface
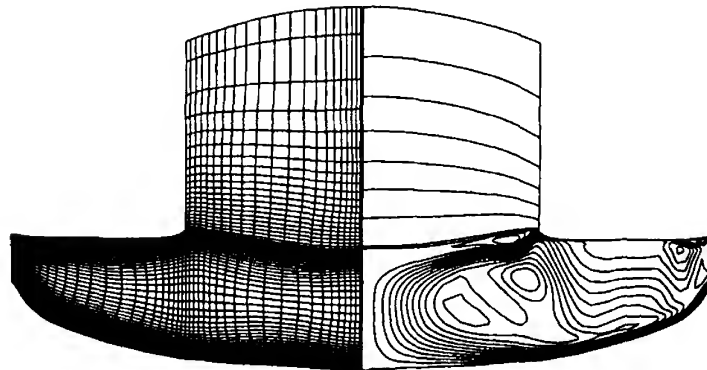
(a)
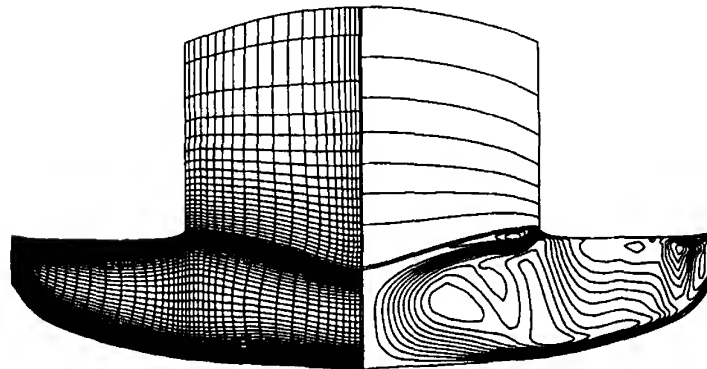
(b)

Fig. 27. Grid distributions and streamfunctions at two selected times for Gr = 10^7, $\mathrm{Re}_s = -\mathrm{Re}_c = 10^4$, and Ma = -10^3 [27].

and the crucible side wall. Small, thin cells have appeared under the free surface and the melt–crystal interface, primarily due to surface tension effects and crystal rotation, respectively. Several other nearly vertical cells are produced because of the increased counterrotations of the crystal and the crucible. The oscillatory behavior of this flow is shown in Fig. 28. Kopetsch [70] has presented a similar flow pattern, as shown in Fig. 27, although he considered a much larger aspect ratio Ar of about unity.

In reality, the interface "inertia" due to the extra release of heat of fusion when the interface deforms is rather high. The oscillation may not be as large as the results indicate here because of the quasi-steady assumption. The dynamics of crystal pull and movement of the free surface with a reduction in melt height also need to be taken into account because the time scale of interface movement is on the same order of the crystal pull. The results presented here assume that the radius of the crystal is kept constant and the pull velocity is calculated from the energy balance. If the pull velocity is kept constant, the interface oscillations may transfer to the oscillations of the crystal radius. This may be an interesting study to perform.

C. EFFECT OF AN APPLIED MAGNETIC FIELD

A magnetic field, when applied to a Cz melt, is known to suppress oscillations and fluctuations [54, 153–156]. However, a direct relation between various Cz parameters and the Hartmann number to produce stable flow regimes is not known. Figure 29 presents a representative
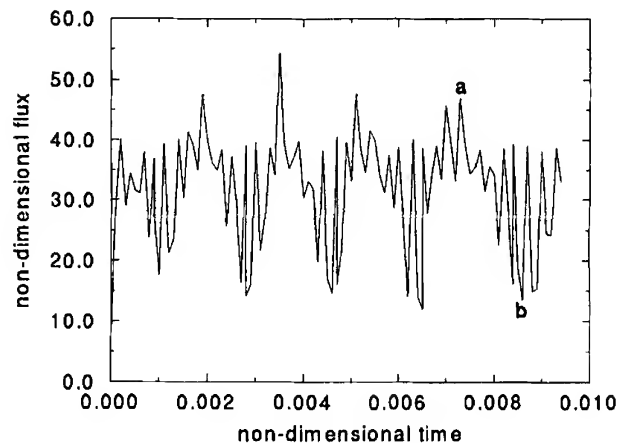
FIG. 28. Flux variation on the side wall of the crucible when $Gr = 10^7$, $Re_s = -Re_c = 10^4$, and $Ma = -10^3$ [27]. a and b correspond to Figs. 27(a) and 27(b), respectively.
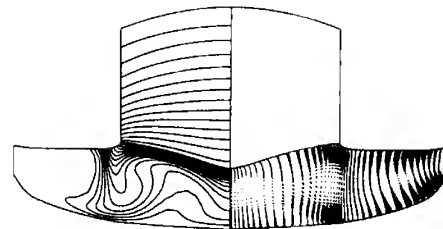
(a)
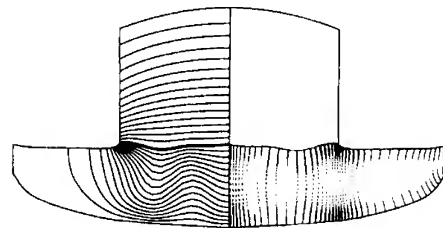
(b)
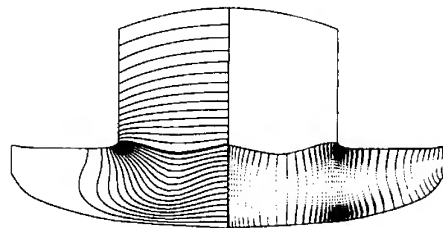
(c)
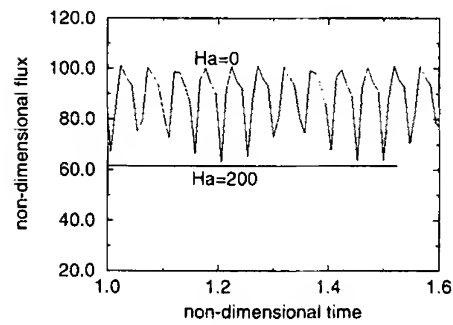
(d)

FIG. 29. Flow field and temperature distributions for (a) Gr = 10^8, Ha = 0; (b) Gr = 10^8, Ha = 200; and (c) Gr = 10^7, Ha = 0. (d) Oscillations of heat flux for the system with and without a magnetic field for Gr = 10^8 (cases a and b) [60].

simulation to demonstrate the effect of an applied magnetic field on flow oscillations. Only buoyancy-induced convection ($Gr = 10^8$) has been considered in this case. The temperature distribution in the absence of a magnetic field is very complex, and there exist three recirculating cells in half of the crucible (Fig. 29(a)). The temperature gradient in the vicinity of the interface and the crystal–melt meniscus is very steep. Both the flow and temperature fields oscillate in this case, resulting in the oscillations of the melt–crystal interface although the interface remains concave.

The effect of an applied magnetic field ($Ha = 200$) on streamline patterns and temperature distribution is presented in Fig. 29(b). Interestingly, the temperature field has changed drastically and shows much less skewness, and this temperature field is much closer to the conduction profile. Although three convective rolls are still present in the melt, their strengths are greatly weakened. The most desirable effect from crystal growth considerations is the flatness of the interface shape achieved with the use of a magnetic field. These considerations also have reduced the steepness of the temperature gradient in the interface and meniscus region. Figure 29(d) shows that the melt flow and temperature are still oscillatory. However, the amplitude of oscillations is very small, and growth conditions are much better than those in Fig. 29(a).

To further examine the strength of melt convection, computations for $Gr = 10^7$ and $Ha = 0$ are presented in Fig. 29(c). We now can very easily see the resemblance between Fig. 29(c) and Fig. 29(b). It is evident that the magnetic field reduces the strength of buoyancy-induced convection by reducing the strength of the body force term in the momentum equation.

D. THREE-DIMENSIONAL EFFECTS

As noted earlier, the flow instability of molten Si in the Cz configuration has been studied by Kakimoto et al. [157] by in situ observation of melt convection using X-ray radiography and by temperature fluctuation measurement during crystal growth. Flow mode was dependent on the aspect ratio of the melt. For a deep, low aspect ratio melt, with growing crystal identical to the shouldering process of the growth, the flow was found to be unsteady and nonaxisymmetric. For a shallow melt without crystal and crucible rotations, the flow was relatively steady and axisymmetric. However, with crystal rotation, the flow became unsteady and nonaxisymmetric for a shallow melt. These observations support the predictions of Anselmo et al. [141, 145]. Figure 30 shows the flow modes for several experimental conditions of crucible and crystal rotation rates. The rotation Reynolds numbers and the aspect ratio are shown in Fig. 30. The Grashof number of
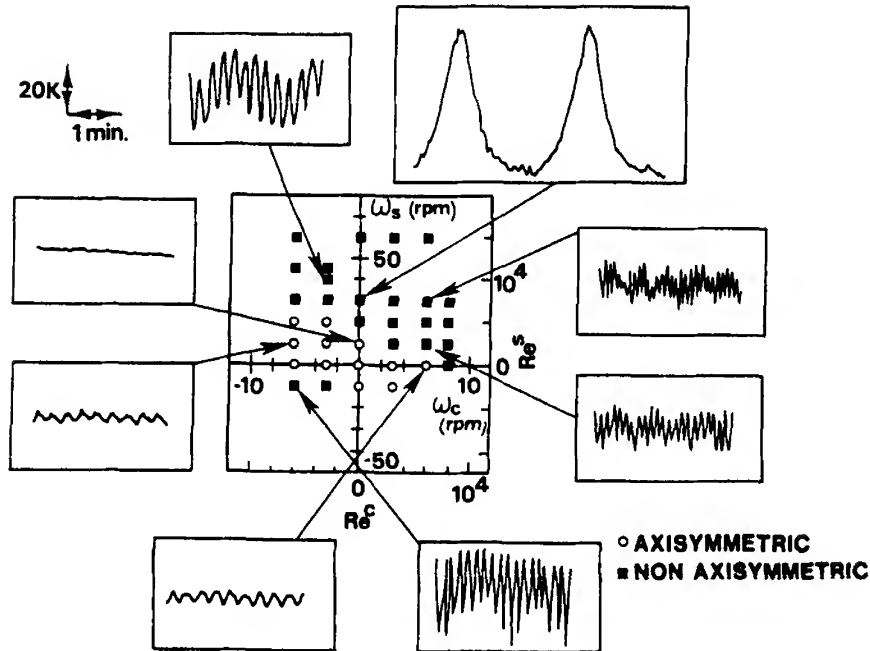
FIG. 30. Flow instability map against crystal and crucible rotation rates. Temperature fluctuation in some crystal and crucible rotation rate conditions are also shown. The aspect ratio is 1.2 [157].

the melt was not reported in the paper. Open circles indicate the flow is steady and axisymmetric, whereas solid squares show time-dependent and nonaxisymmetric flows, respectively. The nature of temperature oscillations at a fixed point in molten Si also is shown around the flow instability map. It was found that the amplitude of the temperature fluctuation for unsteady and nonaxisymmetric flows was larger than that for steady and axisymmetric flows. Kakimoto has concluded that the thermal instability area is identical to the flow instability area, and the Prandtl number has an important effect on flow stability. Munakata and Tanasawa [158] also demonstrated 3D effects using oxides ($Gd_3Ga_5O_{12}$ and $Bi_{12}SiO_{20}$); however, the experimental results were quite different.

Direct experimental measurements and material characterization of Cz grown crystals have convinced the investigators that Cz melt flows for Si growth are three-dimensional. As noted in Section II, extensive efforts have been made to simulate 3D convection in Cz melts with limited

success, primarily because of multiplicity of parameters and their values being in the upper range.

Early 3D simulations were carried out by Bottaro and Zebib [144], and Mihelčić and Wingerath [151] and Anselmo [145]. The results of these 3D calculations are preliminary and not in total agreement. Bottaro and Zebib have argued that buoyancy-driven Cz flow has a large inherent swirl, even at Grashof numbers as low as 0.1, due to the fact that low Pr fluids can become unstable for certain kinds of boundary conditions. Mihelčić et al. also have obtained numerical solutions for 3D natural convection that indicate two flow regimes exist. These solutions are governed by a Grashof number based on a combination of characteristic lengths of crucible radius, crystal radius, and crucible height. Contrary to Bottaro and Zebib's work, their solutions in the low Gr regime indicate that the flow is axisymmetric, steady, and without swirl, while only at high Grashof numbers (Gr > 10^6) does the flow become axisymmetric and oscillatory. This discrepancy between the two results has been noted by both groups of researchers, without any clear explanation.

Anselmo's calculations [145] show that the buoyancy-induced flows in a curved crucible, which is steady at Gr = 10^7 and Ar = 0.25 (Fig. 16), become oscillatory when 3D effects are considered. Interestingly, this oscillatory 3D flow becomes steady when crucible and crystal rotations are imposed with $Re_c = -Re_s = 10^2$.

Time-dependent 2D features of melt flows that occur during the Cz growth of oxide crystals have been analyzed by Xiao and Derby [105] using a theoretical bulk-flow model. Their approach assumes flat surfaces for crystal–melt interface and melt meniscus and imposes idealized thermal boundary conditions. A massively parallel code using a Galerkin FEM is employed to perform these simulations. These authors have found that the temperature distribution after 250 timesteps (represented approximately 3 h for the YAG (yttrium–aluminum–garnet system) seen from the top view in Fig. 31(a) is different from the 2D steady-state solution. The flow shows a 3D annular wave structure (Fig. 31). The figures presented in the paper reveal the axisymmetric dominant velocity fields and asymmetric temperature field. An important issue raised by this study is the utility of 2D models for the analysis of Cz growth systems. The 3D flows significantly influence the overall rate of heat transfer across the melt. However, Xiao and Derby conclude that the 2D simulations are qualitatively valid in Cz modeling, and 3D convection in the melt will change the quantitive accuracy of the model. Since Xiao and Derby [105] performed calculations for oxide melts (high Pr), the validity of their conclusion in the case of semiconductor melts (low Pr) is not clear.
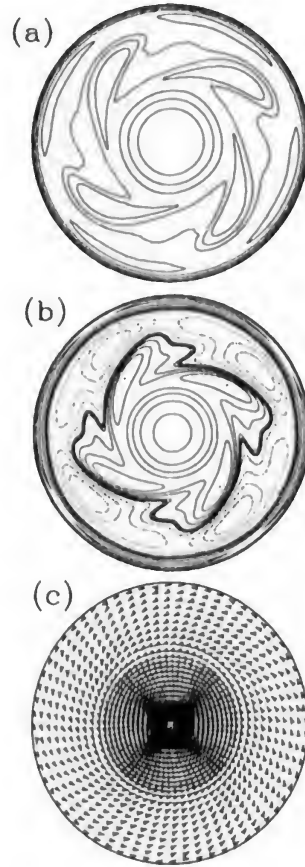
FIG. 31. Top view of the three-dimensional long-time solution for $Gr = 2.54 \times 10^5$, where $Pr = 8$ and $Re_c = 2 \times 10^3$. A horizontal cut through the plane defined by $z = 0.64H$ is shown. (a) The temperature field is represented by isotherms spaced evenly, with $\Delta T = (T_c - T_s)/10$. (b) The axial velocity field is shown by velocity contours spaced evenly, with $\delta v = (v_{z,\max} - v_{z,\min})$. Solid contours indicate positive v_z (upward flow), dotted contours indicate negative v_z (downward flow), and the bold contour represents $v_z = 0$. (c) The azimuthal flow field direction is indicated by velocity vectors [105].

E. SIMULATION EXPERIMENTS

A number of bench experiments (Table IX) have been performed over the years to study the physics of flow and temperature distribution in a Cz system under various regimes of convection. Attempts have been made to reproduce many of the parameters that govern Cz growth. However, it has

TABLE IX

PREVIOUS EXPERIMENTAL WORK[a]

Author	Crucible Rotation	Crystal Rotation	Working Fluid	Tracer	Pr	Gr	Ar	Rr	Ma
Carruthers [134]	Yes	Yes	Glycerine-water	Aniline dye	—	0.0	—	—	—
Shiroki [159]	Yes	Yes	Sugar solution	SiC particles	8.5–30	—	—	—	—
Miller [160]	No	Yes	Water	Rheoscopic fluid	30	—	—	—	—
Jones [12]	Yes	Yes	Water-glycerine	Nigrosine	4.5–7	10^8	—	—	—
Lamprecht [161]	No	Yes	$NaNO_3$ solution	Quartz spheres	9.25	4×10^2	2	0.57	—
Ruiz (86) [162]	No	Yes	Glycerine-water	Magnesium powder	—	—	1.2	0.375	—
Kakimoto [163, 164]	Yes	No	Silicon	Tungsten particles	0.015	—	—	—	—
Munakata [158]	No	Yes	Silicone oil	Liquid crystals	1000	4.5×10^2	—	—	2.12×10^3
Ozoe [165]	No	Yes	Silicone oil	Liquid crystals	4600	3.7×10^2	—	—	—
Hirata [166]	No	Yes	n-Icosane	Aluminum powder	64	—	—	0.6	—
Mukherjee [152]	Yes	Yes	Silicone oil	Liquid crystals	890	1.26×10^2	0.76	0.647	1000

[a] This table is by no means complete, but includes important work.

not been possible to reproduce the relevant Prandtl and Marangoni numbers in these experiments. Semiconductor materials have very low Pr (0.01 to 0.02), which cannot be obtained in bench experiments, particularly if the working fluid must be transparent for visualization and measurements using noninvasive techniques. Materials such as Ga (Pr ≈ 0.02) can be used to achieve a low Prandtl number working fluid; however, they are opaque. Temperatures in these experiments can be measured using only thermocouples, and flows can be traced only by using very expensive techniques such as X-ray radiography. Similarly, the surface tension coefficient of a semiconductor melt is very different from that of the common fluids used in the laboratory. Despite these shortcomings, the bench experiments have provided a much improved understanding of Cz flows over the years. These experiments also have formed a basis for validation of Cz models.

The oldest and the most comprehensive bench experiment to date was executed by Carruthers and Nassau in 1968 [134]. They used aniline dye in a 1 : 1 mixture of glycerine and water. In their simulation experiments, a 70-mm-diameter cylindrical glass crucible filled to a depth of 40 mm and a 25-mm-diameter Al crystal could be rotated, in either direction, by variable speed motors. Their results include a thorough exposition on the different flow patterns when the system is subjected to different rotation rates. Of particular interest are

1. The Taylor-Proudman column that arises in the presence of a stationary crystal in a rotating fluid.
2. The presence of stagnation surfaces that prevent complete mixing except when the crucible rotation rate is zero.

These authors also have shown that when the crystal and the crucible rotate in the same direction, one stagnation surface separates two nonintermixing regions; during counterrotation there are two stagnation surfaces and three nonintermixing regions. Their results on 3D flows below the crystal are well explained in terms of the vertical variations of the radial centrifugal pressure gradient. However, their technique did not explain whether certain motions were induced due to temperature gradients or difference in density between the dye and the test fluid.

Shiroki [159] used warmed sugar solutions (0 to 66 wt%) as test fluids to study the influence of the rate of crystal rotation. The simulated melt crucible was made of quartz, with a 54-mm inner diameter and a 60-mm depth. A 24-mm diameter rotating quartz disk served as a crystal. By varying the concentration of sugar, Shiroki obtained a wide range of viscosities. Different modes of convection were obtained below the rotating disk with changes in viscosity. For the low viscosity solutions (0.5 to 1.1

centistokes) the temperature beneath the rotating crystal was found to vary minimally with the change in the rotation rate. For high viscosity solutions (7.6 to 15 centistokes), the temperature below the rotating disk rises sharply as the rotation rate increases to about 50 rpm. This is correctly attributed to enhanced forced convection of high-temperature fluid from the side and bottom of the crucible and then up to the middle of the crystal. Particles of SiC were used as the dispersion agent.

Miller and Pernell [160] conducted a water bath simulation of oxide melts to show the contribution of Bénard convection on the "wheel spoke" pattern seen in garnet and other oxide melts. The crucible was 130 mm in diameter and 220 mm high. A rheoscopic fluid was mixed with water to view the azimuthal flow pattern from the top. At high temperatures the spoke pattern disappeared. The cause of these wheel spoke patterns has been attributed to a combination of surface tension and buoyancy forces. A series of photographs of the liquid surface is presented as the liquid level is reduced. The most interesting feature of these experiments is that they show how the flow pattern, which is used in garnet growth to define the thermal center, moves off the geometric center as the melt level drops. Therefore, the conclusion is well founded that all of the crystal growth problems resulting from growth in the presence of thermal asymmetry become more severe with reduction in height.

Jones [12] was the first to simulate a Cz system in the laboratory with all of the modes of convection present in the system. He used a mixture of water and glycerol as the working fluid. The diameter of the crucible was 84 mm and that of the crystal was 50 mm. Nigrosine solution was injected into the solution to trace the streamlines. Fish scales were added at the surface to show regions of shearing fluid by the reflection of light. Streak photography with polystyrene beads (0.5 mm in diameter) also was used to provide a measure of the flow velocity. His results on differential heating and rotation are divided into six different regimes:

1. Disk rotation
2. Differential rotation
3. Heating of crucible
4. Disk rotation with heating
5. Differential rotation with heating, with the crucible rotating at 2 rpm
6. Differential rotation with heating, with the crucible rotating at 4 rpm

In regime 1, it was noticed that waves at the surface were created when the rotation rate exceeded 7 rpm. These could well be due to the clash of the buoyance-driven flow with the centrifugally induced flow. In regime 2, an asymmetric 2D flow was found when the crystal was rotated in the same way as the cylinder. In regime 3, temperature fluctuations were observed in

the column of flow descending below the disk and in the horizontal boundary layer. These could arise due to Bénard instability. The flow in regime 6 was different from flow in regime 5 due to increased asymmetry in the horizontal circulation with an increase in crucible rotation rate. This paper serves as a sound base for understanding some of the physics behind the Cz flow patterns.

Lamprecht *et al.* [161] used a sodium nitrate melt, with a crucible diameter of 35 mm and a height of 34 mm, with hollow spheres of quartz glass as tracers to do the following:

1. Verify the contribution of thermocapillary forces
2. Show the interaction of combined buoyant and Bénard convection with forced convection by crystal rotation
3. Present the influence of meniscus height on forced convection

The crystal diameter was 10 mm. Their experiments on buoyant and thermocapillary convection distinctly show that the highest flow velocities were at the free surface. Even when the Grashof number was increased by a factor of four, the surface velocity changed by less than 20%. In addition, the velocities at the surface did not show a square root dependence of the Grashof number, indicating a strong thermocapillary influence. They found that cooling of the crucible bottom enhanced thermocapillary forces, whereas bottom heating masked them.

Ruiz *et al.* [162] devised a flow tracing scheme to compute the velocities in a Cz system. In an isothermal melt (80-mm inner diameter) of 1 : 1 glycerine–water mixture, the flow generated by crystal (30-mm diameter) rotating at 35 rpm was captured by video camera and digitized. The flow field generated by the centrifugal action agreed well with some earlier numerical results.

Kakimoto *et al.* [163, 164] used X-ray radiography to observe convection of molten Si since it has a high free-electron concentration. The melt was housed in a 75-mm diameter silica crucible under 1 atm pure Ar atmosphere. The flow pattern was traced using a multilayered chemically and thermally stable tracer developed in their laboratory. Since tungsten has a high absorption coefficient at the emission wavelength of the X-ray source, it was used along with SiO_2 and carbon as a tracer. The temperature distribution was seen to be highly asymmetric in the melt. The asymmetric flow was attributed to an asymmetric temperature distribution in the crucible holder.

Munakata and Tanasawa [158] used liquid crystals in silicone oil to illustrate the presence of oscillatory flow patterns in the presence of crystal rotation. The crucible was made of Pyrex with a radius of 40 mm and the crystal was made of a cylinder with a copper base (20-mm radius). Their

numerical results agreed very well with their experimental results. The periodicity of flow structures that was observed at a low Reynolds number flow is similar to that observed by Mukherjee *et al.* [152]. A correlation between the frequency of oscillation and frequency of growth striations on an actual crystal was thought to exist. A vertical magnetic field was applied to suppress the temperature oscillation in a GaAs melt. These authors felt that even in the absence of magnetic field it was possible to keep the temperature beneath the crystal almost uniform and, hence, obtain a flat interface shape. However, the temperature oscillations that are generated in the melt due to inherent instabilities contribute directly to the growth of striations. By imposing a vertical magnetic field it is thought that striations can be removed.

Ozoe *et al.* [165] also used liquid crystals in silicone oil to show the transition of flow modes in the Cz melt as a function of the ratio Gr/Re^2. These authors proposed that when the ratio decreased to a value lower than a critical value, the breakage of the shape of the cold plume under the crystal was responsible for the periodic remelting of the crystal rod. Hirata and Tachibana [166] conducted a novel experiment using n-icosane as the test fluid and as the crystal. They were able to show the interface shape as a function of crystal rotation rate. On increasing the crystal rotation rate, the crystal–melt interface shape changed from convex to flat and from flat to concave toward the melt. The interface shape was found to be independent of melt depth. These authors also found Bénard convection to be the dominant mode of convection. In Hirata's experiment, the crystal and crucible diameters were 30 mm and 50 mm, respectively, and Al powder was used as the seeding agent.

Mukherjee *et al.* [152] performed an experiment using a large-scale apparatus (Fig. 32). A 140-mm inner diameter crystal with a 216-mm inner diameter Pyrex cylinder as crucible were simulated such that instabilities associated with a large-diameter crystal could be studied. The radius and aspect ratios of their experiments were 0.647 and 0.76, respectively. The walls of the simulated melt cylinder were isothermal everywhere, as opposed to the one used by Jones [12] where the bottom was insulated. The cylinder was belt-driven at the top by a synchronous motor enabling optical access to the convective medium from the bottom. The crystal cylinder was cooled with recirculating water and rotated by a motor mounted at the top. The principle of flow tomoscopy was implemented to illuminate the flow fields of interest. The simulated melt was seeded with chiral-nematic liquid crystals (Hallcrest, Glenview, Illinois) of two different kinds, each having a bandwidth of 6°C, so that a temperature range of 12°C could be studied.
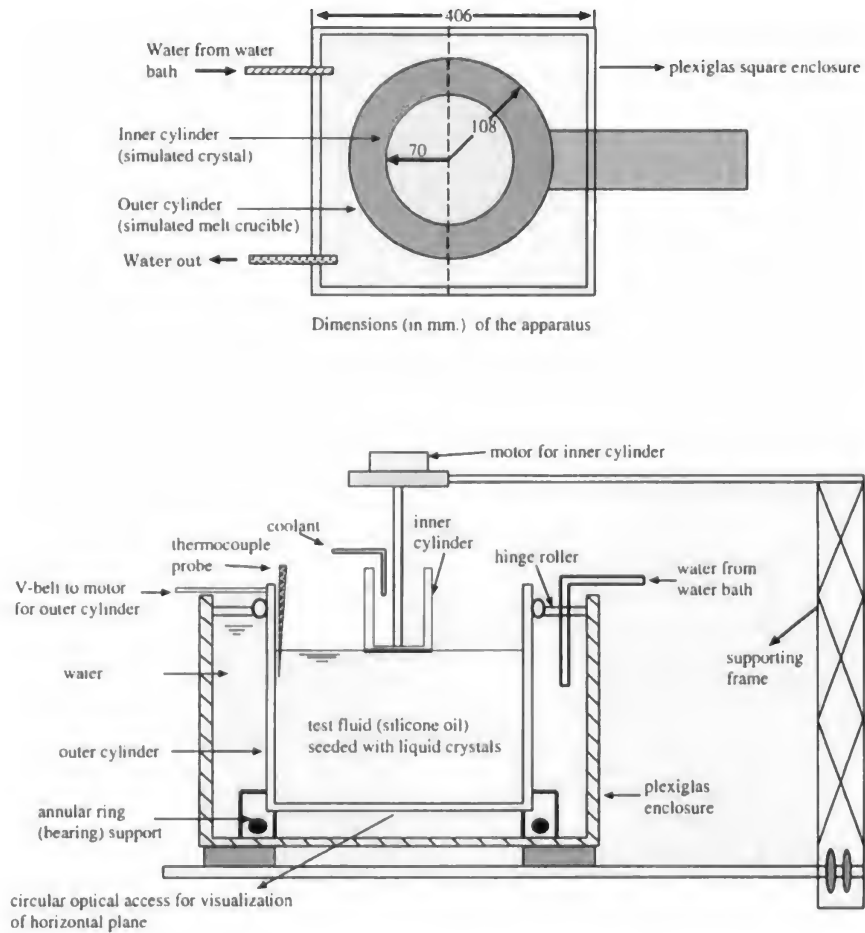
FIG. 32. Experimental apparatus used by Mukherjee *et al.* [152] for visualization of transport phenomena in a simulated Czochralski (Cz) melt.

A charge-coupled device (CCD) camera, Sony XC-711 (Sony Electronics, Inc., Paramus, New Jersey), was used for videography and a still camera was used for still photography. The output of the video camera was digitally analyzed with the help of an image-processing algorithm. A software, XV (an interactive image manipulation program free from Internet, developed by John Bradley at Bryn Mawr, Pennsylvania), was used to relate the RGB (red-green-blue) values of pixels of the digitized image to

temperature. An interpolation routine was then used to compute temperatures between the color bands, thus enhancing the resolution. Once this postprocessed look-up table (LUT) was prepared, temperature and temperature gradients could be computed with ease. Since the images were noisy, due to dark current, transmission errors, or nonuniform response of the CCD array, mean filters were designed to spatially smoothen the images [167, 168]. It is possible to determine the axial and radial temperature gradients (Figs. 24 and 23) by using the software developed by Mukherjee et al. [152]. The color range in their pictures varies from red to blue, with blue denoting the highest axial or radial temperature gradient. Also the postprocessed value of temperature for each pixel was fed to a graphics software, Fieldview (Intelligent Light, Inc., Lyndhurst, New Jersey), to reconstruct the temperature field with a better resolution, and to test the integrity of the calibration scheme. These authors have conducted experiments investigating the effects of crystal and crucible rotations, as described earlier.

F. Growth Experiments

Very few noteworthy growth experiments have been conducted thus far. In 1965, Wilcox and Fullmer [169] conducted an experiment growing calcium fluoride crystals. A 50-mm-diameter molybdenum crucible contained the molten salt. Measurements both with and without crucible rotation were made. In a stationary crucible, the flow was found to be a rolling one typical of free convection flows. At higher rotation rates, the motion makes a transition to a swirl pattern. In the presence of crystal rotation, the turbulence was found to decrease continuously with increasing rotation rate of the crucible. The temperature fluctuations were recorded with thermocouples. Fluctuations on the order of 30°C were shown to cause growth rate fluctuations. The visual observations of these authors coupled with the thermocouple traces convinced them that free-convection–induced flow instability is the source of temperature fluctuations during high-temperature crystal growth. They recommended using afterheaters around the crystal to minimize the vertical temperature gradient and hence the degree of turbulence in the melt. They performed a theoretical analysis on growth rate fluctuations and concluded that to the first approximation, the amplitude of growth fluctuations is proportional to the amplitude of the temperature fluctuations, inversely proportional to the boundary layer thickness, and surprisingly independent of the frequency of temperature oscillations.

In a paper on crystal growth from the melt under destabilizing thermal gradients, Kim et al. [170] correlated the thermal behavior of the melt and

its changes with interface morphology, microscopic growth rate, and dopant segregation in the resulting crystal. Their laboratory experiment was performed on an InSb melt with a 120-mm-long tube furnace. Time markers in the form of electrical pulses were introduced in the growing crystal to correlate location of striations with the recorded temperature. Among other interesting results, these authors found that under conditions of turbulent convection, the microscopic growth rate was about 20 times that of the macroscopic growth rate. In addition, this microscopic growth rate could be controlled by convection in the melt and thermal gradients in the solid.

Kolker [171] conducted experiments where Si was grown under destabilizing temperature gradients in containers without any free melt surface. The free end of a Si rod was fitted tightly in a crucible attached to the rod and was heated by a graphite resistance heater. Growth proceeded from top to bottom by pulling the Si plus container upward at a rate of 1.25 mm/min without rotation. The diameter of the containers (boron nitride and quartz) was typically 10 to 12 mm. The results clearly show that there exists a critical Rayleigh number below which the striations disappear. For free surface melts the critical Rayleigh number is lowered by an order of magnitude. The contribution of surface tension-driven flow was highlighted.

G. GLOBAL HEAT TRANSFER

A Cz furnace is a complex geometric configuration (Figs. 3 and 4). Transport phenomena in a Cz system therefore is governed by the combined effect of heat conduction and radiation in the solid, melt, crucible, resistor, pedestal, pulling axis, radiation shield elements, and other components. Growth conditions are directly influenced by thermal interaction among these components, the melt and the crystal. As noted in Section II, several attempts have been made to examine the global heat transfer in a Cz furnace. However, it is not easy to resolve the accuracy of the numerical solutions both at the local and global levels.

Figure 33(a) shows a schematic of the Cz furnace used by Kakimoto et al. [172-174]. The dotted lines are external walls that are boundary condition-imposed surfaces. The furnace is considered to be made of several macroelements, and these macroelements are used to obtain information on heat fluxes on their outer boundaries for heat exchange calculation by radiation. Convective flows are allowed only in the melt. An iterative method is used to link the outer radiation-conduction domain with convection melt in the melt. Melt convection is therefore decoupled from the conduction-radiation in the furnace. The solution procedure
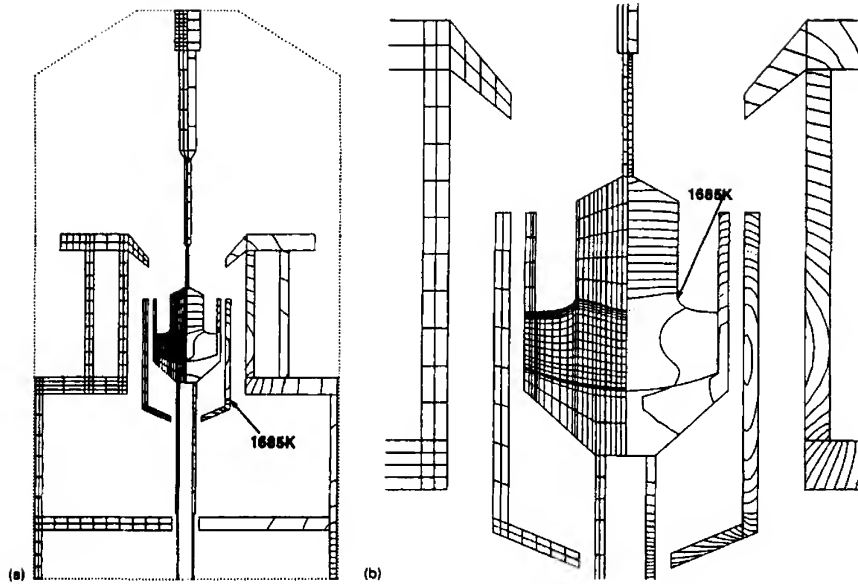
FIG. 33. (a) Global sketch of the finite-element mesh (left) and contour lines of temperature distribution (right) for every 50 K. (b) Zoomed sketch of the finite-element mesh (left) and contour lines of temperature distribution (right) at every 20 K [172].

adopted by Dupret and van den Bogaert [7] is as follows:

1. Calculate the temperature field in the furnace (using the conduction–radiation model) without melt convection.
2. Obtain the temperature distributions on the crucible wall, heat flux on the free surface, and temperature along the crystal surface.
3. Calculate the melt velocities and the temperature field in the melt and the crystal based on the previous boundary conditions.
4. Use the new temperature distributions on melt and crystal surfaces to calculate the global temperature field.
5. Return to 2.

This procedure is justified for Cz and low-pressure LEC growth where gas convection in the furnace has negligible effect. It is not possible to decouple the local transport phenomena at melt level with global gas convection and radiation in a high-pressure system, since they are strongly coupled.

Figures 33(a) and 33(b) show the temperature field and mesh for global calculation with the assumptions of axisymmetric and steady flows. The

dotted lines between crystal and melt correspond to the melting point of Si. The solid lines show contour lines of temperature every 50 K in (a) and 20 K in (b). Dupret's calculations predict a power supply of 15.142 kW, which is almost identical to the experimentally obtained data of electric power supply to the heater of 15 kW for the Cz furnace considered by Dupret.

A 3D combined conduction and radiation heat transfer analysis also has been conducted by Maruyama and Aihara [175]. The radiation heat transfer assumes axisymmetric bodies consisting of numerous arbitrary ring elements. Each ring element has the combined characteristics of specular and diffuse surfaces. The radiation transfer model was combined with the finite-element package ABAQUS for conduction analysis. The heat flux and temperature distributions obtained from this analysis are shown in Fig. 34.

Global numerical simulation for a LEC process for a GaAs growth is shown in Fig. 35(a), which illustrates the typical calculated temperature field in the furnace without gas convection. The simulation has been carried out by Dupret *et al.* [74, 173] using a quasi-steady global FEM, where the radiative heat exchange is modeled as a surface phenomenon. Deformation of the solidification interface and the melt meniscus is clearly
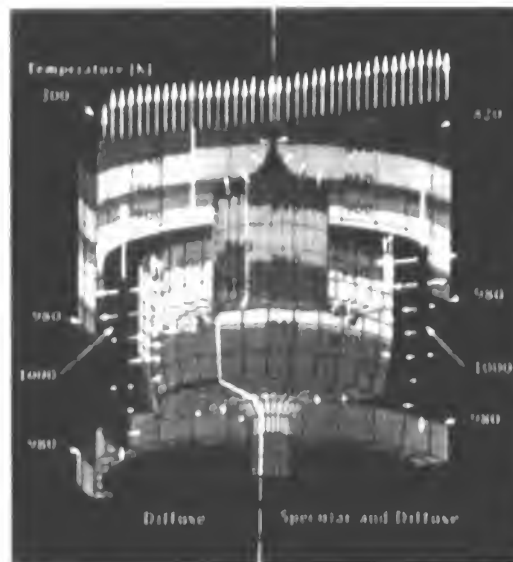
FIG. 34. Temperature distribution and surface heat flux on various surfaces of the radiation–conduction combined heat transfer model [175].

demonstrated by this simulation. Curved interfaces are known to result in increase of grown defects within the crystal. Their results show that the concave interface becomes more concave and the stress level increases as the pull rate increases. Peak stress values are always found at the interface and at the point where the crystal emerges from the encapsulant layer.

A reduction in heater power causes the crystal radius to increase, van den Bogaert and Dupret [174] have shown interesting system responses to a reduction of heater power. Figure 35 (color section) shows the finite-element mesh and temperature field for 1% step decrease in heater power for Cz Si growth. The results of time-dependent global simulations, however, were obtained by neglecting the melt flow. The authors note that the computational cost for calculating melt convection using a classic FEM is generally too high to allow for dynamic simulations. The influence of melt convection on dynamic behavior of the system is of major interest. The calculated heater power appears to be highly dependent on the intensity of the convection, and is expected to increase if convection is taken into account. The representation of the flow in the melt has been achieved by coupling with a global model only under quasi-steady conditions.

H. CONVECTION IN A CONTINUOUS CZOCHRALSKI GROWTH SYSTEM

Many of the inhomogeneities in crystals grown by the conventional Cz batch process are a direct result of the nonsteady nature of the growth kinetics, primarily due to the continuous change in melt volume from start to finish. As discussed earlier, this comes from the fact that the length scale (the decreasing height of the melt) significantly affects the convective flows and temperature fields, which generally are very complex. The unsteady flows within the melt produce defects in the crystal, due to the fluctuations in transport of impurities and interface dynamics.

One possible solution to the limitations of the conventional Cz Si process for growing large-diameter crystals is to use a continuous Cz process. Various liquids and solid-feed schemes have been proposed to develop a continuous process. Anselmo et al. [30] have proposed and investigated a solid polysilicon pellets feed CCz technique (Fig. 36). In this process, silicon pellets of about 1-mm diameter are added continuously to the melt from which more than one crystal can be grown in one furnace cycle. Since the charge is added continuously, a shallow constant height melt may be sufficient to grow the crystal, reducing the buoyancy effect significantly and suppressing many kinds of unsteady kinetics, instabilities, and inhomogeneities. As shown in previous sections, the oscillations can be reduced significantly at low melt heights [30, 141, 145]. The heat input in this process can be constant and the crucible will not need to be moved

1271.00
1251.00
1231.00
1211.00
1171.00
1131.00
1091.00
1051.00
1011.00
971.00
931.00
891.00
851.00

(b)

(a)
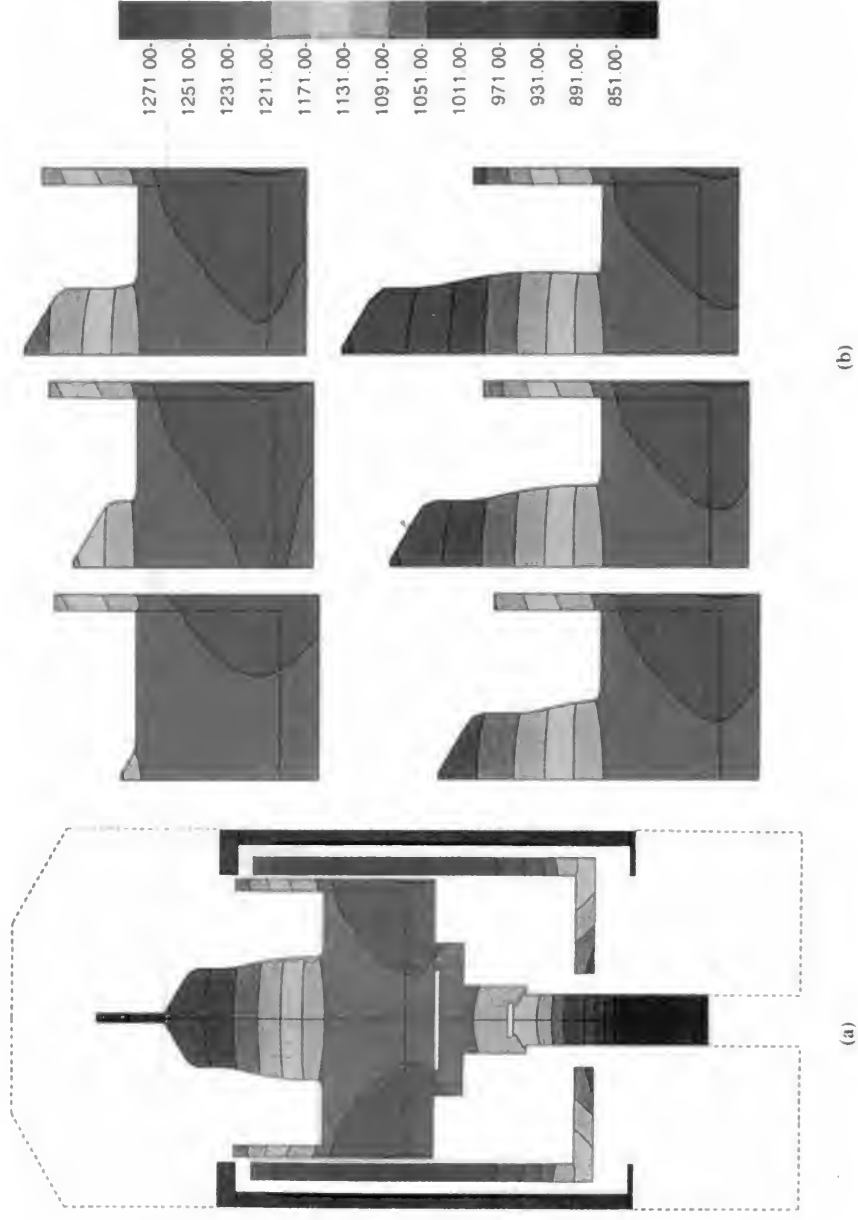
FIG. 35. Response to a 1% step decrease in heater power: (a) finite-element meshes for various stages of growth; and (b) temperature field in the global furnace and temperature field in the melt, crystal, and crucible for various stages of growth [7].

FIG. 43. Flow (right) field and temperature (left) field for the melt, crystal, and gas as the indium phosphide (InP) crystal is grown for $We_m = 2.5 \times 10^{-5}$, $Fr_m = 10^{-8}$, $\rho_s/\rho_m = 1.0$, $k_s/k_m = 0.40$, $C_s/C_m = 0.96$, $Gr_m = Gr_g = 10^7$, and $Re_c = -Re_s = 10^3$, for various crystal heights [28].
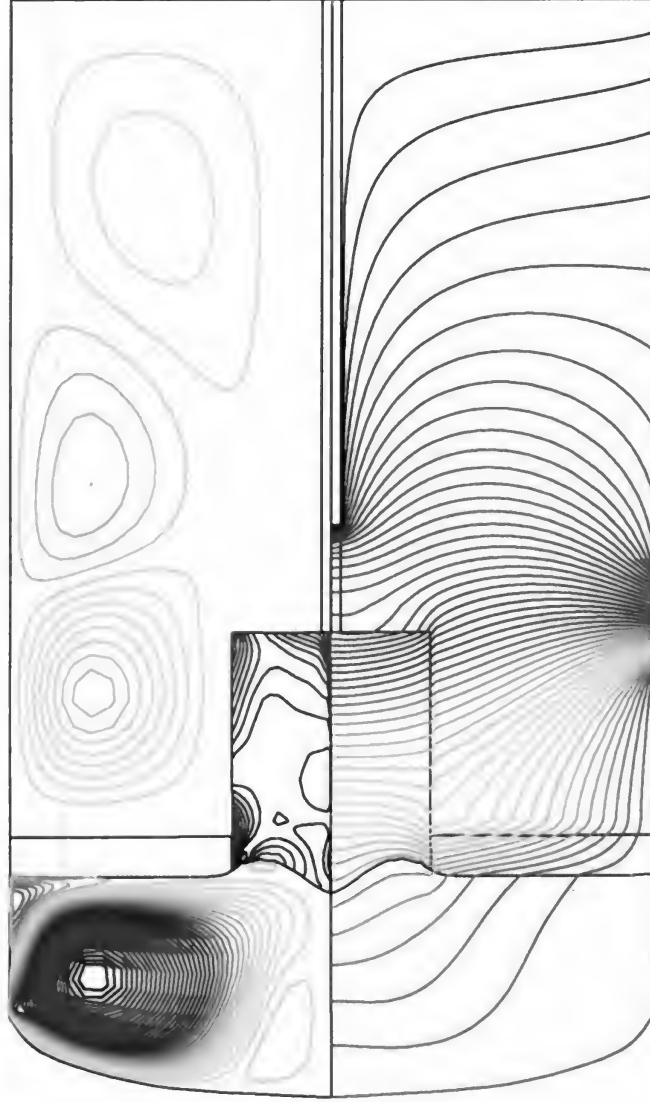
FIG. 45. Distributions of temperature (right), stress (left), and velocity vectors for high-pressure growth at gas Grashof number, $Gr_g = 10^7$ and $Re_s = -10^2$, $Re_c = 10^2$ and $Gr_l = 10^6$ [107].
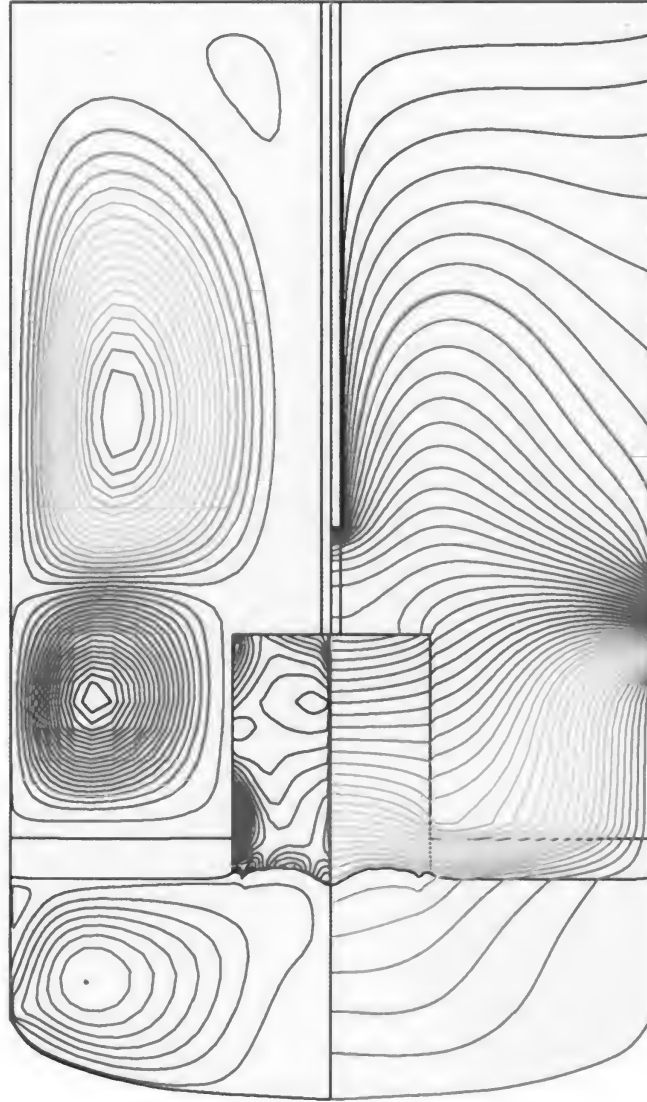
FIG. 46. Distributions of temperature (right), stress (left), and velocity vectors for high-pressure growth at gas Grashof number, $Gr_g = 10^8$ and $Re_s = -10^2$, $Re_c = 10^2$ and $Gr_l = 10^6$ [107].
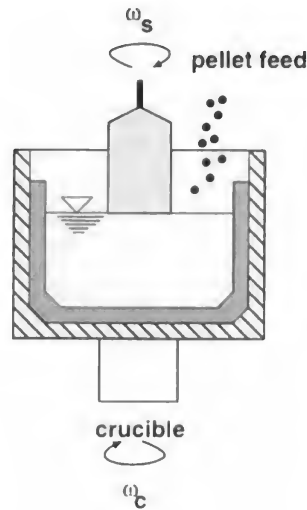
FIG. 36. Schematic of the proposed solid-feed continuous Czochralski process, using polysilicon pellets to replenish the melt [30, 176].

up or down for most of the growth process. Above all, by continuously charging the polysilicon and dopant, the crystal quality can be tightly controlled and production cost substantially reduced. A similar investigation into solid-pellets feed CCz growth also was performed by Ono *et al.* [52]. These authors used a crucible with a partition, whereas no changes were made in the crucible design used by Anselmo *et al.* For the first time, Anselmo *et al.* [176] demonstrated that a solid-pellets feed CCz process is technically feasible.

Preliminary studies on CCz flows also have been reported by Anselmo *et al.* [30] using a 2D model. Although the validity of a 2D model when the pellets are melting on a rotating melt surface is always questionable, these computations demonstrate the qualitative effect of the addition of the pellets to the melt. To simulate a solid pellets-feed CCz process for a given crystal diameter and pull rate, an amount of pellets equal to the mass removed must be added to the melt for the melt height to remain constant. This translates to a heat sink being imposed on the melt surface. When this heat sink reaches a critical value, the melt surface becomes cool enough to either solidify or not support pellets melting as the temperature in a region where the pellets are dropped approaches the melting point of Si. When this happens, the likelihood of stray pellets that move toward the rotating crystal will attach to the crystal and destroy the single crystal structure is increased.

Figures 37(a) to 37(c) present the temperature and flow fields with feed rates of 50, 100, and 150 g/min for a low aspect ratio (Ar = 0.25) melt in a curved crucible. The nondimensional values for these cases were chosen based partially on the first experimental results of Anselmo et al. [30, 176], and partially on the industrial crystal growth rates, which can be about 50 g/min. At 50 and 100 g/min, as shown in Figs. 37(a) and 37(b), the melt temperature remains above the melting point of Si; however, in Fig. 37(c), the temperature decreases to below the melting point of Si, creating problems for pellet melting and crystal growth.

These simulations indicate that the temperature field is largely modified in the region where the pellets are added, whereas away from this region the perturbation is minimal. As a result, the change in flow field is also localized, and the surface tension–driven counterclockwise rotating convection roll remains almost the same in strength and size. On the contrary, the clockwise rotating cell becomes a little weaker and loses its quasi-circular pattern [30]. In fact, this is the roll that is significantly affected by the increase in feed rate (Figs. 37(b) and 37(c)). The overall flow pattern is not changed radically by the addition of pellets when the sink strength is low. However, when the feed rate is 150 g/min, the temperature drops below T_m at a location away from the delivery area (toward the crystal) because the energy from the crucible is largely used to melt the pellets, and cannot maintain a temperature above the freezing point.

I. CONVECTION IN A CZOCHRALSKI MELT WITH PARTITION

Motivated by the research into CCz growth by Anselmo et al. [30, 141, 145, 176], Jafri et al. [177] performed an analysis of the effect of a crucible partition of different sizes on melt convection. Their numerical results indicate that for the melt aspect ratio of 0.5 and conditions close to reality (Pr = 0.015, Gr = 10^8, Re_c = 10^4, Re_s = -10^4, Ma = 10^3, and Rr = 0.5), a short obstruction, h_p $\approx$ 0.25, at the top of the crucible can greatly improve the melt conditions (Figs. 38 and 39). A short partition at the bottom of the crucible, however, does not provide the same benefits. A partition at the top weakens the surface tension–induced flows that are generally very strong in the upper region of the melt. This is a desirable condition. On the contrary, a partition promotes the Bénard convection conditions in the inner region, produces strong flows and instabilities under the crystal, and is undesirable. These effects are much stronger when the partition is tall (Fig. 39). A full-length crucible partition or a double-crucible, as suggested by several investigators and investigated by Ono et al. [52], may not be the correct choice because both result in strong flows directly under the crystal even when the crucible is rotated. In
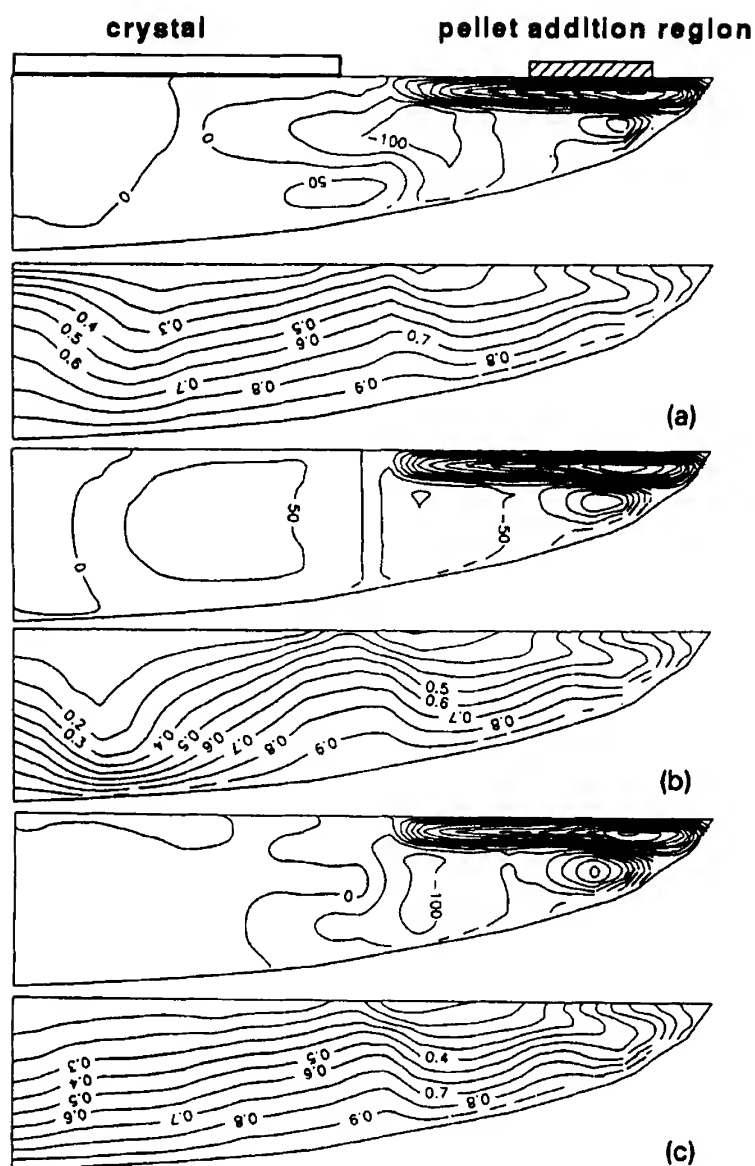
FIG. 37. Effects of polysilicon pellets on flow and temperature field in a continuous Czochralski process for feed rates of (a) 50 g/min, (b) 100 g/min, and (c) 150 g/min. At 150 g/min, $T < T_{melting}$ in a small region on the surface [30].
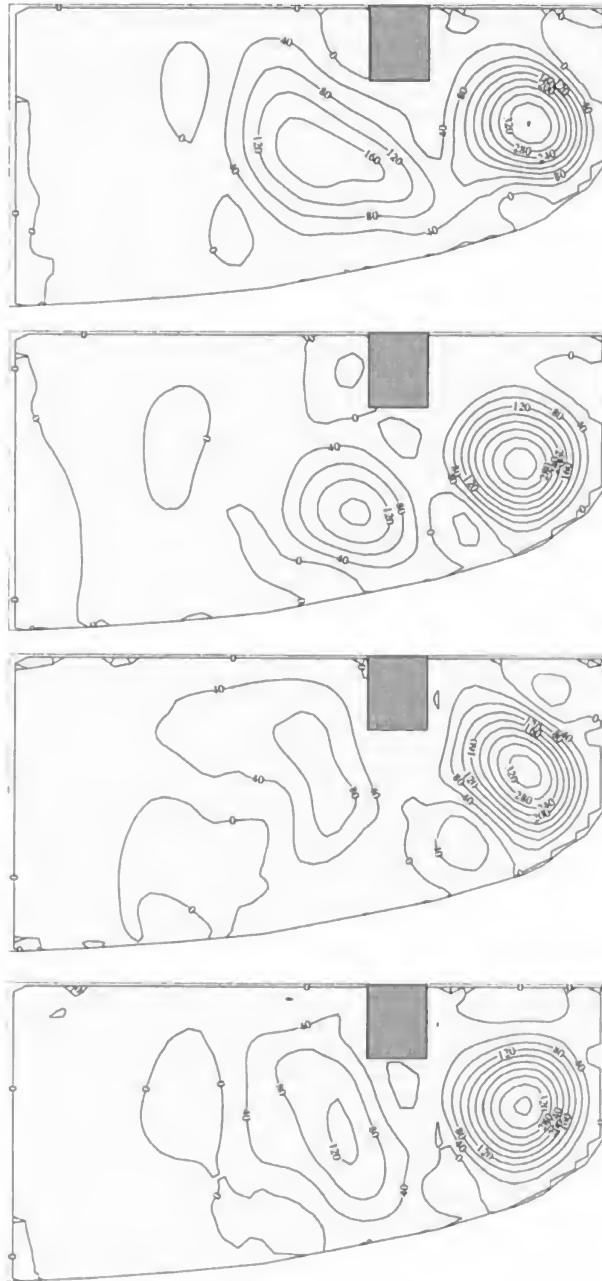
FIG. 38. Oscillatory melt flow fields in a crucible with a short partition in the upper region, where $h_p = 0.25$, $d_p = 0.65$, and $t = 0.1$ [177].
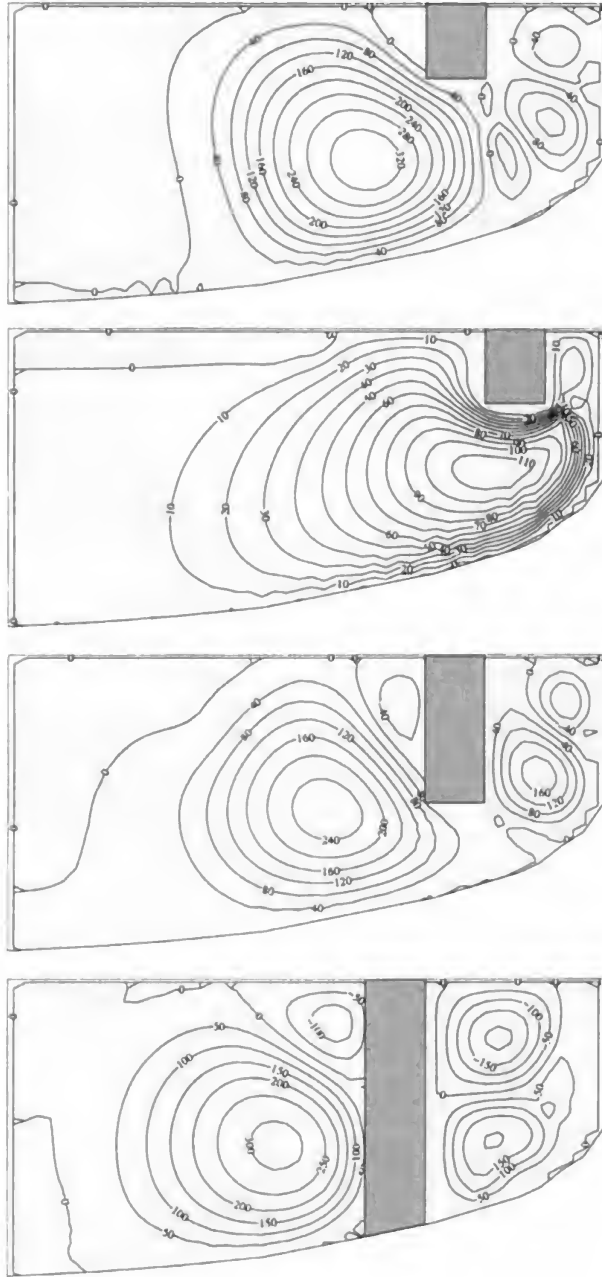
FIG. 39. Representative flow fields for a partition in the upper region. (a) $h_p = 0.25$, $d_p = 0.75$; (b) $h_p = 0.25$, $d_p = 0.85$; (c) $h_p = 0.50$, $d_p = 0.75$; and (d) $h_p = 1.0$, $d_p = 0.65$ [177].

addition, the partition should not be placed very close to the crucible side wall, otherwise the benefits of adding a blockage are either completely diminished or at least reduced.

The results presented by Jafri *et al.* [177] show only a qualitative trend, and a suitable size of the partition and its location will have to be determined for realistic process conditions. These authors have noted that for every aspect ratio and crucible size there is an optimal size of partition, which when added from the top of the crucible, can improve the melt conditions for Cz growth. Thus an added impetus is provided to investigate the solid-pellets feed CCz process. Indeed one of the major problems—that is, the movement of Si pellets (while they are melting) toward the crystal, as experienced by Anselmo *et al.* [145, 176]—easily can be resolved by using a small blockage on the crucible top.

V. Convection in High-Pressure Liquid-Encapsulated Czochralski Growth

As noted earlier, the transport mechanisms in a HPLEC growth is very different from that of a low-pressure Cz Si growth. Although this was recognized by investigators years ago, only recently could it be shown that the thermal interaction between gas and melt flows is complex and must be considered in order to analyze HPLEC growth conditions [26, 28, 68]. Prasad *et al.* [26] estimate that the Grashof number for gas flows in a typical HPLEC system for InP growth may be as high as 10^8 to 10^9. If the height of the furnace is used as the length scale, the Grashof number can be on the order of 10^{11} to 10^{12} (Fig. 6).

The buoyant flow conditions in a HPLEC system do no fit into the definitions of the classic free convection problems of Bénard convection and differentially heated vertical cavities. The hot B_2O_3 surface and the cold injector bottom (Fig. 6), or the cold top surface of the furnace, provide the so-called Bénard conditions; whereas the heated quartz shield in the upper portion and the hot vertical insulation layer in the bottom part of the furnace together with the cold vertical wall represent a differentially heated vertical cavity configuration. Many other hot and cold surfaces that are generally present in the furnace further complicate the situation. The Bénard convection flow is known to start oscillating at Ra > 10^5, leading to random oscillations and turbulent behavior at higher Rayleigh numbers. The vertical cavity flow becomes turbulent at Ra $\cong 10^9$. From theoretical considerations, the gas flow in a HPLEC furnace therefore can be expected to be turbulent. As is well-known, any step change in

the surface over which the flow can trip, a sudden change in the flow path and passage restrictions add further to the turbulent behavior. Flow turbulence was clearly observed by Prasad *et al.* during the HPLEC growth [26]. Indeed, the oscillating nature of the gas flow could also be visualized by watching the movement of stray thin clouds of P-vapor, which appear above the melt from time to time depending on the supersaturation of InP melt.

Although gas convection plays an important role in providing desirable (or undesirable!) conditions in a HPLEC system, radiation dominates the heat transfer from the melt. For example, if the melt surface (at 1100°C) can be treated as a blackbody, it will lose 1.57 kW energy by radiation to a cold ambient at 300 K, while the encapsulant B_2O_3 surface at 1000°C can dissipate a maximum of 0.5 kW by convection to an infinite ambient at 300°C. (An average heat transfer coefficient ($h \cong 100$ W/m^{2}K) obtained from a correlation for turbulent-free convection from a heated surface (Nusselt number, Nu $= 0.15Ra^{1/3}$) has been used to calculate the convection loss [125].) In reality, the radiation loss decreases when we consider a realistic value of emissivity for InP melt and crystal, an appropriate value for absorptivity of B_2O_3, and the presence of P-injector and a heat shield. However, the estimated convective heat transfer will be reduced much more if it is treated as an enclosure (formed by an injector, a heat shield, and the crucible).

It must be mentioned that the overall convection and radiation heat transfer in a HPLEC furnace is much greater than that calculated here because of the heat dissipation by outside surfaces of the susceptor and also by the heater. However, this cannot be expected to affect radiation loss from the melt surface very much. Conversely, the hot gases flowing upward along the outside surface of the heat shield may reduce convection loss from the encapsulant surface by raising the furnace wall temperature. It is not true, however, that gas convection directly above the melt is weak. In fact, 100 to 500 W convection loss represents 1.4 to 7 W/cm^2 heat flux, which must be transferred by buoyancy-induced gas flows. A survey of the electronic cooling literature easily demonstrates that this heat flux, which must be dissipated by free convection, is large [178].

The configuration of the HPLEC system varies depending on whether the furnace is used for *in situ* synthesis and growth of InP crystals or only for the growth. Generally, the InP is first synthesized in a high-pressure furnace and then transferred (as solid) to a HPLEC system for growth. This "two-step" process is expensive and prone to contamination, motivating researchers to study "one-step" *in situ* synthesis and growth processes. Figure 6 presents a schematic of the system being used at the US Air Force Rome Laboratory to develop a one-step process in which In melt is

synthesized by injecting P-vapor. The phosphorus is contained in a quartz ampoule, which is heated by radiation from the melt when the surface injector is moved down, thereby releasing P-vapor after vaporization. After the synthesis is completed, the P-injector is moved up and a seed is brought down for the growth.

In the case of one-step synthesis and growth of GaAs crystals, As is placed directly above the Ga and then is covered by the encapsulant, B_2O_3. Ga and As then react at and above the melting point of GaAs, thereby producing a melt for the growth. Because of this variation in the synthesis processes for InP and GaAs, the two furnaces have different internal configurations.

A. CONVECTION IN THE SYSTEM FOR INDIUM PHOSPHIDE SYNTHESIS AND GROWTH

First, we present the overall convective flow pattern in a HPLEC system used for one-step *in situ* synthesis and growth of InP crystals. Although precise information on most of the thermal and physical properties for InP is lacking, the estimate (Table X) for the calculations presented here have

TABLE X

GOVERNING PARAMETERS USED FOR HIGH-PRESSURE SIMULATION

Parameter	Definition	Value
Density ratio	$\bar{\rho}_s = \rho_s/\rho_m$	1.0
Conductivity ratio	$\bar{k}_s = k_s/k_m$	0.40
Specific heat ratio	$\bar{C}_{ps} = C_{ps}/C_{pl}$	1.0
Melt aspect ratio	$Ar_m = h_m/b$	0.68
Crystal radius ratio	$Rr = a/b$	0.5
Melt Grashof number	$Gr_m = \dfrac{g\beta_m b^3(T_h - T_f)}{\nu_m^2}$	10^7
Gas Grashof number	$Gr_g = \dfrac{g\beta_g b^3(T_h - T_\infty)}{\nu_g^2}$	10^8
Reynolds number for		
Crucible	$Re_c = \omega_c b^2/\nu_m$	10^4
Crystal	$Re_s = \omega_s b^2/\nu_m$	-10^4
Melt Prandtl number	$Pr_m = \nu_m/\alpha_m$	0.015
Biot number	$Bi_r = \varepsilon\sigma_r b/k_m Pr_m$	
	$\times(T^2 + T_\infty^2)(T + T_\infty)$	—
Froude number	$Fr_m = \nu_m^2/gb^3$	10^{-9}
Bond number	$Bo_m = \rho_m gb^2/\sigma_m$	1000
Contact angles	ϕ_{sl}	45°

been obtained from Jordan [179–181]. The computer model MASTRAPP has been used for the simulations presented here. The governing equations in the melt region (consisting of the melt, seed shaft, and crystal) are solved separately, followed by matching at the encapsulant–inert gas and crystal–inert gas interfaces. The procedure used here requires iterations between the two solutions.

Figure 40 shows the temperature and streamfunction distributions in the gas, melt, and crystal phases when the flow is induced by buoyancy at $Gr = 10^8$, $Gr_m = 10^7$, with rotation rates of $Re_c = -Re_s = 10^4$ [68]. A multicellular flow is produced in the melt and the melt–crystal interface is concave with respect to the crystal. Due to $Gr_m/Re_c^2 = 0.1$, the rotational forces are dominant in the melt, which clearly is evident from the velocity field. A counterrotating vortex develops beneath the crystal, in which the fluid flows upward along the axis of symmetry and downward near the edge of the crystal. In fact, the rotation of the crystal induces the flow in a direction opposite to the flow produced by buoyancy effect on the crucible wall. The upward flow along the axis of symmetry pushes the isotherms toward the crystal, thereby increasing the concavity of the interface (Fig. 40(b)). The concavity of the interface extends very close to the crystal periphery, yielding a monotonic concave shape. Figure 40(b) clearly demonstrates almost zero flow conditions in the encapsulant layer due to the extremely high viscosity of B_2O_3, and to a large temperature decrease resulting from the much smaller thermal conductivity of B_2O_3 as compared with that of the InP melt [182]. Radial and axial temperature gradients are also evident in the crystal and are the primary causes of stresses in the crystal.

Figure 40(a) shows the corresponding temperature distribution and velocity field in the inert gas. Due to a low temperature at the seed shaft (cooled by circulating cold water) and a small gap between the shaft and the injector through which it passes, the gas flows downward along the seed. If the flow field reaches steady state, the same amount of gas must leave the inner region through the opening between the shield and the P-injector to maintain continuity. A multicellular flow is produced in the region underneath the injector. These cells are slender and demonstrate strong flows with turning in the bottom and top regions, while in the core the flow is somewhat parallel. Note that this flow is strongly influenced by counterrotations of the crystal and heat shield. (The heat shield sits on the graphite susceptor.) Correspondingly, an upward flow of hot gases is also established outside the heat shield, which is further strengthened by the buoyancy effects induced by the cold furnace walls. This produces a large recirculation in the furnace outside the heat shield and P-injector. A small convective roll is formed in the stagnation region directly above the

(a)

(b)
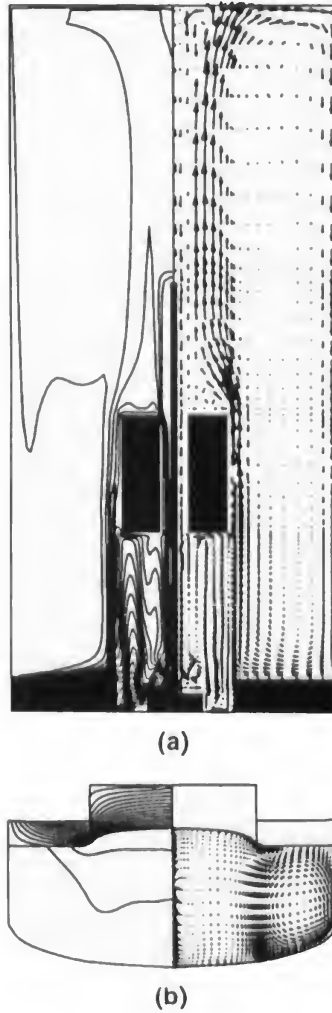
FIG. 40. (a) Temperature distribution and velocity field in the gas region when $Gr_g = 10^8$ for $Re_c = 10^4$. (b) Temperature and streamfunction distributions in the melt for $Gr_m = 10^7$ [182].

injector, as shown in Fig. 40(a). The general flow pattern of the gas in Fig. 40(a) is well supported by the visualized flow behavior in a high-pressure system (Fig. 41).

From Fig. 40, it is evident that an intense gaseous convection is induced in the furnace and takes heat away from the surfaces of the crystal and
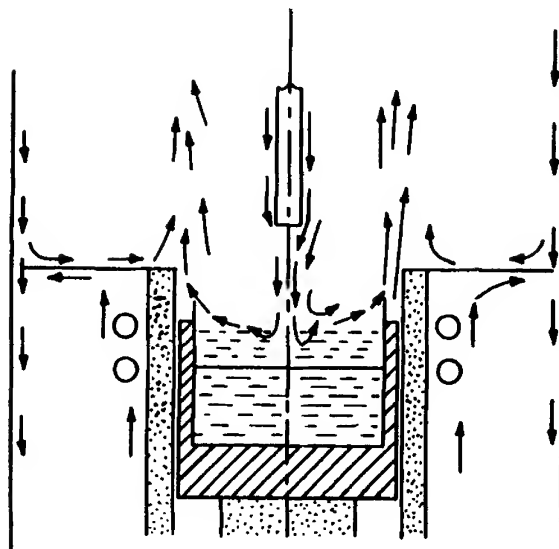
FIG. 41. Visualized recirculatory gas flow pattern in the absence of the phosphorus-injector and the heat shield. A similar gas flow pattern exists when the P-injector and the heat shield are present in the furnace [26].

encapsulant. The temperature distribution in the crystal and the shape of the crystal–melt interface therefore are strongly influenced by the gas flows in the inner and outer regions. The existence of the liquid encapsulant and the high-pressure gas makes the transport mechanism much more complex than that observed in the case of Cz melt flow for Si. An extensive study of the gas flow therefore is necessary to develop an understanding of the HPLEC growth and control of crystal quality.

B. CONVECTION IN HIGH-PRESSURE LIQUID-ENCAPSULATED CZOCHRALSKI GROWTH

Here we concentrate on the flow and temperature fields that directly affect the crystal–melt interface. Zhang et al. [28, 68] were the first to simulate the high-pressure growth process. In their simulation, the thermophysical properties of the gas (N_2) are allowed to vary with temperature at a constant high pressure (600 psi), while the properties of the melt and the crystal are considered to be constant. Figures 42 and 43 show the tempera-

(a)

(b)

(c)

(d)
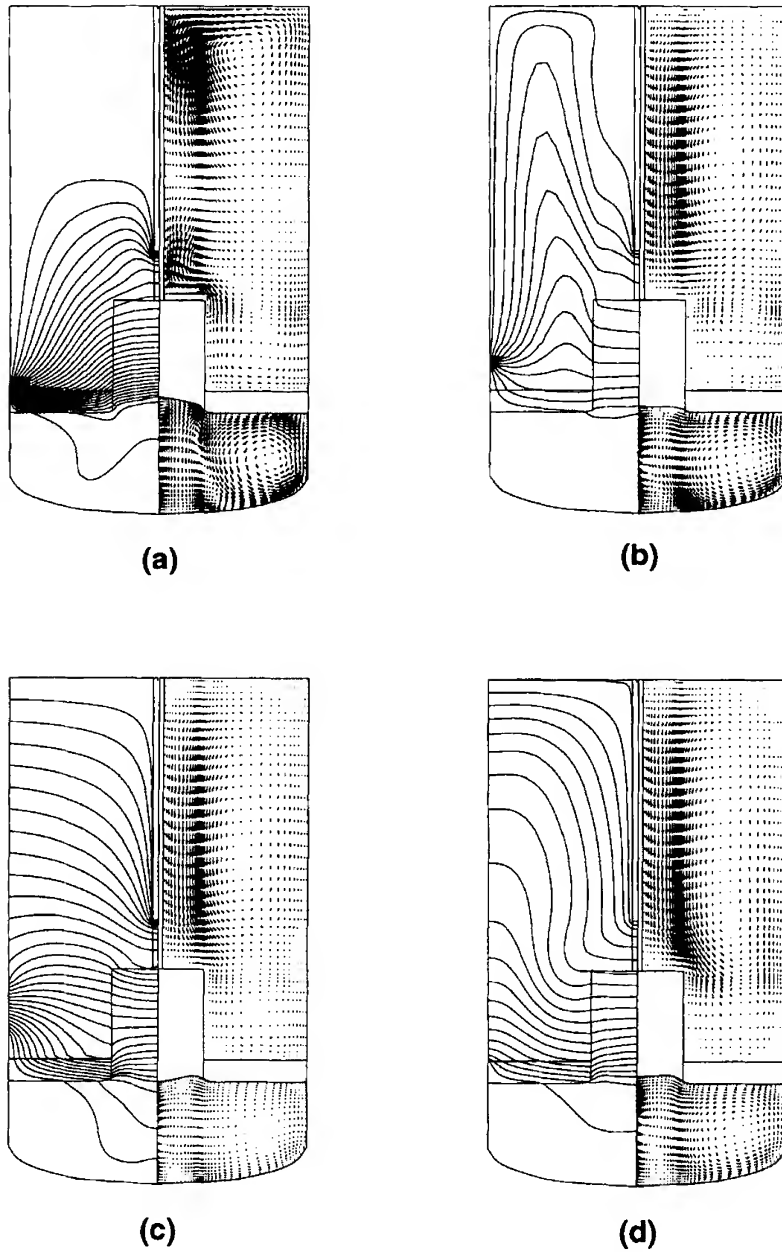
FIG. 42. Effect of the side wall boundary condition on the crystal–melt interface, flow field, and temperature distributions for $Gr_m = Gr_g = 10^7$, $Re_c = -Re_s = 10^3$, and $\sigma_r = 0.2$: (a) cold temperature, (b) cold temperature beyond the crucible height, (c) a given temperature profile, and (d) zero heat flux [28].

ture and flow fields for the growth of InP crystals. The thermophysical parameters used in the simulation are $We = 2.5 \times 10^{-5}$, $Fr = 10^{-8}$, $\rho_s/\rho_m = 1.0$, $k_s/k_m = 0.40$, and $C_{p,s}/C_{p,m} = 0.96$ based on the available data for InP. The contact angles at both the side wall of the crystal and the side boundary are taken to be 45 degrees, and are not allowed to change with the pull rate of the crystal.

Figure 42 shows the effects of the side wall boundary condition on crystal–melt interface, as well as on the temperature distribution in the crystal. Four kinds of boundary conditions have been considered. The parameters used in the simulation are the Grashof numbers, $Gr_m = Gr_g = 10^7$, and the rotation rates of the crystal and crucible, $Re_c = -Re_s = 10^3$. The upper portion of the seed shaft remains at a cold temperature, as in the real situation.

Figure 42(a) presents the velocity field and temperature distribution in the gas and melt phases when the side wall is maintained at a cold temperature. Heat loss takes place at the crystal–gas and melt–encapsulant interfaces. A concave shape of the crystal–melt interface is obtained due to the strong cooling effect on the crystal surface. The flow field in the melt shows that buoyancy is a dominant force. The melt flows upward along the side wall of the crucible and downward in the central region of the crucible. The flow pattern underneath the crystal is quite complex and oscillatory behavior is observed in this region. The temperature profile in the melt is distorted. Figure 42(b) shows the velocity and temperature distributions in the gas and melt phases when the side wall beyond the encapsulant height is considered cold. (The crystal extends beyond the encapsulant level.) A cold temperature therefore is maintained above the edge of the crucible, as shown in Fig. 42. The upper portion of the crystal is now heated due to convective heat exchange with the hot wall of the crucible, while the lower portion of the crystal loses heat by diffusion through the encapsulant layer. The crystal–melt interface is now doubly curved. The gas flow pattern is quite complicated. The melt flow is very similar to that presented in Fig. 42(a).

Figure 42(c) shows the results for a given temperature profile on the side wall (based on a simulation presented in Fig. 40). A high-temperature condition is prescribed in a short distance just above the encapsulant, as a part of the crucible. A linear temperature with large gradient follows beyond the crucible wall and a smaller temperature gradient exists on the rest of the side wall. The crystal is again heated in the upper portion and cooled in the bottom part. A convex shape of the crystal–melt interface is observed in this case. As shown in the figure, the gas flows downward along the seed shaft until it reaches the crystal, and one recirculatory cell is located directly above the encapsulant free surface while two slender cells exist in the upper region. The melt flow is again similar to that in Figs.
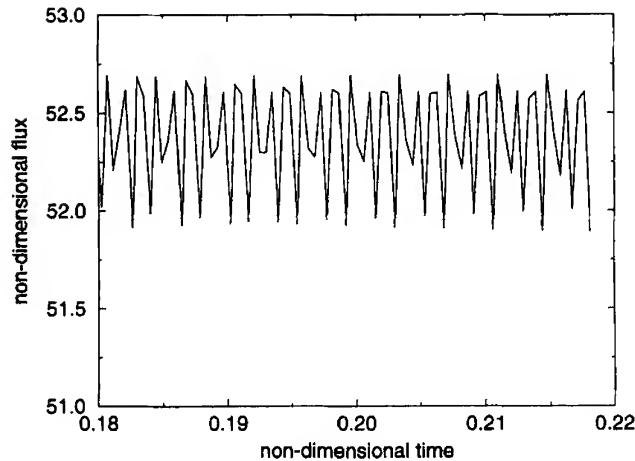
FIG. 44. Oscillation in the heat flux when the crystal is short, corresponding to the case in Fig. 43(a) [28].

42(a) to 42(c). Figure 42(d), however, presents the results of an insulated wall. The flow pattern and temperature distribution are quite similar to those in Fig. 42(c). However, the interface shape is slightly changed due to a change in temperature distribution on the side wall. These results confirm that gas convection plays an important role in high-pressure crystal growth, and the side wall boundary condition has an important influence on the crystal–melt interface shape and its dynamics.

Figure 43 (color section) shows the effect of crystal size for $Gr_m = Gr_g = 10^7$ and $Re_c = -Re_s = 10^3$. The side wall is insulated and the top wall is cold. Figure 43(a) shows the flow field and temperature distribution when the crystal is short. The level of the melt is highest at this time. There is one large cell under the free surface due to buoyancy and one small cell underneath the crystal due to the combined effects of natural convection and rotation. The temperature distribution is again distorted. Figure 44 shows the nondimensional heat flux (heat gain on the crucible wall) for a short period of time for Fig. 43(a). The crystal length remains almost unchanged for this short time period. The oscillations seem periodic, with at least two frequencies and small amplitudes.

As the crystal is grown, the level of the melt drops. The two-cell structure of the melt flow gradually changes to a three-cell structure. The temperature distribution also changes with respect to the flow field. The temperature on the top surface of the crystal decreases from Fig. 43(a) to

43(f) due to an increase in the view factor. The crystal–melt interface changes gradually from a convex to a concave shape. The overall flow and temperature fields in the gas region change a little. The gas flows downward on the seed and the crystal, and after gaining heat from the encapsulant surface, moves up along the side wall. When the crystal is short, the gas flow does not create a cell directly on the surface of the encapsulant, and the cells are slender and extend to the top of the domain. In general, the crystal size has a complex effect on gas and melt flow fields and on the crystal–melt interface.

The effect of gas convection on temperature and stress fields in the growing crystal is significant. The velocity vector and the temperature and stress distributions for a simplified high-pressure growth simulation with a 5-in.-diameter crucible and 1.667-in.-diameter crystal are presented in Figs. 45 and 46 (color section) for two different gas-flow conditions, $Gr_g = 10^7$ and 10^8. For the cases presented here, the other governing parameters are $Gr_l = 10^6$, $Re_c = 10^2$, and $Re_s = -10^2$.

An increase in the Grashof number from 10^7 to 10^8 for the gas changes the gas flow pattern substantially. At $Gr = 10^7$, three recirculating cells are predicted in the gas region and the flow is moderate. Of these three cells, one is located directly between the crucible wall and the crystal; the other two are tall slender cells located between the seed rod and the outer boundary. When the gas Grashof number is increased to 10^8, only two recirculating cells are found, and the flow field is much stronger. The two slender cells merge to form one convective roll. In Figs. 45 and 46, the roll between the crucible wall and the crystal is very strong and has a large impact on the heat loss or gain from the crystal. Since the crucible wall is heated, this cell brings energy from the crucible wall and dissipates it in the upper portion of the crystal, thereby heating its upper part. On the contrary, as it moves down it encounters a higher temperature at the crystal surface (see isotherms in Figs. 45 and 46) and, hence, gains energy in the lower portion. Cooling of the crystal above the encapsulant layer causes a strong temperature decrease in the crystal and produces large stresses in this region. Evidently, this complex behavior of heating and cooling complicates the stress phenomena in the crystal.

Previous models using an average heat transfer coefficient have assumed that the effect of gas flow on the crystal surface is to produce a cooling effect. Obviously, these results do not support this assumption, but suggest that both heating and cooling may be produced in different regions of the crystal surface. Although the location and strength of the bottom cell in the gas region may differ with the governing parameters and the crucible height beyond the melt level, the effect of this "roll" will remain the same and needs to be investigated in much more detail.

C. Stress in High-Pressure Liquid-Encapsulated Czochralski Grown Crystals

From Figs. 45 and 46, it is evident that the gas flow modifies the temperature distribution in the crystal and hence, the stress distribution in the crystal. It also can be seen that the change in gas flow significantly affects the melt–crystal interface profile. This influence is indirect and can be attributed to the flow and heat transfer interactions at the encapsulant–gas and crystal–gas interfaces [107, 108]. The change of the stress pattern in the high-pressure case is much more obvious than that in the low-pressure growth. Large stresses appear in a region close to the B_2O_3–gas. The maximum stress in this region changes from 15.05 to 23.4 MPa with an increase in the gas flow strength. A detailed discussion on stresses in high pressure grown crystals was presented recently by Zou et al. [183, 184].

D. Effect of a Magnetic Field

Zhang and Prasad [60] have investigated the effect of an applied magnetic field on growth conditions that are also influenced by gas convection. They considered the growth of GaAs under 1 atm pressure with $Gr_m = 10^7$, $Pr_m = 0.068$, $Gr_g = 10^7$, $Pr_g = 0.7$, and $P_g = 0.1$ MPa (Fig. 47). It is evident from Fig. 47(a) that even though the gas pressure is only 0.1 MPa, it significantly affects the thermal characteristics of the melt. The melt flow is oscillatory with a larger scale variation in heat flux (Fig. 48). The effect of an applied magnetic field (Ha = 200) for the case considered in Fig. 47(a) is presented in Fig. 47(b). The temperature field
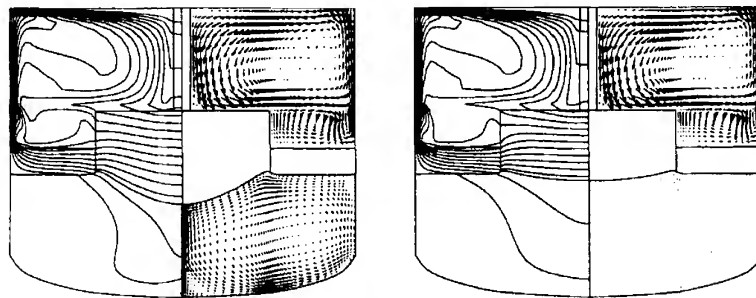
Fig. 47. Flow and temperature fields for the melt and crystal for the growth of (a) without and (b) with an applied magnetic field, for $Gr_m = 10^7$, $Pr_m = 0.068$, $Gr_g = 10^7$, and $Pr_g = 0.7$ [60].

has changed and shows less skewness. The flow in the melt is much weaker than that without a magnetic field. Convection in the gas remains unchanged. The magnetic field has reduced the steepness of the temperature gradient at the interface and in the meniscus region and the interface is much less convex. Figure 48 shows that the melt flow and temperature are still oscillatory. The amplitude of oscillations is small, however, and growth conditions have been greatly improved by the application of this magnetic field.

VI. Concluding Remarks

Transport phenomena in crystal growth processes are quite complex due to melt and gas flows that may be oscillatory, or turbulent, or both; coupled convection and radiation; impurities and dopant distributions; unsteady kinetics of the growth process; melt–crystal interface dynamics; free surface and meniscus; stoichiometry in the case of compound materials, and so on. The multiplicity of governing parameters, complex geometric configurations, complicated boundary conditions, and many times lack of information on the thermophysical properties and boundary conditions make this process very difficult to understand, predict, and control. Because the defects, dislocations, and dopant and impurity distributions in the grown crystals are directly related to transport phenomena in the Cz systems, extensive experimental and theoretical research has been per-
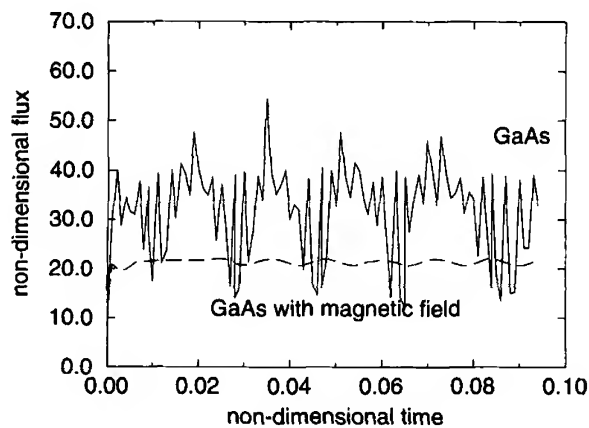
Fig. 48. Oscillations in heat flux for a gallium arsenide (GaAs) crystal growth at 1 atm (with and without a magnetic field) [60].

formed on this topic, particularly in the area of Si crystal growth. With a better understanding of Cz growth, it has been possible to significantly increase the size and quality of grown Si crystals. This has now resulted in a melt size where the flow is considered to be turbulent. The effect of flow turbulence on the melt–crystal interface dynamics, macro- and micro-segregation, and crystal microstructure, however, is not clear. The suitability of conventional turbulence models, such as the k-ε model, for phase-change processes in a rotating system is also questionable.

Our understanding of radiation heat transfer in a Cz and LEC system is also limited. Crystals of optical materials are known to have special radiation characteristics at different wavelengths and can participate in radiation exchange within the growth furnace. Even materials such as Si and Ge, can behave differently at different temperatures. Significant research efforts are needed to understand and predict spectral volumetric radiation in a Cz system. Although extensive research has been performed to examine the 3D behavior of Cz melts, not much is known about its effect on crystal–melt interface shape and dynamics, macro- and micro-segregation, and thermal stresses.

LEC growth of III-V compounds is further complicated by melt stoichiometry, the presence of an encapsulant layer, and large-scale variation in thermal conditions within and outside the encapsulant. (The crystal experiences a thermal shock when it comes out of the encapsulant layer.) The process is further complicated if a high-pressure gas environment is needed to maintain equilibrium vapor pressure at the melting point of the compound. Thermal interaction between the gas, melt, and crystal is then highly complex. Research on transport phenomena in a high-pressure crystal growth system has just been initiated. Modeling of HPLEC growth is a challenging task, particularly if the model must incorporate coupled melt and gas convection; radiation through the encapsulant, and other components of the system; solute distribution in the melt; solidification at the crystal–melt interface; and thermal stresses in the grown crystal. Simulation experiments on high-pressure growth is another area of challenge. Establishing a correlation between the defects, dislocations, and microstructure of the crystal, and the transport phenomena in a growth furnace remains a formidable task.

Acknowledgments

Nomenclature

Ar	aspect ratio, melt height-to-crucible radius, h/b	V_p	pulling velocity, m/sec
$\mathbf{B}$	magnetic field strength	W	weight function for grid concentration
$\mathbf{T}$	total exchange factor matrix	Γ	diffusion coefficient
Bi_r	radiation Biot number, $\varepsilon_{\text{eff}}\,\sigma_r(T_{\text{surf}}^2 + T_x^2)$ $\times(T_{\text{surf}} + T_x)b/k$	a	crystal radius, m
		b	crucible radius, m
		e_x	unit vector in the x-direction
Bo	Bond number, $\rho g b^2/\sigma$	h	surface axial distance, m
C	concentration		melt height, m
C_p	specific heat, J/kgK	h_{sl}	latent heat of fusion, J/kg
D	diffusion coefficient, m²/s	g	acceleration due to gravity, m²/sec
E	current field strength, T·m/sec	j	current density, A
F	force, N/m³	k	thermal conductivity, W/(mK)
	view factor		kinetic energy for k − ε model
Fr	Froude number, v_o^2/gb^3		segregation coefficient
G	weight function of grid orthogonality	$\mathbf{n}$	unit normal vector
		n	normal direction
Gr	Grahsof number, $g\beta b^3(T_h - T_f)/v_o^2$	n_f	refractive index
		p	pressure, Pa
H_1	melt−crystal interface height, H_1^*/b	q''	heat flux, W/m²
		q'''	volumetric heat source, W/m³
H_2	melt−encapsulant interface height, H_2^*/b	r	radial distance, m
		t	time, sec
H_3	encapsulant−ambient gas interface height, H_3^*/b	u	velocity in axial direction, m/sec
		v	velocity in radial direction, m/sec
Ha	Hartmann number, $Bb(\sigma/\rho v)^{1/2}$	w	velocity in swirl direction, m/sec
Ja	Jacobian of transformation, $x_\xi y_\eta - x_\eta y_\xi$	u_g, v_g	grid covariant velocity components, m/sec
M	grid inertial coefficient		
Ma	Marangoni number, $(d\sigma/dT)(T_h - T_f)b/v_o\alpha_o$		
Pr	Prandtl number, v_o/α_o	**GREEK LETTERS**	
Ra	Rayleigh number, $g\beta b^3(T_h - T_f)/v_o\alpha_o$	Ω	swirl, rw, m²/sec
		ω	rotation rate, 1/sec
Re	Reynolds number, $\omega b^2/v_o$	Ψ	electric current streamfunction
Rr	radius ratio, a/b	α	thermal diffusivity, m²/sec
S	source term	β	thermal expansion coefficient, 1/K
Sc	Schmidt number, v_o/D_o	δ	boundary layer thickness, m
Ste_l	liquid Stefan number, $C_{pl}(T_h - T_f)/h_{sl}$	λ	positive coefficient
		ξ, η	axes of curvilinear coordinates
Ste_s	solid Stefan number, $C_{ps}(T_x - T_f)/h_{sl}$	τ	unit tangential direction
		ρ	density, kg/m³
T	temperature, K	ϕ	general variable

ε	emissivity	eff	effective
	dissipation rate for $k - \varepsilon$ model	f	freezing temperature
ε	strain matrix	g	gas
μ	viscosity, kg/msec	h	crucible temperature
μ_e	magnetic permeability, $T \cdot m/A$	i	phase index
ν	kinematic viscosity, m^2/sec	int	interface
σ	Stefan-Boltzman constant,	j	surface
	$W/(m^2 K^4)$	l	melt
	surface tension	m	inertia
	electrical conductivity, $A/V \cdot m$		magnetic
σ	stress tensor	o	reference
Θ	dimensionless temperature,	r	radiation
	$(T - T_f)/(T_h - T_f)$	s	crystal
θ	angular direction	w	weight
Φ	generalized coordinate	ξ, η, ζ	curvilinear coordinates
K	dimensionless thermal conductivity	∞	infinity
		turb	turbulent

SUBSCRIPTS

P	node P
c	crucible
e	encapsulant

SUPERSCRIPTS

$-$	dimensionless properties

References

1. Czochralski, J. (1918). Ein neues verfahren zue messung der kristallisation-geschwindigkeit der metalle. Z. Phys. Chem. **92**, 219–221.
2. Shimura, F. (1989). Semiconductor Silicon Crystal Technology. Academic Press, Orlando, FL.
3. Hurle, D. T. J., and Cockayne, B. (1994). Czochralski growth. In Handbook of Crystal Growth (D. T. J. Hurle, ed.), Vol. **2a**, pp. 99–211. North-Holland, New York.
4. Langlois, W. E. (1981). Convection in Czochralski growth melts. PCH, PhysicoChem. Hydrodyn. **2**, 245–261.
5. Brown R. A. (1986). Interactions between convection, segregation and interface morphology. In Advanced Crystal Growth, (P. M. Dryburgh, B. Cockayne, K. G. Barraclough, eds.) pp. 3–94. Prentice-Hall, Englewood Cliffs, NJ.
6. Müller, G. (1988). Convection and inhomogeneities in crystal growth from melt. In Crystals, (H. C. Freyhardt, ed.) Vol. **12**, Springer-Verlag, Berlin.
7. Dupret, F., and van den Bogaert, N. (1994). Modelling Bridgman and Czochralski growth. In Handbook of Crystal Growth (D. T. J. Hurle, ed.), Vol. **2b**. pp. 875–1010, North-Holland, New York.
8. Prasad, V., and Zhang, H. (1995). Challenging issued in bulk crystal growth modeling. Cryst. Growth Novel Electron. Mater. Cer. Trans. **60**, 3–36.
9. Teal, G. K., and Little, J. B. (1950). The growth of germanium single crystals. Phys. Rev. **78**, 647.
10. Teal, G. K., and Buehler, E. (1952). The growth of germanium single crystals and of single silicon p-n junctions. Phys. Rev. **87**, 190.

11. Kobayashi, N. (1978). Computational simulation of the melt flow during Czochralski growth. *J. Cryst. Growth* **43**, 357–363.

12. Jones, A. D. W. (1983). An experimental model of the flow in Czorhralski growth. *J. Cryst. Growth* **61**, 235–244.

13. Chaney, R. E., and Varker, C. J. (1976). The dissolution of fused silica in molten silicon. *J. Cryst. Growth* **33**, 188–190.

14. Kaiser, W. K., and Kech, P. H. (1957). Oxygen content of silicon single crystals. *J. Appl. Phys.* **28**, 882–887.

15. Cizsek, T. F. (1981). Growth, properties and applications. In *Crystals* (J. G. Grabmaier, ed.), Vol. 5, Springer-Verlag, New York.

16. Ristorcelli, J. R., and Lumley, J. L. (1992). Instabilities, transition, and turbulence in the Czochralski crystal melt. *J. Cryst. Growth* **116**, 447–460.

17. Maiman, T. H. (1960). Simulated optical radiation in ruby. *Nature (London)* **187**, 493–494.

18. Johnson, L. F., Boyd, G. D., Nassau, K., and Soden, R. R. (1962). Continuous operation of a solid-state optical laser. *Phys. Rev.* **126**, 1406–1409.

19. Pressley, R. J. (1971). *Handbook of Lasers with selected data on optical technology*. Chem. Rubber Publ. Co., Cleveland, OH.

20. Cockayne, B. (1977), The melt growth of oxide and related single crystals, *J. Cryst. Growth*, **42**, 413–426.

21. Greiling, P. T. (1993). InP-based microelectronics pilot line for commercial and military applications. *Proc. 5th Int. Conf. InP Relat. Mater.*, pp. 3–6, IEEE, New York.

22. Bliss, D. F., Hilton, R. M., and Adamski, J. A. (1993). MLEK crystal growth of large diameter (100) indium phosphide. *J. Cryst. Growth* **128**, 451–456.

23. Müller, G., Hofmann, D., and Schäfer, N. (1993). Perspectives of the VGF growth processes for preparation of low-defect InP substrate crystals. *Proc 5th Int. Conf. InP Relat. Mater.*, pp. 60–65, IEEE, New York.

24. Kohiro, K., Ohta, M., and Oda, O. (1996). Growth of long-length 3 inch diameter Fe-doped InP single crystals. *J. Cryst. Growth* **158**, 197–204.

25. Akai, S. I., Fujita, K., Yokogawa, M., Marioka, M., and Matsumoto, K. (1989). *Bulk Crystal Growth Technology*. Gordon & Breach, New York.

26. Prasad, V., Bliss, D. F., and Adamski, J. A. (1994). Thermal characterization of the high pressure crystal growth system for in-situ synthesis and growth of InP crystals. *J. Cryst. Growth* **142**, 21–30.

27. Zhang, H., and Prasad, V. (1995). A multizone adaptive process model for low and high pressure crystal growth. *J. Cryst. Growth* **155**, 47–65.

28. Zhang, H., Prasad, V., and Bliss, D. F. (1996). Transport phenomena in high pressure crystal growth systems for III-V compounds. *J. Cryst. Growth* **169**, 250–260.

29. Nunes, E. M., Naraghi, M. H. N., Zhang, H., and Prasad, V. (1996). Combined radiative-convection modeling for materials processes: Application to crystal growth. *Proc. 31st Natl. Heat Transfer Conf.*, Houston, TX, ASME HTD-Vol. 323, 27–37, New York.

30. Anselmo, A. P., Prasad, V., Koziol, J., and Gupta, K. P. (1993). Numerical and experimental study of a solid pellet feed continuous Czochralski growth process for silicon single crystals. *J. Cryst. Growth* **131**, 247–264.

31. Jones, W. P., and Launder, B. E. (1972). The prediction of laminarization with a two-equation model of turbulence. *Int. J. Heat Mass Transfer* **15**, 301–314.

32. Speziale, C. G. (1991). Analytic methods for the development of Reynolds-stress closures in turbulence. *Annu. Rev. Fluid Mech.* **23**, 107–157.

33. Kobayashi, S., Miyahara, S. Fujiwara, T., Kubo, T., and Fujiwara, H. (1991). Turbulence heat transfer through the melt in silicon Czochralski growth. *J. Cryst. Growth* **109**, 149–154.

34. Kinney, T. A., Bornside, D. E., and Brown, R. A. (1993). Quantitative assessment of an integrated hydrodynamic thermal-capillary model for large-diameter Czochralski growth of silicon: Comparison of predicted temperature field with experiment. *J. Cryst. Growth* **126**, 413–434.

35. Kinney, T. A., and Brown, R. A. (1993). Application of turbulence modeling to the integrated hydrodynamic thermal-capillary model of Czochralski crystal growth of silicon. *J. Cryst. Growth* **132**, 551–574.

36. Zhang, T., Ladeinde, F., Zhang, H., and Prasad, V. (1996). A comparison of turbulence models for natural convection in enclosures: Applications to crystal growth processes. *Proc. 31st Natl. Heat Transfer Conf.*, Houston, TX, ASME HTD-Vol. 323, pp. 17–26, New York.

37. Hurle, D. T. J., Jakeman, E., and Pike, E. R. (1969). Striated solute distributions produced by temperature oscillations during crystal growth from the melt. *J. Cryst. Growth* **3**, 633–640.

38. Kobayashi, N. (1991). Oxygen transport under an axial magnetic field in Czochralski silicon growth. *J. Cryst. Growth* **108**, 240–246.

39. Yen, C. T., and Tiller, W. A. (1992). Oxygen partitioning analysis during Czochralski silicon crystal growth via a dopant marker and a simple transfer function modeling technique. II. Growth velocity and applied magnetic field transients. *J. Cryst. Growth* **118**, 85–92.

40. Hurle, D. T. J. (1993). *Crystal Pulling from Melt.* Springer-Verlag, Berlin.

41. Hurle, D. T. J. (1983). Convective transport in melt growth systems. *J. Cryst. Growth* **65**, 124–132.

42. Burton, J. A., Prim, P. C., and Slichter, W. P. (1953). The distribution of solute in crystals grown from the melt. Part I. Theoretical. *J. Chem. Phys.* **21**(11), 1987–1991.

43. Burton, J. A., Kolb, E. D., Slichter, W. P., and Struthers, J. O. (1953). Distribution of solute in crystals grown from the melt. Part II. Experimental. *J. Chem. Phys.* **21**(11), 1991–1996.

44. Wilson, L. O. (1978). A new look at Burton, Prim and Slichter model of segregation during crystal growth from the melt. *J. Cryst. Growth* **44**, 371–376.

45. Wilson, L. O. (1980). The effect of fluctuating growth rates on segregation in crystals grown from the melt. *J. Cryst. Growth* **48**, 435–450.

46. Pfann, W. G. (1966). *Zone Melting.* Wiley, New York.

47. Müller, G., and Ostrogorsky, A. (1994). Convection in melt growth. In *Handbook of Crystal Growth* (D. T. J. Hurle, ed.), Vol. **2b**. 709–819 North-Holland, New York.

48. Favier, J. J., and Wilson, L. O. (1982). A test of the boundary layer model in unsteady Czochralski growth. *J. Cryst. Growth* **58**, 103.

49. Garandet, J. P., Favier, J. J., and Camel, D. (1994). Segregation phenomena in crystal growth from the melt. In *Handbook of Crystal Growth* (D. T. J. Hurle, ed.), Vol. **2b**. 659–707 North-Holland, New York.

50. Riley, N. (1989). Species transport in magnetic field Czochralski growth. *J. Cryst. Growth* **97**, 76–84.

51. Langlois, W. E., Kim, K. M., and Walker, J. S. (1993). Hydro-magnetic flows and effects on Czochralski silicon crystals. *J. Cryst. Growth* **126**, 352–372.

52. Ono, N., Kida, M., Arai, Y., and Sahira, K. (1994). A numerical study on oxygen transport in silicon melt in a double-crucible method. *J. Cryst. Growth* **137**, 427–434.

53. Oreper, G. M., and Szekely, J. (1984). The effect of a magnetic field on transport phenomena in a Bridgman-stockbarger crystal growth. *J. Cryst. Growth* **67**, 405–419.

54. Hjellming, L. N., and Walker, J. S. (1987). Melt motion in a Czochralski crystal puller with an axial magnetic field: Motion due to buoyancy and thermocapillarity. *J. Fluid Mech.* **182**, 335–368.

55. Series, R. W., and Hurle, D. T. J. (1991). The use of magnetic fields in semiconductor crystal growth. *J. Cryst. Growth* **113**, 305–328.

56. Cartwright, R., Ilegbusi, O. J., and Szekely, J. (1989). A comparison of order-of-magnitude and numerical analysis of flow phenomena in Czochralski and magnetic Czochralski systems. *J. Cryst. Growth* **94**, 321–333.

57. Alboussiere, T., Garandet, J. P., and Moreau, R. (1993). Buoyancy-driven convection with a uniform magnetic field. Part 1. Asymptotic analysis. *J. Fluid Mech.* **253**, 545–563.

58. Baumgartl, J., Hubert, A., and Müller, G. (1993). The use of magnetohydrodynamic effects to investigate fluid flow in electrically conducting melt. *Phys. Fluids A* **5**, 3280–3289.

59. Prescott, P. J., and Incorpera, F. P. (1994). Convection transport phenomena and macro-segregation during solidification of a binary metal alloy. I. Numerical predictions. *J. Heat Transfer* **116**, 735–741.

60. Zhang, H., and Prasad, V. (1995). Transport Phenomena of Czochralski crystal growth in low and high pressure. *Proc. ISHMT-ASME Heat Mass Transfer Conf., 2nd* Surathkal, Mangalore, India, pp. 409–415. Tata-McGraw Hill, Bombay.

61. Zhang, H., and Prasad, V. (1996). Effect of an applied magnetic field on buoyancy-driven flows in an enclosure. *Proc. 31st Natl. Heat Transfer Conf.*, Houston, TX, ASME HTD-Vol. 324, 193–201, New York.

62. Ozoe, H., and Okada, K. (1989). The effect of the direction of the external magnetic field on the three-dimensional natural convection in a cubical enclosure. *Int. J. Heat Mass Transfer* **32**(10), 1939–1954.

63. Ozoe, H., and Iwamoto, M. (1994). Combined effects of crucible rotation and horizontal magnetic field on dopant concentration in a Czochralski melt. *J. Cryst. Growth* **142**, 236–244.

64. van der Eerden, J. P. (1994). Crystal growth mechanisms. In *Handbook of Crystal Growth* (D. T. J. Hurle, ed.), Vol. 1a. pp 307–475. North-Holland, New York.

65. Chan, S. H., Cho, D. H., and Kocamustafaogullari, G. (1983). Melting and solidification with internal radiative transfer—a generalized phase change model. *Int. J. Heat Mass Transfer* **26**(4), 621–633.

66. Zhang, H., and Moallemi, M. K. (1995). Numerical simulation of hot-dip metallic coating process. *Int. J. Heat Mass Transfer* **38**(2), 241–257.

67. Zhang, H., Prasad, V., and Moallemi, M. K. (1995). A solution adaptive scheme for deformable free surface flow and heat transfer problems. *Natl. Heat Transfer Conf.*, Portland, OR, ASME HTD-Vol. 311, pp. 119–127.

68. Zhang, H., and Prasad, V. (1995). Multizone adaptive simulations for high pressure crystal growth. *ASME/JSME Therm. Eng. J. Conf.*, Maui, Hawaii, pp. 559–568.

69. Chan, Y. T., Gibeling, H. J., and Grubin, H. L. (1988). Numerical simulation of the Czochralski growth. *J. Appl. Phys.* **64**, 1425–1439.

70. Kopetsch, H. (1989). Numerical simulation of the Czochralski bulk flow of silicon on a domain confined by a moving crystal melt interface and curved melt-gas meniscus. *PCH, PhysicoChem. Hydrodyn.* **11**(3), 357–375.

71. Brown, R. A. (1988). Theory of transport processes in single crystal growth from the melt. *AIChE J.* **43**(6), 881–911.

72. Shapiro, A. B. (1983). FACET, A radiation view factor computer code for axisymmetric, 2D planar and 3D geometries with shadowing. *Lawrence Livermore Lab.* [*Rep.*] *UCID* **UCID-19887**.

73. Atherton, L. J., Derby, J. J., and Brown R. A. (1987). Radiative heat exchange in Czochralski crystal growth. *J. Cryst. Growth* **84**, 57–78.

74. Dupret, F., Necodeme, P., Ryckmans, Y., Wouters, P., and Crochet, M. J. (1990). Global modeling of heat and mass transfer in crystal growth furnaces. *Int. J. Heat Mass Transfer* **33**(9), 1849–1871.

75. Xiao, Q., and Derby, J. J. (1994). Heat Transfer and interface inversion during the Czochralski growth of yttrium aluminum garnet and gandolinium gallium garnet. *J. Cryst. Growth* **139**, 147–157.

76. Hottel, H. C., and Sarofim, A. F. (1967). *Radiative Heat Transfer.* McGraw-Hill, New York.

77. Siegel, R., and Howell, J. R. (1992). *Thermal Radiation Heat Transfer.* Hemisphere, Washington, DC.

78. Modest, M. F. (1993). *Radiative Heat Transfer.* McGraw-Hill, New York.

79. Ramachandran, P. A., and Dudukovič, M. P. (1985). Simulation of temperature distribution in crystals grown by Czochralski method. *J. Cryst. Growth* **71**, 399–408.

80. Motakef, S., and Witt, A. F. (1987). Thermoelastic analysis of GaAs in LEC growth configuration. *J. Cryst. Growth* **80**, 37–50.

81. Naraghi, M. H. N., Chung, B. T. F., and Litkouhi, B. (1988). A continuous exchange factor method for radiative exchange in enclosures with participating media. *J. Heat Transfer* **110**(2), 456–462.

82. Naraghi, M. H. N., and Kassemi, M. (1989). Radiative transfer in rectangular enclosures: A discretized exchange factor solution. *J. Heat Transfer* **111**(4), 1117–1119.

83. Saltiel, C., and Naraghi, M. H. N. (1993). A parallel processing approach for radiative heat transfer prediction in participating media. *J. Thermophys. Heat Transfer* **7**(4), 739–742.

84. Modest, M. F. (1988). Radiative shape factors between differential ring elements on concentric axisymmetric bodies. *J. Thermophys. Heat Transfer* **2**(1), 86–88.

85. Naraghi, M. H. N., and Chung, B. T. F. (1984). A stochastic approach for analysis of radiative heat transfer in enclosures with non-participating media. *J. Heat Transfer* **106**, 690–698.

86. Kimura, S., Sasaki, H., and Terashima, K. (1995). Properties of Si melt near melting point. *Cryst. Growth Novel Electron. Mater., Ceram. Trans.* **60**, 69–82.

87. Glasov, V. M., Chizhevskaya, S. N., and Glagoleva, N. N. (1969). *Liquid Semiconductors.* Plenum, New York.

88. Smithells, C. J. (1983). *Smithells Metals Reference Book*, 6th ed. Butterworth, London.

89. Chang, C. J., and Brown, R. A. (1983). Radial segregation induced by natural convection and melt/solid interface shape in vertical Bridgman growth. *J. Cryst. Growth* **63**, 343–364.

90. Derby, J. J., and Brown, R. A. (1986). Thermal-capillary analysis of Czochralski and liquid encapsulated Czochralski crystal growth I. Simulation. *J. Cryst. Growth* **74**, 605–624.

91. Derby, J. J., Atherton, L. J., and Gresho, P. M. (1989). An integrated process model for the growth of oxide crystals by the Czochralski method. *J. Cryst. Growth* **97**, 792–826.

92. Brown, R. A., Kinney, T. A., Sackinger, P. A., and Bornside, D. E. (1989). Towards an integrated analysis of Czochralski growth. *J. Cryst. Growth* **97**, 99–115.

93. Crowley, A. B., Stern, E. J., and Hurle, D. T. J. (1989). Finite element simulation of Czochralski bulk flow. *J. Cryst. Growth* **97**, 697–719.

94. Sackinger, P. A. (1989). Flows and transitions during solidification: (1) Mode expansion calculations of Rayleigh-Bernard convection in a cylinder: (II) Simulation of hydrodynamics, heat transfer, and free boundaries in Czochralski growth. Ph.D. Thesis, MIT, Cambridge, MA.

95. Koai, K., Seidl, A., Leister, H.-J., Müller, G., and Kohler, A. (1994). Modeling of thermal fluid flow in the liquid encapsulated Czochralski process and comparison with experiments. J. Cryst. Growth 137, 41-47.

96. Baumgartl, J., Bune, A., Koai, K., and Müller, G. (1993). Global simulation of heat transport, including melt convection in a Czochralski crystal growth process-combined finite element/finite volume approach. Mater. Sci. Eng. A 173, 9-13.

97. Moallemi, M. K., and Zhang, H. (1993). Surface tension effects on solidification of thin films via dip coating process. J. Mater. Proc. Manuf. Sci. 2, 233-243.

98. Zhang, H., and Moallemi, M. K. (1995). A multizone adaptive grid generation technique for simulation of moving and free boundary problems. Numer. Heat Transfer, Part B 27, 255-276.

99. Zhang, H., Prasad, V., and Moallemi, M. K. (1996). A numerical algorithm using multizone grid generation for multiphase transport processes with moving and free boundaries. Numer. Heat Transfer, Part B 29, 399-421.

100. Sabhapathy, P., and Salcudean, M. E. (1990). Numerical study of flow and heat transfer in LEC growth in GaAs with an axial magnetic field. J. Cryst. Growth 104, 371-388.

101. Ono, N., Kida, M., Arai, Y., and Sahira, K. (1993). Thermal-analysis of the double-crucible method in continuous silicon Czochralski processing. 2. Numerical analysis. J. Electrochem. Soc. 140, 2106-2111.

102. Gottfried, B. S., and Weisman, J. (1973). Introduction to Optimization Theory. Prentice-Hall, Englewood Cliffs, NJ.

103. Patankar, S. V. (1980). Numerical Heat Transfer and Fluid Flow. McGraw-Hill, New York.

104. Chui, W. K., Climm, J., Tangerman, F. M., and Zhang, H. (1996). Parallel algorithm for simulation of crystal growth processes. Presented at SIAM Ann. Meet., Kansas City, MO.

105. Xiao, Q., and Derby, J. J. (1995). Three-dimensional melt flows in Czochralski oxide growth: High-resolution, massively parallel, finite element computation. J. Cryst. Growth 152, 169-181.

106. Fox, G. C., Johnson, M. A., Lyzenga, G., Otto, S. W., Salmon, J., and Walker, D. (1988). Solving Problems on Concurrent Processors, Vol. 1. Prentice-Hall, Englewood Cliffs, NJ.

107. Zou, Y. F., Zhang, H., and Prasad, V. (1995). Coupled melt flow and stress predictions for Czochralski crystal growth processes. Natl. Heat Transfer Conf., Portland, OR, HTD, Vol. 302, pp. 121-130.

108. Zou, Y. F., Zhang, H., and Prasad, V. (1996). Dynamics of melt-crystal interface and thermal stresses in Czochralski crystal growth processes. J. Cryst. Growth 166, 476-482.

109. Jordan, A. S., Caruso, R., and von Neida, A. R. (1980). A thermoelastic analysis of dislocation generation in pulled GaAs crystals. Bell Syst. Tech. J. 59, 593-637.

110. Jordan, A. S., von Neida, A. R., and Caruso, R. (1981). A comparative study of thermal stress induced dislocation in pulled GaAs, InP, and Si crystals. J. Appl. Phys. 52(5), 3331-3336.

111. Kelly, K. W., Koai, K., and Motakef, S. (1991). Model-based control of thermal stresses during LEC growth of GaAs I. Validation of thermal model. J. Cryst. Growth 113, 254-264.

112. Kelly, K. W., Koai, K., and Motakef, S. (1991). Model-based control of thermal stresses during LEC growth of GaAs II: Crystal growth experiment. J. Cryst. Growth 113, 265-278.

113. Kinney, T. A., and Brown, R. A. (1994). Application of turbulence modeling to the integrated hydrodynamic thermal-capillary model of Czochralski crystal growth of silicon. *J. Cryst. Growth* **142**, 551–574.

114. Bornside, D. E., Kinney, T. A., and Brown, R. A. (1991). Minimization of thermoelastic stresses in Czochralski grown silicon: Application of the integrated system model. *J. Cryst. Growth* **108**, 779–805.

115. Imaishi, N., Tsukada, T., Hozawa, M., Okano, Y., and Hirata, A. (1992). Numerical study of the Czochralski growth of oxide single crystal. In *Heat and Mass Transfer in Material Processing* (I. Tanasawa and N. Lior, eds.), pp. 123–136. Hemisphere, Washington, DC.

116. Völkl, J., and Müller, G. (1989). A new model for the calculation of dislocation formation in semiconductor melt growth by taking into account the dynamics of plastic deformation. *J. Cryst. Growth* **97**, 136–145.

117. Völkl, J. (1994). Stress in the cooling crystal. In *Handbook of Crystal Growth* (D. T. J. Hurle, ed.), Vol. 2b. pp 821–874. North-Holland, New York.

118. Alexander, H., and Haasen, P. (1968). Dislocations in the diamond structure. *Solid State Phys.* **22**, 28.

119. Maroudas, D., and Brown, R. A. (1991). On the prediction of dislocation formation in semiconductor crystals grown from the melt: Analysis of Haasen model for plastic deformation dynamics. *J. Cryst. Growth* **108**, 399–415.

120. Motakef, S. (1989). Thermoelastic analysis of GaAs in LEC growth configuration. *J. Cryst. Growth* **96**, 201–216.

121. Motakef, S., Kelly, K. W., and Koai, K. (1991). Comparison of calculated and measured dislocation density in LEC-grown GaAs crystals. *J. Cryst. Growth* **113**, 279–288.

122. Völkl, V., Müller, G., and Blum, W. (1987). Analysis of generation and movement of dislocations in InP by a study of the deformation behavior. *J. Cryst. Growth* **83**, 383–390.

123. Ishida, M., Katano, K., Kawarata, S., Higuchi, Y., Orito, F., Yamaguchi, Y., Yajima, F., and Okano, T. (1990). Total simulation model of high pressure liquid encapsulated Czochralski crystal growth. *J. Cryst. Growth* **99**, 707–712.

124. Busse, F. H. (1985). Transition to turbulence in Rayleigh-Bénard convection. *Top. Appl. Phys.* **45**, 95–137.

125. Gebhart, B., Jaluria, Y., Mahajan, R. L., and Sammanka, B. (1988). *Buoyancy-Induced Flows and Transport.* Hemisphere, Washington, DC.

126. Krishnamurthi, R. (1984). Some further studies on the transition to turbulent convection. *J. Fluid Mech.* **60**, 285–303.

127. Bejan, A. (1984). *Convection Heat Transfer.* Wiley, New York.

128. Jones, A. D. W. (1988). Scaling analysis of the flow of low Prandtl number Czochralski melt. *J. Cryst. Growth* **88**, 465–476.

129. Balasubramaniam, R., and Ostrach, S. (1984). Fluid motion in the Czochralski method of crystal growth. *PCH, PhysicoChem. Hydrodyn.* **5**, 3–8.

130. Bird, R. B., Stewart, W. E., and Lightfoot, E. N. (1982). *Transport Phenomena.* Wiley, New York.

131. Rosenberger, F., and Müller, G. (1983). Interfacial transport in crystal growth, a parametric comparison of convective effects. *J. Cryst. Growth* **65**, 91–104.

132. Wilkinson, S. P., and Malik, M. R. (1985). Stability experiments in the flow over a rotating disk. *AIAA J.* **23**, 588–595.

133. Birikh, R. V. (1966). Thermocapillary convection in a horizontal layer of liquid. *J. Appl. Mech. Tech. Phys.* **7**, 43–44.

134. Carruthers, J. R., and Nassau, K. (1986). Nonmixing cells due to crucible rotation during Czochralski crystal growth. *J. Appl. Phys.* **39**, 5205–5214.

135. Carruthers, J. R. (1976). Flow transitions and interface shapes in the Czochralski growth of oxide crystals. *J. Cryst. Growth* **36**, 212–214.

136. Kobayashi, N. (1981). Hydrodynamics in Czochralski growth. *J. Cryst. Growth* **52**, 425–434.

137. Chan, Y. T., Gibeling, H. J., Liu, N.-S., and Grubin, H. L. (1987). Three-dimensional numerical studies of the physics of semi-conductor crystal growth. *Tech. Rep., Off. Nav. Res.* AD-A176 808, Rep. R-920018-F.

138. Chandrasekhar, S. (1961). *Hydrodynamics and Hydro-magnetic Stability.* Oxford University Press, England.

139. Langlois, W. E. (1982). A parameter sensitivity study for Czochralski bulk flow of silicon. *J. Cryst. Growth* **56** 15–19.

140. Crochet, M. J., Wouters, P. J., Geyling, F. R., and Jordan, A. S. (1983). Finite-element simulation of Czochralski bulk flow. *J. Cryst. Growth* **65**, 153–165.

141. Anselmo, A. P., Prasad, V., Koziol, J., and Gupta, K. P. (1993). Oscillatory convection in low aspect ratio Czochralski melts. *J. Cryst. Growth* **134**, 116–139.

142. Langlois, W. E., Hjellming, L. N., and Walker, J. S. (1987). Effects of the finite electrical conductivity of the crystal on hydro-magnetic Czochralski flow. *J. Cryst. Growth* **83**, 51–61.

143. Bottaro, A., and Zebib, A. (1988). Bifurcation in axisymmetric Czochralski natural convection. *Phys. Fluids* **31**(3), 495–501.

144. Bottaro, A., and Zebib, A. (1989). Three-dimensional three convection in Czochralski melt. *J. Cryst. Growth* **97**, 50–58.

145. Anselmo, A. P. (1994). Solid-pellets feed continuous Czochralski growth of silicon single crystal. Ph.D. Dissertation, Columbia University, New York.

146. Feigl, G. (1983). Recent advances and future directions in Cz silicon crystal growth technology. *Solid State Technol.* 121–131.

147. Araki, T., and Matsuura, A. (1991). Heat and fluid analysis on the growth of larger diameter silicon single-crystal. *ASME/JSME Therm. Eng. Proc.* **1**, 413–418.

148. Virzi, A. (1991). Computer modeling of heat transfer in Czochralski silicon. *J. Cryst. Growth* **112**, 699–722.

149. Müller, G., Völkl, J., Tomzig, E. (1983). Thermal analysis of LEC InP growth. *J. Cryst. Growth* **64**, 40–47.

150. Seidl, A., McCord, G., Müller, G., and Leister, H.-J. (1994). Experimental observation and numerical simulations of wave patterns in a Czochralski silicon melt. *J. Cryst. Growth* **137**, 326–334.

151. Mihelčić, M., and Wingerath, K. (1989). Instability of the buoyancy driven convection in si melts during Czochralski crystal growth. *J. Cryst. Growth* **97**, 42–49.

152. Mukherjee, D. K., Prasad, V., Dutta, P., and Yuan, T. (1996). Liquid crystal visualization of the effects of crucible and crystal rotation on Cz melt flows. *J. Cryst. Growth* **169**, 136–146.

153. Mihelčić, M., and Wingerath, K. (1985). Numerical simulations of the Czochralski bulk flow in an axial magnetic field: Effects on the flow and temperature oscillations in the melt. *J. Cryst. Growth* **71**, 163–168.

154. Salnik, Z. A. (1992). Oxygen in Czochralski silicon crystals grown under an axial magnetic field. *J. Cryst. Growth* **121**, 775–780.

155. Oshima, M., Taniguchi, N., and Kobayashi, T. (1994). Numerical investigation of three-dimensional melt convection with the magnetic Czochralski method. *J. Cryst. Growth* **137**, 48–53.

156. Hurle, D. T. J., and Series, R. W. (1994). Use of a magnetic field in melt growth. In *Handbook of Crystal Growth* (D. T. J. Hurle, ed.), Vol. **2a**. 99–211 North-Holland, New York.

157. Kakimoto, K., Eguchi, M., Watanabe, H., and Hibiya, T. (1990). Flow instability of molten silicon in the Czochralski configuration. *J. Cryst. Growth* **102**, 16–20.

158. Munakata, T., and Tanasawa, I. (1990). Onset of oscillatory flow in a Czochralski growth melt and its suppression by magnetic field. *J. Cryst. Growth* **106**, 566–576.

159. Shiroki, K. (1977). Simulations of Czochralski growth on crystal rotation influence in fixed crucibles. *J. Cryst. Growth* **40**, 129–138.

160. Miller, D. C., and Pernell, T. L. (1982). Fluid flow patterns in a simulated garnet melt. *J. Cryst. Growth* **57**, 253–260.

161. Lamphrecht, R., Schwabe, D., Scharmann, A., and Schultheiss, E. (1983). Experiments on buoyant, thermocapillary, and forced convection in Czochralski configuration. *J. Cryst. Growth* **65**, 143–152.

162. Ruiz, X., Massons, J., Diaz, F., and Aguilo, M. (1986). Image processing of Czochralski bulk flow. *J. Cryst. Growth* **79**, 92–95.

163. Kakimoto, K., Eguchi, M., Watanabe, H., and Hibiya, T. (1989). Natural and forced convection of molten silicon during Czochralski single crystal growth. *J. Cryst. Growth* **94**, 412–420.

164. Kakomoto, K., Watanabe, M., Eguchi, M., and Hibiya, T. (1994). Flow instability of the melt during Czochralski Si crystal growth: Dependence on growth conditions; a numerical simulation study. *J. Cryst. Growth* **139**, 197–205.

165. Ozoe, H., Toh, K., and Inoue, T. (1991). Transition mechanism of flow modes in Czochralski convection. *J. Cryst. Growth* **110**, 472–480.

166. Hirata, A., and Tachibana, M. (1993). Observation of crystal-melt interface shape in simulated Czochralski method with model fluid. *J. Cryst. Growth* **128**, 195–200.

167. Jahne, B. (1993). *Digital Image Processing.* Springer-Verlag, New York.

168. Mukherjee, D. K. (1995). Use of an intensified charge-coupled device (ICCD) camera for UV Ramam imaging of turbulent flames. MS. Thesis, Vanderbilt University, Nashville, TN.

169. Wilcox, W. R., and Fullmer, L. D. (1965). Turbulent free convection in Czochralski crystal growth. *J. Appl. Phys.* **36**, 2201–2206.

170. Kim, K. M., Witt, A. F., and Gatos, H. C. (1972). Crystal growth from the melt under destabilizing thermal gradients. *J. Electrochem. Soc.* **119**, 1218–1226.

171. Kolker, H. (1980). The behavior of nonrotational striations in Silicon. *J. Cryst. Growth* **50**, 852–858.

172. Kakimoto, K., Nicodeme, P., Lecomte, M., Dupret, F., and Crochet, M. J. (1991). Numerical simulation of molten silicon flow; comparison with experiment. *J. Cryst. Growth* **114**, 715–725.

173. Dupret, F., Necodeme, P., and Ryckmans, Y. (1989). Numerical method for reducing stress level in GaAs crystals. *J. Cryst. Growth* **97**, 162–172.

174. van den Bogaert, N., (1993). Simulation dynamique de la Croissance dans un four Czochralski: Modèle global de calcul des èchanges thermiques et de la forme du cristal sur une géométrievariable, PhD Dissertation, Université Catholique de Louvain, Louvain-la-Neuve, Belgium.

175. Maruyama, S., and Aihara, T. (1994). Radiation heat transfer of a Czochralski growth furnace with arbitrary specular and diffuse surfaces. *Int. J. Heat Mass Transfer* **37**, 1723–1731.

176. Anselmo, A. P., Koziol, J., and Prasad, V. (1996). Full-scale experiments on solid-pellets feed continuous Czochralski growth of silicon crystals. *J. Cryst. Growth* **163**, 359–368.

177. Jafri, I. H., Prasad, V., and Anselmo, A. P. (1995). Role of crucible partition in improving Czochralski melt conditions. *J. Cryst. Growth* **154**, 280–292.

178. Kraus, A. D., and Bar-Cohen, A. (1983). *Thermal Analysis and Control of Electronic Equipment*, Hemisphere, Washington, DC.

179. Jordan, A. S. (1985). Estimated thermal diffusivity, Prandtl number and Grashof number of molten GaAs, InP, and GaSb. *J. Cryst. Growth* **71**, 551–558.

180. Jordan, A. S. (1985). Some thermal and mechanical properties of InP essential to crystal growth modeling. *J. Cryst. Growth* **71**, 559–565.

181. Jordan, A. S., Monberg, E. M., and Clemans, J. E. (1993). Thermal stress theory of dislocation reduction in the vertical gradient freeze (VGF) growth of GaAs and InP. *J. Cryst. Growth* **128**, 444–450.

182. Zhang, H., Prasad, V., Anselmo, A., Bliss, D. F., and Iseler, G. (1996). Transport phenomena in a high pressure crystal growth system: In-situ synthesis for InP melt. *J. Cryst. Growth* (in press).

183. Zou, Y. F. (1997). Coupled convection, segregation, and thermal stress modeling of low and high pressure czochralski crystal growth, Doctoral Dissertation, State University of New York at Stony Brook.

184. Zou, Y. F., Wang, G.-X., Zhang, H., and Prasad, V. (1997). Macrosegregation, dynamics of interface and stresses in high pressure LEC grown crystals. *J. Cryst. Growth* (in press).

INDEX